

10



ДЕСЯТЫЙ
МОСКОВСКИЙ
МЕЖДУНАРОДНЫЙ
СИМПОЗИУМ
ПО ИССЛЕДОВАНИЯМ
СОЛНЕЧНОЙ СИСТЕМЫ

7-11 ОКТЯБРЯ 2019
ИНСТИТУТ
КОСМИЧЕСКИХ
ИССЛЕДОВАНИЙ
МОСКВА

THE TENTH
MOSCOW
SOLAR SYSTEM
SYMPOSIUM

7-11 OCTOBER 2019
SPACE RESEARCH
INSTITUTE
MOSCOW



overview 10M-S³ program

THE TENTH MOSCOW SOLAR SYSTEM SYMPOSIUM (10M-S³)

IKI RAS, 7-11 October 2019

	7 October	8 October	9 October	10 October	11 October				
10.00	OPENING SESSION	session 2. VENUS	session 4. MOON AND MERCURY	session 5. GIANT PLANETS	session 7. SOLAR WIND				
10.20									
10.40									
11.00									
11.20									
11.40	coffee	coffee	coffee	coffee	coffee				
12.00	session 1. MARS	session 3. EXTRASOLAR PLANETS	session 6. SMALL BODIES	session 8. ASTROBIOLOGY	session 8. ASTROBIOLOGY				
12.20									
12.40									
13.00						lunch	lunch	lunch	lunch
14.00									
14.20	coffee	coffee	coffee	coffee	coffee				
14.40									
15.00									
15.20									
15.40									
16.00	POSTER SESSION WELCOME PARTY	SOCIAL EVENTS IN MOSCOW	POSTER SESSION	CONCERT	SOCIAL EVENTS IN MOSCOW				
16.20									
16.40									
17.00									
17.20									
17.40	SOCIAL EVENTS IN MOSCOW	SOCIAL EVENTS IN MOSCOW	SOCIAL EVENTS IN MOSCOW	RECEPTION	SOCIAL EVENTS IN MOSCOW				
18.00									
18.20									
18.40									
19.00									
20.00									

10M-S³ SCIENTIFIC PROGRAM

Monday, 7 October 2019

Lev ZELENYI	Opening Remarks	10.00-10.10
James W. HEAD	The Apollo lunar exploration program: scientific legacy and the road ahead	10.10-11.00

session 1. MARS 11.00-19.00

convener: Oleg KORABLEV

conference hall, second floor

10MS3-MS-01	Alexander TROKHIMOVSKIY et al	Methane and other trace species detection attempts using ACS MIR channel onboard TGO ExoMars mission	11.00-11.20
10MS3-MS-02	Anatoliy PAVLOV et al	A novel mechanism for rapid methane destruction by cosmic rays on Mars	11.20-11.40

coffee-break 11.40-12.00

10MS3-MS-03	Anna FEDOROVA et al	The O ₂ vertical profiles in the Martian atmosphere with ACS-NIR onboard TGO	12.00-12.20
10MS3-MS-04	Mikhail LUGININ et al	Dust and water ice aerosols during the first year of ACS TIRVIM and NIR observations	12.20-12.40
10MS3-MS-05	Dmitrij TITOV et al	Mars Express recent science highlights	12.40-13.00

lunch 13.00-14.00

10MS3-MS-06	Alexey MALAKHOV et al	FREND onboard ExoMars: global near-surface water abundance and local features	14.00-14.20
10MS3-MS-07	Sergei NIKIFOROV et al	Analysis of the water distribution in Martian subsurface estimated by passive measurements with the DAN instrument onboard NASA/MSL	14.20-14.40
10MS3-MS-08	Maya DJACHKOVA et al	Subsurface water content in Gale crater from DAN measurements and its correlation with mineral abundance on the surface	14.40-15.00
10MS3-MS-09	James W. HEAD	Toward an understanding of early Mars climate history: new themes, directions and tests	15.00-15.20
10MS3-MS-10	Ashley PALUMBO et al	Volcanism on early Mars: Exploring the influence of the SO ₂ plume on local and short-term climate change	15.20-15.40

10MS3-MS-11	Mikhail IVANOV and H. HIESINGER	The Acidalia Mensa region on Mars: A key element to test the Mars ocean hypothesis	15.40-16.00
coffee-break			16.00-16.20
10MS3-MS-12	Boris IVANOV	Air shock wave traces on Mars	16.20-16.40
10MS3-MS-13	Vladimir OGIBALOV and G. SHVED	Effect of aerosol scattering on radiative transfer in the CO ₂ and CO infrared bands in the daytime Martian atmosphere under breakdown of vibrational LTE	16.40-17.00
10MS3-MS-14	Maria PILAR VELASCO et al	The Martian atmospheric dust dynamic through fractional differential models and simulations	17.00-17.20
10MS3-MS-15	Thomas DUXBURY and Natalia SEREGINA	Looking Back at Mars 50 years: Mariner Mars 1969 imaging	17.20-17.40
10MS3-MS-16	Mikhail VERIGIN et al	Measurements of the Martian crust magnetization 25 years before its discovery	17.40-18.00
10MS3-MS-17	Marina DÍAZ MICHELENA and C. R. KILIAN	Magnetic measurements in terrestrial analogues of Mars	18.00-18.20
10MS3-MS-18	Marina DÍAZ MICHELENA et al	Newton novel magnetic instrument. Potential application to unveil key questions as the origin of Martian moons	18.20-18.40
10MS3-MS-19	Jose Luis VAZQUEZ-POLETTI et al	Serverless Computing for Mars Exploration and Colonization Applications	18.40-19.00
POSTER SESSION (all sessions)			19.00-20.00

Tuesday, 8 October 2019

session 2. VENUS

10.00-16.00

convener: Ludmila ZASOVA

conference hall, second floor

10MS3-VN-01	Vladimir A. KRASNOPOLSKY	Venus Nighttime Photochemical Model: Night-glow of O ₂ , NO, OH and Abundances of O ₃ and ClO	10.00-10.20
10MS3-VN-02	Peter WURZ et al	Measurement of the composition of Venus atmosphere during aerobreaking	10.20-10.40
10MS3-VN-03	Helmut LAMMER et al	Atmospheric noble gas isotope and bulk K/U ratios as a constraint on the early evolution of Venus and Earth	10.40-11.00
10MS3-VN-04	Maike BAUER et al	Implications of hydrodynamic escape for the Venusian water inventory, constrained by D/H	11.00-11.20
10MS3-VN-05	Richard ERNST et al	Geological tests of global warming models on Venus	11.20-11.40
coffee-break			11.40-12.00
10MS3-VN-06	Leonid KSAFOMALITY	Bright flashes of lightning on Venus were recorded in infrared images of the Akatsuki mission	12.00-12.20
10MS3-VN-07	Dmitry GORINOV et al	Circulation of the lower cloud level on the nightside of Venus from VIRTIS-M (Venus Express) and IR2 (Akatsuki) data in 1.74 μm	12.20-12.40
10MS3-VN-08	Vladimir GUBENKO and I. KIRILLOVICH	Internal waves characteristics in the Venus's atmosphere revealed from the Magellan and Venus Express radio occultation data by two independent methods	12.40-13.00
lunch			13.00-14.00
10MS3-VN-09	Richard GHAIL et al	EnVision: European concept of a mission to Venus	14.00-14.20
10MS3-VN-10	Patricia BEAUCHAMP et al	Proposed Venus Flagship Mission	14.20-14.40
10MS3-VN-11	Ludmila ZASOVA and the JSDT	Venera-D: a potential joint Roscosmos – NASA mission to explore Venus' atmosphere, surface, interior structure and plasma environment	14.40-15.00
10MS3-VN-12	Vladimir GROMOV and Alexander KOSOV	A model of microwave absorption of atmospheric gases for the radiometric experiment in the Venera-D mission	15.00-15.20

10MS3- VN -13	Valentin PARMON et al	Hypothetical living forms on Venus planet and their possible nature	15.20-15.40
10MS3- VN -14	Anastasia KOSENKOVA et al	Maneuverable Entry Vehicles for Venus research	15.40-16.00
coffee-break			16.00-16.20
session 3. EXTRASOLAR PLANETS convener: Alexander TAVROV conference hall, second floor			16:20-18:45
10MS3-EP-01	Daniel ANGERHAUSEN et al	The LIFE mission: a Large Interferometer for Exoplanets	16.20-16.40
10MS3-EP-02	Shingo KAMEDA et al	WSO-UV/UVSPEX for observation of Earth-like Exoplanets	16.40-16.55
10MS3-EP-03	Andreas KRENN et al	Energy-limited escape: an examination of the range of applicability	16.55-17.10
10MS3-EP-04	Valery SHEMATOVICH et al	Atmospheric escape of close-in Neptunes	17.10-17.25
10MS3-EP-05	Ildar SHAIKHISLAMOV et al	3d gasdynamic modeling of transitioning hot exoplanets	17.25-17.40
10MS3-EP-06	Daria KUBYSHKINA et al	The past rotation history of Kepler-11 revealed by the present atmospheres of its planets	17.40-17.55
10MS3-EP-07	Vladislava ANANYEVA et al	Mass distribution of exoplanets considering observation selection effects in the transit detection technique	17.55-18.10
10MS3-EP-08	Vladislava ANANYEVA et al	Mass distribution of transit planets depending on the host star spectral class (considered: K, G, F)	18.10-18.20
10MS3-EP-09	Anastasia IVANOVA et al	RV-exoplanets mass distribution at M-dwarf-type host stars	18.20-18.30
10MS3-EP-10	Leonid KSAFOMALITY and Alexander TAVROV	On a possible role of giant exo-rings of the j1407b type in physical properties of the KEPLER KIC 8462852 object	18.30-18.45

Wednesday, 9 October 2019

session 4. MOON AND MERCURY

10.00-18.00

conveners: Igor MITROFANOV,
Maxim LITVAK

conference hall, second floor

10MS3-MN-01	Johannes BENKHOFF et al	BepiColombo en route to Mercury	10.00-10.20
10MS3-MN-02	Alexande KOZYREV et al.	MGNS: first data en route to Mercury	10.20-10.40
10MS3-MN-03	Evgeny SLYUTA	Geology, geochemistry and geophysics of the Moon: from priority scientific tasks to scientific equipment	10.40-11.00
10MS3-MN-04	James W. HEAD and Lionel WILSON	Rethinking lunar mare basalt regolith formation: new concepts of lava flow protolith and evolution of regolith thickness and internal structure	11.00-11.20
10MS3-MN-05	Jinsong PING et al	Low frequency radio astronomical experi- ments on the Moon	11.20-11.40
coffee-break			11.40-12.00
10MS3-MN-06	Mikhail GERASIMOV et al	Morphologies of impact-simulated condensates	12.00-12.20
10MS3-MN-07	Elliot SEFTON-NASH et al	Targeting lunar volatiles with ESA's PROSPECT payload on LUNA-27	12.20-12.40
10MS3-MN-08	Rahul SHARMA et al	Lunar lava tubes represent vast poten- tial	12.40-13.00
lunch			13.00-14.00
10MS3-MN-09	Sergey VOROPAEV and A.Yu. DNESTROVSKY	Features of the fossil tidal bulge formation for the early Moon	14.00-14.20
10MS3-MN-10	Wang MINGYUAN et al	Prospect of planetary radio emission based on low frequency de- tection of Chang'E-4	14.20-14.40
10MS3-MN-11	Susanne SCHRODER et al	LIBS for in-situ geo- chemical investigations of extraterrestrial sur- faces of atmosphere- less bodies	14.40-15.00
10MS3-MN-12	Egor SOROKIN et al	Experimental simulating of a micrometeorite impact on the Moon	15.00-15.20

10MS3-MN-13	Svetlana DEMIDOVA	Distribution of P-bearing olivines sources in the lunar crust	15.20-15.40
10MS3-MN-14	James W. HEAD and Lionel WILSON	Dike intrusion-related processes in the lunar crust: the role of country rock porosity/permeability in magmatic percolation and thermal annealing, and implications for gravity signatures	15.40-16.00
coffee-break			16.00-16.20
10MS3-MN-15	Alexander BASILEVSKY et al	Potential lunar base on Mons Malapert: Topographic, geologic and trafficability consideration	16.20-16.40
10MS3-MN-16	Zhanna RODIONOVA et al	Topographical Features of the Lunar Maria and Basins	16.40-17.00
10MS3-MN-17	Maya DJACHKOVA et al	Landing site selection for future lunar landers	17.00-17.20
10MS3-MN-18	Maxim LITVAK et al	The nearest perspectives for Lunokhod 2.0	17.20-17.40
10MS3-MN-19	Igor MITROFANOV et al	The concept of LUNA-28 mission for polar soil return	17.40-18.00
POSTER SESSION (all sessions)			18.00-19.00

Thursday, 10 october 2019

session 5 . GIANT PLANETS

10.00-13.10

convener: Scott BOLTON

conference hall, second floor

10MS3-GP-01	Scott BOLTON et al	Result from Juno on the Origin of Jupiter	10.00-10.15
10MS3-GP-02	John CONNERNEY et al	Jupiter's Magnetic Field and Magnetosphere at the Midpoint of the Juno Mission	10.15-10.30
10MS3-GP-03	Alberto ADRIANI et al	Infrared observations of the Jupiter's atmosphere	10.30-10.45
10MS3-GP-04	Masafumi IMAI et al	Observations of radio and plasma waves at Jupiter from Juno Waves investigation	10:45-11:00
10MS3-GP-05	Alessandro MURA et al	Observations of Jupiter Aurorae from Juno	11.00-11.15
10MS3-GP-06	Vladimir KRASNOPOLSKY	Photochemical Model of Pluto's Atmosphere and Ionosphere	11.15-11.30
10MS3-GP-07	John JOERGENSEN et al	Jovian Moon interaction with energetic electrons as measured by the Juno ASC	11.30-11.45

coffee-break

11.45-12.00

10MS3-GP-08	Erica NATHAN et al	Experimental and Numerical Model for Freezing Icy Satellites	12.00-12.15
10MS3-GP-09	Manuel SCHERF et al	The origin and evolution of Titan's nitrogen atmosphere	12.15-12.30
10MS3-GP-10	Igor ALEXEEV et al	Diagnostics of the Jovian magnetospheric state during the Juno mission	12.30-12.40
10MS3-GP-11	Alexander PERMINOV and Eduard KUZNETSOV	The resonant semi-analytical motion theory for giant planets of the Solar system	12.40-12.50
10MS3-GP-12	Valery KOTOV	Rotation of giant planets	12.50-13.00
10MS3-GP-13	Michel BLANC et al	Science objectives and mission scenarios for future missions to the Jupiter system	13.00-13.10

lunch

13.10-14.00

session 6. SMALL BODIES

(including cosmic dust)

convener: Alexander BASILEVSKY,
Alexander ZAKHAROV

conference hall, second floor

14.00-18.00

10MS3-SB-01	Thomas DUXBURY	The International Phobos/Deimos Data Working Group	14.00-14.15
-------------	-----------------------	--	-------------

10MS3-SB-02	Mikhail MAROV and Sergei IPATOV	Migration of planetesimals from different distances outside Mars' orbit to the terrestrial planets and the Moon	14.15-14.30
10MS3-SB-03	Mikhail MAROV et al	Simulations of fragmentation of dust aggregates at the snowline in a protoplanetary disk: first results	14:30-14:45
10MS3- SB-04	Sergei IPATOV	Probabilities of collisions of planetesimals from different parts of the feeding zone of the terrestrial planets with the forming planets, the Moon, and their embryos	14:45-15:00
10MS3- SB-05	Sergey EFIMOV and V. SIDORENKO	Lidov-Kozai cycles in secular dynamics of resonant Kuiper belt objects	15:00-15.15
10MS3- SB-06	Sergey KRASILNIKOV et al	Pinnacles on the surface of the 67P/Churyumov-Gerasimenko comet nucleus	15.15-15:30
10MS3- SB-07	Vladimir BUSAREV and Ekaterina FEOKTISTOVA	Assessment of the possibility of ice presence on 101955 Bennu	15.30-15.45
10MS3- SB-08	Yuri SKOROV	Thermal models of comets. New challenges after the Rosetta mission	15.45-16.00
coffee-break			16:00-16:20
10MS3- SB-09	Sergey VOROPAEV et al	Small bodies' strength: failure model	16.20-16.35
10MS3- SB-10	Ute BOETTGER et al	Raman spectrometer for Phobos in-situ exploration	16.35-16.50
10MS3- SB-11	Ekaterina KOREN and Eduard KUZNETSOV	Features of the Dynamical Evolution of Near-Earth Asteroid Pairs	16.50-17.05
10MS3- SB-12	Eduard KUZNETSOV et al	Search for young asteroid pairs with close orbits	17.05-17.20
10MS3- SB-13	Sergey POPEL et al	Dusty plasmas in environments of Mars	17.20-17.35
10MS3- SB-14	Ilan ROTH	Present solar observations — a catalyst of processes at the birth of solar and death of stellar system	17.35-17.50
	PANEL DISCUSSION		17.50-18.00
	CONCERT		18.00-19.00
	RECEPTION		19.00-20.00

Friday, 11 October 2019

**session 7:
SOLAR WIND INTERACTIONS
WITH PLANETS AND SMALL BODIES**

10.00-12.40

convener: Oleg VAISBERG

room 200, second floor

10MS3-SW-01	Eduard DUBININ et al	What is a main driver for ion losses at Mars and what is a role of the crustal magnetic field?	10.00-10.20
10MS3-SW-02	Lev ZELENYI et al	Thin current sheets of sub-ion scales observed by MAVEN in the Martian magnetotail	10.20-10.40
10MS3-SW-03	Salvador JIMENEZ et al	Induced magnetic field in Mars ionosphere. Solar wind and aurorae	10.40-11.00
10MS3-SW-04	Valery SHEMATOVICH et al	Kinetic Monte Carlo Model of High-Energy H/H+ Precipitation into the Martian Atmosphere	11.00-11.20
10MS3-SW-05	Alexander GRIGORIEV et al	The Fine Structure of the Interface between the Magnetosheath and the Venusian Induced Magnetosphere	11.20-11.40

coffee-break

11.40-12.00

10MS3-SW-06	Andrey DIVIN et al	A Fully Kinetic Study of Electron Acceleration Around a Weak Comet	12.00-12.20
10MS3-SW-07	Vladimir BUSAREV et al	Similarity of sublimation activity of the main-belt primitive asteroids 704 Interamnia, 24 Themis, and 449 Hamburga and solar flares' influence	12.20-12.40

session 8: ASTROBIOLOGY

10.00-17.00

convener: Elena VOROBYOVA,
Oleg KOTSYURBENKO

conference hall, second floor

10MS3-AB-01	Elias CHATZITHEODORIDIS	Biosignature detection with state-of-the-art instrumentation	10.00-10.20
10MS3-AB-02	Sohan JHEETA	Astrochemistry: synthesis of the basic 'building blocks' of life	10.20-10.40
10MS3-AB-03	Vladimir KOMPANICHENKO	Origin of life through the efficient reaction of prebiotic systems to external oscillations: application to Mars, Europa, and Enceladus	10.40-11.00

10MS3-AB-04	Vladimir MATVEEV and A. MALYGIN	Sorption theory of the origin of life	11.00-11.20
10MS3-AB-05	Valeriy SNYTNIKOV	The most likely places to detect traces of extraterrestrial life in the Solar System	11.20-11.40
coffee-break			11.40-12.00
10MS3-AB-06	Martin FERUS	Exoplanets: Natural laboratories of chemical evolution and origin of life	12.00-12.20
10MS3-AB-07	Daniel ANGERHAUSEN et al	Big Data and Machine learning for Exoplanets and Astrobiology: Results from NASA Frontier Development Lab	12.20-12.40
10MS3-AB-08	Valery SHEMATOVICH and M. SACHKOV	Study of exoplanet habitability: potential atmospheric biomarkers O ₂ /O ₃ in ultraviolet	12.40-13.00
lunch			13.00-14.00
10MS3-AB-09	Vinod KUMAR GUPTA	Emergence of photoautotrophic assimilative mechanisms in an irradiated sterilized aqueous mixture of some inorganic and organic substances induced by electromagnetic radiation of Sun	14.00-14.20
10MS3-AB-10	Chandra WICKRAMASINGHE and Richard HOOVER	Comets, carbonaceous chondrites and extraterrestrial life	14.20-14.40
10MS3-AB-11	Sergey BULAT et al	Microbial life under thick glacier sheets: lessons from the subglacial Antarctic Lake Vostok exploration	14.40-15.00
10MS3-AB-12	Richard HOOVER and E.V. PIKUTA	Advances in astrobiology: life in ice	15.00-15.20
10MS3-AB-13	Oleg KOTSYURBENKO	Methanogenic archaea as model microorganisms for astrobiology	15.20-15.40
10MS3-AB-14	Anton RYUMIN and M. KAPRALOV	Astrobiological studies in Dubna	15.40-16.00
coffee-break			16.00-16.20
10MS3-AB-15	Nikita DEMIDOV	Pingos on Spitsbergen and on Mars as astrobiological target	16.20-16.40
	Panel DISCUSSION		16:40-17:00

POSTER SESSION

7 october 19.00-20.00

9 october 18.00-19.00

exhibition hall, ground floor

MARS		
10-MS3-PS-01	Benjamin D. BOATWRIGHT and James W. HEAD	Testing the Effectiveness of Impact Bombardment on Early Mars Landscape Degradation
10-MS3-PS-02	Ashley PALUMBO and James W. HEAD	Rainfall on Noachian Mars: Nature, timing, and influence on geologic processes and climate history
10-MS3-PS-03	Mariya ZHARIKOVA et al	O ₂ nightglow observations in the Martian atmosphere by SPICAM/MEX
10-MS3-PS-04	Natalia SAVELYEVA et al	First measurements of Carbon Monoxide in Martian Atmosphere from ACS-TIRVIM Solar Occultation Observations Onboard ExoMars TGO
10-MS3-PS-05	Ekaterina STARICHENKO et al	Gravity waves in Martian atmosphere from ACS/TGO solar occultations: preliminary results
10-MS3-PS-06	Gennady DOLNIKOV et al	Investigation of the Martian dust dynamics with Dust Complex: Instrument Development and Calibration
10MS3-PS-07	Manuel DOMINGUEZ-PUMAR et al	Performance of a miniature Martian 3d wind sensor in the dust devil scale
10-MS3-PS-08	Yulia IZVEKOVA et al	Hydrodynamic similarity of dust devils on Earth and Mars
10-MS3-PS-09	Victor BENGHIN et al	Comparison of Liulin-MO dosimeter radiation measurements during ExoMars 2016 TGO Mars' a circular orbit with dose estimations based on galactic cosmic ray models
10-MS3-PS-10	Sergei NIKIFOROV et al	The ADRON-RM instrument onboard the ExoMars rover
10-MS3-PS-11	Alexander KOSOV et al	LaRa (Lander Radioscience) on the ExoMars 2020 Kazachok lander
10-MS3-PS-12	Diego RODRÍGUEZ DÍAZ et al	AMR instrument for ExoMars 2020 scientific payload for stationary magnetic measurements on the surface of Mars
10-MS3-PS-13	Imant VINOGRADOV et al	M-DLS experiment for the ExoMars-2020 mission Stationery Landing Platform: instrument design, fabrication and calibration results
10MS3-PS-14	Kirill ZAKHARCHENKO et al	Characterization of space radiation monitor based on diamond sensitive elements for future interplanetary missions
10-MS3-PS-15	Gennady KOCHEMASOV	Warm and wet martian period in comparison with mantle heating in other rocky planets and the Moon
10-MS3-PS-16	Olaga TRETYUKHINA	Multiscale hipsometric web-map of Mars
10-MS3-PS-17	Sergei KULIKOV et al	Possible electromagnetic emissions above the magnetic anomalies: Phobos-2 observations

10MS3-PS-18	Ekaterina GRISHAKINA et al	Physical, mechanical, hydrophysical, and microbiological properties of Martian soil simulant
10MS3-PS-19	Sergey KRASILNIKOV et al	Measuring of volume and thicknesses of remnant massifs of layered deposits on Mars, using altimetry data and math approximation
10MS3-PS-20	Alexandra BERMEJO et al	Controlling electromagnetic waves with all dielectric metamaterials
10MS3-PS-21	Alexey BATOV et al	Estimates of stresses beneath Elysium Planitia on Mars
10MS3-PS-22	Tamara GUDKOVA et al	Estimates of density anomalies beneath Elysium Planitia on Mars
10MS3-PS-23	Inna STEPANOVA et al	Method of S-, and R-approximations in solving the problems of geophysics: application for Mars

VENUS

10MS3-PS-24	Alexey MARTYNOV et al	Development of the Venera-D Spacecraft Design
10MS3-PS-25	Daria EVDOKIMOVA et al	Water vapour distribution in the Venus deep atmosphere by the SPICAV-IR/VEX night observations
10MS3-PS-26	Anatoly GAVRIK	Radio occultation of Venusian ionosphere
10MS3-PS-27	Marina PATSAEVA et al	Dependence of cloud top circulation above Aphrodite Terra on solar-related effects and topography. Variations in the behavior of zonal wind over mission time from VMC/Venus Express wind fields
10MS3-PS-28	Jacob BENHEIM et al	Autonomous aerodynamic repeating diver for Venus atmospheric research of clouds
10MS3-PS-29	Vladimir GUBENKO et al	Activity of small-scale internal waves in the Venus's northern polar atmosphere by using radio occultation measurements of signal intensity ($\lambda = 32$ cm) from the Venera-15 and -16 satellites
10MS3-PS-30	Tamara GUDKOVA and Vladimir ZHARKOV	Corrections to model Love number k_2 due to inelasticity of the interiors of Venus
10MS3-PS-31	Eugenia GUSEVA and Mikhail IVANOV	Topographic configuration of coronae on Venus: supporting evidence for time-dependent styles of resurfacing

MOON AND MERCURY

10MS3-PS-32	James W. HEAD and Boris IVANOV	Ina Irregular Mare Patch (IMP): new insights from observations of superposed impact craters
10MS3-PS-33	James W. HEAD et al	Volcanically-induced transient atmospheres on the Moon: assessment of duration and significance
10MS3-PS-34	Aaron CHERIAN et al	Project Orpheus: lunar laboratory

10MS3-PS-35	Ariel DEUTSCH et al	Investigating diurnal changes in the normal albedo of the lunar surface at 1064 nm: a new analysis with the Lunar Orbiter Laser Altimeter
10MS3-PS-36	Ariel DEUTSCH et al	Distribution of surface water ice on the Moon: an analysis of host crater ages provides insights into the ages and sources of ice at the lunar south pole
10MS3-PS-37	Alexey BEREZHNOY et al	³ He-rich potential landing sites on the Moon
10MS3-PS-38	Sergey KRASILNIKOV et al	Selection of landing site for potential lunar base on Mons Malapert
10MS3-PS-39	Gennady SIZENTSEV et al	Lunar resources to address energy and climate problems on Earth
10MS3-PS-40	Mikhail MALENKOV et al	They are ahead of time: the influence of the Soviet and American lunar rovers on modern planetary research
10MS3-PS-41	Ivan AGAPKIN and Evgeny SLUTA	Problems of studying the physico-mechanical properties of lunar soil in the TERMO-LR experiment for the Luna-Resource-1 project
10MS3-PS-42	Olga TURCHINSKAYA and Evgeny SLUTA	Preliminary data on mapping and outlining of various concentrations of ilmenite in lunar rocks on the visible side of the Moon
10MS3-PS-43	Andrey DIVIN et al	Structure of the electrostatic potential above ion-scale lunar magnetic anomalies
10MS3-PS-44	Alexander BASILEVSKY et al	Rolling boulders and their tracks on lunar slopes
10MS3-PS-45	Ekaterina KRONROD et al	The structure, composition and temperature in the Moon based on the joint inversion of geophysical and geochemical data for a linear temperature profile in the mantle
10MS3-PS-46	Igor ZAVYALOV et al	Implementation of lunar crater catalogue for morphometric studies of the craters (diameter 1-10 km)
10MS3-PS-47	Ekaterina FEOKTISTOVA et al	Thermal regime and regolith parameters of landing site of probe Chang'E
10MS3-PS-48	Svetlana PUGACHEVA et al	Research of the lunar south polar area
10MS3-PS-49	Azariy BARENBAUM	Stratigraphic scale as proof of cyclicity bombardments of solar system by galactic comets
10MS3-PS-50	Azariy BARENBAUM and Michael SHPEKIN	Problems of interpretation crater data in the Solar System
10MS3-PS-51	Nadezhda CHUJKOVA et al	Determination of global density inhomogeneities and stresses inside the Moon
10MS3-PS-52	Maria KOLENKINA et al	Patterns in morphometry of Mercury and the Moon: morphological mapping at the global level

10MS3-PS-53	Maria KOLENKINA et al	Creating a museum collection of archive data of planet research with the help of modern technologies
10MS3-PS-54	Maria KOLENKINA et al	Using relief approximation methods to study the surface of the Moon
10MS3-PS-55	Olaga TRETUKHINA and Evgeny SLYUTA	Interactive globe of the digital elevation model of Moon relief
10MS3-PS-56	Sergey IPATOV	Angular momenta of colliding rarefied condensations and formation of the Earth-Moon system
10MS3-PS-57	Valerii BURMIN and A.G. FATYANOV	The focusing effect of P-wave in the Moon's and Earth's low-velocity core. Analytical solution
10MS3-PS-58	Gennady KOCHEMASOV	Modulated lunar orbiting frequencies and corresponding them structures (Chang'E 3 & 4)
10MS3-PS-59	Rico FAUSCH et al	The neutral gas mass spectrometer for the Luna-Resurs mission
10MS3-PS-60	Veniamin FEDULOV et al	Experimental study of degassing of the early Earth and Moon during accretion
10MS3-PS-61	Vladimir CHEPTSOV et al	Dependence of accuracy of elemental and isotopic composition measurement on the volume of the spectra array for the LASMA-LR instrument onboard Luna-Glob and Luna-Resource missions
10MS3-PS-62	Jianfeng CAO et al	Precise orbit determination of Chang'e 4 lander based on doppler measurement
10MS3-PS-63	Lue CHEN et al	Precise Open-loop Doppler Measurement of Chang'e-4 Probe Based on China's Deep Space Interferometry System

GIANT PLANETS

10MS3-PS-64	Ivan PENSIONEROV et al	Comparison of the Jupiter's current disc model with the magnetic field observations from Juno and Galileo
10MS3-PS-65	Elena BELENKAYA	Jupiter's auroras associated with Galilean moons and the main ovals
10MS3-PS-66	Vladimir VDOVICHENKO et al	Zonal features of the weak ammonia absorption bands behavior on Jupiter
10MS3-PS-67	Anna DUNAEVA et al	Theoretical composition of the Titan's ocean derived from the tidal love numbers
10MS3-PS-68	Victor KRONROD et al	Adjustment of models of the internal structure of Titan with love numbers data
10MS3-PS-69	Gennady KOCHEMASOV	Pluto granules and X-ray emission calculated by modulated orbital frequencies (comparison with Saturn and Jupiter)

10MS3-PS-70 **Gennady KOCHEMASOV** Saturnian hexagon is not alone

SMALL BODIES (including cosmic dust)

10MS3-PS-71 **Maxim ZHELTOBRYUKHOV et al** Polarization of comet 46P/Wirtanen

10MS3-PS-72 **Ekaterina CHORNAYA et al** Fast variations of composition in the 21P/Giacobini-Zinner coma

10MS3-PS-73 **Evgenij ZUBKO et al** Peculiar Polarization of Comet C/2018 V1 (Machholz-Fujikawa-Iwamoto)

10MS3-PS-74 **Timur NOZDRACHEV et al** Small fragments of asteroids and cometary nuclei orbiting Earth: numerical simulation

10MS3-PS-75 **Vladimir BUSAREV and Sergei IPATOV** Estimation of the fraction of ice material delivered to the Main asteroid belt in the early Solar system

10MS3-PS-76 **Arina REZAEVA et al** Modeling of asteroid reflectance with laboratory databases of analog sample

10MS3-PS-77 **Larissa GOLUBEVA and Dmitry SHESTOPALOV** Polarimetric properties of asteroid 3200 Phaethon

10MS3-PS-78 **Aleksei ROSAEV** Numeric modeling of asteroid orbits close to 3:1 resonance

10MS3-PS-79 **Alexander GUSEV et al** Space iron oxide microspheres: origin and typomorphic features

10MS3-PS-80 **Alekander POTOSKUEV et al** The project of multiband photometry of small bodies of the solar system with Robophot

10MS3-PS-81 **Artem KRIVENKO et al** Experimental investigation of mechanical properties of meteorites

10MS3-PS-82 **Nikolay PEROV and V.E. PAKHOMYCHEVA** Interstellar meteoroids sorting in the Solar system

10MS3-PS-83 **Tatiana SALNIKOVA et al** Possible models of the planetary systems formations

10MS3-PS-84 **Markus R EINHARD BENEDIKT et al** Escape of rock-forming volatile elements and noble gases from planetary embryos

10MS3-PS-85 **Gennady KOCHEMASOV** Natural octahedrons of various sizes including hidden ones in Earth and Saturn

10MS3-PS-86 **Elena PETROVA and V.P. TISHKOVETS** Light scattering by discrete random media: pitfalls in the comparison of models and experiments

10MS3-PS-87 **Iliia KUZNETSOV et al** Investigation of the atmosphereless bodies dust dynamics: experimental set-up

10MS3-PS-88 **Yulia IZVEKOVA and Sergey POPEL** Wave effects in dusty plasmas in Martian atmosphere

10MS3-PS-89 **Alexey DEMYANOV and V.V. VYSOCHKIN** Dust Impact Mass-Spectrometer «METEOR-LD»

SOLAR WIND INTERACTIONS WITH PLANETS AND SMALL BODIES

10MS3-PS-90	Sergey KOLOMIETS et al	An experiment and data processing technique aimed at determining the radial speed of solar wind inhomogeneities of various spatial scales
10MS3-PS-91	Georg MINASYAN et al	Methods of Detection of Failures in Phase Data of GNSS and Their Influence on Value of Measurements of the Total Electron Content
10MS3-PS-92	Galina KHACHIKYAN	Observed response of Earth's lithosphere to solar wind and radiation belt variations
10MS3-PS-93	Natalia BULATOVA	Features of the Sun's influence on the Earth lithosphere in periods of minima activity
10MS3-PS-94	Artem SHESTAKOV et al	Complex of low-weight miniature instruments for space weather monitoring
10MS3-PS-95	Oleg KHAVROSHKIN and Vladislav TSYPLAKOV	The observation of the solar flare on the neutrino telescope
10MS3-PS-96	Oleg KHAVROSHKIN and Vladislav TSYPLAKOV	Neutrino Telescope: Problems and Solution
10MS3-PS-97	Ricardo Tomas FERREYRA et al	A new inversion of the Prandtl-Meyer relation

ASTROBIOLOGY

10MS3-PS-99	Richard HOOVER and Alexey ROZANOV	Evidence for indigenous microfossils in carbonaceous chondrites
10MS3-PS-100	Andrey KHARITONOV	The influence of cycles of space weather on geochronology of biological and climatic changes
10MS3-PS-101	Marina RUMENSKIKH et al	3D modeling of transit observations of the hot exoplanets
10MS3-PS-102	Laurenz SPROSS et al	Why Earth-like N ₂ atmospheres are most likely not common on terrestrial planets
10MS3-PS-103	Margarita KRYUCHKOVA et al	How fungal communities of desert soils respond to irradiation by high-energy electrons (HEE)?
10MS3-PS-104	Růžena FERUSOVÁ ŽIVOROVÁ and Martin FERUS	Czech participation on the ARIEL telescope mission - remote sensing of asteroid and cometary impact events
10MS3-PS-105	Vladimir CHEPTSOV et al	Bacteria survival in Europa's surface ice after pulse ejection of subsurface ocean water
10MS3-PS-106	Andrey BELOV et al	Edaphic bacterial communities of the arid Mojave Desert: astrobiological implication
10MS3-PS-107	F. A. I. AZAR and Ilya DIGEL	PARAFAC Algorithm for Resolving Fluorescence Signatures of Life-Specific Compounds

THE APOLLO LUNAR EXPLORATION PROGRAM: SCIENTIFIC LEGACY AND THE ROAD AHEAD

James W. Head, III

*Department of Earth, Environmental and Planetary Sciences,
Brown University, Providence, RI 02912 USA*

Keywords:

Apollo, astronauts, Moon, impact craters, volcanism, planetary formation, evolution, magma ocean, tectonics, volcanism, planetary systems, exoplanets.

Half a century ago, the Apollo lunar exploration missions began the transformation of the Moon, terrestrial planets and outer planet satellites, from objects of astronomical study to objects of geologic exploration and characterization (Figures 1-3). The Apollo missions resolved fundamental questions about the Moon (origin of the Moon and its craters, the age and origin of the maria, the formation of basins; did the Moon form hot or cold?). It also provided a fundamental framework and paradigm for understanding the history and evolution of the terrestrial planets, including Earth [1]. What have we learned about planetary formation and evolution in the ensuing five decades from this Moon-based comparative planetology? Ejecta from a large Mars-sized projectile impacting into early Earth appears to have formed the Moon. Impact cratering plays a fundamental role in initial impact heating and melting to create a molten magma ocean whose thermal and chemical evolution dictates much of subsequent history. Planetary internal heating, melting and extrusion of molten rock (lava) to the surface supplies additional volatiles to the primordial atmospheres and resurfaces significant areas. Earth loses heat through plate tectonics, but smaller bodies lose heat primarily by conduction and rapidly become “one-plate planets”. Planets lose atmospheres as a function of time and Mars is a laboratory for this change, perhaps evolving from warm and wet to today’s sub-freezing desert. The current position of planets relative to their stars is not necessarily where they started out. Abundant planetary environments have the ingredients for life, but life has thus far only been detected on Earth. As usual, astronomers are leading the way to the future, with the discovery of many dozens of exoplanetary systems and thousands of exoplanets. Today astronomers and planetary scientists are teaming up to tackle fundamental questions in comparative planetary systems: How can we use our knowledge about our Solar System and the characteristics and histories of its planets and satellites to interpret the nature of exoplanets? (Figure 4) Where does the Solar System fit in the menagerie of exoplanetary systems? Is our Solar System typical or anomalous?



Fig. 1. Earth-based telescopic view of the Earth’s Moon showing how it was known prior to the Space Age.



Fig. 2. Apollo 11 begins the geological exploration of the Moon and planets, July 20, 1969.

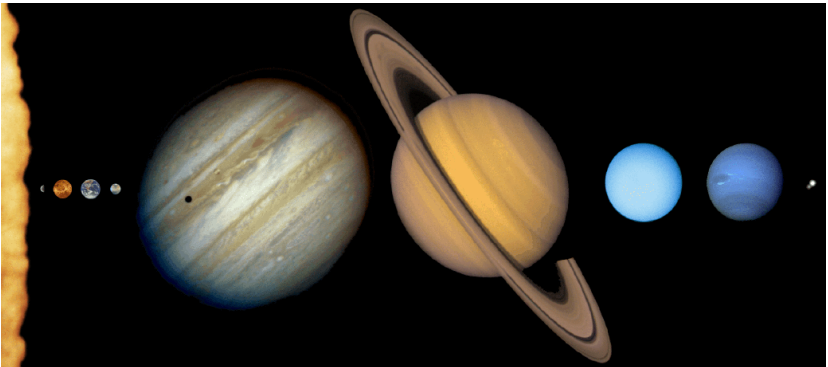


Fig. 3. The Solar System, illustrating the difference between the small, solid terrestrial inner planets, and the outer gas giants. The shadow of one Jovian satellite appears as a black dot on Jupiter.

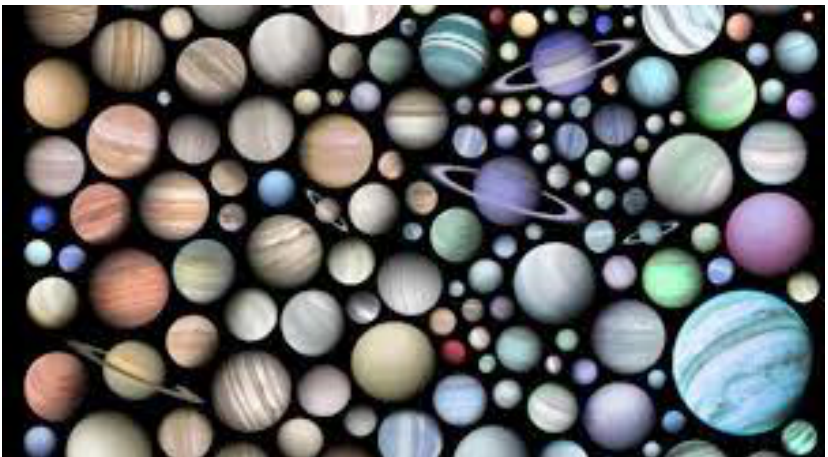


Fig. 4. A small selection of exoplanets known today

References:

- [1] Head, J.W. and Pieters, C.M. (2018) Geological evolution of the terrestrial planets: 60 years of exploration and discovery, in *Sputnik: 60 Years Along the Path of Discoveries*, pp. 209–233, Russian Academy of Sciences, Moscow, Russia.

METHANE AND OTHER TRACE SPECIES DETECTION ATTEMPTS USING ACS MIR CHANNEL ONBOARD TGO EXOMARS MISSION

A. Trokhimovskiy¹, O. Korablev¹, A. Fedorova¹, F. Montmessin²,
K. Olsen², L. Baggio², F. Lefèvre², A. Patrakeev¹, A. Shakun¹

¹ Space Research Institute (IKI) RAS Moscow, Russia, trokh@iki.rssi.ru;

² LATMOS, UVSQ Université Paris-Saclay, Sorbonne Université, CNRS, France

Keywords:

Mars, atmosphere, TGO, ExoMars, methane, trace species, solar occultation.

Introduction:

In this work we present highly sensitive attempts to detect methane and other trace species in the Martian atmosphere by the ACS instrument onboard the ESA-Roscosmos ExoMars Trace Gas Orbiter (TGO) [1]. No methane was detected during the time period of our measurements and over a range of latitudes in both hemispheres. Our upper limit for methane of ~0.05 ppbv is 10-100 times lower than previously reported positive detections [2]. The upper limits for other trace species are also better by at least one and up to several orders of magnitude.

Given its potential implications for exobiology or geochemistry, highly sensitive measurements of atmospheric methane and other trace species were identified as the primary science goal of the TGO mission [3]. The 2-hour circular orbit of the TGO satellite was designed for detecting trace gases using solar occultations, a technique in which the spacecraft instruments observe the atmospheric absorption spectrum of sunlight during sunsets and sunrises [4]. ACS instrument consists of three infrared channels featuring high accuracy, a high resolving power, and broad spectral coverage (0.7 to 17 μm). The mid-infrared (MIR) channel is a high dispersion echelle spectrometer dedicated to solar occultation measurements in the 2.3-4.5 μm range. MIR has been conceived to accomplish the most sensitive measurements of Martian trace gases, while simultaneously profiling more abundant compounds such as CO_2 , H_2O , and their isotopologues. When staring at the solar disk outside the atmosphere, the SNR of the transmittance spectra recorded by ACS MIR channel reaches 10,000. While CH_4 constitutes a central target for the "Breakthrough" science, ACS MIR instrument is used to search and the quantification thereof of the abundance of a suite of companion trace gases: C_2H_2 , C_2H_4 , C_2H_6 , CH_2O , H_2S , H_2O_2 , OCS , N_2O , HCl , HCN and others.

References:

- [1] Korablev O. et al. The Atmospheric Chemistry Suite (ACS) of three spectrometers for the ExoMars 2016 Trace Gas Orbiter. *Space Sci. Rev.* 2018. V. 214:7.
- [2] Korablev O. et al. No detection of methane on Mars from early ExoMars Trace Gas Orbiter observations. *Nature.* 2019. V. 568, P. 517–520.
- [3] Vago J. et al. ESA ExoMars program: The next step in exploring Mars. *Solar System Research.* 2015. V. 49. P. 518–528
- [4] Svedhem H., Vago J.L., Mitschdörfer P., de Groot R., Montagna M., Renaud P.-Y. The ExoMars Trace Gas Orbiter. *Space Sci. Rev.* 2019. 215. In press.

A NOVEL MECHANISM FOR RAPID METHANE DESTRUCTION BY COSMIC RAYS ON MARS

A.K. Pavlov¹, D.A. Tsurkov^{1,2}, A.A. Pavlov³

¹ *Ioffe Physical-Technical Institute, Russian Academy of Sciences, 26 Politekhnicheskaya str., St. Petersburg, 194021, Russia; anatoli.pavlov@mail.ioffe.ru*

² *Peter the Great St. Petersburg State Polytechnic University, 29 Politekhnicheskaya str., St. Petersburg, 195251, Russia;*

³ *Planetary Environments Laboratory, NASA Goddard Space Flight Center, Greenbelt, MD 20771, USA.*

Keywords:

Mars, atmosphere, methane destruction, cosmic rays

Introduction:

Rapid variations of methane abundance in Martian atmosphere is one of the most intriguing problems in Mars exploration. Methane molecules can be produced by a potential martian biosphere. Tunable laser spectrometer on the Curiosity rover detected seasonal variations of methane at sub ppb levels over 5 year period [1]. Such observations are in conflict with the currently accepted photochemical modeling of the Martian atmosphere. According to all published photochemical models the lifetime of CH₄ molecules in the Martian atmosphere should be 300–500 years. Global atmospheric mixing time is about one Martian year. Therefore, additional rapid process of methane destruction is needed to explain global seasonal variations even for local and variable methane sources on Mars [2].

In this work we consider cosmic rays ionization of the Martian atmosphere and subsequent atmospheric ion-molecular reactions as possible process of rapid methane destruction. We demonstrate that the lifetime CH₄ decrease by a factor of 10 and more in comparing to the standard photochemical model (see Fig. 1).

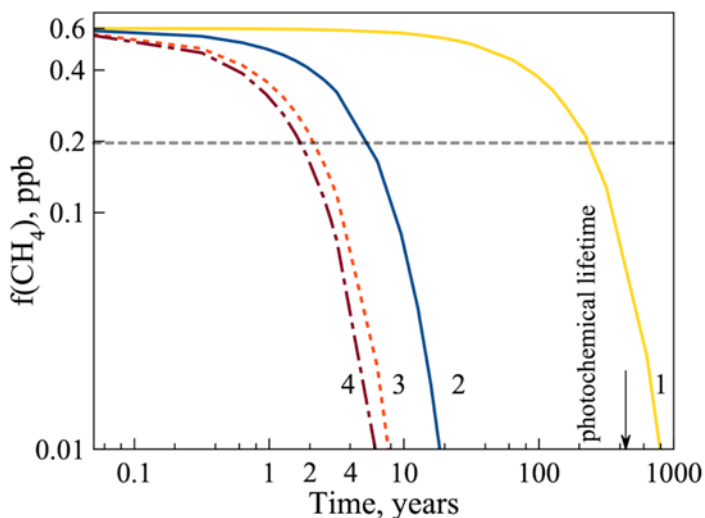


Fig. 1. Atmospheric methane lifetime. Initial methane concentration is 0.6ppb. Curve 1 shows photochemical methane destruction. Curve 2, 3, 4 — ion-molecular methane destruction. Curve 2 — GCR ionization of Molina Cuberos [4]. Curve 3 — GCR ionization with GCR spectra of PAMELA mission 2012 year, Curve 4 — GCR PAMELA 2012 ionization and SCR ionization with spectra index $\gamma=3$ (flux $50 \text{ p}^* \text{cm}^{-2} \text{s}^{-1}$).

We further demonstrate that the global methane loss rate is correlated with seasons due to effective seasonal destruction of methane in the polar regions during winter seasons.

Recently, the observations of ExoMars Trace Gas Orbiter (TGO) discovered very low methane concentration (<50 ppt) in upper atmosphere [3]. It is very unusual result because of the MSL experiments demonstrate variations of methane concentration in range 0.2–0.6 ppb and short time spikes up to several ppb. We simulated a combination of short time emission of subsurface methane and low Eddy diffusion coefficient in framework of our model. This combination can support the observed difference of methane concentration during 600 sols (see Fig. 2).

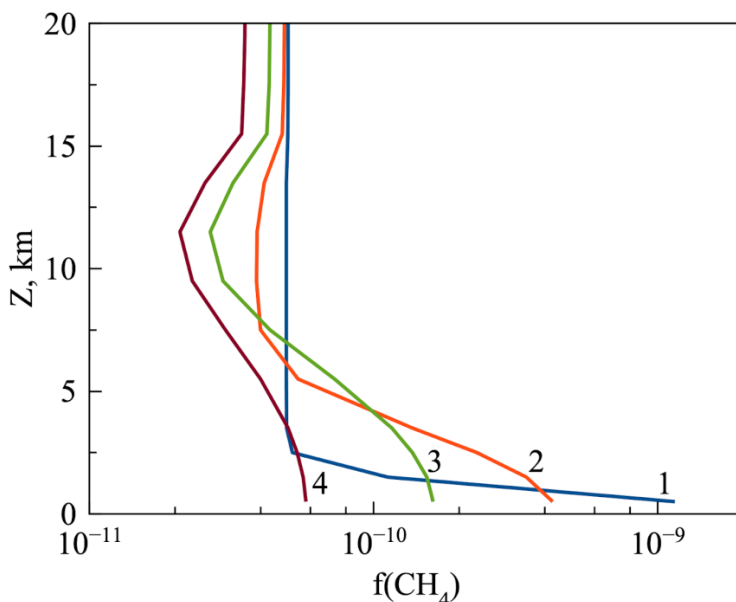


Fig. 2. Evolution of methane profiles after 5-days spike. Curve 1 — is resulting profile of 5 days emission with flux $5 \cdot 10^7$ molecules \cdot cm $^{-2}$ s $^{-1}$. Curve 2 — methane profile after 90 sols; Curve 3 — after 300 sols; Curve 4 — after 600 sols. This profiles was calculated with assumption of eddy diffusion coefficient for mixing of 4km atmospheric layer during 1 martian year ($\sim 2.6 \cdot 10^3$ cm 2 /sec).

References:

- [1] Webster et al 2018, Science 360, 2018. P. 1093–1096
- [2] Giuranna et al., 2019, Nature Geoscience, doi.org/10.1038/s41561-019-0331-9
- [3] Korabiev et al., 2019, Nature, doi.org/10.1038/s41586-019-1096-4
- [4] Molina-Cuberos G.J., Lichtenegger H. and Schwingenschuh K., 2002, JGR, v. 107, NO. E5, 5027, 10.1029/2000JE001447

THE O₂ VERTICAL PROFILES IN THE MARTIAN ATMOSPHERE WITH ACS–NIR ONBOARD TGO

A. Fedorova¹, F. Lefevre², A. Trokhimovsky¹, O. Korablev¹,
F. Montmessin², M. Zharikova^{1,3}, A. Patrakeev¹, J.-L. Bertaux^{2,1}
and the ACS team

¹ Space Research Institute (IKI), Moscow, Russia, fedorova@iki.rssi.ru;

² LATMOS-UVSQ, Guyancourt, France, 3MPII, Dolgoprudnyi, Russia

Keywords:

Mars, atmosphere, spectroscopy, solar occultation, oxygen, CO

Introduction:

The molecular oxygen is the minor constituent of the Martian atmosphere with the mean mixing ratio of $(1.56 \pm 0.06) \cdot 10^{-3}$. As it is a long-lived incondensable species (with the lifetime ~ 60 years) the O₂ mixing ratio should have latitudinal variations induced by condensation and sublimation of CO₂ from the polar caps that result in enrichment and depletion and seasonal variations following the total CO₂ amount in the atmosphere. The O₂ column-averaged mixing ratio was provided by several ground-based observations as well as by Herschel orbiting observatory [1–3]. Now the high precision measurements of the O₂ mean surface mixing ratio were obtained by the quadrupole mass spectrometer as a part of Mars Science Laboratory at the Curiosity rover [4].

Observations:

The Atmospheric Chemistry Suite (ACS) is a set of three spectrometers (-NIR, -MIR, and -TIRVIM) intended to observe Mars atmosphere onboard the ESA-Roscosmos ExoMars 2016 Trace Gas Orbiter (TGO) mission [5]. ACS started a science program on orbit of Mars in Mars 2018. The near infrared channel (NIR) is a compact spectrometer operating in the range of 0.7–1.7 μm with a resolving power of $\lambda/\Delta\lambda \sim 25,000$. It is designed to operate in nadir and in solar occultation modes. In solar occultation mode NIR provides a simultaneous measurement of CO₂ band at 1.56 μm (order 49) to get temperature-pressure profiles (0–110 km), O₂ band at 0.76 μm (order 101) and CO band at 1.56 μm (order 49) for vertical profiling in the low atmosphere (0–60 km). A vertical profiling of the O₂ density is a unique feature of the ACS NIR science in occultation. No other instrument on a Mars orbiting platform being sensitive to O₂ from 10 to 60 km altitude range. The ratio of O₂/CO is also an important indicator of the Martian photochemistry.

Results:

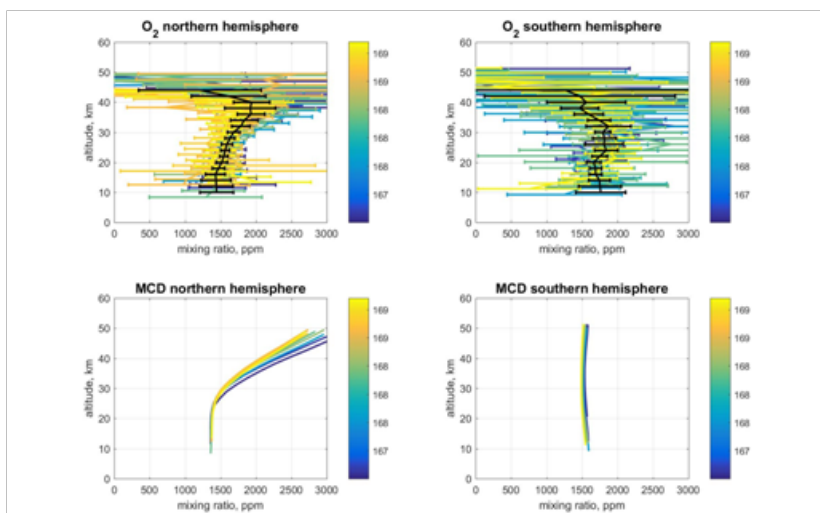


Fig. 1 The O₂ vertical profiles before the MY34 Global Dust storm in the Northern and Southern hemispheres as observed by ACS-NIR and prediction published in MCD 5.3 [6]

The first O₂ profiles were obtained for 36 observations gives a value of : 1582±83 ppm at latitude of 80N and 1756±101 ppm at 44-57S and Ls 167-169 before the dust storm, and 2361±270 ppm at 43-53N and 1877±187 ppm at 80S and Ls 196-198 during the global dust storm.

Here we present the first results of the O₂ density retrievals from the ACS/NIR solar occultations for the first year of observations and a comparison with the LMD General Circulation model.

Acknowledgements:

ExoMars is the space mission of ESA and Roscosmos. The ACS experiment is led by IKI Space Research Institute in Moscow. The project acknowledges funding by Roscosmos and CNES. Science operations of ACS are funded by Roscosmos and ESA. This work has been supported partially by the Ministry of Education and Science of Russian Federation grant 14.W03.31.0017.

References:

- [1] Barker E.S. Detection of O₂ in the Martian Atmosphere with the Echelle-Coudé Scanner of the 107-inch Telescope, BAAS. 1972, V. 4, P. 371
- [2] N. P. Carleton, W. A. Traub, Detection of Molecular Oxygen on Mars. Science. 1972. V. 177. Is. 4053, P. 988–992, DOI: 10.1126/science.177.4053.988
- [3] P. Hartogh et al. Herschel/HIFI observations of Mars: First detection of O₂ at sub-millimetre wavelengths and upper limits on HCl and H₂O₂. A&A. 2010. V. 521. P. L49
- [4] Mahaffy et al. Abundance and Isotopic Composition of Gases in the Martian Atmosphere from the Curiosity Rover. Science. 2013. V. 341. Is. 6143. P. 263-266, DOI:10.1126/science.1237966.
- [5] Korablev O., Montmessin F., and ACS Team. The Atmospheric Chemistry Suite (ACS) of three spectrometers for the ExoMars 2016 Trace Gas Orbiter. Space Sci. Rev.. 2018, V. 214:7.
- [6] Millour E. et al. The Mars Climate Database (MCD version 5.3). Geophysical Research Abstracts. 2019. V. 21. EGU2019–7153.

DUST AND WATER ICE AEROSOLS DURING THE FIRST YEAR OF ACS TIRVIM AND NIR OBSERVATIONS

M. Luginin¹, A. Fedorova¹, N. Ignatiev¹, A. Grigoriev¹, A. Trokhimovskiy¹, A. Shakun¹, F. Montmessin² and O. Korabiev¹

¹ Space Research Institute (IKI), Moscow, Russia,
mikhail.luginin@phystech.edu

² LATMOS-UVSQ, Guyancourt, France

Keywords:

Mars, atmosphere, aerosols, solar occultations, ACS, TGO, ExoMars, TIRVIM, NIR. Aerosols play a big role in the atmospheric circulation, thermal structure, and climate of Mars [1, 2]. Dust particles cause changes in atmospheric dynamics and inflation of the atmosphere through the solar heating of the atmosphere [1]. Water ice particles play fundamental role in photochemistry and transport of volatiles on Mars [1, 3]. Knowledge of the spatial and temporal distribution of dust and water ice aerosols is highly important for better understanding of dust and water cycles on Mars.

The ExoMars Trace Gas Orbiter (TGO) is a joint ESA–Roscosmos mission to Mars [4]. It began orbiting Mars in October 2016 and started its observations in April 2018, just before the beginning of the 2018 global dust storm at the beginning of June (solar longitude $L_s \approx 185^\circ$).

The Atmospheric Chemistry Suite (ACS) is a set of three infrared spectrometers (NIR, MIR, and TIRVIM) featuring high accuracy, high resolving power and a broad spectral coverage (0.7–17 μm). TIRVIM is a Fourier-transform spectrometer capable of operation in nadir and solar occultation modes. In occultations, TIRVIM operates mostly in ‘climatology’ mode, covering the full spectral range of 1.7–17 μm every 0.4 s with spectral resolution $\leq 1 \text{ cm}^{-1}$ [5]. Aerosol properties from TIRVIM solar occultation data were retrieved from 19 wavelengths in the spectral range of 2–6 μm (1700–5000 cm^{-1}), chosen outside of strong-gas-absorption bands. To increase the signal-to-noise ratio, the spectra were averaged using the simple moving mean within a spectral window of 50 cm^{-1} centered at the chosen wavenumbers. NIR is an echelle spectrometer, with selection of diffraction orders performed by an acousto-optical tuneable filter. It operates in nadir and solar occultation modes and covers the spectral range 0.7–1.7 μm . During an occultation, ACS NIR measures 10 preselected diffraction orders in two seconds, including the absorption bands of H_2O , CO_2 , and O_2 . For the aerosol retrieval, diffraction orders centered at 0.76, 0.86, 0.99, 1.38, and 1.57 μm were used.

The first step in retrieval procedure is calculation of aerosol transmission profile. For TIRVIM, it is straightforward and standard for all solar occultation experiments. The reference spectrum for an occultation I_0 is obtained when observing the Sun out of the atmosphere. Inside the atmosphere solar radiance is attenuated by aerosols. Transmittances are obtained by dividing the spectra measured through the atmosphere by the reference spectrum recorded outside the atmosphere: $T = I/I_0$. For NIR, the spectra fitting and retrieval of aerosol transmission profile follow the method described for the SPICAM Mars Express 1.38- μm band [6, 7].

The second step, retrieval of the extinction vertical profiles, is identical to the one used for SPICAM and SPICAV solar occultations [8, 9]; that is by making use of the standard ‘onion peeling’ method.

The final step involves fit of the experimental data to the modelled one. As a result, vertical profiles of size distribution and number density are retrieved (Figure). To distinguish between water ice and dust particles, we applied the optimal-estimation retrieval scheme independently for both types and made the decision based on the fit quality.

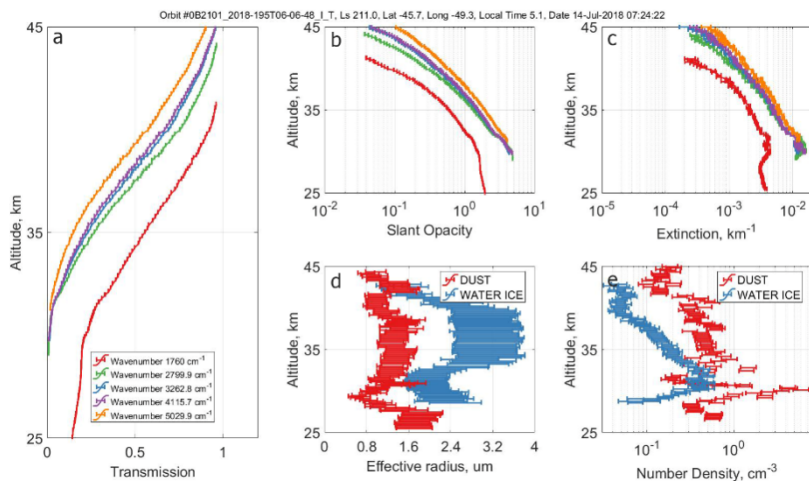


Fig. 1. Retrieved vertical profiles of transmission (a), slant opacity (b), extinction coefficient (c), particle effective radius (d), and number density (e) from orbit #B21_I.

In this work, we will present analysis of retrieved dust and water ice aerosol properties from the first year of observations on the orbit of Mars.

Acknowledgements:

ExoMars is the space mission of ESA and Roscosmos. The ACS experiment is led by IKI Space Research Institute in Moscow. The project acknowledges funding by Roscosmos and CNES. Science operations of ACS are funded by Roscosmos and ESA. M. Luginin acknowledges the support from the Ministry of Science and Higher Education of the Russian Federation, grant №14.W03.31.0017.

References:

- [1] Haberle R.M., Clancy R.T., Forget F., Smith M.D. & Zurek R.W. The Atmosphere and Climate of Mars (Cambridge Univ. Press, Cambridge, 2017).
- [2] Korabely O., et al., 2005. Optical properties of dust and the opacity of the Martian atmosphere. *Adv. Space Res.* 35, 21–30.
- [3] Vandaele A.C., et al., 2019. Martian dust storm impact on atmospheric H₂O and D/H observed by ExoMars Trace Gas Orbiter. *Nature*, 568, 521-525.
- [4] Korabely, O., et al., 2018. The Atmospheric Chemistry Suite (ACS) of Three Spectrometers for the ExoMars 2016 Trace Gas Orbiter. *Space Science Reviews*. V. 214(1). P. 7.
- [5] Shakun A., et al.: ACS/TIRVIM: Calibration and first results, *Proc. SPIE 10765, Infrared Remote Sensing and Instrumentation XXVI*, 107650E (18 September 2018).
- [6] Maltagliati L., et al., 2013. Annual survey of water vapor vertical distribution and water–aerosol coupling in the Martian atmosphere observed by SPICAM/MEX solar occultations. *Icarus* 223, 942–962.
- [7] Fedorova A. et al., 2018. Water vapor in the middle atmosphere of Mars during the 2007 global dust storm. *Icarus* 300, 440–457.
- [8] Fedorova A., et al., 2009. Solar infrared occultation observations by SPICAM experiment on Mars-Express: Simultaneous measurements of the vertical distributions of H₂O, CO₂ and aerosol. *Icarus*, V. 200(1), P. 96–117.

MARS EXPRESS RECENT SCIENCE HIGHLIGHTS

D.V. Titov¹, J.-P. Bibring², A. Cardesin³, T. Duxbury⁴, F. Forget⁵, M. Giuranna⁶, F. González-Galindo⁷, M. Holmström⁸, R. Jaumann⁹, A. Määttä¹⁰, P. Martin³, F. Montmessin¹⁰, R. Orosei¹¹, M. Pätzold¹², J. Plaut¹³, and MEX SGS Team³

¹ ESA-ESTEC, 2200 AG Noordwijk, The Netherlands, dmitri.titov@esa.int;

² IAS-CNRS, Orsay, France;

³ ESA-ESAC, Madrid, Spain;

⁴ George Mason University, Fairfax, VA, USA;

⁵ LMD, Paris, France;

⁶ IAPS-INAF, Rome, Italy;

⁷ IAA, Granada, Spain;

⁸ IRF, Kiruna, Sweden;

⁹ IPF-DLR, Berlin, Germany;

¹⁰ LATMOS/IPSL, CNRS, Guyancourt, France; 11IRA-INAF, Bologna, Italy;

¹² RIU-Uni Cologne, Cologne, Germany; 13JPL, Pasadena, CA, USA

Keywords:

Mars Express, geology, atmosphere, ionosphere, plasma environment, escape.

After 15 years in orbit Mars Express remains one of ESA's most scientifically productive Solar System missions whose publication record now exceeds 1200 papers. Characterization of the geological processes on a local-to-regional scale by HRSC, OMEGA and partner experiments on NASA spacecraft has allowed constraining land-forming processes in space and time. Recent results suggest episodic geological activity as well as the presence of large bodies of liquid water in several provinces (e.g. EridaniaPlanum, Terra Chimeria) in the early and middle Amazonian epoch and formation of vast sedimentary plains north of the Hellas basin. Mars Express observations and experimental teams provided essential contribution to the selection of the Mars-2020 landing sites and supporting characterization of potential landing sites for the Chinese HX-1 mission. Recent discovery by the subsurface radar MARSIS of subglacial liquid water underneath the Southern polar layered deposits has proven that the mission science potential is still not exhausted. The radar will continue searching for subsurface water pockets using its high resolution mode.

More than a decade-long record of the atmospheric parameters such as temperature, dust loading, water vapor and ozone abundance, water ice and CO₂ clouds distribution, collected by SPICAM, PFS, OMEGA, HRSC and VMC together with subsequent modeling have provided key contributions to our understanding of the martian climate. Spectroscopic monitoring of the global dust storm in 2018 revealed dust properties, their spatial and temporal variations and atmospheric circulation.

Recently PFS has reported a firm detection of 15.5 ± 2.5 parts per billion by volume of methane in the Martian atmosphere above Gale crater on 16 June 2013, just one day after the in-situ observation of a methane spike by the Curiosity Rover. Numerical simulations of the Martian atmosphere, using stochastic gas release scenarios, identified a potential source region east of Gale crater. Most importantly, independent geological analysis also pointed to the same region, where faults of Aeolis Mensae may extend into proposed shallow ice of the Medusae Fossae Formation and episodically release gas trapped below or within the ice.

More than 10,000 crossings of the bow shock by Mars Express allowed ASPERA-3 to characterize complex behavior of the magnetic boundary topology as function of the solar EUV flux. Observations of the ion escape during complete solar cycle revealed dependencies of the atmospheric erosion rate on parameters of the solar wind and EUV flux and established global energy balance between the solar wind and escaping ion flow. This led to important conclusion that the ion escape at Mars is production rather than energy

limited. The analysis showed that ion escape can be responsible for removal of about 10 mbar over Mars history that implies existence of other more effective escape channels.

The structure of the ionosphere sounded by the MARSIS radar and the MaRS radio science experiment was found to be significantly affected by the solar activity, the crustal magnetic field, as well as by the influx of meteorite and cometary dust. MARSIS and ASPERA-3 observations suggest that the sunlit ionosphere over the regions with strong crustal fields is denser and extends to higher altitudes as compared to the regions with no crustal anomalies. Several models of the upper atmosphere and plasma environment are being developed based on and in support of the collected experimental data. The models aim at creating user-friendly data base of plasma parameters similar to the Mars Climate Database that would be of great service to the planetary community.

A significant recent achievement was the flawless transition to the “gyroless” attitude control and operations mode on the spacecraft, that would allow mitigating the onboard gyros aging and extending the mission lifetime. The mission operations are now confirmed till the end of 2020 and the mission is notionally extended till the end of 2022. The talk will give the Mars Express status, review the recent science highlights, and outline future plans focusing on synergistic science with TGO.

FREND ONBOARD EXOMARS: GLOBAL NEAR-SURFACE WATER ABUNDANCE AND LOCAL FEATURES

A.V. Malakhov, I.G. Mitrofanov, A.B. Sanin, M.L. Litvak, D.V. Golovin, M.V. Djachkova, S.Yu. Nikiforov, A.A. Anikin, D.I. Lisov, N.V. Lukyanov
Space Research Institute, Moscow, 84/32 Profsoyuznaya st.

Keywords:

Mars, water, hydrogen, neutrons, climate.

Introduction:

FREND stands for Fine Resolution Epithermal Neutron Detector, an instrument orbiting Mars onboard Trace Gas Orbiter spacecraft. It began mapping campaign in May 2018 and we present major mapping results in this work.

Mapping of Hydrogen abundance:

FREND is a neutron telescope instrument installed onboard Roscosmos/ESA ExoMars 2016 mission, Trace Gas Orbiter (TGO) spacecraft.

Its main objective is to map hydrogen (water equivalent) abundance in the shallow subsurface of Mars. The instrument is sensitive to hydrogen up to 1 m deep. Epithermal and fast neutrons ratio, measured from orbit, depends greatly on the content of hydrogen in the subsurface.

Characteristic FREND feature is its collimator that shields detectors from neutrons from outside the field of view. Such technique allows for mapping with spatial resolution of up to 60 km per pixel, which was never before performed on Mars [1].

Global maps and local features:

In this work we will present FREND's latest results — global maps of Martian hydrogen abundance as measured by the instrument.

Thanks to its high spatial resolution, it becomes possible to study also local features in comparison with topography and geomorphology features. We will also present such findings for locations of most interest.

References:

- [1] I. Mitrofanov et al.: Fine Resolution Epithermal Neutron Detector (FREND) Onboard the ExoMars Trace Gas Orbiter, Space Sci Rev (2018), <https://doi.org/10.1007/s11214-018-0522-5>

ANALYSIS OF THE WATER DISTRIBUTION IN MARTIAN SUBSURFACE ESTIMATED BY PASSIVE MEASUREMENTS WITH THE DAN INSTRUMENT ONBOARD NASA/MSL

S.Y. Nikiforov, I.G. Mitrofanov, M.L. Litvak, M.V. Djachkova, D.I. Lisov, A.S. Sanin,

Space Research Institute of the Russian Academy of Sciences (IKI), 117997, 84/32 ProfsoyuznayaSt., Moscow, Russia, nikiforov@np.cosmos.ru.

Keywords:

Mars, Mars exploration, Surface, Water, WEH, Neutron Spectroscopy

Introduction:

During more than 7 years MSL Curiosity is successfully traversing across Mars surface exploring Gale crater. In our study we have used the data received from Dynamic Albedo of Neutron (DAN) instrument installed onboard Curiosity rover. The main objective of the DAN instrument onboard Curiosity rover is to study the bound water in shallow layer of Martian subsurface (up to 0.6 m) [1,2]. We paid our major attention to the DAN passive observations to suggest new technique and to reconstruct continuous profile of subsurface water along the traversed distance in Gale crater. We have also compared our results with previous analyses [5, 6, 7].

Instrumentation: The DAN instrument uses a method of active and passive neutron sensing of the shallow subsurface. Active neutron measurements are provided with the pulsing neutron generator (PNG), which produces 2 microsecond pulses of 14 MeV neutrons at a frequency of 10 Hz. In passive observations, the instrument detects neutrons that are produced by two different sources: 1) the neutrons born in the interactions between charge particles of galactic cosmic rays (GCR) and soil nuclei; 2) the neutrons produced with rover's Multi-Mission Radioisotope Thermoelectric Generator (MMRTG).

Neutrons from the both sources are initially produced with high energies and then moderated down to epithermal and thermal ranges in the subsurface under the rover. The efficiency of the moderation process is known and it depends on the presence of hydrogen in the soil because during a neutron-hydrogen collision, the light nucleus of hydrogen atom takes about the same recoil energy, as the scattered neutron. It means that DAN detects elevated content of hydrogen through the variations of low energy neutron flux leaking from the subsurface.

Data Analysis:

In our analysis, we processed of DAN passive observations over the period of 2100 Sols in the Gale crater.

The estimation of water component is based on the comparison and the calibration of passive data using active ones at the rover stops. This method uses two parameters: the ratio between count rates of thermal and epithermal detectors and the content of neutron absorbers. The last one is described by chlorine concentration as most important (taking into account many factors) neutron absorber in the Martian subsurface [1,3]. For the simplicity, we implemented homogeneous model of the subsurface. This regolith structure is prevailing according to the active measurements (see for details [4]).

Results. The analysis of DAN passive data shows that WEH (water equivalent hydrogen) varies from 0.5% up to 7% along the rover traverse over the period of 2100 Sols and distance up to 20 km. The implemented method shows good correlation with the active measurements (up to 90% degree of correlation for ~ 400 individual spots) and could be used for the continuous monitoring of the average content of subsurface water.

References:

- [1] Mitrofanov I.G. et al. 2014. JGRE, 119, 1579–1596.
- [2] Livak M.L. et al. 2014. JGRE, 119, 1259–1275.

- [3] Hardgrove C.J. et al. 2011. *Nucl. Instr. Meth. Phys. Res. A*, 659(1), 442–445.
- [4] Mitrofanov I.G. et al. 2016. *AstL*, 42, 251–259.
- [5] Tate C.G. et al. 2015. *Icarus*, 262, 102–123.
- [6] Tate C.G. et al. 2018. *Icarus*, 299, 513–537.
- [7] Tate C.G. et al. 2019. *Icarus*, 330, 75–90.

SUBSURFACE WATER CONTENT IN GALE CRATER FROM DAN MEASUREMENTS AND ITS CORRELATION WITH MINERAL ABUNDANCE ON THE SURFACE

M.V. Djachkova¹, I.G. Mitrofanov¹, S.Y. Nikiforov¹, M.L. Litvak¹, D.I. Lisov², A.B. Sanin¹

¹Space Research Institute, Moscow, Russia

Keywords:

Mars, Mars exploration, water content, DAN, hydrated minerals, CRISM.

Introduction:

The Dynamic Albedo of Neutrons (DAN) instrument designed to detect neutrons in order to determine hydrogen abundance in the Martian subsurface (down to 1 m deep) [1, 2] is successfully working onboard Mars Science Laboratory (MSL) rover Curiosity for more than 6 years. The Curiosity rover covered more than 19 km on the Martian surface and crossed a range of terrain types and geological structures of different mineralogical composition. We investigated the possible correlation between water content value as measured by DAN instrument along the Curiosity traverse and the presence of hydrated minerals as seen from orbit (for example, by Compact Reconnaissance Imaging Spectrometer for Mars instrument onboard Mars Reconnaissance Orbiter [3]) in order to connect geochemical features of the surface to the subsurface water measurements. Our cross-analysis of soil water content from DAN passive measurements in Gale crater and special data sets, reflecting distribution of hydrated/hydroxylated minerals on the surface of this crater, shows an increase of the average water content for the surface containing certain types of minerals as related to the surface, which does not contain them. This increase is higher, with the more prominent spectral feature of the mineral on the surface. Thus, certain types of minerals being part of the sedimentary deposits composing the Gale crater surface have considerable thickness, which is insufficient for being detected by the DAN measurements.

References:

- [1] Mitrofanov I.G. et al. J. Geophys. Res. 2014. V. 119. P. 579–1596.
- [2] Livak M.L. et al. J. Geophys. Res. 2014. V. 119. P. 1259–1275.
- [3] Pelkey, S. M., et al., J. Geophys. Res. V 112, P. E08S14.

TOWARD AN UNDERSTANDING OF EARLY MARS CLIMATE HISTORY: NEW THEMES, DIRECTIONS AND TESTS

James W. Head

Department of Earth, Environmental and Planetary Sciences, Brown University, Providence, RI 02912 USA, james_head@brown.edu

Keywords:

Mars, climate history, Noachian, Hesperian, Amazonian, valley networks, rainfall, snowmelt, "warm and wet", "cold and icy".

Discussion and debate continue concerning the nature and evolution of the atmosphere and climate in the Noachian and Hesperian periods of the history of Mars, centering on two end-member hypotheses (Fig. 1): 1) "warm and wet/arid" (WW/A), with fluctuations in the amount and intensity of rainfall (infiltration versus overland flow), and a Late Noachian climate optimum causing overland flow [1], valley network (VN) formation, open and closed basin lakes (CBL/OBL) and a northern lowlands ocean; and 2) "cold and icy" (CI), with mean annual temperatures (MAT) ~ 225 K, an adiabatic cooling effect forming a Noachian Icy Highlands (NIH), and transient perturbations to the ambient CI climate to cause melting of the NIH to form VN, OBL/CBL [2, 3]. Here we outline a series of concepts and themes that are currently emerging from this discussion and identify several directions for the path forward.

Time Period Involved:

The Noachian begins with the formation of the Hellas basin, and continues with Isidis and Argyre (Fig. 2); therefore the Middle and Late Noachian (M-LN) are characterized by significant inheritance from the influence of these large basins on the atmosphere, hydrosphere, surface temperatures, regional to global resurfacing, geomorphology, exposure of deep primary and secondary rock types and anomalous alteration mineralogy. It is also a period of relatively higher impact flux, with temporally decreasing flux offset by decreasing atmospheric pressure. This is all built on top of Pre-Noachian inheritance (Fig. 2).

Nature of the Ambient Background Atmosphere and its Evolution:

What is the nature of the ambient atmosphere, the long-term background atmosphere that exists throughout the 250 Ma Middle-Late Noachian (M-LN)? Critical to this question is how the atmosphere responds to and recovers from impact basin formation, the fate of the magnetic field, and the timing and rates of early loss-to-space mechanisms. These effects are largely poorly known/unknown, but are likely to have occurred and been in place by the M-LN. Atmospheric pressure is unlikely to have exceeded 1 bar, CO₂ is the dominant component, and other greenhouse gases appear to have been minimal. These conditions and Mars' distance from a faint young Sun favor MAT ~ 225 K. Long-term loss-to-space rates decreased atmospheric pressure with time, but it is unlikely that a M-LN ambient atmosphere could have been characterized by sustained MAT > 273 K; sustained evolutionary warming mechanisms to > 273 K appear difficult.

Nature of M-LN Background Climate:

Barring major changes in our understanding (which are certainly possible!), the characteristics of the ambient background atmosphere predict that the background M-LN climate (Fig. 1) is characterized by MAT ~ 225 K, an adiabatic cooling effect, highlands which act as a cold-trap for water, and accumulation and storage of the water as snow and glacial ice there (the 'icy highlands'). This strongly suggests that the abundant geological evidence of surface liquid water may be due to perturbations to this background climate, not to a sustained > 273 K climate itself. In searching for such perturbations, peak annual and seasonal (PAT, PST) temperatures are likely to be important, as well as intermittent (occur for time to time) and heterogeneous (occur in some places but not others) melting conditions.

Nature of Precipitation (rainfall, snowmelt):

Most contributions use the term precipitation and parenthetically add (rainfall, snow; or snowmelt). It is important to distinguish between rainfall and snowmelt in proposed hypotheses for M–LN climate conditions. It is extremely difficult to produce sustained or widespread rainfall in a climate with MAT < 273 K, but such a climate can undergo intermittent or heterogeneous melting of snow and ice under a variety of conditions, producing significant volumes of glacial meltwater.

Hydrological System and Cycle:

End-member climate models predict very different water cycle scenarios. In the WW/A model, the hydrological system is vertically integrated, rainfall is common, groundwater plays an important role, and northern lowland oceans are an important part of the cycle. In the CI model, there is a thick global cryosphere, the hydrological system is horizontally stratified, there is no sustained ocean or connection to the groundwater system, and the majority of the water is located as snow and glacial ice in the uplands above an ELA of $\sim +1$ km. Any ocean formed from the release of groundwater is very short-term, rapidly freezing and returning to upland cold-traps.

Water Budget:

The M-LN surface-near surface estimated water budget is uncertain but may only have been within a factor of 2–3 of the current 34 m GEL [4]. Furthermore, water recycling needs to be considered in all estimates of total water volumes required to erode VN and fill CBL/OBL, and thus estimating the total water budget. Water recycling readily occurs in both WW/A and CI scenarios. Increased total water budget in the CI scenario means more ice in the uplands available to melt during climate perturbations.

Polar Deposits:

The presence of significantly larger ($\sim 2.5\times$ area) LN-EH south polar-circumpolar deposits (the Dorsa Argentea Formation; DAF) are consistent with CI climate models in which the ACE causes ice to reside in the southern uplands and not in the relatively “warmer” northern lowlands.

ML-N Geological Processes:

Impact basin aftermath hot rains may be a critical erosional and alteration process in EN basins [5, 6] but ML-N impact craters have little effect on the climate except for hot ejecta melting surface snow and ice [6]. CI upland glaciation is cold-based except under extreme water budgets, and thus is likely to leave little evidence of its presence except when top-down melting occurs (fluvial) [7]. Flood volcanism is a very significant ML-N-H process, resurfacing >30% of Mars; although gas release may locally contribute to raising PAT/PST toward melting [8], the most important effect may be lava/ice contact/deferred melting, which can produce very significant amounts of meltwater [9].

Mineralogical Perspectives and Constraints:

The surface phyllosilicate and related mineralogical record is an important constraint on climate history but uncertainty as to the provenance and environment of origin of these has precluded definitive application to the climate discussion. Advances are needed in terms of understanding necessary water/rock ratios, temperatures, time-scales and micro-environments; also necessary is a better understanding of the climate implications of preserved salts and olivine.

Lander/Rover Perspectives:

Surface exploration of a variety of local environments will help resolve many of these issues by providing evidence to distinguish between local micro-environments and global climate effects. At the same time, global climate models provide paradigms to test with surface exploration data (e.g., are Meridiani deposits due to fluctuating groundwater table flooding levels or could they be due to intermittent overland flooding and evaporation? Similarly, improved understanding of sediment protoliths and the role of impact pre-processing in influencing sediment grainsize/shape is important [10].

Candidates and Timescales of Climate Perturbations:

A sustained WW/A MAT >>>273 K climate needs only minor perturbations to produce sustained liquid water and runoff; in contrast, a nominal CI MAT ~225 K climate needs significant perturbations to produce the same effects. Among the types of variability and Intermittencies are: 1) Episodic/Periodic: Two scales: Normal atmospheric system variability: This episodic intermittency operates on < 1–103 years timescales; Spin axis/orbital variation-forced climate cycles: This periodic intermittency operates on 103–106 year timescales. 2) Punctuated: Two types: Variability in effusive/explosive volcanic processes: Volcanism is likely to be punctuated and more episodic than periodic, with uncertain intermittency; External stochastic variability: Impact cratering: Episodic and punctuated (but vary in magnitude); durations of atmospheric effects estimated at 102–103 years [5, 6]. Introduction of additional greenhouse gases can also cause significant perturbations of uncertain duration. Examination of the durations of fluvial activity (Fig. 3) suggest that the required duration of individual perturbations may be short and their total number may not be large.

The Early Mars Climate Aftermath:

All Noachian climate models must account for LH and Amazonian events [11] in an evolutionary manner.

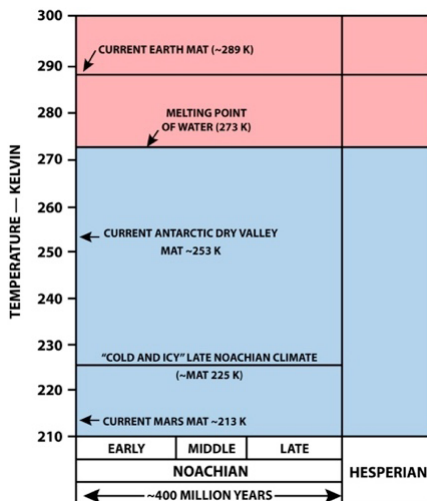


Fig. 1. Temperature-time framework [12].

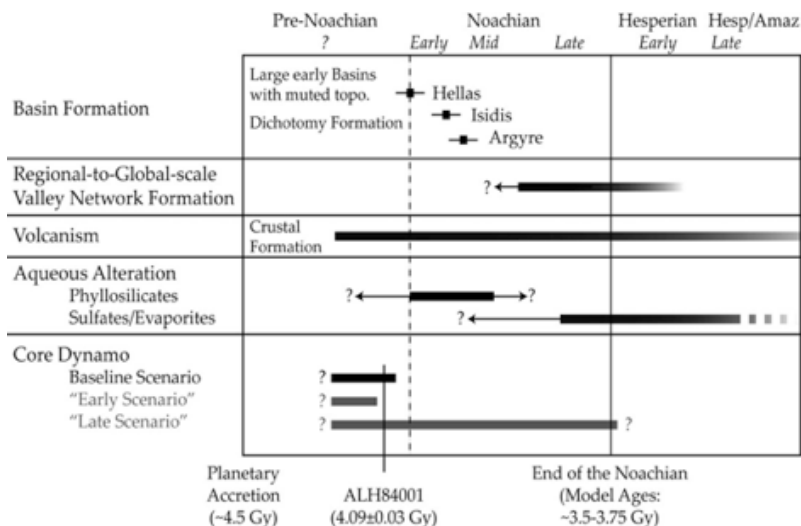


Fig. 2. Major factors in early Mars history [13].

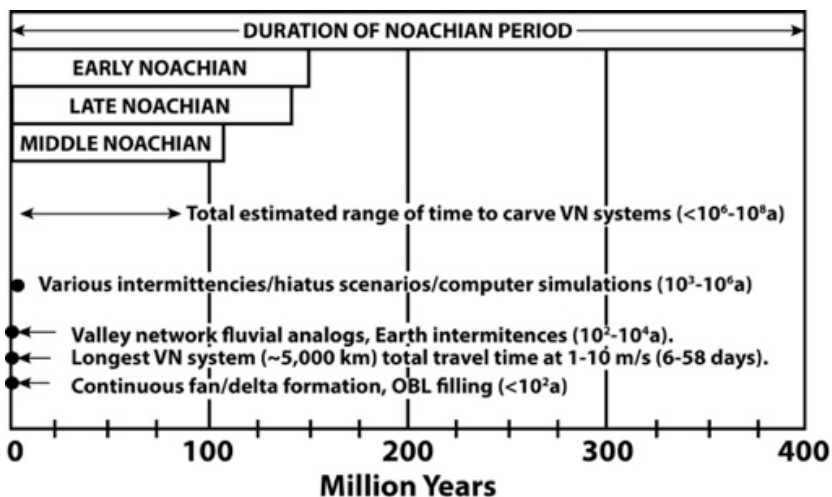


Fig. 3. Process duration estimates [12-14].

References:

- [1] Ramirez and Craddock. 2018. V. NG 11. P. 230
- [2] Wordsworth et al. 2015. V. JGR 120, P. 1201
- [3] Head and Marchant. 2015. V. AS 26. P. 774
- [4] Carr and Head. 2015. V. GRL 42. P. 1
- [5] Palumbo and Head. 2017. V. MAPS 53. P. 687
- [6] Turbet et al. 2019. V. LPSC 50
- [7] Fastook and Head. 2015. V. PSS 86. P. 102
- [8] Palumbo et al. 2019. V. LPSC 50
- [9] Cassanelli and Head. 2016. Icarus 271, 237
- [10] Arp et al. 2019. Icarus 321. P. 531
- [11] Carr and Head. 2010. EPSL 294. P. 185
- [12] Head et al. 2017. 4th Early Mars
- [13] Fassett and Head. 2011. Icarus 211, 1204;
- [14] Buhler et al. 2014. Icarus 241. P. 130.

VOLCANISM ON EARLY MARS: EXPLORING THE INFLUENCE OF THE SO₂ PLUME ON LOCAL AND SHORT-TERM CLIMATE CHANGE

A.M. Palumbo¹, J.W. Head¹, and R.D. Wordsworth²

¹ Dept Earth, Environmental & Planetary Sciences, Brown University, Providence, RI 02912 USA, Ashley_Palumbo@Brown.edu

² Sch Engineering & Applied Sciences, Harvard University, Cambridge, MA 02138 USA

Keywords:

volcanism, climate, Noachian, rainfall, cold and icy

Introduction: The nature of the early martian climate is a compelling scientific problem [1]. Widespread valley networks (VNs) [2] and lakes [3, 4] suggest that there was abundant liquid water on the surface during the Late Noachian-Early Hesperian (LN-EH). This has led to suggestions that the early climate was “warm and wet”, with mean annual temperature (MAT) > 273 K and abundant rainfall [e.g. 5]. In contrast, recent climate modeling suggests that the climate may have been “cold and icy”, with MAT ~ 225 K and water ice in the highlands [6, 7, 8]. In this “cold and icy” scenario, fluvial activity would have occurred during periods of transient heating, ice melting, and runoff. Many transient heating mechanisms exist, including volcanism-induced heating [9–14].

Background:

SO₂ and H₂S are strong greenhouse gases in the martian atmosphere because they have fundamental absorptions in the IR atmospheric window [10]. Thermochemical modeling suggests that martian magmas are more sulfur enriched than terrestrial magmas [15], implying that large quantities of sulfur can be released for relatively small eruption volumes. Further, at least 30% of Mars was resurfaced with basaltic plains by LN-EH flood volcanism [16, 17]. For these reasons, volcanism was an active and important process in the LN-EH, when the VNs and lakes formed. Understanding the influence of volcanism on the early climate is critical for interpreting the geologic and climatic history of Mars.

Previous studies have used climate and radiative transfer models to estimate the heating from volcanic gases in the martian atmosphere [9, 11–13, 18]. Many concluded that sulfur-based gases cannot produce the necessary climate change because (1) MAT does not exceed 273 K for reasonable gas concentrations [12] when considering global gas distribution, (2) temperatures above freezing can occur in the summer for modest concentrations of globally-distributed SO₂ [19], but the percentage of the year above freezing is low and ice melting and runoff is insignificant, and (3) heating may only last a few months to years [11, 20] due to rapid conversion to aerosols, which are atmospheric cooling agents. Although the influence of volcanism-induced heating has been extensively studied, one important aspect has not been explored in detail: localized heating is predicted to occur when gases are concentrated near the source and have not yet dispersed globally. This effect is well-established for terrestrial analogues, such as the 2001 Mt. Pinatubo eruption, but has not yet been analyzed for early Mars.

Methods:

We use the 3D Laboratoire de Météorologie Dynamique (LMD) global climate model (GCM) for early Mars to assess the localized SO₂ greenhouse heating that occurs following a volcanic eruption, before the gas distributes globally. The ambient background climate is simulated as 1 bar CO₂ [21], 34 m GEL water [22], 25–55° obliquity [23], 0–0.17 eccentricity [23], and 0 ppm SO₂; these conditions produce a “cold and icy” climate.

We run the model with this ambient, SO₂-free atmosphere until it reaches equilibrium, then simulate the eruption ‘plume’ by introducing 10 ppm SO₂ near a LN-EH volcanic edifice (Fig. 1); 10 ppm is an upper limit for atmo-

spheric SO_2 concentration during this period of high volcanic outgassing rates [9]. Specifically, the ‘plume’ is simulated as an SO_2 column above a volcanic edifice. The column has a lateral SO_2 gradient, with most SO_2 concentrated in the center, and the column is continuous until ~ 28 km altitude (following [24,25]). As the model progresses through time, we track the distribution of SO_2 in the atmosphere and the associated heating of the surface. We do not account for photochemical effects, including OH radical attack, which convert the SO_2 to aerosols; our temperature predictions are maxima.

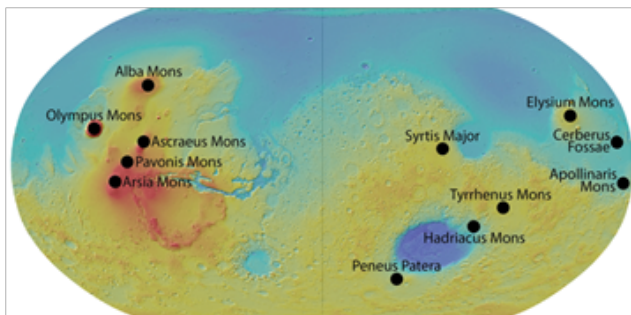


Fig 1. Locations of volcanoes which are used as starting points for plumes.

Results and Discussion:

Based on our results, we identify two key phases of atmospheric SO_2 distribution following a volcanic eruption. Phase one is defined as the period of time in which SO_2 is focused near the volcanic edifice and spreading through a latitudinal band. By day 45, the SO_2 has dispersed through the latitudinal band (Fig. 2A). Phase two is defined as the period of time in which the SO_2 is spreading poleward and becomes globally distributed. After the eruption, the SO_2 has reached the poles (Fig. 2A). After the SO_2 has reached the poles, it continues to redistribute for 10s of days longer until it is relatively homogeneously distributed across the planet. Next, we analyze the SO_2 -related greenhouse warming in phase one and phase two.

Phase one. The first 45 days following an eruption introduce important local climate change; the SO_2 greenhouse effect is focused near the eruption site and then within a latitudinal band, strengthening the local greenhouse effect. To quantitatively understand the localized greenhouse warming, we compare the temperature at the eruption site as a function of time for two different scenarios: following an eruption and for an SO_2 -free atmosphere (Fig. 2B). Recall that an SO_2 -free atmosphere is the ambient background Noachian “cold and icy” climate. To describe our results, we assess local warming following a single eruption at Hadriacus Mons (HM). The simulated eruption occurs at southern hemispheric spring equinox, obliquity is 25° , eccentricity is 0, there is 1 bar CO_2 , and the 10 ppm SO_2 plume is initiated as a column.

In the first 10 days following an eruption at HM, the temperature near the eruption site is predicted to be ~ 15 K warmer than in the SO_2 -free case (Fig. 2B). Summer temperatures at HM are ~ 5 -10 K warmer following the eruption than in the SO_2 -free climate, but average daily temperatures do not exceed 273 K (Fig. 2B). Note that an eruption at the beginning of the local summer season, instead of spring equinox, would be required to increase temperatures above 273 K locally, but even in that case, the heating would be short-lived (10s of days) because the plume rapidly disperses and the magnitude of localized heating decreases. For comparison, in the Antarctic Dry Valleys, temperatures are only >273 K for 20–25 days each year, but sufficient meltwater is produced to activate the ~ 30 km long Onyx River.

Phase two. Temperatures continue to be warmer in the post-eruption case than in the SO_2 -free case. However, in phase two, as the SO_2 disperses poleward and distributes globally, the difference in temperature between the post-eruption and SO_2 -free cases becomes smaller (~ 5 K; Fig. 2B) than in phase one. Although temperatures globally are higher than in an SO_2 -free atmosphere, the amount of warming in phase two is not enough to increase

temperatures above 273 K at the eruption site, regardless of the season in which the eruption occurs. In agreement with previous work [e.g. 12], we find that phase two conditions, 10 ppm globally distributed SO_2 , are not sufficient to increase temperatures >273 K for more than a few hours yearly anywhere on the planet. Further, photochemical conversion to aerosols causes atmospheric SO_2 concentration and associated warming to decrease after the first few months [11, 25]. In summary, the most drastic heating occurs during phase one, immediately following the eruption (Fig. 2B).

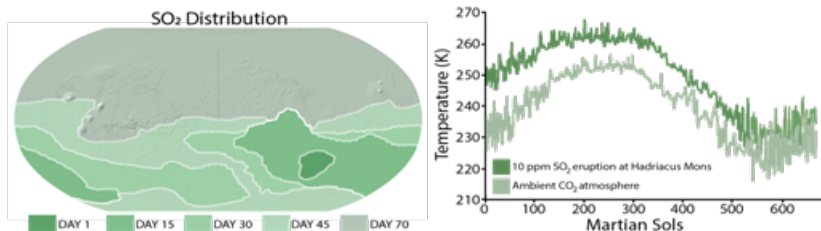


Fig. 2. (A, left) Dispersal of 10 ppm SO_2 following eruption at HM ($31^\circ\text{S } 92^\circ\text{E}$). The plume spreads latitudinally then poleward. (B, right) Time series of mean daily temperature at HM after an eruption (green) and in an SO_2 -free atmosphere (gray).

Conclusions:

We used a 3D GCM to explore localized heating following volcanic eruptions on early Mars. We identify two phases: phase one, in which the plume is focused near the volcanic edifice and spreading in a latitudinal band, and phase two, in which the SO_2 reaches the poles and becomes homogeneously distributed. During phase one, significant heating can occur locally and regionally. For specific conditions, including an eruption at the beginning of local summer, the local heating may cause average daily temperatures >273 K for 10s of days, which may cause some ice melting and runoff. Although heating is local and short-lived, the cumulative amount of heating and melting from all LN-EH volcanism could produce significant volumes of meltwater and potentially contribute to formation of VNs and lakes.

Acknowledgments:

This work was supported by NASA Headquarters under NESSF to AMP; Grant 90NSSC170487.

References:

- [1] Wordsworth et al. 2018. *Nat. Geosci.*11, P. 888.
- [2] Hynke et al. 2010. *JGR Planets*115, E09008.
- [3] Fassett & Head 2008. *Icarus*198, P. 37.
- [4] Goudge et al. 2015. *Icarus*260, P. 346.
- [5] Craddock & Howard. 2002. *JGR Planets*107, P. 5111.
- [6] Wordsworth et al. 2013. *Icarus*222, P. 1.
- [7] Forget et al. 2013. *Icarus*222. P. 81.
- [8] Head & Marchant. 2014. *Ant. Sci.* 26(6), P. 774.
- [9] Halevy & Head. 2014. *Nat. Geosci.*7, P. 865.
- [10] Postawko & Kuhn. 1986. *JGR Solid Earth*91, P. 431.
- [11] Kerber et al. 2015. *Icarus*261, P. 133.
- [12] Mischna et al. 2013. *JGR Planets*118, P. 560.
- [13] Johnson et al. 2009. *JGR Planets*114, P. E11011.
- [14] Wordsworth et al. 2017. *GRL*44, 2016GL071766.
- [15] Gaillard & Scaillet. 2009. *EPSL*279, P. 34.
- [16] Head et al. 2002. *JGR Planets*107, P. 3.
- [17] Tanaka et al. 2014. *PSS*95, P. 11.
- [18] Johnson et al. 2008. *JGR*, 113, E08005.
- [19] Palumbo et al. 2018. *LPSC*49, Abs 2169.
- [20] Tian et al. 2010. *EPSL*295, P. 412.
- [21] Jakosky et al. 2017. *Science*355, P. 1408.
- [22] Carr & Head 2015. *GRL*42, 2014GL062464.
- [23] Laskar et al. 2004. *Icarus*170, P. 343.
- [24] Glaze & Baloga. 2002. *JGR Planets*107, P. 16.
- [25] Kerber et al. 2013. *Icarus*223, P. 1.

THE ACIDALIA MENSA REGION ON MARS: A KEY ELEMENT TO TEST THE MARS OCEAN HYPOTHESIS

M.A. Ivanov¹ and H. Hiesinger²

¹ Vernadsky Institute, RAS, 19, Kosygin st., 119991 Moscow, Russia, mikhail_ivanov@brown.edu;

² Institut für Planetologie, Westfälische Wilhelms-Universität, Münster, Wilhelm-Klemm-Str. 10, 48149 Münster, Germany

Keywords:

Mars, Acidalia Mensa, ocean, Vastitas Borealis Formation, chronology

Introduction:

The giant circum-Chryse system of outflow channels are likely the principal source of water that may have flooded the northern plains [1, 2]. The Chryse basin is the region of convergence of the largest outflow channels and the Acidalia basin is at continuation of the northward trend of the channels and their possible floods. The basins represent the first sizable lowlands where the channels effluents may have been deposited.

Acidalia Mensa is the largest positive topographic feature that is at the projection of the outflow channels into the northern plains. The overall morphology of Acidalia Mensa suggests that this features existed prior to the emplacement of the VBF [3, 4]. Despite the lines of evidence suggesting the presence of an ocean-sized body of ice/water/mud in the northern plains, the topographic characteristics of Acidalia Mensa and its interpretation as an outcrop of the ancient uplands could be strong arguments against this hypothesis. Indeed, the topographic position of Acidalia Mensa below the level of the proposed shorelines would be inconsistent with the ocean hypothesis if the surface of the Acidalia plateau always remain subaerial.

The potential conflict between the consequences of the ocean hypothesis and possible nature of the surface in Acidalia Mensa motivated our photogeological study of the Acidalia Mensa region (43–50 N, 15–35 W) that was oriented to address the following questions relevant to the Mars ocean problem. What is the inventory and nature of materials exposed in Acidalia Mensa? What is the crater retention age of the surfaces within Acidalia Mensa and its surroundings? Is there evidence in Acidalia Mensa of its surface being either subaerial or submerged? Did Acidalia Mensa control the outflow channel floods? Is there evidence for the 3.6 Ga old resurfacing in Acidalia Mensa?

Data:

We conducted our study using available medium- and high-resolution images and topographic measurements in combination. Our database included:

1) THEMIS-IR daytime and nighttime images, resolution is 100 m/px. 2) CTX images, resolution is 5 m/px. 3) HiRISE images, resolution is 25-50 m/px 4) The topographic data of MOLA; 1/128 degree gridded topography.

Topography of the study region:

The study region represents flat plains slightly sloped toward northeast; the topographic amplitude of the majority of the plains is slightly less than ~400 m. The Acidalia plateau represents an elevated feature, the base of which occurs mostly at about -4.6 km (corresponds to the mean elevation of the surface of the VBF around the plateau). The tops of the Acidalia plateau are ~500-600 m above the surrounding plains. About 80% of the plateau, is within a 200-meters-interval above its base. The plateau is below the level of -3.92 km (the mean elevation of the VBF boundary in the Chryse-Acidalia region [5]).

Material units and structures in the study area

Smooth plains of Acidalia plateau (unit Nsp_m)

These plains make up the majority of the Acidalia plateau. Walls of an impact crater (~8.5 km diameter) demonstrate the deeper subsurface of this unit represents stacks of thick layers with jagged and blocky edges. Knobby ter-

rain (unit Hkt): Occurrences of this unit are around the edges of the Acidalia plateau. Mesas within this unit suggest that the knobby terrain consists of disintegrated pieces of the plateau. Background plains (Unit HVBi) is the most abundant unit in the study area and correspond to the Vastitas Borealis interior unit mapped by [4]. Mantling flow-like materials (units Hmmp, Hmmd, and Hmnr) form extensive material units on the surface of the background plains and occur throughout the map region except for the areas occupied by the Acidalia plateau plains and the knobby terrain. Occurrences of the mantling units usually have flow-like and/or lobe-like shapes. These units, Hmmp (preserved), Hmmd (degraded), and Hmnr (relicts), are similar morphologically to the flow-like features that have been detected in Utopia Planitia and in Acidalia Planitia and interpreted as mudflows [6, 7]. Thick flows (unit Hfm) occur in the map area exclusively in close spatial association with the Acidalia plateau. This unit forms broad bands (tens of kilometers wide) with lobate margins usually bounded by low scarps. The shape of the flow edges resembles that observed along the edges of the VBF [8, 5]. The flows of unit Hfm extends downslope at higher elevations and are controlled by a moat-like topographic depression that outlines the base of the Acidalia plateau. Small cones/mounds (unit Hbm) usually appear as cones with a summit pit. They overlay the surface of the background plains and the mantling flows embay the cones. Areas occupied by the plateau smooth plains (unit Nspm) and knobby terrain (unit Hkt) represent regions free of the bright cones/mounds. Troughs of the polygonal terrain [9] are relatively narrow linear and curvilinear topographic depressions that cut the surfaces of both the background plains and the mantling flows; materials of the thick flows (Hfm) cover the troughs.

We recognize three distinctly different morphologies of ejecta in the study area. Many larger craters (several kilometers diameter and larger) show heavily degraded ejecta. These craters with the pancake-like ejecta [10] are typical features of the northern plains [11]. Pedestal-like craters present [10] the second type of ejecta in the study area. Ejecta of these craters form a plateau-like features bounded by sharp scarps. In contrast to the pancake-like ejecta, the pedestal ejecta show no evidence for fluidized features or enhanced degradation within the ejecta blankets. Ballistic ejecta represent the third type of impact-related morphologies. Craters with the ballistic ejecta are usually small (<1 km).

Chronology:

In order to estimate the AMAs of key units in the study area, we counted craters using THEMIS-IR daytime images with resolution of 100 m/px. In our study, we estimated AMAs for the most widespread units in the study area: (1) unit Nspm, (2) unit HVBi, and (3) unit Hfm. These units are extensive and represent distinctly different stratigraphic levels.

The CSFD curve for craters on the Acidalia plateau has a complex shape and likely reflects multiple ages. The size-frequency distribution of the largest (3-50 km diameter) craters defines an oldest isochron that gives the age of $3.92 \pm 0.04 / -0.05$ Ga; this age corresponds to the Noachian epoch. The second isochron corresponds to the age of 3.65 ± 0.02 Ga. This age is close to the range of ages determined for the edges of the VBF in many regions of the northern plains [5]. We interpret the AMA of the background plains as the age of the emplacement of the Vastitas Borealis Formation materials in the study area. The size-frequency distribution of craters in a diameter range from 0.7 to 4 km on the surface of the flow-like materials on the Acidalia plateau (unit Hfm) is also better fit by a single isochron that corresponds to the age of $3.47 \pm 0.04 / -0.05$ Ga.

Discussion:

The apparent sequence of events in the study area begins with the formation of the Acidalia plateau plains ~ 4 Ga ago. The darker smooth plains of the plateau (unit Nspm) show a specific texture at depth formed by rough layers. The similarity of the subsurface textures of the plains of the Acidalia plateau with that in the volcanic provinces suggests that the Acidalia plains are also

of volcanic origin and that the Acidalia Mensa represented originally a volcanic province.

The Noachian age of the Acidalia volcanic plateau suggests that potentially it could be a subject of the late modification. Three lines of evidence support this suggestion.

(1) Although the subsurface of the Acidalia plains is morphologically identical to that of the volcanic provinces, its surface is strongly different and characterized by hummocky texture with abundant boulders. This specific small-scale morphology of the surface of the Acidalia plains suggests that the Acidalia plateau was modified by the deposition of poorly sorted materials.

(2) The larger impact craters (>10 km) on the plateau belong to the ancient, Noachian in age, population. These craters show no evidence for the ejecta blankets, are unusually shallow, and have lower rims than their counterparts elsewhere within the cratered uplands. This topographic configuration of the older craters on the Acidalia plateau indicates that the plateau was strongly degraded since its formation and accumulation of the ancient crater population.

(3) The SFD curve for all craters on the Acidalia plateau indicate that the plateau was resurfaced and suggests that the resurfacing was related not to a single event but was rather prolonged and consisted of multiple episodes. During these episodes, however, resurfacing was broadly distributed that prevented formation of localized erosional landforms such as valley networks or features that characterize the outflow channels (e.g., streamlined islands and/or steep-sided banks).

We interpret the surface texture of the Acidalia plains, the topographic configuration of the larger impact craters and the lack of localized erosion features as evidence that the sheet-wash removal and re-deposition of materials were responsible for the resurfacing in the Acidalia plateau.

References:

- [1] Baker, V.R., Strom R.G., Gulick V.C. et al. Ancient oceans, ice sheets and the hydrological cycle on Mars // *Nature*. 1991. V. 352. P. 589-594.
- [2] Carr M.H. *Water on Mars*, New York, Oxford University Press, 1996. 229 p.
- [3] Scott D.H., Tanaka K.L. Geologic map of the western equatorial region of Mars, 1:15,000,000 scale, USGS Map I-1802-A, 1986.
- [4] Tanaka K.L., Skinner J.A., Hare T.M. Geologic map of the Northern Plains of Mars, USGS Map I-2888, 2005.
- [5] Ivanov M.A., Erkeling G., Hiesinger H. et al. Topography of the Deuteronilus contact on Mars: Evidence for an ancient water/mud ocean and long-wavelength topographic readjustments // *Planetary Space Sci.* 2017. V. 144. P. 49–70.
- [6] Ivanov M.A., Hiesinger H., Erkeling G., Reiss D. Mud volcanism and morphology of impact craters in Utopia Planitia // *Icarus*. 2014. V. 228. P. 121–140.
- [7] Ivanov M.A., Hiesinger H., Erkeling G., Reiss D. Evidence for large reservoirs of water/mud in Utopia and Acidalia Planitiae on Mars // *Icarus*. 2015. V. 248, P. 383–391.
- [8] Parker T.J., Gorsline D.S., Saunders R.S., Pieri D.C., Schneeberger D.M. Coastal geomorphology of the Martian northern plains // *Journ. Geophys. Res.* 1993. V. 98, P. 11061–11078.
- [9] Hiesinger H., Head J.W. Characteristics and origin of polygonal terrain in southern Utopia Planitia, Mars: Results from Mars Orbiter Laser Altimeter and Mars Orbiter Camera data // *Journ. Geophys. Res.* 2000. V. 105, P. 11999–12022.
- [10] Barlow N.G., Boyce J.M., Costard F.M., et al. Standardizing the nomenclature of Martian impact crater ejecta morphologies // *Journ. Geophys. Res.* 2000. V. 105, P. 26733–26738.
- [11] Tanaka K.L., Skinner J.A., Hare T.M., et al. Resurfacing history of the northern plains of Mars based on geologic mapping of Mars Global Surveyor data // *Journ. Geophys. Res.* 2003., V. 108, doi:10.1029/2002JE001908.

AIR SHOCK WAVE TRACES ON MARS

B.A. Ivanov

Institute for Dynamics of Geospheres, Russian Academy of Science, Leninsky Prospect 38-1, Moscow, Russia, 119334, baivanov@idg.chph.ras.ru

Keywords:

Mars, impact craters, atmospheric shock waves, dust, HiRIse.

Introduction:

Atmospheric shock waves (ASW) generated by high velocity entry of small meteoroids are well known phenomenon — see, for example, the recent Chelyabinsk meteorite fall [1]. The rarified Martian atmosphere is able to fragment small meteoroids, as well as to support ASW generation and propagation. High resolution HiRISE images of new impact craters on Mars in many cases revealed dark “fresh” dusty halo around craters, as well as albedo/color contrast curved strips near craters [2] named “parabola” and “scimitar” (Fig. 1). The most spectacular case has been analyzed in [3], where the air shock waves were proposed as the most probable cause of the elongated curved “scimitar”. The analysis [4] supports that the impact-related ASW a most probable mechanism of halo’s formation. We assume that two kinds of ASW could act: 1) the ballistic “sonic boom” formed during meteoroid’s flight through the atmosphere, 2) the spherical (quazi-spherical) “blast” ASW, driven by fast impact products injected to the atmosphere at the moment of meteoroid’s collision with the surface. ASW could mobilize the near surface dust creating a concentric halo [4], and strips along the trace of two colliding shock fronts [2].

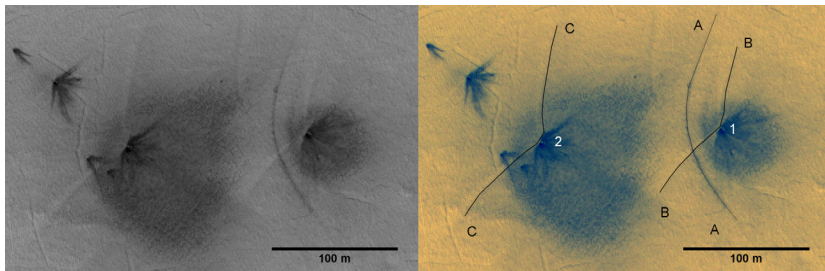


Fig. 1. A fragment crater’s cluster (ESP_022299_2040) where ~ 33 craters occupy an ellipse $\sim 1000 \times 200$ m (left-b/w image, right-stretched color image with outlined features). Craters 1 and 2 have diameters of ~ 4 and 2.5 m. The parabola A-A could be traced up to ~ 100 m from the crater 1 ($\sim 25 D$). Scimitars B-B (attached to the crater № 1) and C-C (attached to the crater № 2) are visible up to 100 m from “parent” craters ($\sim 25 D$ for № 1 and $\sim 40 D$ for № 2). The cluster is formed between December 2002 and March 2008, imaged in April 2011 (https://www.uahirise.org/ESP_022299_2040). The cluster is 6 ± 3 years old.

The idea to visualize shock wave passage along the dusted (sooty) surface has been proposed and tested by Ernst Mach [5]. Using sooty glass Ernst Mach found the irregular air shock wave reflection, known today as Mach reflection. Here we present some new thoughts about air blast generation by impacts in a tiny Martian atmosphere, illustrated with a reconnaissance numerical modeling of the process.

ASW impact efficiency:

The strength of ballistic shock waves may be estimated for known meteoroid’s diameter, its entry velocity, and possible ablation and deceleration [6]. The intensity of a spherical blast wave due to cratering impacts is poorly known. We find only one experimental paper with direct measurements of a laboratory impact ASW [7], where the air shock blast corresponded to an explosion with energy $\sim 1.7\%$ of the impact kinetic energy (KE). P. Schultz [8] estimated the energy of expanding impact vapors in a range of 1% to 20% of KE.

To constrain the minimum impact ASW efficiency we use the numerical modeling where a rocky projectile fly through the atmosphere (ideal gas CO_2) and collide the rocky surface (Fig. 2). The air shock wave front motion is compared with theoretical results for point source explosion, and the effective energy of this explosion serves as a proxy for the impact ASW efficiency.

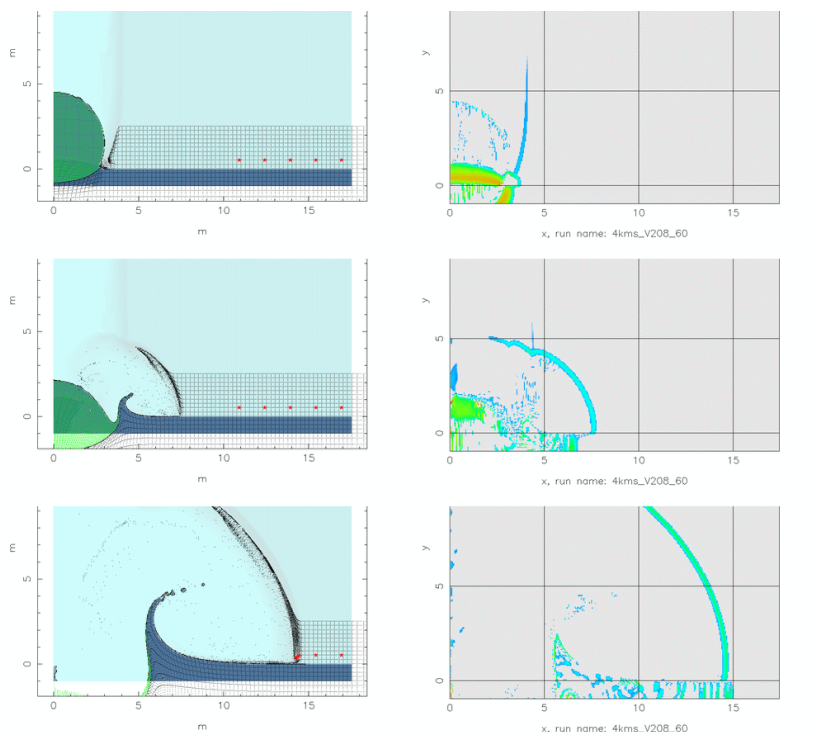


Fig. 2. Selected time moments of the vertical impact of a sphere ($D_{pr} = 6\text{m}$) with the velocity of $4\text{ km}\cdot\text{s}^{-1}$ after the passage through the Martian atmosphere (up to down: 0.4, 1.0, and 2.5 ms after the first touch). Left column—density, right column — artificial viscosity, outlining air shock wave fronts. The lower part of the computational grid is covered with Lagrangian massless tracers. The visible gridat left panels is formed with plotting of each 5th row and each 5th column.

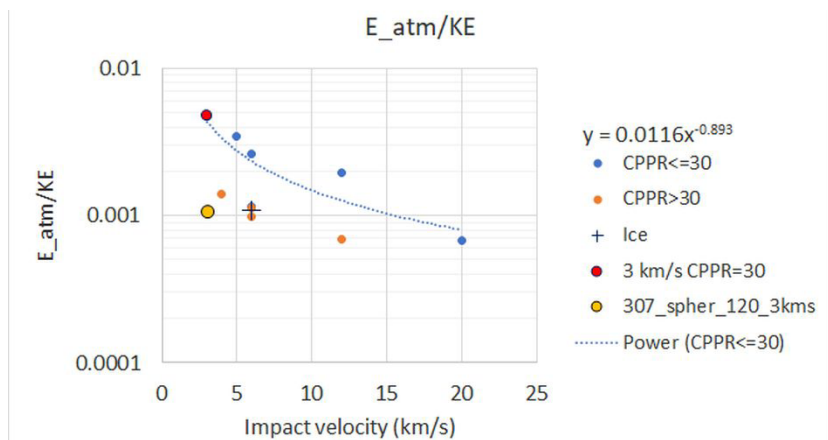


Fig. 3. The ratio of energy of an equivalent atmospheric point explosion to the kinetic energy of a projectile for a range of impact velocities and spatial resolutions.

The modeling shows that the efficiency decreases as the impact velocity increases (Fig. 3). The problem of a spatial resolution is not still resolved,

and we see that the efficiency decreases factor of 4 when we compare the projectile of 30 computational grid cells per radius (CPPR) and model runs with CPPR = 100. Anyway, we can conclude that for a vertical impact in the Martian atmosphere the spherical air blast wave may be estimated with the point source solution with the source energy equal to 0.1 % to 0.4% KE.

The obtained result allows us to estimate shock wave intensity and duration at maximal distances where we see crater related haloes, parabolas, and scimitars. These estimates are necessary for the further analysis of Martian ASW collision, regular and irregular reflection and refraction. The quantitative knowledge of ASW pressures and durations could help to interpret dust layering around fresh impact sites.

Conclusion:

We estimate that a minimal efficiency of a quazi-spherical air shock wave in the Martian atmosphere is in the range of 0.1 % to 0.5 % of KE. The efficiency could be enhanced for oblique impacts and the volatile presence near the surface.

Acknowledgments:

The work is supported within the Russian Academy of Science project "Origin and evolution of Space studied with telescopic observations and space missions" (the former Program 28 and Program 12).

References:

- [1] Popova O.P., Jenniskens P., Emel'yanenko V. and 52 others. Chelyabinsk Airburst, Damage Assessment, Meteorite Recovery, and Characterization // *Science*. 2013. V. 342 (6162). P. 1069–1073.
- [2] Ivanov B.A., Melosh H.J., McEwen A.S. New Small Impact Craters in High Resolution HiRISE Images—III // 41st Lunar and Planetary Science Conference. 2010. Abs. #2020.
- [3] Burleigh K.J., Melosh, H.J., Tornabene, L.L., Ivanov, B., McEwen, A.S., Daubar, I.J. Impact airblast triggers dust avalanches on Mars // *Icarus*, 2012. V. 217. P. 194–201.
- [4] Bart G.D., Daubar I., Ivanov B.A., Dundas C.M., McEwen A.S. Dark halos produced by current impact cratering on Mars // *Icarus*. 2019. P. 45–57.
- [5] Reichenbach H. Contributions of Ernst Mach to Fluid Mechanics // *Annual Review of Fluid Mechanics*. 1983. V. 15. P. 1–29.
- [6] Ivanov B.A., Melosh H.J., McEwen A.S., New Small Craters in High Resolution HiRISE Images — IV // 45th Lunar and Planetary Science Conference. 2014, abs. #1812.
- [7] Gee D.J., Reinecke W.G., Levinson S.J. Blast phenomena associated with high-speed impact // *International Journal of Impact Engineering*. 2007. V. 34. P. 178–188.
- [8] Schultz P.H. Effect of impact angle on vaporization // *Journal of Geophysical Research*. 1996. V. 101. P. 21117–21136.

EFFECT OF AEROSOL SCATTERING ON RADIATIVE TRANSFER IN THE CO₂ AND CO INFRARED BANDS IN THE DAYTIME MARTIAN ATMOSPHERE UNDER BREAKDOWN OF VIBRATIONAL LTE

V.P. Ogibalov, G.M. Shved

Department of Atmospheric Physics, St.Petersburg State University, Ulyanovskaya st. 1, St.Petersburg-Petrodvorets, 198504 Russia, vpo563@mail.ru;

Keywords:

Radiative transfer, planetary atmospheres, aerosols, Mars, non-LTE, molecular bands, carbon dioxide

Introduction:

The Martian atmosphere consisting of almost 95 per cent carbon dioxide has a relatively low density. Therefore, the rarity of molecular collisions, on the one hand, and the high rate of excitation of the vibrational states of the CO₂ and CO molecules due to the absorption of solar radiation in the near-infrared (NIR) spectral range of ~1.05–5 μm, on the other hand, result in the breakdown of the Boltzmann distribution in values of the concentrations (populations) of the vibrational states of these molecules. By another words, the breakdown of the local thermodynamic equilibrium (LTE) over the vibrational degrees of freedom of these molecules (vibrational non-LTE) takes place. The altitude of the level in the Martian atmosphere, lower which one needs to take into account for the vibrational non-LTE effects when assessing the populations of vibrational states of the CO₂ and CO molecules, varies depending on the wavelengths of the fundamental band (FB) in which the excitation of these states by absorption of the solar NIR radiation from the molecular ground state takes place. Thus, these altitude levels may even descend to the planet's surface for vibrational states of the main isotopologue ¹²C¹⁶O₂ (or 626, in the HITRAN notification) which are excited by solar radiation in the ro-vibrational (R-V) transitions of the CO₂ molecule with the wavelengths shorter than 1.6 μm.

Since the Martian atmosphere is sufficiently rarified already at the surface, the breakdown of vibrational local thermodynamic equilibrium (LTE) for the CO₂ and CO molecules starts in the daytime from the troposphere. As the Mars lower atmosphere is dusty, the scattering of infrared solar radiation by aerosols should affect the vibrational state populations of these molecules. The problem of radiative transfer in the ro-vibrational molecular bands under condition of local thermodynamic equilibrium breakdown in a planetary atmosphere is generalized for the case taking into account the extinction (i.e. scattering and absorption) of the continuum radiation produced by aerosols. The method for calculating the non-equilibrium populations of vibrational states of gas molecules in the planetary atmospheres is developed. The report presents the first results of modeling the radiative transfer under non-LTE conditions in the CO₂ and CO bands in the wavelength range of 1–5 μm, taking into account the radiation scattering by aerosols.

Methodology:

In the papers [1, 2], the radiative transfer problem for the R-V bands of CO₂ and CO molecules with accounting the vibrational LTE breakdown in the Martian atmosphere has been solved by using the technique of Accelerated Lambda Iterations (ALI) which allows to find out effectively the non-equilibrium values of the populations of the CO₂ vibrational states [3].

The model takes into account for the 206 vibrational states of 7 isotopologues of CO₂ molecule (the most high excited state included into the model is the 20031 vibrational state of the molecule ¹²C¹⁶O₂ with the energy of the order of 9500 cm⁻¹) and the 8 vibrational states of 2 isotopologues of CO molecule (the most high state is the one excited four times in the fundamental

stretch mode). In total the 555 vibrational transitions numbering about 64200 R-V lines within the spectral range of $1.05\div 15\ \mu\text{m}$ are considered. The spectroscopic parameters of the R-V lines of the CO_2 and CO molecules (the frequency, intensity, and Lorentz half-width) are taken from the HITRAN database. The abundances of isotopologues of the CO_2 and CO molecules correspond to the terrestrial ones. The intensities of extraterrestrial solar radiation correspond to the mean distance of Mars from the Sun, 1.52 AU.

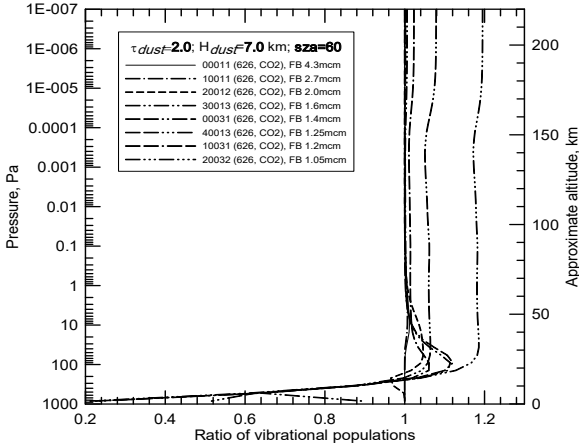


Fig. 1. The ratio of some vibrational states (according to the nomenclature of the HITRAN database) of the main isotopologue $^{12}\text{C}^{16}\text{O}_2$ for the case of the presence of aerosols (model parameters $\tau_{\text{dust}}=2.0$ and $H_{\text{dust}}=7.0\ \text{km}$) in the Martian atmosphere to such populations obtained for the case of aerosol absence. Conditions: Lambertian surface albedo for bright areas [5]; $\varphi=70\text{N}$, $\lambda=45\text{E}$, local time $t=12\text{h}$, $L_s=90^\circ$, solar zenith angle $\text{SZA}=60^\circ$. In the legend, the most optically thick fundamental ro-vibrational transition (FB) within the corresponding CO_2 band is shown.

Atmospheric and aerosol optical models:

The models of the Martian atmosphere and its composition were borrowed from the Mars Climate Database (Version 5.2) [4].

Reflective properties of the surface of Mars correspond to those for orthotropic (Lambertian) one with the spectral dependence of the surface albedo λ_{surf} borrowed from the paper [5].

To explore qualitatively the effects on the values of the non-equilibrium populations of the CO_2 and CO molecules when accounting for the aerosol scattering of radiation, the simple model of aerosols in the Martian atmosphere from the study [6] has been supplemented. The vertical profile of concentration of the aerosol particles was assumed to be exponential with the height scale H_{dust} . The concentration of aerosols at the surface of Mars is determined by the value τ_{dust} of the total optical depth of the Martian aerosol. The phase function of aerosol particles is supposed to be of Henyey-Greenstein type with parameter g . The spectral dependence both of values g and the values of the aerosol single-scattering albedo λ_{dust} are borrowed from the paper [7].

Results:

The presented results correspond mainly to the conditions of $j=70^\circ\text{N}$, $l=45^\circ\text{E}$, solar longitude $L_s=90^\circ$, local time $t=12\text{h}$. The values of λ_{surf} correspond to the ones for bright areas [5]. Thus, the input parameters are the values: τ_{dust} at the wavelength $\lambda=0.55\ \text{mcm}$, height scale H_{dust} , and solar zenith angle SZA .

It is convenient for presenting the results of numerical modeling the values

n_l , it was chosen the ratio $\rho_l^d(z) = \frac{n_l^{\text{dust}}(z)}{n_l^{\text{no-dust}}(z)}$, where $n_l^{\text{dust}}(z)$ is the population of the vibrational states of molecules calculated with accounting

for the interaction of radiation with aerosols, $n_l^{\text{no-dust}}(z)$ is the population of the vibrational states obtained for the case of absence of aerosols in the Martian atmosphere (examples are given in Fig. 1, 2).

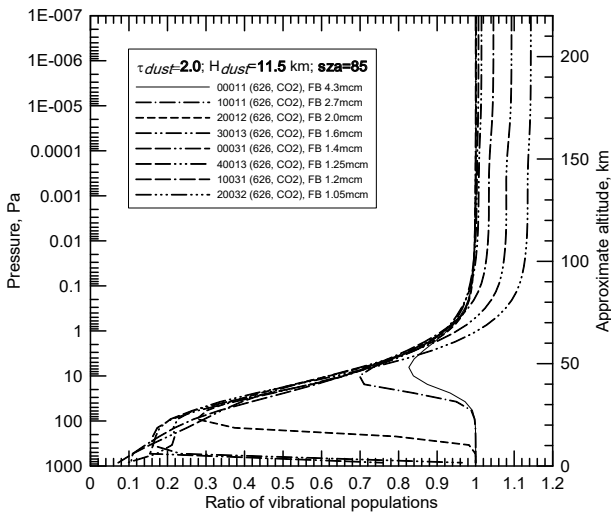


Fig. 2. The same as in the Figure 1 but for the aerosol model parameters $\tau_{dust}=2.0$ and $H_{dust}=11.5$ km, and solar zenith angle SZA=85°.

Conclusions:

The populations were studied depending on the optical thickness both of the aerosol layer and of the bands, the vertical distribution of aerosols, the solar zenith angle, and the aerosol parameters describing the scattering and absorption of radiation. The weaker the band, the stronger the aerosol effect on a population. This effect manifests as an increase and a decrease in population above and below a certain altitude level, respectively.

References:

- [1] Ogibalov V.P., Shved G.M. An improved model of radiative transfer for the NLTE problem in the NIR bands of CO₂ and CO molecules in the daytime atmosphere of Mars. 1. Input data and calculation method // *Solar Syst. Res.* 2016. V. 50. No. 5. P. 316–328. doi:10.7868/S0320930X16050042.
- [2] Ogibalov V.P., Shved G.M. An improved model of radiative transfer for the NLTE problem in the NIR bands of CO₂ and CO molecules in the daytime atmosphere of Mars. 2. Population of vibrational states // *Solar Syst. Res.* 2017. V. 51. No. 5. P. 373–385. doi:10.1134/S0038094617050070.
- [3] Kutepov A.A., Gusev O.A., Ogibalov V.P. Solution of the non-LTE problem for molecular gas in planetary atmospheres: Superiority of the accelerated lambda band iteration // *J. Quant. Spectrosc. Radiat. Transfer*, 1998. V. 60. No. 2. P. 199-220.
- [4] <http://www-mars.lmd.jussieu.fr/mars/access.html>.
- [5] Erard S.A spectro-photometric model of Mars in the near-infrared // *Geophys. Res. Lett.* 2001. V. 28. P. 1291–1294.
- [6] Ogibalov V.P. Radiative Transfer in the near-infrared CO₂ bands taking account of continuum absorption by aerosol particles in the Martian atmosphere // *Vestnik of St. Peterburg Univ. (Series 4)*. 2008. V. 3, P. 27-36.
- [7] Ockert-Bell M.E., J.F. Bell III, J.B. Pollack, C.P. McKay, Forget F. Absorption and scattering properties of the Martian dust in the solar wavelengths // *J. Geophys. Res., Planets*, 1997. V. 102. P. 9039–9050.

THE MARTIAN ATMOSPHERIC DUST DYNAMIC THROUGH FRACTIONAL DIFFERENTIAL MODELS AND SIMULATIONS

M.P. Velasco¹, D. Usero², S. Jiménez¹, J.L. Vázquez-Poletti², L. Vázquez²

¹ Universidad Politécnica de Madrid, mp.velasco@upm.es, s.jimenez@upm.es;

² Universidad Complutense de Madrid;

umdavid@mat.ucm.es, jlvazquez@fdi.ucm.es, lvazquez@fdi.ucm.es

Keywords:

Dust, Solar Radiation, Fractional Calculus, Mittag-Leffler functions, Fractional Ordinary and Partial Differential Equations, Cloud Computing.

Introduction:

The dust storms are very frequently seen features of Mars and they play an important role in governing the climate of Mars [1, 2]. For instance, the global storms alter the planet's total heat balance, promote variations in seasonal frost formation and dissipation, and greatly affect the distribution of water vapour.

One of the effects of the atmospheric dust is the solar radiation scattering. This is a complex phenomenon, which depends on many space and time scales associated to the concentration, distribution and size of the dust as well as the radiation wavelength. The theory of radiative transfer establishes that the attenuation of the solar radiation traversing the atmosphere due to the dust aerosols is modeled by the Lambert-Beer-Bouguer law, where the aerosol optical thickness plays an important role. Through Angstrom law [3], the aerosol optical thickness can be approximated as a second order moment of a non-ordinary diffusive process. This dynamic is governed by different-time/space scales and, thus, it is natural to think about diffusive integro-differential equations to describe a better modeling [4, 6].

By continuing the work started in [7, 9], we define fractional diffusion models to obtain a more accurate model of the attenuation of the solar radiation traversing the atmosphere and we obtain information of higher order moments, which is relevant to understand the atmospheric dynamic. We discuss some questions of the model: interpretation of variables, statement of initial and boundary conditions, analytic and numerical solutions in one and three space dimensions, and computational simulations vs observational data. Furthermore, our objective is to apply these models in the context of the development of the sensors of Universidad Carlos III de Madrid, and to deal possible experiments in the Planetary Atmosphere and Surface Chamber of the Astrobiology Center.

Acknowledgements:

The authors thank to the support of MINECO of Spain, through the projects ESP2016-79135-R, TIN2015-65469-P.

References:

- [1] Cachorro V.E., de Frutos A.M., Casanova J.L. Determination of the Angstrom turbidity parameters // *Applied Optics*. 1987.V. 26. No. 15. P. 3069–3076.
- [2] Córdoba C., Vázquez L. Characterization of atmospheric aerosols by an in-situ photometric technique in planetary environments // In Bearman G.H., Beauchamp P.M. (eds.). *First Jet Propulsion Laboratory In Situ Instruments Workshop*. SPIE. 2003. V. 4878.
- [3] Angstrom A. On the atmospheric transmission of sun radiation and on dust in the air // *Geografiska Annaler*. 1929. V. 11. P. 156-166.
- [4] Diethelm K. *The analysis of fractional differential equations*. Springer, 2010.
- [5] Kilbas A.A., Srivastava H.M., Trujillo J.J. *Theory and Applications of Fractional Differential Equations*. Elsevier, 2006.
- [6] Zaslavsky G.M., Baleanu D., Tenreiro J.A. *Fractional Differentiation and its Applications*. *Physica Scripta*, 2009.
- [7] Velasco M.P., Usero D., Jiménez S., Aguirre C., Vázquez L. Mathematics and Mars Exploration // *Pure and Applied Geophysics*. 2015. V. 172. No. 1. P. 33–47.

- [8] Velasco M.P., Usero D., Jiménez S., Vázquez-Poletti J.L., Vázquez L. Modeling and simulation of the atmospheric dust dynamic: Fractional Calculus and Cloud Computing // International Journal of Numerical Analysis and Modeling. 2018. V. 15. No. 1–2. P. 74-85.
- [9] Velasco M.P., Usero D., Jiménez S., Vázquez-Poletti J.L., Vázquez L. Fractional diffusion models for the atmosphere of Mars // Fractal and Fractional. 2018. V. 2. No. 1.

LOOKING BACK AT MARS 50 YEARS: MARINIER MARS 1969 IMAGING

T.C. Duxbury¹, N.V. Seregina²

¹ *Physics and Astronomy Department, George Mason University, Fairfax, Virginia, 22030, USA, tduxbury@gmu.edu;*

² *Physics and Astronomy Department, George Mason University, Fairfax, Virginia, 22030, USA, mars1e@yahoo.com*

Keywords:

Mars, Mariner 1969, Imaging.

Introduction: The Far and Near Encounter images from the Mariner 6 and 7 spacecraft on the Mariner Mars 1969 Mission have been restored. In addition, new NAIF SPICE kernels have been created, making this archive fully useable using today's SPICE-based image processing. The images [1] view the surface of Mars 50 years ago, including some of today's landing sites. The restored archive is found at:

http://pds-geosciences.wustl.edu/missions/mariner/duxbury_mariner69.htm

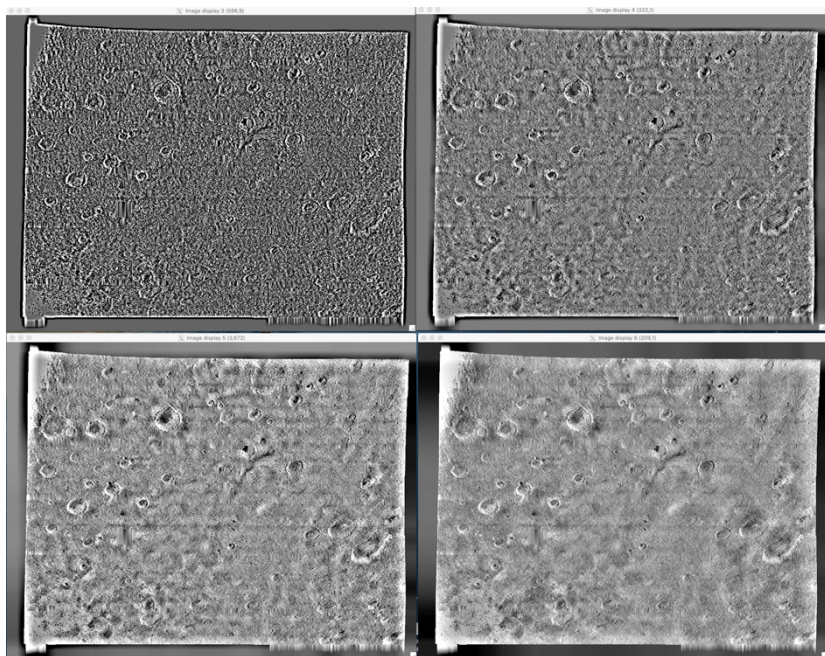


Fig. 1

References:

- [1] R.B. Leighton, B.C. Murray, One Year's Processing and Interpretation – An Overview, JGR, 10 January 1971, V. 76, No. 2, P. 293–296.

MEASUREMENTS OF THE MARTIAN CRUST MAGNETIZATION 25 YEARS BEFORE ITS DISCOVERY

M.I. Verigin ¹, G.A. Kotova ¹, J.A. Slavin ²

¹ Space Research Institute of Russian Academy of Sciences, Moscow 117997, Profsoyuznaya 84/32, Russia. verigin@iki.rssi.ru kotova@iki.rssi.ru

² University of Michigan, Ann Arbor, MI, USA. jaslavin@umich.edu

Keywords:

Mars 3 orbiter, Martian crust magnetization, “stagnating” magnetopause, plasmashet heavy ions acceleration processes.

Introduction:

About 45 years ago, in the late 1971, Mars 3 spacecraft was placed into orbit around Mars. On January 21, 1972 this orbiter recorded strong (~ 27 nT) and regular magnetic field in the vicinity of its closest (~ 1500 km) approach to the day side of the planet. This observation was originally interpreted by Dolginov et al. [1] and Gringauz et al. [2] as an evidence of planetary dipole magnetic field. Later Russell [3] qualified the same observations in terms of magnetic field draped over the Martian obstacle. After analyzing the data of early planetary missions, Slavin & Holzer [4] concluded that “Mars most probably possesses a small intrinsic field magnetosphere”. Subsequent Mars 5, Phobos 2, MGS, MEX, MAVEN and other missions revealed many exclusive features of complicated Martian magnetosphere, and clarified an essential role in its formation of multipole magnetic field of planetary crust and planetary atmosphere.

Earlier Mars 3 data will be revisited in the present paper. It will be shown that this orbiter observed strong and regular magnetic field exactly above the region of the strongest magnetization of the Martian crust in the southern hemisphere of the planet revealed by Acuña et al. [5] according to MGS measurements. Magnetic field and plasma measurements from Mars 3 are compared with those of MGS to provide evidences that Mars 3 really detected the magnetic field of Martian crust in the early 1972 about 25 years before MGS.

Reanalysis of Mars 3 measurements:

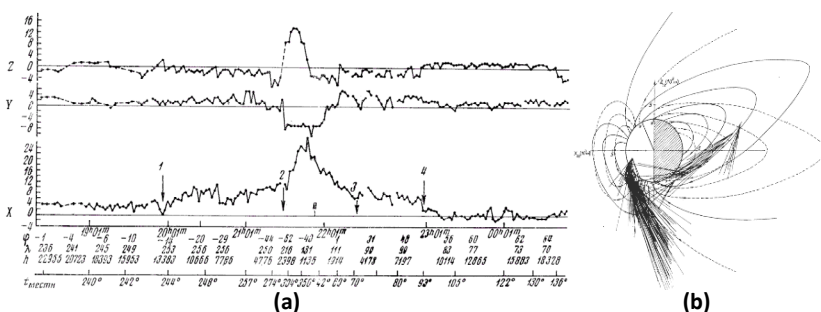


Fig. 1. Magnetic field measurements aboard Mars 3 on Jan. 21, 1972 (a) and its interpretation as inclined planetocentric dipole (b).

Fig. 1a[1] presents results of flux gate magnetometer aboard Mars 3 orbiter on Jan. 21, 1972. During this period the orbiter first crossed the bow shock (1), then twice crossed the magnetopause (2, 3) and exited to solar wind after final bow shock crossing (4). The strongest (~ 27 nT) and regular magnetic field was measured in the vicinity of the closest approach (~ 1500 km) by Mars 3 to the day side of the planet. These measurements were originally interpreted as an evidence of planetary dipole magnetic field $M_m = 2.4 \times 10^{22}$ G cm^3 (Fig. 1b, [6]). Later Russell [3] draw a conclusion that “observed magnetic field was draped over the Martian obstacle as expected if the field were

simply shocked and compressed solar wind magnetic field." Their deduction looksto be inconsistent with magnetic field direction (Fig. 2, multiple black lines) to those one expected for simple draping (Fig. 2, blue line) in the closest approach region, marked in Fig.2 by orange arrows. After analysis of early Mars 2, 3, 5 planetary mission data Slavin&Holzer[4]accepted theexistence of small intrinsic field in Martian magnetosphere.

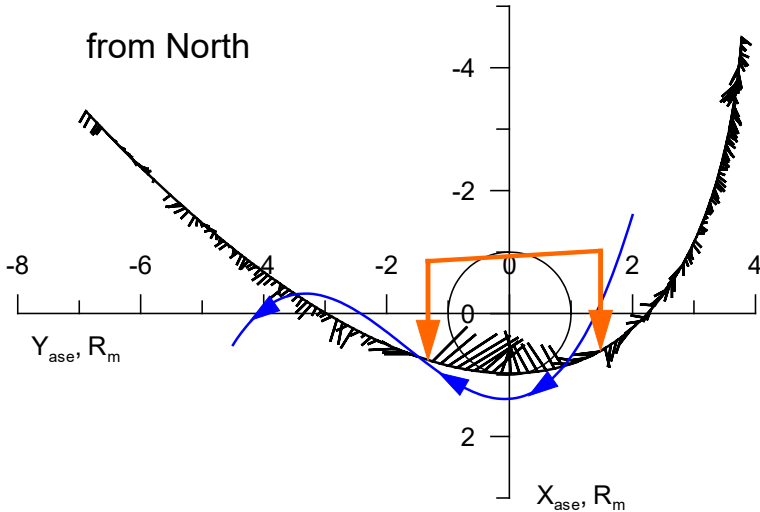


Fig. 2. Projection of magnetic field measurements aboard Mars 3 on Jan. 21, 1972 taken from Fig. 1 onto (X_{ase}, Y_{ase}) plane.

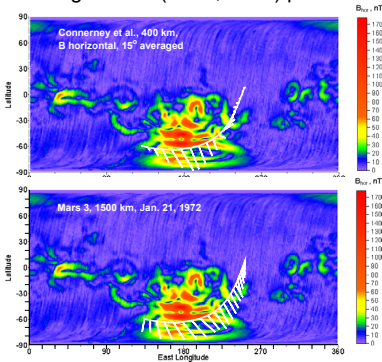


Fig. 3. Comparison of MGS and Mars 3 magnetic field observations above the same planetary region.

Color plates in Fig. 3a,b are taken from [7] and are representing complicated distribution of Martian crust magnetic field horizontal component at 400 km above planetary surface as deduced from MGS measurements. Smooth white lines in Fig. 3a,b are projection of closest approach region of Mars 3 orbit onto planetary surface. White arrows in Fig. 3a are 150 averaged MGS magnetic field horizontal component and white arrows in Fig. 3b are the same component from Mars 3 magnetic field measurements. It is obvious that Mars 3 orbiter observed strong and regular magnetic field exactly above the region of the strongest magnetization of the Martian crust in the southern hemisphere of the planet revealed by MGS measurements, and that directions of magnetic field over both orbiters data are in close correspondence to each other. Thus Mars 3 really detected the magnetic field of Martian crust in the early 1972 about 25 years before MGS. Unquestionably, Mars 3 observations were not properly interpreted before MGS crustal magnetization discovery.

Discussion:

Solar wind ram pressure during Mars 3 magnetic field measurements can be evaluated with the aid of IMP 6 Earth's orbiter and Mars 3 electron spectra observations. In this period, heliocentric distances to the Earth and Mars were 0.98 a.u. and 1.49 a.u., respectively, while the Earth was ahead of Mars by 62.40. Thus, with the velocity of 455 km/s (IMP 6) the solar wind emitted from the certain place of the solar corona reaches Mars 2.8 days earlier than the Earth. Taking into account proper radial scaling, the ram pressure at Mars can be evaluated as 0.4 nP. Thus, magnetic field of Martian crust observed by Mars 3 can reliably stagnate/deflect impacting solar wind.

It is worth mentioning that above Mars 3 magnetic field measurements were realized at low solar wind ram pressure conditions: $0.4 \text{ nP} < 2 \text{ (} 0.98/1.49 \text{)}^2 \sim 0.9 \text{ nP}$ when effect of Martian core magnetization can prevail in solar wind deflection around planet. On the other case, under high solar wind ram pressure conditions planetary ionosphere effects can prevail in solar wind deflection around Mars. What is the ram pressure margin between the two prevailing effects?

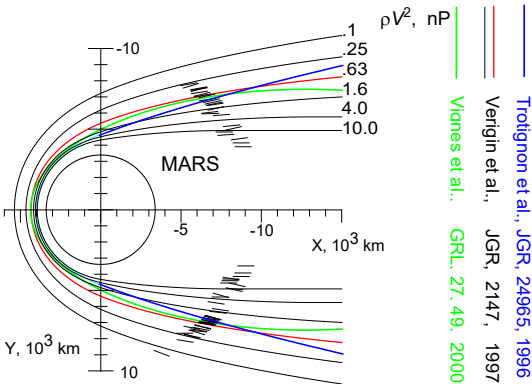


Fig. 4. Comparison of different Martian magnetopause models.

topause when the ram pressure increases to values $> 0.6 \text{ nP}$ when planetary ionosphere effects start to prevail in solar wind deflection around Mars [8]. The same $\sim 0.6 \text{ nP}$ margin separates different prevailing processes of oxygen

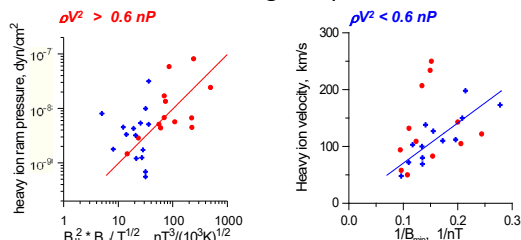


Fig. 5. Solar wind ram pressure 0.6 nP is the margin that separates different prevailing processes of oxygen ion acceleration in the plasmashet of Martian magnetotail: magnetic field lines stress acceleration (left panel) and cross tail electric field acceleration (right panel).

are prevailing in solar wind deflection around Mars [9]. When solar wind ram pressure $< 0.6 \text{ nP}$ (blue points in Fig. 5) heavy ion velocity in the Martian plas-

masheet correlates with $\frac{1}{B_{\min}}$ (right panel in Fig. 5) thus implying that in this

case plasmashet heavy ions gain energy via cross tail electric field and planetary magnetic field is prevailing in solar wind deflection around Mars.[9].

Conclusions:

- Mars 3 data (Dolginov et al. [1], Gringauz et al. [2]) are revisited in the present talk. It is shown that this orbiter observed strong and regular magnetic field exactly above the region of the strongest magnetization of the Martian crust in the southern hemisphere of the planet found by Acuña et al. (1998) by MGS data.
- Magnetic field directions by both Mars 3 and MGS measurements are in close correspondence to each other. Thus Mars 3 really detected the magnetic field of Martian crust in 1972 about 25 years before MGS.
- There are two different regimes of solar wind flow around Mars. At low solar wind ram pressure conditions $< 0.6 \text{ nP}$ the effect of Martian core magnetization prevails in solar wind deflection around planet,

Fig. 4. [8] presents variation of the shape of the Martian magnetopause modeled according to the Phobos 2 data with increase of solar wind ram pressure (red and black lines). The short lines are centered on the individual magnetopause crossings and they are inclined to the X axis at their deduced flaring angles. The specific feature of the models is the "stagnation" of the subsolar magne-

topause when the ram pressure increases to values $> 0.6 \text{ nP}$ when planetary ionosphere effects start to prevail in solar wind deflection around Mars [8]. The same $\sim 0.6 \text{ nP}$ margin separates different prevailing processes of oxygen ion acceleration in the plasmashet of Martian magnetotail. When solar wind ram pressure $> 0.6 \text{ nP}$ (red points in Fig. 5) heavy ion ram pressure in the Martian plasmashet correlates with (left panel in Fig. 5) thus implying that in this case heavy ions gain energy via magnetic field line stress acceleration process and planetary ionosphere effects are prevailing in solar wind deflection around Mars [9]. When solar wind ram pressure $< 0.6 \text{ nP}$ (blue points in Fig. 5) heavy ion velocity in the Martian plas-

masheet correlates with $\frac{1}{B_{\min}}$ (right panel in Fig. 5) thus implying that in this case plasmashet heavy ions gain energy via cross tail electric field and planetary magnetic field is prevailing in solar wind deflection around Mars.[9].

Conclusions:

- Mars 3 data (Dolginov et al. [1], Gringauz et al. [2]) are revisited in the present talk. It is shown that this orbiter observed strong and regular magnetic field exactly above the region of the strongest magnetization of the Martian crust in the southern hemisphere of the planet found by Acuña et al. (1998) by MGS data.
- Magnetic field directions by both Mars 3 and MGS measurements are in close correspondence to each other. Thus Mars 3 really detected the magnetic field of Martian crust in 1972 about 25 years before MGS.
- There are two different regimes of solar wind flow around Mars. At low solar wind ram pressure conditions $< 0.6 \text{ nP}$ the effect of Martian core magnetization prevails in solar wind deflection around planet,

the magnetosphere is compressible, and plasmashet heavy ions gain energy via cross tail electric field.

- At high solar wind ram pressure conditions > 0.6 nPMartian magnetopause subsolar part is “stagnating”, and plasmashet heavy ions gain energy via magnetic field line stress acceleration.
- Mars 3 magnetic field measurements were realized at low solar wind ram pressure conditions < 0.6 nP when effect of Martian core magnetization prevails in solar wind deflection around planet.

Acknowledgements:

The paper completed over the general NIR plan of IKI RAN with partial support of program № 12 PRAN.

References:

- [1] Dolginov Sh. Sh., Yeroshenko E.G., Zhuzgov L.N. Magnetic field in the close vicinity of Mars by Mars 2 and Mars 3 orbiter measurements // *Doklady AN SSSR*. 1972. V. 207. No. 6. P. 1296–1299.
- [2] Gringauz K.I., Bezrukikh V.V., Breus T.K., Verigin M.I., Volkov G.I., Dyachkov A.V. Solar plasma studies around Mars and at Earth-Mars trajectory by charged particle traps aboard soviet spacecraft of 1971–1973 years. 2. Characteristics of electrons along orbits of Mars 2 and Mars 3 Martian orbiters // *Kosm. Issled.*, 1974. V. 12. No. 4. P. 585–599.
- [3] Russell C.T. The magnetic field of Mars: Mars 3 evidence reexamined // *Geophys. Res. Letters*. 1978. V. 5. No. 1. P. 81–84.
- [4] Slavin J.A., Holzer R.E. The solar wind interaction with Mars revisited // *J. Geophys. Res.* 1982. V. 87. No. B12. P. 10285–10296.
- [5] Acuña M.H., Connerney J.E.P., Wasilewski P., Lin R.P., Anderson K.A., Carlson C.W., McFadden J., Curtis D.W., Mitchell D., Rème H., Mazelle C., Sauvaud J.A., d’Uston C., Cros A., Medale J.L., Bauer S.J., Cloutier P., Mayhew M., Winterhalter D., Ness N.F. Magnetic field and plasma observations at Mars: Initial Results of the Mars Global Surveyor mission // *Science*. 13 March 1998. V. 279. No. B12. P. 1676–1680.
- [6] Dolginov Sh. Sh., Yeroshenko Ye.G., Zhuzgov L.N. The magnetic field of Mars according to the data from the Mars 3 and Mars 5 // *J. Geophys. Res.* 1976. V. 81. No. 19. P. 3353–3362.
- [7] Connerney J.E.P., Acuña M.H., Wasilewski P.J., Kletetschka G., Ness N.F., Rème H., Lin R. P., Mitchell D.L. The global magnetic field of Mars and implications for crustal evolution // *Geophys. Res. Letters*. 2001. V. 28. No. 21. P. 4015–4018.
- [8] Verigin M., Kotova G., Shutte N., Remizov A., Szego K., Tatrallyay M., Apathy I., Rosenbauer H., Livi S., Richter A.K., Schwingenschuh K., Zhang T.-L., Slavin J., Lemaire J. Quantitative model of the Martian magnetopause shape and its variation with the solar wind ram pressure based on Phobos 2 observations // *J. Geophys. Res.* 1997. V. 102, No. A2, P. 2147–2156.
- [9] Kotova G.A., Verigin M.I., Remizov A.P., Shutte N.M., Rosenbauer H., Livi S., Riedler W., Schwingenschuh K., Tatrallyay M., Szegö K., Apathy, Heavy ions in the magnetosphere of Mars: Phobos 2/TAUS observations // *Physics and Chemistry of the Earth*. V. 25. No. 1-2. P. 157–160.

MAGNETIC MEASUREMENTS IN TERRESTRIAL ANALOGUES OF MARS

M. Diaz-Michelena¹, **C.R. Kilian**²

¹ *Instituto Nacional de Técnica Aeroespacial (INTA), Madrid 28850, Spain;*

² *University of Trier, Geology, Trier, Germany*

Keywords:

High resolution magnetometry, terrestrial analogues, magnetic signature of geological features.

Mars, as it is the Earth, presents a complex geological map. Its crust has been formed by means of a whole variety of processes and shows different compositions, mineralogies and evolutions, which should provide typical magnetic signature patterns.

Many of the scenarios, which appear on Mars might have representatives on Earth. The investigation of these analogues can be of much help in the interpretation of magnetic data on the surface of Mars.

In the frame of the investigations of Exomars 2020 mission, AMR team has developed a number of scientific surveys of high resolution in different terrestrial analogues.

They comprise results of the magmatic and tectonics in an active continental margin, different craters associated to volcanism or impacts, as well as the result of alteration processes like fluvial valleys, which are the main landing scenarios for the Exomars-2020.

In this work, the team would like to present some of the main results and interpretations derived from the measurements with special attention in Rio Tinto area, considered as analogue of the landing site target. This target, Mawrth valley, is a Northward running valley formed during an early fluvial activity. It is located at 22.3°N, 343.5°E (Oxia Pallus) with an elevation approximately two kilometers below datum. This valley casts low magnetic anomalies from the the satellites due to ist mineralogy with a mixture of fine grained phyllosilicates, silicates as well as iron oxides and hydroxides.

Acknowledgements:

This project has received funding from the European Union's Horizon 2020 research and innovation program under grant agreement No 730041 and the Spanish Programme of Research, Development and Innovation oriented to the challenges of the society under grant ESP2017-88930-R.

NEWTON NOVEL MAGNETIC INSTRUMENT. POTENTIAL APPLICATION TO UNVEIL KEY QUESTIONS AS THE ORIGIN OF MARTIAN MOONS

M. Díaz-Michelena ¹, J.L. Mesa ¹, A. Arlensíu ¹, J. de Frutos ¹, V. González ¹,
C. Aroca Hernández-Ros ², M. Pérez Jiménez ², M. Maicas ², M.M. Sanz ²,
C. Lavín García ³, R. Marante ³, B. Langlais ⁴, R. Kilian ⁵, Ó. Baeza ⁵, F. Ríos ⁵,
M.Á. Rivero ⁶

¹ National Institute for Aerospace Technology, INTA Torrejón de Ardoz, Madrid. Spain,

² Physical Electronics Department, Technical University Madrid, UPM Madrid. Spain,

³ TTI Norte, Santander, Spain,

⁴ Centre National de la Recherche Scientifique — Laboratoire de Planétologie et Géodynamique — (CNRS), France.

⁵ Geology Department, University of Trier, Germany.

⁶ ISDEFE as external consultant at INTA.

Keywords:

Susceptometer, magnetic susceptibility, magnetic measurements, origin of Phobos and Deimos.

The main objective of this contribution is to present the evolution of NEWTON novel magnetic susceptometer for planetary exploration, a state of the art sensor for the measurement of the complex magnetic susceptibility developed in the frame of an EU H2020 funded project [1].

The magnetic susceptibility is a complex parameter dependent on the external magnetic field amplitude, direction and frequency. NEWTON susceptometer has been developed to determine the magnetic susceptibility of rocks and soils, with the capability to determine not only the real part but also the imaginary part of the susceptibility. The NEWTON susceptometer is on an advanced stage of its development and last efforts have been focused on its calibration.

The calibration and validation process for the susceptometer prototype casted very good results in comparison with other commercial and high resolution laboratory devices, reaching a resolution in the order of $\chi = 10^{-4}$ (I.S. Vol. Susceptibility), representative of Earth, Moon and Mars rocks. The critical parts of the prototype have been subjected to different tests, i.e. vibration and TVT, to verify the capability to withstand the hard environmental conditions of interplanetary missions.

His new generation of instruments can play a key role in the unveiling of some unanswered questions in the planetary context as the origin of Phobos and Deimos.

Some works [2,3] suggest that the moons could be accreted within an impact generated disk, which could have formed as well the Borealis basin of Mars.

In the near future, MMx seems to be the mission to explore the Martian moons with a mission including a landing on one of them as well as collection and return of samples to ground.

The mission is very well equipped with powerful scientific instruments, which will be able to image the moon, generate morphologic maps, determine the composition of surface rocks, etc.

In this work we discuss the potential improvement of the scientific investigation which could take place in case that NEWTON instrument would be part of the landing module instrumentation.

Acknowledgements:

This project has received funding from the European Union's Horizon 2020 research and innovation program under grant agreement No 730041 and the Spanish Programme of Research, Development and Innovation oriented to the challenges of the society under grant ESP2017-88930-R.

References:

- [1] M. Diaz Michelena, J.L Mesa Uña, M. Perez Jimenez, M. Maicas Ramos, P. Cobos Arribas, C. Aroca Hernandez-Ros, *Sensors and Actuators, A: Physical*, V. 263, P. 471–479 (2017)
- [2] Hyodo, Ryuki&Genda, Hidenori&Charnoz, Sébastien& Rosenblatt, Pascal. On the Impact Origin of Phobos and Deimos I: Thermodynamic and Physical Aspects. *The Astrophysical Journal*. 2017. V. 845. P. 10.3847/1538–4357/aa81c4.
- [3] Hyodo, Ryuki& Rosenblatt, Pascal &Genda, Hidenori&Charnoz, Sébastien. (2017). On the Impact Origin of Phobos and Deimos II: True Polar Wander and Disk Evolution. *The Astrophysical Journal*. V. 851. 10.3847/1538–4357/aa9984.

SERVERLESS COMPUTING FOR MARS EXPLORATION AND COLONIZATION APPLICATIONS

J.L. Vázquez-Poletti ¹, I.M. Llorente ¹, M. Ruiz-Ramos ², P.J. Pascual ³, M. Ramírez-Nicolás ¹, A. Sanz-Cobena ², S. Jiménez ², A. Rodríguez ^{2,4}, D. Usero ¹, L. Vázquez ¹, V.Yu. Makovchuk ⁵, E.A. Grishakina ⁵, A.A. Belov ⁶, V.S. Cheptsov ^{6,7}, Z.S. Ezhelev ⁶

¹ Universidad Complutense de Madrid (UCM), Spain.

² Universidad Politécnica de Madrid (UPM), Spain.

³ Universidad Autónoma de Madrid (UAM), Spain.

⁴ Universidad de Castilla La Mancha (UCLM), Spain.

⁵ Vernadsky Institute of Geochemistry and Analytical Chemistry, RAS, Moscow, Russian Federation.

⁶ Lomonosov Moscow State University, Moscow, Russian Federation.

⁷ Space Research Institute, RAS, Moscow, Russian Federation.

Keywords:

Mars; ionogram; crop simulation; serverless computing; cloud computing

Introduction:

Cloud computing is a dynamic, elastic and on-demand resource provision solution [1] that starts to be used widely in Space Exploration. The main reason is that budget restrictions and non-dedicated environments prevent the use of in-house solutions (like supercomputers) [2].

Serverless computing represents a new step further, where massive short data-intensive tasks can be executed in almost real time. The user only needs to upload the code and define the events that would trigger the execution.

In this contribution we explain two use cases where Amazon Web Services Lambda serverless framework [3] is being used.

MARSIS ionogram processing:

In the first use case data from the active ionospheric sounding (AIS) experiment from the MARSIS instrument is processed. The objective is to identify magnetic fields to, for instance, study the effects of solar wind and understand dust storms.

Magnetic fields are identified through an image processing algorithm [4]. These images are a result of AIS dataset conversion. Processing times depend on the data file size and range from seconds to a few minutes. The file retrieval pattern prevents relying on a dedicated machine by means of budget.

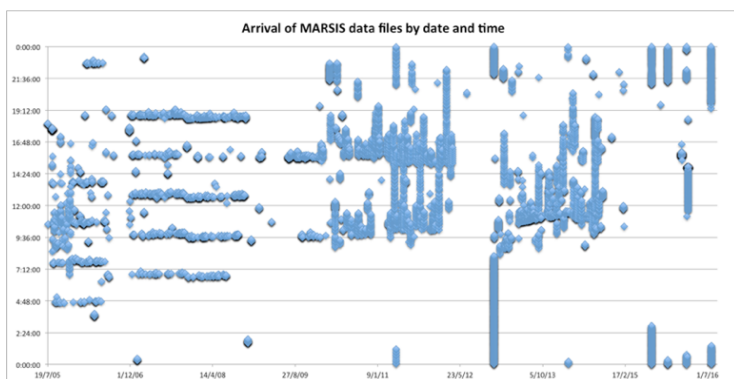


Fig. 1.

In the serverless solution, code for processing the AIS dataset and the resulting images is directly uploaded to AWS Lambda and declared as a service or function. This function, coded in Node.js and acting as a wrapper of a C executable, is triggered every time a file is uploaded to a repository (bucket) hosted by AWS Simple Storage Service [5].

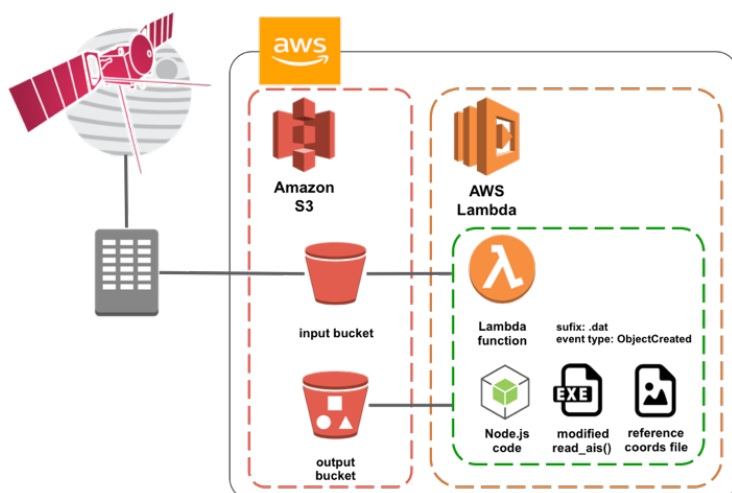


Fig. 2.

This architecture allows parallel processing in almost real time, as a new function is started upon each file arrival. Experimental results show an improvement in both execution time and cost when comparing this solution with a traditional server architecture [6].

Martian crop model simulation:

The second use case deals with the simulation of crops using Martian soil, in order to find the best conditions for future production during colonization efforts.

Crop models use a high number of parameters to define aspects of crop genetics, soil, weather and crop management. Within each of these, many variables need to be specified, resulting in an increase of the number of simulations.

For crop genetics, varietal parameters related to potential (under no limitation) and attainable (under biotic or abiotic stress) crop yield as well as to crop architecture and phenology (development) are required. For soil, the crop model uses a by layer description of moisture limits (field capacity, saturation and wilting points), density and depth, among others. Radiation, temperatures, precipitation (or applied water), wind, [CO₂], and possibly other features relevant under Martian environment have to be considered in relation to weather.

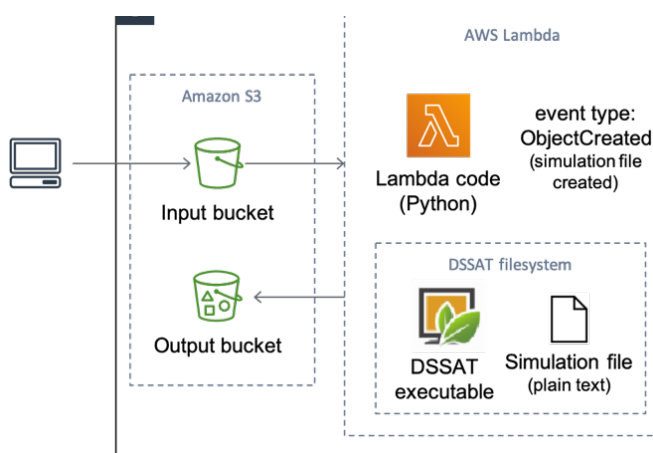


Fig. 1.

Finally, crop management encompasses a large number of options specified by the corresponding parameters: operation dates and frequency (tillage or soil preparation, sowing, fertilization, irrigation), intensity (seeds/ha or m⁻², kg ha⁻¹

of fertilizer, mm of applied water), efficiencies (e.g. 0.95 in dripping irrigation), etc. This large list of parameters results in a huge number of combinations to be simulated for a single crop, unaffordable with classic computational approaches.

In the proposed solution, crop simulations are done with DSSAT, which is a widely used software, which contains dynamic growth simulation models for many crops [7]. Its FORTRAN source code is available under request and the version used in our serverless architecture is 4.7. Its execution time falls into the limits imposed by AWS Lambda.

This time, the function that wraps the DSSAT executable is coded in Python and it is launched every time a simulation file is uploaded to the AWS S3 bucket. The resulting architecture allows a massive execution of the model with permutations of all possible parameter values, improving the quality of the study by means of a deeper analysis and maintaining a reasonable cost.

Acknowledgments:

Authors would like to thank the support of the European Commission under the project IN-TIME (grant agreement 823934), the Ministerio de Ciencia, Innovación y Universidades (Spain) under the project EdgeCloud (RTI2018-096465-B-I00), Spanish National Institute for Agricultural and Food Research and Technology and Agencia Estatal de Investigación (grant no. MACSUR02-APCIN2016-0005-00-00) and Comunidad de Madrid (Spain) and Structural Funds 2014-2020 (ERDF and ESF) under project AGRISOST-CM S2018/BAA-4330.

References:

- [1] Peter M. Mell, Timothy Grance, The NIST Definition of Cloud Computing, Technical Report SP 800-145, NIST, 2011.
- [2] J.L. Vazquez-Poletti, M.P. Velasco, S. Jimenez, D. Usero, I.M. Llorente, L. Vazquez, O. Korablev, D. Belyaev, M.V. Patsaeva and I. V. Khatuntsev: Public "Cloud" Provisioning for Venus Express VMC Image Processing. Communications on Applied Mathematics and Computation, Volume 1, Number 2, pp. 253-261, 2019. Springer.
- [3] Amazon Web Services Lambda. <https://aws.amazon.co-m/lambda>.
- [4] M. Ramírez-Nicolás, B. Sánchez-Cano, O. Witasse, P.-L. Blelly, L. Vázquez, M. Lester, The effect of the induced magnetic field on the electron density vertical profile of the Mars' ionosphere: A Mars Express MARSIS radar data analysis and interpretation, a case study, Planetary and Space Science, Volume 126, 2016, Pages 49-62.
- [5] Amazon Web Services Simple Storage Service. <https://aws.amazon.com/s3/>.
- [6] J.L. Vazquez-Poletti and I.M. Llorente: Serverless Computing: From Planet Mars to the Cloud. Computing in Science & Engineering, Volume 20, Number 6, pp. 73-79, 2018. IEEE Computer Society Press.
- [7] Hoogenboom, G., Jones, J.W., Wilkens, P.W., Porter, C.H., Boote, K.J., Hunt, L.A., Singh, U., Lizaso, J.I., White, J.W., Uryasev, O., Ogoshi, R., Koo, J., Shelia, V., Tsuji, G.Y., 2015. Decision Support System for Agrotechnology Transfer (DSSAT) Version 4.6. DSSAT Foundation, Prosser, Washington. <http://www.dssat.net>.

VENUS NIGHTTIME PHOTOCHEMICAL MODEL: NIGHTGLOW OF O₂, NO, OH AND ABUNDANCES OF O₃ AND ClO

Vladimir A. Krasnopolsky

*Moscow Institute of Physics and Technology, Moscow, Russia,
vlad.krasn@verizon.net*

Keywords:

Venus Atmosphere; Photochemistry; Nightglow; Atmospheric Composition Pl

Introduction:

Detections and first studies of Venus' nightglow were made four decades ago using the Venera 9–10 [8, 6] and Pioneer Venus [15] orbiters and ground-based high-resolution spectroscopy [2, 13]. Later, long-term observations by Venus Express in 2005–2014 provided the most detailed studies of the O₂ nightglow at 1.27 μm [11] and in the visible range [4] and the NO UV nightglow [5, 16]. The NO band at 1.224 μm [3] and the OH rovibrational bands [10, 14] were discovered on Venus. Nighttime ozone layers near 95 km [9] were detected using the SPICAV stellar occultations from Venus Express. Recently ClO [12] was detected on the Venus night side using ground-based high-resolution spectroscopy in the submillimeter range.

All these phenomena refer to the altitude range of 85–120 km in the nighttime atmosphere. Lifetimes of atoms, radicals, and some molecules are smaller than the duration of Venus' night (≈2 Earths days) at these altitudes. Therefore the global-mean models are inapplicable for comparison with observations of short-living species on the night side. Here we update our previous nighttime photochemical model [7] using the recent detection of ClO.

Model

The nighttime chemistry at 80–130 km is induced by transport of atomic species from the day side, where the density at 150 km exceeds that of the night side at this altitude by a factor of ≈30. The model involves 86 reactions of 29 species. Downward fluxes of O, N, H, and Cl at 130 km are the model parameters to fit the observed mean intensities of the O₂, NO, OH nightglow and abundances of O₃ and ClO. The chosen fluxes are $\Phi_{\text{O}} = 3 \times 10^{12}$, $\Phi_{\text{N}} = 1.2 \times 10^9$, $\Phi_{\text{H}} = 9 \times 10^9$, and $\Phi_{\text{Cl}} = 4 \times 10^9$, all in cm⁻² s⁻¹. The model chemistry converts the flux of O at 130 km completely to flux of O₂ at 80 km, the flux of N to flux of N₂, the fluxes of H and Cl return a flux of HCl at 80 km, and the excess of H over Cl returns almost equal fluxes of H₂ and H₂O formed by the reactions of HCl with H and OH, respectively. Flux of CO $\Phi_{\text{CO}} = 2 \times 10^{12}$ cm⁻² s⁻¹ is included to simulate the nighttime CO bulge and returned unchanged at 80 km. The calculated mean nighttime composition of the atmosphere is shown in Fig. 1.

The measured ClO [12] is either 2.6 ± 0.6 ppb in a 10 km layer at 90 km or 2.3 ± 0.5 ppb at 85–100 km (Fig. 2). The model profile of the ClO mole fraction peaks at 88 km with $f_{\text{ClO}} = 4.3$ ppb and full width at half maximum FWHM = 3.7 km. Averaging of the mole fraction within 10 km gives 1.7 ppb at 87.5 km, while a ratio of the averaged ClO and total density is 2.3 ppb at 90.5 km (Fig. 2). The same for the layer at 85–100 km is 2.2 ppb. Therefore the model agrees with the observed ClO.

The calculated ozone (Fig. 1a) peaks at 93 km with $[\text{O}_3] = 1.4 \times 10^8$ cm⁻³ and FWHM = 6.3 km. Its peak limb column abundance is 7.8×10^{15} cm⁻², in accord with the SPICAV occultations [9].

Calculated vertical profiles of the nightglow of O₂, NO, and OH are shown in Fig. 3. Here we assume that the OH nightglow is excited by $\text{H} + \text{O}_3 \rightarrow \text{OH}(v) + \text{O}_2$ only. The observed mean nightside intensities of the OH bands (1–0), (2–1), (3–2), and (4–3) are 2.74, 2.40, 0.57, and 0.44 kR, respectively [14, 7]. The adopted yields of v'' in quenching of OH (v') by CO₂ are those of the collisional cascade model $v'' = v' - 1$ with corrections to fit the observed line distribution.

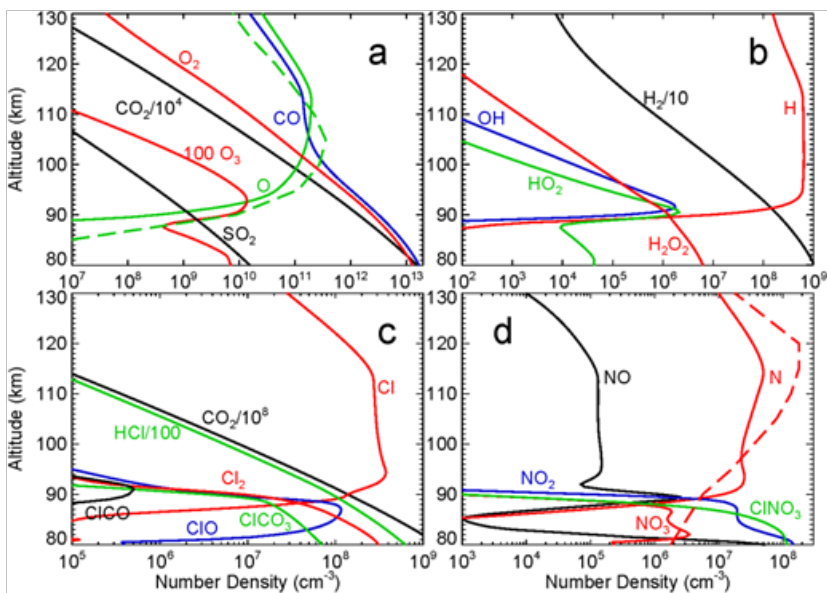


Fig. 1. Chemical composition of the mean nighttime atmosphere at 80–130 km: (a) CO_2 products and SO_2 , (b) hydrogen species, (c) chlorine species, and (d) nitrogen species. The dashed curves are the midnight density profiles of O and N from VTGCM [1]

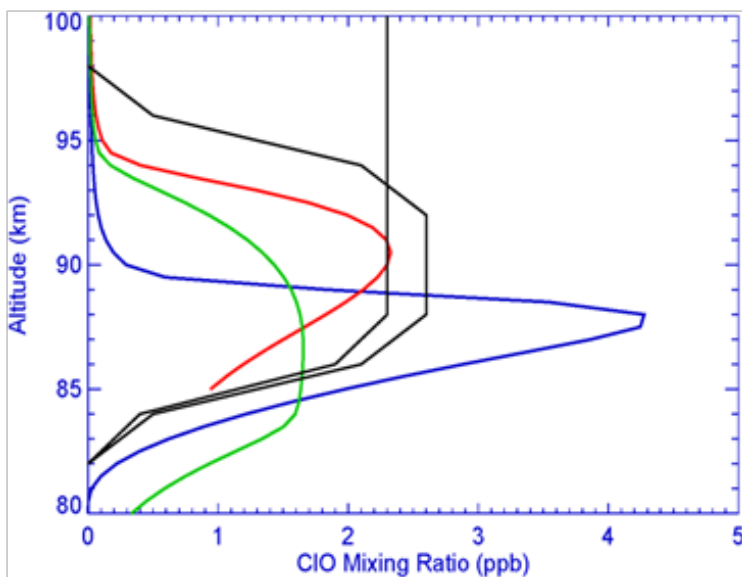


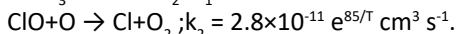
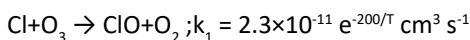
Fig. 2. ClO mixing ratio in the model (blue) and in two versions of a ten-km layer (green and red) are compared with those adopted in [12] to fit their observations (black)

The fluxes of O, N, H, and Cl are properly chosen to fit the observed mean nightglow intensities and the abundances of O_3 and ClO. However, the model does not have parameters to fit the observed altitudes of the nightglow and species layers. Peaks of volume emission rate are typically ≈ 2 km above those observed on the limb. The excellent agreement of the model with the observations confirms adequacy of the model.

Variations of the nighttime composition and nightglow

The fluxes of O, N, H, and Cl vary on the night side and result in variations of the nightglow and abundances of O_3 and ClO. The model is a convenient tool to study these variations. While the predicted variations of the nightglow and

O_3 are moderate, those of ClO may exceed two orders of magnitude. Major reactions that control ClO are



If transport is neglected, then

$$[ClO] \approx 0.8 e^{-285/T} [Cl][O_3]/[O]$$

All species involved are highly variable near 90 km (Fig. 1).

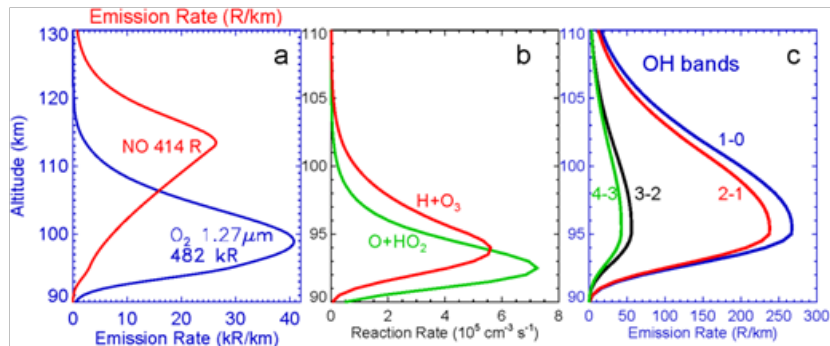


Fig. 3. Calculated vertical profiles of the O_2 , NO, and OH nightglow and two reactions that may form OH(v)

Variations of the O_2 , NO, OH nightglow and abundances of O_3 and ClO may be approximated by analytic relationships that make it possible to convert the fluxes into nightglow intensities, O_3 and ClO abundances and vice versa. Modeling of dynamic and composition of the Venus upper atmosphere, including fluxes from the day side to the night side and their variations, are among the problems under consideration by the Venus Thermosphere GCM, and some results on this subject are presented in [1].

References

- [1] Brecht A.S. et al. JGR 116, E08004, 2011
- [2] Connes P. et al. Astrophys. J. 233, L29–L32, 1979
- [3] Garcia Munoz A. et al. Proc. Nat. Acad. Sci. 106, 985–988, 2009
- [4] Garcia Munoz A. et al. JGR 114, E12002, 2009
- [5] Gerard J.C. et al. JGR 113, E00B03, 2008
- [6] Krasnopolsky V.A. In “Venus” (Hunten D.M. et al., ed.), Univ. Arizona Press, USA, P. 459–483, 1983
- [7] Krasnopolsky V.A. Planet Space Sci. 85, 78–88, 2013
- [8] Krasnopolsky V.A. et al. Cosmic Res. 14, 789–795, 1976
- [9] Montmessin F. et al. Icarus 216, 82–85, 2011
- [10] Piccioni G. et al. Astron. Astrophys. 483, L29–L33, 2008
- [11] Piccioni G. et al. JGR 114, E00B38, 2009
- [12] Sandor B.J. and Clancy R.T. Icarus 313, 15–24, 2018
- [13] Slinger T.G. et al. Science 291, 463–465, 2001
- [14] Soret L. et al. Planet. Space Sci. 73, 387–396, 2012
- [15] Stewart A.I.F. et al. JGR 85, 7861–7870, 1980
- [16] Stiepen A. et al. Icarus 226, 428–436, 2013

MEASUREMENT OF THE COMPOSITION OF VENUS ATMOSPHERE DURING AEROBREAKING

P. Wurz, S. Gruchola, A. Galli, A. Vorburger,

Physics Institute, University of Bern, Sidlerstrasse 5, 3012 Bern, Switzerland, peter.wurz@space.unibe.ch

Keywords:

Venus atmosphere composition, aero-breaking measurements, noble gases

Introduction:

Venus is the closest and most similar planet to Earth in the whole solar system, yet, basic measurements are still missing. The atmospheric composition has been studied to some extent with the Pioneer Venus Orbiter mission and the more recent Venus Express, however, the concentration of many species and their isotopic ratios are not yet known with satisfying accuracy. Especially when it comes to the heavy noble gases as Kr and Xe, there are little to no collected data in this field. These elements form a key link to the reconstruction of the atmospheric evolution, which would provide crucial information on the formation of Earth-like bodies. Knowing the abundances of the noble gases may allow us to answer the question why Venus did not evolve to a potentially habitable planet like its neighbour Earth.

We present a review of existing observations of Venus' upper atmosphere and exosphere and from that developed an exospheric model for the thermal and hot atmosphere of Venus above the homopause. Mass spectra for possible future Venus missions are predicted, as for example for the planned EnVision mission of ESA. The main focus of the present work are the heavy noble gases and requirements for the trajectories of the flybys and measurement per for mance are proposed. In addition, mass spectra and recommended integration times for the Venus flyby of ESA's JUICE mission are derived.

Modelling:

The simulation package used to obtain the models of the Venus atmosphere is based on a Monte Carlo simulation originally developed for Mercury and the Moon [1, 2], now extended to Venus [3]. Strictly speaking, the programme is therefore only applicable to the atmospheric region, where collisions are negligible, namely the exosphere. We cover the altitudes below the exobase by analytic extensions [3]. In this region, the mean free path is larger than the scale height. The simulations should start at the exobase, which is located at around 210 km on the dayside and drops to around 150 km on the nightside because of the cooling by IR emission from the CO₂ atmosphere [4]. The difference between the exobase levels comes from the heating by the Sun, which heats up the dayside thermosphere, resulting in larger scale heights.

In the exospheric model presented in this paper, collisions as well as other processes which take place above the homopause as e.g. sputtering, charge exchange or photolysis are not addressed. However, we focus on the noble gases, which do not undergo photochemical dissociation and have a lower cross section for ionisation and charge exchange than non-noble gases. Also, the abundance of the heavy noble gases Kr and Xe at the exobase is negligible, therefore atmospheric sputtering is not relevant. The uncertainty in the knowledge of the abundance of those noble gases at the homopause is much larger than the model's deviation from the actual conditions due to the processes mentioned before.

Most species in the Venusian exosphere can be modeled as the sum of a thermal and a hot particle distribution. For the thermal component, the temperature equals that of the thermosphere, which implies that the typical velocity of a particle is determined by the temperature of the atmosphere around it. The particles forming the hot component have much higher energies and therefore higher velocities. We simulate the hot atmosphere in the same way as the thermal one only with a much higher initial temperature. The hot

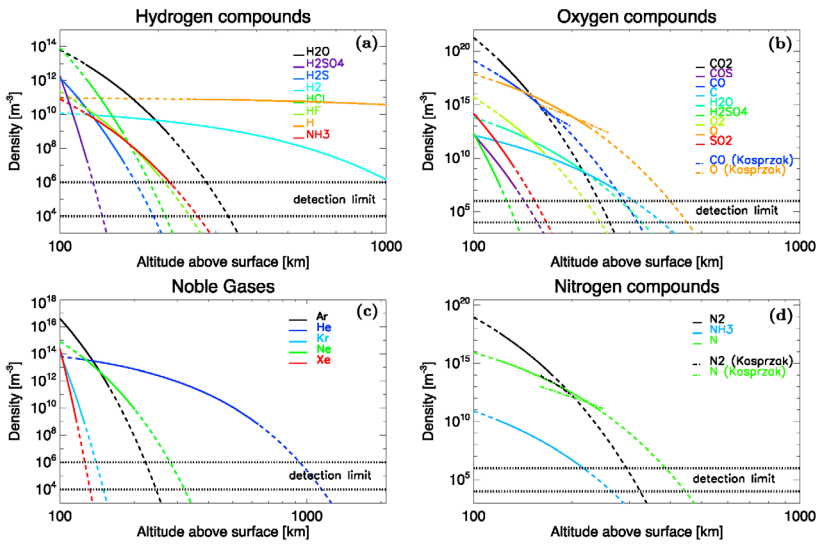


Fig. 1. Number density profiles of thermal hydrogen compounds (panel 1a), oxygen compounds (panel 1b), noble gases (panel 1c) and nitrogen compounds (panel 1d). The solid lines indicate the computed particle trajectories, whereas the dashed lines show from where on the density has been extrapolated [3]. The dotted horizontal lines show the detection limit of the mass spectrometer, the upper and lower lines correspond to integration time of 1 s and 104 s (~ 2.8 h), respectively.

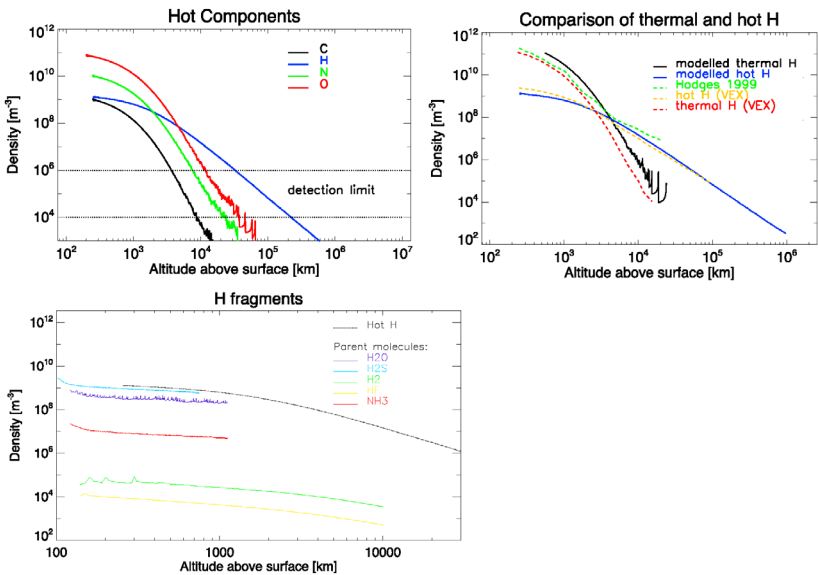


Fig. 2. Left: number density profiles of hot species. The dotted lines show the detection limit of the mass spectrometer, upper and lower lines corresponding to integration times of 1 s and 10^4 s (~ 2.8 h), respectively. Right: comparison of the modelled thermal and hot hydrogen density profiles with the model derived [8] and the measurements made by SPICAV/VEX [9]. Bottom: Hydrogen fragments produced by photochemical dissociation of hydrogen bearing parent molecules (see the legend).

In Fig. 1 two lines are shown, assuming a performance of an instrument that was developed for lunar research [7], for integration times of 1 s and 104 s, respectively. When having a closer look at Fig. 1, one can see that the heavy noble gas xenon is hardly detectable by the mass spectrometer, which has a detection limit of 1 cm^{-3} for an integration time of 1 s, corresponding to a signal-to-noise ratio (S/N) of about 3. Whereas with an integration time of 100 s, which is realistic for an aero-breaking trajectory like the one planned for EnVision, the Xe signal is detectable with $S/N \approx 30$.

The species of the hot component are the result from dissociation processes in the exosphere. The results for these species are shown in Fig. 2, with a comparison of our calculations to earlier theoretical and measured one [8, 9]. For H the contributions from different parents are also identified.

References:

- [1] P. Wurz and H. Lammer, Monte-Carlo Simulation of Mercury's Exosphere, *Icarus*, 164. 2003, 1–13.
- [2] P. Wurz, U. Rohner, J.A. Whitby, C. Kolb, H. Lammer, P. Dobnikar, and J.A. Martín-Fernández, The lunar exosphere: The sputtering contribution, *Icarus* 191. 2007. 486–496.
- [3] S. Gruchola, A. Galli, A. Vorburger, and P. Wurz, The upper atmosphere of Venus: Model predictions for mass spectrometry measurements, *Plan. Sp. Sci.*, 170(2019), 29–41
- [4] W.T. Kasprzak, Keating G.M., Hsu N., Stewart A.I.F., Colwell W.B., Bougher S.W., Solar activity behavior of the thermosphere, in *Venus II: Geology, Geophysics, Atmosphere, and Solar Wind Environment*, University of Arizona Press, ed. S.W. Bougher, D.M. Hunten, and R.J. Phillips. 1997. 225–258.
- [5] Keating G.M., et al., Bertaux J.L., Bougher S.W., Cravens T.E., Dickinson R.E., Hedin A.E., Krasnopolsky V.A., Nagy A.F., Nicholson J.Y., Paxton L.J., Zahn U.V., Models of venus neutral upper atmosphere: structure and composition. *Adv. Space Res.* 5 (11). 1985. 117–171.
- [6] J.L. Bertaux et al., Vandaele A.C., Korabiev O., Villard, E. Fedorova, A. Fussen D., Quémerais E., Belyaev D., Mahieux A., Montmessin F., Muller C., Neefs E., Nevejans D., Wilquet V., Dubois J.P., Hauchecorne A., Stepanov A., Vinogradov I., Rodin A., Nevejans D., Montmessin F., Fedorova A., Cabane M., Chassefière E., Chaufray J.Y., Dimarellis E., Dubois J.P., Hauchecorne A., Leblanc F., Lefèvre F., Rannou P., Quémérais E., Villard E., Fussen D., Muller C., Neefs E., Van Ransbeeck E., Wilquet V., Stepanov A., Vinogradov I., Zasova L., Forget F., Lebonnois S., Titov D., Rafkin S., Durry G., Gérard J.C., Sandel B., A warm layer in Venus' cryosphere and high-altitude measurements of HF, HCl, H₂O and HDO. *Nature* 450. 2007. 646–649.
- [7] P. Wurz, D. Abplanalp, M. Tulej, and H. Lammer, A Neutral Gas Mass Spectrometer for the Investigation of Lunar Volatiles, *Planet. Sp. Science* 74. 2012. 264–269.
- [8] Hodges R.R., An exospheric perspective of isotopic fractionation of hydrogen on Venus. *J. Geophys. Res.* 104. 1999. 8463–8471.
- [9] J.Y. Chaufray, Bertaux J.L., Quémerais E., Villard E., Leblanc F., Hydrogen density in the dayside venusian exosphere derived from Lyman- α observations by SPI-CAV on Venus Express, *Icarus* 217. 2012. 767–778.

ATMOSPHERIC NOBLE GAS ISOTOPE AND BULK K/U RATIOS AS A CONSTRAINT ON THE EARLY EVOLUTION OF VENUS AND EARTH

H. Lammer¹, M. Scherf¹, M. Leitzinger^{2,1}, P. Odert^{2,1}, D. Kubyskhina¹, C. Burger³, C.P. Johnstone³, T. Maindl³, M. Güdel², N. Tosi^{4,5}, N.V. Erkaev^{6,7} L. Fossati¹

¹ Space Research Institute, Austrian Academy of Sciences, Graz, Austria (helmut.lammer@oew.ac.at);

² Institute of Physics/IGAM, University of Graz, Austria;

³ Institute of Astrophysics, University of Vienna, Vienna, Austria;

⁴ Institute of Planetary Research, Department of Planetary Physics, DLR, Berlin, Germany;

⁵ Department of Astronomy and Astrophysics, Berlin Institute of Technology, Germany;

⁶ Institute of Computational Modelling SB RAS, Krasnoyarsk, Russian Federation;

⁷ Siberian Federal University, Krasnoyarsk, Russian Federation;

Keywords:

Venus, Earth, atmosphere evolution, planetary evolution, noble gases, isotopes, fractionation

While early Venus and Earth were accumulating mass within the solar nebular these protoplanets also captured significant hydrogen dominated atmospheres by picking up gas from the circumstellar disk during the formation of the Solar System (e.g. [1]). We apply hydrodynamic upper atmosphere and impact erosion models for studying the fractionation of various elements along solar activity tracks. These primordial atmospheres were then quickly lost by hydrodynamic escape and impact erosion of planetary embryos after the disk dissipated. After a short but efficient boil-off phase the EUV-driven hydrodynamic flow of H-atoms dragged heavier elements with it at different rates, leading to changes in their isotopic and elemental ratios [2, 3, 4], which is reflected in the present-day atmospheric noble gas isotope and elemental ratios of Venus and Earth. Depending on the disk lifetime and the initial composition $^{36}\text{Ar}/^{38}\text{Ar}$, $^{20}\text{Ne}/^{22}\text{Ne}$ and bulk K/U ratios observed for both planets can be best explained if the Sun was born between a weakly and moderately active star and if Venus and Earth had grown to ~85–100% and ~53–58%, respectively, of their current masses by the time the nebula gas dissipated approximately 3.5 Myr after formation of the Sun. If proto-Earth accreted its mass from up to 40% carbonatous chondritic-like (CC) material [5] then the planet must have been grown to about 80% of its final mass as long as it was surrounded by the escaping primordial atmosphere (~7 Myr). Our results are in agreement with a fast accretion of thermally processed disk material planetary embryos, with Hafnium-Tungsten chronometric fast accretion scenarios of the proto-Earth (e.g. [6]), and a noble gas origin based on a mixture of primitive meteoroids with a delivery of $\geq 75\%$ CC-like material after the escape of a small remnant of the proto-solar nebula [7]. Moreover, new precise measurements of noble gas isotope ratios in Venus' atmosphere will constrain not only the evolution of proto-Venus but also the history of the young Sun's activity evolution.

References:

- [1] Stökl, A., Dorfi, E.A., Johnstone, C.P., Lammer, H.: Dynamical Accretion of Primordial Atmospheres around Planets with Masses between 0.1 and 5 M in the Habitable Zone. *Astrophys. J.* 2016.V. 825. P. 86–96.
- [2] Hunten, D.M., Pepin, R.O., Walker, J.C.G.: Mass fractionation in hydrodynamic escape. *Icarus.* 1987.V. 69. P. 532–549.
- [3] Zahnle, K., Pollack, J.B., Kasting, J.F. Mass fractionation of noble gases in diffusion-limited hydrodynamic hydrogen escape. *Icarus.* 1990. V. 84. P. 502–527.
- [4] Odert, P, Lammer, H, Erkaev, N.V, Nikolaou, A., Lichtenegger, H.I.M., Johnstone, C.P., Kislyakova, K.G., Leitzinger, M., Tosi, N. Escape and fractionation

of volatiles and noble gases from Mars-sized planetary embryos and growing protoplanets, *Icarus*. 2018. V. 307. P. 327–46.

- [5] Schiller, M., Bizzarro, M., Fernandes, V.A. Isotopic evolution of the protoplanetary disk and the building blocks of Earth and the Moon. *Nature*. 2018.V. 555. P. 507–510.
- [6] Yu, G., Jacobsen, S.B. Fast accretion of the Earth with a late Moon-forming giant impact. *Proceedings of the National Academy of Science*. 2011. V. 108, P. 17604–17609.
- [7] Lammer, H., Leitzinger, M., Odert, P., Burger, C., Kubyshkina, D., Johnstone, C., Maindl, T., Schäfer, C.M., Güdel, M., Tosi, N., Nikolaou, A., Marcq, E., Erkaev, N.V., Noak, L., Kislyakova, K.G., Fossati, L., Pilat-Lohinger, E., Ragossnig, F., Dorfi E.A. Measured atmospheric $^{36}\text{Ar}/^{38}\text{Ar}$, $^{20}\text{Ne}/^{22}\text{Ne}$ noble gas isotope and bulk K/U ratios constrain the early evolution of Venus and Earth. *Icarus* submitted (revised). 2019.

IMPLICATIONS OF HYDRODYNAMIC ESCAPE FOR THE VENUSIAN WATER INVENTORY, CONSTRAINED BY D/H

M. Bauer¹, H. Lammer², M. Scherf², P. Odert³, M. Leitzinger³

³ *Institute of Physics, IGAM, University of Graz, Universitätsplatz 5, 8010 Graz, Austria, maik.bauer@uni-graz.at;*

² *Space Research Institute, Austrian Academy of Sciences, Schmiedlstr. 6, 8042 Graz, Austria*

³ *Institute of Physics, IGAM, University of Graz, Universitätsplatz 5, 8010 Graz, Austria*

Keywords:

Venus, D/H ratio, hydrodynamic escape, water inventory, isotope ratios

Isotope ratios provide valuable insights into the atmospheric evolution of various solar system bodies. If a planet's isotope ratios differ drastically from the protosolar values, something must have caused the predominant escape of one isotope. The Venera landing probes and the Pioneer Venus provided some present-day isotope ratios for Venus, revealing that the planet's atmosphere is enriched in several heavy isotopes, amongst them deuterium (D). One escape process of particular interest for the early evolution of the Venusian atmosphere is hydrodynamic escape of H and D during a possible captured nebula-based H₂-envelope and/or a magma-ocean related outgassed steam atmosphere. The high levels of extreme ultraviolet (EUV) radiation emitted by the young Sun are likely to have been sufficient for the planet's atmosphere to enter into a hydrodynamic regime. We model the hydrodynamic escape of an outgassed atmosphere from Venus at multiple starting points using different atmospheric compositions and surface temperatures and aim to reproduce present-day isotope ratios. Moreover, we also consider the scenario that Venus might have had a liquid water ocean until about 700 My ago that was proposed by Way et al. [1] and investigate the influence that the presence of an ocean would have had on the D/H ratio and a possible accumulation of oxygen in the atmosphere.

References:

- [1] Way M.J., Del Genio, A.D., Kiang, N.Y., Sohl, L.E., Grinspoon, D.H., Aleinov, I., Kelley, M., Clune, T. 2016. Was Venus the first habitable world of our solar system? *Geophys. Res. Lett.* 2016. V. 43. P. 8376–8383.

GEOLOGICAL TESTS OF GLOBAL WARMING MODELS ON VENUS

R. Ernst^{1,2}, S. Khawja¹, C. Samson^{1,3}

¹ Department of Earth Sciences, Carleton University, 1125 Colonel By Drive, Ottawa, Ontario K1S 5B6, Canada, main author contact e-mail

² Faculty of Geology and Geography, Tomsk State University, 36 Lenin Avenue, Tomsk 634050, Russia

³ Department of Construction Engineering, École de Technologie Supérieure, 1100 rue Notre-Dame Ouest, Montréal, Quebec H3C 1K3, Canada

Keywords:

global warming, climate change, tesserae, erosion, basalt flow, Venus

Introduction:

On the basis of the current extreme high temperatures (450°C) and the absence of free water, it has generally been assumed that water erosion did not operate on Venus. This is consistent with surface morphology in most regions that shows good preservation of primary surface structures and local topographic relief, except where overlain or overprinted by younger volcanic units and structures.

Recent mapping [10–3], however, suggests that erosion might have significantly affected the older complexly deformed terranes, termed tesserae, an observation that is consistent with a recent global climatic model [4], that suggests Earth-like climatic conditions on Venus until approximately 700 Ma. This time is inferred to mark the transition from tesserae to widespread younger mafic volcanic resurfacing (with massive CO₂ release and associated global greenhouse hyper-warming).

Evidence for Erosion in Tessera:

Our analysis is focusing on portions of tesserae that were partially flooded by younger mafic flows. The volcanic flooding provides a semi-horizontal datum to distinguish local elevated areas (peaks and ridges) from valleys. The pattern of peaks and ridges cannot be solely explained by primary topography caused by folding or faulting. However, the distribution of “valleys” is consistent with terrestrial-type stream drainage patterns indicating significant water erosion. The potential role of wind and glacial erosion is also being considered.

A More Earth-Like Climate during Early Post-Tessera Mafic Volcanism?:

This global warming model and our evidence for water erosion during tessera time, would also suggest that the earliest mafic lava flows (post-tessera time) would have been emplaced during more habitable climate conditions, while later (younger) flows would have been emplaced under conditions of progressively higher temperature, atmospheric pressure and CO₂ content. We are therefore assessing older and younger generations of lava flows in terms of flow morphology and surface textures that can be indicative of temperature (Earth-like vs 450°C) and low vs high atmospheric pressure and CO₂ content.

References:

- [1] Khawja S., Ernst R.E., Kuiper Y.D., Samson C. (2019a). Structural analysis of Salus tessera, Venus: Interpreting surface lineament sets using topographic profiles. 50th Lunar and Planetary Science Conference 2019 (LPI Contrib. No. 2132), abstract no. 1967.
- [2] Ernst R.E., Samson C., Kuiper Y.D., Khawja S. (2019). Geological testing of climate change models on Venus. 50th Lunar and Planetary Science Conference 2019 (LPI Contrib. No. 2132), abstract no. 2382.
- [3] Byrne P.K., Ghail R.C., Gilmore M.S., Şengör, A.M.C., Klimczak C., Solomon S.C., Khawja S., Ernst R.E. (2019). Geological significance of preserved interior structures in Venus tessera units. Abstract 624747, American Geophysical Union. Annual Meeting, Dec. 9–13, San Francisco, USA.
- [4] Way M.J., Del Genio A.D., Kiang N.Y., Sohl L.E., Grinspoon D.H., Aleinov I., Kelley M., Clune, T. (2016) Was Venus the first habitable world of our solar system? *Geophys. Res. Letters*, v. 43, p. 8376–8383.

BRIGHT FLASHES OF LIGHTNING ON VENUS WERE RECORDED IN INFRARED IMAGES OF THE AKATSUKI MISSION

L.V. Ksanfomality

Space research institute of the RAS

Keywords:

Venus lightning EM-radiation optical flashes AKATSUKI mission

Electrical phenomena and lightnings in the atmosphere of Venus were discovered in 1978 Ksanfomality, 1979; Ksanfomality, 1980). On December 21 and 25, 1978, the GROZA instrument onboard the VENERA-11, -12 landers recorded numerous electromagnetic pulses, such as Earth atmospheric, in the 10–80 kHz range. 3 days later, the same result, but in the whistler mode, was obtained using the OEFD instrument on the Pioneer-Venus orbiter (Scarf et al., 1980; Ksanfomality et al., 1980). A signature of electric discharges was their pulsed electromagnetic emission in the range of 10–80 kHz (Fig. 1). But the accompanying optical flashes were not observed, although their search was organized first on the same VENERA-11, -12 orbiter modules, fly-by spacecrafts GALILEO, CASSINI and orbiters VENERA-15, -16 and VENUS-EXPRESS.

In all cases, numerous electromagnetic discharges (counting rate up to 30 s^{-1}) were confidently recorded in the absence of optical flashes, which were searched on the night side of the planet.

Interest in electrical atmospheric discharges on Venus is connected, in particular, with the question of the origin of small components in its atmosphere. Lightning, on the one hand, destroys the molecular bonds of the medium in the discharge channel, on the other hand, it causes fast chemical reactions with the appearance of new nonequilibrium chemical compounds, which, among other things, can be associated with subsequent biochemical processes. The nature of charge accumulation in the atmospheric clouds of different planets may vary, but the general physics of the processes is similar. From the moment of discovery, for many years, Venus has been carrying out an unsuccessful search for optical flares, which must accompany

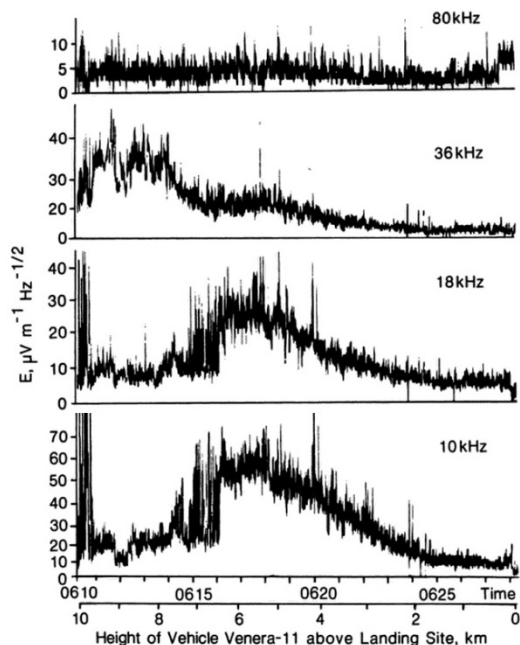


Fig. 1.

electromagnetic pulses. Many papers have been published in which the authors offer some explanation of this paradox. Detailed information about the conducted search for can be found in the review "Lightning detection on Venus: a critical review" (Lorenz, 2018). The author points out that by 2018, the number of published papers on the topic was 180. Note that the task of searching for lightning also belonged to the main goals of the AKATSUKI orbital mission of the Japanese space agency JAXA.

Fig. 1. The field strength of numerous electromagnetic impulses regis-

tered on December 21, 1978 with the GROZA instrument on the VENERA-11 descent module, referred to lightning in a remote source. A fragment of the record is from a height of 10 km to the surface. The origin of the difference in the curves at 18 and 36 kHz remains unknown.

The search was conducted in the UV range (365 nm) on the night side of the planet with a specially designed instrument with a high sampling rate (Takahashi et al., 2019). Search results are not reported. The possible reason for the absence of flares following electrical discharges in the atmosphere of Venus was considered by the author in a number of published articles. If discharges occur in the lower layers of clouds, a significant extinction in the optical range weakens the flashes so that their registration from Venus satellites becomes impossible (Ksanfomality, 1984). In the case of Venus, the optical thickness of clouds τ is very significant. The strongly attenuated radiation in the optical range practically does not reach the detectors of satellite. The extinction is much lower in the near IR range (2 μm), but the necessary data in Venus research for a long time could not be found. In 2016, in the IR experiments with the IR2 camera of the AKATSUKI mission, rich observational material was obtained (the JAXA "DARTS" website). It was the results of observations with the IR2 camera and the materials were used as the basis for the search for lightning flashes in the present work.

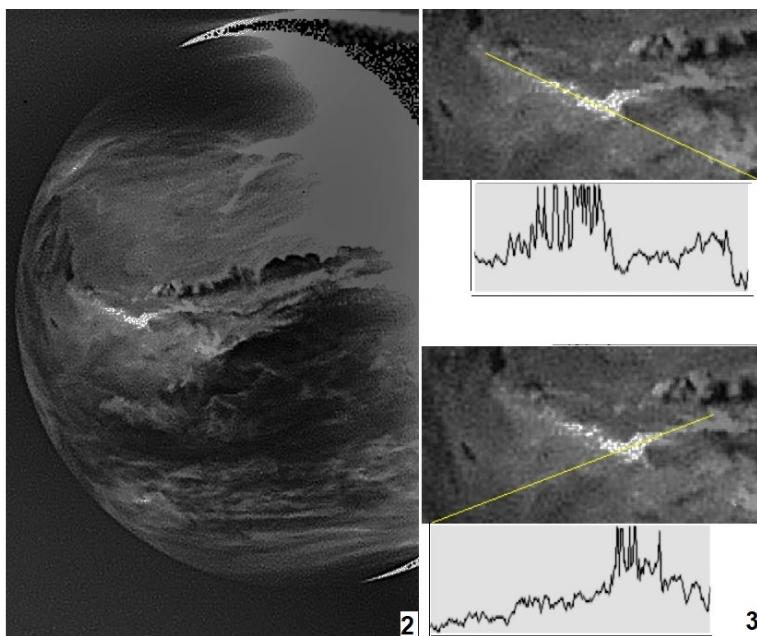


Fig. 2. Photo taken on October 20, 2016, with a bright band in the equatorial region, with a threshold of reproducible brightness $> 140 \text{ mW m}^{-2} \mu\text{m}^{-1} \text{ sr}^{-1}$, demonstrating flashes of lightning. On the right - the distribution of brightness along the section lines. All bright dots correspond to the saturation level of the detector pixels. Coordinates of the sub-satellite point are 8.26°S , 182°E .

While searching for lightning, IR images have important advantages over images in the optical range. Most of the pictures were taken with a 7-second exposure. Apart from the fact that scattering is less than 6 times as the $2\pi r / \lambda$ ratio, due to the high brightness of the flashes, their images gradually accumulate on the detector matrix, in fact, recording during the 7-second exposure, regardless of the short duration (0.2 s) of the flash itself. We managed to find the required flashes, and their brightness exceeds the saturation level of the detector. For the flash image to be fixed on the detector array, the flash brightness must be at least $(7\text{s} / 0.2\text{s})$ times brighter than the average brightness of the image details. Of course, the linearity and saturation threshold of the detector play an important role. The success of the search is due to the highest transparency of the atmosphere at a wavelength

of 2.26 microns. Numerous lightning flashes were detected during image processing obtained in the 2.26 μm band, taken on October 20, 2016, from a distance of 202 thousand km from the upper boundary of clouds (Fig. 2). The bright band in the equatorial belt (Fig. 2.2) turned out to be non-uniform. The threshold of reproducible brightness in Fig. 2.2, at the center, was set at about $140 \text{ mW m}^{-2} \mu\text{m}^{-1} \text{sr}^{-1}$. When the black level rises, the bright area splits into individual bright pixels (in saturation), single, or combined by 2 or 4 pixels. The length of the active region is 1300 km, width from 100 to 340 km.

All, even the brightest, other details of the image were below this level, and only a wide band is distinguished by numerous bright dots. The pixel resolution in the image corresponds to 40 km on the cloud layer. Apparently, the band turned out to be a rupture of clouds above the level of thunderstorms, exposing numerous direct flashes of lightning (not their scattered light). None of the other details of the image having similar structure were detected, with the exception of a small (600 km) spot north of the center of the cluster of flares. Here, a small part of the thunderstorm, about 10 flashes, is covered with a cloudy environment. The optical thickness of the medium above the thunderstorm is small, $\tau < 1$. The sections (Fig. 2.3) show convincingly that all the peaks have the same height — the saturation level of the detector. Image analysis also shows that there are practically no outbreaks in the adjacent area, and the occurrence of thunderstorms is likely due to the formation of gaps and is concentrated in them.

Other images show that cloud ruptures above the lightning level, revealing thunderstorm activity, turned out to be a global phenomenon on Venus, but were recorded differently on different dates, which is probably due to the period of superrotation. Unfortunately, there is no necessary sequence of images for such approval.

References

- [1] L. Ksanfomality, H. Kashimura. IR-observations of the AKATSUKI mission explain the origin of the global Y-structure of the cloud layer and the non-isotropic character of the natural illumination in the VENERA landing sites. // *Solar System research*, 2019, in press.
- [2] R.D. Lorenz. Lightning detection on Venus: a critical review // *Progress in Earth and Planetary Science*, 2018, V. 5 p. 34.
- [3] Y.Takahashi, J. Yoshida, Y. Yair, T. Imamura, M. Nakamura, Lightning detection by LAC onboard the Japanese Venus climate orbiter, Planet-C // *Space Sci. Rev.* 2008, V. 137, P. 317–334.
- [4] L.V. Ksanfomality, F.L. Scarf, W.W. Taylor. The electrical activity of the atmosphere of Venus // *Venus*. Eds D.M. Hanten, L.Colin. 1983. The University of Arizona Press. P. 565–603.
- [5] L.V. Ksanfomality Discovery of frequent lightning discharges in clouds on Venus // *NATURE*, 1980, V. 284, P. 244–246.
- [6] F.L. Scarf, Taylor W.W., Russell C.T., Brace L.H. Lightning on Venus: Orbiter detection of whistler signals. // *JGR*, 1980, V. 85, P. 8158–8166.
- [7] L.V. Ksanfomality. Circumstantial evidence for the occurrence of volcanism on Venus // *Solar System research*, 1984. V. 18, P. 310–320.

CIRCULATION OF THE LOWER CLOUD LEVEL ON THE NIGHTSIDE OF VENUS FROM VIRTIS-M (VENUS EXPRESS) AND IR2 (AKATSUKI) DATA IN $1.74 \mu\text{m}$

D.A. Gorinov, I.V. Khatuntsev, L.V. Zasova, M.V. Patsaeva and A.V. Turin
Space Research Institute RAS, Moscow, Russia, dmitry_gorinov@rssi.ru

Keywords:

Venus, cloud layer, dynamics, wind tracking

Introduction:

The thick cloud layer of Venus rotates around the planet in the westward direction with the peak velocity 60 times higher than that of the planet itself, approximately 100ms^{-1} for the altitudes of 65-70 km (upper cloud level) above the surface [1], the phenomenon known as retrograde superrotation. In the altitude range of 10-90 km the atmospheric motion is predominantly zonal. The velocity decreases for altitude levels farther from the upper cloud level and for latitudes closer to the poles.

On the nightside, the inhomogeneous distribution of the cloud opacity in the infrared spectral range (thermal emission) leads to a complex morphology of small-scale features of various contrasts. By tracking their displacement one can derive horizontal wind speed at the altitude of remote sensing.

In the spectral window of $1.74 \mu\text{m}$ on the nightside, the thermal radiance comes from beneath the main cloud level, subsequently passing through the lower clouds at the altitudes of 44-48 km [2]. Thus, the motion of the observed features is associated with atmospheric dynamics at these altitudes.

Experimental data and approach:

The infrared channel of the imaging spectrometer VIRTIS-M onboard Venus Express performed observations of the nightside from April 2006 to October 2008 with a spectral resolution of 16 nm and pixel size of 10-40 km. Most of its observations covered Southern Hemisphere, primarily high and middle latitudes. To calculate wind velocities using manual wind tracking technique [3], 988 image pairs in $1.74 \mu\text{m}$ were considered, resulting in 45191 vectors in total. Time intervals between pairs were varying from 1 to 3 hours.

The IR2 camera onboard Akatsuki operated in 2016 and one of its channels collected images in a $1.713\text{--}1.755 \mu\text{m}$ band [4]. Although there were fewer images compared to VIRTIS-M, they had better spatial resolution, thus resulting in more retrieved vectors per pair, 15275 for 145 pairs.

Heading styles:

Recent studies indicated significant differences between results from the two instruments [5]. Our findings confirm that the mean zonal speed was significantly higher in the results of IR2. The difference in values was the highest (78 m s^{-1} compared to 62 m s^{-1}) in the equatorial latitudes, in fact, the shape of the IR2 profile displayed an equatorial "jet", an effect which was not observed by VIRTIS-M. One of the possible explanations could be that the observed cloud details relate to different altitudes; in that case by implying the vertical wind shear of about $2 \text{ m s}^{-1} \text{ km}^{-1}$ we would assume an altitude difference of $\sim 8 \text{ km}$. On the other hand, the meridional component was resting at the same magnitudes for both experiments, reaching 0-2 m s^{-1} (equatorward direction). Unfortunately, results cannot be compared for the northern latitudes.

Longitudinal profiles of the mean wind speed for both instruments show variability, which can be partially attributed to the influence of the stationary gravity waves. Isolines of zonal and meridional velocities tend to correlate with the shapes of major underlying topographic features.

Acknowledgements:

D.A. Gorinov, I.V. Khatuntsev and M.V. Patsaeva were supported by the Ministry of High Education and Science of Russian Federation grant 14.W03.31.0017. A. Turin and L. Zasova would like to thank the program #AAAA-A18-118052890092-7 of the Ministry of High Education and Science of Russian Federation for the support.

References:

- [1] Gierasch, P.J., Goody, R.M., Young, R.E., Crisp, D., et al.: The general circulation of the Venus atmosphere: an assessment. In: Bucher J.W., Hunten D.M., Phillips R.J. (Eds.), *Venus II — Geology, Geophysics, Atmosphere, and Solar Wind Environment*. University of Arizona Press, Tucson, P. 459–500, 1997.
- [2] Sánchez-Lavega A., Lebonnois S., Imamura T., Read, P., Luz, D.: The atmospheric dynamics of Venus, *Venus III*, P. 1541–1616, 2017.
- [3] Khatuntsev I.V., Patsaeva M.V., Titov D.V., Ignatiev N.I., et al.: Winds in the middle cloud deck from the near-IR imaging by the Venus Monitoring Camera onboard Venus Express; *J. Geophys. Res. Planets*, Vol. 122, P. 2312–2327, 2017.
- [4] Satoh T.M., Nakamura M., Ueno K., Uemizu M. et al.: Development and in-flight calibration of IR2: 2- μ m camera onboard Japan's Venus orbiter, Akatsuki, *Earth, Planets and Space*, 68:74, 2016.
- [5] Peralta J., Muto K., Hueso R., Horinouchi T., et al.: Nightside winds at the lower clouds of Venus with Akatsuki/IR2: longitudinal, local time, and decadal variations from comparison with previous measurements, *The Astrophysical Journal Supplement Series*, 239:29, 2018.

INTERNAL WAVES CHARACTERISTICS IN THE VENUS'S ATMOSPHERE REVEALED FROM THE MAGELLAN AND VENUS EXPRESS RADIO OCCULTATION DATA BY TWO INDEPENDENT METHODS

V.N. Gubenko, I.A. Kirillovich

*Kotel'nikov Institute of Radio Engineering and Electronics RAS, Vvedenskii
Square 1, Fryazino, Moscow Region, 141190, vngubenko@gmail.com;*

Keywords:

Radio occultation measurements, Magellan and Venus Express spacecrafts, Venus's atmosphere, vertical temperature profiles, internal gravity waves.

Introduction:

Internal gravity waves (IGWs) are vertically propagating waves that have buoyancy force as the restoring force. IGWs are often generated by vertical displacement of the atmosphere due to flow over topography or by convection, or by wind shear instability in the background flow. The existence of IGWs in the Venus's atmosphere is well established from UV images of clouds [1], temperature [2] and wind [3] profiles, and radio occultation (RO) measurements [4–7]. Authors of paper [5] used RO data from Venera–15 and –16 to investigate the thermal structure of the middle atmosphere. They noted that wave-like structure commonly appears in retrieved temperature profiles at altitudes above ~ 60 km, where the static stability is large. The Pioneer Venus (PV) RO experiments have yielded important results concerning the thermal structure of the neutral atmosphere [8], however, little effort has been made to investigate atmospheric waves. Magellan has important advantages over PV for studies of atmospheric waves. The dual-wavelength radio signals transmitted by Magellan have a higher signal-to-noise ratio (SNR) than their counterparts on PV. The orbital period of Magellan (3.26 hrs in 1991) is much shorter than that of PV (24 hrs), so that the rotation of the Venus's atmosphere between successive occultations is proportionately smaller. This provides much finer resolution for studies of zonal structure [4]. Authors of work [4] suggested that radiative damping is the principal process to dissipate internal atmospheric waves having vertical wavelengths shorter than 4 km, and this approach was used for the analysis of Magellan RO data. They showed that the observed wave structures were consistent with pure internal gravity waves that are attenuated by radiative damping during the vertical ascent. It was found that the amplitude and vertical wavelength are about 4 K and 2.5 km, respectively, at altitude of 65 km. A model for radiative damping implies that the wave intrinsic frequency is $\sim 2 \cdot 10^{-4}$ rad/s, and the corresponding ratio between horizontal and vertical wavelengths is ~ 100 [4]. A similar approach was also used by authors of work [7] for the analysis of Venus Express RO temperature data.

We have developed an alternative independent method of identifying discrete wave events and reconstructing IGW parameters from an analysis of the individual vertical temperature, density, or squared Brunt–Vaisala (buoyancy) frequency profile in a planetary atmosphere. Our method does not require any additional information not contained in the profile and can be adopted to analyze vertical profiles obtained by various techniques. The threshold discrimination criterion was formulated and justified for identifying wave events; its fulfillment assumes that the analyzed temperature or density variations to be manifestations of waves [9–14].

This method relies on the analysis of the relative wave amplitude, determined from the vertical profile of temperature or density, as well as on the concept of the linear IGW theory, which suggests that the wave amplitude is limited by threshold values due to wind dynamic (shear) instability in the atmosphere of planet. It is expected that when the internal wave amplitude reaches the wind shear instability threshold as the wave propagates upward,

Table 1. Internal gravity wave characteristics in the Venus's atmosphere inferred by two independent methods from the radio occultation temperature data, collected on 5–6 October 1991 during three successive orbits (orbit numbers 3212–3214) of the Magellan spacecraft

Input radio occultation data taken from HJ-paper [4] for analysis	
Solar zenith angle (SZA)	109°
Local true solar time (LTST)	22 h 05 m
Latitude, φ	67°N
Longitude	127°E
Altitude, h (Venus's radius $R_0 = 6052$ km)	≥ 57 km
Acceleration of gravity a, g	8.7 m/s ²
Angular rotation rate of the atmosphere, Ω	$-1.5 \cdot 10^{-5}$ rad/s (westward)
Coriolis parameter, $f = 2\Omega \cdot \sin\varphi $	$2.7 \cdot 10^{-5}$ rad/s (at 67°N latitude)
Inertial period, $\tau_f = \frac{2\pi}{ f }$	~ 64.6 hrs ≈ 2.7 days (at 67°N latitude)
Background temperature $a, *, T_b$	~ 230 K
Background buoyancy frequency $a, *, N_b$	$\sim 2.13 \cdot 10^{-2}$ rad/s
Vertical wavelength $a, T' $	2.5 km
Vertical wave number $a, m $	$\sim 2.5 \cdot 10^{-3}$ m ⁻¹
Amplitude of temperature perturbations $a,$ $\lambda = \frac{2\pi}{ m }$	4.0 K
Normalized amplitude of temperature perturbations $a, *, \frac{ T' }{T_b}$	$\sim 17.4 \cdot 10^{-3}$
Internal wave characteristics found by two independent methods	
Relative wave amplitude $a,$	~ 0.84 (our results) 0.82 (was calculated by us for HJ-paper results)
Intrinsic wave frequency a, ω	$\sim 3.9 \cdot 10^{-5}$ rad/s (our results) $2 \cdot 10^{-4}$ rad/s (parameter σ in HJ-paper)
Intrinsic wave period $a,$	~ 44.8 hrs ≈ 1.9 days (our results) ~ 9 hrs (value $2\pi/\sigma$ in HJ-paper)
Ratio	~ 0.69 (our results) ~ 0.14 (value f/σ in HJ-paper)
Intrinsic horizontal phase speed $a,$	~ 11.8 m/s (our results) 8.5 m/s (value N/m in HJ-paper)
Horizontal wave number $a,$	$\sim 0.33 \cdot 10^{-5}$ m ⁻¹ (our results) $\sim 2.33 \cdot 10^{-5}$ m ⁻¹ (was calculated from HJ-paper)
Horizontal wavelength $a,$	~ 1895 km (our results) 270 km ("meridional" wavelength in HJ-paper)
Amplitude of wind speed perturbations along the horizontal propagation vector,	~ 9.9 m/s (our results) 7.0 m/s ("meridional" amplitude in HJ-paper)

Amplitude of speed perturbations transverse to the horizontal propagation vector,	~6.8 m/s (our results) 0.7 m/s (“zonal” speed amplitude in HJ-paper)
Amplitude of vertical wind speed perturbations,	~1.3 10 ⁻² m/s (our results) 0.07 m/s (vertical speed amplitude in HJ-paper)

a At 65 km altitude, * was calculated by us for results of HJ-paper [4]

wave energy dissipation occurs so that the IGW amplitude stays at the atmospheric instability threshold (wave amplitude saturation). The application of the method to the analysis of RO temperature data enabled us for the first time to identify wave events in the atmospheres of Earth and Mars, to determine the key characteristics of detected waves, including intrinsic frequency of IGW, vertical fluxes of wave energy and momentum [9–12]. Numerical simulation data and analysis of independent radar and probe measurements in Earth’s atmosphere demonstrate high efficiency of our method and high reliability of scientific results it yields [15]. It is important to notice that authors of work [4] supposed the wave amplitude is not sufficient to cause convective instability, an alternative damping mechanism. Similarly, they believed, possibly erroneously in our opinion, that wind shear instability is not likely to be the cause of the observed attenuation, since the wave amplitude appears to be insufficient to trigger this effect.

We used parameters of the Magellan temperature profiles oscillations remaining after high-pass filtering for wavelengths < 4 km [4] as input RO data for our reanalysis of IGWs in the Venus’s atmosphere. The results obtained by two independent methods are presented, compared, and discussed in this work. Internal gravity wave characteristics in the atmosphere inferred by two methods from the RO temperature data, collected on 5–6 October 1991 during three successive orbits (orbit numbers 3212–3214) of the Magellan spacecraft have been shown in Table 1.

The work was carried out within the framework of the state task and partially was supported by the Russian Foundation for Basic Research, the project No. 19-02-00083 A.

References:

- [1] Rossow W.B., Del Genio A.D., Limaye S.S., Travis L.D., Stone P.H. Cloud morphology and motions from Pioneer Venus images // *J. Geophys. Res.* 1980. V. 85. P. 8107–8128.
- [2] Seiff A., Kirk D.B., Young R.E., Blanchard R.C., Findlay J.T., Kelley G.M., Summer S.C. Measurements of thermal structure and thermal contrasts in the atmosphere of Venus and related dynamical observations: Results from the four Pioneer Venus probes // *J. Geophys. Res.* 1980. V. 85. P. 7903–7933.
- [3] Counselman C.C. III, Gourevitch S.A., King R.W., Loriot G.B. Zonal and meridional circulation of the lower atmosphere of Venus determined by radio interferometry // *J. Geophys. Res.* 1980. V. 85. P. 8026–8030.
- [4] Hinson D.P., Jenkins J.M. Magellan radio occultation measurements of atmospheric waves on Venus // *Icarus*. 1995. V. 114. P. 310–327.
- [5] Yakovlev O.I., Matyugov S.S., Gubenko V.N. Venera–15 and –16 middle atmosphere profiles from radio occultations: Polar and near-polar atmosphere of Venus // *Icarus*. 1991. V. 94. No. 2. P. 493–510. DOI: 10.1016/0019-1035(91)90243-M.
- [6] Gubenko V.N., Andreev V.E., Pavelyev A.G. Detection of layering in the upper cloud layer of Venus northern polar atmosphere observed from radio occultation data // *J. Geophys. Res.* 2008. V. 113. No. E03001. DOI: 10.1029/2007JE002940.
- [7] Tellmann S., Hausler B., Hinson D.P., Tyler G.L., Andert T.P., Bird M.K., Imamura T., Patzold M., Remus S. Small-scale temperature fluctuations seen by the VeRa Radio Science Experiment on Venus Express // *Icarus*. 2012. V. 221. P. 471–480.
- [8] Kliore A.J., Patel I.R. Vertical structure of the atmosphere of Venus from Pioneer Venus Orbiter radio occultations // *J. Geophys. Res.* 1980. V. 85. P. 7957–7962.
- [9] Gubenko V.N., Pavelyev A.G., Andreev V.E. Determination of the intrinsic frequency and other wave parameters from a single vertical temperature or density profile measurement // *J. Geophys. Res.* 2008. V. 113. No. D08109. DOI: 10.1029/2007JD008920.

ENVISION: EUROPEAN CONCEPT OF A MISSION TO VENUS

R. Ghail¹, C.F. Wilson², T. Widemann³, D.V. Titov⁴, T. Voirin⁴, V. Ansan⁵, F. Bovolo⁶, D. Breuer⁷, L. Bruzzone⁸, B. Campbell⁹, G. Comatsu¹⁰, C. Dumoulin⁵, J. Helbert⁷, A. Le Gall¹¹, W. Kiefer¹², E. Marcq¹¹, P. Mason¹³, J. Romstedt⁴, P. Rosenblatt¹⁴, A. Rugina⁴, A.-C. Vandaele¹⁵, A. Wielders⁴

¹ Royal Holloway University of London, UK,

² University of Oxford, UK,

³ Paris Observatory, France,

⁴ ESA-ESTEC, the Netherlands,

⁵ University of Nantes, France,

⁶ Center for Information and Communication Technologies, Trento, Italy,

⁷ IPF-DLR, Berlin, Germany,

⁸ University of Trento, Italy,

⁹ Smithsonian Institution, USA,

¹⁰ Università G.D'Annunzio, Pescara, Italy,

¹¹ LATMOS, France,

¹² LPI, Houston, USA,

¹³ Imperial College London, UK,

¹⁴ LPG, Nantes, France,

¹⁵ BIRA/IASB, Bruxelles, Belgium.

Keywords:

Venus, EnVision, geology, volcanism, atmosphere, evolution.

EnVision is a Venus orbiter mission that will investigate the nature and current state of volcanic and geological activity on Venus, and its relationship with the atmosphere, to understand how and why Venus and Earth evolved so differently. EnVision is a finalist in ESA's M5 Space Science mission selection process. The concept is currently in Phase A study in collaboration with NASA. Selection of one mission out of three candidates is expected in June 2021. If selected and later adopted in 2024, EnVision will be launched in 2032 by Ariane 6.2 into a six month cruise to Venus. Aerobraking would bring the spacecraft into a near-circular polar orbit. The nominal science phase would last at least 4 Venus sidereal days (2.7 Earth years).

Venus and Earth were probably very similar in the past, before their evolutionary paths diverged. Why are these sister-planets so different now? Understanding how and why this occurred is crucial to revealing the diversity of terrestrial planets and their habitability. Complementing Venus Express that focused on the atmosphere and plasma environment of the neighbouring planet, the EnVision orbiter will undertake science investigations in three thematic areas: (1) Is Venus geologically active today and how? (2) How did Venus surface evolve? (3) How did Venus' climate reach its present state?

EnVision will carry three instruments and perform a radio science investigation. The Synthetic Aperture Radar (SAR) will obtain images at a range of spatial resolutions from 30 m (regional scale) to 1m (local scale), measure topography at <20 m resolution vertically and <100 m spatially from stereo and interferometric SAR observations (InSAR), detect cm-scale changes through differential InSAR observations to characterize current volcanic and tectonic activity and estimate rates of weathering and surface alteration. SAR will also characterize surface physical properties and weathering through multi-polarisation radar, and emissivity mapping.

The Subsurface Sounder (SRS) will characterize the vertical structure and stratigraphy of geological units including volcanic flows, contacts between lowlands and tesserae, determine the depths of weathering and aeolian deposits, discover as yet unknown structures buried below the surface.

The Venus Spectrometer suite (VenSpec) consisting of three spectrometers will search for temporal variations in surface temperatures, as an indicator of active volcanism, obtain global maps of surface emissivity in the near-infrared to constrain surface composition and inform evolution scenarios, map

tropospheric gases, searching for volcanic plumes and studying surface-atmosphere interactions, monitor variability of volcanic gases in the mesosphere, in order to link these variations to tropospheric variations and volcanism.

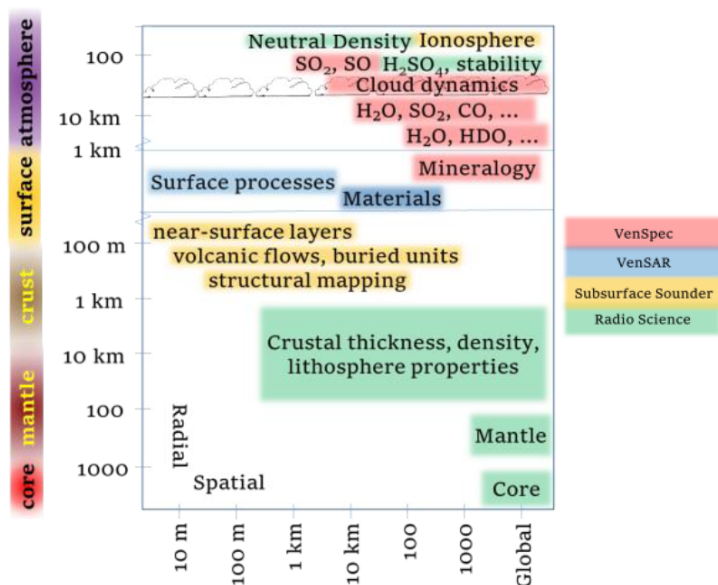


Fig. 1.

The Radio Science and Geodesy investigation will determine crustal and lithospheric structure at finer spatial resolution than Magellan, constrain interior structure through measurement of tidal response (gravitational Love number k_2), sound the atmospheric structure and H₂SO₄ abundance with radio occultation. The figure outlines how the EnVision payload would address the major science themes in different areas on the planet.

The talk will describe science objectives and investigations, payload and mission scenario, and status of the mission study at ESA.

PROPOSED VENUS FLAGSHIP MISSION

A. Martha S. Gilmore¹, Patricia M., Beauchamp² and the 2019 Venus Flagship Mission Study Team

¹ *Department of Earth and Environmental Sciences, Wesleyan University, 265 Church St. Middleton CT 06459 [mgilmore@wesleyan.edu]*

² *Jet Propulsion Laboratory, California Institute of Technology, 4800 Oak Grove Drive, Pasadena, CA. 91109, USA [pbeauch@jpl.nasa.gov]*

Keywords:

Flagship, mission, multi-platform

Introduction:

More than any other known planet, Venus is essential to our understanding of the evolution and habitability of Earth-sized planets in the solar system and throughout the galaxy. Similarly, more than any other group, volatile elements have strong influence on the evolutionary paths of rocky bodies and are critical to understanding planetary evolution. It is clear that Venus experienced a very different volatile element history than the Earth, resulting in a different evolutionary path. The science objectives of the Venus Flagship Mission (VFM) focus on understanding volatiles on Venus. The mission concept's science goals, similar to those for other solar system bodies that were shaped by volatiles such as Mars and Europa, are: to 1) assess the volatile reservoirs, inventory, and cycles over Venus history, and 2) use the understanding of the environments created by and availability of these volatiles to constrain the habitability of Venus. The VFM aims to address two critical questions for planetary science: How, if at all, did Venus evolve through a habitable phase? What circumstances affect how volatiles shape habitable worlds? It is clearly time to focus on Venus and Table 1 shows the advancements possible with such a mission.

The Venus Flagship Mission would provide major, unprecedented advancements in our understanding of the formation, evolution and habitability of terrestrial planets.

First mission to trace volatile inventory, phase, movement, reservoirs and loss over Venus history.

First measurements of the isotopes and inventory of all major atmospheric noble gases.

First measurement of global surface composition from orbit.

First modern, multiple measurements of lower atmosphere in situ and over time via orbital spectroscopy.

First measurement of the seismicity of Venus

First measurement of the isotopes and volatile content of rocks, and the first measurement of the chemistry of the oldest rocks on Venus.

First measurement of interior structure and remanent magnetism.

First deployment of SmallSats at Venus and simultaneous measurements of the exosphere.

First deployment of a Long-lived surface platform.

Table 1.

Objectives and Overview

The VFM concept study enables us to understand the:

- 1) History of volatiles and liquid water on Venus and determine if Venus was habitable.

- 2) Composition and climatological history of the surface of Venus and the present-day couplings between the surface and atmosphere.
- 3) The geologic history of Venus and whether Venus is active today.

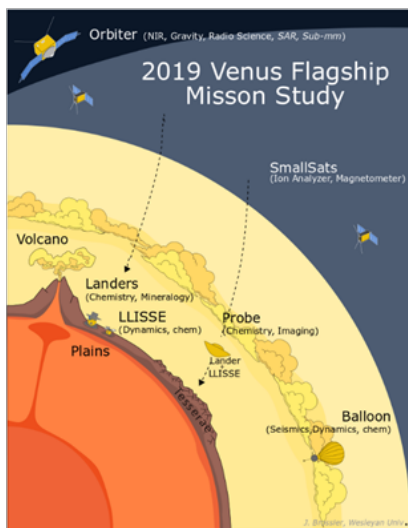


Fig. 1. The Venus Flagship Mission Concept would fill major, long-standing questions about the formation of habitable planets.

the only access to rocks from the first 80% of the history of the planet. One lander would carry a longer-lasting technology demonstration, the Long-Lived In-Situ Solar System Explorer (LLISSE), which measures surface temperature, pressure, wind and atmospheric chemistry as a function of time. The proposed study will also examine the possibility of detecting ground motions via a landed seismometer or by an infrasound technique from aerial platforms.

Technical Approach and Methodology

Many in-depth studies of Venus mission concepts were accomplished in the last decade under the umbrella of proposal developments and down-selects. Proposals for Discovery (VERITAS, DaVINCI, Vesper) and New Frontiers (SAGE, VISAGE, VICI and VOX) advanced several key technologies. Four Venus mission concepts were part of the Planetary Science Deep Space SmallSat Studies (PSDS3). VEXAG was also directed by SMD to study a \$200M "Venus Bridge" mission to explore more options for Venus [VBST 2018]. PSD funded the Surface Platform study and the Aerial Platforms for the Scientific Exploration of Venus.

A Venus Flagship mission, similar to prior flagship missions such as Galileo and Cassini, would accomplish scientific discoveries greater than the sum of what is possible with the individual instruments, employing synergistic observations that work together to answer the 'big questions' relating to Venus' evolutionary path. Although we will be specifying a point-design, we will provide future mission proposers a range of mission implementation strategies at a number of cost points that can address significant science goals. This study will also evaluate and make recommendations for future technology investments and maturation schedules.

Acknowledgements:

This work could not have been accomplished without substantial inputs from the rest of the Science Definition Team comprised of:

The information presented about the VFM concept is pre-decisional and is provided for planning and discussion purposes only.

The cost information contained in this document is of a budgetary and planning nature and is intended for informational purposes only. It does not constitute a commitment on the part of JPL and/or Caltech.

Name of Co-I/Collaborator	Institution
Sushil Atreya	Univ. of Michigan
Penelope Boston	Ames Research Center
Mark Bullock	Science & Technology Corp
Shannon Curry	U.C. Berkeley
Robbie Herrick	Univ. of Alaska
Jennifer Jackson	Caltech
Stephen Kane	U.C. Riverside
Alison Santos	GRC
David Stevenson	Caltech
Colin Wilson	Oxford University
Janet Luhmann (Collaborator)	UC Berkeley
Robert Lillis (Collaborator)	UC Berkeley
Joshua Knicely (student)	Univ. of Alaska

VENERA-D: A POTENTIAL MISSION TO EXPLORE VENUS' ATMOSPHERE, SURFACE, INTERIOR STRUCTURE AND PLASMA ENVIRONMENT

L. Zasova¹, T. Gregg², A. Burdanov³, T. Economou⁴, N. Eismont¹, M. Gerasimov¹, D. Gorinov¹, J. Hall⁵, N. Ignatiev¹, M. Ivanov⁶, K. Lea Jessup⁷, I. Khatuntsev¹, O. Korablev¹, T. Kremic⁸, S. Limaye⁹, I. Lomakin¹⁰, A. Martynov¹⁰, A. Ocampo¹¹, S. Shuvalov¹, O. Vaisberg¹, V. Voron¹², V. Vorontsov¹⁰

¹ Space Research Institute RAS, Russia,

² NASA Goddard Spaceflight Center, USA, ³ TSNIIMASH, Russia,

⁴ Enrico Fermi Institute, USA,

⁵ Jet Propulsion Laboratory, USA,

⁶ Vernadsky Inst. RAS, Russia,

⁷ Southwest Research Institute, USA,

⁸ NASA Glenn Research Center, USA,

⁹ Univ. of Wisconsin, USA,

¹⁰ Lavochkin Assoc., Russia,

¹¹ NASA Headquarters, USA,

¹² Roscosmos, Russia.

Keywords:

Venus, atmosphere, surface, interior, plasma, mission Venera-D.

Introduction:

Venus and Earth were formed approximately the same distance from the Sun, and have almost the same masses and volumes: they should be the most similar pair of planets in the Solar System. An outstanding question is how and when these planets diverged in their evolutions. Significantly, did ocean and life exist in Venus early history? Recent investigations [1] based on similarity of “unknown UV-absorber” and spectra of some bacteria suggest that microbial life may still exist in Venus’ cloud deck. Venus presents us with fundamental questions about the origin and evolution of planetary bodies and life in our Solar System. Venera-D (D stands for “long-lived:” *dolgozhivushaya*) is a potential mission that combines simultaneous observations of Venus’ atmosphere, plasma environment, and surface to try to answer these essential questions.

Venera-D Baseline Architecture:

Based on the initial report from the Venera-D Joint Science Definition Team (composed of scientists from both Russia and the USA) [2], a baseline Venera-D mission would include an orbiter, a VEGA-style lander and attached to it a Long-lived In-Situ Solar System Explorer (LLISSE) [3] on the surface. In addition, the Joint Science Definition Team (VDJSDT) identified the additional science objectives (relying on the NASA Planetary Decadal Survey [4] and VEXAG [5]) that could be addressed by incorporating additional potential elements (e.g., additional long-lived stations, an aerial platform or subsatellites).

Orbiter Science Goals:

Despite the fact that Venus is the planet nearest to Earth, it is a planet of mysteries, one of the most intriguing of them is the dynamics of the atmosphere. In the troposphere and mesosphere, the main circulation mode is retrograde zonal superrotation (RZS), while in the thermosphere — sub-solar — anti-solar circulation (SS-AS)

Although recent investigations, based on the ESA Venus Express and JAXA’s Akatsuki spacecraft data analysis, showed the determining factors influencing the dynamics of the atmosphere, are insolation (in particular solar tides [6], [7]) and surface relief [7], [8], possibly through the generation of gravity waves [9], [10]. An orbiter associated with the Venera-D mission would need to examine the thermal tides, atmospheric composition and structure, examine the atmosphere in the ultraviolet, visible, and infrared wavelengths, study the possible surface thermal activity on the night side and look at the interaction between the upper atmosphere, ionosphere, and magnetosphere with the solar wind. Ideally, the orbiter would take measurements for a minimum of 3 years.

Lander Science Goals:

During descent, the lander would investigate the physical structure and chemical composition of the atmosphere down to the surface, including composition and distribution of atmospheric aerosols. Once below the cloud deck, cameras would image the surface to provide a geologic context for the landing site; on the surface, the chemical composition of the landing site would be measured, the drilling and soil sampling and study the sample inside will be performed and additional cameras would image the near- and far-field. Combining measurements of the surface and the adjacent atmosphere would allow us to constrain the chemical interactions occurring at that interface. A VEGA-style lander would likely live on the surface for 2–3 hours.

LLISSE Science Goals:

A LLISSE would measure surface winds (velocity and direction), pressure, temperature, and chemical composition over a lifetime of 2 – 3 months on the Venusian surface. Ideally, the LLISSE would transition from the dayside to the nightside during this time.

Potential Elements:

The Joint Science Definition Team is examining the science return from potential additional elements, depending on the mass and volume available, which in turn are controlled at least partly by the precise launch date.

Additional contributed augmentations being discussed include additional LLISSEs or a long-lived seismic instrument such as the Seismic and Atmospheric Exploration of Venus (SAEVe) [11], a variable altitude balloon, a sub-satellite(s) placed at the Lagrange point L1 (L2).

References:

- [1] Limaye, S.S. et al. (2018) *Astrobio*. 18(10), doi: 10.1089/as. 2017. P. 1783.
- [2] Venera-D Joint Science Definition Team (2017), <https://www.lpi.usra.edu/vexag/reports/Venera-D-STD013117.pdf>.
- [3] Kremic, T. et al. (2017) LPSC 49, Abstract #2986.
- [4] National Research Council (2011) ,<https://solarsystem.nasa.gov/resources/598/vision-and-voyages-for-planetary-science-in-the-decade-2013-2022/>.
- [5] VEXAG (2017) https://www.lpi.usra.edu/vexag/reports/GOI-Draft-SpacePhy-sAdds_v4.pdf.
- [6] Zasova, L.V., et al.(2007). *PSS*, V. 55(12), P. 1712–1728. doi.org/10.1016/j.pss.2007.01.011
- [7] Khatuntsev, et al.(2017),*JGR. Planets*, V. 1 22, P 2312–2327. doi.org/10.1002/2017JE005355
- [8] Gorinov et al.,*GRL*, 45. 2018. doi.org/10.1002/2017GL076380 .
- [9] Horinouchi, T. et al. 2017. *Nature Geosci*. V. 10 P. 646-651.
- [10] Bertaux, J.-L., et al. 2016. *JGR*, V. 121, P. 1087–1101. doi.org/10.1002/2015JE004958
- [11] Kremic, T. et al. 2018. LPSC 49, Abstract #2744.

A MODEL OF MICROWAVE ABSORPTION OF ATMOSPHERIC GASES FOR THE RADIOMETRIC EXPERIMENT IN THE VENERA-D MISSION

V.D. Gromov, A.S. Kosov

IKI RAS, 84/32 Profsovnaya, Moscow, Russia, 117997.

Contact: vgromov@iki.rssi.ru

Keywords:

Venusian Atmosphere; Microwave Radiometer; Remote Sensing; Carbon Dioxide; Sulfur Dioxide; Sulfuric Acid vapor.

Introduction:

Microwave radiometer [1] of the Venera-D orbiter provide unique possibilities for investigation of sub-cloud atmosphere of Venus, while other remote sensing instruments are pointed mainly to higher layers. Retrieving of profiles of atmospheric parameters [2] requires sufficient accuracy of determination of microwave absorptivity by atmospheric components in extremal conditions of Venus. Now it exists only a limited volume of laboratory measurements partly covering these conditions (see [3–4, 9–11]). It requests for adequate model for extrapolation of the experimental data to wide region of temperatures and pressures.

In microwave region, or, more precisely, on centimeter and millimeter waves, corresponding to spectral bands of the instrument [1], the absorptivity is generated mainly by rotational transitions of molecules CO_2 , N_2 , SO_2 and H_2SO_4 . Collisional interactions change strongly a linear spectrum of molecules for high density of Venusian atmosphere. For non-polar molecules CO_2 and N_2 , we should take into account only collision induced absorption, while for other molecules, “line-transitions” distorted by collisions play an important role. In a first approximation, effect of collisions is considered separately for each line, treated as independent oscillator. Its spectrum of absorption is described as “line-profile”, determined by one of models of collisions, usually in approximation of low rate of collisions. There is a great volume of data on molecular transitions, collected, for example, in a data base HITRAN [5], which permits detailed calculation of molecular spectra, at relatively low pressures.

Nevertheless, the model of independent oscillators is not sufficient for description of microwave molecular absorption even for pressure of the Earth atmosphere. It was shown by extensive literature on atmospheric absorption by water vapor. A solution is a combination of line-spectrum calculated “line-by-line” on molecular data, with continuum-spectrum, produced on base of absorption measurements, to correct inaccuracy of the oscillator model. This approach was used successfully for Earth atmosphere, and it is implemented in this work. Their adequacy for extrapolation was proven particularly for prediction of Terahertz windows in Antarctic [6], by measurements at South pole and in similar dry condition in the high mountain desert Atakama.

Collision induced absorption by non-polar molecules:

The data on collision induced molecular absorption are included in current version of the HITRAN data base [7]. The equations based on theoretical consideration [8] gives the same numerical results. For a limited spectral region discussed here, the simplified equation could be used:

$$\alpha = \alpha_q \cdot \left(\frac{p}{p_0}\right)^2 \cdot \left(\frac{\nu}{\nu_0}\right)^2 \cdot \left(\frac{T}{T_0}\right)^{-n+m \cdot \ln\left(\frac{T}{T_0}\right)} \quad (1)$$

where α is a microwave absorption coefficient, p_0 , T_0 , ν_0 are reference pressure, temperature, and frequency, correspondingly,

$$\alpha_q = \alpha_0 \left(q_{\text{CO}_2}^2 + 0.25 q_{\text{CO}_2} q_{\text{N}_2} + 0.0054 q_{\text{N}_2}^2 \right) \quad (2)$$

where mixing ratios in Venus atmosphere are: $q_{\text{CO}_2} = 0.965$, $q_{\text{N}_2} = 0.035$.

For frequencies from 0 to 150 GHz, and temperatures from 200 to 800 K, Eq. (1) could be used with accuracy about 1%. For $p_0 = 1$ atm (101325 Pa), $T_0 = 273.15$ K, $\nu_0 = 100$ GHz, parameters of Eq. (1) are: $\alpha_0 = 0.1265$ km⁻¹, $n = 4.892$, $m = 0.852$.

Absorption by polar molecules:

“Line-by-line” coefficient of absorption is:

$$\alpha_L = C_L \cdot q \cdot \frac{p}{p_0} \cdot \left(\frac{T_0}{T}\right)^2 \sum_{j=1}^N (S_j(T_0) e^{-\left(\frac{hc}{k}\right) E_j^l \left(\frac{1}{T} - \frac{1}{T_0}\right)}) f(\nu, \nu_j, \nu_j, \dots), \quad (3)$$

where C_L is a constant, q is the number mixing ratio of the gaseous component, N is the number of lines, S_j is the line intensity, E_j^l is the lower state energy in cm⁻¹, $f(\nu, \nu_j, \nu_j, \dots)$ is a line profile, ν_j is the line frequency, the line width

$$\gamma_j(T, p) = \gamma_j(T_0, p_0) \cdot \left(\frac{p}{p_0}\right) \cdot \left(\frac{T}{T_0}\right)^{-n_j}$$

The spectral line profile according to Ben-Reuven is written as

$$f_{BR}(\nu, \nu_j, \gamma, \delta, \zeta) = \frac{2}{\pi} \frac{\nu^2}{\nu_j^2} \cdot \frac{(\gamma - \zeta)\nu^2 + (\gamma + \zeta) \left[(\nu_j + \delta)^2 + \gamma^2 - \zeta^2 \right]}{\left[\nu^2 - (\nu_j + \delta)^2 - \gamma^2 + \zeta^2 \right]^2 + 4\nu^2\gamma^2} \quad (4)$$

where δ is the frequency shift parameter, ζ is the coupling parameter. Index j for parameters γ , δ , ζ is omitted for brevity. The Gross profile is a modification of the Ben-Reuven profile with $\delta=0$, $\zeta=\gamma$. VVW-profile (Van Vleck-Weisskopf) corresponds to $\delta=\zeta=0$.

There is a lot of publications comparing advantages of these profiles. For Venus atmosphere, a numerical difference is not large. In any case, a continuum term could correct a resulting difference between profiles. Finally, the VVW-profile was used in numerical calculations here.

In a general case, an absorption coefficient α could be a sum of lines and a continuum term, which includes effects of non-resonant collision induced absorptivity:

$$\alpha = \alpha_L + \alpha_C \quad (5)$$

In many cases, a continuum term could be written in power-law form as

$$\alpha_C = c_C \cdot f^s \cdot p^n \cdot T^{-m} \cdot q \quad (6)$$

where c_C is a constant, f is frequency in Gigahertz, p is pressure in atmospheres, and T is temperature in degrees Kelvin.

Absorption by sulfur dioxide molecules:

Parameters S_j , E_j^l , ν_j , γ_j , n_j of SO₂ lines could be found in the HITRAN-2016 [5] data base. The number of lines with $\nu_j < 300$ cm⁻¹, used in our calculations, is $N = 36015$. Laboratory measurements of the microwave opacity of SO₂ under simulated conditions for the deep atmosphere of Venus [9] was approximated by authors using Eq. (6) with $s=2$, resulting in values of parameters: $n=1.20$, $m=3.1$, $c_{SO_2} = 2.54 \times 10^7$ dB/km. Altitude dependence $\alpha_{SO_2}(H)$ calculated by Eq. (6) with these parameters is similar to $\alpha_L(H)$ calculated by Eq. (3) with T and p typical for the sub-cloud atmosphere, but values calculated “line-by-line” explains only $\sim 60\%$ of the measured absorption.

Therefore, it is possible to write $\alpha_{SO_2} = \alpha_L + \alpha_C$ following Eq. (5), with the coefficient in Eq. (6): $\alpha_C \approx 1 \times 10^7$ dB/km. This representation has an advantage of that such approximation doesn't flatten spectral details, in spite of a small number of experimental points in a spectrum. These details are important signs for separation of atmospheric components during retrieving of radiometric data received from the orbital sounder.

Absorption by sulfuric acid vapors:

Lines of the H₂SO₄ are not presented in HITRAN-2016 data base. Line parameters was taken from JPL catalog (v. 4, 2013, <https://spec.jpl.nasa.gov/>). The number of lines with $\nu_j < 1$ THz included in the calculations are $N = 20939$.

There are discrepancies between laboratory measurements of microwave absorption by sulfuric acid vapors [3–4, 10–11], and the “line-by-line” calculations of α_c . The difference achieves about 4 times. It is much more than that of sulfur dioxide, so a continuum term in (5) is more important. For determination of optimal parameters in Eq. (6) we used weighted least squares method, because the experimental data for H_2SO_4 vapors are highly inhomogeneous on measurement accuracy. Thus, it was revealed that, square dependence of α_c from frequency, $s=2$ in Eq. (6) definitely doesn't correspond to experimental data, and exponent s was included among the varied parameters. Otherwise, the temperature dependence $\alpha_c \sim T^{-3}$, predicted by some theoretical models, doesn't contradict to experimental data. It was fixed $m=3$, because of absence of statistically reliable ground for any other value.

The result of approximation of all the data: $s=0.909$, $n=1.435$, $c_c = 6.9 \times 10^9$ dB/km.

Conclusions:

The quantitative model of microwave absorption of the sub-cloud Venusian atmosphere is developed. It has a maximum accuracy available with modern laboratory experimental data. It is optimized for remote sensing of atmosphere of Venus by orbital radiometric instrument. Numerical parameters of the model are given in the work.

References:

- [1] Gromov V.D., Kosov A.S. The radiometer for thermal sounding of low atmosphere and sulfur compound detection // Proceedings of the Venera-D Modeling Workshop. Moscow, Russia. 2017. P. 181-184.
- [2] Gromov V.D., Kosov A.S. An accuracy of the retrieving of Venusian atmospheric data from the radiometer instrument in the Venera-D mission // The Ninth Moscow Solar System Symposium Abstracts. Moscow, Russia. 2018. P. 269–271 (9MS3-PS-35).
- [3] Akins A.B., Steffes P.G. Laboratory Measurements of Sulfuric Acid Vapor Opacity at Millimeter Wavelengths Under Venus Conditions // AAS Division for Planetary Sciences Meeting Abstracts. 2017. V. 49. P. 417.04.
- [4] Akins A.B., Steffes P.G. Millimeter Wavelength Opacity of H_2SO_4 Vapor at Venus: Initial Results // Lunar and Planetary Science Conference. 2018. V. 349. P. 2306.
- [5] Gordon, I.E., Rothman, L.S., Hill, C. et al. The HITRAN2016 molecular spectroscopic database // JQSRT. 2017. V. 203. P. 3–69.
- [6] Burova L.P., Gromov V.D. et al. Low humidity and submillimeter transparency above the Vostok Antarctic station. // Soviet Astronomy Letters. 1987. V. 12, P. 339–341.
- [7] Richard C., Gordon I.E., Rothman L.S., et al. New section of the HITRAN database: Collision-induced absorption (CIA) // JQSRT. 2012. V. 113. P. 1276-1285.
- [8] Gruszka M., Borysow A. Roto-Translational Collision-Induced Absorption of CO_2 for the Atmosphere of Venus at Frequencies from 0 to 250 cm^{-1} , at Temperatures from 200 to 800 K // Icarus. 1997. V. 129. P. 172–177.
- [9] Steffes, P.G., Eshleman, V.R. Sulfur dioxide and other cloud-related gases as the source of the microwave opacity of the middle atmosphere of Venus // Icarus. 1981. V. 46, P. 127-131.
- [10] Kolodner M.A., Steffes P.G. The Microwave Absorption and Abundance of Sulfuric Acid Vapor in the Venus Atmosphere Based on New Laboratory Measurements // Icarus. 1998. V. 132. P. 151–169.
- [11] Jenkins, J.M. and Kolodner, M.A. and Butler, B.J. and Suleiman, S.H. and Steffes, P.G. Microwave Remote Sensing of the Temperature and Distribution of Sulfur Compounds in the Lower Atmosphere of Venus. Icarus. 2002. V. 158. P. 312–328.

HYPOTHETICAL LIVING FORMS ON VENUS PLANET AND THEIR POSSIBLE NATURE

V.N. Parmon¹, L.V. Ksanfomality², L.M. Zelenyi², V.N. Snytnikov¹

¹ *Bereskov Institute of Catalysis SB RAS, Novosibirsk, Russia, parmon@catalysis.ru*

² *Space Research Institute, Moscow, Russia, leksanf@gmail.com*

Keywords:

Venera missions, TV experiments, astrobiology, origin of life

The authors in their report will present their views on the possibility of the existence of life forms on the surface of Venus in the light [1] and the creation of the "Venus-D" mission.

References:

- [1] Ksanfomality L.V., Zelenyi L.M., Parmon V.N. Snytnikov V.N. Hypothetical signs of life on Venus:revising results of 1975 - 1982 TV experiments// First Physics Uspekhi.2019. V. 62. No. 4. P. 378-404.

MANEUVERABLE ENTRY VEHICLES FOR VENUS RESEARCH

A.V. Kosenkova, A.B. Martynov

*Lavochkin Association, Russia, Khimki, Leningradskaya 24, 141402,
tarasova_av@laspace.ru*

Keywords:

Venus, Spacecraft, Maneuverable, Atmosphere, Surface, Design.

Introduction:

Basing on the results of the successful soviet Venera and VEGA missions [1], along with the Pioneer, Magellan [2, 3], and more recent Venus Express and Akatsuki missions [4, 5] on Venus research, established in 2015 joint NASA Roscosmos/IKI Science Definition Team (JSDT) started international cooperation for more complex project on Venus research. Within the overarching goal of understanding why Venus and the Earth took divergent evolutionary paths, the JSDT has the task of defining the science and architecture of a comprehensive Venera-D (Venera-Dolgozhivuschaya (long-lasting)) mission. The baseline Venera-D concept includes two elements, an Orbiter and a Lander, with the payload for distance and contact analysis, including detachable elements such as aerial platforms that can flow in the atmosphere, small long-lived surface stations, small satellite(s) and maneuverable entry vehicles. In January 2017, the JSDT finished the first phase and published a report of NASA–Roscosmos/IKI collaboration [6]. The second phase was completed in January 2019 that was mainly focused on refining the science investigation, undertaking a compressive development of the core Orbiter and Lander mission architecture, a detailed examination of contributed elements and aerial platforms that could address key Venus science [7, 8, 9]. Current activities are connected with more precise definition of the payload, landing sites, orbits and landing itself, including consideration of different configurations of maneuverable landers.

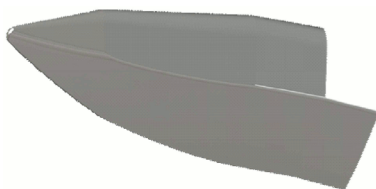


Fig. 1.

Maneuverable Entry Vehicle (MEV) is a “lifting body” type of a lander [10] that can perform significant maneuvers in the Venus atmosphere to provide wide scope of landing site selection with the ability to make measurements during the descent process.

References:

- [1] Sagdeev, R.V., et al. 1986. *Science*. V. 231, P. 1407–1408.
- [2] Colin, L., et al. 1980. *JGR*, 85, A13.
- [3] Saunders, R.S. et al. 1992. *JGR*, 97, 13067.
- [4] Svedhem, H. et al. 2009. *JGR*, 114, E00B33.
- [5] Nakamura, M. et al. 2011. *Earth, Planets and Space*, 63, 443.
- [6] Venera-D JSDT. 2017. http://iki.rssi.ru/events/2017/venera_d.pdf
- [7] Venera-D JSDT, 2019. <http://www.iki.rssi.ru/events/2019/Venera-DPhaseIIFinal-Report.pdf>
- [8] Cutts, J. et al. 2017. *Planetary Science Vision 2050 Workshop*, 1989.
- [9] Cutts, J. 2017. 15th Meeting of the Venus Exploration Analysis Group (VEXAG), 8015.
- [10] Kosenkova, A.V.; Minenko, V.E.; Bykovsky S.B., and Yakushev, A.G., 2018, Investigation of aerodynamic characteristics of lander alternative forms to study Venus. *Inzhenernyy zhurnal: nauka i innovatsii—Engineering Journal: Science and Innovations*, no. 11, <http://dx.doi.org/10.18698/2308-6033-2018-11-1826>.

THE LIFE MISSION: A LARGE INTERFEROMETER FOR EXOPLANETS

Daniel Angerhausen^{1,2}, and the LIFE team

¹ Center for Space and Habitability, University of Bern, Switzerland

² Blue Marble Space Institute of Science, USA

Keywords:

Exoplanets, space telescopes, nulling interferometry, biosignature detection, exoplanet spectroscopy, mid infrared

Summary

The atmospheric characterization of a significant number of terrestrial planets, including the search for habitable and potentially inhabited planets, is arguably the major goal of exoplanetary science and one of the most challenging questions in 21st century astrophysics. However, despite being at the top of the agenda of all major space agencies and ground-based observatories, none of the currently planned projects or missions worldwide—neither in Europe, nor in the US, Russia, China or India—has the technical capabilities to achieve this goal. Here we present the LIFE Mission, which addresses this issue by investigating the scientific potential and technological challenges of an ambitious mission employing a formation-flying nulling interferometer in space working at mid-infrared wavelengths (Quanz et al., 2018; Defrere et al., 2018a). Breakthroughs in our understanding of the exoplanet population as well as significant progress in relevant technologies justify the need, but also the feasibility for a future mission like LIFE to investigate one of the most fundamental questions of mankind: are we alone in the Universe?

Context

One of the long-term objectives of extrasolar planet research is the investigation of the atmospheric properties for a large number (~ 100) of terrestrial exoplanets. This is partially driven by the idea to search for and identify potential biosignatures, but such a dataset is — in a more general sense - invaluable for understanding the diversity of planetary bodies. While exoplanet science is omnipresent on the roadmaps of all major space agencies and ground-based observatories and first steps in this direction will be taken in the coming 10-15 years with funded or selected ground- and space-based projects and missions, none of them will be able to deliver such a comprehensive dataset. An alternative to the currently discussed large space-based coronagraphic missions or the starshade concept is to separate the photons of the planet from those of its host star by means of an interferometer. In Defrere et al. (2018b) for example they showed that Proxima B is an ideal target for a space-based nulling interferometer with relatively small apertures.

LIFE is a new project initiated in Europe with the goal to consolidate various efforts and define a roadmap that eventually leads to the launch of a large, space-based MIR nulling interferometer to investigate the atmospheric properties of a large sample of primarily terrestrial exoplanets. Centered around clear and ambitious scientific objectives the project will define the relevant science and technical requirements. The status of key technologies will be re-assessed and further technology development will be coordinated. LIFE is based on the heritage of ESA/Darwin and NASA/TPF-I, but significant advances in our understanding of exoplanets and newly available technologies will be taken into account in the LIFE mission concept.

First results

In Kammerer & Quanz (2018) we used Monte Carlo simulations to demonstrate that a MIR space-based nulling interferometer, could yield at least as many exoplanet detections as a large, single aperture optical/NIR telescope. The details and exact number of planets depend on the assumed technical specifications and the underlying exoplanet populations, but from an exoplanet science perspective such an interferometer should be considered an attractive mission concept, at least complementary if not superior to an optical/NIR mission.

Future Steps

Our analysis also shows that getting a better handle on the overall planet statistics is crucial for planning larger future missions. Another key aspect that we will investigate more closely in the future is a specific treatment of stellar leakage and exozodiacal light in our simulations. A critical look at the stellar input sample and its properties is also warranted with a specific focus on multiplicity. Sensitivity, wavelength coverage and spectral resolution requirements will be defined using atmospheric retrieval analyses. As most detected planets will be warmer than Earth, going as short as $3\ \mu\text{m}$ seems useful; at the red end $25\ \mu\text{m}$ seems sufficient. This wavelength range features absorption bands of CO_2 ; H_2O ; O_3 ; CH_4 ; $(\text{N}_2)_2$; and N_2O and also contains windows to probe surface emission. The spectral resolution ($R \sim 20\text{--}100$) is very likely to be driven by the need to avoid line contamination of certain molecules such as N_2O and CO_2 around $4.15\ \mu\text{m}$, as well as CH_4 and also N_2O and H_2O between 7.7 and $8\ \mu\text{m}$.

References:

- [1] Defrere D., Leger A., Absil O., et al. 2018a, *Experimental Astronomy*, 46, 543, doi:10.1007/s10686-018-9613-2
- [2] Defrere D., Leger A., Absil O., et al. 2018b, in *Society of Photo-Optical Instrumentation Engineers (SPIE) Conference Series*, Vol. 10701, *Optical and Infrared Interferometry and Imaging VI*, 107011H
- [3] Kammerer J., & Quanz, S. P. 2018, *A&A*, 609, A4,
- [4] Quanz S.P., Kammerer J., Defrere D., et al. 2018, in *Society of Photo-Optical Instrumentation Engineers (SPIE) Conference Series*, Vol. 10701, *Optical and Infrared Interferometry and Imaging VI*, 107011I

WSO-UV/UVSPEX FOR OBSERVATION OF EARTH-LIKE EXOPLANETS

S. Kameda¹, A. Tavrov², T. Muraoka¹, G. Murakami³, K. Enya³, T. Kodama⁴, N. Narita⁵, M. Ikoma⁶, O. Korabiev², M. Sachkov⁷

¹ Rikkyo University, Japan, kameda@rikkyo.ac.jp

² IKI, Russia;

³ ISAS/JAXA, Japan;

⁴ Universite de Bordeaux;

⁵ NAOJ, Japan;

⁶ The University of Tokyo, Japan;

⁷ INASAN, Russia;

Keywords:

exoplanet, exosphere, oxygen, ultraviolet, space telescope

Introduction:

Many Earth-sized planets have been discovered and some appear to lie in the habitable zone. Moreover, several Earth-sized planets were recently detected around low temperature stars near the solar system. However, it is difficult to characterize them as Earth-like or Venus-like. Transit spectroscopy for exoplanetary atmosphere has been performed to characterize larger exoplanets but it requires very high accuracy because of their small size. Hydrogen exosphere has been detected around Neptune-sized exoplanet [1], but an Earth-sized exoplanetary exosphere has not been detected. Recently, Earth's hydrogen exosphere was re-investigated and it was revealed that the Earth's exosphere is extended to ~ 38 Earth radii [2]. On the other hand, Venus' and Mars' hydrogen exosphere is not so much extended because of its low temperature of upper atmosphere. This is caused by the difference of mixing ratio of CO_2 in the upper atmosphere. Venus and Mars have CO_2 -rich atmospheres with a lower exospheric temperature. On Earth, CO_2 was removed from its atmosphere by a carbon cycle with its ocean and tectonics [3]. Translating these arguments to exoplanets in a habitable zone presents a possible marker to distinguish an Earth-like planet from a Mars-like or Venus-like planet. The expanded exospheres can be observed in UV, during the exoplanet transit event in a primary eclipse. It reduces the stellar flux, when an exoplanet orbiting in front of the host star.

Instrumentation:

High sensitivity (photon counting) is required for M-type star faint in UV. Spectral resolution of 0.5 nm is enough for separating major emission lines of exospheric atoms. The spectral resolution will be achievable by spectrometers in the main WUVS block, however, it is difficult to measure the weak stellar emission from M-type stars without a photon-counting detector. To realize exoplanet transit observations in oxygen spectral lines with the desired accuracy, we equip the WSO-UV telescope with the UVSPEX spectrograph. The dominant engineering requirements for the UVSPEX are following. The spectral resolution is better 0.5 nm to separate O I line from other spectral lines. The spectral range is to exceed the wavelengths from 115 nm to 135 nm to detect at least H Lyman alpha 121.6 nm to O I 130 nm. The throughput is better 0.3% accounting more than four terrestrial exoplanets distanced at 5 pc. To achieve these requirements, a simple spectrograph design is proposed, containing the slit, the concave (toroidal) grating as a disperse element and the imaging photo-detector. This optical concept is conventional and used in the other space missions for UV spectroscopy.

Spectrometer slit is aligned at primary focus of the telescope from off-axial sub-FoV. Slit width is 0.2 mm, corresponding to 5 arc-sec. The concave grating is laminar type with groove density of 2400 grooves per mm. It has a toroidal shape with the curvature radii of 266.4 mm in horizontal direction and of 253.0 mm in vertical direction. The effective area has nearly \varnothing 25 mm and the focal length is ~ 250 mm. The surface is coated by Al + MgF2 to increase the reflectance, and diffraction efficiency of $\sim 29\%$ can be achieved.

UVSPEX is planned to be a part of Field Camera Unit (FCU). In this presentation, we show the configuration of UVSPEX instrument and its science objectives.

References:

- [1] Ehrenreich, D. et al., A giant comet-like cloud of hydrogen escaping the warm Neptune-mass exoplanet GJ436b. *Nature* 522, 459–461, 2015.
- [2] Kameda, S. et al., Ecliptic North-South Symmetry of Hydrogen Geocorona. *Geophysical Research Letters* 44, 11,706-11,712, 2017.
- [3] Abbot, D. S., Cowan, N.B. & Ciesla, F.J., Indication of insensitivity of planetary weathering behavior and habitable zone to surface land fraction, *Ap. J.* 756:178(13pp), title// *First Example Journal*. 2016. V. 1. No. 1. P. 1–100.

ENERGY-LIMITED ESCAPE: AN EXAMINATION OF THE RANGE OF APPLICABILITY

A. Krenn¹, H. Lammer², L. Fossati², D. Kubyshkina²

¹ *Institute of Physics/IGAM, University of Graz, Universitaetsplatz5, 8010 Graz, Austria, andreas.krenn@edu.uni-graz.at;*

² *Space Research Institute, Austrian Academy of Sciences, Schmiedlstr. 6, 8042 Graz, Austria, helmut.lammer@oeaw.ac.at;*

Keywords:

Particle escape rates, energy-limited escape, hydrodynamic escape, hydrogen envelopes, atmospheric evolution

A protoplanet can catch a significant envelope of hydrogen gas while forming within the protoplanetary disc. Once the disc has disappeared this envelope will start to interact with the incident extreme ultraviolet (EUV) radiation of the host star. The EUV radiation is absorbed in the upper atmosphere and some of the energy is used to drive hydrodynamic escape, leading to the loss of particles. An upper limit to the maximum particle escape driven by EUV radiation can be found, when looking at the amount of available EUV energy. Watson et al. [1] did such an investigation of the energy-limited escape rate for the first time in 1981. They provided a set of equations to calculate the height of the EUV absorption in the atmosphere and the maximum particle escape rate. However, they used a variety of assumptions, like a thin absorption layer and an absorption of all the EUV energy below the sonic level of the system, that limit the scope of applicability of the equations. We provide lower and upper boundaries for system parameters like mass, radius or incident EUV flux, that still satisfy the above-mentioned assumptions and compare the resulting energy-limited escape rates with escape rates provided by hydrodynamic numerical simulations. In addition, we examine a variety of recently published papers, using the energy-limited escape equations, on whether they stay within the determined boundaries of applicability. Finally, we also compare the upper boundary limits to the gravitational potential limit found by Salz et al. [2].

References:

- [1] Watson, A.J., Donahue, T.M., Walker, James C.G. The dynamics of a rapidly escaping atmosphere: Applications to the evolution of Earth and Venus. *Icarus*. (1981)V. 48(2). P. 150-166
- [2] Salz, M., Schneider, P.C., Czesla, S., Schmitt, J.H.M. M. Energy-limited escape revised. The transition from strong planetary winds to stable thermospheres. *Astron. Astrophys.*(2016). V. 585. P. L2.

ATMOSPHERIC ESCAPE OF CLOSE-IN NEPTUNES

V.I. Shematovich¹, Ya.N. Pavlyuchenkov¹, E.S. Kalinicheva¹

¹ *Institute of Astronomy of the Russian Academy of Sciences, Moscow, Russia; shematov@inasan.ru*

Keywords:

Hot Jupiters and Neptunes, sporadic stellar activity, atmospheric mass loss, aeronomic model.

Introduction:

Exoplanets with substantial hydrogen/helium atmospheres have been discovered in abundance, many residing extremely close to their parent stars. The extreme irradiation levels that these atmospheres experience cause them to undergo hydrodynamic atmospheric escape. Ongoing atmospheric escape has been observed to be occurring in a few nearby exoplanet systems through transit spectroscopy both for hot Jupiters and for lower-mass super-Earths and mini-Neptunes. Hot-Neptunes are exoplanets with masses and radii close to the parameters of Neptune in the Solar System, but with much higher thermospheric temperatures, up to 104 K. High thermospheric temperature is caused by absorption of the high-energy stellar flux, which is very strong for close-in planets [1].

Despite the identification of a great number of Jupiter-like and Earth-like planets at close-in orbits, the number of hot Neptunes — the planets with 0.6–18 times of Neptune mass and orbital periods less than 3 days—turned out to be very small. The respective region in the mass-period distribution was assigned as the “short-period Neptunian desert”. The common explanation of this fact is that the gaseous planet with a few Neptune masses would not survive in the vicinity of host star due to intensive atmosphere outflow induced by heating from stellar XUV radiation. To check this hypothesis we used the previously developed self-consistent 1D model of hydrogen-helium atmosphere with suprathermal electrons accounted [2]. The two-scale structure of the close-in (hot) Neptune atmosphere was found. The gaseous envelope of hot Neptune consists from dense atmosphere with exponential density decrease and extended corona in which the gas density decreases according to the power law. The mass-loss rates as a function of orbital distances and stellar ages are presented. We conclude that the desert of short-period Neptunes could not be entirely explained by evaporation of planet atmosphere caused by the radiation from a host star [3]. While for the case of light Neptune-like planet, the estimated upper limits of the mass outflows are consistent with the estimates [1] of the atmosphere photo-evaporation, in the case of heavy Neptune-like planets this mechanism does not allow to drop away the significant fraction of the planet atmosphere mass.

Acknowledgments:

This study was supported by the Russian Science Foundation (project 18-12-00447).

References:

- [1] Owen J.E. Atmospheric Escape and the Evolution of Close-In Exoplanets // *Annu. Rev. Earth Planet. Sci.* 2019. V. 47. P. 67–90.
- [2] Ionov D.E., Shematovich V.I., Pavlyuchenkov Ya.N. Influence of Photoelectrons on the Structure and Dynamics of the Upper Atmosphere of a Hot Jupiter // *Astron. Reports.* 2017. V. 61. P. 387–392.
- [3] Ionov D.E., Pavlyuchenkov Ya.N., Shematovich V.I. Survival of a planet in short-period Neptunian desert under effect of photo-evaporation // *MNRAS.* 2018. V. 476. Issue 4. P. 5639–5644.

3D GASDYNAMIC MODELING OF TRANSITING HOT EXOPLANETS

I.F. Shaikhislamov¹, M.L. Khodachenko², A.G. Berezutsky¹,
I.B. Miroshnichenko¹ and M.S. Rumenskikh¹

¹ *Institute of Laser Physics SB RAS, Novosibirsk, Russia, ildars@ngs.ru;*

² *Space Research Institute, Austrian Acad. Sci., Graz, Austria*

Keywords:

Exoplanets, planetary wind, transit absorption.

Introduction:

Using a global 3D, fully self-consistent, multi-fluid gas-dynamic aeronomic model, we simulate the dynamically expanding upper atmosphere of a warm Neptune GJ436b. The complex spatial structure of the escaping upper atmospheric planetary material, energized by the stellar XUV and driven further by tidal forces, while interacting with the stellar wind plasma is revealed in course of the modeling. We calculate transit absorption in Ly α and find that it is produced mostly by Energetic Neutral Atoms outside the Roche lobe, due to the resonant thermal line broadening.

A series of observations by HST/STIS (Kulow et al. 2014, Ehrenreich et al 2015, Lavie et al. 2017) revealed that the warm Neptune GJ 436b has a very deep transit in Ly α line reaching up to 60%. Moreover, this strong absorption takes place mostly in a blue wing of the line in the range of Doppler shifted velocities of [-120; -40] km/s. The good signal/noise ratio allowed to reveal clearly, for the first time in VUV observations of hot exoplanets, such details of transit curve as early ingress (Ehrenreich et al 2015) and extended egress (Lavie et al. 2017). The obtained data are of sufficient quality to test quantitatively the existing theoretical concepts and numerical models.

The aim of the present report is to apply, for the first time, a fully self-consistent 3D gasdynamic model (Shaikhislamov et al. 2016, 2018) to simulate the Ly α line absorption features of GJ 436b. Moreover, the applied code is multi-fluid and aeronomic, as it includes hydrogen plasma-photo chemistry. We not only determine parameters of planetary outflow, stellar XUV flux and plasma wind at which a good agreement of synthetic and experimental line absorption profiles and transit curves is obtained, but describe also how different physical processes may affect the observations. It should be noted that HD/MHD modeling of hot exoplanets is steadily progressing from 1D to 3D codes. However, so far they had not reached the same level of complexity present in the first generation of 1D aeronomy models which allows self-consistent simulating of planetary outflow. We believe that the present model is the first one which can be directly compared with involved 1D aeronomy simulations of the subject on the one hand, and which is able to calculate plasma environment in the whole 3D planet-star system on the other. It includes, also for the first time, all the physics present in Monte-Carlo simulations, such as radiation pressure and charge exchange, so can be directly compared with them as well.

Results

Figure 1 show spatial structure of interaction between planetary and stellar winds for simulation with assumed typical parameters: base temperature of the planet atmosphere $T_{\text{base}}=750$ K, Helium abundance $\text{He}/\text{H}=0.1$; GJ436 ionizing radiation $F_{\text{XUV}}=0.86$ erg cm^{-2} s^{-1} at 1 a.u., staller corona temperature $2 \cdot 10^6$ K, stellar mass loss rate $\dot{M}_{\text{sw}}=2.5 \cdot 10^{-11}$ g/s; SW parameters at planet orbit $T_{\text{sw}}=6 \cdot 10^5$ K, $V_{\text{sw}}=170$ km/s, $n_{\text{sw}}=4 \cdot 10^3$ cm^{-3} . Note that assumed stellar radiation and mass loss are about 5–10 times weaker than that of the Sun, mostly due to smaller size of GJ436. At those parameters the simulation gives for the planetary mass loss rate a value of $\dot{M}_{\text{pw}}=2 \cdot 10^9$ g/s.

Energetic Neutral atoms (ENAs) are generated. The neutral atoms of planetary origin which come close to ionopause penetrate through the shocked region where they become uncoupled from protons and interact with stellar protons via charge exchange.

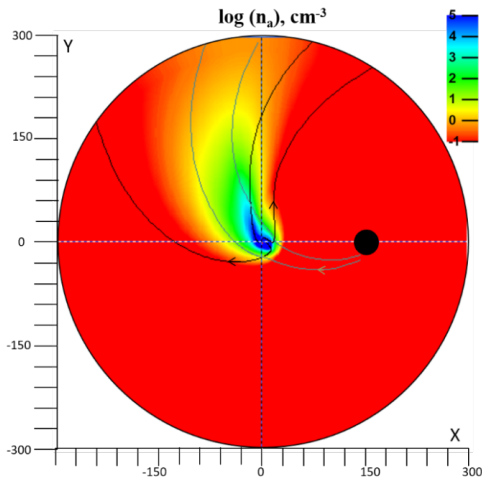


Fig. 1 Color plot showing distribution of density of hydrogen atoms in the equatorial X-Y plane. Black lines show velocity streamlines of atoms, khaki - streamlines of stellar protons. Distance is in units of planet radius.

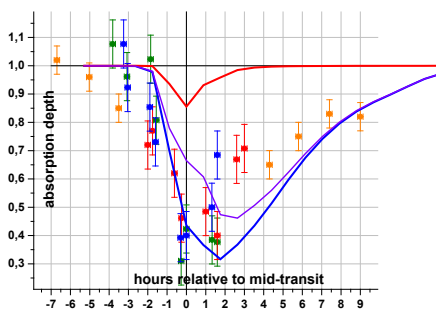


Fig. 2 Light curves in the blue [-120; -40] and red [30; 110] km/s wings of Ly α line (blue and red lines respectively). Violet line shows part of absorption by ENAs in the blue wing. Colored squares show measurement data from different visits (Lavie et al. 2017).

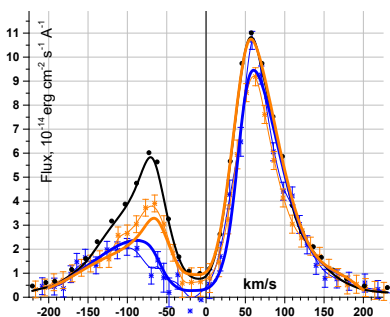


Fig. 3 Modeled Ly α line profiles in mid-transit (blue dots) and post-transit $t=5$ h (orange dots). Measured profiles out of transit and at mid-transit are shown by black and blue lines/symbols respectively.

Plots reveal that SW sweeps away PW and redirects all planetary material in the trailing tail. There is compressed layer (shock) in front of the planet where

Next figures describe modeled absorption in Ly α . For comparison with observation, measured data are plotted as well. One can see deep absorption with early ingress and long egress, mostly in the blue high velocity part of the line. All this features are in good general agreement with observations.

Acknowledgements

This work was supported by the Russian Science Foundation RSF project 18-12-00080, SB RAS basic research program (project II.10 №0307-2017-0015), and Austrian Science Foundation FWF, projects I2939-N27, S11606-N16, S11607-N16. Parallel computing has been performed at Computation Center of Novosibirsk State University, Siberian Supercomputer Center of SB RAS, Supercomputing Center of the Lomonosov Moscow State University and Joint Supercomputer Center of RAS.

References:

- [1] Kulow J. R. et al. 2014, ApJ, 786(2), 132.
- [2] Ehrenreich et al., 2015, Nature, 522, 459.
- [3] Lavie et al. 2017, A&A, 605, L7.
- [4] Shaikhislamov et al. 3D, 2018, MNRAS, 481(4), 5315.
- [5] Shaikhislamov et al. ApJ, 2016, 832(2), 173.

THE PAST ROTATION HISTORY OF KEPLER-11 REVEALED BY THE PRESENT ATMOSPHERES OF ITS PLANETS

D.I. Kubyskhina¹, P.E. Cubillos¹, L. Fossati¹, N.V. Erkaev^{2,3}, C. Johnstone⁴, K.G. Kislyakova^{4,1}, H. Lammer¹, M. Lendl¹, P. Odert^{5,1}

¹ Space Research Institute, Austrian Academy of Sciences, Schmiedlstrasse 6, A-8042 Graz, Austria;

² Institute of Computational Modelling, FRC "Krasnoyarsk Science Center SB RAS", 660036, Krasnoyarsk, Russian Federation;

³ Siberian Federal University, 660041, Krasnoyarsk, Russian Federation;

⁴ Institute for Astronomy, University of Vienna, Türkenschanzstrasse 17, A-1180 Vienna, Austria;

⁵ IGAM/Institute of Physics, University of Graz, Universitätsplatz 5, A-8010 Graz, Austria

Keywords:

exoplanets; upper atmospheres; atmospheric escape; hydrodynamical modelling; planetary evolution; stellar evolution

Planet atmospheric escape induced by high-energy stellar irradiation is a key phenomenon shaping the structure and evolution of planetary atmospheres. Therefore, the present-day properties of a planetary atmospheres are intimately connected with the amount of stellar flux received by a planet during its lifetime, thus with the evolutionary path of its host star.

Recently we developed the method, where using the analytic approximation based on hydrodynamic simulations for atmospheric escape rates, we track within a Bayesian framework the evolution of a planet as a function of stellar flux evolution history, constrained by the measured planetary radius [1]. We find that the ideal objects for this type of study are close-in sub-Neptune-like planets, as they are highly affected by atmospheric escape, and yet retain a significant fraction of their primordial hydrogen-dominated atmospheres. In [1] we tested the method for the wide range of parameters, finding the range of applicability, and then applied it to two real systems, each containing one planet appropriate for our analysis (in sense of its parameters and observational uncertainties).

Kepler-11 system hosts six closely packed planets of sizes between super-Earth and sub-Neptune orbiting the Sun-like star [2, 3]. At least five of them fall in the range of parameters which allows the use of our approach, except the outermost planet where only the upper limit for the mass is known. Using the multi-planet approach allows to better constrain the past rotational history of the star.

Given by initial studies [2, 3], the planets in system have an average densities between 0.6 and 1.7, what is very different to the planets in Solar system. The later work [4] reanalyses the properties of the star and arriving to higher planetary masses and densities, but yet much lower than planets in Solar system at the similar orbital distances.

All together, it makes Kepler-11 system particularly interesting for our study. We present the method and testing results, and results obtained for Kepler-11 system.

References:

- [1] Kubyskhina, D., Cubillos, P.V., Fossati, L., et al. // *ApJ*, 879, 1, 26, 2019.
- [2] Lissauer, J.J., Fabrycky, D.C., Ford, E.B., et al. // *Nature*, 470, 53. P. 10-13, 2011.
- [3] Lissauer, J.J., Jontof-Hutter, D., Rowe, J.F., et al. // *ApJ*, 770, 131, 2013.
- [4] Bedell, M., Bean, J.L., Meléndez, J., et al. // *ApJ*, 839, 94, 2017

MASS DISTRIBUTION OF EXOPLANETS CONSIDERING OBSERVATION SELECTION EFFECTS IN THE TRANSIT DETECTION TECHNIQUE

V. Ananyeva^{1, *}, A. Ivanova¹, I. Shashkova¹, A. Venkstern¹, A. Tavrov¹
and J.-L. Bertaux^{1,2}

¹ Space Research Institute of the Russian Academy of Sciences; 84/32
Profsoyuznaya Str, Moscow, Russia, 117997;

² LATMOS/IPSL/CNRS/UVSQ, 78280, Guyancourt, France

Keywords:

Exoplanets, mass distribution, Kepler Space Telescope.

While the radial velocity technique (RV) allows to determine only the product $m \cdot \sin i$ of the mass m of one exoplanet by $\sin i$ (i , angle of inclination of orbital pole to the observer), when it is applied to a planet already detected while transiting its host star, the true mass m is determined, since angle i is near 90° and $\sin i \sim 1$. Therefore, the mass distribution of transiting exoplanets discovered by photometric observations is of particular interest. However, there are some selection effects that distort the true (original) mass distribution into the observed mass distribution. We have studied the whole observed mass distribution of transiting exoplanets that were discovered from spaceborne and ground-based surveys [1], see Fig. 1.

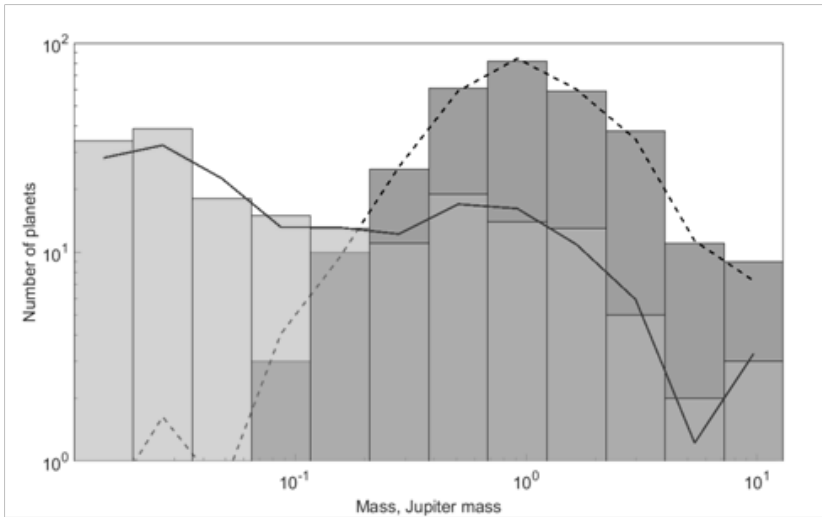


Fig. 1. Mass distributions of transit planets with masses measured by the RV method as directly obtained from the catalogue [1]. They are biased by observation selection effects. Gray bars show the distribution of Kepler planets, and a solid line shows the dependency smoothed by considering the associated measurement error via the KDE with the Gaussian window. Darker bars show the distribution of transit planets discovered by the ground-based surveys and the CoRoT mission, and a dashed line accounts for the inaccuracies in the mass measurements by the KDE.

We have corrected observed mass distributions from some selection effects to retrieve a de-biased true mass distribution, see Fig. 2. For this, we take into account two factors: the probability of mass determination and the probability of transit configurations. The first factor is a bias introduced by a number of effects inherent to the RV method. The bias factor could be estimated by computing the fraction of transiting planets for which the mass was determined from the RV method. Photometric surveys for transit detection allow determining the planetary radii, and the bias factor was estimated for various bins of plan-

etary sizes. The second factor is the transit probability, a geometrical factor which is precisely known for each detected transiting planet and therefore easy to account for. The mass distribution of exoplanets corrected for these two factors (de-biased) was analyzed, and it is found that this distribution can be well approximated by a power law: $dN/dm \propto m^{-2}$. The significances of the local minima in the retrieved mass distribution have been estimated by the Kolmogorov-Smirnov test.

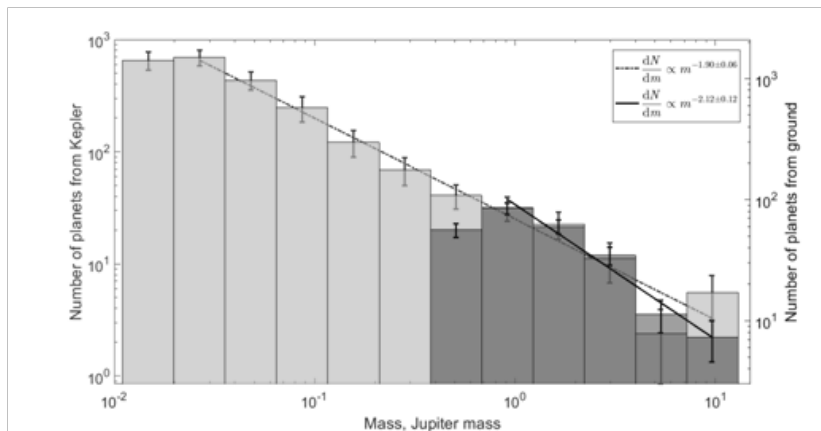
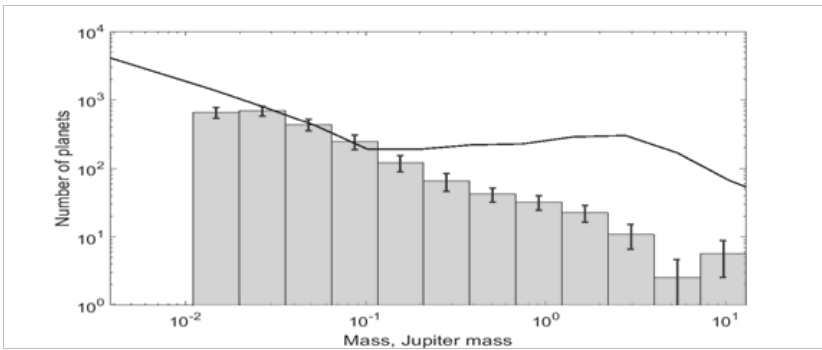


Fig. 2. Comparison of the mass distributions $N(m)$ of transiting planets obtained by different photometric surveys and corrected for the observation selection effects (by considering the factor of mass determination). The mass distribution of the Kepler planets is shown with gray histogram bars with numbers on the left y-axis, and that for transiting planets discovered by ground-based surveys and the CoRoT ST is shown with the darker histogram bars (numbers on the right y-axis). Lines show the power law approximations specified in the caption box. Error bars are built using the Poisson criterion for numbers of planets in each mass bin for ground-based group and for Kepler group.

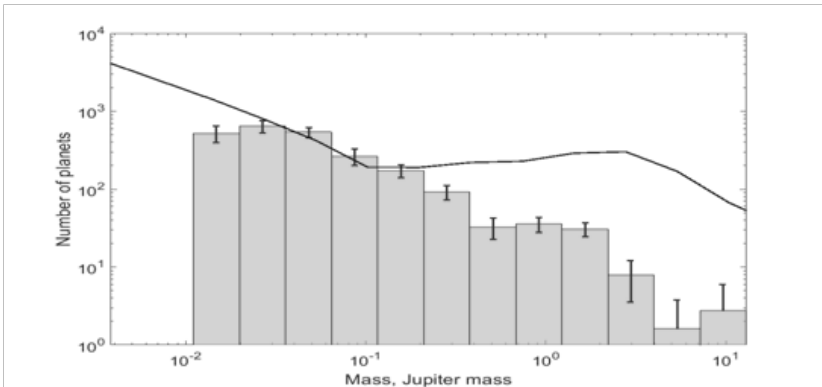
Our de-biased mass distribution was compared to the theoretical model of [2], where planetary population synthesis linked a theoretical model of planet formation and evolution, and the theoretically derived planet mass distribution may be compared to observations, the de-biased planetary mass distribution.

The predicted planetary mass distribution displayed in the Fig. 10 (top left panel in [2]) can be described as follows (shape also shown here as a blue line on Fig. 3). In the mass domain of 1–30 Earth mass (0.003–0.1 Jupiter mass) the distribution follows a power law with a -2 exponent: $dN/dm \propto m^{-2}$ which agrees with our de-biased distribution. In the mass domain of 0.1-5 Jupiter mass, the predicted mass distribution follows a power law with exponent -1: $dN/dm \propto m^{-1}$ (resulting in a plateau in log of mass_bins, or even a slight increase), and in the domain above 5 Jupiter mass the exponent of the power law approaches -2.

In Fig. 3 we can compare the de-biased mass distribution of Kepler planets (discussed above) with result [2]. In panel (a) of Fig.3 we compare the de-biased mass distribution without considering the probability of transit configurations, in panel (b) when considering the probability of transit configurations. For comparison, the scale of mass distribution from [2] was normalized to the number of planets and was artificially shifted vertically to be merged with the bins in 0.020 to 0.116 Jupiter mass domain. The de-biased mass distribution accounting for the probability of transit configuration shows a shape closer to mass distribution from [2], in particular there is a hint of three consecutive bins around 1 Jupiter mass with equal number of planets, reminiscent of the predicted theoretical plateau. The slopes are similar, but a plateau present in the model in the range 0.3-3 Jupiter mass is absent in the data, possibly due to the lower sensitivity of RV and transit method to planets at far distances.



(a)



(b)

Fig. 3. Mass distribution of Kepler planets (green bars) and distribution predicted by [2] (black line). (a) de-biased mass distribution without considering the probability of transit configurations, (b) de-biased mass distribution when considering the probability of transit configurations.

Acknowledgments

We acknowledge the support from the Government of Russian Federation and Ministry of Education and Science of Russian Federation (grant N14.W03.31.0017).

References:

- [1] NASA Exoplanet Archive. 2019. <https://exoplanetarchive.ipac.caltech.edu/>
- [2] Mordasini, C., Planetary Population Synthesis, Handbook of Exoplanets, H. J. Deeg, J. A. Belmonte (eds.) (2018), https://doi.org/10.1007/978-3-319-30648-3_143-1

MASS DISTRIBUTION OF TRANSIT PLANETS DEPENDING ON THE HOST STAR SPECTRAL CLASS (CONSIDERED: K, G, F)

V. Ananyeva^{1,*}, J.-L. Bertaux^{1,2}, and A. Tavrov¹

¹ Space Research Institute of the Russian Academy of Sciences; 84/32 Profsoyuznaya Str, Moscow, Russia, 117997;

² LATMOS/IPSL/CNRS/UVSQ, 78280, Guyancourt, France

Keywords:

Exoplanets, mass distribution, comparative planetology.

The statistics of planetary masses in the Solar System is useful, but not fully significant and representative because the number of planets (and dwarf planets) in the Solar System is not large. Retrieving the true mass distribution of exoplanets allows determining the abundance of planets of various types in the Galaxy at host stars of different spectral classes.

The mass distribution of transiting exoplanets corrected for observation selection was analyzed and was de-biased, and it is found that this distribution can be well approximated by a power law: $dN/dm \propto m^{-2}$, see Fig. 1.

Is this distribution widely universal, e.g. if one traces planetary systems on the host stars of different spectral classes? K, G, F spectral classes are presently considered. However, as is known, the number of giant planets increases with increasing mass and with increasing the metallicity of the host star [1, 2]. On the contrary, the number of small masses planets, increases with decreasing the mass and with decreasing the metallicity of the host star [3]. Therefore, the mass distribution of the planets at host stars of various spectral classes may be possibly different....

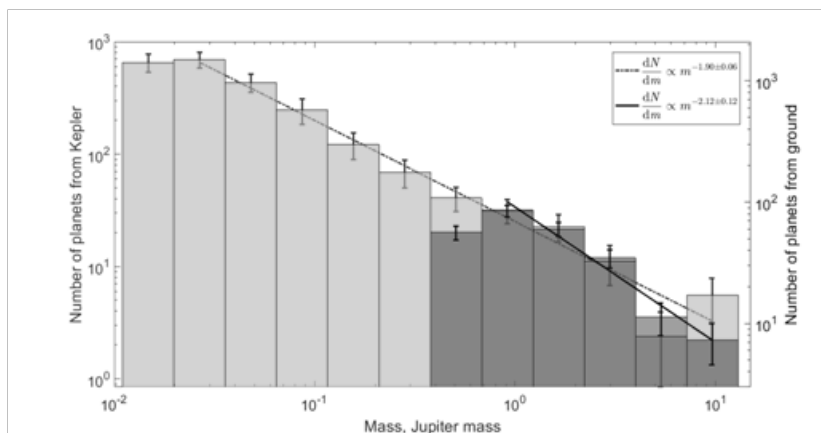


Fig. 1. De-biased mass distributions $N(m)$ of transiting planets obtained by different photometric surveys and corrected for the observation selection effects. The mass distribution of the Kepler planets is shown with gray histogram bars with numbers on the left y-axis, and that for transiting planets discovered by ground-based surveys and the CoRoT is shown with the darker histogram bars (numbers on the right y-axis). Lines show the power law approximations specified in the caption box. Error bars are built using the Poisson criterion.

From [4], we organized the Kepler transit planets into three groups depending on the host star effective temperature, see Fig. 2:

group K with an effective temperature below 5000 K, 531/33 (531 exoplanets mass was measured at 33);

group S – from 5000 to 6200 K (stars from about the spectral class from F8 to K2 fall into this group), 1856/157;

group F – with effective temperatures above 6200 K, 177/20.

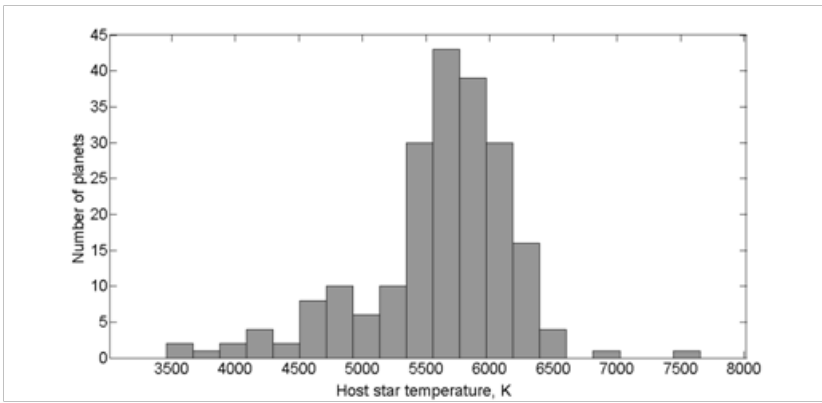


Fig. 2. Distribution by effective temperatures of the host stars of Kepler's transit planets with measured mass.

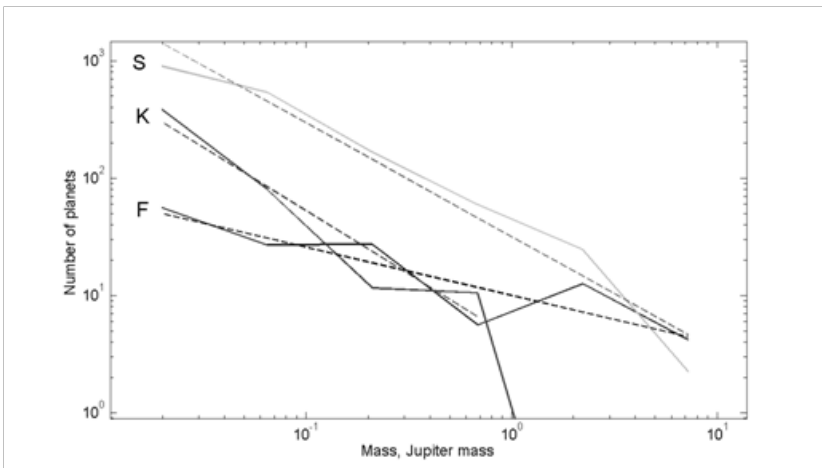


Fig. 3. De-biased mass distributions $N(m)$ of the Kepler planets from the F, K and S groups. De-biasing took into account the mass measurement coefficients. Dotted lines show power dependencies approximating them with exponents of -1.41 ± 0.10 (F), -2.08 ± 0.24 (K) and -1.97 ± 0.11 (S).

The Fig. 3 illustrates that the power law exponents in the distributions of the Kepler planets from groups K and S are well consistent (within the error-bar (not shown here)), then the distribution of planets from group F is noticeably different from them. To consider whether this difference is objective, or whether it is a consequence of observational selection, we examined the distribution of Kepler planets from the F, K, and S groups by their radii. Comparison of the radii of the distributions of the planets from groups F, K, and S demonstrates a clear deficit of small planets in group F in comparison with the groups K and S. This may be due to the fact the Kepler incompleteness for the F group. Ground-based surveys, do prove this hypothesis (power law dependence has exponent -1.84 ± 0.28), Fig. 4.

In conclusion by the first approximation we do not determine any feasible difference in the mass distribution of the planets at host stars of different spectral classes considering K, G, F.

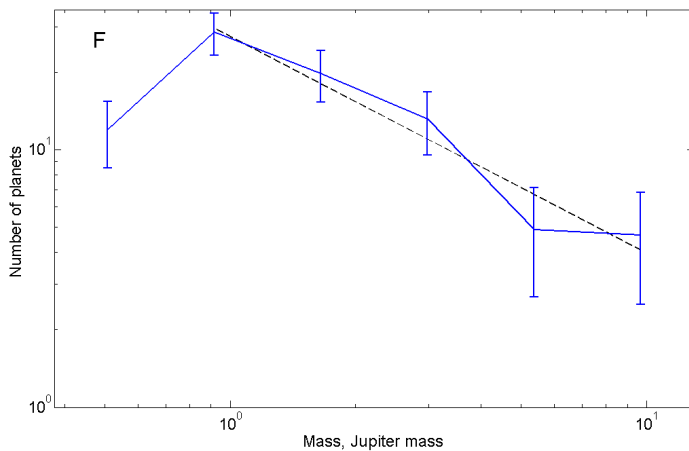


Fig. 4. De-biased mass distributions $N(m)$ of the exoplanets from ground-based surveys for the F group.

Acknowledgments

We acknowledge the support from the Government of Russian Federation and Ministry of Education and Science of Russian Federation (grant N14.W03.31.0017).

References:

- [1] Udry et al.: A Decade of Radial-Velocity Discoveries of Exoplanets, 2005 <https://www.lpi.usra.edu/books/PPV/8058.pdf>
- [2] Perryman M., The Exoplanet Handbook, 2011.
- [3] John M. Brewer, Songhu Wang, Debra A. Fischer, and Daniel Foreman-Mackey, Compact multi-planet systems are more common around metal poor hosts, 2018 <https://arxiv.org/pdf/1810.10009.pdf>
- [4] NASA Exoplanet Archive. 2019. <https://exoplanetarchive.ipac.caltech.edu/>

RV-EXOPLANETS MASS DISTRIBUTION AT M-DWARF-TYPE HOST STARS

A. Ivanova^{1*}, V. Ananyeva¹, I. Shashkova¹, A. Venkster¹, A. Tavrov¹ and J.-L. Bertaux²

¹ Space Research Institute of the Russian Academy of Sciences; 84/32 Profsoyuznaya Str, Moscow, Russia, 117997;

² LATMOS/IPSL/CNRS/UVSQ, 78280, Guyancourt, France

Keywords:

Exoplanets, mass distribution, RV exoplanets, comparative planetology.

Exoplanets orbiting around M-dwarf-type host stars are now of great interest because of their abundance and a planet occurrence in a habitable zone can be investigated. Therefore we study the mass distribution of exoplanets discovered with the method of measuring the radial velocities (RV) and orbiting around M-dwarf type host stars. We take into consideration the observation selection factors aiming to regularize initially inhomogeneous data. We use and modify the detectability-window method [1] by accounting for the detection probabilities (e. g. evaluated in [2]) to form a homogeneous series of exoplanets collected from different surveys. We focused to minority of detected exoplanets which orbit around M-dwarf host stars. Considered different surveys: HIRES/Keck, PFS/Magellan, HARPS/ESO, and UVES/VLT, Lick Observatory Hamilton Echelle Spectrometer, Automated Planet Finder, Anglo-Australian Planet Search, UCLES, Hobby Eberly Telescope, CORALIE and ELODIE, HARPS-North, All Sky Automated Survey, they all have different sensitivities and completeness. Here a detectability-window method [1] is a practical tool, applied to regularize exoplanets data captured by different instrumental errors of spectrographs. The method bounds a nearly rectangular area: the minimal projective mass, denoted by $m_p \sin i$, along the vertical axis, and the exoplanet orbital period P along the horizontal axis, see Fig. 1. The left down boundary of $m_p \sin i$ is associated with an instrument detection limit, while the right down boundary of P is associated with the host star observing time. If we set a binary border of a detectability-window of a particular host star (i.e. a zero multiplier outside and a unit multiplier inside) as in [1], that procedure filters the great majority of exoplanets. An alternative way to keep initial number of exoplanets being detected is to estimate the probability accounting for observation selection as partial incompleteness of a survey, as made in [2], see Fig. 2 of proceeded analysis for M-dwarf type stars.

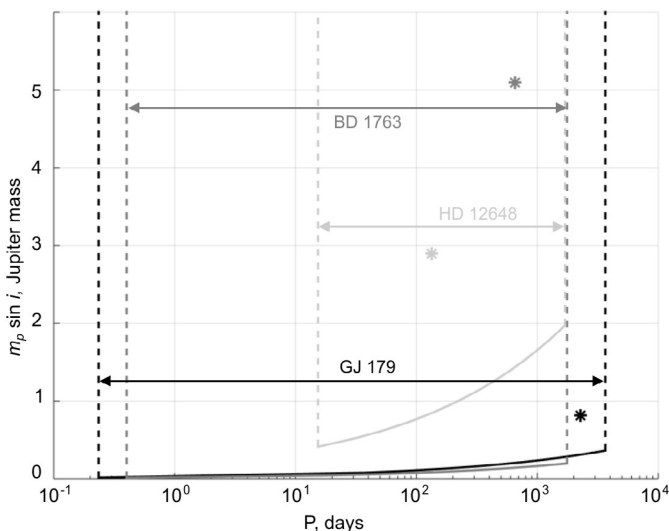


Fig. 1. Examples of the detectability windows on the plane of the orbital period and the projective mass for the planetary systems BD-17 63, HD 12648, and GJ 179. The stars show the planets BD-17 63 b, HD 12648 b, and GJ 179 b.

Required compilation of the earlier observational programs with a low accuracy in the radial-velocity measurements and long observational periods, on the one hand, and the relatively recent observational programs with a higher measurement accuracy but a shorter duration, on the other hand, can be made by a colored detectability-window as having different probability of detection.

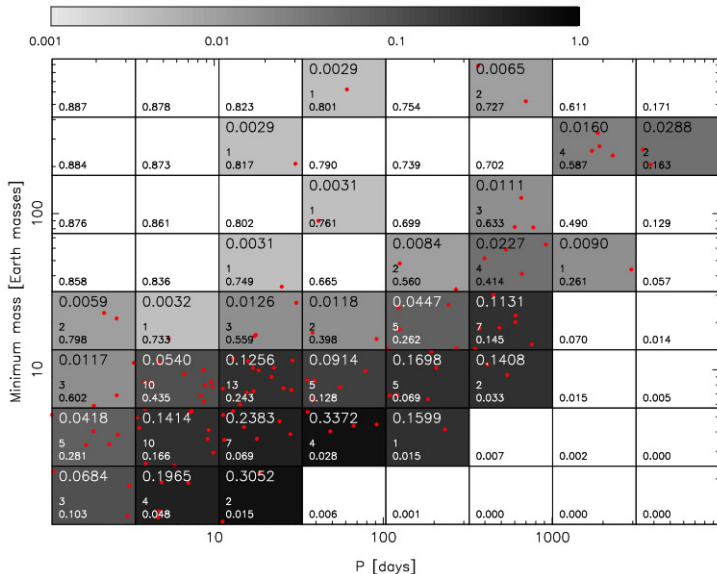


Fig. 2. [2]: Detectability window being colored by detection probability denoted by the number in cell, the number of planets is denoted in cell middle, exoplanets candidates are depicted by red dots and occurrence rate is denoted in cell upper number.

Having these data collected we integrated dataset along P axis and obtained de-biased mass dependence for M-dwarf host stars exoplanets, while we have considered their projective masses.

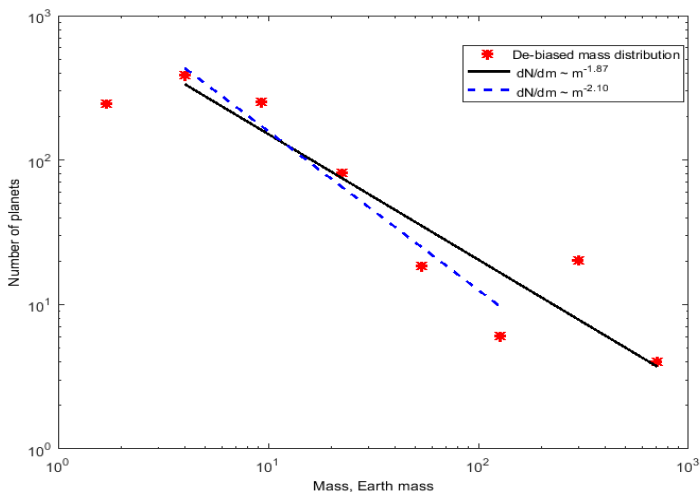


Fig. 3. De-biased mass distribution of exoplanets orbiting around M-stars. Power-law approximations are shown: $dN/dm \sim m^{-1.87 \pm 0.38}$ (solid black line) and $dN/dm \sim m^{-2.10 \pm 0.15}$ (dashed blue line).

Additionally we studied several randomized models to understand the effect of projective mass transformation to the histogram of true masses for several a-priori known power laws.

Finally we compare M dwarf type exoplanets mass histogram obtained by RV with K, G, H spectral classes host stars transiting exoplanets.

Acknowledgments

We acknowledge the support from the Government of Russian Federation and Ministry of Education and Science of Russian Federation (grant N14.W03.31.0017).

References:

- [1] Ananyeva, V.I., Venkstern, A.A., Churbanov, D.V., Shashkova I.A., Tavrov, A.V., Korablev, O.I., Bertaux, J.-L. The distribution of exoplanet giants by the true and projective masses. Accounting observational selection. *Solar System Research*, 2019, Vol. 53, No. 2, pp. 124–137.
- [2] M. Tuomi, H.R. A. Jones, R. P. Butler, P. Arriagada, S. S. Vogt, J. Burt, G. Laughlin, B. Holden, S.A. Shectman, J. D. Crane, I. Thompson, S. Keiser, J.S. Jenkins, Z. Berdiñas, M. Diaz, M. Kiraga, J.R. Barnes, Frequency of planets orbiting M dwarfs in the Solar neighbourhood, 2019, <https://arxiv.org/abs/1906.04644>

ON A POSSIBLE ROLE OF GIANT EXO-RINGS OF THE J1407B TYPE IN PHYSICAL PROPERTIES OF THE KEPLER KIC 8462852 OBJECT

L.V. Ksanfomality, A.V. Tavrov

Space research institute of the RAS

Keywords:

exoplanet giant rings transit photometry

The experimental data on the features of the emission of the KIC-8462852 star (Boyajian et al., 2016), obtained at the KEPLER mission, have not been adequately explained in the past 3 years. Assumptions about the nature of the object, like a swarm of cometary bodies, fragments of a catastrophic collision of asteroids or an exoplanet KIC-8462852b are encountered with serious difficulties (Ksanfomality, Tavrov, 2017) and even contradict Kepler's laws if the eclipsing object is considered as a physical body orbiting the central star. Another possible hypothesis considering here would be the assumption that there is a giant rings system surrounding the KIC-8462852b object.

Mamajek et al. (2012) reported on exoplanet j1407b (belonging to the star 1SWASP), which has a giant ring system. It is huge. If the radius of the outer ring F of Saturn is 140,000 km, then the radius of the outer ring of j1407b is estimated to be 0.6 AU, about 90 million kilometers - 640 times more than the outer ring F of Saturn. The unusualness of the 1SWASP J1407b system was reviewed by Sucerquia et al., (2018), in "Anomalous lightcurves of young tilted exorings" paper. The authors performed numerical simulations and showed that in the presence of a third body (an emerging satellite) in exoplanet's rings and inclination of rings to its orbit reveal short-term changes in shape and orientation of rings, which manifests itself as strong changes in the depth and duration of the transit, even between successive orbits. Changes in the geometry, density and structure of the rings are observed, which the authors explain by the influence of a massive satellite (built into the rings) through the Lidov-Kozai mechanism. The authors conclude that motions of ring structures can explain the peculiarities and strangeness of the transits of light curves of already known exoplanets.

These features could be considered to be properties of the photometry curves of assumed transits of the KIC-8462852b object (Boyajian et al., 2016). None of the proposed physical explanations of the KIC-8462852 transit curves proved to be successful, although some of the data undoubtedly indicates some kind of regular phenomenon or event, the nature of which remains unclear and even contradictory (Ksanfomality, Tavrov, 2017). It is therefore interesting to compare the photometric data of the KIC-8462852 object and the photometry curves of the transit model of rings J1407b. The transit direction can be oriented arbitrarily, as well as its completeness.

The 1SWASP J1407 star has a class K5 IV (orange dwarf) and a magnitude 12.4. The exoplanet j1407 b has a large semi-axis of the orbit 3.9 ± 1.7 AU and a huge mass of $20 \pm 6 M_J$, exceeding the criterion of $13M_J$, therefore, more typical for a brown dwarf than for a planet. On the Earth's orbit, the scale of the rings and the orbit would look like that shown in Figure 1. But the real semi-axis of the j1407b orbit is 3.9 ± 1.7 AU, so the system of giant rings j1407b in the sky of the Earth would be visible at an angle of up to 24° , 48 times larger than the Moon, and, like the Moon, it would remain visible during the day.

The ring system J1407b has at least 37 rings, the total mass of which is about 100 times the mass of the Moon (the mass of the Saturn rings is approximately 1/1000 of the mass of the Moon). The fragmentary photometry of the transit of rings j1407b shown on the website <https://www.google.com/search> and is presented in Fig.2.

The model of rings J1407b, built on the basis of observations, was used to construct an arbitrarily oriented photometry curve of transit through J1407b

rings. It is shown in Fig. 3. It is assumed that the transit, same as in the case of KIC-8462852, was non-central. One can see that the curve has a complex structure, which hardly permits to suggest in advance that it is namely a system of rings in transit.

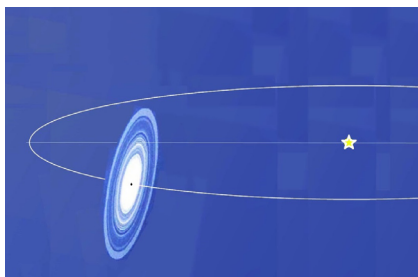


Fig. 1. Scale of rings of exoplanet j1407b, conditionally placed on Earth's orbit.

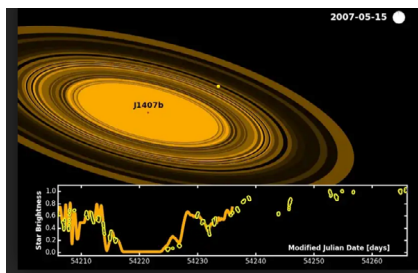


Fig.2. Photometry of transits of J1407b rings, according to <https://www.google.com/search>.

It is interesting to compare Fig. 3 with the KIC-8462852b object's transit curves (Fig. 4) obtained by the KEPLER mission. An interval of 98-105% is presented, and the deepest minimum reaches 78%. A strange result should also include a temporary increase in flow up to 102% in the range of 1550–1560 days. One would assume that a large body is present in a relatively low orbit, reflecting the star's light. But calculation performed rejects this possibility.

In some cases as, for example, details at the mark of 1540, similar as in Fig. 3, it is possible to see regular details of the curve. Nevertheless, it is impossible to ascribe them with confidence to the transit of rings or some other structure, keeping in mind, moreover, that there are no measurements after the 1680 mark.

Thus, in the hypothesis of giant rings, the experimental data on the object KIC-8462852, obtained in the KEPLER mission, also do not find an adequate explanation. Further observations of the object are needed, performed by terrestrial and especially orbital astronomical means. Both long-term MLS-observations and the search for transits of the KIC 8462852 are important.

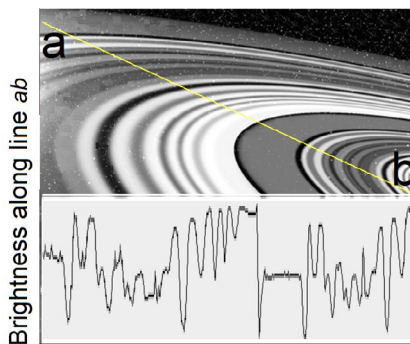


Fig. 3. The model curve of the incomplete transit through the J1407b rings.

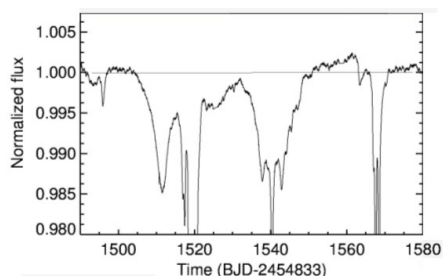


Fig. 4. Hypothetical incomplete transit of KIC 8462852, with a maximum depth of the light attenuation up to 22% (interval 98-105%).

Acknowledgements:

The work was partially supported by Programs P12, P17 and P28 of the Presidium of the Russian Academy of Sciences.

References

- [1] Boyajian T.S., LaCourse D.M., Rappaport S.A. et al. Planet Hunters IX. KIC 8462852 - where's the flux? // *Monthly Notices of the Royal Astronomical Society*, 2016. V. 457, Iss. 4, p. 3988-4004.
- [2] Mamajek E.E., Quillen A.C., Pecaut M.J., Moolekamp F., Scott E.L., Kenworthy M.A., Collier Cameron A., Parley N. R. // *Planetary Construction Zones in Occultation: Discovery of an Extrasolar Ring System Transiting a Young Sun-like Star and Future Prospects for Detecting Eclipses by Circumsecondary and Circumplanetary Disks.* // *The Astronomical Journal*, 2012, V.143, Iss. 3 , article id. 72, 15 p.
- [4] Ksanfomality L.V., Tavrov A.V. Heritage of the Kepler Mission: Special Object KIC 8462852 and Criticism of the Cometary Hypothesis // *Solar System Research*, 2017, V. 51, No. 5, p. 422–435.

BEPICOLOMBO EN ROUTE TO MERCURY

J. Benkhoff, J. Zender¹, G.D. Murakami²

¹ *European Space Research and Technology Centre, Keplerlaan 1, 2200AG Noordwijk ZH, Netherlands, Johannes.Benkhoﬀ@esa.int, Joe.Zender@esa.int*

² *Department of Solar System Science, Institute of Space and Astronautical Science (ISAS), Japan Aerospace Exploration Agency (JAXA), 3-1-1 Yoshinodai, Chuo, Sagami-hara, Kanagawa 252-5210, Japan, go@stp.isas.jaxa*

Keywords:

BepiColombo, Mercury, planetary orbiter, magnetospheric environment

BepiColombo is a joint project between the European Space Agency (ESA) and the Japanese Aerospace Exploration Agency (JAXA). The Mission consists of two orbiters, the Mercury Planetary Orbiter (MPO) and the Mercury Magnetospheric Orbiter (MIO). Both spacecraft has been launched with an ARIANE V in October 2018 for an arrival at Mercury in 2025. From their dedicated orbits the two spacecraft will be studying the planet and its environment.

On its route BepiColombo will pass by Earth, two times Venus, and six times Mercury before jettisoning its orbiters and putting them into orbit around the innermost planet.

Instrumentation on the two orbiters will study and understand the composition, geophysics, atmosphere, magnetosphere and history of Mercury, the least explored planet in the inner Solar System. In addition, the two satellites will provide a rare opportunity to collect multi-point measurements in a planetary environment. This will be particularly important at Mercury because of short temporal and spatial scales in the Mercury's environment. The foreseen orbits of the MPO and MIO will allow close encounters of the two spacecrafts throughout the mission.

The MPO scientific payload comprises eleven instruments/instrument packages; The MIO comprises 5 instruments/instrument packages to the study of the environment. The Bepi spacecraft will focus on a global characterization of Mercury through the investigation of its interior, surface, exosphere and magnetosphere. In addition, it will be testing Einstein's theory of general relativity. The MIO spacecraft is more focused on the plasma and particle environment around Mercury. Together, the scientific payload of both spacecraft will provide the detailed information necessary to understand Mercury and its magnetospheric environment and to find clues to the origin and evolution of a planet close to its parent star. The BepiColombo mission will complement and follow up the work of NASA's MESSENGER mission by providing a highly accurate and comprehensive set of observations of Mercury. The mission has been named in honor of Giuseppe (Bepi) Colombo (1920–1984), who was a brilliant Italian mathematician, who made many significant contributions to planetary research and celestial mechanics.

In this talk on overview about the mission, the launch and the health status of the instruments will be given. The observation plans during the flybys will be discussed, too.

MGNS: FIRST DATA EN ROUTE TO MERCURY

A.S. Kozyrev et al.

Space research institute of the RAS

Mercury Gamma-ray and Neutron Spectrometer (MGNS) is the Russian contributed instrument of ESA BepiColombo project. The main goal of the instrument is to measure gamma-ray and neutron emission from the surface of the planet for studying the elementary composition of the soil. Also, the instrument will record gamma-ray bursts and solar flares. MGNS is operating in the cruise flight providing the monitoring data for local radiation background and gamma-ray bursts. These data are useful for instrument in-flight calibrations and for participation in the International Network for localization of sources of gamma-ray bursts.

GEOLOGY, GEOCHEMISTRY AND GEOPHYSICS OF THE MOON: FROM PRIORITY SCIENTIFIC TASKS TO SCIENTIFIC EQUIPMENT

E.N. Slyuta

Vernadsky Institute of Geochemistry and Analytical Chemistry, Moscow, Kosygina str. 19, Russia, slyuta@mail.ru.

Keywords:

Moon, geological methods, geochemical methods, geophysical methods, lunar soil, implanted volatiles, drilling, Lunar basic network, lunokhod.

Introduction:

The study and exploration of the Moon as a geological object, i.e. of the same object as the Earth and other planets, is one of the main tasks of the development and formation of a scientific research program at the present stage. This determines the basic research methods and, accordingly, the complex of scientific equipment and technical means necessary to solve the priority scientific problems of geochemistry, geology and geophysics of the Moon.

Priority Research Objectives:

The priority scientific tasks of research and exploration of the Moon at the present stage over the past 20 years are quite well developed and agreed upon by the international scientific community on the basis of numerous scientific publications and discussions at scientific conferences [1] (Table) and ranked by 10 points scale according to importance and priority [2]. Each scientific task is characterized by its own research methods and for its solution requires special technical means and a certain set of scientific equipment.

Research methods:

Geological methods include a complex of morphological and structural-geological studies of the lunar surface at the places of sampling of regolith and drilling wells for the purpose of detailed characterization of sampling points with accurate cartographic reference and reference to a specific geological situation.

The task of geochemical methods is to study the chemical and mineral composition of lunar rocks, the chemical and isotopic composition of volatile components and cosmogenic isotopes in lunar regolith, determine the absolute age of rocks and minerals, the age of exposure of individual regolith layers, the age of formation of large impact basins, etc.

Geophysical studies are aimed at obtaining information about the internal structure of the moon, about gravitational and magnetic fields, about the internal heat flux, about the temperature distribution in the bowels, about the thermophysical and electromagnetic properties of lunar rocks. Geophysical exploration is also auxiliary to geological and geochemical exploration and exploration of lunar resources.

DS(Drilling and Sampling):

The delivery of lunar rock samples to Earth is a necessary and key element in the exploration of the Moon. Only in laboratory conditions is it possible to conduct a detailed study of the texture, structure and microstructure of rocks and minerals, determine and study the main, accessory and rare minerals and inclusions, analyze the chemical composition with any degree of accuracy, including basic, subordinate and rare elements, analyze the relations of any stable and radiogenic isotopes, determination of the absolute age of minerals, rocks, and, accordingly, geological structures and the processes associated with their formation. These data are the basis of knowledge about the origin, conditions of formation and evolution of local and regional structures, the lunar crust and the entire planetary body as a whole.

The location and method of sampling is extremely important. Lunar soil has a complex layered structure and its own stratigraphic and geochemical history, which can be traced from the moment of formation of underlying

ing rocks. The larger the crater, the farther the ejections fly. Accordingly, the stratified regolith column provides information on the composition and age of the regolith and underlying rocks not only at the drilling site, but also within a fairly wide adjacent area. The optimum drilling depth and sampling is 10–15 m, i.e. the full thickness of the loose layer of regolith to the underlying rock. The first LB–9 automatic drilling rig to take a stratified regolith sample to a depth of more than 2 m was successfully worked out on board the Soviet Luna-24 spacecraft in 1976. A design of a new generation LB–15 drilling rig is being developed at the Vernadsky Institute, which will allow sampling a regolith column to a depth of 6 m, and in the long term to a depth of 10–15 m.

Table. 1. Priority Research Objectives and Research Methods*

#	ID	ScientificTask	Rating, point	Researchmethods
1	mG1	Origin and dynamic history of the Earth - Moon system	10	LBN, DS
2	mG10	The study of implanted volatiles in the lunar regolith (composition of the primary atmosphere of the Earth, the formation time of the Earth's magnetosphere, the appearance time of biogenic oxygen on the Earth, the synchronization time of rotation of the Moon)	10	DS
3	mG2	The Global dichotomy, the degree of differentiation and the internal structure of the Moon	10	LBN
4	mG3	The history of the formation of the early crust on the Moon	10	DS, LRG
5	mG4	The structure of the lunar crust and the origin of gravitational anomalies - mascones	9	LBN
6	mG8	The internal heat flux of the Moon	9	LBN
7	mG9	The origin of the ancient lunar magnetic field	9	LBN, DS
8	mG5	Regional lateral heterogeneity of the composition of the lunar crust and mantle	9	LRG, DS
9	mG6	History of Lunar Magmatism and Volcanism	9	LRG, DS
10	mG7	Lunarchronology	9	LRG, DS
11	mG11	The study of weakly coupled and frozen volatiles in lunar regolith at Polar regions	9	LGP
12	mG12	The presence in the regolith of a rare asteroidal and cometary matter and relict matter of the young Earth	7	DS
13	mG13	Changes in the activity and composition of the solar wind and galactic cosmic rays over a period of 4 billion years or more	6	DS

*Description of research methods and scientific instruments are given in the text.

LBN (Lunar Basic Network):

Lunar basic network of automatic scientific stations for long-term monitoring of container type. The optimal number of stations on the entire surface of

the Moon is 8-10 [3]. This is a fully autonomous container weighing about 50-70 g, which is installed on the lunar surface and activated from the orbiter or from the Earth. In addition to energy and service radio transmitting equipment (a beacon, antennas), the composition of scientific equipment includes a seismometer, gravimeter, a three-channel magnetometer, a logging thermal probe self-deepening to a depth of 3 meters, a TV camera (TV-spectrometer), an angular reflector for optical navigation. The operating time of the station is at least 10 years.

LRG (Lunokhod "Robot-Geologist"):

The Robot-Geologist (LRG) heavy automatic lunar rover is being developed at RTC (Russian State Scientific Center for Robotics and Technical Cybernetics, Saint-Petersburg) at the initiative of the Vernadsky Institute and under the supervision of Roscosmos for thematic geological, geochemical and geophysical survey with soil sampling from the surface and shallow (up to 6 m) drilling of several (at least 5) wells along an extended route of about 500 km [4, 5]. A set of basic and auxiliary scientific equipment is divided into three main complexes: the scientific navigation complex, the geochemical survey complex and the geophysical survey complex. The main tool is a drilling rig for sampling a stratified regolith column and with a mass spectrometer for simultaneous in situ study of weakly bound volatiles in the lunar soil, as well as a manipulator for sampling from the surface along the lunar rover route.

LGP (Lunokhod "Geologist-Prospector"):

To carry out exploration work to assess the content, distribution and contouring of weakly bound and frozen volatile deposits in the Polar regions of the Moon, an automatic lunar rover project (Geologist-Prospector) is being developed by the initiative of the Vernadsky Institute and under by the leadership of Roscosmos. This is an average type of lunar rover with a mass of 250-350 kg and a scientific payload with a mass of 50–60 kg. The length of the route is up to 50-60 km. There are three main scientific complexes on the lunokhod: the scientific navigation complex, the geochemical survey complex and the geophysical survey complex. The main tool is an auger drilling rig with a mass-spectrometer, which provides a study of the chemical and isotopic composition and concentration of weakly bound and frozen volatiles to a depth of 2 m in situ without soil sampling [6].

References:

- [1] Slyuta E.N., Galimov E.M., Marov M.Ya. Problems of selenology. In: Basic space research, V. 2, Solar System. Moscow, Fizmatlit, 2014. P. 52–97.
- [2] Shearer, C., Neal, C., Borg, L., et al. Analysis of Lunar Sample Mass Capability for the Lunar Exploration Architecture // Unpublished white paper. 14 p. posted May 2007 by the Curation and Analysis Planning Team for Extraterrestrial Materials (CAPTEM). 2007. <http://www.lpi.usra.edu/captem/>.
- [3] Slyuta E.N., Galimov E.M., Marov M.Ya. Thematic geological survey and preliminary geological exploration (on the Moon). In: Basic space research, V. 2, Solar System. Moscow, Fizmatlit, 2014. P. 103–128.
- [4] Vasiliev A., Dalyaev I., Slyuta E. Design concept of lunar rover for the Moon geological exploration. 28th Daaam International Symposium on Intelligent Manufacturing and Automation, Vienna, Austria. 2017. P. 0780-0786. DOI:10.2507/28th.daaam.proceedings.110.
- [5] Slyuta E.N., Vasilev A.V., Dalyaev I.Yu. Lunokhod "Robot-Geologist": Scientific tasks and technical configuration. 48th Lunar Planet. Sci. Conf., Houston, 2017. ID #1929.
- [6] Slyuta. E. Problems of research and mining of gas deposits on the Moon. Mining of Mineral Deposits, 2017. V. 11(4). P. 117-125. DOI: 10.15407/mining11.04.117.

RETHINKING LUNAR MARE BASALT REGOLITH FORMATION: NEW CONCEPTS OF LAVA FLOW PROTOLITH AND EVOLUTION OF REGOLITH THICKNESS AND INTERNAL STRUCTURE

J. Head¹ and L. Wilson^{2,1}

¹ Brown Univ., Providence RI, USA; James_Head@brown.edu

² Lancaster Univ., Lancaster, UK. L.wilson@lancaster.ac.uk

Keywords:

mare regolith, auto-regolith, lava flows, degassing, vesicle formation, regolith protolith, impact cratering.

Introduction:

Lunar mare regolith is traditionally thought to have initiated its growth from impact bombardment of newly emplaced coherent solidified basalt [1]. We use new models of the ascent, eruption and emplacement of lunar mare basalt magma [2] to map out the characteristics, thicknesses, surface topography and internal structure of lava flows, the lunar mare regolith parent rock, or protolith. We show that variations in phases and styles of basaltic eruptions [3] can produce widely varying initial conditions for regolith protolith, including production of 1) “auto-regolith”, a meters-thick surface deposit of fragmental material that mimics regolith in physical properties, and 2) flows with significant near-surface vesicularity and macro-porosity. These factors have important implications for the growth, maturation and regional variability of regolith deposits and suggest that the properties and thickness of similar-aged regolith may vary widely due to the nature of the protolith. While regolith has traditionally been viewed as a blanketing and obscuring layer, orbital and surface documentation of regolith characteristics may instead provide key insights into the mare basalt protolith and its mode of emplacement.

Updated Lava Flow Emplacement Paradigm:

Assessment of mare basalt gas release patterns [4] during individual eruptions [3] provided the basis for predicting the effect of vesiculation processes on the structure and morphology of associated features: typical lunar eruptions are subdivided into four phases (Fig. 1): P1, dike penetrates to surface, transient gas release phase; P2, dike base still rising, high-flux hawaiian eruptive phase; P3, dike equilibration, lower flux hawaiian to strombolian transition; P4, dike closing, strombolian vesicular flow phase. These four mare basalt volatile release phases, together with total dike volumes, initial magma volatile content, vent configuration, and magma discharge rate, define the wide range of initial mare basalt extrusive products and consequent regolith protoliths produced in space and time.

Mare Basalt Protolith Types and Some Implications for Regolith Evolution:

1. Traditional Solidified Coherent Mare Basalt: Magma largely degassed at the vent during P2, several 100 km long generally flat smooth-surfaced flows, low vesicularity, solidified basalts up to tens of m thick. Traditional regolith evolution model. 2. Inflated Flows: Surface topography: P4 causes flow inflation of P2 flows, elevates and distorts pre-existing solidified flow surface, introduces irregular topography with several-m scale irregularities to solidified flow. Forms extremely irregular protolith surface. 3. Inflated Flows: Vesicularity and meso-macro porosity: Internal structure of P4 inflated flow is very porous at depths of a few meters due to intrusion of very vesicular P3 magma; creates layers of solidified low-density vesicular basalt of significant thickness, and m-scale void spaces from coalescence of vertically migrating gas pockets. Potential collapse craters, regolith drainage. 4. Inflated Flows: Second boiling, vertical volatile migration and extrusion of magmatic foam: Further evolution of P4-inflated P2 flows causes in situ generation of additional vesicular layers, and active upward migration of foams in pipes to deform the lava flow surface, create m-scale shallow void space and per-

haps extrusion of foams to form RMDSSs [5]. Early-stage porous substrate, regolith drainage, unusual foam mounds, heterogeneous target. 5. Foam flows and "Auto-Regolith" Formation: Very vesicular P4 flows extrude out into the surface vacuum and undergo catastrophic fragmentation and disruption that can destroy the entire meters-thick flow, leading to production of a fragmental layer (an auto-regolith); this auto-regolith layer can comprise the entire flow unit thickness in a point-source eruption, and a significant amount of the flow thickness in fissure flows (Fig. 2). Regolith formation begins with meters-scale "auto-regolith". 6. Foam flows with coherent surfaces: Some P4 flows develop a coherent upper thermal boundary layer, inhibiting initial catastrophic foam flow disruption and resulting in extremely vesicular, low density meters-thick flows with a solidified carapace, and perhaps some initial collapse pits. Impacts cause surface collapse, regolith drainage. 7. Pyroclastic layers: During P2, regions surrounding the vent can accumulate significant thicknesses (up to many 10s of m) of pyroclastic beads out to ranges of several tens of km (Fig. 2); layers likely to be overlain by (or intercalated with) associated lava flow layers. Creates heterogeneous target, pseudo-regolith layers. 8. Emplacement of anomalous "xenolithic" volcanic glass beads: Initial minutes of eruption (P1) disperses pyroclasts very widely, well beyond the associated subsequent flow deposits (P2-4). Candidate source of "xenolithic" pyroclasts in all regolith deposits. 9. Volcanic Pit Crater Floor Surfaces: If P3 occurs in a depression (pit or collapse crater) than P3 activity can concentrate strombolian pyroclasts and P4 foamy lavas, resulting in extremely high concentration of volatiles and magmatic foams developing below a solidified and evolving thermal boundary layer of unusual micro and macrovesicularity; disruption of the layer has been proposed to cause extrusion of magmatic foams to form mounds [6]. Produces extremely underdense and layered targets; regolith drainage

Summary of New Perspectives on Regolith Protolith Development:

Analysis of the phases of mare basalt eruptions [3] provides a forward-model of the formation of regolith protolith and shows that the traditional view of a solid basaltic regolith protolith [1] is only one of a wide array of regolith protolith outcomes. These results provide predictions, potential new insights and an interpretative framework to revisit regolith-forming processes.

Application of Protolith Concepts to Formation and Evolution of Regolith:

1) Basal regolith-substrate interfaces:

The starting conditions for regolith development can vary widely from solid basalt to a meters-thick "auto-regolith"; initial topography can vary up to tens of meters. 2) Energy partitioning in regolith-forming impacts: Efficiency of cratering will vary as a function of the protolith surface and subsurface structure. The ratio of rock substrate deformation to ejection will vary in space and time. 3) Regolith growth rates: "Auto-regolith" formation can provide both an initial meters-thick "regolith" layer and a buffering layer influencing regolith growth rates. 4) Regolith thickness with age: Regolith thickness/age relationships should take into account the nature of the initial substrate topography, structure (vertical and horizontal) and the potential presence of an auto-regolith; high thickness variability in space and time is likely. 5) Regolith components and maturation rates: Expected diversity of initial protolith conditions will map out into the relative proportions of components (e.g., indigenous and xenolithic pyroclastic glass, glass shards, vesicularity, grain sizes and shapes, mesostasis, etc.) in evolving regolith. 6) Morphology of superposed impact craters: These should differ widely in early protolith bombardment on the basis of energy partitioning in different substrates; this will cause sequential morphological differences as regolith thickens between and within flows. 7) Degradation of superposed craters with time: Energy partitioning in different substrates will yield different initial crater morphologies and morphometries, influencing the interpretation of crater degradation and lifetime; very porous macrovesicular substrates can also produce initial and subsequent collapse craters that can mimic degraded primary impacts. 8) Impact crater size-frequency distribution measurements and surface ages: Variable protolith characteristics in space and time result in variable superposed crater energy partitioning that can influence fresh

and degraded impact crater morphology and morphometry, CSFD measurements, and determination of population equilibrium diameters. An extreme case of these types of effects is predicted to occur in pit crater floors (P3-4) (Irregular Mare Patch mounds and hummocky terrain in Ina [6]). 9) Vertical structure of lava flows: Individual lava flow cross-sectional vertical structure should vary widely (in both space and time), in contrast to the simple solid basalt cooling unit often assumed. Despite this diversity and complexity, eruption phase parameter space (Fig. 1) offers promise to unravel the eruption history of individual cross-section exposures of intercalated lava flows and regolith layers [7].

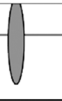
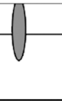
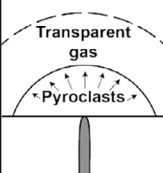
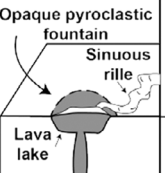
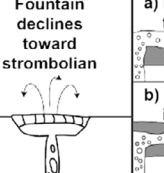
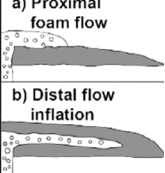
Eruption Phase	PHASE 1	PHASE 2	PHASE 3	PHASE 4
		Dike penetrates to surface, transient gas release phase	Dike base still rising, high flux hawaiian eruptive phase	Dike equilibration, lower flux hawaiian to strombolian transition phase
Dike Configuration				
Surface Eruption Style				
Magma Rise Speed	30 to 20 m/s	20 to 10 m/s	5 to <1 m/s	< 1 m/s
Magma Volume Flux	$\sim 10^6$ m ³ /s	10^6 to 10^5 m ³ /s	10^5 to $\sim 10^4$ m ³ /s	$\sim 10^4$ m ³ /s
Percent Dike Volume Erupted	<5%	$\sim 30\%$	$\sim 30\%$	$\sim 35\%$
Phase Duration	~ 3 minutes	5-10 days	2-3 days	10-100 days
Flow Advance Rate	n/a	~ 3 to 0.1 m/s	0.03 m/s	0.01 m/s
Flow Advance Distance	n/a	300 km	305 km	335 km
Vesicularity of Flow	n/a	zero	low, but increasing	very high

Fig. 1. Stages in mare basalt eruptions [3].

Future Work:

Documentation of these differences in initial flow characteristics and regolith protolith can enhance the understanding of the true complexity of regolith development and lead in turn to a paradigm for the variation in basaltic lava flow surface and internal structure in time and space. Predictions of the forward model of lava flow emplacement [3] can provide specific goals and objectives for further exploration of the nature and initial emplacement environment of the regolith protolith, and the evolution and current state of the resulting regolith. Some promising areas of investigation include: 1) Analysis of orbital remote sensing data for their ability to detect and map variations in protolith/regolith parameter space (e.g., radiometry, radar, surface roughness, photometry, mineralogy, maturity indices, etc.). 2) Measurements of

the vertical structure of lava flows and regolith in order to test and refine the protolith/regolith parameter space (e.g., in crater walls and lava pit craters [7]). 3) Reassessment of assumptions about regolith thickness and internal structure for seismic, heat flow, radar (surface and orbital GPR) and SEP data. 4) Analyzing assumptions about CSFD ages and crater degradation processes to take into account potential varying protolith and regolith processes. 5) Revisiting the Apollo/Luna/Chang'E data on the lunar regolith in the context of this forward-model protolith/regolith growth paradigm.

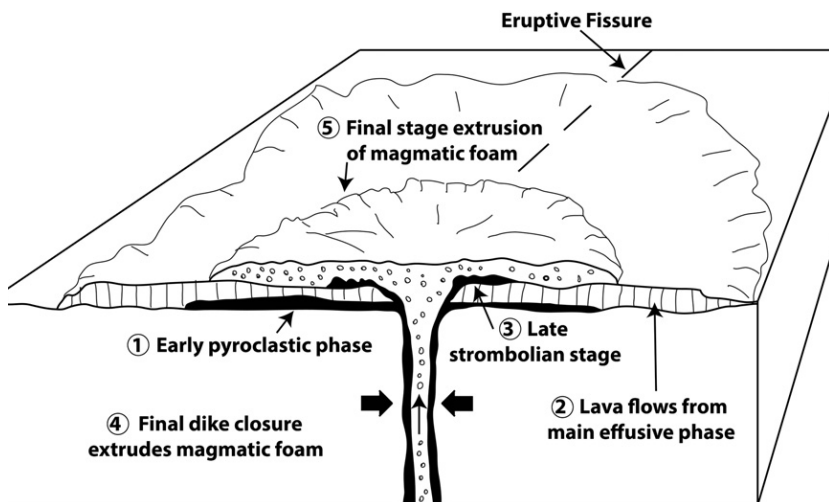


Fig. 2. Cross-sectional flow sequence in single fissure flow [6].

References:

- [1] Langevin & Arnold. 1977. *Ann. Rev.* 5, 449; McKay et al. (1991) Ch. 7, *Lunar Sourcebook*; Wilcox et al. (2005) *MAPS* 40, 695;
- [2] Head & Wilson. 2017. *Icarus* 283, 176; Wilson & Head (2017) *Icarus* 283, 146;
- [3] Wilson & Head. 2017. *GRL* 45, 5852;
- [4] Rutherford et al. 2017. *AM* 102, 2045;
- [5] Wilson & Head. 2017. *LPSC* 49 #1326;
- [6] Wilson & Head. 2017 *JVGR* 335, 113;
- [7] Kerber et al. 2019. *LPSC* 50 #1163.

LOW FREQUENCY RADIO ASTRONOMICAL EXPERIMENTS ON THE MOON

J.S. Ping¹, Y.C. Ji², M.Y. Wang¹, L.J. Chen¹, M. Zhang¹,
M.H. Huang¹, Y.H. Yan¹, G.Y. Fang², B. Zhao²

¹ National Astronomical Observatories, CAS, Datun Rd. 20A, Beijing, China, 100101, jsping@bao.ac.cn;

² Institute of Electronics, CAS, Haidian, Beijing, China, 100080, ycji@mail.ie.ac.cn.

Keywords:

Low frequency, radio astronomy, moon, farside.

Introduction:

On the ground, the Earth ionosphere blocks the low frequency radio signal from out space. Open this electron-magnetic wave window is one of the key channels for astronomers to uncover the unknown cosmic world. To kick off this work, CE-4 lunar project selected monopole antenna systems for both of the far-side lander landed in SPK basin and for a relay-satellite flying at L2 Earth-Moon Lagrange Point.

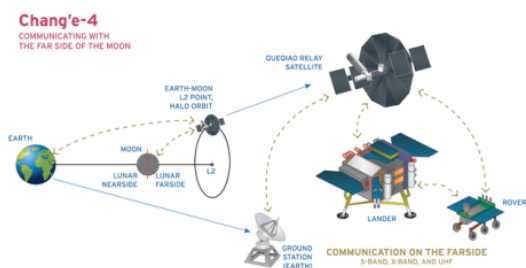


Fig. 1. CE-4 Lunar Mission Concept

On the lander, three orthogonal 5-meter mono-pole antennas and a 30-cm calibration antenna has been used. The data obtained between 100KHz ~ 40MHz will be transferred to spectra information and sent back to the Earth via the relay satellite. The narrow data rate limited the observation, which makes the facility focus on lower band measurement below 2MHz, where the short antenna will be a nice tool to remove the near field noise.



Fig. 2. Low Frequency Antenna on CE-4 Lander

On the relay satellite, identical system had been designed by Chinese radio astronomers originally. To improve output of the science by means of using top level payloads, and to improve the international collaboration of Chinese lunar exploration, the relay satellite finally selected a joint Netherlands-China low frequency mission. Also, three orthogonal 5-meter mono-pole antennas are used. The data obtained between 80KHz ~ 80MHz will be obtained and sent back to the Earth via the relay satellite. The high data rate will be used in the near future so as to obtain wideband information during the observation.

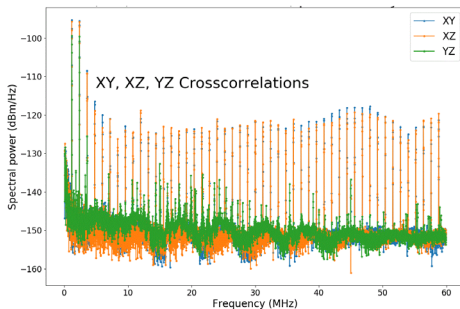


Fig. 3. Initial cross-correlation spectra for NCLE

Coordinating observations will be carried out between above to facilities, as well as with ground facilities of same or similar band. A first Earth-Moon low frequency VLBI observation may also be carried out, with the Sun or Jupiter, or an artificial object being a possible common radio target source.

The most important output of above missions will be the low frequency electron-magnetic emission background in the lunar orbiter, and in the orbit of Earth-Moon surround the Sun. This will be the 1st step for the future low frequency radio astronomical array in the Earth-Moon space. Additionally, the top band which overlaps the FAST low band, can benefit the future radio astronomical studies.

MORPHOLOGIES OF IMPACT-SIMULATED CONDENSATES

M.V. Gerasimov¹, O.I. Yakovlev², Yu.P. Diko³

¹Space Research Institute, Profsoyuznaya, 84/32, Moscow, 117997, mgerasim@mx.iki.rssi.ru,

²Vernadsky Institute of Geochemistry and Analytical Chemistry, Moscow, 117975, Kosygina, 19,

³Institute of Ore Deposits, Petrography, Mineralogy and Geochemistry, Moscow 109017, Staromonetny per., 35.

Keywords:

Vaporization, condensation, Lunar regolith, morphology of condensates, nano-globules.

Introduction:

Processing of silicates during hypervelocity collisions is a fundamental process which affects the evolution of solid material in the universe and in the Solar system as well. Impacts on planetary surfaces proceed at velocities in excess of 10 km/s and provide partial or complete vaporization of colliding material. Subsequent expansion and cooling of impact-generated vapor plumes produce condensed particles with nanometer to micron sizes. Investigation of trends of differentiation of silicate material during impact-induced vaporization is important for understanding of early evolution of planetary bodies. Laboratory simulation of impact-induced vaporization - condensation processes is limited to a few millimeter scales. It is important to know the relevance of laboratory produced condensates to that produced in nature during real impacts. We tried to compare laboratory produced condensates with that found on Luna regolith samples based on their morphology and chemical structure.

Simulation of lunar condensates: The Moon has preserved impact-produced condensates which can be found on surfaces of lunar rocks and glasses. These condensates have composition noticeably different from melts [e.g. 1, 2] that shows deep differentiation of silicate material during high-temperature pulse processing.

The goal of our work was to produce experimentally impact-simulated condensates with different elemental composition and compare their morphology with that of lunar condensates. Simulation of impact-generated condensates was done using laser pulse technology [3]. We used diverse samples representing terrestrial rocks and minerals, meteorites, and volatile-rich mixtures to simulate cometary impacts.

We have discovered several types of condensates many of which have twins among lunar condensates (e.g. Fig. 1 and 2). Histograms indicate that both lunar condensed particles and that from experiments have the main mode about 30–50 nm.

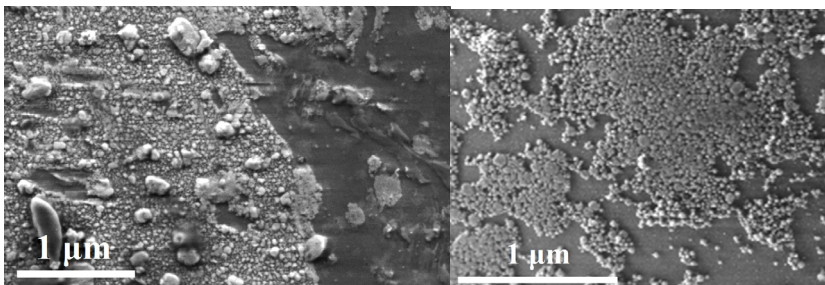


Fig. 1. Condensed particles on a surface of Apollo-17 glass spherule.

Fig. 2. Condensed nano-globules on surface of a melted droplet from experiment with carbonaceous chondrite (CM2) Murchison.

Acknowledgment:

This work was supported by the RAS program П12.

References:

- [1] Keller L.P., McKay D.S. The nature and origin of rims on lunar soil grains // *Geochim. et Cosmochim. Acta.* 1997. V. 61. No. 11. P. 2331–2341.
- [2] P. H. Warren Lunar rock-rain: Diverse silicate impact-vapor condensates in an Apollo-14 regolith breccias // *Geochim. et Cosmochim. Acta.* 2008. V. 72. P. 3562–3585.
- [3] Gerasimov, M.V., et al. Physics and chemistry of impacts // *Earth, Moon, and Planets.* 1998. V. 80. No. 1–3. P. 209–259.

TARGETING LUNAR VOLATILES WITH ESA'S PROSPECT PAYLOAD ON LUNA 27

E. Sefton-Nash¹, R. Fisackerly¹, R. Trautner¹, D.J.P. Martin², J.D. Carpenter¹, B. Houdou¹ the ESA Lunar Exploration Team, the PROSPECT Science Team and the PROSPECT Industrial Team.

¹ ESTEC, European Space Agency, Noordwijk, The Netherlands, e.sefton-nash@cosmos.esa.int

² ECSAT, European Space Agency, Harwell, Didcot, UK.

Keywords:

Moon, volatiles, polar, Luna Resource, PROSPECT

Introduction:

The Package for Resource Observation and in-Situ Prospecting for Exploration, Commercial exploitation and Transportation (PROSPECT) is a payload in development by ESA for use at the lunar surface. Development is in progress for its flight on Roscosmos' Luna-Resource (Luna 27) lander mission, which will target the south polar region of the Moon. PROSPECT is designed to perform an assessment of the volatile inventory in near surface regolith (down to ~1 m), and elemental and isotopic analyses to determine the abundance and origin of any volatiles discovered. Lunar polar volatiles present compelling science and exploration objectives for PROSPECT, but solar wind-implanted volatiles and oxygen in lunar minerals (extracted via ISRU techniques) constitute potential science return anywhere on the Moon, independently of a polar landing site. PROSPECT is comprised of the ProSEED drill module and ProSPA analytical laboratory [1] (Fig. 1). In ensemble, PROSPECT has a number of sensors and instruments (ion-trap and magnetic sector mass spectrometers, cameras, and sensors for temperature, pressure, permittivity and torque) that form the basis for a range of science investigations [2]. These investigations are led by the PROSPECT Science Team (appointed in 2019).

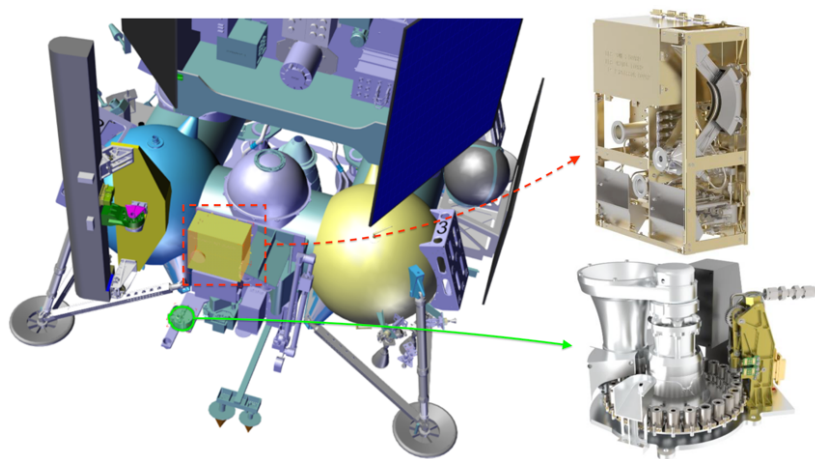


Fig. 1. Renderings — Left: PROSPECT mounted on Luna 27, including ProSEED drill module (left), Solids Inlet System [SIS] (green circle), and analytical lab. drawer (yellow box) containing ProSPA gas processing system and instruments. Upper right: ProSPA analysis package containing magnetic sector and ion-trap mass spectrometers. Lower right: Solids Inlet System to receive samples from drill sampling mechanism, with sample camera assembly (Sam-Cam) and carousel of ovens for volatile extraction from regolith samples.

Development Status and Current Activities:

Tests of the PROSPECT Drill Module, ProSEED, in 2019 are intended to demonstrate drilling and sampling functionality in ambient, cold and thermal vacuum (TV) laboratory conditions. Drill development model tests comprise drilling into, and sampling from, lunar regolith simulant, which comprised

of NU-LHT-2M, supplied by Zybek Advanced Products (grain sizes <1 mm), mixed with chips of anorthosite representing coarser size fractions supplied by the Sample Analogue Curation Facility (SACF) at ESA/ECSAT, UK [3]. Regolith density-depth profiles and grain size distributions in test materials are selected to cover plausible ranges expected for lunar regolith, informed by parameters measured from Apollo cores and retrieved from thermal infrared orbital observations [e.g. 4]. Most relevant to polar regions, material for tests in TV is prepared with water content representative of regolith that ranges from 'dry' to 'saturated' (0 – ~ 10 wt. %). In addition, both completed work [5] and on-going efforts seek to better quantify the potential effect of possible volatile loss during sampling, including the effect on measured D/H of sublimation of lunar water ice.

Access to subsurface volatiles:

There is currently focus on the abundant evidence for water ice on the lunar surface and in the sub-surface (visible to far-IR [e.g. 6, 7], morphology [8], radar, neutrons, LCROSS [9]), but there remain questions about the precise spatial distribution and abundance of volatiles in the lunar polar sub-surface at spatial scales relevant to landed missions. Work by [10] identified regions of volatile stability, where temperatures never exceed a volatility threshold (~ 110 K, but dependent on diffusion rates of water molecules in regolith) such that sublimation to vacuum results in loss rates <1 kg m $^{-2}$ Ga $^{-1}$ (Fig. 2). Many locations at the lunar south pole show such zones, and many zones extend to the surface in PSRs (lightest blue in Fig. 2).

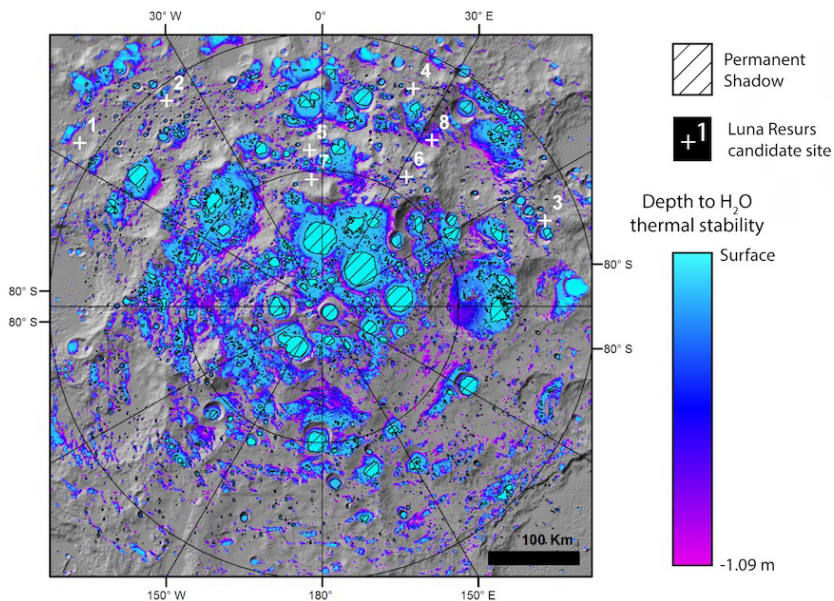


Fig. 2. Lunar south polar region; Zones of thermal stability in the sub-surface permitting the presence of water-ice, data from [9]. Candidate sites identified by IKI/Roscosmos and Permanently Shadowed Regions (PSRs) [11] are also marked. The Luna 27 lander will not operate in PSRs.

The majority of zones of water-ice stability have upper boundaries shallower than 1m (Fig. 3). Thus, where water ice exists and is stable in the lunar polar sub-surface, it is likely to be accessible in the top few 10s of cm. This result introduces a trade-space where competing requirements are oppositely-sensed for solar-powered spacecraft, such that solar illumination must be maximised for the purposes of power and thermal operational constraints, but simultaneously minimised such as to target areas where illumination is not so high that volatile stability criteria are not met in the shallow sub-surface. Indeed, for missions targeting subsurface volatiles it is clear that careful landing site selection, precision landing and consideration of locally and seasonally-timed illumination conditions are of high importance.

The delivery function for lunar water is not well constrained over geologic time, and convolved with that uncertainty is another introduced by seasonal variation of insolation [12]. Moreover, Gyr-scale variations in lunar orbit and obliquity probably modified the available cold-trapping area over time [13].

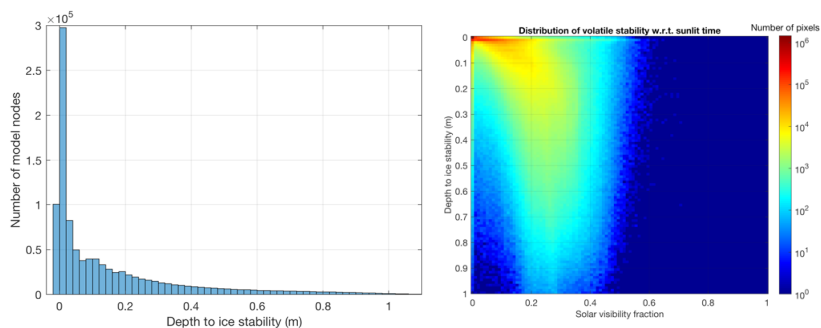


Fig. 3. Left: For locations where the water ice stability criterion is met in [8] (Fig. 2), distribution of depth to stability. Right: Distribution of depth to thermal volatile stability [8] as a function of mean sunlit time, as determined by [9].

The relative importance of scattering and shadowing to the lunar thermal environment increases at high latitudes, which has led to [14] combining a 1D heat-flow parameterisation [4] and ray-tracing models [10, 15] in order to better constrain subsurface thermal environments in lunar polar regions. This type of work will be crucial for lunar polar mission planning.

Acknowledgements:

The PROSPECT Industrial Consortium and development of ProSEED is led by Leonardo (Italy). The development of ProSPA is led by the Open University (UK).

References:

- [1] Barber, S. et al., (2018), Euro. Lunar Symp. Abstract #099.
- [2] Sefton-Nash, E. et al., (2018), Euro. Lunar Symp., Abstract 114.
- [3] Martin, D. and Duvet, L. (2019) 50th LPSC, LPI Contrib. No. 2132, Abstract #2663.
- [4] Hayne, P. et al. (2017), J. Geophys. Res., 10.1002/2017JE005387.
- [5] Mortimer, J. et al., (2018), Plan. Space Sci. 158, p. 25-33.
- [6] Li, S. et al., (2018), PNAS, 115 (36), p. 8907-8912.
- [7] Sefton-Nash, E. et al., (2019), Icarus 332, p. 1-13.
- [8] Rubanenko, L. et al. (2019), Nature Geoscience 12, p. 597-601.
- [9] Colaprete, A. et al., (2010), Science 330, p. 463-468.
- [10] Paige, D. A. et al. (2010), Science, 330, p. 479.
- [11] Mazarico, I., et al., (2011), Icarus 211, p. 1066-1081.
- [12] Williams, J.-P. et al. (2019), 50th LPSC, LPI Contrib. No. 2132, Abstract #2852.
- [13] Seigler, M. A. et al. (2015), Icarus 255, p. 78-87.
- [14] Vasavada, A. et al. (1999) J. Geophys. Res. 141, p. 179-193.
- [15] Warren, T. et al., (2019) 50th LPSC, LPI Contrib. No. 2132, Abstract #2040.

LUNAR LAVA TUBES REPRESENT VAST POTENTIAL

R. Sharma, A.A. Mardon, C.C. Mardon

Antarctic Institute of Canada (#303 – 11919 – 82 Street, Edmonton, Alberta, Canada T5B 2W4),

According to Wikipedia, a lava tube is “a natural conduit formed by flowing lava which moves beneath the hardened surface of a lava flow”. These tubes exist on the Earth and various celestial bodies, including the moon. The tube forms when the lava drains and leaves a hardened crust.

NASA scientists are studying lava tubes on Earth in order to learn about those on the moon. As potential sites for future lunar colonies, they offer protection from surface radiation and the wide temperature swings (over 250°C) on the moon’s surface. The interior of the tubes are still quite cold, however, sitting at about 100°C.

The aforementioned scientists map terrestrial lava tubes from the surface using portable instruments such as ground penetrating radar, a magnetometer, and a gravimeter. The data from these instruments combine to provide a detailed picture of each tube. This is vital in knowing the depth of the tubes, any obstructions therein, etc. “Until you explore it, it’s just a pit”, says Kelsey Young, a geologist at NASA.

Since humans first landed on the moon, they have not remained continuously for more than 3 days at a stretch. Space suits are a short term solution for the moon’s harsh environment.



Fig. 1.

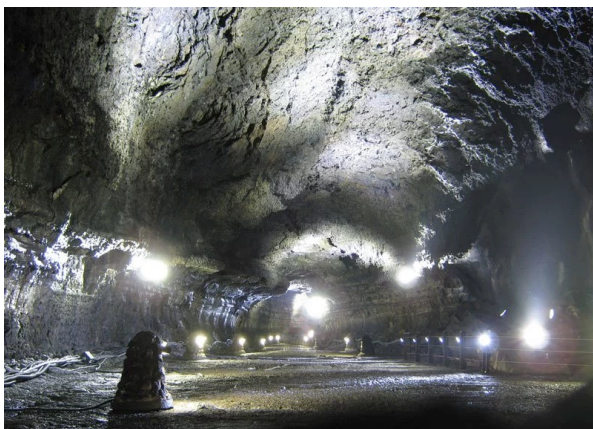


Fig. 2.

If gravity analyses are correct, there is a lava tube [https://twistedstifer.com/2012/08/pictures-of-lava-tubes-around-the-world/on the moon big enough to house the city of Philadelphia](https://twistedstifer.com/2012/08/pictures-of-lava-tubes-around-the-world/on-the-moon-big-enough-to-house-the-city-of-Philadelphia).

On October 5/2017, U.S Vice – President Mike Pence <https://www.space.com/41921-exploring-lava-tubes-for-moon-landings.html> stated that “the moon will be a stepping stone, a training ground, a venue to strengthen our commercial and international partnerships, as we re-focus America’s space program towards human space exploration”.

Furthermore, NASA’s Lunar Reconnaissance Orbiter (LRO) has provided images that suggest that a network of lava tubes beneath the moon’s surface could provide astronauts with easy access to water. These would alleviate the need to excavate the surface.

Certain peaks on the moon provide potential opportunities for the installation of solar arrays. These would provide electricity to potential lunar colonies.

References:

- [1] <https://twistedstifer.com/2012/08/pictures-of-lava-tubes-around-the-world/>
- [2] <https://www.space.com/39404-lava-tube-skylights-discovered-moon-images.html>
- [3] <https://www.livescience.com/60733-moon-lava-tube-could-shelter-astronauts.html>
- [4] <https://www.space.com/41921-exploring-lava-tubes-for-moon-landings.html>

FEATURES OF THE FOSSIL TIDAL BULGE FORMATION FOR THE EARLY MOON

S.A. Voropaev, A.Yu. Dnestrovsky

GEOKHI RAS, Moscow, Kosygina str. 19. Voropaev@geokhi.ru

Keywords:

Moon, Earth, tidal, gravimetric, orbit, stress, strain.

Introduction:

From the end of the 18th century, starting with Laplace's research, it has been known that the Moon's tidal bulge is abnormally large. It is larger than that predicted from the hydrostatic theory for the present-day lunar rotational and orbital states. Recent measurements by the Gravity Recovery and Interior Laboratory (GRAIL) mission showed that the (normalized) spherical harmonic coefficients $|C_{20}|$ and C_{22} of the Moon's gravitational field, which characterize the size of the bulges, are 203.2×10^{-6} and 22.4×10^{-6} , respectively [1]. This is about 22 and eight times larger than their corresponding hydrostatic values [2]. After correcting for the effects from large sea basins (basalts) and displacement of the axis of rotation, the coefficients $|C_{20}|$ and C_{22} are reduced to values of 156×10^{-6} and 38.8×10^{-6} , respectively, which remains approximately 17 and 14 times their corresponding hydrostatic values.

At present, the prevailing hypothesis for the Moon's excess bulge is a "frozen in" fossil bulge, which remained from the early Moon when the Moon was closer to the Earth, spun faster, and experienced larger tidal forces from the Earth than at present [3]. As the Moon subsequently receded from the Earth due to Earth's tidal dissipation and cooled, the formed strong outer layer (lithosphere) was partially or fully retained against the hydrostatic compensation of the planet's shape [4]. From the geophysical and geochemical points of view, the development of the tidal bulge of the Moon

is a continuous dynamic process, closely associated with the formation of the crust and mantle. In this paper we analyze the initial phase of the development of the tidal bulge using the semi-analytical method and modern seismological data, and obtain, by its refined dimensions, restrictions on the orbital parameters and the density distribution of the early Moon.

Analytical procedure:

The tidal-rotational influence on the formation of the early crust and mantle of the Moon depends on its rotational rate and orbital state. In [5] it was shown that the bulge could not have been formed in an orbit with a large eccentricity due to the large elastic deformations that occurred. In this work, we also assume that at the beginning of the formation of the tidal bulge, the Moon was in a circular and synchronous orbit with respect to the Earth; i.e., tidal capture had already occurred. In the Cartesian coordinate system with the origin placed at the center of inertia of the Moon and the X axis directed to the Earth, the internal tidal potential takes the following form:

$$V_t = \frac{-GM_E}{D^3} \cdot \left[x^2 - \frac{1}{2y^2} - \frac{1}{2z^2} \right] \quad (1)$$

where G is the gravitational constant, M_E is the mass of the Earth, and D is the lunar orbital semimajor axis. The centrifugal potential inside the Moon is determined by the expression

$$V_\omega = -\frac{1}{2\omega^2} \cdot [x^2 + y^2] \quad (2)$$

where $\omega = 2\pi/T$ is the angular velocity and T is the period of rotation of the Moon. The synchronous rotation of the Moon on a circular orbit leads to $GM_E/D^3 = \omega^2$ (Kepler's third law), and then, the total potential can be written as

$$V_t + V_\omega = -\frac{1}{2\omega^2} \cdot [3x^2 - z^2], \quad (3)$$

Since at the initial stage the elastic lithosphere of the Moon had not yet formed, the primary crust, which does not have significant viscosity, should take the form of an equipotential surface in the form of a three-axial ellipsoid, eliminating shear stresses. For the homogeneous case, the internal gravitational potential of the Moon will be determined by the expression

$$V_g = G\pi\rho \cdot abc \cdot [-U_0 + U_a x^2 + U_b y^2 + U_c z^2] \quad (4)$$

where a , b , and c are the principal semiaxes of the ellipsoid ($a > b > c$), and ρ is the mean density,

$$U_0 = \int \frac{ds}{\Delta}, \quad \Delta = [(a^2 + s)(b^2 + s)(c^2 + s)]^{\frac{1}{2}} \quad (5)$$

$$U_a = \int \frac{ds}{(a^2 + s) \cdot \Delta}, \quad U_b = \int \frac{ds}{\pi(b^2 + s)\Delta}, \quad U_c = \int \frac{ds}{(c^2 + s)\Delta}$$

and integrals are taken from 0 to ∞ . In what follows, we will use the dimensionless analogs of expressions (5) using the semiaxis relations $T_1 = (b/a)^2$ and $T_2 = (c/a)^2$; the equatorial (E_1) and polar (E_2) eccentricities of the outer surface are equal: $E_1 = 1 - T_1$ and $E_2 = 1 - T_2$, respectively. Since the eccentricities are small, a linear approximation for the components of the gravitational potential can be used with good accuracy:

$$U_a \approx 2/3 + 1/5 \cdot (E_1 + E_2), \quad U_b \approx 1/5 \cdot (3E_1 + E_2) + 2/3, \quad U_c \approx 1/5 \cdot (E_1 + 3E_2) + 2/3$$

The resulting force acting on the substance inside the Moon will be determined by the expression

$$F = -grad \cdot V, \quad V = V_t + V_w + V_g \quad (6)$$

In the case of a completely homogeneous, isotropic and isothermal early Moon, the hydrostatic theory of a planet with a mantle substance in the form of a viscous fluid without an elastic lithosphere (to maintain long-term shear stresses) predicts a figure in the form of a three-axial ellipsoid with a fixed eccentricity ratio: $E_1 \approx 3/4E_2$ and their absolute values depending on $d = D/R_E$

$$[U_a(T_1, T_2) - T_1 U_b(T_1, T_2)] \sqrt{T_1 T_2} \approx \frac{2 \cdot \rho_E}{\rho} \cdot \frac{1}{d^3} \quad (7)$$

For example, for $d = D/R_E = 20$, the difference of the main semiaxes will be $a - b \approx 1.35$ km and $a - c \approx 1.81$ km. At the same time, the current values of the average density of the Earth – 5520 kg/m³ and the density of the Moon – 3345 kg/m³ are taken. In the homogeneous model, the ratio of the coefficients $|C_{20}|/C_{22}$ is constant and equal to 3.3, which significantly differs from the range of values of the observed relations: $|C_{20}|/C_{22}$ from 9.2 to 4 (after correction), $a - b \approx 1$ km and $a - c \approx 2$ km. Variations of the orbit parameter $d = D/R_E$ from 10 to 40 do not allow us to approach the observed ratios of the differences of the semiaxes of the body. Therefore, it is necessary to take into account the heterogeneity of the internal structure of the early Moon.

Model of the magma “Mantle–Crust” ocean:

Geochemical data on lunar rocks collected by the Soviet automatic interplanetary stations Luna–16, –20, and –24 and Apollo missions 11–17 indicate a melted magmatic ocean that covered the entire surface of the early Moon at least 200 million years after its formation. Light smelting, predominantly of anorthosite composition with a density of ≈ 2600 –2700 kg/m³, formed the primary crust with a thickness of about 70 km, and denser basalts with a high content of iron and titanium of density ≈ 3300 –3800 kg/m³ formed the primary mantle. A semi-analytical approach using equipotential surfaces for layers of different densities (see Fig.1) allows us to make the necessary estimates of the functional relationship of their eccentricities.

If we neglect in our calculations the ellipsoidal shape of the inner layer, then its contribution to the total gravitational potential $V_g = V_g^{(1)} + V_g^{(0)}$ can be described by an expression simpler than (7)

$$V_g^1(x, y, z) = \frac{G\Delta M}{r}, \quad r^2 = x^2 + y^2 + z^2, \quad M = M_0 + \Delta M, \quad \rho_1 = \rho_M - \rho_{Crust} \quad (8)$$

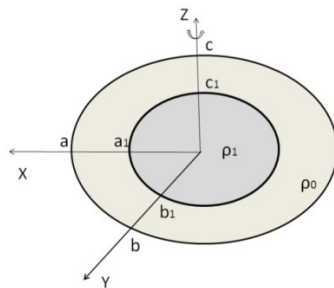


Fig. 1. Two-layer model of the early Moon.

With a good approximation, the outer surface can be represented by a three-axial ellipsoid, the principal semi-axes of which are a , b , and c (or the eccentricities E_1 and E_2) that are determined by the relations for the total potential (6)

$$U_a^{(0)}(T_1, T_2) - T_1 U_b^{(0)} - \Delta \frac{M}{M_0} \cdot \frac{3}{4} \cdot \left(\frac{1}{\sqrt{T_1} - 1} \right) = \frac{3}{2} \cdot \frac{\omega^2}{G\pi\rho_0} \cdot \sqrt{T_1 \cdot T_2}$$

and

$$\frac{T_1}{T_2} \cdot U_b^{(0)} - U_c^{(0)} - \frac{\Delta M}{M_0} \frac{3}{4} \left(\frac{1}{\sqrt{T_2}} - \frac{1}{\sqrt{T_1}} \right) \cdot \frac{1}{T_2} = \frac{1}{2} \cdot \frac{\omega^2}{G\pi\rho\sqrt{T_1 \cdot T_2}}$$

respectively. Their comparison allows us to eliminate the unknown factor ω (d) and determine the heterogeneity of the early Moon: $\Delta M/M_0 = 0.711$, taking $E_1 = 1.196 \cdot 10^{-3}$ and $E_2 = 2.495 \cdot 10^{-3}$ according to the observed value of the fossil tidal bulge. Taking into account the found inhomogeneity value, one can determine d : $d = D/R_\epsilon \approx 31.5$ Considering that $\Delta M/M_0 = M/M_0 - 1$

$$\rho_0 = \frac{\rho_B}{1 + \frac{\Delta M}{M_0}}, \quad \rho_0 = \rho_{Crust} = 19565 \text{ kg/m}^3$$

With the above estimates of heterogeneity, we get more agreement with the observed data for the fossil tidal bulge than for the homogeneous model [6]:

$$\frac{|C_{20}|}{C_{22}} = 6.11$$

The simple two-layer model of the early Moon considered by us reproduces quite well the main observable characteristics of the fossil tidal bulge under the assumption that the early Moon was at a distance of $d = D/RE \approx 31.5$ and the density of the upper layer of the MO was 1956 kg/m^3 before solidification.

Later, when the volatile remains were degassed, the Moon's crust had apparently thickened and acquired its present-day values

Acknowledgments

This work was supported by the Russian Science Foundation, project no. 17-17-01279.

References:

- Williams J.G., Konopliv A.S., Boggs D.H., et al., // *J. Geophys. Res.: Planets*. 2014. V.119. No 7, P.1546-1558.
- Zharkov V.N., Pan'kov V.L., Kalachnikov A.A., and Osnach A.I., *Introduction to lunar physics*. Izd. Nauka, Moscow, 1969, 312 p.[in Russian].
- Mazarico E., Barker M., Neumann G., Zuber M., and Smith D., // *Geophys. Res. Lett.* 2014. V. 41. P. 2282-2287.
- Zhong S. and Zuber M. // *J. Geophys. Res.* 2000. V. 105. No 2. P. 4153-4160.
- Wahr J., Selvans Z., Mullen M., Barr A., Collins G., Selvans M., and Pappalardo R. // *Icarus*. 2009. V.200 No 1, P.188-196.
- Voropaev S., Dnestrovsky A., Marov M. // *Doklady Physics*. 2019, V 64, No. 2, P.80-83.

PROSPECT OF PLANETARY RADIO EMISSION BASED ON LOW FREQUENCY DETECTION OF CHANG'E-4

Wang Mingyuan¹, Ping Jinsong¹, Zhang Mo¹, Chen Linjie¹,
Marc Klein Wolt²

¹ National Astronomical Observatories, Chinese Academy of Sciences,
Beijing, China, wangmy@nao.cas.cn

² Dept. of Astrophysics, Radboud University

Keywords:

Low frequency, NCLE, CE-4, AKR

Introduction:

On Earth, low frequency observations below ~30 MHz are hard to achieve because the peak plasma frequency of Earth ionosphere is 5–10 MHz. Spacecraft of lunar orbit and lunar farside will reveal a new window for low frequency radio-astronomy. Last year, Chang'E-4 relay satellite, lander and rover were launched successfully. Both the relay satellite and the lander of Chang'E-4 have very low frequency detection payloads: Low Frequency Spectrometer [1] for the lander and Netherlands-China Low-Frequency Explorer (NCLE) for CE-4R. These payloads provide an opportunity to understand the variation of Earth AKR radiation and Jupiter radio burst. In this report, we review the research status of Earth AKR radiation and Jupiter radio burst, then discuss the possible contribution of both LFS and NCLE in AKR and Jupiter radio burst detection.

References:

- [1] Ji Y.C., Zhao B., Fang G.Y., et al. Key technologies of very low frequency radio observations on the lunar far side [J]. Journal of Deep Space Exploration, 2017, 4 (2): 150-157.
- [2] Woan G. A very low frequency radio telescope on the far side of the moon, 1998.
- [3] Jia Y., Zou Y., Xue C., et al., Scientific objectives and payloads of Chang'E-4 mission. Chin J. Space Sci., 2018, 38(1):118-130.

LIBS FOR IN-SITU GEOCHEMICAL INVESTIGATIONS OF EXTRATERRESTRIAL SURFACES OF ATMOSPHERELESS BODIES

S. Schröder¹, D.S. Vogt¹, K. Rammelkamp¹, S. Kubitzka¹, S. Frohmann¹, E. Dietz¹, P.B. Hansen¹, U. Böttger¹, S.G. Pavlov¹, A. Börner¹, A. Wedler², M. Gensch^{1,3}, H.-W. Hübers^{1,4}

¹ *Institute of Optical Sensor Systems, German Aerospace Center (DLR), Rutherfordstr. 2; 12489 Berlin, Germany, susanne.schroeder [at] dlr.de*

² *Institute of Robotics and Mechatronics, German Aerospace Center (DLR), Muenchener Str. 20; 82234 Wessling, Germany*

³ *Technische Universität Berlin, Institute of Optics and Atomic Physics, Straße des 17. Juni 135, 10623 Berlin, Germany*

⁴ *Humboldt-Universität zu Berlin, Department of Physics, Newtonstr.15, 12489 Berlin, Germany*

Keywords:

LIBS, laser-spectroscopy, elemental analysis, geochemistry, in-situ exploration, Moon, asteroids

Introduction:

Laser-induced breakdown spectroscopy (LIBS) is a type of atomic emission spectroscopy for the elemental analysis at a sub millimeter scale [1]. LIBS permits rapid in-situ multi-elemental analysis without sample preparation and only optical access over distances of up to several meters, making it particularly interesting as a scientific payload for robotic missions. The LIBS technique has already been proven very useful for in-situ geochemical analysis on the martian surface [2–4] and is discussed for future missions to explore also other bodies of the Solar System. It was proposed as payload for the exploration of bodies with thin or no atmospheres like asteroids and the Moon [e.g., 5], but also for high pressure environments such as on Venus [6]. The DLR Institute of Optical Sensor Systems develops LIBS for future robotic in-situ exploration of extraterrestrial environments.

LIBS:

LIBS relies on ablating material from the sample by focusing a pulsed laser onto its surface [1]. This produces an expanding plasma of atoms, ions, and electrons. The emitted photons, which feature characteristic wavelengths of the elements composing the sample, are collected and analyzed spectroscopically. It was shown that LIBS is suitable even with a low-energy laser in ultra-high vacuum environments [7]. LIBS data obtained during a mission will probably mostly be a time and spatially integrated signal. The LIBS plasma is, however, not a homogeneously emitting uniform source but complex with different distributions of particles inside that change over time. Time- and spatially-resolved LIBS data opens up a way to study the transient inhomogeneous LIBS plasma and its characteristics and is investigated at the DLR Institute of Optical Sensor Systems with focus on low-pressure environments.

Laboratory Works:

Our laboratory LIBS setups are constructed especially for the purpose of testing and developing LIBS for applications in planetary science. The setups allow for the exchange and coupling of different components to enable testing and studying of single components and prototypes. Since both the pressure and composition of the ambient atmosphere have great influence on the characteristics of the laser-induced plasma, the setups are combined with dedicated experimental chambers for the simulation of planetary conditions (atmospheric composition, pressure, temperature) to test the performance and suitability of LIBS for different applications in planetary science. Recent activities of the group focused on applications on Mars and on bodies without atmospheres such as the Moon. In particular, a Vacuum-UV LIBS is currently being developed, since this wavelength range allows for an improved detection of volatile elements such as sulfur, chlorine, and phosphorous [8].

Miniaturized components and prototypes are developed and tested in the facilities of the DLR. Together with partners (von Hoerner&Sulgar and Laserzentrum Hannover e.V.), a very compact and light-weight low-energy LIBS laser was developed for ESA's ExoMars rover when LIBS was still a part of the intended payload. A small echelle type spectrometer allowing for the detection of highly resolved LIBS spectra from 230-780 nm was developed together with the ISAS (Leibniz Institut für Analytische Wissenschaften) and von Hoerner & Sulgar. Miniaturized Czerny-Turner spectrometers are tested as well for different applications. Depending on the goal of the mission, different configurations can be considered for the LIBS instrument to maximize the scientific return.

At the DLR Institute of Optical Sensor Systems, a setup for time-resolved plasma imaging was recently implemented and combined with a simulation chamber to experimentally simulate different low-pressure environments [9]. The goal is to provide a better understanding of the particular characteristics of extraterrestrial LIBS plasmas, their dynamics, and their typical spatial and temporal evolution. The results are used to give input for instrument designs, and for data analysis and interpretation of real mission data such as from Mars.

Combination of LIBS and Raman spectroscopy

Besides LIBS we also investigate and develop Raman spectroscopy for robotic missions. Together with partners from Spain and Japan (INTA, JAXA), a small Raman spectrometer is currently being developed for the DLR/CNES Martian Moon eXploration MMX rover [10, 11] to investigate the surface of Phobos.

The combination of LIBS and Raman spectroscopy is particularly promising for in-situ surface analysis in robotic missions since the data are complementary [12, 13] and hardware components can be shared. The DLR is working on combining both techniques into a single instrument to provide information about the elemental composition together with the molecular or lattice structure.

LIBS on robotic platforms:

The DLR is currently working on implementing a LIBS module into a mobile DLR robot in the framework of the Helmholtz ARCHES project [14]. The Lightweight Rover Unit (LRU) is equipped with a versatile robotic arm to which different modular instruments can be connected. A demonstration of the LRU performing LIBS in an environment similar to extraterrestrial surfaces is scheduled for next year (2020) on the hillside of the volcano Etna on Sicily. DLR is moreover involved in an EU Horizon 2020 project, developing a LIBS instrument for the LUVMI-X rover under the lead of Space Applications Belgium (<https://www.h2020-luvmi-x.eu/about/>). The lightweight rover and its payload will be designed to explore the polar regions of the Moon and to search there in particular for water and other volatiles.

References:

- [1] D.A. Cremers and L. Radziemski, Handbook of Laser-Induced Breakdown Spectroscopy, Wiley, 2013.
- [2] S. Maurice et al., The ChemCam instrument suite on the Mars Science Laboratory (MSL) rover: Science objectives and mast unit description, Space Sci. Rev., 2012. №. 1–4. V. 170. P. 95–166.
- [3] R.C. Wiens et al., The ChemCam instrument suite on the Mars Science Laboratory (MSL) rover: Body unit and combined system tests, Space Sci. Rev., 2012. V. 170. №1–4, P. 167–227.
- [4] S. Maurice et al., Chem Cam activities and discoveries during the nominal mission of the Mars Science Laboratory in Gale crater, Mars, J. Anal. At. Spectrom. 2016. V. 31, №. 4, P. 863–889.
- [5] J. Lasue et al., Remote laser-induced breakdown spectroscopy (LIBS) for lunar exploration, J. Geophys. Res. E Planets, 2012. V. 117, №. 1, P. 1–18.
- [6] Z.A. Arp, D.A. Cremers, R.D. Harris, D.M. Oschwald, G.R. Parker, and D.M. Wayne, Feasibility of generating a useful laser-induced breakdown spectroscopy plasma on rocks at high pressure: Preliminary study for a Venus mission, Spectrochim. Acta — Part B At. Spectrosc., 2004. V. 59, №. 7, P. 987–999.
- [7] S.G. Pavlov, S. Schröder, I. Rauschenbach, E.K. Jessberger, and H.W. Hübers, Low-energy laser induced breakdown spectroscopy for in-situ space missions

- to solar system bodies without atmospheres, *Planet. Space Sci.*, 2012. V. 71, №. 1, P. 57–63.
- [8] L. Radziemski, D.A. Cremers, K. Benelli, C. Khoo, and R.D. Harris, Use of the vacuum ultraviolet spectral region for laser-induced breakdown spectroscopy-based Martian geology and exploration, *Spectrochim. Acta – Part B At. Spectrosc.*, 2005. V. 60, №. , P. 237–248.
- [9] D.S. Vogt et al., Time-resolved spectral imaging of LIBS plasma at low pressures for the exploration of Solar System bodies, EPSC conference Berlin. 2018. №754.
- [10] J. Bertrand et al., Roving on Phobos: challenges of the MMX Rover for space robotics, *Proc. Of the 15th Symposium on Advanced Space Technologies in Robotics and Automation (ASTRA)*, 2019.
- [11] U. Böttger et al., Raman spectrometer for Phobos in-situ exploration, this conference 10MS3 Moscow, 2019.
- [12] K. Rammelkamp et al., Low-level LIBS and Raman data fusion in the context of Martian exploration, *J. Raman Spectrosc.* 2019. P. 1–20.
- [13] S. Schröder et al., Effects of Pulsed Laser and Plasma Interaction on Fe, Ni, Ti, and their oxides for LIBS Raman Analysis in Extraterrestrial Environments, *J. Raman Spectrosc.*, accepted, 2019.
- [14] A. Wedler et al., From single autonomous robots toward cooperative robotic interactions for future planetary exploration missions, *Proc. of the 69th IAC, International Astronautical Federation (IAF)*, Bremen, 2018.

EXPERIMENTAL SIMULATING OF A MICROMETEORITE IMPACT ON THE MOON

E.M. Sorokin¹, M.V.Gerasimov², M.A. Zaitsev², V.D. Shcherbakov³, K.M. Ryazantsev¹, O.I. Yakovlev¹, E.N. Sluta¹, S.P. Krasheninnikov¹

¹ Vernadsky Institute of Geochemistry and Analytical Chemistry RAS, Moscow, Russia

² Institute of Space Research, RAS, Moscow, Russia

³ Lomonosov Moscow State University, Department of Geology, Moscow, Russia

Keywords:

impact, micrometeorite bombardment, evaporation differentiation, experiment, laser, nanophase iron, npFe⁰.

Introduction

The study of surface processes on airless bodies, in particular on the Moon, is an important task today and in the future. Most remote sensing data is obtained from the surface layer of such bodies. This loose surface layer is called regolith. It is the result of the interaction of the surface of airless bodies with outer space. One such interaction is the micrometeorite bombardment. In this work we will show simulating of such process in laboratory by laser. We use two targets - basalt with crystalline structure (further - crystalline basalt) and basalt glass. It will be shown that basalt glass undergoes evaporation differentiation to a greater extent than crystalline basalt. About 90% of the glass spherules from basalt glass underwent evaporation differentiation, whereas in crystalline basalt only 25%.

Investigation of the initial sample

The target in the experiment was a sample of basalt, similar in composition to the basalts of the mare regions of the Moon and basalt glass of a similar composition. This sample was studied before the experiment, with such techniques as: micro-X-ray analysis, X-ray diffraction analysis and X-ray fluorescence analysis (in %: LOI-2,12, Na₂O-2,03, MgO-6,54, Al₂O₃-14,01, SiO₂-48,71, P₂O₅-0,12, K₂O-0,26, CaO-11,54, TiO₂-1,05, MnO-0,20, Fe₂O₃-13,0).

Experimental technique

We use millisecond Nd-glass pulse laser with a laser radiation wavelength of 1.06 μm, pulse duration of 10⁻³ s, and pulse energy of ~600–700 J. The energy flux density was ~106–107 W/cm². The temperature created in the vaporized cloud was about 4000–5000 K, which corresponded to the temperature of vaporization upon hypervelocity impact processes with collision velocities of about 10–15 km/s. The target—a slice of basalt in a seal—was placed into a hermetic ~500 cm³ volume chamber with an optical window of fused silica. The chamber was purged with the model gas mixture at atmospheric pressure with a volume flow rate of 300–400 cm³/min. After the purging, the gas mixture supply was decreased to ~5 cm³ without closing it completely to avoid ingress of the atmospheric air into the chamber. [1].

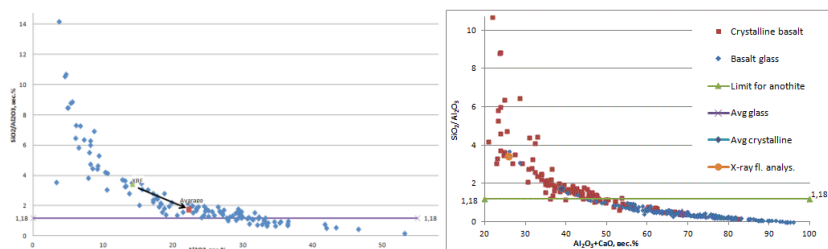


Fig. 1. Ratio SiO₂/Al₂O₃ against Al₂O₃ in the glass beads that have been analyzed by SEM. Beads below line at 1,18 correspond to the process of evaporative differentiation.

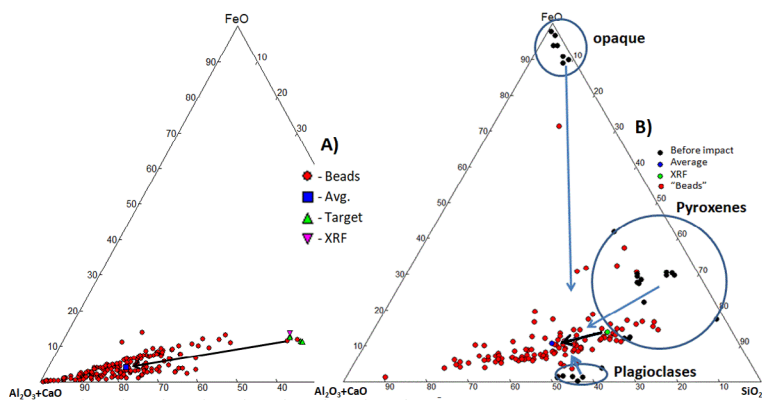


Fig. 2. Triangular diagram, in the corners of which are located oxides of different volatility. The arrows show approximate displacements of the compositions of the initial minerals during melting and evaporation.

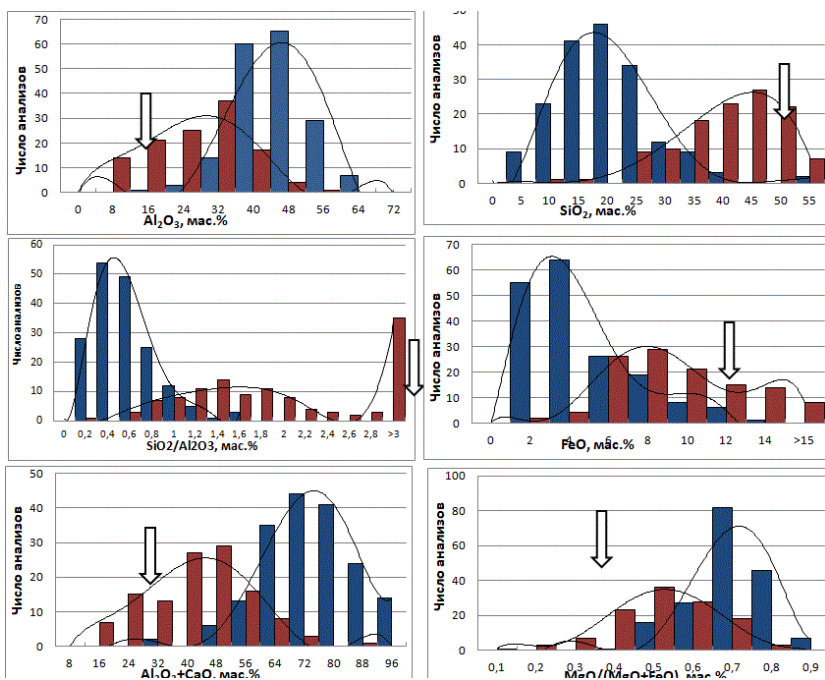


Fig. 3. Histograms that shows difference between two experiments. Red bars are responsible for the experiment with crystalline basalt, while blue bars are responsible for basalt glass. The arrow indicates the average content of the initial sample (according to XRF).

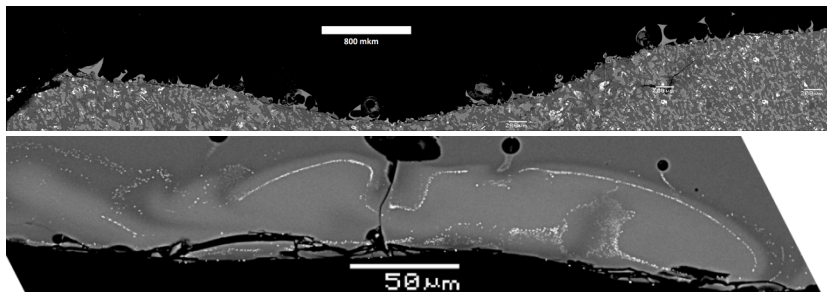


Fig. 4. The craters obtained by laser impacts. A – Crystal Basalt Crater. It has a diameter of about 6 mm, and a depth of 0.6 mm. B – Part of the crater obtained from basalt glass. Here we can see nanophase iron (npFe⁰).

Results

After the laser "impact", the ejection products from the craters and the craters itself were analyzed by various methods. Melt and condensation beads were analyzed by scanning electron microscope. It is shown that some of the beads have undergone of evaporative differentiation, and correspond to the high-aluminous HASP glasses found on the Moon ($\text{Al}_2\text{O}_3 > 34 \text{ wt}\%$, $\text{SiO}_2 < 32\%$) (fig.1). On this figure it can be seen that about 25% of glass beads in the case of crystalline basalt and 90% in the case of basalt glass undergoes of evaporation differentiation. The value of 1,18 (and line with it) shows minimal ratio of $\text{SiO}_2/\text{Al}_2\text{O}_3$ in anorthite, so dots below this line correspond to the process of evaporative differentiation [2, 3]. One of the important conclusions in the paper is the wide heterogeneity of the compositions of the melt glasses (fig. 2b) for the experiment with crystalline basalt. This is the result of mixing melts in various proportions obtained by melting the original minerals (the black dots on the figure 2b) of the target. This is shown by blue arrows. Genesis upon impact of such glasses is shown on partially melted grains of minerals in the crater (fig. 4a). On the other hand, almost all (90%) glass beads that one which was measured in the experiment with basalt glass is undergone of evaporation differentiation. It is possible indicates that fact tha in the glass condition almost all binds in crystal structure was already broken and thus the components (oxides) evaporated more easily (fig. 2a). Another important conclusion is that the evaporative differentiation gone much further in the experiment with basalt glass (fig. 3.). For example, in the experiment with basalt glass Al_2O_3 has a minimum at about 14.5 wt.%, maximum – at 60 wt.%, average – at 40 wt.%; SiO_2 has minimum at about 0.8 wt.%, max - at 53 wt.%, avg. - at 17.7 wt.%; FeO min – 0.01 wt.%, max – 12.1 wt.%, avg. – 3.7 wt.%. The same for experiment with crystalline basalt is: Al_2O_3 has a minimum at about 3.3 wt.%, maximum – at 53 wt.%, average – at 22 wt.%; SiO_2 has minimum at about 9 wt.%, max - at 61 wt.%, avg. - at 38.5 wt.%; FeO min – 1.1 wt.%, max – 52 wt.%, avg. – 9.29 wt. % (fig. 3). In both experiments easily volatile oxides was evaporated and the average chemical composition of the glass beads shifts toward the refractory region (fig. 2.).

The craters obtained after the laser impacts were analyzed by SEM. In case of crystalline basalt, it revealed traces (or roots) of those formations that were found in the ejected material or, in other words, traces of the flows (schlieren) (fig. 4a). In case of basalt glass, nanophase iron (npFe^0) was found here in crater (fig.4.b).

References:

- [1] Zaitsev M.A., Gerasimov M.V., Safonova E.N., Vasilieva A.S. Peculiarities in the formation of complex organic substances in the nitrogen-methane atmosphere during Hypervelocity Impacts // *Astronomicheskii Vestnik*, 2016, Vol. 50, No. 2, p. 123-140.
- [2] Yakovlev O.I., Shornikov S.I., Ryazantsev K.M. Inversion of the flying of silica and magnesium oxides in the evaporation of hasp-glasses on the moon // *Geochemistry*, 2018, №1, p.77-81.
- [3] Yakovlev O.I., Gerasimov M.V., Dikov Yu.P. Estimation of the temperature conditions for the formation of HASP- and GASP glasses of lunar regolith // *Geochemistry*, 2011, №3, p.227-238.

DISTRIBUTION OF P-BEARING OLIVINES SOURCES IN THE LUNAR CRUST

S.I. Demidova¹

¹ Vernadsky Institute of Geochemistry and Analytical Chemistry, Russian Academy of Sciences, Kosygin St. 19, Moscow, 119991 Russia, demidova.si@yandex.ru

Keywords:

P-bearing olivine, lunar rocks, lunar samples, lunar meteorites.

Introduction:

Olivine is a common mineral of the lunar rocks and the only rock-forming mineral which can concentrate incompatible element phosphorus. Rocks with P-bearing olivine were found in lunar meteorites Dhofar 1442, 287, 961, 025 and in "Apollo — 14" (lunar sample 14321), "Luna — 16, 20 and 24" lunar samples. Analysis of the lithological composition of both the landing sites regolith from known locality and meteorites obtained by occasional sampling of the lunar crust constrains P-bearing olivine sources distribution areas on the lunar surface and may shed some light to the connection with other lunar rocks.

Results:

Mg-rich olivines containing up to 0.4 wt% P_2O_5 (type 1) were found in the highland anorthositic-noritic (gabbro-noritic)–troctolitic (ANT) rock series enriched in phosphorus and other incompatible elements. Fe-rich varieties (type 2) are present in a late-stage products of low-Ti basalts crystallization (table 1). The rocks are not related to typical KREEP rocks commonly free of olivine.

Table. 1. Abundance of rock fragments with P-bearing olivines in lunar samples and meteorites

Type	Olivine	Rock fragments	L16	L20	L24	A14	Dho 1442	Dho 287	Dho 961
1	Fo ₅₁₋₈₈ (<0.4 wt % P_2O_5)	Anorthosite – norite (gabbro-norites) – (spinel) troctolites.	10	14	3	1	0	0	1
2	Fo ₂₋₅₂ (<0.4 wt % P_2O_5)	Low-Ti basalts	1	0	2	0	2	1	0

A link of type 1 olivines with HMS rocks has been recently established based on its chemical composition [1], but impact-induced mixing and melting could significantly affect the composition of the rocks. In spite of the abundance of the highland ANT suite in the lunar crust and the occurrence of P-bearing olivine in many meteorites and "Luna" and "Apollo" landing sites, this phase is extremely rare. In the highland Dho 733, 1436 and group Dho 302 meteorites with a remarkably diverse rock series (including the HMS suite) P-bearing olivine was not found. Its absence in the olivine-bearing rocks in source areas of these meteorites indicates either a localized distribution of sources of P-bearing olivines in the lunar highlands, or their limited abundance.

Mare basalts represent another potential source of the P-bearing olivine, but its content in them should not be significant. Modeling fractional crystallization of compositions of some "Luna — 16, 24" basalts showed that the normative content of ferroan olivine (type 2) in the rocks does not exceed 1 % [2].

The sources of P-bearing olivines could assimilate KREEP material, which is considered to be related to the giant Mare Imbrium impact basin. Indeed, the "Apollo — 14" mission, delivered rock samples of the Fra Mauro Formation, thought to be lithified material ejected from the Mare Imbrium

crater basin [e.g. 3]. The Dho 1442 and 961 meteorites contain a KREEP component, but they are not definitely ejected from the Mare Imbrium. However, the “Luna” landing sites were located far from the Mare Imbrium, and “Luna — 16, 20 and 24” samples are practically devoid of KREEP, nevertheless with rare evidence for the presence of the component enriched in incompatible elements [4, 5]. The “Luna — 16, 20 and 24” samples taken both from the highland area between the Mare Fecunditatis and Mare Crisium (L-20), as well as from the Mare Fecunditatis (L-16) and Mare Crisium (L-24), have significantly different amounts of the highland component [6–8]. It is believed that the highland material in “Luna — 16” samples was obtained from the highland domain 70–80 km north of the Langren Crater, 300 km southeast of the sampling site [6]. The closest highland area is located 40 km from the “Luna — 24” drill core site [9]. The largest number of rock fragments with P-bearing olivine was found in the “Luna — 20” samples, which also contain rocks with possibly primary igneous texture. The content of these rocks is lower in the “Luna — 16” samples and even lower in the “Luna — 24” samples (table 1). Only one “Luna — 16” rock fragment with P-bearing olivine has an primary igneous texture, while others are represented by breccias and agglutinates. If the studied sampling is representative, this may reflect the amount of highland component in samples of these areas or indicate that the “Luna — 20” landing site is located most closely to a source of P-bearing olivines. The characteristic feature of this source could be enrichment of olivine-normative melts in Cr [1, 10]. This feature differs them from primary highland HMS rocks, but is typical of some olivines from mare basalts and is also predicted for the deep-seated early lunar magma ocean cumulates [11]. So, at least one source of P-bearing olivines should be located in the eastern part of the lunar nearside. This area likely contains a previously unknown type of olivine-bearing highland rocks enriched in incompatible elements.

The “Luna” and “Apollo — 14” landing sites are characterized by the development of low-Ti or very low-Ti mare basalts. The Dho 961, 1442, and 025 meteorites, in addition to the widespread highland material, contain single clasts of basaltic rocks too. This indicates that a source of P-bearing olivines may be confined to the mare-highland boundary.

It is remarkable the presence of single fragments of evolved rocks found in 14321 lunar sample [12] and Dho 1442, 961 meteorites [13, 14]. According to the orbital data, rare granitic domes are localized in the area of the Gruithuisen, Hansteen, Aristarchus, Lassell, Mairan, Compton and Belkovich craters [15, 16, 17]. Most of these areas are confined to the Oceanus Procellarum, except for the Compton–Belkovich area located on the dark side of the Moon. These rocks are interpreted to be derived through a deep differentiation of silicate melts, or partial melting of a source enriched in incompatible elements or through liquid immiscibility of these melts [e.g. 17]. It is known that during immiscible splitting of the melt into ferrobasaltic and granitic liquids, phosphorus is accumulated in the ferrobasaltic melt, where its solubility could reach a few percents [18]. Addition of such a melt to the HMS source could significantly affect source composition, in particular, lead to its enrichment in phosphorus and other incompatible elements. Noteworthy is the recently discovered exposure of magnesian rocks (containing Mg spinel) in the silica-rich setting of the Hansteen Alpha [19]. However, the contribution of such melts should not be significant, since experimental studies demonstrated a strong influence of phosphorus on the crystallization sequence of basic melts up to the disappearance of olivine [20]. Thus, the potential distribution area of these olivines could be some domains of the Oceanus Procellarum.

Conclusions:

Analysis of the lithological components of both the landing site regolith and the meteorites suggests that sources of P-bearing olivines are restricted to the lunar nearside. The association with mare basalts likely indicates their confinement to the mare-highland boundary. The presence of fragments of evolved rocks in the studied breccias suggests that some olivine

sources are linked with the recently described occurrences of felsic rocks in the Oceanus Procellarum and Compton–Belkovich area on the dark side of the Moon. However, it is possible that the “Luna” landing site contains a previously unknown type of olivine-bearing highland rocks, which are enriched not only in incompatible elements, but also in chromium.

References:

- [1] Demidova S.I., Anosova M.O., Kononkova N.N. et al. Phosphorus-bearing olivines of lunar rocks: sources and localization in the lunar crust // *Geochem. Intern.* 2019. V. 57. No. 8. P. 873–892.
- [2] Demidova S.I., Badekha K.A., Kononkova N.N. Modeling conditions of crystallization of P-bearing fayalites of lunar mare basalts // *Proc. VESEMPG-2018. Moscow. Russia.* 2018. P. 302–306.
- [3] Grieve R.A., McKay G.A., Smith H.D., Weill D.F. Lunar polymict breccia 14321: a petrographic study // *Geochim. Cosmochim. Acta.* 1975. V. 39. P. 229–245.
- [4] Pavlenko A.S., Tarasov L.S., Shevaleevskii I.D., Ivanov A.V. Petrology of lunar rocks from the Mare Fecunditatis // In *Regolith from the Mare Fecunditatis.* Ed. Vinogradov A.P. 1974. P. 56–64 (in Russian).
- [5] Cameron K.L., Papike J.J., Bence A.E., Sueno S. Petrology of fine-grained rock fragments and petrologic implications of single crystals from the “Luna — 20” soil // *Geochim. Cosmochim. Acta.* 1973. V. 37. P. 775–793.
- [6] Tarasov L.S., Shevaleevskii I.D., Nazarov M.A. Petrographic and mineralogical studies of magmatic rocks from the Mare Fecunditatis // In *Regolith from the Mare Fecunditatis.* Ed. Vinogradov A.P. 1974. P. 129–147 (in Russian).
- [7] Florensky K.P., Polosukhin V.P., Bazilevsky A.T., Konopikhin A.A. Geology and Geomorphology of the “Luna — 20” landing site // In *Regolith from the Moon,* Ed. Barsukov V.L. and Surkov Yu.A. 1979. P. 41–51 (in Russian).
- [8] Bence A.E., Grove T.L. The “Luna — 24” highland component // In *Mare Crisium: The View from “Luna — 24”.* Ed. Lerrill R.B. and Papike J.J. *Geochim. Cosmochim. Acta.* 1978. V. 9. P. 429–444.
- [9] Florensky K.P., Pronin A.A., Bazilevsky A.T. Geology of “Luna — 24” landing site // In *Regolith from the Mare Crisium.* Ed. Barsukov V.L. 1980. P. 7–18 (in Russian).
- [10] Demidova S.I., Ntaflou T., Brandstätter F. P-bearing olivines from the “Luna — 20” soil samples, their sources and possible phosphorus substitution mechanisms in lunar olivine // *Petrology.* 2018. V. 26. N. 3. P. 314–327.
- [11] Elardo S.M., Draper D.S., Shearer Jr.C.K., Lunar magma ocean crystallization revisited: bulk composition, early cumulate mineralogy, and the source regions of the highlands Mg-suite // *Geochim. Cosmochim. Acta.* 2011. V. 75. P. 3024–3045.
- [12] Lindstrom M.M., Knapp S.A., Shervais J.W., Taylor L.A. Magnesian anorthosites and associated troctolites and dunite in “Apollo — 14” breccias // *Proc. Lunar Planet. Sci. Conf.* 15. *J. Geophys. Res.* 1984. P. C41–C49.
- [13] Demidova S.I., Nazarov M.A., Anosova M.O., et al. U-Pb zircon dating of the lunar meteorite Dhofar 1442 // *Petrology.* 2014. V. 22. N. 1. P. 1–16.
- [14] Demidova S.I., Nazarov M.A., Ntaflou Th., Brandstaetter F. Possible serpentine relicts in lunar meteorites // *Petrology.* 2015. V. 23. N. 2. P. 116–126.
- [15] Glotch T.D., Lucey P.G., Bandfield J.L. et al. Highly silicic compositions on the Moon // *Science.* 2010. V. 329. P. 1510–1513.
- [16] Greenhagen B.T., Lucey P.G., Wyatt M.B., et al. Global silicate mineralogy of the moon from the Diviner lunar radiometer // *Science.* 2010. V. 329. P. 1507–1509.
- [17] Jolliff B. L., Wiseman S.A., Lawrence S.J., et al. Compton Belkovich: non mare silicic volcanism on the Moon’s farside // *Nature Geosci.* 2011. V. 4. P. 566–571.
- [18] Watson E.B. Apatite saturation in basic to intermediate magmas // *Geophys. Res. Lett.* 1979. V. 6. P. 937–940.
- [19] Dhingra D., Glotch T.D., Prissel T.C., et al. Mg-spinel exposures within silica rich setting on Hansteen Alpha: probing the geologic context // *Lunar Planet. Sci. Conf. V. 48.* 2017. P. 2104.
- [20] Toplis M.J., Libourel G., Carroll M.R. The role of phosphorus in crystallization processes of basalt: an experimental study // *Geochim. Cosmochim. Acta.* 1994. V. 58. P. 797–810.

DIKE INTRUSION-RELATED PROCESSES IN THE LUNAR CRUST: THE ROLE OF COUNTRY ROCK POROSITY/PERMEABILITY IN MAGMATIC PERCOLATION AND THERMAL ANNEALING, AND IMPLICATIONS FOR GRAVITY SIGNATURES

J.W. Head¹ and L. Wilson^{1,2}

¹ *Department of Earth, Environmental and Planetary Sciences, Brown University, Providence, RI 02912 USA;*

² *Lancaster Environment Center, Lancaster University, Lancaster LA1 4YQ UK.*

Keywords:

dike, lunar basalt, sill, magmatic percolation, thermal annealing.

Introduction:

Shallow crustal country rock on the Moon is demonstrably more fractured and porous than deeper crustal bedrock, and GRAIL gravity data have shown that deeper crustal bedrock is more porous than previously thought. This raises the question of how crustal porosity and permeability will influence the nature of magmatic dike and sill intrusions in terms of: 1) the ability of ascending magma to intrude and occupy this pore space (magmatic percolation), and 2) the influence of the intruded magma on annealing of this porosity and permeability (thermal annealing), thus densifying the country rock [1]. We analyze quantitatively the emplacement of basaltic dikes and sills on the Moon and assess these two factors in the context of the most recent data on micro- and macro-scale porosity of lunar crustal materials. We then assess the influence of these two densification processes in contributing to gravity signals associated with these intrusions.

Processes:

1) Magmatic Percolation:

Magma injection into pre-existing fractures: We model fractures of various mean widths W and inject lunar magma under a pressure gradient of the same order as buoyancy, where $\rho \Delta z$. Lunar magmas have low viscosities in comparison with terrestrial basalts and may initially move in a turbulent fashion even when injected into narrow fractures. This results in efficient heat transfer to the walls of the fracture, rapid cooling, the progressive formation of crystals, and the onset of non-Newtonian rheology. We therefore assume that in general the magma being injected has a yield strength that depends on the current crystal volume fraction [2]. The crystal fraction is assumed to increase linearly as the temperature decreases from the liquidus to the solidus. The temperature-dependent viscosity of crystal-free lunar basalt is well-approximated by a power law [3]; we use the viscosity data for a low-Ti mare basalt [4]. The bulk viscosity is then related to the liquid viscosity via a correction factor that is again a function of the crystal content [5].

Standard fluid mechanics formulae [e.g., 6] then give the flow speed of the magma in laminar or turbulent flow. An initially turbulent fluid will make the transition to laminar motion when its Reynolds number decreases below some critical value determined by the current value of the Hedstrom number, a function of both the yield strength and bulk viscosity. While motion is turbulent, heat is transferred from the magma to the walls of the fracture at a rate per unit area that can be obtained from industrial data on heat exchangers [3]. The heat loss causes a decrease in the lava temperature as the lava advances. Cooling leads to increases in the yield strength, the viscosity, the Hedstrom number and the critical Reynolds number. The increases in viscosity and yield strength cause the flow speed to decrease, and so the initially high Reynolds number decreases until it intersects the increasing critical Reynolds number and the motion becomes laminar. We note the distance that the magma has travelled when this occurs, Z_l . From this point onward, thermal boundary layers grow against the walls of the fracture, and motion stops when the two boundary layers meet in the center of the flow.

This criterion is the basis of the Grätznuber treatment for the maximum travel distances of laminar lava flows [7], and adapting it to flow in a planar fracture we find the maximum additional distance that the magma can advance, Z_p . The maximum penetration distance of magma into the fracture is then $Z_m = Z_t + Z_p$. Figure 1 shows the values of Z_p , Z_t and Z_m for magma injections into fractures with widths, W , from 1 cm to one meter. The penetration distance increases dramatically for fractures more than a few tens of cm wide. However, there is little evidence that such wide fractures will exist in the lunar crust. Fractures are extremely common at the 10-20 microns scale in impact-modified rocks [8] but exposures at the Vredefort impact structure [9] suggest that at larger scales the commonest fracture width is in the range 1–3 cm. We conclude that lunar magmas driven by the pressure gradients expected for volcanic intrusions would penetrate less than one meter in such cracks. Thus, magmatic percolation should not be common at distances greater than about a meter from the edge of an intruding dike or sill, and since the majority of cracks are predicted to be in the 10–20 micron range, where significant intrusion is unlikely, the cumulative effect of magmatic percolation on the density structure should be negligible.

2) Thermal Annealing:

Consequences of dike and sill intrusions: Wieczorek et al. [10] called on viscous deformation due to elevated temperatures with depth in the crust to decrease porosity and increase density (thermal annealing). The strong temperature dependence of viscosity causes this effect to occur over a narrow depth interval (<5 km) and [10] used representative lunar historical temperature gradients to find that (depending on the heat fluxes and rheologies assumed) the minimum depth where this transition would take place is ~40 km. On the other hand, penetration of dikes to the shallow crust and surface and potential intrusion of shallow sills (as in the case proposed by [1]) should be accompanied by thermal annealing as well. We now consider such a case to assess the importance of thermal annealing and its role in offsetting the density of the intruded basaltic sill.

The thermal consequences of the abrupt injection of a sill into much cooler rocks can be modelled analytically using treatments by Carslaw and Jaeger [11; article 2.4.i]. For the present case the most useful approximation is a horizontal sheet of magma at temperature T_m emplaced rapidly into an infinitely extensive body of host rock at temperature T_a . For cases where the top of the sill is at a depth less than or comparable to the thickness of the sill an alternative analytical solution approximating to the geometry would be that in article 2.4.iv [11], in which the top of the sill would be exactly at the planetary surface. In practice that both treatments yield essentially the same results for the penetration of heat from the sill into the country rocks.

A number of simple relationships emerge. First, the interface between the sill and the host rocks almost instantly reaches a temperature that is the average of the temperatures of the magma and host. The highest liquidus temperature for a lunar magma reported by [4] is 1440 °C, i.e., 1713 K, for a low-Ti basalt. A representative thermal conductivity for lunar crustal rocks is ~1.3 W m⁻¹ K⁻¹ [12] and the lunar geothermal heat flow is ~3×10⁻² W m⁻² [13]. With an average surface ambient temperature of ~250 K, the temperature at a depth of ~10 km in the Moon will be ~480 K; injection of the above magma will lead to an interface temperature of 1097 K, i.e., 824 °C. [1] quotes data from [14] and [15] showing that lunar rocks experienced significant annealing if held at >800 °C for the order of a year. Heat transfer from a sill to its host rocks will occur on a much longer time scale, but the peak temperature experienced by the host rocks will decrease approximately exponentially with distance from the sill margin, and a given temperature will be experienced for a duration that increases as the square of the sill thickness. In our model we conservatively assume that a temperature of 700 °C is needed for efficient annealing. The gravity models of [1] imply that sills up to 6 km in thickness might be needed to explain the gravity data he analyzed. Using this extreme sill thickness in our model, we find that the 700 °C isotherm extends for 600 m into the host rock for a period of ~250,000 years. If this results in com-

plete elimination of, say, 30% pore space in these host rocks, both above and below the sill, the crust overlying the area of the sill intrusion would subside by ~360 m, 6% of the sill thickness. For a 3 km thick sill the corresponding values have the 700 °C isotherm extending for 300 m into the host rock for a period of ~30,000 years and again producing subsidence equal to 6% of the sill thickness. It is of course the case that greater volumes of crust are heated to lower temperatures than 700°C for longer times but, given that we have used the highest plausible magma temperature and a conservative annealing temperature, we cannot see a situation where annealing would eliminate more than a small fraction of the topographic signature of the intrusion.

Conclusions:

For the range of plausible micro/macro-scale porosity and permeability (microns to cm) and open crack lateral continuity (mm to tens of cm), we find 1) that rapid conductive cooling of injected magma due to the very large surface area to volume ratio restricts magmatic percolation to very limited areas (maximum several tens of cm) adjacent to the ascending dike, even in the upper several hundred meters of the lunar crust; 2) that the conductive heat loss from intruded dikes and sills results in a thermal wave decay rate that is predicted to limit the effects of intrusion-adjacent thermal annealing to less than ~6% of the thickness of the intruded body. The extremely rapid rise rate of magma in dikes derived from sources in the lunar mantle disfavors the lateral migration of dikes to form sills in the crust, except in specific shallow crustal environments influenced by impact crater-related environments (e.g., floor-fractured craters). We conclude that magmatic percolation and thermal annealing in association with lunar mare basalt magmatic dike and sill emplacement should be taken into consideration in interpreting gravity signatures, but that the effects are likely to be minor, compared with the density contrast of the solidified magmatic intrusion itself.

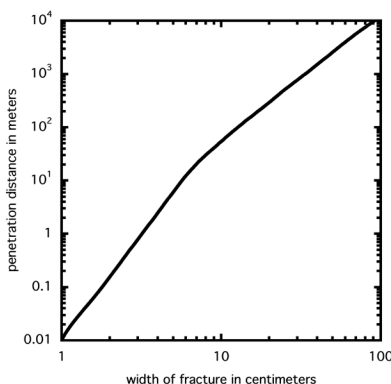


Fig. 1. Variation of the maximum distance that magma can penetrate into a fracture before cooling halts its progress shown as a function of the fracture width. Note that the vast majority of cracks are at the 10–20 microns scale in impact-modified rocks, and that fractures and pore space in the crust are at the mm to cm scale; thus the penetration distance of apophyses (small intrusive features adjacent to and emanating from the sill margins) is typically well below a meter.

References:

- [1] Kiefer, W. (2013) *JGR-P* 118, 733.
- [2] Ishibashi, H. & Sato, H. (2010) *J. Min. and Pet. Sci.*, 105, 334.
- [3] Hulme, G. (1973) *Modern Geology* 4, 107.
- [4] Williams, D. A., et al. (2000) *JGR* 105, 20,189.
- [5] Pinkerton, H. & Stevenson, R.J. (1992) *J. Volcanol. Geotherm. Res.* 53, 47.
- [6] Knudsen, J.G. & Katz, D.L. (1958) *Fluid Dynamics and Heat Transfer*. McGraw-Hill, New York. 576 pp.
- [7] Pinkerton, H. & Wilson, L. (1994) *Bull. Volcanol.* 56, 108.
- [8] Kenkmann, T. et al. (2014) *J. Structural Geology* 62, 156.
- [9] Lieger, D. et al. (2009) *Earth Planet. Sci. Letts.* 279, 53; Lieger, D. et al. (2011) *Geochim. Cosmochim. Acta* 75, 4490.
- [10] Wicczorek, M., et al. (2013) *Science* 339, 671.

- [11] Carslaw, H. S. & Jaeger, J.C. (1959) *Conduction of Heat in Solids*. 2nd ed. Oxford University Press, 510 pp.
- [12] Robertson, E.C. (1988) U.S.G.S. Open File Report 88-441, 106 pp.
- [13] Vaniman, D., et al. (1991) The lunar environment. Chapter 3, pp. 27-60, in *The Lunar Source Book*, Cambridge Univ. Press.
- [14] Simonds, C. (1973) *Am. J. Sci.*, 273, 428.
- [15] Uhlmann, D. R. et al. (1975) *Proc. Lunar Sci. Conf.* 6, 693.

POTENTIAL LUNAR BASE ON MONS MALAPERT: TOPOGRAPHIC, GEOLOGIC AND TRAFFICABILITY CONSIDERATION

A.T. Basilevsky^{1,2}, S.S. Krasilnikov¹, M.A. Ivanov¹, M.I. Malenkov³, G.G. Michael², T. Liu⁴, J.W. Head⁵, D.R. Scott⁵, L. Lark⁵

¹ Vernadsky Institute of Geochemistry and Analytical Chemistry, RAS, Kosygin Str., 19, 119991, Moscow, Russia, atbas@geokhi.ru

² Planetary Sciences and Remote Sensing, Institute of Geological Sciences, FreieUniversitaet Berlin, MalteserStrasse 74-100, 12249, Berlin, Germany

³ Space Research Institute, Profsoyuznaya Str., 84/32, 117997, Moscow, Russia

⁴ Institute of Geodesy and Geoinformation, Technische Universität Berlin, 10623, Germany,

⁵ Department of Earth, Environmental and Planetary Sciences, Brown University, 02912, Providence, RI, USA

Keywords:

The Moon, lunar base, topography, geology, trafficability, rover.

Introduction:

Due to the near constant solar illumination and the potential presence of water ice in the regolith, polar areas of the Moon are candidates for construction of a lunar base [e.g., 1, 2]. The mountain Mons Malapert (MM) near the South Pole of the Moon (a massif that is part of the outer ring of the South Pole Aitken basin) is a key candidate for the location of such a base [e.g., 3, 4, 5]. MM is an ~ 30x50 km mountain elongated in a WNW-ESE direction with a NNE extension (Fig. 1). Its summit stands ~5 km above the 1838 km datum, has constant visibility from Earth and long periods of sunlight (87 to 91% of the year).

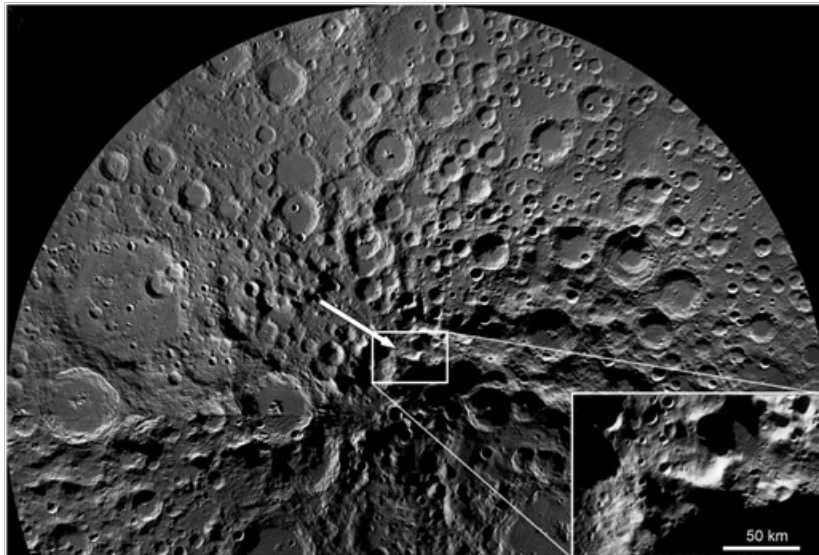


Fig. 1. Mons Malapert (arrow) seen in the LROC WAC mosaic P900S0000_032P of the lunar South Pole region (NASA/ASU).

In this analysis we consider the topographic, geologic and trafficability characteristics of Mons Malapert, which need to be taken into account in the further consideration of MM as a lunar base location. Potential landing sites for a lunar base in the Mons Malapert area are discussed in [6].

Topography and Geology:

The topography and its derivatives of MM were studied using LROC WAC images and the LOLA-based DTM. South of MM lie the ~50-km craters

Haworth and Shoemaker whose floors are in permanent shadow and show a neutron spectrometric signature of high water-ice content [7] that may be a source of water for the base. The geology of the MM region is defined by its position on the rim of the South-Pole-Aitken basin, the largest and most ancient impact basin on the Moon [8]. The ancient age of this area is confirmed by crater spatial density which shows ages of ~ 4.2 Ga [9]. The MM slopes are mostly rather steep: from ~ 20 to 30° , while slopes on its summit and base are more gentle (Fig. 2).

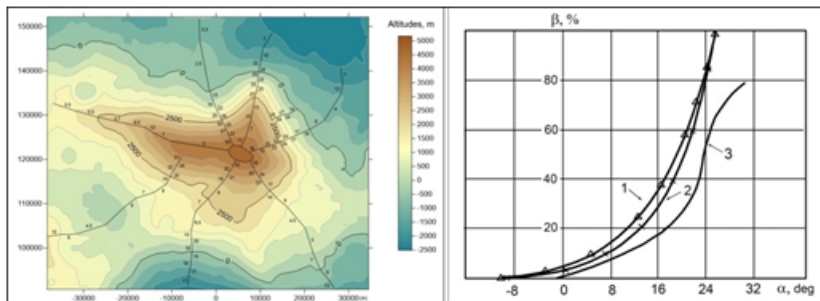


Fig. 2. Left — Topographic map of Mons Malapert based on the LOLA-based DTM LDEM80S20M_a1 calculated values of slope steepness shown. Right — Dependence of slip ratio (β) on steepness (α) of the slope on which the rover is climbing. 1 and 2 — Lunokhod 1 measurements on the Moon and on Earth analogs, correspondingly [10]. 3 — the Apollo Lunar Rover Vehicle measurements on terrestrial analogs [11].

LROC NAC images of this area show that while the summit and base of MM are covered by numerous small craters, its steep slopes show a deficit of craters and are complicated by low ridges approximately perpendicular to the downslope direction. These characteristics of the steep slopes suggest effective downslope movement of the regolith material that, in turn, suggests that the mechanical properties of the surface layer here are relatively weak.

Trafficability

The siting, building and operation of a lunar base implies activity not only at the base and in close proximity, but also traverses to other distant sites of interest for resources and scientific investigations. So planning the Mons Malapert base requires the detailed analysis of the trafficability of the region. To consider this issue we return to experience gained by the operations of Soviet Lunokhod 1, 2 and the US Apollo Lunar Roving Vehicles (LRV) [10, 11]. On the basis of new and evolving technology, rovers designed for the MM lunar base may significantly differ from earlier rovers, but consideration of trafficability of the earlier rovers is important for future planning. Our analysis shows that neither Lunokhods nor the Apollo LRV could successfully climb most of the slopes of Mons Malapert. The acceptable trafficability appears to be only possible along the WNW crest of the mountain. For emergency cases wheel-walking rovers may be considered. Mons Malapert seems to be a good locality for the lunar base but more studies are needed [12].

Acknowledgments

This work was partly supported by Russian Science Foundation, project #17-17-01149, and Institute für Geologische Wissenschaften, Freie Universität Berlin. We gratefully acknowledge financial support from the NASA Solar System Exploration Research Virtual Institute (SSERVI) grant for Evolution and Environment of Exploration Destinations under cooperative agreement number NNA14AB01A at Brown University.

References:

- [1] Burke J.D. Merits of lunar polar base location // Lunar Bases and Space Activities of the 21st Century. Ed. W.W.Mendel. Houston. 1985. P. 77–84.
- [2] Zelenyi L. Milestones of the Russian space science program for the decade 2016–2025 // The 7-th Moscow Solar System Symposium, Space Research Institute, Moscow, Russia. Moscow. 2016, 7MS3_OS_01.
- [3] Sharpe B.L. and Schrank D.G. Malapert mountain: Gateway to the Moon // Advances in Space Research. 2003. V. 31. No 11. P. 2467-2472.

- [4] Cooper B.L. and Simon T. ISRU production of life support consumables for a lunar base // SAE Technical Report 2007-01-3106. 2007. 7 p.
- [5] Schrunk D., Sharpe B., Cooper B.L., and Thangavelu M. The first lunar base. In: The Moon. Springer Praxis Books. Praxis. 2008. P. 83-95.
- [6] Krasilnikov S.S., Basilevsky A.T., Ivanov M.A. Landing site for potential lunar base on Mons Malapert // The 10-th Moscow Solar System Symposium, Space Research Institute, Moscow, Russia. Moscow. 2019, 8MS3_OS_01.
- [7] Sanin A.B., Mitrofanov I.G., Litvak M.L. and 17 coauthors. Hydrogen distribution in the lunar polar regions // Icarus. 2017. V. 283. P. 20–30.
- [8] Ivanov M.A., Hiesinger H., van der Bogert C.H., Orgel C., Pasckert J.H., Head J.W. Geologic history of the northern portion of the South Pole-Aitken basin on the Moon // Journal of Geophysical Research - Planets. 2018. V. 123 (10). P. 2585–2612.
- [9] Basilevsky A.T., Krasilnikov S.S., Ivanov M.A. and 6 coauthors. Potential lunar base on Mons Malapert: Topographic, geologic and trafficability considerations // Solar System Research. 2019 (in press).
- [10] Malenkov M.I. Extreme Robotics: Design of driving systems of planetary rovers. St. Peterburg. Polytechnical University Press. 2008. 159 p. (in Russian).
- [11] Asnani V., Delap D. and Creager C. The Development of Wheels for the Lunar Roving Vehicle, NASA/TM—2009-215798.2009. 26 p.
- [12] Malenkov M.I., Volov V.A., Guseva N.K., Lazarev E.A. Increasing the mobility of Mars rovers by improving the locomotion systems and their control algorithms. Russian Engineering Research, 2015. V. 35. No. 11. P. 824–831.

TOPOGRAPHICAL FEATURES OF THE LUNAR MARIA AND BASINS

Zh.F. Rodionova¹, E.A. Grishakina², A.Yu. Zharkova^{1,3}, V.V. Shevchenko¹

¹ Sternberg Astronomical Institute, Moscow State University, Moscow, 119234, Russia;

² Vernadsky Institute of Geochemistry and Analytical Chemistry, Russian Academy of Sciences, Moscow, 119991, Russia;

³ Moscow State University of Geodesy and Cartography (MIIGAik), MIIGAik Extraterrestrial Laboratory, Moscow, 105064, Russia

Keywords:

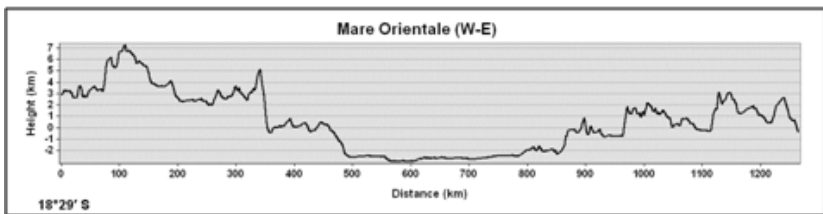
The Moon, topography, maria, basins, elevation, range heights, Bouguer anomaly.

Introduction:

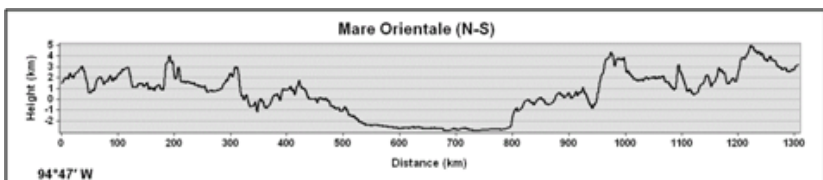
Several previously unrecognized pre-Nectarian impact basins and other previously suspected basins have been verified by Clementine laser altimeter data [1]. The GRAIL inventory of lunar basins improves upon earlier lists that differed in their totals by more than a factor of 2. The size-frequency distributions of basins on the near side and far side hemispheres of the Moon differ substantially [2]. The book “The Moon’s Largest craters and basins” [3], which incorporates information collected by the Kaguya, Lunar Reconnaissance Orbiter and GRAIL missions, also contains the Catalog of 72 impact features more than 200 km in diameters. The sequence numbers have been established as embodiment of several lines of evidence of relative ages of the 72 lunar impact features in this Catalog. The numbers of features from 1 to 44 refer to Pre-Nectarian period, from 45 to 64 — to Nectarian period, from 66 to 69 — to Early Imbrian period, and, finally, numbers from 70 to 72 correspond to Late Imbrian period [3]. The study of such parameters of large basins and maria profiles as absolute elevations of their bottoms and rims heights was performed in our abstract. Correlation of the Byrne’s sequence numbers with the measured parameters was fulfilled.

Methods:

The profiles in western-eastern and north-south directions of 36 lunar maria and large basins were compiled using global digital elevation model (DEM) with a resolution of 118 m/pixel [4]. Figure 1 shows an example of profiles for Mare Orientale.



a)



b)

Fig. 1. Profiles of Mare Orientale: a) in W-E direction; b) in N-S direction.

The Table 1 shows the next parameters: the name of feature (Name), latitude (Lat.), longitude (Long.), diameter in kilometers (Dkm), absolute height

of bottom (Hbot), Bouguer anomaly contrast (Anom.), sequence numbers (SN), range of heights (Hr), rim's maximum height (hmax), rim's minimum height (hmin), difference between rim's heights (Δh).

Table 1. Example of table structure for lunar maria and large basins parameters

Name	Lat.	Long.	Dkm	Hbot	Anom.	SN	Hr	hmax	hmin	Δh
Orientele	-20	-95	960	-2.5	720	69	8.5	7.2	3.1	4.1

Discussion and Conclusion:

We analyzed the correlations between the features diameters and Bouguer's Anomalies. There is dependence between them. But we have not found the connection with Byrne Sequence Numbers (Fig. 2).

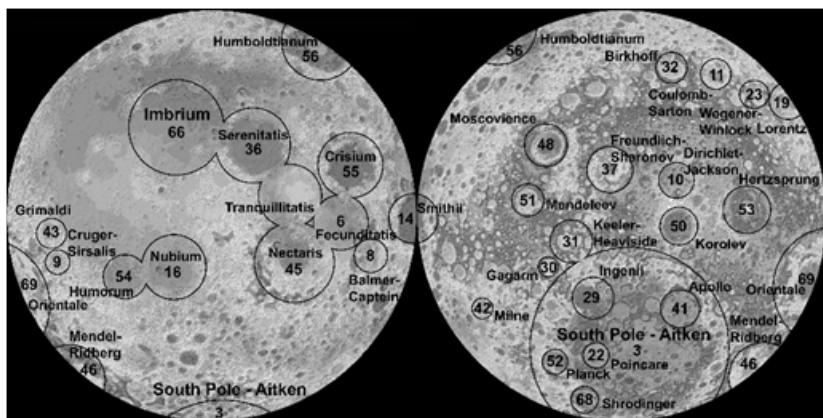
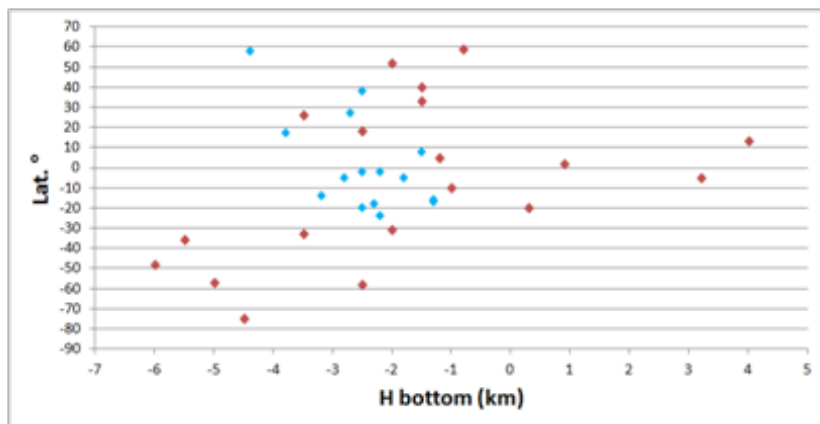


Fig. 2. Byrne Sequence Numbers shown on our Lunar map [5].

Our study shows that it is possible to compile three groups of large basins and maria in dependence of the difference of rim's heights (Δh): 1 – rim's heights from 6 km till 2.9 km; 2 – from 2.2 km till 1.5 km; 3 – rim's heights are less than 1.2 km.

Figure 3 below shows the dependence of the parameters on latitudes and longitudes. Blue points are on near side, red ones – far side.

The absolute heights of the maria and basins' bottoms on the near hemisphere of the Moon are less than on the far hemisphere. The dependence of the studied formations' depths on the longitude is traced. On the far hemisphere, the elevation differences of the formations (range heights) under study are substantially greater than on the near hemisphere.



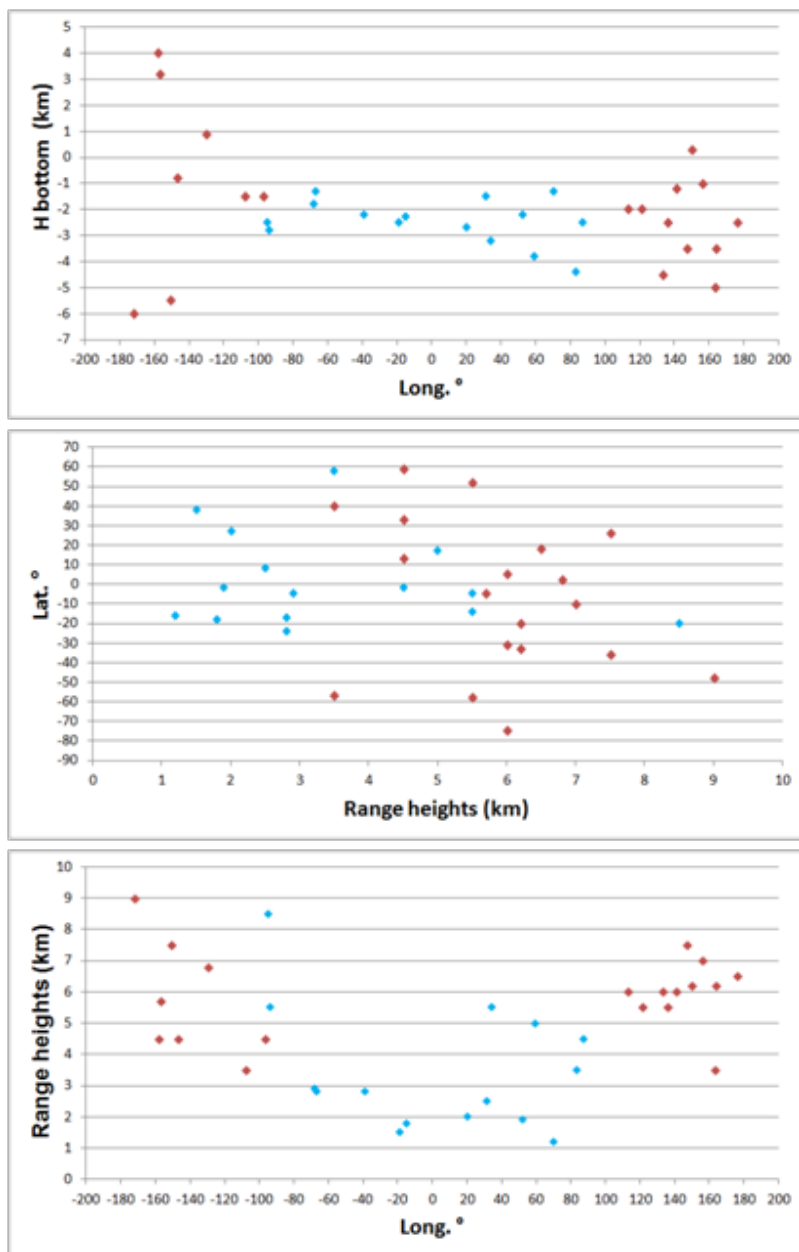


Fig. 3. Dependence of absolute H bottom and Range heights from latitudes and longitudes

References:

- [1] Cook A.C., Watters T.R., Robinson M.S., Spudis P.D., Bussey D.B.J. Lunar Polar topography derived from Clementina stereoimages. J.G.R. 2000 V. 105, № E5, P. 12,023-12,033
- [2] Neumann G. A., Zuber M. T., Wieczorek M. A., Head J. W. et. al. Lunar impact basins revealed by Gravity Recovery and Interior Laboratory measurements. Sci. Adv. 2015. P. 1-10
- [3] Byrne C. J. The Moon's Largest Craters and Basins. 2016. Springer. 246 p.
- [4] Scholten F., Oberst J., Matz K.-D., Roatsch T., Wählisch M., Speyerer E.J., Robinson M.S. GLD100: The near-global lunar 100 m raster DTM from LROC WAC stereo image data, J. G. R. 2012, 117, E00H17.
- [5] Grishakina E., Rodionova Zh., Shevchenko V., Slyuta E., Obzornaya Karta Lunu, scale 1:13 000 000. Sternberg Astronomical Institute (MSU), Vernadsky Institute of Geochemistry and Analytical Chemistry (RSSI). 2018.

LANDING SITE SELECTION FOR FUTURE LUNAR LANDERS

M.V. Djachkova, I.G. Mitrofanov, M.L. Litvak, A.B. Sanin

Space Research Institute, Moscow, Russia

Keywords:

Moon, landing site, landing site selection, Luna-25, Luna-27.

Introduction:

The landing site selection method primarily developed by our team for Luna-25 mission allowed us to identify several areas suitable for landing and surface operations in the South Polar Region of the Moon. These areas can be considered as possible landing sites for future lunar missions such as Luna-27, and their size depends on the landing precision of the mission. For example, the landing precision of 1 km gives an opportunity to explore quite an extensive area close to the South Pole. The features of this area will be discussed.

THE NEAREST PERSPECTIVES FOR LUNOKHOD 2.0.

M.L. Litvak, I.G. Mitrofanov, V.I. Tretyakov

*Space Research Institute, Russia, Moscow, 117997, Profsouznaya str. 84/32,
litvak@mx.iki.rssi.ru*

Keywords:

Russian lunar program, Luna-28, polar sample return, lunokhod, geological survey

Introduction:

The Russian lunar exploration program is implementing now as a sequence of lunar robotic missions Luna – 25,26,27 and Luna – 28. The last one in this row is the lunar polar sample return (LPSR) mission. Its primary science and technology goals, and implementation capabilities are under discussion now and will be reviewed at the stage of technical proposal by the end of 2019.

It is being considered that this type of the mission should not be only limited by short living polar lander supplied with ascent module to deliver lunar samples to the Earth. The one of the prioritized mission scenarios proposes small or middle size lunar rover that can substantially expand mission capabilities during sample acquisition as well as after launch of ascending rocket with samples. The following potential tasks for such a rover could be proposed:

To help with sample collection: some samples could be delivered to the lander from the vicinity area (stones, regolith samples).

To install some instruments in the vicinity of lander: seismic instrumentations, some regolith probes.

To help with remote sampling: To bring samples cached onboard Luna – 27.

To conduct surveys: Photos of lander operations, survey of landing area after launch of ascending rocket.

Long living operations: geological survey after launch of ascending rocket at distances up to 30 km.

In this study we would like to present our vision of this scenario, to discuss science goals, required technologies, design, capabilities of the rover and propose science instrumentation that should be installed onboard rover.

THE CONCEPT OF LUNA-28 MISSION FOR POLAR SOIL RETURN

I.G. Mitrofanov et al.

*Space Research Institute, Russia, Moscow, 117997, Profsovnaya str. 84/32,
litvak@mx.iki.rssi.ru*

The concept of the project “Luna-Grunt” is presented. The main goal of the mission is to return the samples of frozen regolith from the area at the vicinity of south pole of the Moon. Scenario of mission implementation is presented and science payload is described.

RESULT FROM JUNO ON THE ORIGIN OF JUPITER

S.J. Bolton¹, **J. Connerney**², **S. Levin**³

¹ *Southwest Research Institute, San Antonio, TX, USA, sbolton@swri.edu*

² *SRC, Annapolis, MD, USA*

³ *Jet Propulsion Laboratory and the Juno Science Team*

Juno's investigation into the origin of Jupiter is focused on the study of Jupiter's gravity and magnetic fields combined with the study of Jupiter's atmosphere. The interior structure, and in particular constraints on the core of heavy elements deep within Jupiter discriminate among formation theories. We know Jupiter is composed primarily of hydrogen and helium and hence must have formed early while the protoplanetary nebula was still present. How this happened, however, remains unclear after many decades of modeling. A primary goal of the Juno mission is to constrain properties of Jupiter that are diagnostic of how giant planets form. Two possible mechanisms are generally considered: (i) direct instability of the disk itself and (ii) accretion of a solid core inducing local collapse of gas around it. Differences between these scenarios are profound, particularly in terms of the mass of a heavy element core. Juno's gravity field investigation suggests that the concentration of heavy elements deep down is larger than expected and diffuse. The magnetic field indicates large asymmetries similar to the gravity field indicates as well as can be seen in the atmospheric wind profiles. The oxygen abundance within Jupiter—also a key goal of the Juno mission—indicates water potentially above solar abundance at the equatorial region. Results from these three investigations will be presented from the first half of the mission in the context of progress on the origin of Jupiter.

JUPITER'S MAGNETIC FIELD AND MAGNETOSPHERE AT THE MIDPOINT OF THE JUNO MISSION

J.E.P. Connerney^{1,2}, D.J. Gershman², S. Kotsiaros^{2,3}, J.L. Joergensen⁴, P.S. Joergensen⁴, J.M.G. Merayo⁴, J. Bloxham⁵, K.M. Moore⁵, S.J. Bolton⁶, S.M. Levin⁷

¹ *Space Research Corporation, Annapolis, MD, United States, jack.connerney@nasa.gov*

² *NASA Goddard Space Flight Center, Greenbelt, MD, United States*

³ *University of Maryland College Park, College Park, Maryland, United States*

⁴ *Technical University of Denmark (DTU), Lyngby, Denmark*

⁵ *Harvard University, Cambridge, MA, United States.*

⁶ *Southwest Research Institute, San Antonio, TX, United States*

⁷ *Jet Propulsion Laboratory (JPL), Pasadena, CA, United States.*

Keywords:

Jupiter's magnetic field; magnetosphere; magnetodisc;

Introduction:

The Juno spacecraft, orbiting Jupiter since July 4, 2016, maps Jupiter's magnetic and gravitational potential fields and probes its deep atmosphere in search of clues to the planet's formation and evolution [1]. From its unique vantage point of a high inclination, 53-day polar orbit, Juno also conducts an in-depth exploration of the polar magnetosphere and auroral phenomena [2].

Juno's magnetometer investigation (MAG) is equipped with two magnetometer sensor suites [3], located 10 and 12 m from the center of the spacecraft at the end of one of Juno's three solar panel wings. Each contains an accurate (100 ppm absolute vector accuracy) fluxgate magnetometer (FGM) sensor and a pair of co-located non-magnetic star tracker camera heads. The co-located star cameras monitor the attitude of the magnetometer sensors continuously (up to 4 quaternions/s), correcting for the slight deformation of the spacecraft solar array experienced during maneuvers and perijove passes. Such deformations, if not measured and corrected, would otherwise compromise measurement vector accuracy.

Juno's highly elliptical 53.5-day orbit carries her science payload from pole to pole in ~2 hours, with a closest approach to within ~1.05 R_J of the center of the planet (one R_J = 71,492 km, Jupiter's equatorial radius). Repeated periapsis passes will eventually encircle the planet with a dense net of observations equally spaced in longitude (<12° at the equator) and optimized for characterization of the Jovian dynamo [3]. Such close passages are sensitive to small spatial scale variations in the magnetic field and therefore many such passes are required to bring the magnetic field into sharp focus. Nevertheless, a dramatically detailed 10 degree and order model ("JRM09", for Juno Reference Model after 9 orbits) was extracted from a partial solution to a 20 degree/order model representation, providing the first new information about Jupiter's magnetic field in decades. Having passed the midpoint of Juno's baseline mapping mission, now with orbits separated by ~22.5 degrees of longitude, a model ("JRM17") with increased spatial resolution of the main field is obtained. The new model extends to degree and order 12 to 14 (with limited parameter resolution) and evidences more compact source geometry, as one might expect with increasing spatial resolution.

Jupiter's internal magnetic field exhibits a dramatic hemispheric asymmetry, with a very non-dipolar northern hemisphere contrasting a southern hemisphere that appears very dipolar [4, 5]. An equatorial belt of positive radial flux is interrupted by an isolated reverse-polarity patch situated near the equator at about 90 degrees system III west longitude. Comparison with earlier magnetic field models is suggestive of secular variation [6, 7] but inconsistencies among prior analyses call for caution in interpretation. A thorough retrospective analysis [8] of Voyager, Pioneer, and Ulysses observations obtained several decades ago provides the first unambiguous evidence of Jovian magnetic

secular variation and relates the variation to the penetration of zonal winds into the electrically conducting interior.

The evolution of Juno's orbit now brings the spacecraft through the magnetodisc in the inner magnetosphere (Figure 1), affording an opportunity to improve magnetodisc models [9, 10, 11] and provide a measure of magnetospheric activity during Juno's mission.

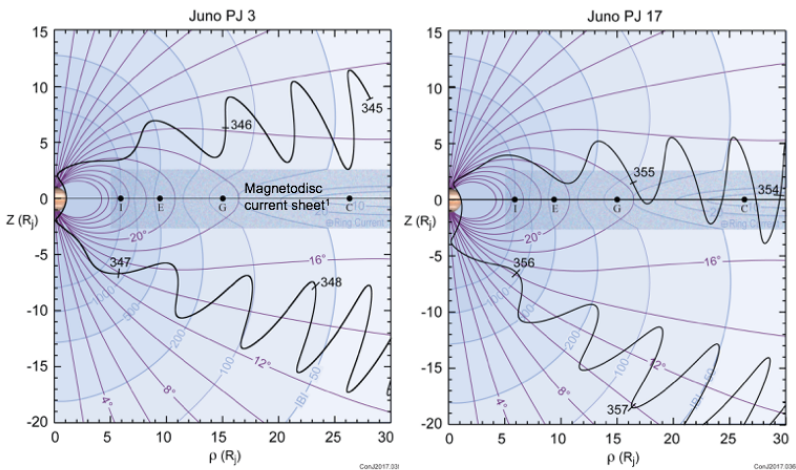


Fig. 1. Evolution of Juno's orbit illustrated in magnetic equatorial coordinates. Spacecraft trajectory in this coordinate system (black) oscillates due to the ~ 10 tilt of the Jovidipole. The equatorial azimuthal magnetodisc currents (shaded region) draw magnetic field lines (purple) outward along the equator, where field magnitudes (blue contours) are reduced.

Observations of the Jovian magnetosphere obtained throughout Juno's first 18 orbits have been used to optimize the geometric parameters of an azimuthally symmetric magnetodisc model, facilitating studies of time variability (parameterized via time-dependent current density). Combined with a model of radial currents providing torque to outflowing plasma, we obtain a measure of the time variability of the magnetodisc. The radial current system evidences significant time variability ($\sim 50\%$) whereas the magnetodisc currents thus far prove remarkably stable ($\sim 6\%$ variability). We present an overview of the magnetometer observations obtained during Juno's first two years in orbit [12, 13] in context with prior observations.

References:

- [1] Bolton, S.J. and the Juno Science Team (2010). The Juno mission. Proceedings of the International Astronomical Union Symposium, No. 269: 92–100.
- [2] Bagenal, F., Adriani, A., Allegrini, F., et al.: Magnetospheric science objectives of the Juno mission, *Space Sci. Rev.*, doi 10.1007/s11214-014-0036-8.
- [3] Connerney, J.E.P., Benn, M., Bjarno, et al. 2017. The Juno Magnetic Field Investigation, *Space Sci. Rev.*, doi: 10.1007/s11214-017-0334-z.
- [4] Connerney, J.E.P., Kotsiaros, S., Oliverson, R.J., Espley, J.R., Joergensen, J.L., Joergensen, P.S. et al. (2018). A new model of Jupiter's magnetic field from Juno's first nine orbits. *Geophys. Res. Lett.*, 45, doi: 10.1002/2018GL077312.
- [5] Moore, K., Rakesh, Y., Kulowski, L., et. al. 2018. A complex dynamo inferred from the hemispheric dichotomy of Jupiter's magnetic field, *Nature*, 561, 76–78, doi:10.1038/s41586-018-0468-5.
- [6] Connerney, J.E.P., & Aćuna, M.H. 1982. Jovimagnetic secular variation. *Nature*, 297, 313–315.
- [7] Ridley, V.A., and Holme, R. 2016. Modeling the Jovian magnetic field and its secular variation using all available magnetic field observations, *J. Geophys. Res. Planets*, 121, doi:10.1002/2015JE004951.
- [8] Moore, K.M., H. Cao, J. Bloxham, D.J. Stevenson, J.E. P. Connerney, and S.J. Bolton. 2019. Time-variation of Jupiter's internal magnetic field consistent with zonal wind advection, *Nature Astronomy*, doi:10.1038/s41550-019-0772-5.
- [9] Connerney, J.E.P., Aćuna, M.H. & Ness, N.F. (1981). Modeling the Jovian current sheet and inner magnetosphere. *J. Geophys. Res.*, 86, 8370–8384.

- [10] Alexeev, I.I., and E.S. Belenkaya, 2005. Modeling of the Jovian magnetosphere. *Annales Geophysicae*, 23(3), 809–826. doi:10.5194/angeo-23-809-2005.
- [11] Pensionerov, I.A., I.I. Alexeev, E.S. Belenkaya, J.E.P. Connerney, and S.W.H. Cowley, 2019. Model of Jupiter's current sheet with a piecewise current density, *Journal of Geophysical Research: Space Physics*, 124, doi:10.1029/2018JA026321.
- [12] Bolton, S.J., Adriani, A., Adumitroaie, V., et al.: Jupiter's interior and deep atmosphere: the first pole-to-pole pass with the Juno spacecraft, *Science*, doi: 10.1126/science.aal2108, 2017.
- [13] Connerney, J.E.P., Adriani, A., Allegrini, F., et al., Jupiter's Magnetosphere and Aurorae Observed by the Juno Spacecraft During its First Polar Orbits, *Science*, 10.1126/science.aam5928, 2017.

INFRARED OBSERVATIONS OF THE JUPITER'S ATMOSPHERE

A. Adriani, A. Mura, and the JIRAM team

INAF-IAPS Rome, Italy

Keywords:

Jupiter, Atmosphere, spectral-imaging, poles, water, ammonia, phosphine, germane, arsine, limb.

The Jovian InfraRed Auroral Mapper (JIRAM) [1] on board the Juno [2, 3] spacecraft, is equipped with an infrared camera and a spectrometer working in the spectral range 2–5 μm . JIRAM was built to study the infrared aurora of Jupiter as well as the Jupiter's atmosphere. The infrared camera is able to image auroral H3+ emissions and the thermal emission from the planet's atmosphere. The instrument is on board of the NASA mission Juno and it used for studying atmospheric morphological and dynamical structures and for investigating the abundance of some chemical species that have importance in the atmosphere's chemistry, microphysics and dynamics.

The spacecraft was inserted in the Jupiter's orbit in August of 2016. Since then, and with the exception of orbits 2 and 3, JIRAM has performed several observations from the equator to poles. Juno orbital design allows the spacecraft to fly over the planet's polar regions. This fact permitted unprecedented views of the polar atmospheric structures that have been acquired for the first time during orbit 4 [4]. Other observations permit to study the baroclinic waves extending for significant longitudinal span in the Northern Equatorial Belt [5] and over the polar structures. Spectral measurements provided the opportunity to measure abundances of water, ammonia, phosphine, germane and arsine at all latitudes down to pressures of 4–5 bars. Limb observations at the low latitudes permit to profile abundances of methane and trihydrogen cation in the stratosphere and the thermosphere of the planet.

We present results from the most significant atmospheric observations performed by the instrument since the start of the mission.

References:

- [1] Adriani, A. et al., JIRAM, the Jovian Infrared Auroral Mapper. *Space Science Reviews*, 2017, vol. 213, P. 393–446.
- [2] Bolton S.J. et al., Jupiter's interior and deep atmosphere: The initial pole-to-pole passes with the Juno spacecraft. *Science*, 2017, V. 356, P. 821–825.
- [3] Connerney J.E.P. et al., Jupiter's magnetosphere and aurorae observed by the Juno spacecraft during its first polar orbits. *Science*, 2017, V. 356, P. 826–832
- [4] Adriani, A., et al., Clusters of Cyclones Encircling Jupiter's Poles. *Nature*, 2018, V. 555, P. 216–219.
- [5] Adriani, A. et al., Characterization of Mesoscale Waves in the Jupiter NEB by Jupiter InfraRed Auroral Mapper on board Juno, *The Astronomical Journal*, 2018, V. 156, P. 246.

OBSERVATIONS OF RADIO AND PLASMA WAVES AT JUPITER FROM JUNO WAVES INVESTIGATION

M. Imai¹, W.S. Kurth¹, G.B. Hospodarsky¹, S.S. Elliott¹, A.H. Sulaiman¹, D.A. Gurnett¹, I. Kolmašová^{2,3}, O. Santolík^{2,3}, P. Louarn⁴, C.K. Louis⁴, P. Zarka⁵, S.J. Bolton⁶, J.E.P. Connerney^{7,8}

¹ Department of Physics and Astronomy, University of Iowa, Iowa City, Iowa, USA

² Department of Space Physics, Institute of Atmospheric Physics, The Czech Academy of Sciences, Prague, Czechia

³ Faculty of Mathematics and Physics, Charles University, Prague, Czechia

⁴ IRAP, Toulouse, France

⁵ LESIA, CNRS, Observatoire de Paris, Meudon, France

⁶ Space Science and Engineering Division, Southwest Research Institute, San Antonio, Texas, USA

⁷ Space Research Corporation, Annapolis, Maryland, USA

⁸ NASA Goddard Space Flight Center, Greenbelt, Maryland, USA

Keywords:

Jupiter, Juno, Waves, radio and plasma waves

Introduction:

The Juno spacecraft has, since its arrival at Jupiter on July 5, 2016, observed Jovian polar magnetosphere and atmosphere from its unique polar orbit [1]. In concert with insitu particle and field measurements [2–4] and the remote ultraviolet spectrometer and imager [5], the Waves instrument was designed to observe the electric component of waves from 50 Hz to 41 MHz and the magnetic component of waves from 50 Hz to 20 kHz [6]. In the polar cap region, upward-moving whistler-mode waves has been frequently observed concurrently with upward-moving energetic electrons [7]. According to theoretical studies [8, 9], the whistler-mode waves originate from upward-moving, field-aligned electron beams via a beam-plasma instability and contribute to pitch angle scattering and energization of the electrons. Over the main auroral oval region, Waves has recorded downward-moving intense broadband whistler-mode waves [10] correlated with broadband energetic precipitating electrons. This correlation may imply that the whistler-mode waves are involved in the stochastic acceleration of the electrons. Juno has also passed through magnetic field lines connected to Io's footprint tails for several cases [11]. For most of these cases, the broadband whistler-mode waves were accompanied by both downward- and upward-moving electrons precipitating along the common field lines. Some examples clearly show distinctive whistler-mode saucer-like waves near the field line connecting to the footprint tail. Hence, whistler-mode waves appear to play an essential role in Jupiter's auroras.

At radio frequencies, Jovian auroral radio emissions are regularly observed with Waves both remotely and in situ [12–20]. The nonthermal radio sources are distributed along auroral magnetic field lines at emission frequencies very close to the local cyclotron frequency via the electron cyclotron maser instability (CMI). Juno's wave, particle, and field observations indicate that unstable electron distributions that drive CMI are either loss-cone or conic type, with the latter being 5–10 times more efficient for the CMI growth rate than the former [18, 19]. The auroral radio emissions can be divided into decametric (DAM), hectometric (HOM), and broadband kilometric (bKOM) radio components depending on their spectral shapes. The first concurrent radio-ultraviolet aurora observations from Juno, using the RM09 internal magnetic field and washer-shaped current sheet models [21, 22], revealed that bKOM radio sources are tied to the main auroral oval [20].

Juno's close perijove passes provide a unique opportunity to monitor Jovian lightning in the atmosphere [23–26]. Waves has recorded two kinds of low-frequency electromagnetic waves related to the lightning. The first is comprised of Jovian low-dispersion whistlers observed at frequencies below 20 kHz [24, 25]. These whistlers may possibly propagate up to several

thousand km horizontally away from lightning strokes below the ionosphere before ultimately escaping the inner magnetosphere [25]. Initial whistler observations show that the lightning flash rate is 3–30 flashes/year/km² at midlatitudes, with greater rates in the northern hemisphere than the southern hemisphere [24]. The second kind is comprised of dispersed millisecond pulses called Jupiter dispersed pulses (JDPs), observed at frequencies below 150 kHz. JDPs propagate directly from lightning strokes but can leak into the inner magnetosphere only where the ionospheric density is sufficiently low, either in localized holes or over the night side [26]. Therefore, the synoptic observations of lightning-induced whistlers and JDPs improve our understanding of the physical process of lightning discharges in Jupiter's atmosphere. In this talk, we present the recent observations of radio and plasma waves at Jupiter from Juno Waves investigation, and compare them with some theoretical considerations including the wave-particle interactions and radio wave propagation.

References:

- [1] Bolton, S.J., et al. The Juno Mission // *Space Sci. Rev.* 2017. V. 213. P. 5–37.
- [2] McComas, D.J., et al. The Jovian Auroral Distributions Experiment (JADE) on the Juno Mission to Jupiter // *Space Sci. Rev.* 2017. V. 213. P. 547–643.
- [3] Mauk, B.H., et al. The Jupiter Energetic Particle Detector Instrument (JEDI) Investigation for the Juno Mission // *Space Sci. Rev.* 2017. V. 213 P. 289–346.
- [4] Connerney, J.E.P., et al. The Juno Magnetic Field Investigation // *Space Sci. Rev.* 2017. V. 213. P. 39–138.
- [5] Gladstone, G.R., et al. The Ultraviolet Spectrograph on NASA's Juno Mission // *Space Sci. Rev.* 2017. V. 213. P. 447–473.
- [6] Kurth W.S., et al. The Juno Waves investigation // *Space Sci. Rev.* 2017. V. 213. P. 347–392.
- [7] Tetrick, S.S., et al. Plasma waves in Jupiter's high-latitude regions: Observations from the Juno spacecraft // *Geophys. Res. Lett.* 2017. V. 44. P. 4447–4454.
- [8] Elliott, S.S., et al. Pitch Angle Scattering of Upgoing Electron Beams in Jupiter's Polar Regions by Whistler Mode Waves // *Geophys. Res. Lett.* 2018. V. 45. P. 1246–1252.
- [9] Elliott, S.S., et al. The Acceleration of Electrons to High Energies Over the Jovian Polar Cap via Whistler Mode Wave-Particle Interactions // *J. Geophys. Res. Space Physics.* 2018. V. 123. P. 7523–7533.
- [10] Kurth, W.S., et al. Whistler Mode Waves Associated With Broadband Auroral Electron Precipitation at Jupiter // *Geophys. Res. Lett.* 2018. V. 45. P. 9372–9379.
- [11] Szalay, J.R., et al. In-Situ Observations Connected to the Io Footprint Tail Aurora // *J. Geophys. Res. Planets* 2018. V. 123 P. 3061–3077.
- [12] Connerney, J.E.P., et al. Jupiter's magnetosphere and aurorae observed by the Juno spacecraft during its first polar orbits // *Science* 2017. V. 356 P. 826–832.
- [13] Kurth, W.S., et al. A new view of Jupiter's auroral radio spectrum // *Geophys. Res. Lett.* 2017. V. 44 P. 7114–7121.
- [14] Imai, M., et al. Latitudinal beaming of Jovian decametric radio emissions as viewed from Juno and the Nançay Decameter Array // *Geophys. Res. Lett.* V. 44. P. 4455–4462.
- [15] Imai, M., et al. Statistical study of latitudinal beaming of Jupiter's decametric radio emissions using Juno // *Geophys. Res. Lett.* V. 44. P. 4584–4590.
- [16] Imai, M., et al. Direction-finding measurements of Jovian low-frequency radio components by Juno near Perijove 1 // *Geophys. Res. Lett.* V. 44. P. 6508–6516.
- [17] Louis, C. K., et al. Io-Jupiter decametric arcs observed by Juno/Waves compared to ExPRES simulations // *Geophys. Res. Lett.* V. 44. P. 9225–9232.
- [18] Louarn, P., et al. Generation of the Jovian hectometric radiation: First lessons from Juno // *Geophys. Res. Lett.* 2017. V. 44. P. 4439–4446.
- [19] Louarn, P., et al. Observation of Electron Conics by Juno: Implications for Radio Generation and Acceleration Processes // *Geophys. Res. Lett.* 2018. V. 45. P. 9408–9416.
- [20] Imai, M., et al. Probing Jovian Broadband Kilometric Radio Sources Tied to the Ultraviolet Main Auroral Oval With Juno // *Geophys. Res. Lett.* 2019. V. 46. P. 571–579.
- [21] Connerney, J.E.P., et al. A New Model of Jupiter's Magnetic Field from Juno's First Nine Orbits // *Geophys. Res. Lett.* 2018. V. 45. P. 2590–2596.
- [22] Connerney, J.E.P., et al. Modeling the Jovian current sheet and inner magnetosphere // *J. Geophys. Res. Space Physics* 1981. V. 186. P. 8370–8384.
- [23] Brown S., et al. Prevalent lightningferics at 600 megahertz near Jupiter's poles // *Nature* 2018. V. 558(7708). P. 87–90.

- [24] Kolmašová I., et al. Discovery of rapid whistlers close to Jupiter implying similar lightning rates to those on Earth // *Nat. Astron.* 2018. V. 2. P. 544–548.
- [25] Imai, M., et al. Jupiter lightning-induced whistler and spheric events with Waves and MWR during Juno perijoves // *Geophys. Res. Lett.* 2018. V. 45. P. 7268–7276.
- [26] Imai, M., et al. Evidence for low density holes in Jupiter's ionosphere // *Nat. Commun.* 2019. V. 10. P. 2751.

OBSERVATIONS OF JUPITER AURORAE FROM JUNO

A. Mura, A. Adriani, the JIRAM Team

INAF-IAPS Rome Italy

Keywords:

Jupiter, Aurorae, Footprints, H3+.

NASA's Juno mission has been observing the Jovian aurorae since 2016 from a polar, highly elliptical orbit [1, 2, 3]. From this very favourable position above the poles, Juno obtained unprecedented in-situ measurements of Jupiter magnetosphere, and unique, remote-sensing views of the auroral regions both in the infrared and the ultra-violet ranges. Direct excitation of molecular hydrogen in the ionosphere by precipitating electrons results in Lyman and Werner bands in the UV; the same electron precipitation also produces, indirectly, H3+ thermal emission in the IR range. Images of aurorae in these two ranges are collected, respectively, by the Ultra Violet camera (UVS) and the Jovian InfraRedAuroral Mapper (JIRAM) [4], at each Juno perijove pass. In the main oval, the field aligned electric currents have very low densities, less than what was previously assumed to explain the intense auroral emissions. Juno observed the high energy (>100 keV) auroral electron, but also a lower energy component (~1 keV), which plays a substantial role. Inside the main oval, persistent upward broadband high-energy (~1 MeV) electron are observed. Also, intense auroral emissions are observed in regions where little or no precipitating electron flux is detected, possibly indicating excitation from strong ionospheric electric currents. The different mechanisms leading to H2 and H3+ emission explain the relations between the energy of precipitating electrons and the variability of the relative UV/IR intensities. Juno also revealed a puzzling structure in the electromagnetic interactions between Jupiter and its moons [5], whose signature is the presence of auroral footprints. These are a peculiar series of emission features extending downstream of the leading one, and look like a repeating pattern of swirling vortices. These multiple features have a very small scale (~100 km), which is not compatible with the simple paradigm of multiple Alfvén wave reflections. Observations of Io's footprint well downstream of the leading feature reveal a pair of closely spaced parallel arcs where previously only one was resolved. Both of Ganymede's footprints (main and secondary) appear as a pair of emission features that provide a remote measure of Ganymede's magnetosphere.

References:

- [1] Connerney J.E.P. et al., Jupiter's magnetosphere and aurorae observed by the Juno spacecraft during its first polar orbits. *Science*, DOI: 10.1126/science.aam5928, 2017.
- [2] S. Bolton, et al. Jupiter's interior and deep atmosphere: The initial pole-to-pole passes with the Juno spacecraft, *Science*. 2016. V. 356, Issue 6340, P. 821–825
- [3] F. Bagenal et al., Magnetospheric Science Objectives of the Juno Mission, SSR DOI 10.1007. 2017.
- [4] Adriani A. et al., JIRAM, the Jovian Infrared Auroral Mapper. *Space Sci. Rev.*, DOI 10.1007/s11214-014-0094-y, 2014.
- [5] Mura et al., *Science* 361, 774–777. 2018

PHOTOCHEMICAL MODEL OF PLUTO'S ATMOSPHERE AND IONOSPHERE

Vladimir A. Krasnopolsky

Moscow Institute of Physics and Technology, Moscow, Russia, vlad.krasn@verizon.net

Keywords:

Pluto; Pluto's Atmosphere; Pluto's Ionosphere; Photochemistry; Atmospheric Composition

Introduction:

The New Horizons flyby of Pluto [1, 2, 8] along with the ALMA [5] and VLT/CRIRES [4] high-resolution spectroscopy and the recent stellar occultations resulted in significant progress in Pluto's atmosphere. These new data require updated photochemical modelling. The model by Wong et al. [7] includes detailed neutral chemistry at 40 levels up to 1300 km. To fit the observations, the authors adopted saturated vapor densities of C₂H₄ and C₂H₆ equal to those of C₂H₂, though they differ by orders of magnitude. Here we present a model that does not require the revision of the laboratory data on the saturated vapor densities and involves ion chemistry that affects the neutral composition and is missing in Wong et al. [7].

Model

The model by Krasnopolsky [3] that reproduces fairly well the observed properties of Titan's atmosphere and ionosphere is adjusted to the conditions of Pluto during the New Horizons flyby. It involves 83 neutrals and 35 ions and extends up to the exobase at 1600 km. Thermal escape of neutrals and diffusion of ions are the upper boundary conditions. Condensation on the haze and surface are the lower boundary conditions.

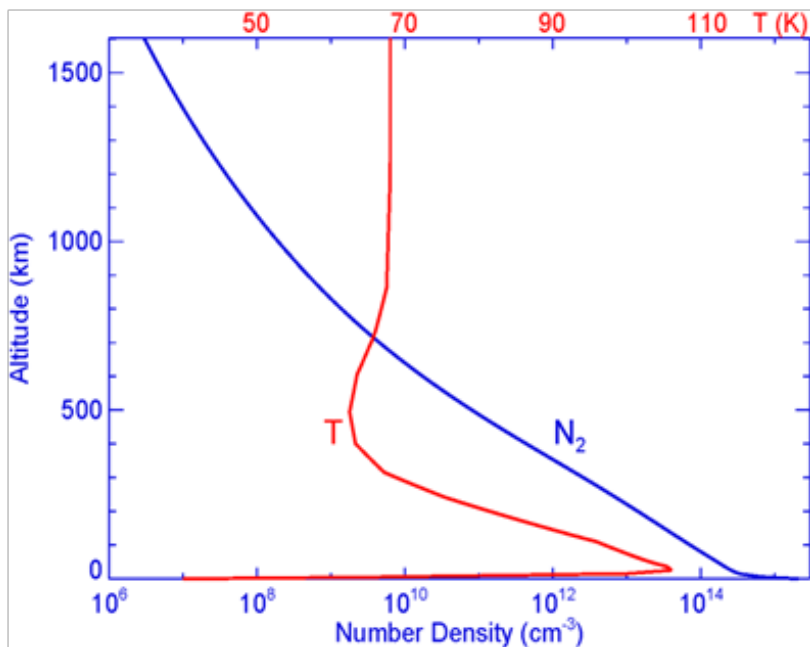


Fig. 1. The observed temperature and calculated N₂ density profiles

Model results

The adopted eddy diffusion $K = 3 \times 10^4 \text{ cm}^2 \text{ s}^{-1}$ facilitates transport and condensation of C₂H₆ on the surface (Fig. 2) and does not require the revision of the laboratory data on the saturated vapor densities. The CH₄ homopause is at 90 km for this K , and the CH₄ profile is mostly controlled by molecular diffusion and agrees with the observations (Fig. 2).

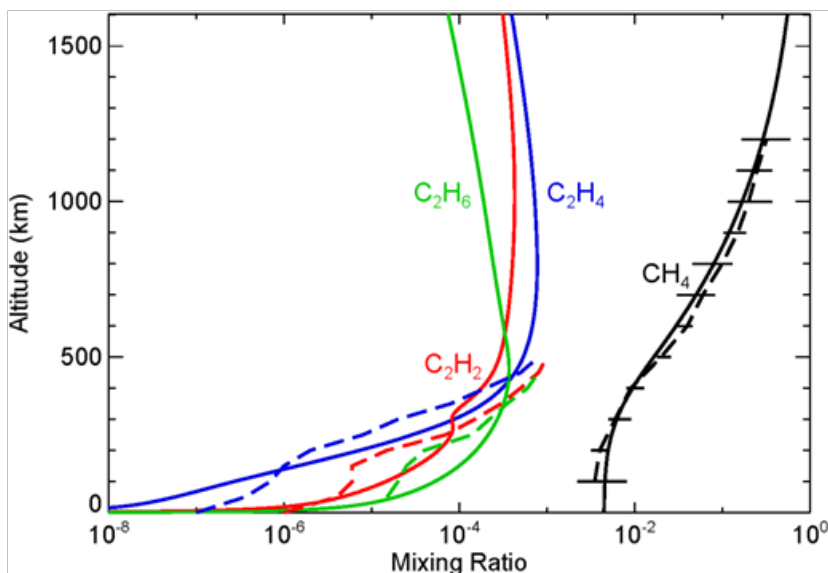


Fig. 2. Observed (dashed curves) and calculated (solid curves) profiles of the main hydrocarbons

Major production and loss processes of the observed species are briefly discussed. Ion chemistry significantly contributes to those. The most abundant C3, C4 hydrocarbons and benzene are shown in Fig. 3a, b. Diacetylene C4H2 is effective in polymerization with C6H and C3N. Sticking coefficients for condensation of hydrocarbons and nitriles are adopted at 0.002 and 0.01, respectively.

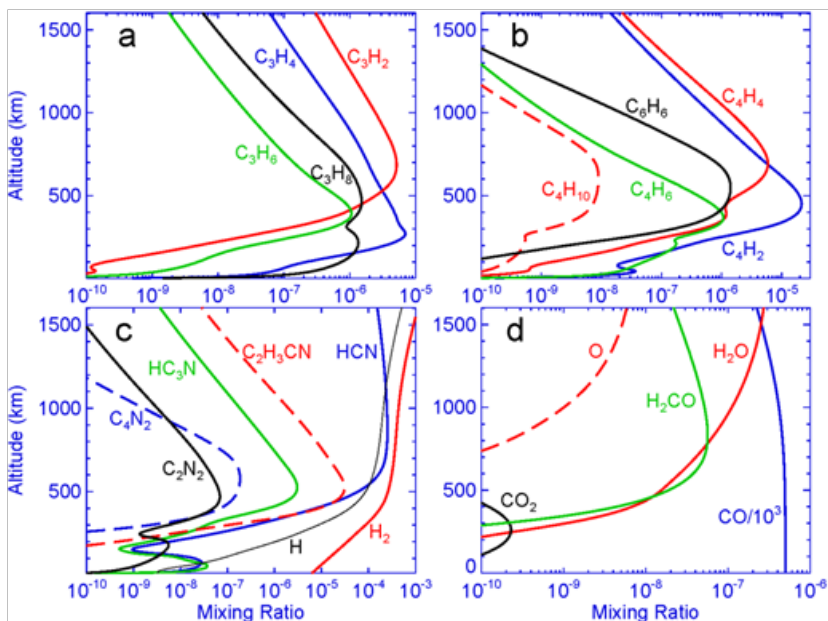


Fig. 3. Vertical profiles of C3 hydrocarbons (a), C4 hydrocarbons and benzene (b), nitriles, H, and H2 (c), and oxygen species (d)

Some nitriles and H2 are depicted in Fig. 3c. The HCN abundance agrees with the ALMA [5] observations. The HC3N warm layer below 150 km constitutes 90% of its column abundance and is weakly sensitive to the adopted sticking and slightly exceeds the observed upper limit.

H and H₂ are formed by photolysis of hydrocarbons. 60% of the production of H escape, and the remaining 40% react with radicals and form H₂. Almost all H₂ escapes. Its mole fraction increases up to 400 km due to diffusive separation. Further increase reflects a balance between the production and escape.

Oxygen chemistry (Fig. 3d) is stimulated by CO and the meteorite H₂O that is very weak, according to the interplanetary dust dynamic model [6].

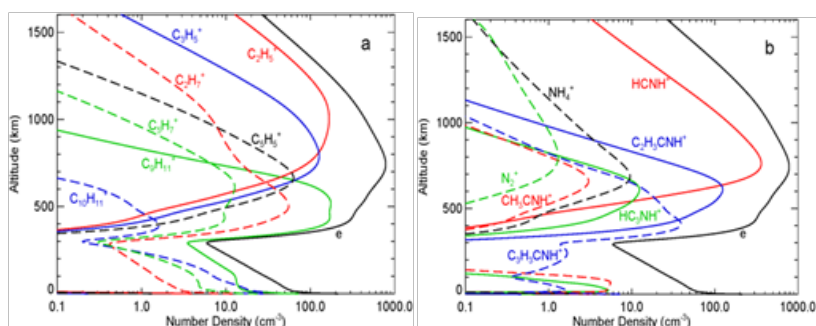


Fig. 4. The most abundant hydrocarbon (a) and nitrogen-bearing (b) ions

Ionosphere is formed by the solar EUV ionization and the galactic cosmic rays that dominate below 300 km (Fig. 4). The ionospheric peak is at 750 and 850 km with $n_{max} = 800$ and 300 cm^{-3} on the day side and near the terminator, respectively. It agrees with the New Horizons upper limit of 1000 cm^{-3} . The heavy ion C₉H₁₁⁺ is the most abundant below 650 km (Fig. 4a). The main ions above 650 km are HCNH⁺, C₂H₅⁺, and C₃H₅⁺. The predicted ion densities are well within the range of the Cassini Ion-Neutral Mass Spectrometer.

Evolution: The calculated annual mean rates are $150 \text{ g cm}^{-2} \text{ Byr}^{-1}$ for escape of CH₄ + CH₃ and H₂ + H, 150 and $50 \text{ g cm}^{-2} \text{ Byr}^{-1}$ for precipitation of hydrocarbons and nitriles, respectively. The surface is young, and the surface mixing is significant.

Pluto and Triton: The great differences (by orders of magnitude) between the atmospheres and ionospheres of Pluto and Triton are caused by the methane abundances. Transition from Triton's conditions observed in the Voyager flyby to Pluto's conditions in the New Horizons flyby is expected near CH₄ $\approx 0.05\%$. Both Triton and Pluto undergo these transitions during their annual cycles.

References

- [1] Gladstone G.R. et al. Science 351, aad8866, 2016
- [2] Hinson D.P. et al. 2017. Icarus 290, P. 96–111,
- [3] Krasnopolsky V.A. 2014. Icarus 236, 83–91,
- [4] Lellouch E. et al. Astron. 2011. Astrophys. 530, L4,
- [5] Lellouch E. et al. Icarus 286, 2017. 289–307,
- [6] Poppe A.R. and Horanyi M. Astron. Astrophys. 2018. 617, L5,
- [7] Wong M.L. et al. Icarus 287, 2017. 110–115,
- [8] Young L.A. et al. Icarus 300, 2018. 174–199,

JOVIAN MOON INTERACTION WITH ENERGETIC ELECTRONS AS MEASURED BY THE JUNO ASC

J.L. Joergensen¹, P.S. Joergensen¹, M. Benn¹, J.M. Merayo¹, M. Herceg¹, T. Denver¹, J.E.P. Connerney^{2,3}, S.J. Bolton⁴, S.M. Levin⁵

¹ Technical University of Denmark (DTU), Lyngby, Denmark

² Space Research Corporation, Annapolis, MD, United States

³ NASA Goddard Space Flight Center, Greenbelt, MD, United States

⁴ Southwest Research Institute, San Antonio, TX, United States

⁵ Jet Propulsion Laboratory (JPL), Pasadena, CA, United States

Keywords:

Jupiter's energetic electrons; Jovian Moon interaction; Magnetosphere; Magnetodisk.

Introduction:

Juno was placed in an elliptical polar orbit about Jupiter on July 4th 2016 to study the formation and structure of the gas giant, its atmosphere and polar magnetosphere. The orbit was chosen to give optimum spatial coverage of the planets potential fields, while avoiding excessive radiation exposure. Juno orbits every 53 days, diving under the main radiation belts at perijapsis and distributing longitudes at closest approach for optimal gravity and magnetic mapping.

The magnetic mapping experiment consist of two vector field magnetometers placed on a boom near the tip of one of the spacecraft's solar arrays, at 10m and 12m, well away from any artificial disturbance fields [1]. Each vector magnetometer is supported by two star tracker units collocated with the magnetic sensors to provide accurate attitude information and eliminate any thermal or mechanical biases. Because of the proximity to the vector magnetometer sensors, and to eliminate any potential magnetic disturbances, the star trackers are equipped with limited radiation shielding. As a consequence, high energy particles can penetrate to the focal array sensor (CCD), leaving an ionization charge which is measured and recorded. The star tracker shielding will stop electrons with an energy less than 20MeV and protons with an energy less than 100 MeV, but particles with higher energy will penetrate. Each passing particle will deposit a local charge, which is recorded, providing a measure of the high energy flux at Juno's position. Using this technique, the Juno high energy particle environment is continuously monitored [2].

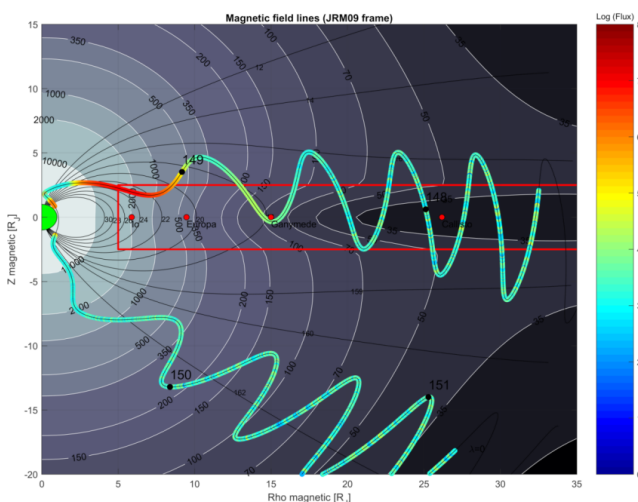


Fig. 1. The Juno orbit of the 20th perijove passage, in magnetic coordinates. The colors, blue to red, show the measured particle flux (mainly >20MeV electrons). Magnetic field lines are shown in black. In this orbit, field lines connecting to the Ganymede orbit, are crossed 5 times inbound (upper wiggle) and once outbound.

The gravity field from the fast rotating, oblate, Jupiter, forces the line of apsides of the elliptic Juno orbit to drift, from its initial position near the equatorial plane, towards an ever more southerly position of the apoaxis. While this motion offers a unique profiling of the Jovian high energy particle environment, it also causes Juno to pass through magnetic field lines that intersect the orbit of Jovian satellites. Most often such crossings appear through field lines leading or lagging the actual moon in longitude, but sometimes the Juno orbit happens to pass through the field lines connecting directly to a moon. In all cases, a profound effect on the measured radiation flux is observed, as a direct consequence of the moon's interaction with the trapped high energy flux.

We present particle signatures from passages of the field lines thus connecting to Callisto, Ganymede, Europa, Io, Amalthea, Metis and the gossamer rings. We also present an interpretation for the highly variable signatures from satellite to satellite and whether the passage is of field lines in front, on, or behind the moon.

References:

- [1] Connerney, J.E.P., Benn, M., Bjarno, et al. 2017. The Juno Magnetic Field Investigation, *Space Sci. Rev.*, doi: 10.1007/s11214-017-0334-z
- [2] Becker, H.N., Alexander, J. W., et al. 2017. The Juno Radiation Monitoring (RM) Investigation, *Space Sci. Rev.*, doi: 10.1007/s11214-017-0345-9

EXPERIMENTAL AND NUMERICAL MODEL FOR FREEZING ICY SATELLITES

E. Nathan¹, M. Berton², T. Girona³, H. Karani⁴, C. Huber¹, J. Head¹, P. Williard⁵

¹ Department of Earth, Environmental and Planetary Sciences, Brown University, Providence, RI 02912, USA, erica_nathan@brown.edu

² College of Engineering, Virginia Commonwealth University

³ Jet Propulsion Laboratory, California Institute of Technology

⁴ Department of Engineering Sciences and Applied Mathematics, Northwestern University

⁵ Department of Chemistry, Brown University

Keywords:

Icy satellites, ice, experimental and laboratory work, numerical model

Introduction:

The icy satellites of the outer solar system are a compelling class of bodies to study for their complicated and diverse geology as well as their astrobiological potential. Many icy satellites have or have had oceans, some of which are likely not to exist in a thermal equilibrium and may be freezing [1–5]. Above these oceans, ice shells are covered by extensional features and fractures [6, 7]. Although there are many processes that contribute to the extensional stresses affecting the evolution and surface features of icy satellites, we focus on the stresses associated with the expansion of water upon freezing [8]. In the present study, we investigate the role of water-ice phase change on surface expressions such as fractures using a combination of analog experiments and numerical simulations.

Physical Model:

We solve the mass and energy conservation equations numerically, tracking the evolution of the ice shell thickness and the pressure in liquid (Eq. 1–2).

$$\frac{\partial T}{\partial t} = \frac{\kappa}{r^2} \frac{\partial}{\partial r} \left(r^2 \frac{\partial T}{\partial r} \right) - \frac{L}{c_w} \frac{\partial f}{\partial t} \quad (\text{Eq. 1})$$

$$\frac{1}{\beta_w} \frac{dp}{dt} = \frac{3}{R(t)} \frac{dR}{dt} \left(\frac{\rho_i}{\rho_w} - 1 \right) \quad (\text{Eq. 2})$$

Here, T is the temperature, t is the time, κ is the thermal diffusivity, r is a radial coordinate, L is the latent heat of solidification, c_w is the specific heat of water, f is the melt fraction, β_w is the bulk modulus, p is the pressure in the water between fracture events, R is the radius of the liquid, ρ_i is the density of the ice, and ρ_w is the density of the water.

Experimental Methods:

Experiments are performed with non-degassed and degassed pure deionized water. Degassing is achieved by boiling the water under reflux for one hour with vigorous stirring and then chilling the water in an ice bath under vacuum for four hours with ultrasound pulsing for thirty minutes. Water is injected in a spherical acrylic mold (7cm or 10cm diameter) (Fig. 1A), which is placed within a freezing chamber that uses vaporized nitrogen to control ambient temperatures from -15°C to -70°C. When the ice shell freezes to a thickness of 5mm, as determined in calibration experiments, the acrylic mold is removed to ensure the mold has limited influence over subsequent fracture formation (Fig. 1B). The sphere continues to freeze and fracture until a critical fracture leads to the failure of the sphere (Fig. 1C–D).

Throughout the experiment, three webcams record video and audio data, four thermocouples monitor freezing chamber temperature, and a Kulite-miniature pressure transducer records the pressure evolution of the liquid within the sphere. Measurements of ice shell thickness are taken upon the conclusion of the experiment (Fig. 1D).

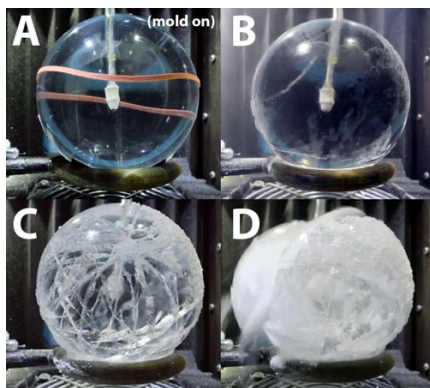


Fig. 1. Snapshots from left camera at different stages of the experiment: A. after filling mold with water, B. after mold removal with a 5 mm thick ice shell, C. during further freezing, D. at the moment of final fracture.

Results:

Experiments with degassed and non-degassed water were conducted for 7 cm and 10 cm spheres at freezing temperatures in the range -20°C to -60°C in 10°C intervals. Additional degassed experiments were conducted at 5°C intervals and experiments for 14 cm spheres are in progress.

Dissolved gas.

Several observations from degassed and non-degassed water experiments:

- 1) Degassed water spheres experience a critical fracture later than non-degassed spheres and have a thicker final ice shell.
- 2) Peak water pressure is higher for degassed than non-degassed experiments. Peak pressure is higher at warmer freezing temperatures.
- 3) The interfracture time is shorter for degassed than non-degassed water spheres and thus more fractures are formed over an experiment for degassed water (Fig. 2).
- 4) For degassed water spheres, a dramatic change in interfracture time is observed before final fracture.
- 5) The estimated ice fracture toughness is similar for degassed and non-degassed experiments.

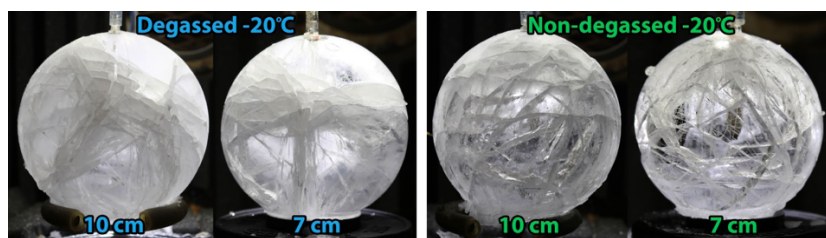


Fig. 2. Comparison of final crack coverage for 10 cm and 7 cm spheres of degassed and non-degassed water.

Sphere size.

When normalized by sphere radius, the final ice shell thickness and time freezing until final fracture are temperature independent for experiments with 7 cm and 10 cm spheres (Fig. 3). The calculated final hoop stress and fracture toughness are also similar for both sphere sizes.

Discussion:

The effects of gas on the compressibility of the water can explain the observed differences in the evolution of freezing spheres of degassed or non-degassed water. Since the ice shell fracture toughness is consistent between both water types, the sudden change in interfracture time for degassed water spheres can be explained by the exsolution of gas into the liquid during the

freezing process, resulting in an abrupt change in compressibility of the liquid phase. This hypothesis is supported by estimation of the time required to reach the abrupt interfracture regime change which compares well to experimental results. Future work will further assess scaling of results between all sphere sizes and investigate the effects of curvature, particularly for understanding the mechanism of the final critical fracture.

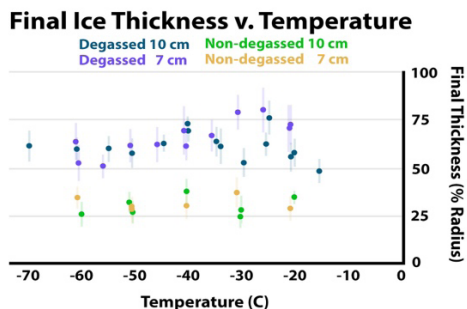


Fig. 3. Final ice shell thickness normalized as a percentage of total sphere radius.

References:

- [1] Head J., N. Sherman, R. Pappalardo, C. Thomas, R. Greeley, and Galileo SSI Team. LPSC XXIX. 1998. 1491 (abstract).
- [2] Head J., R. Pappalardo. *Journal of Geophysical Research*. 1999. V. 104. No. 27. P. 143–27, 155.
- [3] Nimmo F., M. Manga. In: Pappalardo, R., W. McKinnon, K. Khurana (Eds.), *Europa*. Arizona Press Space Science Series. 2009. P. 119–134.
- [4] Schubert G., H. Hussmann, V. Lainey, D. Matson, W. McKinnon, F. Sohl, C. Sotin, G. Tobie, D. Turrini, T. Van Hoolst. *Space Science Reviews*. 2010. V. 153. P. 447–484.
- [5] Johnston S., L. Montési. *Journal of Geophysical Research: Planets*. 2017. V. 122. No. 6. P. 1258–1275.
- [6] Manga M., C. Wang. *Geophysical Research Letters*. 2007. V. 34, No. L07202.
- [7] Kimura J., Y. Yamagishi, K. Kurita. *Earth Planets Space*. 2007. V. 59. No. 2. P. 113–125.
- [8] Wildeman S., S. Sterl, C. Sun, D. Lohse. *Physical Review Letters*. 2017. V. 188. No. 084101.

THE ORIGIN AND EVOLUTION OF TITAN'S NITROGEN ATMOSPHERE

M. Scherf¹, N. Erkaev^{2,3}, S. Thaller⁴, H. Lammer¹

¹ *Space Research Institute, Austrian Academy of Sciences, Austria*(manuel.scherf@oeaw.ac.at);

² *Institute of Computational Modelling SB RAS, Krasnoyarsk, Russian Federation;*

³ *Siberian Federal University, Krasnoyarsk, Russian Federation;*

⁴ *Institute of Physics/IGAM, University of Graz, Austria*

Keywords:

Titan, atmospheric evolution& origin, atmospheric escape, N₂, isotope fractionation.

Introduction:

Titan is the only satellite in the solar system with a significant nitrogen atmosphere. Its origin, however, is yet a matter of debate. Within this presentation we will present simulations of thermal atmospheric nitrogen escape at Titan through time and discuss its implications for the origin and evolution of the atmosphere of Saturn's biggest moon.

Atmosphere structure and thermal escape:

For the simulation of nitrogen loss at Titan we applied a time-dependent 1-D hydrodynamic upper atmosphere model that solves the system of the fluid equations for mass, momentum, and energy conservation (see [1]). An important input into this model is the evolution of the solar EUV-flux over time which is strongly depending on the rotational evolution of the Sun [2]. The simulated total thermal escape of nitrogen from Titan therefore strongly varies in dependence of the initial rotation rate of the Sun, i.e. from ~0.3 (slow rotator) to ~1.1 (moderate) and up to ~11 times the present-day atmospheric mass for a fast rotator. The main fraction of the thermal escape takes place early in the solar system at a time when the EUV flux of the young Sun was significantly higher than at present-day. Other escape processes such as sputtering or photochemical loss of nitrogen are less important during this early phase.

The origin and evolution of the atmosphere:

An insight into the origin and evolution of Titan's nitrogen atmosphere can be gained by the isotopic fractionation of 14N/15N which can be significantly modified by atmospheric loss, since escape preferentially removes the lighter isotope from the atmosphere. Cassini measured Titan's present-day atmospheric 14N/15N ratio to be at about 168 [3] which is in the range of cometary ammonia [4, 5]. This might suggest NH₃ to be a potential source of Titan's nitrogen. If escape, however, modified the 14N/15N ratio over time, the origin of its atmospheric N₂ might be a different one such as the solar nebula, chondrites or refractory organics.

Our simulations show that atmospheric escape does not alter 14N/15N significantly over time. Taking into account fractionation by thermal escape, sputtering and photochemistry, the original fractionation in Titan's atmosphere could not have been higher than ~165 for a slow, ~171 for a moderate and ~194 for a fast rotating Sun, indicating that the origin of Titan's atmosphere might have been indeed protosolar ammonia which is in agreement with a recent study by Mandt et al. [6]. Moreover, if Titan's atmosphere originated endogenically through decomposition of NH₃ and subsequent outgassing as N₂ [7], then our study further suggests that either for a moderate to fast rotating young Sun Titan's atmosphere could not have originated before ~4.3 billion years ago or the Sun was a slow to moderate rotating young G-type star.

References:

- [1] Erkaev N.V., Lammer H., Odert P., Kulikov Yu.N., Kislyakova K.G. Extreme hydrodynamic atmospheric loss near the critical thermal escape regime // *Mont. Notes Roy. Astron. Soc.* 2015. V. 448. 1916.

- [2] Tu L., Johnstone C.P., Güdel M., Lammer H. The extreme ultraviolet and X-ray Sun in Time: High-energy evolutionary tracks of a solar-like star // *Astron. Astrophys.* 2015.V. 577. L3.
- [3] Niemann H.B., Atreya S. K., Demick J.E.,Gautier D., Haberman J.A., Harpold D.N., Kasprzak W.T., Lunin J.I., Owen T.C., Raulin F.Composition of Titan’s lower atmosphere and simple surface volatiles as measured by the Cassini-Huygens probe gas chromatograph mass spectrometer experiment // *Nature.*2010. V. 115. E12006.
- [4] Rousselot P., Pirali O., Jehin E., Vervloet M., Hutsemékers D., Manfroid J., Cordier D., Martin-Drumel M.A., Gruet S., Arpigny C., Decock, A., Mousis, O.Toward a unique nitrogenisotopic ratio in cometaryices // *Astrophys. J. Lett.* 2014. V. 780. 2–6.
- [5] Shinnaka Y., Kawakita H., Kobayashi H., Nagashima M., Boice D.C.14NH₂/15NH₂ ratio in comet C//2012 S1 (ISON) observed during its outburst in 2013 November // *Astrophys. J.* 2014. V. 782 .L16.
- [6] Mandt K.E., Mousis O., Lunine J.I., Gautier D. Protosolar ammonia as the unique source of Titan’s nitrogen // *Astrophys. J. Lett.* 2014. V. 788. L24.
- [7] Glein C.R. Noble gases, nitrogen, and methane from the deep interior to the atmosphere of Titan // *Icarus.* 2015. V. 250.570–586.

DIAGNOSTICS OF THE JOVIAN MAGNETOSPHERE STATE DURING THE JUNO MISSION

I.I. Alexeev, E.S. Belenkaya, A.S. Lavrukhin, I.A. Pensionerov

Federal State Budget Educational Institution of Higher Education
M.V. Lomonosov, Skobeltsyn Institute of Nuclear Physics (SINP MSU),
Moscow State University, Moscow, Russian, iialexeev@mail.ru

Keywords:

Magnetosphere, Jupiter, equatorial current disk, global magnetospheric current systems, magnetic field, disk parameters.

Introduction:

In the Earth's magnetosphere the contribution of the ring current generated by the magnetospheric plasma is essential only during a magnetic storm, while in a quiet time this contribution is less or of the order of the other magnetospheric current systems field (see [1]). In the case of Jupiter the magnetospheric magnetic field is mainly determined by the equatorial current disk (see [2]), formed by the magnetospheric plasma obtained after ionization of volcanic eruptions of the Io. In the inner magnetosphere ($<20 R_J$), the dipole field prevails, however, the contribution of the disk magnetic field (about -100 nT) is almost 100 times greater than the contribution of the other global magnetospheric current systems (see, [3, 4]). In the outer magnetosphere, the disk field is 2.5–3 times higher than the dipole field of Jupiter [3] and is of the same order of the magnetopause currents field, which is approximately equal to 1.44 multiplied by the disk field. Therefore, the dynamics of the external magnetosphere, in particular the magnetic flux in the tail lobes of the magnetosphere of Jupiter, is determined by the disk parameters.

Magnetospheric dynamics:

The dimensions of the magnetosphere and the projection of its equatorial plane onto ionospheric heights are mainly determined by the dynamics of the equatorial current disk. For this reason, many models of the Jupiter's magnetosphere are limited to considering only the internal field and the disk field ([4] and references therein). These models are sufficient for determination of the field on the surface of Jupiter and for calculation of the position of auroral spots from the Galilean satellites of Jupiter. If we confine ourselves to the Ganymede orbit and not interested in the area inside the main polar oval, we can ignore the other global magnetospheric current systems [5], but to understand the global magnetospheric dynamics and to forecast the polar cap aurora dynamics we should take into account the model of the outer magnetospheric current systems.

Based on the parameters of the equatorial disk obtained in [4] during the first 9 revolutions of Juno, we find the characteristic dimension of the magnetosphere (the distance to the subsolar point), the magnetic field in the tail lobes, and magnetic flux in the open field lines bundle. The dynamics of the outer magnetosphere is compared with the dynamics of the aurora observed during the flight of Juno in Jupiter's magnetosphere.

References:

- [1] I.I. Alexeev, E. S. Belenkaya, S. Y. Bobrovnikov, and V. V. Kalegaev. Modeling of the electromagnetic field in the interplanetary space and in the earth's magnetosphere. *Space Science Reviews*, 107(1/2):7–26, 2003. DOI: 10.1023/A:1025542915800
- [2] Alexeev, I.I. and Belenkaya, E.S.: Modeling of the Jovian Magnetosphere // *Ann. Geophys.*, 23, 809–826, <https://doi.org/10.5194/angeo-23-809-2005>, 2005
- [3] Pensionerov, I.A., Alexeev, I.I., Belenkaya, E.S., Connerney, J. E. P., Cowley, S. W. H. (2019). Model of Jupiter's current sheet with a piecewise current density. // *Journal of Geophysical Research: Space Physics*, 124. 2019. <https://doi.org/10.1029/2018JA026321>
- [4] I.A. Pensionerov, E.S. Belenkaya, Stanley W.H. Cowley, I.I. Alexeev, V.V. Kalegaev, and David A. Parunakian, Magnetodisc modelling in Jupiter's magnetosphere

using Juno magnetic field data and the paraboloid magnetic field model // *Ann. Geophys.*, 37, 101–109, <https://doi.org/10.5194/angeo-37-101-2019>, 2019

- [5] Hess, S.L.G., B. Bonfond, P. Zarka, and D. Grodent. 2011. Model of the Jovian magnetic field topology constrained by the Io auroral emissions // *J. Geophys. Res.*, 116, A05217, doi:10.1029/2010JA016262.

THE RESONANT SEMI-ANALYTICAL MOTION THEORY FOR GIANT PLANETS OF THE SOLAR SYSTEM

A.S. Perminov¹, E.D. Kuznetsov²

¹ Ural Federal University, 620000, Yekaterinburg, 51 Lenin Avenue, perminov12@yandex.ru;

² Ural Federal University, 620000, Yekaterinburg, 51 Lenin Avenue, eduard.kuznetsov@urfu.ru

Keywords:

Resonant semi-analytical motion theory, Hori–Deprit method, the second system of Poincare elements, giantplanets of the Solar system.

The investigation of the dynamical evolution of planetary systems is one of the important problems of celestial mechanics. The most vital feature of any planetary system, including our Solar system, is its stability. From the time of Laplace and Lagrange to modern researchers it has been shown that the Solar system is stable over cosmogonic time scales. But the question about the stability of arbitrary planetary systems remains open. Any researches of the dynamical evolution of planetary systems over so long-time intervals require the using of averaged methods. The essence of any averaged method is the elimination from the Hamiltonian of the planetary system all terms corresponding to short-periodic perturbations in planet-planet interactions. Consequently, it becomes possible to increase the time step of the integration and sufficiently reduce whole integration time.

After the averaging process, denominators, which are represented by linear combinations of mean longitudes of the planets, appear in the terms of the averaged Hamiltonian of the second order and higher. If the planetary system is close to a resonance of mean motions of the planets, some denominators can become small quantities, which lead to the extreme growth of corresponding terms. Thus classical averaging methods are not applicable to the resonant or near-resonant planetary systems. In this case for the investigation of the dynamical evolution of resonant planetary systems, it is necessary to introduce a new resonant variable, which is slowly changing in the vicinity of the resonance [1]. Usually, it is the linear combination corresponding to the mean motion resonance.

The resonances of mean motions of the planets play an important role in dynamical evolution both the Solar system and extrasolar planetary systems. There are two well-known examples. The first is “the great inequality” – the closeness of mean motions of Jupiter and Saturn to resonance 2:5. The second is mean motion resonance 2:3 of Neptune and Pluto, which prevents both planets from colliding. Moreover, some planets in extrasolar systems are, also, in mean motion resonance. The long term dynamical evolution of such resonant planetary systems requires study.

In this work, the resonant averaged semi-analytical motion theory is constructed up to the second order of planetary masses. The Hamiltonian of the planetary problem is written in Jacobi coordinates and it is expanded into the Poisson series in the small parameter and elements of the second system of Poincare. The ratio of the sum of planetary masses to the mass of the star plays the role of the small parameter. The way to introduce additional resonant variable and its canonically conjugated one is shown. After that, the averaging process of the Hamiltonian is performed by Hori–Deprit method [2]. The equations of motion are constructed up to the second degree of the small parameter and the fifth degree of eccentric and oblique Poincare elements. The transformations between osculating and averaged elements are provided by the functions for the change of variables. All analytical transformations with series are performed by using of computer algebra system Piranha [3], which is echeloned Poisson series processor.

This work is a direct continuation of previous research of authors [4] for the non-resonant case of the planetary problem. The resonant variable is introduced as the linear combination of mean motions of Jupiter and Saturn, corresponding to resonance 2:5. Then the constructed equations of motion for giant-planets of the Solar system are integrated over time interval 10 billion years.

In the future, this resonant theory can be applied to the investigation of extra-solar planetary systems.

References:

- [1] Ferraz-Mello S. On Hamiltonian averaging theories and resonance // CM&DA. 1996. V. 66. No. 1. P. 39–50.
- [2] Kholshchikov K.V. Asimptoticheskiy metod dynebesnoimekhaniki (Asymptotic methods for celestial mechanics). Leningrad: Leningrad. Univ, 1985. 208 p.
- [3] Biscani F. The Piranha computer algebra system. <https://www.github.com/bluescarni/piranha>. 2018.
- [4] Perminov A.S., Kuznetsov E.D. Orbital evolution of the Sun – Jupiter – Saturn – Uranus – Neptune four planet system on long-time scales // Sol. Syst. Res. 2018. V. 52. No. 3. P. 241–259.

ROTATION OF GIANT PLANETS

V.A. Kotov

*Crimean Astrophysical Observatory, Nauchny, Crimea 298409, Russia,
vkotov@craocrimea.ru*

Spin periods of Jupiter, Saturn, Uranus and Neptune are specified by the analysis of the resonant motion of their large satellites: 0.445(2), 0.448(1), 0.673(9) and 0.561(7) days, respectively. They are near-commensurate with the period $P_0 \approx 0.111$ days of the cosmic oscillation, discovered first in the Sun, then in other variable objects of the Universe. The like analysis of spin rates of the total set of the largest and fastest rotators of the Solar system (planets, asteroids, satellites) resulted in the best commensurable, or «synchronizing», timescale of 0.111 days, coinciding well with P_0 too (a probability the two timescales could agree by chance, is less than 10^{-5}). True origin of this odd resonance of our planetary system is unknown, but it is supposed the phenomenon reflects the P_0 oscillations of gravity operating within the Solar system.

SCIENCE OBJECTIVES AND MISSION SCENARIOS FOR FUTURE MISSIONS TO THE JUPITER SYSTEM

M. Blanc^{1,4}, N. André⁴, X. Wang¹, L. Li¹, M. Li¹, C. Wang¹, Y. Wang¹, O. Mousis², D. Hestroffer³, O. Prieto-Ballesteros⁵

¹ NSSC, China

² LAM, France

³ IMCCE, France

⁴ IRAP, France

⁵ INTA-CAB, Spain

Keywords:

Space missions; giant planets; origin of planets; origin of life; planetary systems

Jupiter is the dominant planet in the Solar System: gathering just by itself 76% of the total mass of planets and small bodies, it nearly forms a “binary system” with the Sun. To properly answer our key scientific questions about the Solar System as a whole, and even more generally about Planetary Systems (how do they form, how do they evolve and give birth to the diversity of their objects and of their architectures, how do they work, do they harbor habitable worlds and can we find life there), one must apply these questions to the Jupiter System and find answers there using the power of in situ planetary exploration. Three of these key questions should be addressed in priority beyond the horizon of the missions currently in operation (Juno) or in preparation (JUICE, Europa Clipper):

A-How did the Jupiter System form? One can read answers to this question by studying the objects that have been left basically unaltered since this formation occurred, about four billion years ago: Callisto, the outermost of the Galilean satellites, seems to have been only partly differentiated; its bulk composition, interior and surface terrains still bears the records of its early eons and can tell us the story of the formation of the Galilean satellites; the 77 or so irregular satellites which are wandering, mostly on retrograde orbits, far out of the region occupied by the Galilean satellites, are likely unique and precious remnants of the populations of planetesimals which orbited the outer Solar System, beyond the ice line, at the time of the formation of Jupiter.

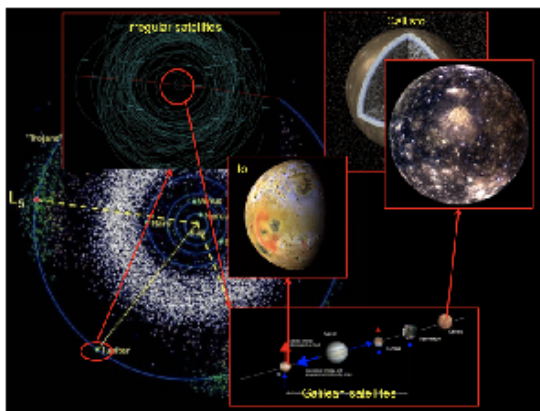


Fig. 1. This synthetic picture of the Jupiter System shows that it has to be studied at different spatial scales, from the large scale (whole solar system) at which one can encompass the Trojan Asteroids orbiting the L4 and L5 Lagrangian points of the Sun-Jupiter system, through the intermediate scale of the irregular satellites, to the Galilean satellites and finally to Jupiter itself. Among the Galilean moons, Io must focus our attention to better understand how the Jupiter System globally works; Callisto, on the other hand, has likely best preserved the memories of the times of the formation of the Jupiter system, and should be the priority of a mission to unravel the mysteries of its Origins.

B-How does it work? One can best address this question by studying and understanding the great chain of energy transfer operating today in the Jupiter System: how is gravitational energy from Jupiter transferred to Io's interior via tidal heat dissipation to feed its unique volcanic activity? How does this activity in turn store energy into the Io plasma torus to drive the whole magnetosphere into motion? How does the interplay between the Io torus and the solar wind finally dump energy into heating of Jupiter's upper atmosphere, or release it into the tail and interplanetary space?

China is currently designing an exploration mission that will fly to Jupiter in the 2030's. This mission will capitalize on the legacy of previous missions to Jupiter and to develop unique international collaborations with other missions in flight (NASA's Juno mission) or in preparation (ESA's JUICE and NASA's Europa Clipper).

The exciting science goals of this mission, which we will call Gan De, can be reached thanks to a dual-platform architecture combined with an innovative design of its instrument suite based on four standard instrument packages to be used as elementary bricks for the science operations of its different flight elements.

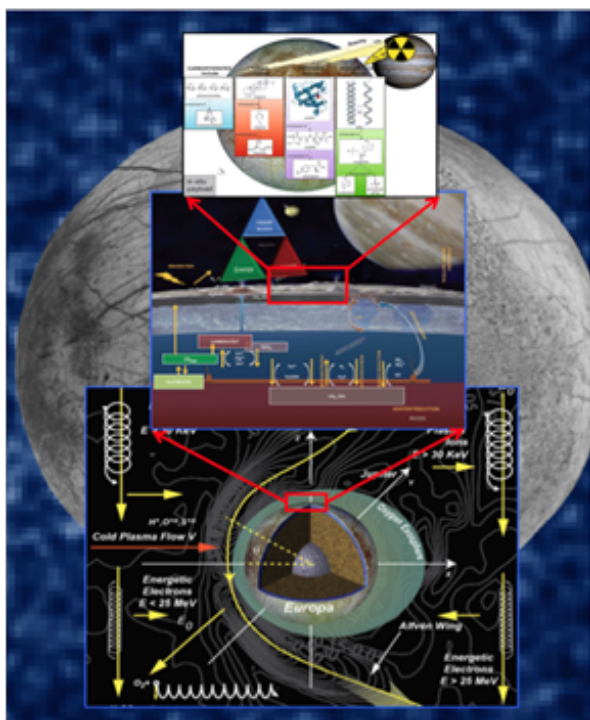


Fig. 2. This logical chart of the proposed JEM Science Plan shows the three successive scales investigated by JEM, from bottom upwards: (1) the global Europa, a complex system responding to the two main types of Jovian forcing, tidal forcing and magnetospheric forcing; (2) the scale of Europa's potential biosphere (median figure), at which we will more particularly characterize the ocean and ice sheet and (3) finally the local scale at which we will perform life detection experiments.

C- Does the Jupiter system bear life? Here the main target for our investigations is Europa, whose habitability will be studied by NASA's Europa Clipper mission. Europa, together with Enceladus, is the best possible destination to search for and possibly find life in the outer solar system. Strong indications that Europa may indeed be inhabited come from recent key discoveries: the Galileo discovery of a sub-surface ocean in contact with a silicate floor that could be a source of the key chemical species for biomolecules, the many indications that the icy crust is active and may be partly permeable to the transfer of materials, including elementary forms of life, and the identification

of candidate thermal and chemical energy sources necessary to drive a metabolic activity. To understand how the Europa system works and whether it may have developed a biosphere under the effect of its proper evolution and of forcing by the other components of the Jupiter System we need to design and fly to this Ocean World a multi-scale, multi-platform, interdisciplinary mission that will perform combined orbiter and lander science investigations. We will summarize the science and technology strategy of this proposed Joint Europa Mission (JEM), based on the combination of an astrobiology lander concept and of an orbital platform which will carry and deliver the lander to its destination, relay its data back to Earth and will finally perform science operations on a European orbit for about three months. While the orbiter will perform an in-depth investigation of Europa's geophysics, ocean and habitability, investigations by the Europa lander will be focused on the search for bio-signatures in solid and liquid samples.

We will emphasize the key role that international cooperation between the major space-faring nations should play in implementing this ambitious program.

THE INTERNATIONAL PHOBOS/DEIMOS DATA WORKING GROUP

T.C. Duxbury¹, PDDWG Advisory Committee²

¹ Physics and Astronomy Department, George Mason University, Fairfax, Virginia, USA;

² International Group from ESA, JAXA, NASA and Roscosmos

Keywords:

Phobos, Deimos, Derived Data, Space Agencies

Introduction:

The International Phobos/Deimos Data Working Group (PDDWG) was created by European Space Agency (ESA), Japanese Aerospace Exploration Agency (JAXA), National Aeronautics and Space Administration (NASA) and Russian Space Agency (Roscosmos) personnel and scientists to: 1) derive higher level datasets to support sample site selection, and proximity and sample collection operation for the JAXA Martian Moon Exploration (MMX) mission and evolving ESA, NASA and Roscosmos Phobos/Deimos missions; 2) encourage existing Mars missions to continue or implement new observations to support 1); 3) develop searchable data catalogs covering MEX, Viking, Phobos 88, etc. archives to allow the international science community to identify datasets for their use in deriving datasets for 1); develop PDS4-compliant catalog and derived data standards / recommendations to insure international operability with evolving GIS tools; and 5) keep the science community and public informed and involved.



Fig. 1. Phobos surface coverage of 3 ODYSSEY THEMIS IR observation sequences

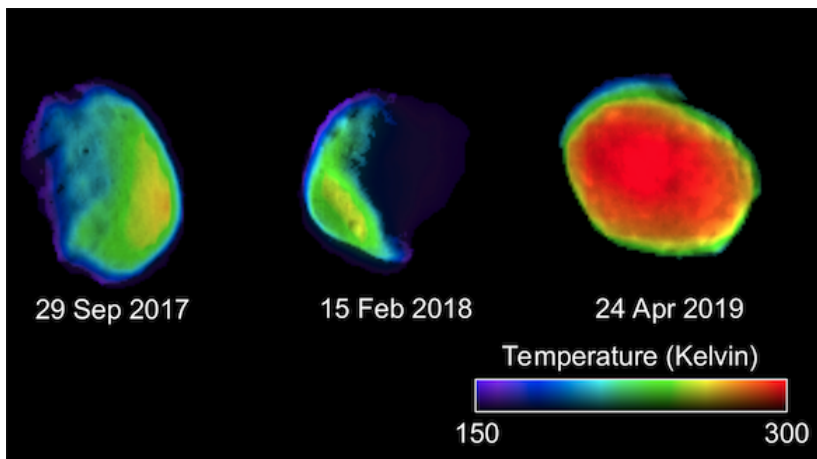


Fig. 2. Phobos surface temperatures from the 3 ODY THEMIS IR sequences

An international Advisory Committee and Charter have been created. ESA MEX and NASA ODY have agreed to continue / make new and unique observations of the Martian moons. Draft PDS4-compliant catalog and derived data standards have been completed and the initial validation with the PDS started. Draft catalog and derived data have been produced for evaluation and validation. The PDDWG is working through NASA Planetary Science Division Small Bodies Advisory Group and presenting at international conferences to involve the science community and public. Initial efforts are concentrating on completing the validation of PDS4 compliant catalog and derived data standards and produce archival catalog and derived registered and map projected datasets from many thousands of MEX HRSC/SRC/OMEGA, Viking Orbiter Imaging, Phobos 88 Imaging, new THEMIS IR and VIS Imaging [1], etc., datasets for international archive and distribution.

References:

- [1] J. L. Bandfield, et. al., Mars Odyssey THEMIS observations of Phobos: new spectral and thermophysical measurements. 49th Lunar and Planetary Science Conference, 2018 (LPI Contrib. No. 2083).

MIGRATION OF PLANETESIMALS FROM DIFFERENT DISTANCES OUTSIDE MARS' ORBIT TO THE TERRESTRIAL PLANETS AND THE MOON

M.Ya. Marov, S.I. Ipatov

Vernadsky Institute of Geochemistry and Analytical Chemistry of Russian Academy of Sciences, Moscow, Russia, marovmail@yandex.ru, siipatov@hotmail.com

Keywords:

Planetesimals, migration, ocean water, terrestrial planets, the Moon

Introduction:

Earth's ocean water and its D/H ratio could be the result of mixing water from several exogenous and endogenous sources with high and low D/H ratios. Endogenous water sources could include direct hydrogen adsorption from nebular gas to magma melts followed by H_2 reaction with FeO, which could increase the D/H ratio in the Earth's oceans by 2–9 times and water accumulation by particles of the protoplanetary disk before the start of gas dissipation in the inner part of the early Solar System. The exogenous sources included the migration of bodies from the outer part of the main asteroid belt and the migration of planetesimals from beyond the orbit of Jupiter. In a number of papers, the outer asteroid belt was considered as the main source of water on the Earth. Earlier, we studied the migration of bodies with initial orbits close to the orbits of known Jupiter family comets (e.g., [1–3]), and the migration of planetesimals with initial values of semi-major axes of their orbits from 4.5 to 12 AU [4]. Below we consider the migration of planetesimals from different (from 2.5 to 40 AU) distances from the Sun and the probability of collisions of such planetesimals with the terrestrial planets and the Moon. In addition to our previous studies [5] of migration of bodies from different distances from the Sun to the terrestrial planets and the Moon, below we consider a greater number of calculations. For example, besides initial eccentricities e_0 of planetesimals equaled to 0.3, we also consider $e_0=0.05$.

The model and initial data used for calculations:

For our calculations of the migration of planetesimals from different distances from the Sun to the terrestrial planets and the Moon, we used the symplectic code from the Swift integration package [6]. The gravitational influence of 7 planets (from Venus to Neptune) or of 5 planets (from Venus to Saturn) was taken into account. Initial semi-major axes a_0 of planetesimals varied from a_{\min} to a_{\max} with a number of initial planetesimals with a_0 proportional to $a_0^{1/2}$. In our calculations $a_{\max}=a_{\min}+2.5$ AU and a_{\min} varied with a step of 2.5 AU from 2.5 to 40 AU. Initial eccentricities e_0 of planetesimals equaled to 0.05 or 0.3. Initial inclinations i_0 equaled to $e_0/2$ rad. The mean eccentricities equaled to 0.3 could be reached due to mutual gravitational influence of planetesimals during evolution of a disk of planetesimals in the feeding zone of the giant planets [7]. Integration was done until planetesimals reached 2000 AU from the Sun or collided with the Sun. Nevertheless, some calculations with a large value of a_{\min} were stopped after several tens or hundreds of millions of years, if the probabilities of collisions of planetesimals with the Earth had not changed for some long time, and a small number of planetesimals was left in the disk. Each calculation was made for 250 initial planetesimals with different orientations of their initial orbits. Several runs were made for the same a_{\min} . The orbital elements of migrated planetesimals were recorded in computer memory with a step of 500 years. Based on these arrays of the orbital elements, similar to the calculations presented in [1–4], we calculated the probabilities of collisions of planetesimals with the terrestrial planets, the Moon, and their embryos.

Delivery of water to the terrestrial planets from beyond the Jupiter's orbit:

In our calculations [4] with $a_{\min}=4.5$ AU and $a_{\max}=12$ AU the probability p_E of a collision of a planetsimal during its dynamic lifetime with the Earth was about 2×10^{-6} . For recent calculations, the values of p_E at $n_{pl}=7$ are presented in Table 1

for $e_o=0.05$ and $e_o=0.3$ at several values of a_{min} (p_E is the average value for several calculations, each with 250 planetesimals). Due to several planetesimals with much higher probabilities p_E than for other planetesimals, two values of p_E ($p_E=3.8 \times 10^{-4}$ at $a_{min}=7.5$ AU and $e_o=0.3$, and $p_E=3 \times 10^{-5}$ at $a_{min}=10$ AU and $e_o=0.05$) in Table 1 are much greater than other values of p_E with $5 \leq a_{min} \leq 10$ AU. For $a_{min} \leq 10$ AU the values of p_E in Table 1 were not less than 2×10^{-6} . When considering thousands of planetesimals with $5 \leq a_{min} \leq 10$ AU the average value of p_E may be greater than 2×10^{-6} at least by a factor of several. This means that if most of the total mass of planetesimals in the feeding zone of Jupiter and Saturn was in a large number of relatively small planetesimals, then, for large embryos of Uranus and Neptune, the values of p_E could be greater than 10^{-5} . On average, for the distance from the Sun between 20 and 40 AU, p_E can be about 10^{-6} . This area could also play an important role in the migration of ice bodies to the Earth. For $n_{pl}=5$ and $e_o=0.3$, a a_{min} equal to 5, 7.5 and 10 AU, the average (for 750 planetesimals) value of p_E was close to 2×10^{-6} , 2×10^{-6} and 1.2×10^{-6} , respectively. For $n_{pl}=5$, the value of p_E (calculated for 750 planetesimals at each value of a_{min}) was smaller than that for $n_{pl}=7$, but for different runs with 250 planetesimals p_E could also vary by more than a factor of 10.

Table 1. Probabilities p_E of a collision of one planetesimal during its dynamical lifetime with the Earth at $n_{pl}=7$ (p_E is the mean value for several calculations, each of which was with 250 planetesimals).

a_{min} , AU	2.5	5.	7.5	10
$e_o=0.3$	$5 \cdot 10^{-5}$	$4 \cdot 10^{-6}$	$3.8 \cdot 10^{-4}$	$2 \cdot 10^{-6}$
$e_o=0.05$	$2 \cdot 10^{-2}$	$6 \cdot 10^{-6}$	$2 \cdot 10^{-6}$	$3 \cdot 10^{-5}$
a_{min} , AU	15	20	30	40
$e_o=0.3$	$1 \cdot 10^{-6}$	$6 \cdot 10^{-7}$	$6 \cdot 10^{-7}$	$1 \cdot 10^{-6}$
$e_o=0.05$	$1 \cdot 10^{-6}$	$2 \cdot 10^{-6}$	$6 \cdot 10^{-7}$	$8 \cdot 10^{-7}$

The ratio of probabilities of collisions with the Earth and the Moon of planetesimals migrated from beyond the Jupiter's orbit estimated to be about 16–17. The mass of water in the planetesimals migrated from beyond the orbit of Jupiter collided with the Moon could be not more than 20 times smaller than that for the Earth. Due to a smaller mass of the Moon, the fraction of the material evaporated and ejected from the Moon at collisions of planetesimals with the Moon was greater than that at collisions with the Earth.

For Mars, the ratio of the mass of water in planetesimals delivered from beyond the orbit of Jupiter to a planet to the mass of the planet was approximately two to three times greater than that for the Earth. In absolute values, the mass of water delivered to Mars was 3 to 5 times smaller than the mass of water delivered to the Earth [4]. The mass of water delivered to Mercury or Venus, calculated per unit mass of the planet, was a little greater than that for the Earth. These mass fractions would result in relatively large ancient oceans on Mars and Venus [8].

Most of the planetesimals from the Jupiter's feeding zone were ejected into hyperbolic orbits in a few Myr. Most of collisions with the Earth of bodies initially located in the zone at 5–30 AU from the Sun took place in less than 20 Myr. This testifies in favor of that the planetesimals from beyond the Jupiter's orbit could fall onto the Earth and the Moon in the process of their growth, and the matter, including water and volatiles, delivered from beyond the orbit of Jupiter was incorporated into the internal layers of the Earth and the Moon. The delivery of matter to the Earth and the Moon from the zone of Uranus and Neptune depended on when these giant planets acquired large masses and began to move in orbits close to their present orbits. After the formation of the giant planets, the typical time until the collisions of the planetesimals with the Earth and the Moon often did not exceed 20 Myr, but a small fraction of the planetesimals could fall onto the Earth during hundreds of Myr.

Conclusions:

The amount of material delivered from beyond the Jupiter's orbit to the Earth could exceed the mass of Earth's oceans. Some fraction (may be 1/3) of this material was composed of water and volatiles. The total mass of planetsimals migrated from beyond the Jupiter's orbit and collided with the Moon was by a factor of 16 or 17 smaller than that for the Earth. The mass of the material delivered to a planet to the mass of the planet for Mars was about two times greater than that for the Earth, and such ratios for Mercury and Venus were a little greater than that for the Earth. Some material from beyond the Jupiter's orbit was delivered to the forming Earth.

Acknowledgements

The work was supported by the grant of Russian Science Foundation № 17-17-01279 (migration to the Moon) and by the Program of Fundamental Studies of the Presidium of RAS № 16 (migration to the terrestrial planets).

References:

- [1] Ipatov S.I., Mather J.C. Migration of Jupiter-family comets and resonant asteroids to near-Earth space // *Annals of the New York Academy of Sciences*. 2004. V. 1017. P. 46–65. <http://arXiv.org/format/astro-ph/0308448>.
- [2] Ipatov S.I., Mather J.C. Comet and asteroid hazard to the terrestrial planets // *Advances in Space Research*. 2004. V. 33. N 9. P. 1524-1533. <http://arXiv.org/format/astro-ph/0212177>.
- [3] Ipatov S.I., Mather J.C. Migration of comets to the terrestrial planets // *Proc. of the IAU Symposium No. 236 "Near-Earth Objects, Our Celestial Neighbors: Opportunity and Risk" (14-18 August 2006, Prague, Czech Republic)*, ed. by A. Milani, G.B. Valsecchi, & D. Vokrouhlický, Cambridge Univ. Press, Cambridge. 2007. P. 55-64. <http://arXiv.org/format/astro-ph/0609721>.
- [4] Marov M.Ya., Ipatov S.I. Delivery of water and volatiles to the terrestrial planets and the Moon // *Solar System Research*. 2018. V. 52.P. 392-400.
- [5] Ipatov S.I. Migration of bodies to the Earth and the Moon from different distances from the Sun // *The Ninth Moscow Solar System Symposium 9M-S3*, <https://ms2018.cosmos.ru/>, 2018. #9MS3-SB-11. P. 104-106.
- [6] Levison H.F., Duncan M.J. The long-term dynamical behavior of short-period comets // *Icarus*. 1994. V. 108.P. 18-36.
- [7] Ipatov S.I. Migration of bodies in the accretion of planets // *Solar System Research*. 1993.V. 27. P. 65–79.
- [8] Marov M.Ya., Grinspoon D.H. *The planet Venus*, New Haven: Yale University Press, 1998. 442 p.

SIMULATIONS OF FRAGMENTATION OF DUST AGGREGATES AT THE SNOWLINE IN A PROTOPLANETARY DISK: FIRST RESULTS

M.Ya. Marov¹, A.V. Rusol¹, A.B. Makalkin²

¹ Vernadsky Institute of Geochemistry and Analytical Chemistry RAS, Kosygin St. 19, 119991 Moscow,

² Schmidt Institute of Physics of the Earth RAS, B. Gruzinskaya St. 10-1, 123242 Moscow, Russia

Keywords:

protoplanetary disk, planetesimal formation, dust aggregate, fragmentation, snowline, fractal aggregate

Introduction:

Fragmentation of dust aggregates in the protoplanetary disk through evaporation of ice is important to define position of the planetesimals formation on the snowline. The process involves the ratio of sizes and/or densities of aggregates before and after evaporation of ice and allows us to determine whether they would accumulate near by the snowline or move to smaller radial distances of inner planets formation [1, 2].

The effect of icy dust aggregates structure near the snowline was evaluated in the earlier studies [3] but how the structure of icy aggregate affects the parameters of fragments and planetesimals formation was not clarified. The problem is addressed in this study.

The structure, composition, size, and density of ice containing dust aggregates was constrained using the cometary nucleus data available including those of 67P/Churyumov-Gerasimenko comet revealed by the Rosetta mission [4], as well from several Kuiper Belt objects (see [5] and references therein). In particular, a high refractory-to-ice mass ratio inside the nucleus ($\delta > 3$) was derived [5]. The cometary nucleus is composed of fairly dense pebbles consisting mainly ($\sim 90\%$) of silicates, sulphides and a large fraction of organic matter, and only $\sim 10\%$ of water ice [4]. The mass ratio of pebbles is up to $\sim 99\%$ and only $\sim 1\%$ amounts to fluffy dust particles. Experiments with collisions of small particles of fractal structure showed that initially fractal dimension growths resulting in sticking fractal clusters and then it is replaced by bouncing when aggregate sizes reach ~ 1 cm for stony and at least tenfold larger icy aggregates (see [4] and references therein). This is confirmed by the results of modeling [8].

Input parameters and method:

With regard to these data, we consider a pebble-sized icy aggregate near the snowline having various fractal dimension meaning its variable porosity. It was suggested that a spherical aggregate consists of two smaller sets of spherical particles (pebbles) of different size and density due to their different composition/origin. One type of particles is assumed to consist mostly of ice evaporating completely at the snowline, a minor fraction of refractory grains inside being neglected. The other type of particles are refractories, which consists mainly of silicates, sulphides and organics while a minor fraction of water ice inside is ignored. These particles are assumed to fully preserve when crossing the snowline. In our model we vary size and density of both types of particles thus simulating the porosity and composition of the medium. The fractal icy assembly approach and the modified permeable particle method [9–11] were used. For the both types of particles a selected size range and the inversed power-law size distribution with variable exponent was accepted. Following the data available on the pebble sizes achievable in the protoplanetary disc, the aggregate diameter varied in the range from 1 to 10 cm. The smallest diameter of each type particles inside the aggregate was at least one two-hundredth of the aggregate's diameter due to computational limits.

Results and discussion:

The results of our modeling was obtained for the following set of parameters: Diameter of the aggregate is 10 cm; fractal dimension is 2.75; diameters of refractory particles are varied from 0.05 to 0.1 cm; diameters of ice particles are varied from 0.5 cm to 1 cm, i.e. ten times larger; exponent in the inverse power-law size distribution is equal to 3.5 (similar to interstellar dust particles and crater sizes), which yields the average diameters ~ 0.06 cm and 0.6 cm, respectively; density of refractory particles is taken equal to 1.2 g cm^{-3} ; density of ice particles is assumed to be 0.1 g cm^{-3} corresponding to rather high porosity ~ 0.9 . The total mass of the aggregate was obtained to be 60.1 g , the masses of refractory and ice components are 54.2 and 5.9 g , respectively; their ratio is similar to that in the 67P nucleus.

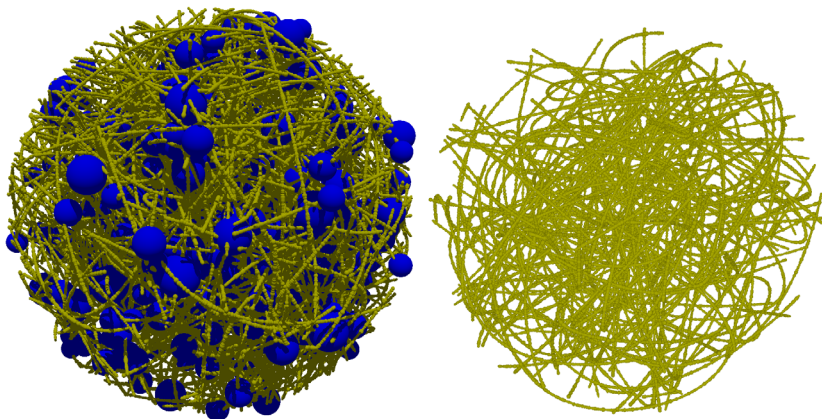


Fig. 1. Left: The dust aggregate with diameter of 10 cm and total number of particles $N = 306336$ before evaporation of ice at the snowline. Blue balls are ice particles, yellow are the chains of refractory particles. Right: The largest refractory fragment resulting from evaporation of ice; number of particles $N_1 = 107487$, that is 35% of the total number; the maximum size $L = 7.7 \text{ cm}$.

Mass of the largest fragment (shown in Fig. 1) is $\sim 32\%$ of the total mass of aggregate before the ice evaporation; size of this fragment is $\sim 77\%$ of the aggregate diameter. Mass of the second large fragment is 7.5 times less. In the option with greater ice mass fraction and higher density of ice particles, similar result of massive large fragments was derived. Such large fragments drift from the snowline with rather high velocity into the inner planet formation zone [2]. However, in the case of smaller ice particles than refractory ones our modeling yields very small fragments of only several particles left. In such a case they will be slow down by the gas drag and accumulate in the asteroid formation zone.

It is aware that the results of modeling is to be analyzed in the whole range of the input parameters possible variations, which would allow us to estimate characteristics of the resulting fragments at the inner side of the snowline. Another goal is to assess the rate of sticking and aggregation of fragments at the snowline, jointly with their radial drift and influence of turbulent diffusion in the disk gas. Providing the aggregation of fragments was efficient, it would drastically affect the radial motion and distribution of dust aggregates implying significant impact on the formation of planetesimals.

This work was supported by the Russian Foundation for Basic Research (Project 17-02-00507).

References:

- [1] Ida S., Guillot T. Formation of dust-rich planetesimals from sublimated pebbles inside of the snow line // *Astron. and Astrophys.* 2016. V. 596. Article id. L3. 5 p. L3. 5 p.
- [2] Makalkin A.B. and Artyushkova M.E. On the formation of planetesimals: radial contraction of the dust layer interacting with the protoplanetary disk gas // *Sol. Syst. Res.* 2017. V. 51. No. 6. P. 491–526.

- [3] Schoonenberg D., Ormel C.W. Planetesimal formation near the snowline // *Astron. and Astrophys.* 2017. V. 602. Article id. A21. 19 p.
- [4] Blum J., Gundlach B., Krause M., Fulle M. et al. Evidence for the formation of comet 67P/Churyumov-Gerasimenko through gravitational collapse of a bound clump of pebbles // *Mon. Notic. Roy. Astron. Soc.* 2017. V. 469. P. S755–S773.
- [5] Fulle M., Blum J., Green S.F., Gundlach B., Herique A., Moreno F., Mottola S., Rotundi A., Snodgrass C. The refractory-to-ice mass ratio in comets // *Mon. Notic. Roy. Astron. Soc.* 2019. V. 482. P. 3326–3340.
- [6] Marov M.Ya., Rusol A.V. Gas-dust protoplanetary disc: Modeling collisional interaction of primordial bodies // *J. Modern Phys.* 2015. V. 6. P. 181–193.
- [7] Marov M.Ya., Rusol A.V. Gas-dust protoplanetary disc: Modeling primordial dusty clusters evolution // *J. Pure Appl. Phys.* 2015. V. 3. P. 16–23.
- [8] Marov M.Ya., Rusol A.V. Estimating the parameters of collisions between fractal dust clusters in a gas–dust protoplanetary disk // *Astron. Lett.* 2018. V. 44: P. 474–481.

PROBABILITIES OF COLLISIONS OF PLANETESIMALS FROM DIFFERENT PARTS OF THE FEEDING ZONE OF THE TERRESTRIAL PLANETS WITH THE FORMING PLANETS, THE MOON, AND THEIR EMBRYOS

S.I. Ipatov

Vernadsky Institute of Geochemistry and Analytical Chemistry of Russian Academy of Sciences, Moscow, Russia, siipatov@hotmail.com

Keywords:

Planetesimals, migration, terrestrial planets, the Moon

Initial data and the model of calculations:

In previous papers (e.g. [1]) the studies of fractions of planetesimals, initially located at different distances from the Sun, collided with different terrestrial planets were based on computer simulations of the evolution of disks of gravitating bodies combined at their collisions. Recently [2] I used another approach for estimates of such fractions. I made computer simulations of migration of planetesimals, initially located in a ring, under the gravitational influence of planets or their embryos. Based on the arrays of orbital elements of migrated planetesimals, I calculated the probabilities of collisions of planetesimals with the planets or their embryos. In this integration, the collisions of planetesimals with planets were not simulated, but the planetesimals were excluded from integration when they collided with the Sun, or their distances from the Sun exceeded 2000 AU. In the series MeN of runs, the migration of planetesimals, originally located in a relatively narrow ring, is studied under the gravitational influence of all planets (from Mercury to Neptune). In the series Me₀₁S of calculations, I considered the embryos of the terrestrial planets with masses equal to 0.1 of the present masses, moving in present orbits of the planets, and also Jupiter and Saturn with their present masses and their present orbits (Uranus and Neptune were excluded). For series Me₀₃N, masses of the embryos of the terrestrial planets equaled to 0.3 of the present masses of the planets, and all giant planets were considered. The influence of gas was not taken into account. The orbital elements of the migrated planetesimals were recorded in the computer memory with a step of 500 years. Based on these arrays, similar to the calculations presented in [3–4], for the considered time interval T, the probabilities of collisions of planetesimals with planets and the Moon and with their embryos were calculated.

250 initial planetesimals were considered in each variant of calculations. The semimajor axes a_0 of the initial orbits of the planetesimals changed from a_{0min} to $a_{0min} + d_a$ AU, and the number of planetesimals with a_0 was proportional to $a_0^{1/2}$. The values of a_{0min} varied with a step of 0.2 AU from 0.3 to 1.5 AU for different runs. $d_a = 0.5$ AU for $a_{0min} = 1.5$ AU. For all other runs $d_a = 0.2$ AU. In some variants of the MeN calculations, initial eccentricities e_0 of orbits equaled to 0.05, and in other runs they were 0.3. For Me₀₁S and Me₀₃N calculations I considered only $e_0 = 0.05$. The initial inclinations i_0 were equal to $e_0/2$ rad. The probabilities of collisions of planetesimals during considered time interval T (equaled to 1, 2, 5, 10, 20 or 50 Myr) with the Earth, Venus, Mars, Mercury, Jupiter, Saturn, the Moon and the Sun are denoted by $p_{E'}$, $p_{V'}$, $p_{Ma'}$, $p_{Me'}$, p_J , p_S , p_M and $p_{Sun'}$, respectively. The probabilities of collisions of planetesimals with embryos of the Earth, Venus, Mars, Mercury, and Moon with masses equal to 0.1 of their present masses are denoted by $p_{E01'}$, $p_{V01'}$, $p_{Ma01'}$, $p_{Me01'}$, and $p_{Mo01'}$, respectively. The tables with the values of the above probabilities for different calculations were presented in [2]. The considered model doesn't take into account the mutual gravitational influence of planetesimals, which increased their eccentricities and mixing of planetesimals in the zone of the terrestrial planets.

Probabilities of collisions of planetesimals with forming terrestrial planets:

For Me_{01} S runs, at each considered ring, planetesimals collided mainly only with one embryo, and probabilities of collisions of planetesimals with other embryos were zero or were much smaller than those for that embryo. So inner layers of a terrestrial planet were formed by accumulation mainly of material from the neighbourhood of the planetary orbit. It was shown that Venus and the Earth, starting from 0.1 of their masses, could accumulate most of the planetesimals from the zone at 0.7–1.1 AU in less than 5 Myr, and Venus could accumulate most of the planetesimals from the zone at 0.5–0.7 AU in not more than 10 Myr. The embryos of the Earth and Venus grew faster than the embryos of Mercury and Mars. For Me_{01} S runs and the zone at 0.3–0.5 AU, p_{Me01} equaled to 0.03 at $T=5$ Myr. For the total mass M_b of planetesimals in the zone equaled to $0.1m_E$ (where m_E is the Earth's mass), $M_b p_{Me01} = 0.03m_E$ is about a half of the mass of Mercury ($0.055m_E$). Therefore, Mercury could accumulate a considerable fraction of its mass from neighbourhood of its orbit. For Me_{01} S runs and the zone at 1.3–1.5 AU, p_{Ma01} equaled to 0.011 and 0.035 at T equaled to 5 and 20 Myr, respectively. For the total mass of planetesimals in the zone $M_b = 0.2m_E$ and p_{Ma01} equaled to 0.011 and 0.035, we have $M_b p_{Ma01} = 0.02m_E$ and $M_b p_{Ma01} = 0.07m_E$, respectively. For Me_{01} S runs and the zone at 1.5–2.0 AU, p_{Ma01} equaled to 0.0075 and 0.032 at T equaled to 5 and 20 Myr, respectively. So compared to other terrestrial planets, Mars (with its present mass of $0.107m_E$) could acquire a smaller fraction of its mass during the considered 5 Myr. However, at $T=20$ Myr and the mass of material in the zone at 1.3–2.0 AU greater than $0.3m_E$, Mars could acquire most of its mass from this zone.

Probabilities of collisions of planetesimals with the terrestrial planets:

Analysis of Me_{03} N runs showed that probabilities of collisions of the planetesimals, originally located at distances from 0.7 to 0.9 AU from the Sun, with the embryos of the Earth and Venus with masses equal to 0.3 from the masses of the present planets, differed for these embryos by no more than a factor of 2. The estimates based on MeN calculations correspond to the last stages of the formation of the planets. The ratio p_v/p_E of the probabilities of collisions of planetesimals with Venus and the Earth was in the range from 0.5 to 1.9 for a_{omin} in the range from 0.7 to 1.1 AU. For $a_{omin} = 1.3$ AU, the ratio was also close to this interval (0.5, 1.9), e.g., at $T=5$ Myr it was 0.48 and 0.38 for $e_o = 0.05$ and $e_o = 0.3$, respectively ($p_v/p_E = 0.78$ at $T=20$ Myr and $e_o = 0.3$). Therefore, the amounts of material from different parts of the zone from 0.7 to 1.5 AU from the Sun, which entered into almost formed the Earth and Venus, differed, probably, by no more than a factor of 2. For initial planetesimals with $a_o < 0.7$ AU, the fraction of planetesimals that fell onto Venus was at least several times higher than the fraction of planetesimals that fell onto the Earth. The ratio p_{Ma}/p_E exceeded 0.1 in the majority of calculations for $a_{omin} \geq 1.1$ AU, and for $a_{omin} \leq 0.9$ AU in two calculations it reached 0.045 and 0.087. The p_{Me}/p_E ratio was close to 100 at $a_{omin} = 0.3$ AU, and $p_{Me} \approx 0.5$ for $a_{omin} = 0.3$ AU, $e_o = 0.05$, and $T=5$ Myr. In other variants, p_{Me}/p_E was significantly smaller, although it reached 0.07 for $a_{omin} = 0.7$ AU, $e_o = 0.3$ and $T=20$ Myr. The results of the MeN calculations testify in favor of the accumulation by almost formed terrestrial planets and the Moon of the matter originally located near other planets. In some runs with a_{omin} equaled to 0.3, 1.1, 1.3, and 1.5 AU, more than 10% of planetsimals could fall onto the Sun. The ejection of matter into hyperbolic orbits and the probabilities of collisions of planetesimals with the giant planets were insignificant.

The Earth and Venus could acquire more than a half of their mass in 5 million years. The ejection of the matter at collisions of planetesimals with planets, that was not taken into account in the considered model, can increase the time of accumulation of the planets. At a small mass of the Mars's embryo, the embryo grew slowly. The formation of a Mars's embryo with a mass that was several times smaller than that of Mars, as a result of the compression of a rarefied condensation, can explain the relatively rapid growth (not more than 10 Myr; such estimates were based on the Martian mantle Hf/W ratio) of the main mass of Mars. We can also suppose [2] the formation of Mercury's embryo with a mass of 0.02 of the Earth's mass by similar compression.

The features of the formation of the terrestrial planets can be explained with a relatively smooth decrease of the semi-major axis of Jupiter caused by its ejection of planetesimals into hyperbolic orbits, without considering Jupiter's migration to Mars's orbit and back (the Grand Tack model) and without sharp changes in orbits of the giant planets for the Nice model.

Probabilities of collisions of planetesimals with the Moon:

At the ratio of the masses of the embryos of the Earth and the Moon equaled to 81 (the ratio of the masses of the Earth and the Moon), the ratio of probabilities of planetesimals collided with the embryos of the Earth and the Moon in the considered calculations did not exceed 54 and was maximum at the masses of embryos about three times smaller than the present masses of the Earth and the Moon. The ratio of the total mass of the planetesimals that fell onto the Earth to the mass of the planetesimals that fell onto the Moon, in the considered MeN variants of calculations ranged from 16.9 (for $a_{\text{omin}}=1.1$ AU and $e_0=0.3$) to 35.6 (for $a_{\text{omin}}=0.9$ AU and $e_0=0.05$).

Conclusions:

The embryos of the terrestrial planets with masses which were not more than 0.1 of masses of the planets accumulated mainly material from neighbourhoods of their orbits. The amount of material from different parts of the zone from 0.7 to 1.5 AU from the Sun, which collided with almost formed the Earth and Venus, differed for these planets, probably, by no more than a factor of two. Inner layers of each terrestrial planet could be accumulated mainly from planetesimals from the neighbourhood of the orbit of this planet. The outer layers of the Earth and Venus could accumulate similar planetesimals from different regions of the feeding zone of the terrestrial planets. At the ratio of the masses of the embryos of the Earth and the Moon equaled to 81 (the ratio of the masses of the Earth and the Moon), the ratio of probabilities of planetesimals collided with the embryos of the Earth and the Moon in the considered calculations did not exceed 54.

Acknowledgements:

The studies of the growth of Mars and Mercury were supported by the Program of Fundamental Studies of the Presidium of RAS № 12. The studies of the formation of the Earth-Moon system were supported by the grant of Russian Science Foundation N 17-17-01279.

References:

- [1] Ipatov S.I. Migration of bodies in the accretion of planets // Solar System Research. 1993. V. 27. P. 83–101.
- [2] Ipatov S.I. Probabilities of collisions of planetesimals from different regions of the terrestrial feeding zone with forming planets and the Moon // Solar System Research. 2019. V. 53. № 5.
- [3] Ipatov S.I., Mather J.C., Comet and asteroid hazard to the terrestrial planets // Advances in Space Research. 2004. V. 33, N 9. P. 1524–1533.
- [4] Marov M.Ya., Ipatov S.I. Delivery of water and volatiles to the terrestrial planets and the Moon // Solar System Research. 2018. V. 52. P. 392–400.

LIDOV-KOZAI CYCLES IN SECULAR DYNAMICS OF RESONANT KUIPER BELT OBJECTS

S.S. Efimov¹, V.V. Sidorenko²

¹ *Moscow Institute of Physics and Technology, 9 Institutskiy per., 141701 Dolgoprudny, Russia, efimov.ss@phystech.edu;*

² *Keldysh Institute of Applied Mathematics, 4 Miusskaya sq., 125047 Moscow, Russia*

Keywords:

Mean motion resonance, perturbation theory, averaging method, Kuiper belt, twotinos, plutinos, Lidov-Kozai resonance, trans-Neptunian objects.

Lidov-Kozai cycles — long-term periodic synchronous variations of an object's eccentricity e , inclination i , and argument of periapsis ω — are a key concept for describing secular evolution of the orbit. They are also instrumental in understanding dynamical structure of planetary systems as well as debris disks and belts.

We study secular dynamics of Kuiper belt objects (KBOs) in mean motion resonance (MMR) within restricted three-body problem (R3BP). For a “Sun-planet-KBO” system MMR ($p+q$): p can be defined as an orbital configuration in which the KBO completes $p+q$ rotations around the Sun in the same time the planet completes p rotations (p and q are integer numbers). Special attention is paid to the exterior first order MMRs ($q=-1$). In Kuiper belt these resonances are represented by large populations such as twotinos and plutinos, which are the objects in 1:2 ($p=2$) and 2:3 ($p=3$) MMRs with Neptune, respectively.

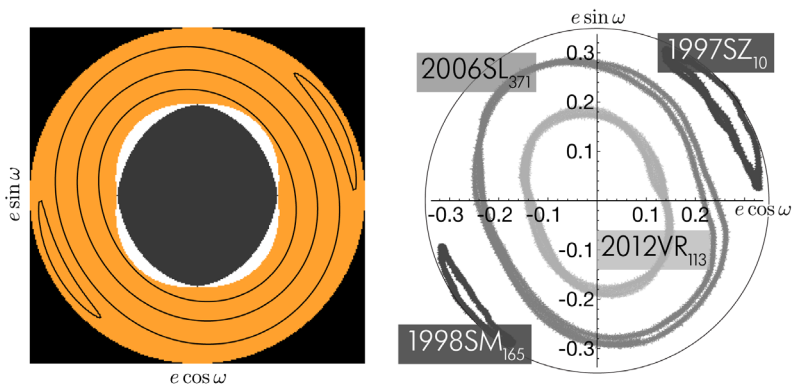


Fig. 1. Secular evolution of twotinos: model (left) vs numerical simulation of the entire solar system (right). Objects 1997SZ₁₀ and 1998SM₁₆₅ are in Lidov-Kozai resonances with ω librating about the values that are neither 0° , 90° , 180° , nor 270° .

A key feature that distinguishes our model from the prior art, is its applicability to orbits with arbitrary values of eccentricity and inclination. It became possible owing to a combination of the approach developed by Wisdom [1] with semi-analytical methods based on numerical averaging of disturbing function. Thus, the complete survey of secular dynamics in first-order MMR within R3BP is carried out, revealing a broad variety of Lidov-Kozai cycles. Many specific cases of secular evolution are illustrated by examples from dynamics of actual KBOs (Fig. 1). Some of the described Lidov-Kozai cycles are well-known and exist outside of MMR as well [2, 3], some were previously encountered only in numerical simulations involving fictitious particles [4], while some appear to be new and unique (Fig. 1) and are not replicated by low-order models of the resonance [5].

Furthermore, our model allows revising the results of [6] and discussing the role of giant planets (other than Neptune) in secular dynamics of resonant KBOs.

Acknowledgements:

This work was supported by the Ministry of Science and Higher Education of the Russian Federation (Project КП19-270 "Origin and evolution of the Universe problems involving ground observations and space research").

References:

- [1] Wisdom J. A perturbative treatment of motion near the 3/1 commensurability // *Icarus*. 1985. V. 63. P. 272-289.
- [2] Thomas F. and Morbidelli A. The Kozai resonance in the outer solar system and the dynamics of long-period comets // *Celestial Mechanics and Dynamical Astronomy*. 1996. V. 64. P. 209–229.
- [3] Vashkov'yak M. A. Evolution of orbits in the restricted circular twice-averaged three-body problem I. Qualitative investigation // *Cosmic Research*. 1981. V. 19(1). P. 1–10.
- [4] Gallardo T., Hugo G., Pais P. Survey of Kozai dynamics beyond Neptune // *Icarus*. 2012. V. 220. P. 392-403.
- [5] Sessin W. and Ferraz-Mello S. Motion of two planets with periods commensurable in the ratio 2:1. Solutions of the Hori auxiliary system // *Celestial Mechanics and Dynamical Astronomy*. 1984. V. 32. P. 307-332.
- [6] Wan X.-S. and Huang T.-Y. An exploration of the Kozai resonance in the Kuiper Belt // *MNRAS*. 2007. V. 377. P. 133–141.

PINNACLES ON THE SURFACE OF THE 67P/CHURYUMOV-GERASIMENKO COMET NUCLEUS

S.S. Krasilnikov^{1,2}, A.T. Basilevsky^{1,2}, Y.V. Skorov^{2,3}, S.F. Hviid⁴, U. Mall², H.U. Keller³

¹ Vernadsky Institute of Geochemistry and Analytical Chemistry RAS Moscow, Russia, krasilnikovruss@gmail.com;

² Max Planck Institute for Solar System Research, Göttingen, Germany;

³ Institute of Geophysics and Extraterrestrial Physics, Braunschweig University of Technology, Braunschweig, Germany;

⁴ Institute of Planetary Research, German Aerospace Center (DLR), Berlin, Germany

Keywords:

Pinnacles, comet, 67P, Churyumov-Gerasimenko, sublimation.

Introduction:

Pinnacles, which are local promontories of various shapes including spires with pointed tops, are known in several geologic environments on Earth [e.g., 1]. They mostly represent erosional remnants created by a loss of material surrounding spots of the more-erosion-resistant material. On comet nuclei they were first briefly described on the nucleus of comet Wild 2 [2] and then discussed along with other surface features by [3] and [4]. In the case of comet nuclei, the pinnacle-forming erosion is most probably sublimational loss of surface material to coma and further to open space. Such mechanism of pinnacle formation suggests that their maximum heights on the nucleus represent a measure of minimum depth of the surface erosion and their number and sizes provide information on degree of inhomogeneity of the nucleus material. On the nucleus of comet 67P/Churyumov-Gerasimenko, pinnacles (Figure 1) were first identified and described in its northern part by [5]. The current paper briefly discuss progress in studying of the 67P pinnacles achieved through the comprehensive analysis of the OSIRIS camera [6] images and high-resolution shape model SHAP7 [7] of the total nucleus surface.

Analysis of pinnacles on the surface of 67P

Inhomogeneity of a nucleus structure can be observed on different size levels. The highest level of inner inhomogeneity forms are regional ridges and depressions. These ridges have about a hundred meters in width and a few hundreds of meters length. Lower level of the material inhomogeneity can be observed in the surface structure of individual boulders and finer. In the current work, medium size of inhomogeneity (pinnacles) is considered (fig.1).

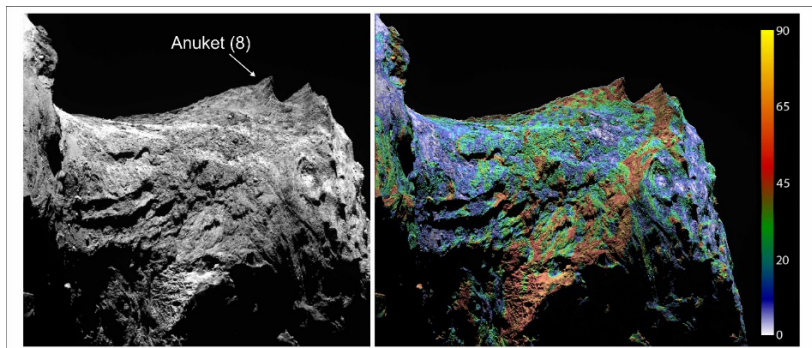


Fig. 1. Fragment of OSIRIS NAC image (left) and image with superposed color-coded values of the slope steepness (90°—vertical, 0° — horizontal) (right) with pinnacle Anuket-1 in the Anuket region (OSIRIS image N201601277232331219ID30F41).

Using the mentioned high-resolution data, 166 pinnacles were identified on the surface of the nucleus. For these pinnacles, morphometric measure-

ments were made — one of them is measuring of the interval in the base of pinnacle in smaller (d) and bigger (D) planimetric directions. The pinnacles were divided into two types: 1) those with rounded planimetric shape ($d/D > 0.7$) and 2) local ridges ($d/D \leq 0.7$). 54 rounded pinnacles with heights from 10 to 93 meters, with mean ratio of high (h) to smaller axes (d) ~ 0.4 and 112 ridges with heights from 9 to 137 meters with mean dependence of $h/d \sim 0.6$, were observed (fig.2).

In lateral views, pinnacles are typically asymmetric and have both gentle and steep slopes with the average slopes' angle to be $\sim 60^\circ$. Pinnacles typically deviate from plumb line suggesting that their shapes almost do not controlled by gravitational forces. Inclination of pinnacles from plumb line is sufficiently high. Mean deviation from the plumb line is $\sim 34^\circ$ with standard deviation $\pm 20^\circ$ ($\pm 1\sigma$) and statistical dispersion near 90° .

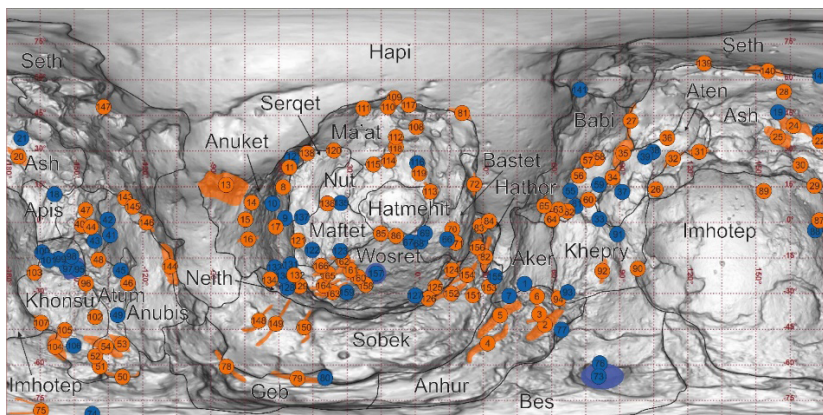


Fig. 2. Global map of the pinnacle distribution with separation them in the rounded ones (violet) and local ridges (orange).

Analysis of the OSIRIS images of the 67P nucleus shows that pinnacles represent outcrops of consolidated material with knobby texture, similar to consolidated material outside of pinnacles. In the south hemisphere of the 67P nucleus at the base of pinnacles' boulders were observed. Frequently, in the northern regions, pinnacles are usually surrounded by both smooth material and boulders. It is assumed that boulders around pinnacles are fragments of pinnacle material.

The observed heights of pinnacles vary on regional scale, which makes it possible to estimate a minimum thickness of lost material in different regions. The average height of 10 highest pinnacles were calculated for regions mainly with solid material (generally in south hemisphere) was found to be 80 ± 8 m thickness and, for regions with smooth material, (generally in northern hemisphere) -98 ± 13 m. So, estimates of minimum thickness of the erosionally lost material in the nucleus south and north are practically the same. Using a thickness of lost material, a time period needed for these processes can be calculated.

Acknowledgment:

KSS supported by Deutscher Akademischer Austauschdienst. Work of KSS and BAT was partly supported by grant 0137-2018-0038, Program 1.28 by Presidium of Russian Academy of Sciences. Yu.S. thanksthe Deutsche Forschungsgemeinschaft (DFG) for support undergrant SK 264/2-1.

References

- [1] Migon P. Rock and earth pinnacle and pillar. // Encyclopedia of Geomorphology Routledge, A.S. Goudie, ed., Taylor and Francis Group. 2004. 876.
- [2] Brownlee D.E., Horz F., Newburn R.L., Zolensky M., Duxbury T.C., Sandford S., Sekanina Z., Tsou P., Hanner M.S., Clark B.C., Green S.F., Kissel J. Surface of young Jupiter family comet 81 P/wild 2: view from the Stardust spacecraft // Science.2004. 304 (5678), 1764–1769.
- [3] Basilevsky A.T. and Keller H.U. 2006. Comet nuclei: morphology and implied processes of surface modification. Planet. Space Sci. 54 (8), 808–829.

- [4] Cheng A.F., Lisse C.M., A'Hearn M., 2013. Surface geomorphology of Jupiter family comets: a geologic process perspective. *Icarus* 222, 808–817.
- [5] Basilevsky A.T., Krasilnikov S.S., Mall U., Hviid S.F.S., Skorov Yu.V., Keller H.U. 2017. Pinnacles on the 67P comet nucleus: Evidence for large scale erosion and hierarchical agglomeration of the nucleus. *Planet. Space Sci.* 140. 80–85.
- [6] Keller, H.U., Barbieri, C., Lamy, P., et al., 2007. OSIRIS – The Scientific Camera System Onboard Rosetta. *Space Sci. Rev.* 128, 433
- [7] Preusker F., Scholten F. et al. 2017. The global meter-level shape model of comet 67P/ Churyumov-Gerasimenko. *A&A* 607, L1. 5.

ASSESSMENT OF THE POSSIBILITY OF ICE PRESENCE ON 101955 BENNU

V.V. Busarev, E.A. Feoktistova

*Lomonosov Moscow State University, Sternberg Astronomical Institute, University Av., 13, Moscow, 119992, Russian Federation
busarev@sai.msu.ru, Hrulis@yandex.ru*

Keywords:

NEAs, dust activity, ice sublimation, thermal modeling, Bennu thermal evolution.

Introduction:

101955 Bennu is one of the near-Earth asteroids (NEAs) of taxonomic type B with the most primitive mineralogy, similar to CI and CM carbonaceous chondrites with a predominance of hydrated compounds [1]. Using the OSIRIS-REx spacecraft studying the asteroid at the present time, it was first discovered dust activity of Bennu [2]. This process is explained by the formation of ice dust particles during cracking and drying of hydrosilicates, which make up a significant proportion of Bennu's substance, during stay of the asteroid at elevated subsolar temperatures [3].

Problem formulation and results:

As follows from the experiments, the heating of CI-CM carbonaceous chondrites to temperatures of $\sim 1000^\circ\text{C}$ leads to the release of up to 30 wt. % bound water [4]. At the same time, estimates show that although the temperature increase on the surface of Bennu near perihelion (the eccentricity of its orbit $e = 0.203745$) can reach several hundred degrees, at the depth of only a few centimeters, the temperature decreases by 100 degrees [5]. Therefore, another mechanism of dust activity of such primitive asteroids deserves attention – sublimation of ice (mainly H₂O), located in the near-surface or deeper layers of such bodies, where the “heat wave” reaches when the temperature on the surface increases. A similar variant of the activity of primitive-type NEAs was considered by us on the example of the asteroid 162173 Ryugu, which has a taxonomic type close to Bennu, using an analytical model based on the assumption of the presence of water ice in interiors of the body (at least at the beginning of its stay in the near-Earth space) [6]. Aim of the work is a computer simulation of the temperature regime of Bennu and searching areas where the presence of water ice is possible under its surface.

Assumptions and modeling.

To calculate the temperature distribution on Bennu and into its interiors, we used a model obtained from observations of the asteroid using ground-based radar at a wavelength of 12.6 cm (band S), which includes 49152 surface elements [7, 8]. Variations in near-surface properties and regolith structure of asteroids are currently not well determined and radar is a useful tool for investigations of NEAs [9]. Given the low average density of the asteroid [10], as well as its belonging to the low-temperature type B, we assumed that its composition is a mixture of silicates, hydrosilicates and water ice. We also assumed that the asteroid is covered by a layer of regolith, the thickness of which is minimal at the poles (~ 1 m) and increases linearly to the equator, reaching 4 m. According to our model, the shares of different compounds in the depths of the asteroid are: water ice – 15%, and hydrosilicates and silicates – 45 and 40%, respectively. Porosity of the upper layer of regolith (within 0–0.5 of its total thickness), consisting mainly of smaller and more packed particles, was assumed to be 0.35, and of the lower layer, presumably consisting of larger blocks, – to be 0.54. The average density of denser high-temperature minerals and oxides (olivines, pyroxenes, magnetite, etc.) and of low-temperature hydrosilicates and hydroxides we adopted equal to 3.5 g/cm^3 and 2.4 g/cm^3 , respectively, where the last value is close to the density of carbonaceous chondrites of CI-group [11]. Thus, density of the upper layer of regolith according to our model was 1.638 g/cm^3 ,

the density of the lower regolith layer — 1.170 g/cm^3 , and the average density of Benu turned out to be 1.190 g/cm^3 , which is in good agreement with an estimate from [10].

The temperature regime of the asteroid is determined by the solution of the heat equation

$$c(T)\rho(z)\frac{dT}{dt} = \frac{d}{dz}\left(k(z,T)\frac{dT}{dz}\right) \quad 0 < z < L \quad (1)$$

with appropriate boundary and initial conditions:

$$k(z,T)\frac{dT}{dz}\Big|_{z=0} = \varepsilon\sigma T_0^4 - (1-a)F_0(M)$$

$$k(z,T)\frac{dT}{dz}\Big|_{z=L} = 0$$

where z is the depth in m, $c(T)$ is the heat capacity of the considered asteroid soil layer, for which we used the expression from [12], $k(z,T)$ is the coefficient of thermal conductivity of the soil, $\rho(z)$ is the density of the soil substance; T_0 is the initial temperature distribution in the soil; L is the penetration depth of the heat wave; $F_0(M)$ is the flux of radiation from the Sun falling on a given area of the surface, M is the true anomaly determining the position of the asteroid in orbit, ε is the radiation coefficient (in this work it is assumed to be 0.95 similar to the coefficient for the Moon and Mercury), a is the average Benu's surface albedo to be equal to 0.044 [13]; σ is the Stefan-Boltzmann constant. The heat flux from the interior of the asteroid is assumed to be 0. The heat equation (1) was solved for each of the mentioned 49152 surface elements.

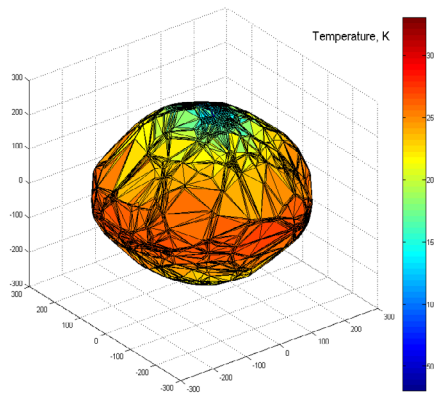


Fig. 1. The temperatures below the limit of the diurnal oscillations on Benu after 10,000 years of its stay in the near-Earth space.

Figure 1 shows the temperatures below the penetration depth of the diurnal temperature oscillation. Using these results, we investigated the possibility of water ice existence in the composition of Benu. The duration of the existence of volatile compounds deposits (in this case, water ice) is determined by the rate of their sublimation [12]:

$$E = \frac{\alpha P}{\sqrt{2\pi k T \mu}}, \quad (2)$$

where α is the condensation coefficient, k is the Boltzmann constant, P is the pressure of saturated water vapor, T is the temperature, μ is the mass of H_2O molecule. According to our calculations, in the area of the asteroid poles

there are small areas (with a total area of about 300 m²) in which water ice can exist on the surface of the asteroid for a long time. In addition, we investigated the possibility of existence of water ice in the body of Bennu under a layer of “dry” (i.e., not containing volatile compounds) regolith. To do this, we modeled the regolith consisting of two layers: the upper layer was a soil without water ice and the lower one was taken consisting of a mixture of water ice (15%) and dry regolith (85%). Different thermophysical parameters of the lower layer, such as density, thermal conductivity and heat capacity of the mixture were calculated as

$$N = N_{\text{regolith}} \gamma + N_{\text{water}} (1 - \gamma) \quad (3)$$

where N_{water} — a parameter of water ice, N_{regolith} — a parameter of regolith, γ — a share of regolith, $(1 - \gamma)$ — a share of water ice in the matter.

The change in the proportion of volatile compounds (in this case water) in the soil is characterized by the flow of the particles through the soil layer to the surface. For a soil layer of Δz thickness, this value is defined as [12]

$$J = \frac{\mu E}{2\Delta z} \quad (4)$$

where l is the size of the soil granules, Δz is the thickness of the soil layer, E is the evaporation rate of volatile compounds.

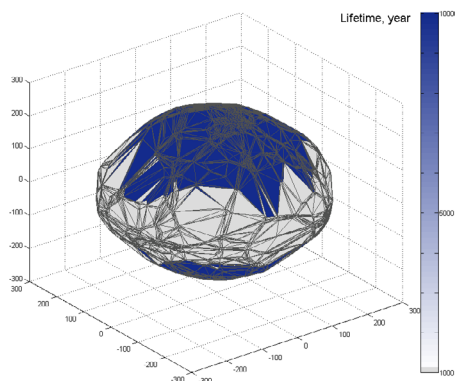


Fig. 2. Areas where water ice can be stable against evaporation up to the center of Bennu for 10,000 years.

Conclusions:

According to the results obtained by solving one-dimensional equation (1) (in the vertical direction), the existence of water ice on Bennu is impossible at any depth in the near-equatorial zone ($\phi < \pm 45^\circ$) after its revolution around the Sun in the near-Earth space. For 10,000 years of the asteroid movement in the present orbit, water ice is possible only in the area closer to the poles ($\phi \geq \pm 45^\circ$) (Fig.2).

However, in this paper we neglected the lateral energy transfer between adjacent elements of the asteroid. But the presence of water ice in the regolith significantly affects the thermophysical parameters of the soil. In particular, the thermal conductivity of the soil significantly increases, and for correct calculation of the temperature distribution in the asteroid, it is necessary to take into account the horizontal heat transfer. Perhaps this will explain the activity of the asteroid near the aphelion of its orbit (it was just the case considered by us previously for asteroid 162173 Ryugu [6]). This will be the subject of our further investigations.

References:

- [1] Clark B.E., Binzel R.P., Howell E.S. et al. Asteroid (101955) 1999 RQ36: Spectroscopy from 0.4 to 2.4 μm and meteorite analogs // *Icarus*. 2011. V. 216. P.462–475.

- [2] <https://www.nasa.gov/press-release/nasa-mission-reveals-asteroid-has-big-surprises>
- [3] Hergenrother C.W., Maleszewski C.K., Nolan M.C. et al. The operational environment and rotational acceleration of asteroid (101955) Bennu from OSIRIS-REx observations // *Nature Communications*. 2019. V. 10. P.1291-1300.
- [4] King A.J., Solomon J.R., Schofield P.F., Russell S.S. Characterising the CI and CI-like carbonaceous chondrites using thermogravimetric analysis and infrared spectroscopy // *Earth, Planets and Space*. 2015. V. 67. P.198–219
- [5] Delbo M., Michel P. Temperature history and dynamical evolution of (101955) 1999 RQ 36: A potential target for sample return from a primitive asteroid // *Astrophysical J. Lett.* 2011. V. 728. L42–L46.
- [6] Busarev V.V., Makalkin A.B., Vilas F., Barabanov S.I., Scherbina M. P. New candidates for active asteroids: Main-belt (145) Adeona, (704) Interamnia, (779) Nina, (1474) Beira, and near-Earth (162,173) Ryugu // *Icarus*, 2018. V. 304. P. 83–94.
- [7] <https://www.asteroidmission.org/updated-bennu-shape-model-3d-files/>
- [8] Nolan M., Magri C., Howell E. et al. Shape model and surface properties of the OSIRIS-REx target asteroid (101955) Bennu from radar and lightcurve observations // *Icarus*. 2013. P. 629–640.
- [9] Hickson D., Boivin A., Daly M.G. et al. Near surface bulk density estimates of EAs from radar observations and permittivity measurements of powdered geologic material // *Icarus*. 2018. V. 306. P. 16–24.
- [10] Lauretta D.S., Al Asad M.M., Ballouz R.-L. et al. The OSIRIS-REx arrives at asteroid (101955) Bennu: Exploration of a hydrated primitive near-Earth asteroid // 50 th Lunar. Planet. Sci. Conf. 2019. Abstract №2608.
- [11] Flynn G.J., Consolmagno G.J., Brown P., Macke R.J. Physical properties of the tone meteorites: Implications for the properties of their parent bodies // *Chemie der Erde*. 2018. V. 78. P. 269–298.
- [12] Schorghofer N., Taylor G.J. Subsurface migration of H₂O at lunar cold traps // *JGR*. 2007. V. 112. E02010.
- [13] DellaGiustina D.N., Emery J.P., Golish D.R. et al. Properties of rubble-pile asteroid (101955) Bennu from OSIRIS-REx imaging and thermal analysis // *Nature Astron.* 2019. V. 3. P. 341–351.

THERMAL MODELS OF COMETS. NEW CHALLENGES AFTER THE ROSETTA MISSION

Yu. Skorov

IGEP, TU Braunschweig, Germany, skorov@mps.mpg.de

Keywords:

comets, comet 67P/Churyumov/Gerasimenko, thermal model.

Comets are among the most primitive bodies of our solar system. Following classical dynamical scenarios, comets were formed during the early stages of the solar system, 4.5 billion years ago, and have since been stored far from the Sun in a very cold environment. Thus, they hold clues to constrain the formation and evolution of our solar system, including insights on prebiotic molecular chemistry and the origin of life on Earth. Composed of minerals, organics, and ices (mainly H₂O, CO₂, and CO ice) comets become active, when approaching the Sun: ices sublimate and comets erode by losing gas and dust, forming their well-known and characteristic coma and tail that can extend over millions of kilometers. Cometary activity has been observed since the Antiquity, but only understood as resulting from ice sublimation in the 50's (Whipple's model). While this overall picture is still valid today, the details are far from being understood and we still do not have a comprehensive view of cometary activity.

Our physical understanding of cometary activity really started in the 50's with the comet nucleus model of the "dirty snowball" developed by Whipple, which demonstrated the key role of water ice sublimation. Following this initial model, progress has been made using different methods: i) Observations of comae with Earthbased telescopes, with a breakthrough in cometary composition, ii) Theoretical numerical models, iii) Laboratory experiments, mainly since the early90's starting with the KOSI experiments, and, finally, iv) In-situ observations of comae and nuclei by dedicated space missions; six comets have been visited by spacecraft since the 80's, which cumulated with the two year continuous observation of comet 67P by Rosetta in 2014-2016. From all these remote or in-situ observations, laboratory experiments and theoretical models, emerges a picture of activity driven by ices, which sublimate when the comet approaches the Sun, dragging dust in the coma as Whipple had envisaged but with many questions still remaining concerning the details..

Looking at the numerous and fundamental discoveries made in space, there remains a lag in the theoretical field in some areas: our understanding of the microphysical processes responsible for the transfer of energy and mass in the cometary nucleus (which determine cometary activity) has hardly improved significantly. We still do not understand the most basic (fundamental) things: 1) we cannot explain how the activity changes depending on the heliocentric distance; 2) we do not understand what serves as a driver of dust activity (how dust is released). These two questions set the boundaries of the problem: we need new models applicable for the analysis of both macro- and microscopic problems.

Since the beginning of the Rosetta mission, it was clear that theoretical models claiming to describe cometary activity should explicitly take into account the fact that volatile sublimation does not occur from the surface of the nucleus, but from under a porous dusty crust. Such model was first proposed by [3] and later applied in [2, 4, 5]. In these thermophysical models, the explicit two-layer model of the near-surface region was applied with varying degrees of rigor. The authors focused on various specific features of the transfer processes (weakening of the efficiency of sublimation, radiative heat transfer, porosity and bulk ice/dust ratio). However, in all published theoretical models, without exception, it was assumed that the properties remain unchanged both with a change in the heliocentric distance and for different regions of the nuclear surface. This used basic model assumption can be called an assumption of a static dust layer. Here it is important to explain

one nontrivial detail: the concept of static does not mean that the layer does not change, quite the opposite, in these models it is assumed implicitly that the dust particles on the upper boundary of the layer are constantly carried away by the gas flow, and this ablation is exactly offset by the addition of new particles on the lower boundary of the layer (so we have at the same time a fixed layer thickness and non-zero dust production).

It seems obvious that this assumption is artificial and non-physical. However, today we do not have more adequate models. It is not surprising, therefore, that none of the models mentioned can explain two very important observable effects: an accelerated increase in gas production near perihelion and a shift in maximum gas production. At the same time, it was shown in [1, 4] that these effects are well explained by the hypothesis of variability in activity. Unfortunately, in the proposed form, this hypothesis is essentially just a model parametrization. It does not contain a consistent micro-physical model describing the observed changes (this task was not posed by the authors). Nevertheless, it gives us important clues about what micro-physical processes should be included in future models. We can expect that the changeable activity may be due to the activation of previously inactive (or weakly active) areas. The main question arises: How can we significantly increase activity in a microphysical model built on first principles?

We will present the recent results of modeling heat transfer in a cometary nucleus at different spatial scales: micro, meso and macro. Problems arising from the use of simplifying assumptions about the constant structure of the dust layer will be analyzed.

References:

- [1] Attree, N., L. Jorda, O. Groussin, and 11 colleagues 2019. Constraining models of activity on comet 67P/Churyumov-Gerasimenko with Rosetta trajectory, rotation, and water production measurements, *Astronomy and Astrophysics*, in press (<https://doi.org/10.1051/0004-6361/201834415>)
- [2] Blum J., B. Gundlach, M. Krause, and 19 colleagues 2017. Evidence for the formation of comet 67P/Churyumov-Gerasimenko through gravitational collapse of a bound clump of pebbles, *Monthly Notices of the Royal Astronomical Society* 469, S755-S773
- [3] Fanale, F.P., Salvail, J.R., 1984. An idealized short-period comet model — Surface insolation, H₂O flux, dust flux, and mantle evolution, *Icarus*, V. 60, P. 476–511
- [4] Keller, H.U., Š. Mottola, B. Davidsson, and 44 colleagues 2015. Insolation, erosion, and morphology of comet 67P/Churyumov-Gerasimenko, *Astronomy and Astrophysics* 583, A34
- [5] Skorov, Y.V., L. Rezac, P. Hartogh, and 2 colleagues 2016. A model of short-lived outbursts on the 67P from fractured terrains, *Astronomy and Astrophysics* 593, A76

SMALL BODIES' STRENGTH: FAILURE MODEL

S.A. Voropaev¹, Y. Jianguo², J.-P. Barriot³

¹ GEOKHI RAS, Moscow, Kosygina str. 19. Voropaev@geokhi.ru

² The State Key Laboratory of Information Engineering in Surveying, Mapping and Remote Sensing, Wuhan University, China.

³ Geodesy observatory of Tahiti, University of French Polynesia, BP 6570, 98702 Faa'a, Tahiti, French Polynesia.

Keywords:

Moon, Earth, asteroid, stress, strain, fracture.

Introduction:

It was assumed that barrage of comets and asteroids produced many young lunar basins (craters over 300 km in diameter) during an impact spike at ~ 3.7 Ga (Late Heavy Bombardment, LHB). Many authors assume the LHB ended about 3.7 to 3.8 billion years (Gyr) ago with the formation of Orientale basin, but recent analysis of the possible 40 Ar diffusion in Apollo samples make this assumption questionable [1]. Evidence for LHB sized blasts on Earth extend into the Archaean and early Proterozoic eons, in the form of global ejecta layers of impact spherule beds. At least seven spherule beds, formed between 3.23 and 3.47 Gyr ago, have been found, four between 2.49 and 2.63 Gyr ago, and one between 1.7 and 2.1 Gyr ago [SM]. Recently, in the geological time scale, late Eocene impact clusters were formed: the Mt Ashmore structural dome at Timor sea ($D \sim 90$ km, 35.4 ± 0.1 Ma), Popigai in East Siberia ($D \sim 100$ km, 35.7 ± 0.2 Ma) and the Chesapeake Bay in North America ($D \sim 85$ km, 35.3 ± 0.1 Ma). The formation event could have been a rupture of a huge asteroid with a size of 30-40 km into pieces under 10 km.

New data on the east Antarctic gravity field from the Gravity Recovery and Climate Experiment (GRACE) mission revealed a prominent positive free-air gravity anomaly over ca. 500 km diameter subglacial basin centered on (70° S, 120° E) in north central Wilkes Land [2]. The inferred impact crater is nearly three times the size of the Chicxulub crater ($D \sim 180$ km, 65 ± 0.2 Ma) and presumably formed at the beginning of the greatest extinction of life on Earth at ca. 260 Ma. The Siberian Traps were antipodal to it. Potential sources of such uninvited guests are near-Earth asteroids families — Apollons, Atons, etc. Their debris regularly cross the Earth's orbit and, once in a hundred years, the fall of a body with size ~ 10 m occurs. The probability of significantly larger falling fragments, at a size of ~ 1 km, is much smaller, with a recurrence of a few million years. Nevertheless, disastrous consequences for the entire Earth's biosphere makes detailed studies of their strength and rate of decay under the action of tidal forces an active subject

Failure model:

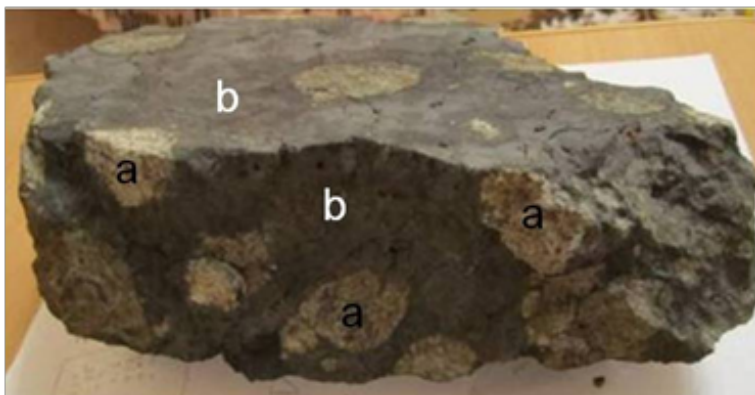


Fig. 1. Meteorite Chelyabinsk' LL5 fragment: **a)** pristine ordinary chondrite; **b)** impact melt. Breccias size $\sim 35 \times 25 \times 15$ cm, mass ~ 4 kg, mean density ~ 3.2 g/cm³.

At present, the geological composition of small bodies of the Solar system is better known from a number of spacecraft missions to asteroids and comets (Hayabusa, NEAR-Shoemaker, Rosetta etc.). They are mainly consolidated bodies, made of rocks, metal compounds and ice, with dramatic surface structures full of large craters and/or system of cracks which should disappear in the case of full fragmentation and subsequent re-accumulation. A detailed study of the meteorite Chelyabinsk (LL5 S3 W0 ordinary chondrite, fall 15 February, 2013) revealed that its parent body's composition was breccias of pristine chondrite material and crystallized impact melts with hard coupling with each other. One of its main rest' fragment is shown on Fig. 1 and thoroughly done measurements provided the mechanical strength of underlying surface rocks [3].

Apparently, melting and subsequent solidification are common processes following shock wave propagation on asteroids and comets after impact events. Therefore, to consider small bodies' failure states of stress, we need a failure model, as used in rock mechanics.

The Grady & Kipp [4] dynamic fragmentation model treats the fracturing material as if it were a continuum. The average effect of many individual fractures is incorporated into a scalar parameter called damage, D . The parameter D is defined such that $D = 0$ corresponds to intact, undamaged rock, and $D = 1$ means the material is completely fragmented and unable to transmit tensile stress — i.e. the body is a collection of separate fragments. In this model, the yield strength, Y , is given by

$$Y = (1 - D) \cdot Y_i + D \cdot Y_d, \quad (1)$$

where Y_i and Y_d are the yield strengths of intact and shock-damaged rock, respectively. The yield strength Y_d is well established and is known as the Coulomb friction law,

$$Y_d = Y_{coh} + \mu_{dam} \cdot P, \quad (2)$$

where Y_{coh} , μ_{dam} and P are the cohesion, internal friction and pressure, respectively. The Y_d is limited by the von Mises plastic limit, which is typically 1–5 GPa under strong compression. The maximum value of $\mu_{dam} \sim 0.6$ is typical for rocky granular media.

Recent observations have indicated that rubble pile asteroids ($D = 1$) may have a small, but finite, level of tensile strength allowing them to have rotation rates above their spin deformation limit [5]. Estimation of maximum possible tensile strength provides only value ~ 10 KPa. Popova et al. [PO] assembled data on 13 cases of meteoritic falls and estimated the bulk strength of the objects corresponding to their earliest observed fragmentation in the high atmosphere. In all 13 cases, the strengths were much less than the compressive or tensile strength reported for that class of stony meteorites. Bulk compressive strengths upon atmospheric entry of these bodies were shown to be very low: 0.1 – 1 MPa on first breakups and 1 – 10 MPa on final breakups.

From the [6] we can see that pre-entry, 10–100 meter scale interplanetary meteoroids are typically highly fractured ($0.5 < D < 0.8$) and can break up under tensile stresses of $0.03 + 1$ MPa. The exception is the fall (September 15, 2007) of the Carancas stony meteorite at Peru which caused the formation of a 13 m wide impact crater. It was classified as an ordinary chondrite H4–5 with an estimated initial size $\sim 0.9 + 1.7$ m, a compressive strength $\sim 20 + 40$ MPa and a tensile strength $\sim 1.2 + 2.4$ MPa, depending of the trajectory. So, the Carancas meteorite is a rare example of a monolithic meteoroid that was almost free of internal cracks ($0 < D < 0.2$).

Results:

One of the most important questions in this context is at what distance from a large planet such a body may split, and how this distance depends on the physical properties of the body. This has been under debate ever since Edouard Roche, calculating his famous expression for the splitting distance, D , as

$$D = 2.45 \cdot \left(\frac{\rho_p}{\rho_0} \right)^{\frac{1}{3}} \cdot R_p \text{ or } \delta = \frac{D}{R_p} \left(\frac{\rho_0}{\rho_p} \right)^{\frac{1}{3}} = 2.45, \quad (3)$$

where R_p and ρ_p are the radius and density of the planet, and ρ_0 is the density of the small body. Roche used a homogeneous, self-gravitating liquid satellite on a circular orbit around a solid planet, no reference to any other property of the body than its density.

Let us consider the stability of a rotating prolate body during a close encounter with Earth, in a general scaling form. As we know from the detailed analysis [7], the tensile (positive) stress, σ_{xx} , appears first on the surface equator at the point $x = z = 0$, $y = c$, for some distance D_c ("down" case). The parameter D_c could be defined as

$$\sigma_{xx}^{(e)}(D, \nu, \varepsilon) = \frac{I_g}{Z(k, t)} \left[\left(\frac{1}{\delta^3} \right) \cdot T(k, t) + 3 \cdot \left(\frac{I_\omega}{I_g} \right) \cdot R(k, t) - 6 \cdot (f_1(\varepsilon) \cdot F_1(k, t) + f_2(\varepsilon) \cdot F_2(k, t)) \right], \quad (4)$$

where $k(\nu) = \left(\frac{1-\nu}{1-2\nu} \right)$, $t = 1 - \varepsilon^2 = \frac{c^2}{a^2}$, ν is the Poisson' ratio, as usual (see [SV] for details about functions $T(k, t)$, etc.). Therefore, δ_c is defined by the condition $\sigma_{xx}^{(e)}(D_c, \nu, \varepsilon) = 0$:

$$(\delta_c)^3 = \frac{T(k, t)}{3 \cdot \left[2 \cdot (f_1(\varepsilon) F_1(k, t) + f_2(\varepsilon) \cdot F_2(k, t)) - \left(\frac{I_\omega}{I_g} \right) \cdot R(k, t) \right]} \quad (5)$$

This scaling form, connecting the dimensionless variables $\delta = \frac{D}{R_p} \left(\frac{\rho_0}{\rho_p} \right)^{\frac{1}{3}}$ and

$$\chi = \frac{I_\omega}{I_g} = \frac{\rho_\omega}{\rho_0}, \quad \rho_\omega = \frac{\pi}{G \cdot T^2},$$

allows to analyze the critical distance for any possible combination of physical parameters of asteroid and planet. For a sphere $\varepsilon = 0$, δ_c takes the simplest form

$$(\delta_c)^3 = \frac{5 \cdot (1 - \nu^2)}{\left[(7 + 5\nu)(1 - 2\nu) - \chi \cdot 6 \cdot (4 - 3\nu - 5 \cdot \nu^2) \right]} \quad (6)$$

In the future, it is planned a further development of the Griffiths theory to study the conditions of cracks growth at small bodies' environments.

Acknowledgments

This work was supported by the Russian Science Foundation, project no. 17-17-01279.

References:

- [1] Boehnke, P. et al. // PNAS. 2016. V. 113. No. 39. P. 10802-10806.
- [2] von Freese R.R.B. et al. // Geochemistry and Geophysics Geosystems. 2009. V. 10. No. 2.
- [3] Voropaev S., Jianguo Y. et al. // Doklady Astronomy & Mechanics. 2017. V. 62. No. 10. P. 486-489.
- [4] Grady D.E., Kipp M.E. Fracture Mechanics of Rocks, Academic, San-Diego. 1987. P. 475
- [5] Holsapple K.A. // Icarus. 2007. V. 187, P. 500-509.
- [6] Popova O. et al. // Meteoritics & Planetary Science. 2011. V. 46. No. 10. P. 1525-1550.
- [7] Voropaev S., Jianguo Y. and Barriot J.-P. // Solar System Research, 2019 (in publication)

RAMAN SPECTROMETER FOR PHOBOS IN-SITU EXPLORATION

U. Böttger¹, M. Buder¹, Y. Cho², E. Dietz¹, T. Hagelschuer¹, F. Hanke¹, H.-W. Hübers¹, S. Kameda³, E. Kopp¹, A. Moral⁴, C. Paproth¹, G. Peter¹, K. Rammelkamp¹, P. Rodriguez⁴, F. Rull⁵, C. Ryan¹, T. Säuberlich¹, F. Schrandt¹, S. Schröder¹, S. Ulamec⁶, T. Usui⁷, R. Vance¹, and I. Weber⁸

¹ German Aerospace Center (DLR), Institute of Optical

Sensor Systems, Rutherfordstraße 2, 12489 Berlin,

Germany, Ute.Boettger@dlr.de; Maximilian.Buder@dlr.de;

Enrico.Dietz@dlr.de; Till.Hagelschuer@dlr.de; Franziska.Hanke@dlr.de;

Heinz-Wilhelm.Huebers@dlr.de; Emanuel.Kopp@dlr.de;

Carsten.Paproth@dlr.de; Gisbert.Peter@dlr.de;

Kristin.Rammelkamp@dlr.de; Conor.Ryan@dlr.de; Saeuberl@

dlr.de; Friedrich.Schrandt@dlr.de; Susanne.Schroeder@dlr.de;

Roderick.Vance@dlr.de

² Department of Earth and Planetary Science, Graduate School of Science, University of Tokyo, 7-3-1 Hongo, Bunkyo, Tokyo 113-0033 Japan. cho@eps.s.u-tokyo.ac.jp

³ Department of Physics, College of Science, Rikkyo University, 3 Chome-34-, Nishiikebukuro, Tokyo 171-8501, Japan, kameda@rikkyo.ac.jp

⁴ Instituto Nacional de TécnicaAerospacial (INTA), Ctra. Ajalvir, Km 4, 28850 Torrejón de Ardoz, Spain, moralia@inta.es; rodriguezpp@inta.es

⁵ Universidad de Valladolid –UnidadAsociada UVA-CSIC Centre de Astrobiología, Av. Francisco valles, 8, Parque Tecnológico de Boecillo, Parcela 203, E-47151 Boecillo, Valladolid, Spain, rull@fmc.uva.es

⁶ German Aerospace Center (DLR), Microgravity User Support Center, Linder Höhe, 51147 Cologne, Germany, Stephan.Ulamec@dlr.de

⁷ Japan Aerospace Exploration Agency (JAXA), Institute of Space and Astronautical Science, Department of Solar System Sciences, 3-1-1 Yoshinodai, Chuo, Sagamihara, Kanagawa, 252-5210, Japan, usui.tomohiro@jaxa.jp

⁸ Institut für Planetologie, Wilhelm-Klemm-Str. 10, 48149 Münster, Germany, sonderm@uni-muenster.de

Keywords:

Raman spectroscopy, mineralogy, in-situ exploration, Phobos, MMX, RAX

Introduction:

The Martian Moons eXploration (MMX) mission to be launched 2024 by the Japan Aerospace Exploration Agency (JAXA) will conduct remote sensing observations of both Mars moons, Phobos and Deimos, and will as well carry out in-situ observations on and return samples from the surface of Phobos [1] back to Earth. A rover provided by DLR/CNES will be delivered to Phobos and perform scientific measurements on the surface including Raman spectroscopy with an instrument developed by DLR/INTA/JAXA.

Raman spectroscopy for mineral phase identification on Phobos.

Phobos occupies a unique position in the exploration of the Solar System. It is a low-gravity object inside the gravity well of Mars. The origins of both, Phobos and Deimos, are uncertain and studying both provides insights into the formation of the inner Solar System, including the terrestrial planets [2]. Gaining knowledge about the origin, evolution, and formation of Solar System bodies is the main objective of MMX and the accompanying rover mission. For this purpose information about Phobos' mineralogical and geochemical composition will be obtained in-situ using Raman spectroscopy [3]. The investigation of returned samples in laboratories on Earth allows more detailed analyses and provides the most unambiguous means to distinguish among the different hypotheses about the moons' origin.

RAX (Raman spectrometer for MMX) is a compact, low-mass Raman instrument with a volume of approximately $81 \times 98 \times 125 \text{ mm}^3$ and a mass of less than 1.4 kg developed by DLR, INTA/UVA and JAXA/UTOPS/Rikkyo. It will per-

form spectroscopic measurements to identify the mineralogy of the Phobos surface. The RAX data will support the characterization of a potential landing site for the MMX space craft and the selection of samples for the return to Earth. The RAX measurements will be compared with Raman measurements obtained from the RLS instrument during the ExoMars 2020 mission, to provide evidence for the Martian or non-Martian origin of the surface minerals of Phobos.

References:

- [1] Kuramoto, K., Kawakatsu, Y., Fujimoto, M., Genda, H., Imamura, T., Kameda, S., Matsumoto, K., Miyamoto, H., Morota, T., Nagaoka, H., Nakamura, T., Ogawa, K., Otake, H., Ozaki, M., Sasaki, S., Senshu, H., Tachibana, S., Terada, N., Usui, T., Wada, K., Watanabe, S., and MMX study team, 2018, Martian moons exploration (mmx) conceptual study update. *Lunar Planet. Sci* 49, (abstract #2143)
- [2] Pieters, C., Calvin, W., Cheng, A., Clark, B., Clemett, S., Gold, R., McKay, D., Murchie, S., Mustard, J., Papike, J., Schultz, P., Thomas, P., Tuzzolino, A., Yeomans, D., Yoder, C., Zolensky, M., Barnouin-Jha, O., Domingue, D., 1999. Aladdin: exploration and sample return of Phobos and Deimos. *Lunar Planet. Sci.* 30 (abstract #1155).
- [3] Murchie, S., Eng, D., Chabot, N., Guo, Y., Arvidson, R., Trebi-Ollennu, A., Seelos, F., Adams, E., Fountain, G., 2012. Merlin: Mars–Moon exploration, reconnaissance and landed investigation. *Acta Astronaut.*, <http://dx.doi.org/10.1016/j.actaastro.2012.10.014>.

FEATURES OF THE DYNAMICAL EVOLUTION OF NEAR-EARTH ASTEROID PAIRS

E.S. Koren, E.D. Kuznetsov

Ural Federal University, Lenina Avenue, 51, Yekaterinburg, 620000, Russia, eduard.kuznetsov@urfu.ru, modaeru@gmail.com

Keywords:

Asteroid pairs, numerical simulation, Yarkovsky effect, Kholoshevnikov metrics, Hill radius, escape velocity.

Introduction:

The dynamical evolution of asteroids pairs on close orbits has been studied for more than 10 years. Such asteroid pairs may be of a common origin. They can be formed as a result of the ejection of fragments of the large asteroids substance during non-catastrophic collisions of these asteroids with other small bodies. Asteroid pairs also can be formed in the process of crushing an asteroid under the action of the YORP effect, and as a result of the decay of binary and multiple systems of asteroids due to the BYORP effect. Analysis of asteroid pairs distribution shows that close pairs are concentrated in the main asteroid belt, but they are not found among the known near-Earth asteroids. The reason may be the gravitational scattering of the forming asteroid pairs due to approaches with the terrestrial planets.

In order to study the mechanisms of gravitational scattering, dynamical evolution of asteroid pairs on close orbits has been investigated in the terrestrial planet region. Evolution in the past is considered for several asteroid pairs: (3200) Phaethon, (155140) 2005 UD, (225416) 1999 YC, 2012 KT42, and others. The cluster 3200–155140–225416 could be formed by rotational fission of a critically spinning parent body. We investigate the evolution of this group of asteroids in order to estimate the time when these pairs appeared.

Method:

Numerical modeling of the motion of asteroid pairs was performed for 200 kyr into the past, using the code Orbit9 of the OrbFit software [1]. Orbital elements of the asteroids, taken from the AstDyS database (Asteroids Dynamic Site1), for the epoch $T_0 = \text{MJD}58400$ (00h 00m 00s 09/10/2018), were used as initial ones. The equations of motion of the asteroid, the eight major planets and the dwarf planet Pluto were integrated together. Oblateness of the Sun, relativistic effects and semimajor axis drift due to the Yarkovsky effect were also taken into account.

In order to take the Yarkovsky effect into account, we tried to estimate the maximum values of the semimajor axis drift $\frac{da}{dt}$ for asteroids of the group, using

physical parameters and $\frac{da}{dt}$ of asteroid (101995) Bennu, which are well-known at the moment [2]:

physical parameters and $\frac{da}{dt}$ of asteroid (101995) Bennu, which are well-known at the moment [2]:

$$\left(\frac{da}{dt}\right) = \left(\frac{da}{dt}\right)_B \frac{\sqrt{a_B(1-e_B^2)} D_B \rho_B \cos\phi}{\sqrt{a}(1-e^2) D \rho \cos\phi_s} \frac{A}{1-A_B}$$

Here e is the eccentricity of the orbit, D is the diameter of asteroid, ρ is the bulk density of asteroid, ϕ is the obliquity (angle between the spin axis and the normal to the orbit plane), and A is the Bond albedo ($A = \frac{1}{3} p_v$,

where p_v is the geometric albedo). The symbols with a "B" refer to asteroid

(101995) Bennu. For asteroid Bennu: $\left(\frac{da}{dt}\right)_B = (19 \pm 0.1) \cdot 10^{-4}$ au/Myr,

$$D_B = (0.492 \pm 0.020) \text{ km}, \quad \rho_B = (1.26 \pm 0.07) \text{ g/cm}^3, \quad \rho_{V_B} = 0.046 \pm 0.005, \\ \phi_B = (175 \pm 4).$$

The search of the new groups of asteroids on close orbits was performed using the Kholshvnikov metrics ζ_2 , which is the distance between two orbits in the five-dimensional space of Keplerian orbits [3,4]. The group was defined as a group, if $\zeta < 0.04 \text{ au} \frac{1}{2}$ for each pair in the group.

Results:

We estimated the maximum absolute value of the semimajor axis drift $\frac{da}{dt}$. If we

do not know the inclination of the asteroid rotation axis to the orbital plane,

we consider both cases with $+\left(\frac{da}{dt}\right)_{\max}$ and with $-\left(\frac{da}{dt}\right)_{\max}$, a case with

a half of $\left(\frac{da}{dt}\right)_{\max}$, and also a zero drift case. For (3200)Phaethon, we accept

three cases: nominal drift value, $\left(\frac{da}{dt}\right)_{\min}$ and $\left(\frac{da}{dt}\right)_{\max}$ (within the standard

deviation). So, for (3200)Phaethon: $\frac{da}{dt} = -(6.9 \pm 1.9) \times 10^{-4} \text{ au/Myr}$ [5].

Table 1 shows the estimations of the close approach moments (Δt from MJD58400 to backward), the relative distance Δr , and the relative velocity Δv , as well as the rates of the semimajor axis drift $\frac{da}{dt}$ for both aster-

oids of the pair, the Hill radius R_H for the primary asteroids of the pairs, and the escape velocity v_{esc} for the secondary asteroid with respect to the primary asteroid. For (3200) Phaethon, radius of the Hill sphere is accepted to be 78 km at the distance equal to the value of semimajor axis [6]. For aphelion $R_H = 113 \text{ km}$, and for perihelion $R_H = 6.6 \text{ km}$. The escape velocity on the surface of the Hill sphere in aphelion $v_{\text{esc}} = 1.29 \text{ m/s}$, in perihelion $v_{\text{esc}} = 1.68 \text{ m/s}$. For $R_H = 78 \text{ km}$, $v_{\text{esc}} = 1.55 \text{ m/s}$.

Table 1. Approaches of asteroids for pairs with close values of the Kholshvnikov metrics

Asteroid 1 (Primary) — Asteroid 2 (Secondary)	$\left(\frac{da}{dt}\right)_1$, au/Myr	$\left(\frac{da}{dt}\right)_2$, au/Myr	Δt , years	Δr , km	R_H , km	Δv , m/s	v_{esc} , m/s
(3200)Phaethon — (155140) 2005 UD	6.9E-04	9.8E-05	82678	3 329341	113	11.77	1.29
(3200) Phaethon — (225416) 1999 YC	6.9E-04	1.2E-04	166522	1 563532	113	7.22	1.29
(3200) Phaethon — 2012 KT42	6.9E-04	0.4E-03	104758	3 672321	113	12.27	1.29

We have considered only nominal trajectories, and we haven't found any close approaches within 200 kyr. Further, it is planned to increase the integration interval up to 400 kyr, and to consider the nearest clones of the trajectories within the limits of orbital elements definition errors.

The Yarkovsky effect and well-determined orbital elements was required to take into account accurately to carry out precise simulation of the dynamical evolution of the asteroid pairs. Determination of physical and rotational parameters of asteroids as well as precise orbit determination are needed to solve this problem.

In addition, we found some new groups of asteroids using the Kholshchevnikov metrics for further consideration: the first one consists of 2010 CL35, 2008 EK60, 2006 DY217; the second one consists of 1999 TS224, 2007 RW5, 2009 SK141.

Acknowledgments:

The study was funded by RFBR (the research project no. 18-02-00015)

References:

- [1] OrbFit Consortium, OrbFit: Software to Determine Orbits of Asteroids. Astrophysics Source Code Library. 2011. arXiv:1106.015.
- [2] Del Vigna A., Faggioli L., Milani A. et al. Detecting the Yarkovsky effect among near-Earth asteroids from astrometric data // *Astronomy and Astrophysics*. 2018. V. 617. Article id. A61.
- [3] Kholshchevnikov K.V., Kokhirova G.I., Babadzhanov P.B., Khamroev U.H. Metrics in the space of orbits and their application to searching for celestial objects of common origin // *Monthly Notices of the Royal Astronomical Society*. 2016. V. 462. P. 2275–2283.
- [4] Kuznetsov E., Safronova V. Application of metrics in the space of orbits to search for asteroids on close orbits // *Planetary and Space Science*. 2018. V. 157. P. 22–27.
- [5] Hanuš J., Vokrouhlický D., Delbo' M. et al. (3200) Phaethon: Bulk density from Yarkovsky drift detection // *Astronomy and Astrophysics*. 2018. V. 620. Article id. L8.
- [6] Jewitt D., Mutchler M., Agarwal J., Li J. Hubble Space Telescope Observations of 3200 Phaethon at Closest Approach // *The Astronomical Journal*. 2018. V. 156. P. 238.

SEARCH FOR YOUNG ASTEROID PAIRS WITH CLOSE ORBITS

E.D. Kuznetsov¹, A.E. Rosaev², E. Plavalova³, V.S. Safronova¹, M.A. Vasileva¹

¹ Ural Federal University, Lenina Avenue, 51, Yekaterinburg, 620000, Russia, eduard.kuznetsov@urfu.ru, vika483@bk.ru, maxa1907@icloud.com;

² Yaroslavl State University, Sovetskaya Street, 14, Yaroslavl, 150000 Russia, hegem@mail.ru;

³ Mathematical Institute of the Slovak Academy of Sciences, [Stefanikova 848/49, 81473, Bratislava, Slovakia](#) plavalova@komplet.sk

Keywords:

Asteroid pairs, numerical simulation, Yarkovsky effect, Kholshchevnikov metrics, Hill radius, escape velocity.

Introduction:

Recently, a significant interest is the study of close pairs of asteroids, very likely having a common origin [1–3]. Pairs can be formed by collisional disruptions of massive asteroids. YORP-induced spin up may lead to rotational fission of fast spinning asteroids. In this case, the disparate fragment must exceed the escape velocity under the effect of the centrifugal force. Break-ups of binary or multiple asteroid systems could also result in the formation of paired asteroids with close orbits. Examination of the dynamical evolution of asteroid pairs with close orbits allows estimating their ages. If an asteroid pair has been produced by fragmentation, of particular interest are physicochemical properties of the relatively young surface, which has had brief contact with the space environment.

Method:

The search of candidates for young asteroid pairs has been carried out by means of the computation of the values of the Kholshchevnikov metrics ζ_2 and ζ_5 [4]. The metric ζ_2 is the distance between two orbits in the five-dimensional space of Keplerian orbits. The metric ζ_5 is a distance in three-dimensional factor-space of positional orbital elements. Osculating elements of orbits were used to calculate the metric ζ_2 and proper elements of orbits were used to calculate the metric ζ_5 . Orbital elements of asteroids have been taken from Asteroids Dynamic Site — AstDyS¹. Criteria for finding the new young asteroid pairs are $\zeta_2 < 0.004 \text{ au}^{1/2}$, $\zeta_5 < 0.001 \text{ au}^{1/2}$, and $\zeta_2 - \zeta_5 < 0.001 \text{ au}^{1/2}$. Also, we consider some asteroid pairs with common origin from [5].

To study the dynamical evolution of some selected close asteroid pairs, the equations of the motion of the systems were numerically integrated 1 Myr into the past, using the N-body integrator Mercury [6].

We made three series of integration. In the first, we use only major planets perturbations. In the second we add Ceres, Vesta, Juno, and Pallas. In the third series of our numeric integration, we try to estimate the non-gravitational Yarkovsky effect. In addition to distance during the encounter, we perform calculation relative velocity along with integration by Nesvorný and Vokrouhlický [7] and by our previous paper [8] expression.

We perform numerical integrations of the orbits of all pairs of asteroids which were selected using the Kholshchevnikov metrics over 100 kyr backward in time with the code known as Orbit91 [9]. Major planets' perturbations, oblateness of the Sun, relativistic effects and semimajor axis drift due to the Yarkovsky effect were taken into account. We used the relation between drift value and physical parameters of asteroid (101995) Bennu and asteroids' parameters in order to estimate their maximal drift values. Evolution scenarios with altered semimajor axis drift values were investigated. The moment of pair formation corresponds to the conditions that the distance between asteroids has the same order as the Hill radius and the relative velocity has comparable value with the escape velocity.

Results:

Using the Kholshchikov metrics, we found six new members of Rampo family (2009 SR371, 2013 RL101, 2013 VC30, 2015 TA367, 2015 TM372, 2017 UH21) which did not list in [1]. One new member of Hobson family (2017 SQ83) was detected that did not list in [2]. The two new asteroid clusters were discovered that comprising three asteroids ((381362) 2008 EP15, (405843) 2006 BT227, 2012 XC32 and (338073) 2002 PY38, 2012 TZ97, 2016 SQ14) in each.

We considered conditions of the asteroids approaches for the asteroid pairs with close values of the Kholshchikov metrics and . Table 1 shows the estimations of the close approach moments (Δt from MJD58400 to backward), the relative distance Δr , and the relative velocity Δv , as well as the rates of the semimajor axis drift da/dt for both asteroids of the pair, the Hill radius R_H for the primary asteroids of the pairs, and the local escape velocity for the secondary asteroid with respect to the primary asteroid.

Table 1. Approaches of asteroids for pairs with close values of the Kholshchikov metrics ρ_2 and ρ_5 .

Asteroid 1 (Primary) — Asteroid 2 (Secondary)	$\left(\frac{da}{dt}\right)_1$, au/Myr	$\left(\frac{da}{dt}\right)_2$, au/Myr	Δt , years	Δr , km	R_H , km	Δv , m/s	v_{esc} , m/s
(355258) 2007 LY4 — (404118) 2013AF40	-0.0012	-0.00081	8200	2029	136	0.18	0.005
(53576) 2000 CS47 — (421781) 2014 QG22	-0.00015	0.00089	6121	5738	381	0.85	0.014
(180906) 2005 KB6 — (217266) 2003 YR67	0.00064	0.00061	11788	2199	180	0.16	0.008
(87887) 2000 SS286 — (415992) 2002 AT49	0.00011	0.00019	5635	1133	621	0.06	0.049
(320025) 2007 DT76 — (489464) 2007 DP16	-0.00016	-0.00032	1632	1218	696	0.11	0.054

Table 2 presents the estimations of ages of asteroid pairs. We used the N-body integrator Mercury. The exception is the pair (46829) McMahan–2014 VR4 that we integrated both Mercury and Orbit9. In some cases, we obtain for the pair age values very different from the values in paper [5] (boldface typed pairs in Table 2). For example, if the Yarkovsky effect produces (46829)

McMahan's semimajor axis drift $\frac{da}{dt} = -1.8 \dots 10^{-5}$ au/Myr then the estimation of the age of this pair is 26 kyr only. This problem required the future careful studying in each case.

The Yarkovsky effect was required to take into account accurately to carry out precise simulation of the dynamical evolution of the asteroid pairs. Determination of physical and rotational parameters of asteroids is needed to solve this problem.

Table 2. Estimations of ages of asteroid pairs

#pair	Asteroid 1 (Primary)	Asteroid 2 (Secondary)	Age, kyrs [5]	Age, kyrs
1	(5026) Martes	2005 WW113	18	18
2	(1741) Giclas	(258640) 2002 ER36	200	180
3	(3749) Balam	(312497) 2009 BR60	400	270
4	(46829) McMahon	2014 VR4	800	150 (Mercury) 950(Orbit9)
5	(4765) Wasserburg	(350716) 2001 XO105	200	100

Acknowledgments:

The study was funded by RFBR (the research project no. 18-02-00015)

References:

- [1] Pravec P., Vokrouhlický D. Significance analysis of asteroid pairs // *Icarus*. 2009.V. 204. P. 580–588.
- [2] Rosaev A., Plavalova E. On the young family of 18777 Hobson // *Icarus*. 2017. V. 282. P. 326–332.
- [3] Kuznetsov E., Safronova V. Application of metrics in the space of orbits to search for asteroids on close orbits // *Planetary and Space Science*. 2018. V. 157. P. 22–27.
- [4] Kholshevnikov K.V., Kokhirova G.I., Babadzhanov P.B., Khamroev U.H. Metrics in the space of orbits and their application to searching for celestial objects of common origin // *Monthly Notices of the Royal Astronomical Society*. 2016. V. 462. P. 2275–2283.
- [5] Pravec P., Fatka P., Vokrouhlický D. et. al. Asteroid pairs: A complex picture // *Icarus*. <https://doi.org/10.1016/j.icarus.2019.05.014>.
- [6] Chambers J.E. A hybrid symplectic integrator that permits close encounters between massive bodies // *Monthly Notices of the Royal Astronomical Society*. 1999. V. 304. P. 793–799.
- [7] Nesvorný D., Vokrouhlický D. New candidates for recent asteroid breakups // *The Astronomical Journal*. 2006. V. 132. P. 1950–1958.
- [8] Rosaev A., Plavalova E. On relative velocity in very young asteroid families // *Icarus*. 2018. V. 304. P. 135–142.
- [9] Orfit Consortium, Orfit: Software to Determine Orbits of Asteroids. *AstrophysicsSource Code Library*. 2011. arXiv:1106.015.
- [10] Del Vigna A., Faggioli L., Milani A. et al. Detecting the Yarkovsky effect among near-Earth asteroids from astrometric data // *Astronomy and Astrophysics*. 2018. V. 617. Article id. A61.

DUSTY PLASMAS IN ENVIRONMENTS OF MARS

S.I. Popel, A. P. Golub', A.V. Zakharov, L.M. Zelenyi

*Space Research Institute of the Russian Academy of Sciences (IKI), 84/32
Profsoyuznaya Str, Moscow 117997, Russia, popel@iki.rssi.ru*

Keywords:

Mars, Phobos, Deimos, ionosphere, dusty plasmas, photoelectric effect

Introduction:

Investigation of dusty plasma systems beyond the Earth's atmosphere is of considerable interest not only from the viewpoint of understanding and describing the processes occurring in nature, but also in connection with the planning of space missions, including those to Mars and its satellites, as well as with the interpretation of data obtained in the existing and future space missions. In the Martian atmosphere, the presence of dust grains was never questioned, because grains of the Martian soil can be lifted from the surface due to various processes. The dust component can play a substantial (in some cases, decisive) role in the radiation balance. Dust grains get charged under the action of solar radiation, interaction with charged particles of the atmosphere and solar wind, triboelectric effect in dust devils, and other factors.

The Martian atmosphere is somewhat similar to the Earth's atmosphere. In particular, there is an ionosphere on Mars with the maximum electron density of up to 10^5 cm^{-3} at altitudes of 135-140 km. The lower boundary of the ionosphere lies at 80 km; however, it can come down to 65 km in some cases [1]. This fact points to the possibility of the development of dusty plasma processes in the atmosphere of Mars that have a certain similarity with the processes of the formation of dusty plasma clouds occurring in the Earth's atmosphere [2]. An adequate description of dusty plasma processes in the atmosphere of Mars appears to be very important and timely from the point of view of developing its models.

Interest in investigation of the Martian satellites — Phobos and Deimos stems from the fact that the satellites of Mars are more accessible for manned missions than Mars itself due to their weak gravity. For example, the gravitational acceleration on Phobos is about 0.0057 m/s^2 , and landing a spacecraft on its surface is more reminiscent of docking to another spacecraft rather than landing on a planet. According to observations made from the Viking [3, 4] as well as Phobos — 2 and Mars—Express spacecrafts [5], the surface of Deimos is covered with a dust consisting of small separate regolith grains formed as a result of bombardment of the surface by microscopic meteoroids. Weak gravity enhances the role of dust on Phobos and Deimos, because even a small perturbation can lead to the formation of a massive dust cloud above the surface of these Martian satellites. Among the aims of the future Boomerang (Phobos—Grunt 2) mission are to detect dust particles in an orbit around Mars and near the surface of Phobos and to determine the main parameters of dust particles (momentum, mass, velocity, and charge). Furthermore, the measurement of the plasma parameters and the determination of the local electric field near the surface of Phobos are expected. To these ends, piezoelectric impact sensors, whose operation is based on the impact action of a dust particle, and probes for measurements of the parameters of the plasma and the local electric field near the surface of Phobos will be used.

The purpose of this work is a brief review of the results of studies of fine particles and dusty plasmas in the atmosphere of Mars and in the vicinity of its satellites Phobos and Deimos, carried out recently at the Space Research Institute of the Russian Academy of Sciences.

Dust in the atmosphere of Mars:

The atmosphere of Mars is much thinner than the Earth's atmosphere, and its ability to hold dust grains for a long time is very low. High dust number density is observed only during dust storms or other events that lift dust

from the Martian surface. The data on the presence of dust in the Martian atmosphere were obtained from Mars rovers and instruments installed on orbital stations. However, estimates made by different methods yield somewhat different values of the main physical parameters of dust grains [6]. These discrepancies can be explained, e.g., by the presence of clouds of condensed grains. At altitudes of 100 km in the mesosphere, where the temperature is sufficiently low for carbon dioxide freezing, clouds formed of dust grains with a size of about 100 nm (similar to noctilucent clouds in the Earth's atmosphere) were observed by means of the SPICAM infrared spectrometer installed on Mars — Express orbiter [7]. In addition, clouds of micron-size grains were observed at altitudes of about 80 km by means of the OMEGA spectrometer onboard Mars — Express [8]. A theory study of the role of condensation processes in the formation of dusty plasmas in the Martian ionosphere has been carried out in [9]. The calculations within the framework of the model [9] allow us to draw the following main conclusions concerning clouds of condensed particles.

- 1) Ice particles of CO_2 , which are initially in the zone of supersaturation of CO_2 vapor, collect on their surfaces most of the CO_2 vapor and are precipitated downward together with absorbed CO_2 molecules. Particles of different dust layers absorb different amounts of carbon dioxide molecules. This leads to the possibility of the interfusion of layers and the formation of dust clouds. The characteristic time for the sedimentation of solid dust particles consisting of CO_2 molecules in the condensation zone is about several minutes. Below the condensation zone, the particles evaporate. Accordingly, the characteristic time for the sedimentation of dust in the condensation zone determines the characteristic time for the existence of dust clouds similar to noctilucent clouds [2] in the Earth's ionosphere. In the condensation zone, particles of CO_2 ice can reach sizes of the order of 100 nm. This value is in accordance with the data of observations performed by the Mars — Express orbiter using the SPICAM IR spectrometer [7]. In the daytime, dust particles can acquire charges of the order of 100 e, where -e is the charge of an electron.
- 2) Similar to the situation at the Earth, particles with a characteristic size of several nanometers may exist in the Martian ionosphere over the condensation zone due to the bombardment of Mars by micrometeorites. Those particles that are initially located above the upper boundary of the condensation zone (even when reaching the condensation zone in definite time) cannot be significantly increased in size due to the insufficient (residual) amount of CO_2 molecules in this zone. These nanoscale particles exist at altitudes from 112 to 115 km during several hours, which can lead to phenomena in the atmosphere of Mars, which are similar to polar mesosphere summer echoes [2] at the Earth.

Dusty plasmas at Phobos and Deimos:

In accordance with theory results [10, 11], due to the lower gravity, substantially larger dust grains ($a \sim 1 \mu\text{m}$) are lifted above the surfaces of Phobos and Deimos relative to those lifted above the surface of the Moon ($a \sim 0.1 \mu\text{m}$). In this case, the role of adhesion, which seems to significantly hamper the detachment of dust grains from the lunar surface is substantially reduced on Phobos and Deimos. In fact, it can be stated that the formation of dusty plasmas above the surfaces of Phobos and Deimos is related to photoelectric and electrostatic processes. The role of meteoroids in the formation of dusty plasmas in the near-surface layer above each of the satellites of Mars also turns out to be much smaller relative to the conditions existing on the Moon. At the same time, at long distances from Phobos and Deimos (substantially larger than their linear dimensions of $\sim 10 \text{ km}$), the effect of meteoroids leads to the formation of a dust halo consisting of grains with a size of about $10 \mu\text{m}$ and number density of $N_d \sim 10^3 \text{ km}^{-3}$ [12]. This density is much smaller than the number density of dust grains, which is established near the surfaces of Phobos and Deimos due to photoelectric and electrostatic processes. As to the specific features of dusty plasma near the surface of Deimos compared to that near Phobos, it should be noted that the size

and electric charge of dust grains at certain altitudes above the surface of Deimos are larger than those at the same altitudes above the surface of Phobos. In this case, the number densities of dust grains at the same altitude above Deimos and Phobos are nearly the same. This is related to the fact that the gravitational acceleration on Deimos is smaller than that on Phobos.

Acknowledgments:

This work was supported in part by the Russian Foundation for Basic Research (project no. 18-02-00341-a) and within Major Project of RF Ministry of Education and Science (Moscow, Russia) MP19-270 "Problems of the Origin and Evolution of the Universe with the Use of Methods of Ground-Based Observations and Space Research".

References:

- [1] Pätzold M., Tellmann S., Häusler B., et al., A sporadic third layer in the ionosphere of Mars // *Science*. 2005. V. 310. No. 5749. P. 837-839.
- [2] Klumov B.A., Morfill G.E., Popel S.I., Formation of structures in a dusty ionosphere // *J. Exp. Theor. Phys.* 2005. V. 100. No. 1. P. 152-164.
- [3] Thomas P. Surface features of Phobos and Deimos // *Icarus*. 1979. V. 40. No. 2. P. 223-243.
- [4] Thomas P., Veverka J. Downslope movement of material on Deimos // *Icarus*. 1980. V. 42. No. 2. P. 234-250.
- [5] Zakharov A., Horányi M., Lee P., et al. Dust at the Martian moons and in the circummartian space // *Planet. Space Sci.* 2014. V. 102. P. 171-175.
- [6] Dlugach Z.M., Korabev O.I., Morozhenko A.V., et al., Physical properties of dust in the Martian atmosphere: analysis of contradictions and possible ways of their resolution // *Solar Syst. Res.* 2003. V. 37, No. 1, P. 1-19.
- [7] Montmessin F., Bertaux J.L., Quémerais E., et al. Subvisible CO₂ ice clouds detected in the mesosphere of Mars // *Icarus*. 2006. V. 183. No. 2. P. 403-410.
- [8] Montmessin F., Gondet B., Bibring J.P., et al. Hyperspectral imaging of convective CO₂ ice clouds in the equatorial mesosphere of Mars // *J. Geophys. Res.* 2007. V. 112. P. E11S90.
- [9] Dubinskii A.Yu., Reznichenko Yu.S., Popel S.I. On formation and evolution of dusty plasma structures in ionospheres of Earth and Mars // *Plasma Phys. Rep.* 2019. V. 45. No. 10, in press.
- [10] Popel S. I., Golub' A. P., Zakharov A. V., Zelenyi L. M. Dusty plasma near the surface of Phobos // *JETP Lett.* 2017. V. 106. No. 8. P. 485-490.
- [11] Popel S. I., Golub' A. P., Zelenyi L. M., Dusty plasma near the Martian satellite Deimos // *Plasma Phys. Rep.* 2018. V. 44. No. 8. P. 723-728.
- [12] Krivov A. V., Hamilton D. P. Martian dust belts: Waiting for discovery // *Icarus*. 1997. V. 128. No. 2. P. 335-353.

PRESENT SOLAR OBSERVATIONS — A CATALYST OF PROCESSES AT THE BIRTH OF SOLAR AND DEATH OF STELLAR SYSTEM

I. Roth

Space Sciences University of California

Analysis of heliospheric anomalous abundances of energetic elements and isotopes points to the existence of an efficient physical mechanism through nuclear or resonant plasma interactions. When processes involving nuclear reactions do not show consistency with experiments, one must envision acceleration mechanisms involving plasma processes in the presence of solar or interplanetary magnetic field. The most spectacular heliospheric enhancement with unusual abundances involves the ^3He isotope and heavy elements (mainly Mg, Ne, Si, and Fe) in impulsive solar flares. The cosmic value of coronal He isotope ratio $^3\text{He}/^4\text{He} \sim 2.0 \cdot 10^{-4}$ is enhanced during impulsive flares by several orders of magnitude due to resonant wave-particle interaction with electromagnetic ion cyclotron (emc) waves. These observations may help in explaining two astrophysical observations (1) at the birth of solar system formation and (2) at the death of a stellar system.

Observations of Calcium-Aluminum Inclusions in meteorites with enhanced abundance of ^{26}Mg . This stable isotope requires existence of the parent radioactive ^{26}Al isotope, which decays into the observed fossil element ^{26}Mg with lifetime of ~ 1 Myears. The observations of fossil radioactive elements in meteorites is connected intimately to the formation of the solar system. The young solar-like stars emit copious amount of x-rays indicating intense magnetic activity. Their irradiation of pre-solar grains by solar cosmic rays ($\text{H}, ^4\text{He}$) which were accelerated in CME shocks may give the correct yield of the radioactive- ^{41}Ca and ^{53}Mn , but too low for ^{26}Al . Supernova abundances are also at odds with other element abundances. Possible solution would include the young Sun with strong flare activity, resulting in large enhancement of MeV ^3He . These energetic ^3He ions are crucial in the formation of ^{26}Al through $^{24}\text{Mg}(^3\text{He}, p)^{26}\text{Al}$ and similar reactions. Therefore, plasma acceleration of rare isotopes in the early solar system contributes to selective formation of radioactive elements which are observed as fossil elements in the meteorites.

Observation of enhanced abundances of ^3He in planetary nebulae. The presently observed ^3He abundance in galactic HII regions is similar to the Big Bang Nucleosynthesis yield of $^3\text{He}/\text{H} \sim 2.0 \cdot 10^{-5}$, in contrast to the evolutionary galactic models, which enhance this ratio. An extra nonstandard rotation-induced mixing in a red giant branch, required to explain the anomaly in $^{12}\text{C}/^{13}\text{C}$, which decreases also the ratio $^3\text{He}/\text{H}$, does not support the measurements of the known planetary nebulae which show abundance ratio of $^3\text{He}/\text{H} \sim 10^{-4}$ - 10^{-3} for the inferred mass of the progenitor star with $M < 2 M_{\odot}$, in contrast to the nonstandard mixing. It is suggested therefore that enrichment of a subset of minority elements at progenitor star with a low mass and intense magnetic activity causes the $^3\text{He}/^4\text{He}$ enhancements, solving partly the "astrophysical ^3He problem", with important implications for galactic evolution and cosmology.

WHAT IS A MAIN DRIVER FOR ION LOSSES AT MARS AND WHAT IS A ROLE OF THE CRUSTAL MAGNETIC FIELD?

E. Dubinin¹, M. Fraenz¹, M. Pätzold², O. Vaisberg³, L. Zelenyi³,
J. McFadden⁴, J. Halekas⁵, J. Connerney⁶, F. Eparvier⁷

¹ *Max-Planck-Institute for Solar System Research, Germany;*

² *Rhenish Institute for Environmental Research, Germany;*

³ *Institute of Space Research, Moscow, Russia;*

⁴ *University of California, Berkeley, USA;*

⁵ *University of Iowa, USA;*

⁶ *NASA Goddard Space Flight Center, USA;*

⁷ *Laboratory for Atmospheric and Space Physics, University of Colorado
Boulder, Boulder, Colorado, USA*

Keywords:

Mars, Solar wind, Solar EUV flux, Ion losses, Crustal magnetic field

Introduction:

The paradigm is that Mars loses the ionosphere by ablation process forced by solar wind. However, there is another important driver — solar irradiance which carries a much higher energy. We will discuss the role of both drivers for ion losses. It will be shown that processes of ion escape driven by the solar wind and the EUV radiation are very different. It occurs that solar irradiance is more efficient driver. The EUV radiation not only heats and ionizes the atmospheric gases. The subsequent energy transfer process drives ion acceleration by the ambipolar electric field, their outflow and escape. There is also no consensus about the role of the crustal magnetic field. Whether it shields the ionosphere from solar wind and weakens ablation or enhances ion outflow by the processes similar to ones operating at the Earth. We will show that answer on this question depends on the solar wind conditions and the IMF orientation.

THIN CURRENT SHEETS OF SUB-ION SCALES OBSERVED BY MAVEN IN THE MARTIAN MAGNETOTAIL

L.M. Zelenyi¹, E.E. Grigorenko¹, G. DiBraccio², V.N. Ermakov¹,
S.D. Shuvalov¹, H.V. Malova^{3,1}, V.Y. Popov^{4,5,1}

¹ Space Research Institute of RAS, Moscow, Russia

² NASA Goddard Space Flight Center, Greenbelt, Maryland, USA

³ Moscow State University, Moscow, Russia

⁴ Higher School of Economics, National University, Moscow, Russia

⁵ Department of Physics of Moscow State University, Moscow, Russia

Current Sheets (CSs) play a crucial role in the storage and conversion of magnetic energy in planetary magnetotails. Using high resolution magnetic field data from MAVEN spacecraft we report the existence of Super Thin Current Sheets (STCSs) in the Martian magnetotail. The typical half-thickness of the STCSs is ~ 5 km, and it is much less than the gyroradius of thermal protons (ρ_p). The STCSs are embedded into a thicker sheet with $L \geq \rho_p$ forming a multiscale current configuration. The formation of STCS does not depend on ion composition but it is controlled by the small value of the normal component of the magnetic field at the neutral plane (BN). A number of the observed multiscale CSs are located in the parametric map close to the tearing-unstable domain and, thus, the inner STCS can provide an additional free energy to excite ion tearing mode in the Martian magnetotail.

INDUCED MAGNETIC FIELD IN MARS IONOSPHERE, SOLAR WIND AND AURORAE

S. Jimenez¹, M. Ramírez-Nicolás², D. Usero², P.J. Pascual³, M.P. Velasco¹, L. Vázquez²

¹ Universidad Politécnica de Madrid, Spain

² Universidad Complutense de Madrid, Spain

³ Universidad Autónoma de Madrid Spain, s.jimenez@upm.es

Keywords:

Mars, Dipolar/Quadrupolar magnetic field, ionosphere, crustal magnetic field, Solar wind, aurorae, MARSIS.

Introduction:

Using data from the Mars Advanced Radar for Subsurface and Ionospheric Sounding (MARSIS) onboard Mars Express [1], we retrieve the magnetic field in Mars ionosphere [2]. We consider the effect due to the crustal fields and to the Solar wind. This is relevant in the context of the observed aurorae in Mars under Solar storms, either localized above crustal fields [3] or diffuse above both the nocturnal and the diurnal zones of the planet [4]. We also aim at considering the information arising from crossing the corresponding datasets from Spicam and MAVEN.

In relation to that, we study the mechanism of particle confinement that is at the basis of the aurora, considering dipolar and quadrupolar terms [5, 6]. Quadrupolar magnetic fields provide a mechanism similar to that of dipolar fields that enables confinement. For fields with similar strength, the quadrupolar field appears to bound more energetic particles than the dipolar.

References:

- [1] R. Orosei, R.L. Jordan, D.D. Morgan, M. Cartacci, A. Cicchetti, F. Duru, D.A. Gurnett, E. Heggy, D.L. Kirchner, R. Noschese, W. Kofman, A. Masdea, J.J. Plaut, R. Seu, T.R. Watters, G. Picardi. "Mars Advanced Radar for Subsurface and Ionospheric Sounding (MARSIS) after nine years of operation: A summary", *Planetary and Space Science*. 2015. V. 112, P. 9–114.
- [2] M. Ramírez-Nicolás, B. Sánchez-Cano, O. Witasse, P.-L. Blelly, L. Vázquez. "The effect of the induced magnetic field on the electron density vertical profile of the Mars' ionosphere: A Mars Express MARSIS radar data analysis and interpretation, a case study", *Planetary and Space Science*. 2016. V. 126. P. 49–62.
- [3] J.-L. Bertaux, F. Leblanc, O. Witasse, E. Quemerais, J. Lilensten, S.A. Stern, B. Sandel & O. Korabely, "Discovery of an aurora on Mars", *Nature* volume. 2005. V. 435. P. 790–794 .
- [4] J. Deighan, S.K. Jain, S. Chaffin, X. Fang, J.S. Halekas, J.T. Clarke, N.M. Schneider, A.I.F. Stewart, J.-Y. Chaufray, J.S. Evans, M.H. Stevens, M. Mayyasi, A. Stiepen, M. Crismani, W.E. McClintock, G.M. Holsclaw, D.Y. Lo, F. Montmessin, F. Lefèvre & B.M. Jakosky, "Discovery of a proton aurora at Mars", *Nature Astronomy* volume 2. 2018. P 802–807.
- [5] L. Vázquez, S. Jiménez, "Motion of a charge in a magnetic dipole field I. Painlevé, Analysis and a conservative numerical scheme", *Applied Mathematics and Computation* 25. 1988. P. 207–217.
- [6] M. Ramírez-Nicolás, D. Usero, M.P. Velasco, L. Vázquez, "Numerical study of a charged particle in a general magnetic field", *International Journal of Pure and Applied Mathematics*. 2016. No. 2, V. 106. P. 401–414.

KINETIC MONTE CARLO MODEL OF HIGH-ENERGY H/H+ PRECIPITATION INTO THE MARTIAN ATMOSPHERE

V.I. Shematovich¹, D.V. Bisikalo¹, J.-C. Gérard², B. Hubert²

¹ *Institute of Astronomy of the Russian Academy of Sciences, Moscow, Russia; shematov@inasan.ru*

² *Laboratoire de Physique Atmosphérique et Planétaire, STAR Institute, Université de Liège, Belgium*

Keywords:

Mars, solar wind, high-energy proton and hydrogen atom precipitation, auroral phenomena, atmospheric ultraviolet emissions, kinetic Monte Carlo model.

Introduction:

Observations with the SPICAM and ASPERA-3 instruments on board the ESA Mars Express and the IUVS spectrograph on board the NASA MAVEN spacecraft have identified three types of aurorae on Mars, two of them (electron diffuse and proton aurorae) profoundly different from comparable types on Earth and other planets.

The results of model calculations of precipitation of the high-energy protons and hydrogen atoms (H/H+) from solar wind and/or magnetosheath into the Martian atmosphere are presented. A modification of the kinetic Monte Carlo model [1, 2] developed earlier to analyze the data of the MEX/ASPERA-3 instrument onboard the ESA Mars Express and MAVEN/SWIA instrument onboard the NASA MAVEN spacecraft was used. In the presented modification of the kinetic model for the first time the arbitrary (three-dimensional) structure of the magnetic field of Mars is taken into account [3]. Because the local measurements of all three components of the magnetic field by MAVEN/MAG magnetometer are now available, it is possible to describe not only the flux of protons penetrating into the atmosphere, but also the deposition of the H/H+ flux along the spacecraft orbit, as well as the formation of the scattered by atmosphere upward fluxes of protons and hydrogen atoms. Comparison of the calculations and measurements of proton fluxes at low altitudes received by the MAVEN/SWIA instrument during the MAVEN deep-dip maneuvers allowed us to conclude about the efficiency of charge exchange processes between the solar wind protons and the extended hydrogen corona of Mars. It is also found that the induced magnetic field plays an important role in the formation of the upward (scattered by the atmosphere) proton flux and actually controls its value.

The developed kinetic Monte Carlo model of proton and hydrogen atom precipitation into the atmosphere of Mars will be used to calculate the brightness and line profiles of the atomic hydrogen emission in the Ly- α line for comparison with the observations of the recently discovered proton aurora [4] at Mars. For such calculations, the simultaneous measurements of the intensity of the induced magnetic field by the MAVEN/MAG magnetometer and the energy spectra of H/H+ fluxes precipitating into the Mars atmosphere measured by the MAVEN/SWIA analyzer will be used.

Acknowledgments:

This study was supported by the Russian Science Foundation (project 19-12-00370).

References:

- [1] Shematovich V.I., Bisikalo D.V., Diéval C., et al. Proton and hydrogen atom transport in the Martian upper atmosphere with an induced magnetic field // *J. Geophys. Res.* 2011. V. 116. P. A11320.
- [2] Bisikalo D.V., Shematovich V.I., Gérard J.-C., Hubert B. Monte Carlo simulations of the interaction of fast proton and hydrogen atoms with the Martian atmosphere and comparison with in situ measurements // *J. Geophys. Res.* 2018. V. 123. P. 58.
- [3] Shematovich V.I., Bisikalo D.V., Gérard J.-C., Hubert B. Kinetic Monte Carlo model of the precipitation of high-energy proton and hydrogen atoms into the Martian

atmosphere with taking into account the measured magnetic field // *Astron. Reps.* 2019. V. 63. No. 10 (in press).

- [4] Deighan J., Jain S.K., Chaffin M.S., et al. Discovery of proton aurora at Mars // *Nature Astronomy.* 2018. V. 2. P. 802.

THE FINE STRUCTURE OF THE INTERFACE BETWEEN THE MAGNETOSHEATH AND THE VENUSIAN INDUCED MAGNETOSPHERE

A. Fedorov¹, E. Knizhnikova¹, A. Grigoriev¹, S. Barabash²

¹ IRAP-UPS-CNRS, Toulouse, France

² IRF, Kiruna, Sweden

Keywords:

Venus, solar wind, mass loading, interplanetary magnetic field, induced magnetosphere boundary

There are two essential effects inherent to the interaction of non-magnetic bodies with the solar wind: (1) the generation of the planetary magnetosphere by the currents induced in the almost superconducting ionosphere and (2) the mass loading of the incident solar wind by a continuously ionized exosphere. Both effects alter the solar wind magnetic field and create a solar wind void near the planetary body. The mass loading and the direct interaction of the interplanetary magnetic field (IMF) with the ionosphere fill the void with accelerated planetary ions.

Several physical mechanisms lead to the formation of a separation boundary between the Venusian induced magnetosphere and the magnetosheath flow. Ionospheric currents create a “magnetic barrier” separating the solar wind and the induced magnetosphere. This boundary naturally extends to the Venusian wake as a boundary of the solar wind void, but on the nightside it loses some characteristic features and obtains more complexity.

To call this separator in the tail region we prefer to use a term “Induced Magnetosphere Boundary”. Actually this boundary does have so complex nature, thus to characterize it we have to investigate a broad region around the separator. The present paper is devoted to a detailed study of such interface region around the ionosphere of Venus on the nightside of the planet.

A FULLY KINETIC STUDY OF ELECTRON ACCELERATION AROUND A WEAK COMET

A.V. Divin¹, J. Deca², P. Henri³, A. Eriksson⁴, S. Markidis⁵, V. Olshevsky⁵

¹ St. Petersburg State University, St. Petersburg, Russia;

² Laboratory for Atmospheric and Space Physics (LASP), University of Colorado Boulder, 80303, USA;

³ LPC2E, CNRS, Orléans, 45071, France;

⁴ Swedish Institute of Space Physics, Uppsala, Sweden;

⁵ KTH Royal Institute of Technology, SE-100 44, Stockholm, Sweden

Keywords:

Particle-in-Cell (PIC) simulations; electron acceleration; ambipolar electric field; high-performance computing

Introduction:

Comets are small Solar system bodies, “ice balls” [1] composed of a mixture of rocks, dust and frozen volatiles and organics. The cometary nucleus becomes active when sufficiently close to the Sun as Solar radiation heats the nucleus’ surface. The slowly expanding atmosphere gets gradually ionised as it moves away from the nucleus. The newly-formed charged particles have nearly zero velocity with respect to the persistent supersonic magnetized solar wind, and as a result, the plasma flow experiences soft “mass-loading”. Most recently the ESA/Rosetta spacecraft accompanied a weak comet 67P, providing an unprecedented perspective into the evolution of a comet.

The dynamics of the cometary plasma have been studied extensively using numerical models to predict and explain the complex plasma observations. With the advent of modern high-performance supercomputers large scale three-dimensional simulations become possible. In order to understand Rosetta’s measurements and particle heating in the weak outgassing case it is of primary importance to include electron-scale kinetic physics in the model [2]. We performed numerical 3D full kinetic (PIC) simulations of a plasma source which mimics the kinetic-scale comet-solar wind interaction [3]. Our main finding is that the electron pressure gradient supports the ambipolar electric field which in turn confines the low-energy part of electron population. The accelerating parallel potential is generated, which controls the parallel electron temperature and total density. The population of passing electrons has temperatures on average of several times the solar wind temperature in weak comet case [4]. The high solar wind electron density near the comet compensates the charge imbalance, briefly trapping/ decelerating fast-moving electrons and confirming the coupled four-fluid scenario. As a result, such process substitutes electrons of cometary origin with the electrons of solar wind origin near the nucleus.

References:

- [1] Whipple, F. L. A comet model. I. The acceleration of Comet Encke // *Astrophys. J.* 111 (1950): P. 375–394.
- [2] Deca, J., Divin, A., Henri, P., Eriksson, A., Markidis, S., Olshevsky, V., & Horányi, M. (2017). Electron and Ion Dynamics of the Solar Wind Interaction with a Weakly Outgassing Comet // *Phys.Rev.Lett.*, 118(20), 205101
- [3] Deca, J., Henri, P., Divin, A., Eriksson, A., Galand, M., Beth, A., Ostaszewski, K. and Horányi, M., 2019. Building a weakly outgassing comet from a generalized Ohm’s law. *Phys. Rev. Let.*, 123(5), p.055101.
- [4] Nilsson, H., et al., Size of a plasma cloud matters the polarisation electric field of a small-scale comet ionosphere, *A. & A.*, 2018, V. 616, A50.

SIMILARITY OF THE SUBLIMATION ACTIVITY OF THE MAIN-BELT PRIMITIVE ASTEROIDS 704 INTERAMNIA, 24 THEMIS, AND 449 HAMBURGA AND SOLAR FLARES' INFLUENCE

V.V. Busarev, M.P. Scherbina, T.R. Irsambetova

Lomonosov Moscow State University, Sternberg Astronomical Institute (SAI MSU), University Av., 13, Moscow, 119992, Russian Federation; busarev@sai.msu.ru

Keywords:

Primitive asteroids, UVBRI-reflectance, ice sublimation, solar flares.

Introduction:

We confirmed sublimation activity near perihelion of 704 Interamnia and discovered similar activity of 24 Themis and 449 Hamburga, main-belt primitive asteroids. To study the phenomenon, a spectral method is used [1].

Observations and results:

24 Themis (C-type [2] or B-type [3]), 449 Hamburga (C-type [2]) and 704 Interamnia (F-type [2] or B-type [3]) were quite near perihelion in time of the observations that allowed to test presence of ices (predominately water ice) in their matter at elevated sub-solar temperatures due to the effect of ice sublimation. The effect leads to formation of a temporal subtle exosphere consisting of micron-sized particles of water ice which could be detected by optical methods. Relevant for the case dynamical parameters of asteroids in addition to eccentricity (e) are semi-major axis of the orbit (a) and orbit inclination (i). In particular, these are for 24 Themis: $a = 3.13617$ AU, $e = 0.124743$, $i = 0^\circ.752$; for 449 Hamburga: $a = 2.551006$ AU, $e = 0.172769$, $i = 3^\circ.085$; for 704 Interamnia: $a = 3.057946$ AU, $e = 0.154658$, $i = 17^\circ.310$ [4]. It should be also noted that these asteroids had close equatorial coordinates at our observations.

We used a spectrophotometric method of registration of asteroid sublimation activity. It will be discussed in more details in the next section. For obtaining UVBRI-reflectance of mentioned asteroids (at effective wavelengths 0.366, 0.436, 0.545, 0.641, and 0.800 μm), UVBRI-photometry of these bodies, solar analog star (HIP 29759) and standard stars were performed by means of 60-cm telescope and a CCD-camera in the Crimean Observatory of SAI MSU in March 2019. To control the stability of the spectral transparency of terrestrial atmosphere, standard stars on common with asteroids CCD-frames were utilized. Normalized UVBRI reflectance curves of 24 Themis, 449 Hamburga and 704 Interamnia on 17, 18, and 19 March are shown in figures 1–3, 7–9 and 13–15 followed by corresponding figures with records of relative intensity of standard stars. The latter show that atmospheric observational conditions were predominately stable.

Discussion and interpretation of the results:

Previously we have discovered a simultaneous sublimation activity of four main-belt primitive-type asteroids passing near perihelion, one of which was 704 Interamnia [1]. It points to a widespread character of this process among such asteroids and presence of ice (predominately H_2O) in their substance. Considerable eccentricity of orbits some of these bodies creates possibility to test presence of ice in the matter at elevated temperature. As demonstrated our study of reflectance spectra of four primitive asteroids with strong sublimation activity [7], a maximum arising at 0.4–0.65 μm is a diagnostic feature of the process. According to the Mie theory [8], spectral position of the maximum is determined by micron-sized spherical particles of H_2O ice scattering light.

Here we confirm sublimation activity of 704 Interamnia and report the detection of this process on 24 Themis and 449 Hamburga passing perihelion. It is important to note that presence of water ice was discovered on the surface of 24 Themis with IR-observations near 3 μm [7]. As seen from the UVBRI-reflectance curves on Figs 1 and 3, 7 and 9, 13 and 15 obtained

on 17 and 19 March, the asteroids demonstrated very similar spectral appearance: combination of a lower maximum (at $0.44 \mu\text{m}$) a higher one (at $0.66 \mu\text{m}$). We interpret those as light-scattering by submicron particles of H_2O ice (the first maximum) and micron-sized silicate particles (second). However, it should be confirmed by a special modeling of the light scattering and other conditions. Surprisingly, these curves are very similar for all three asteroids. Another strange thing is strictly different appearance of the UBVRi-reflectance curves of all asteroids on 18 March (Figs 2, 8 and 14). On this day, reflectance spectra of all asteroids looked as if the process of sublimation completely stopped, and they acquired the usual appearance. To show this, we compare the UBVRi-reflectance curves of Themis (Fig. 2) and Interamnia (Fig. 14) and their known SMASSII reflectance spectra [5, 6]. Let us try to explain the phenomenon.

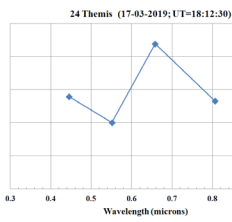


Fig. 1.

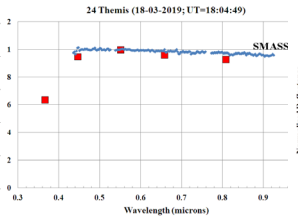


Fig. 2.

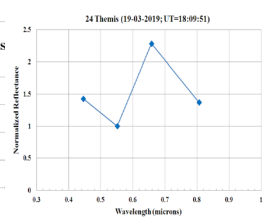


Fig. 3.

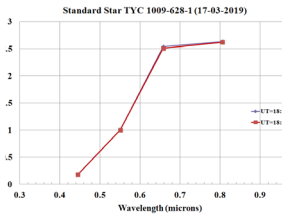


Fig. 4.

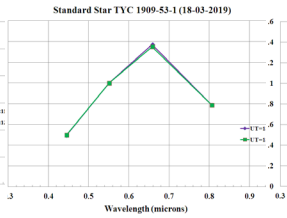


Fig. 5.

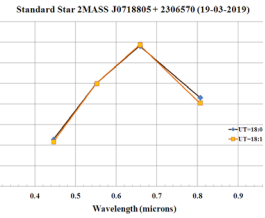


Fig. 6.

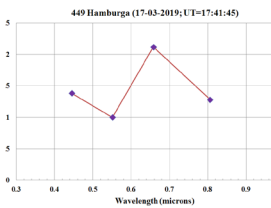


Fig. 7.

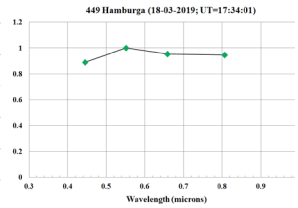


Fig. 8.

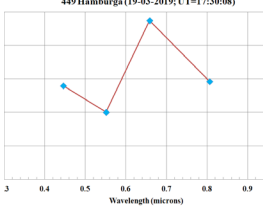


Fig. 9.

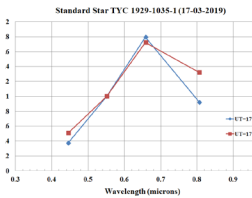


Fig. 10.

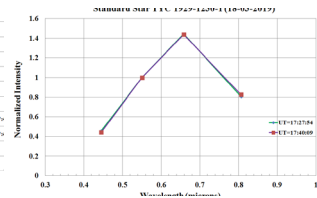


Fig. 11.

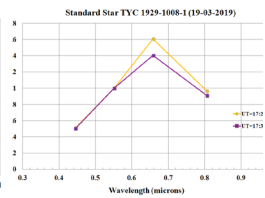


Fig. 12.

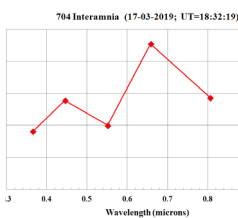


Fig. 13.

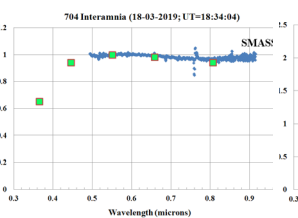


Fig. 14.

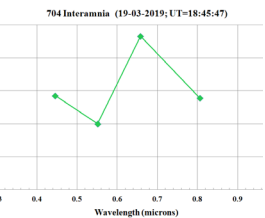


Fig. 15.

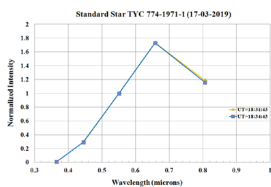


Fig. 16.

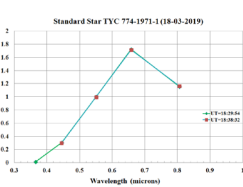


Fig. 17.

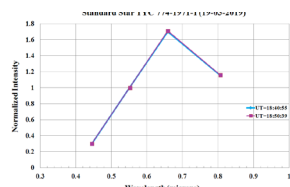


Fig. 18.

Previously, we reported the detection of solar activity effect to the shape of reflectance spectra of active asteroids obtained in 2012 (a high solar activity) and in 2016–2018 (low solar activity) [10]. Obvious explanation is the influence of different intensity of the solar wind to the surface matter of a primitive asteroid incorporating water ice and related consequences to the parameters of sublimation exosphere. In the period of a minimal solar activity the flow of solar wind from the Sun becomes more smooth (e. g., [11]). This is probably a reason of the unusual similarity of the shape of the reflectance spectra of the considered active asteroids determined by the physical state of their sublimation exosphere. Yet weak solar flares are possible in such a period. It was such a small solar flare that occurred shortly, 10 days before our observations on March 18 [12] (maybe, this time had been enough for the solar wind oscillations to reach the asteroids at a speed of ~ 550 km/s). The power of the flare was possibly sufficient to create a spherical shock-wave in the solar wind and blow away sublimation exospheres of the asteroids in the anti-sun direction. Thus, it allowed observations of asteroid bare surface without any noise (i.e., in the absence of an exosphere).

References:

- [1] Busarev V.V., Barabanov S.I., Rusakov V.S., Puzin V.B., Kravtsov V.V. Spectrophotometry of (32) Pomona, (145) Adeona, (704) Interamnia, (779) Nina, (330825) 2008 XE3, and 2012 QG42 and laboratory study of possible analog samples // *Icarus*. 2015. V. 262. P. 44–57.
- [2] Tholen D.J. Asteroid taxonomy: From cluster analysis to photometry // Ph. D. thesis. Tucson: University of Arizona, 1984.
- [3] Bus S.J., Binzel R.P. Phase II of the Small Main-Belt Asteroid Spectroscopic Survey. A Feature-Based Taxonomy // *Icarus*. 2002. V. 158. P. 146–177.
- [4] <https://ssd.jpl.nasa.gov/sbdb.cgi?help=1>
- [5] Bus S., Binzel R.P. 24 Themis Average CCD Spectrum. EAR-A-I0028-4-SBN0001/SMASSII-V1.0:24_00_TAB. NASA Planetary Data System, 2003.
- [6] Lazzaro D., Angeli C.A., Carvano J.M., Mothe-Diniz T., Duffard R., Florczak M., Small Solar System Objects Spectroscopic Survey V 1.0. EAR-A-I0052-8-S3OS2-V1.0. NASA Planetary Data System, 2006.
- [7] Busarev V.V., Barabanov S.I., Puzin V.B. Material composition assessment and discovering sublimation activity on asteroids 145 Adeona, 704 Interamnia, 779 Nina, and 1474 Beira // *Solar Sys. Research*. 2016. V. 50. No. 4. p. 281–293.
- [8] Hansen J.E., Travis L.D. // *Space Sci. Rev.* 1974. V. 16. P. 527–610.
- [9] Rivkin A., Emery J. Detection of ice and organics on an asteroid surface // *Nature*. 2010. 464, 1322–1323.
- [10] Busarev V.V., Scherbina M.P. Barabanov S.I. et al. // The Ninth Moscow Solar System Symposium, 8–12 October 2018, Space Research Inst., Abstract 9MS3-SB-08.
- [11] Cliver E.W., Von Steiger R. Minimal magnetic states of the Sun and the solar wind: Implications for the origin of the slow solar wind space // *Sci. Rev.* 2017. V. 210. P. 227–247.
- [12] https://tesis.lebedev.ru/sun_flares.html?m=3&d=8&y=2019

BIOSIGNATURE DETECTION WITH STATE-OF-THE-ART INSTRUMENTATION

E. Chatzitheodoridis

*National Technical University of Athens, School of Mining and Metallurgical Engineering, Department of Geological Sciences, 9 HeroonPolytechniou str., 15780 Zografou, Athens, Greece.
eliasch@metal.ntua.gr*

Keywords:

Biosignatures, Time-of-Flight mass spectrometry, Martian Meteorites, Laser Desorption mass spectrometry, spaceTOF

Introduction:

The detection of life on other planets requires a good understanding on the trace organic substances and inorganic element chemical anomalies that extinct microorganisms have left behind. Among other evidence, such as mineralogical, isotopic, and morphological, the organic and inorganic anomalies constitute some of the evidence that we call biosignatures. Chemical biosignatures as such are usually preserved in trace amounts within minerals (i.e., clay) and as small-scale geochemical environments. To detect them we require state-of-the-art instruments for which we must define a good set of analytical methodologies.

Mass spectrometric techniques constitute state-of-the-art tools to detect potential biosignatures. In this work we will initially review how mass spectrometry is used to detect chemical patterns that could define a good set of biomarkers which will be used in the direct or indirect search of life on other planets. We will then focus on instruments such as high mass resolution and mass resolving power Time-of-Flight mass spectrometers which detect secondary ions, molecular or elemental (isotopic), which are produced with ion sputtering, often with laser assisted ionization [1] or laser desorption mechanisms [2]. We will also present a new methodology to detect patterns of hydrocarbon fragments during sputtering that have the potential to distinguish among organics that have a different source. With reference materials, such as tetracene ($C_{18}H_{12}$), we will demonstrate that it is possible to clearly separate this molecule and its fragments from background organics of other origin (Figure 1).

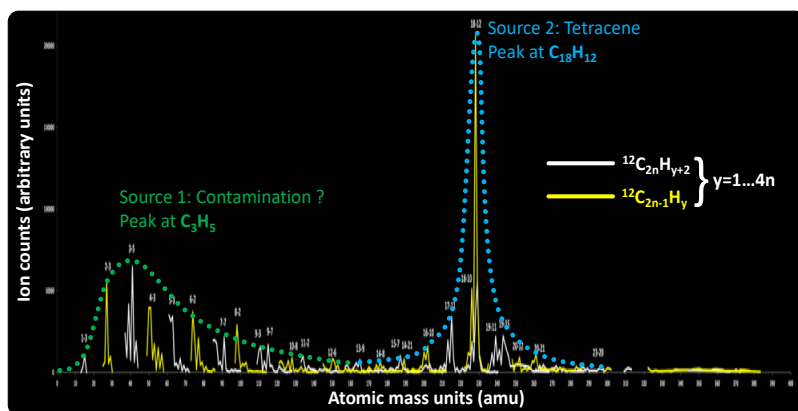


Fig. 1. Pattern distribution of odd- and even-numbered carbon hydrocarbons clearly distinguishing the tetracene substance ($C_{18}H_{12}$; blue distribution of peaks) and its fragments from another component (green distribution of peaks) which is possibly contamination.

To acquire the above information a labour intensive data processing procedure is required, which is highly aided and automated with a software we developed in-house, the "spaceTOF". This is a fully interactive software capable to handle the massive data files produced by ToF-SIMS instruments, especially those that can perform high-spatial resolution ion mapping.

Biosignature interpretation is generally performed using a small number of characteristic peaks from reference materials, and statistical or labelling techniques. Biochemical phases that have been investigated in the literature include proteins and their aminoacids [3], extracellular polymeric substances [4], lipids in tissues and cells [5, 6, 7, 8], and PAHs in meteorites [9, 10]. It is concluded that no unique peaks are characteristic of the different biological samples, while mass spectra are much further complicated by the large number of molecular fragments. Additionally, the absence of repeatability and the large number of artefacts [3] (Quong et al., 2005) complicate interpretation. Contamination is common in the samples, and it should be considered when studying geobiological and astrobiological samples [7], therefore its signatures should be also included in the database.

To perform the above task and demonstrate our methodology, we use all the peaks of a mass spectrum to produce patterns such as in Figure 1, which appear to be distinct and characteristic, similarly to the mass patterns resulting from the tetracene TOF-SIMS mass spectra. High mass resolution spectra together with fine mass calibration, separate for the elemental/isotopic and molecular ions, fully benefit an automated interpretation [11]. We apply the methodology to real samples, including a Martian meteorite (Nakhla), fossilised cyanobacteria by hematite from Milos Island in Greece, mass spectra from the comet 67P/Churyumov-Gerasimenko made by the COSIMA Instrument of the Rosetta Mission, and from stalactite samples from Icaria Island, Greece.

References:

- [1] Henkel T., Tizard J., Blagburn D.J., Lyon I. Interstellar dust laser explorer (IDLE): A new instrument for submicron analyses of stardust-quantification of laser SNMS. *Applied Surface Science*. 2006, V. 252. No. 19. P. 7117–7119. DOI: 10.1016/j.apsusc.2006.02.139
- [2] Sabbah H., Bonnamy A., Papanastasiou D., Cemichao J., Martín-Gago J.-A., Joblin C. Identification of PAH Isomeric Structure in Cosmic Dust Analogs: The AROMA Setup. *The Astrophysical Journal*. 2017, V. 843:34, 8 pp. <https://doi.org/10.3847/1538-4357/aa73dd>
- [3] Quong J.N., Quong A.a., Wu K.-J., Kercher J.R. A Signature-Based Method to Distinguish Time-Of-Flight Secondary-Ion Mass Spectra from Biological Samples. *Chemistry & Biodiversity*. 2005. V. 2. P. 1495–1502. DOI: 10.1002/cbdv.200590121
- [4] De Brouwer J.F.C., Cooksey K.E., Wigglesworth-Cooksey B., Staal M.J., Stal L.J., Avci R. *Journal of Microbiological Methods*. 2006. V. 65. No. 3. P. 562–572. <https://doi.org/10.1016/j.mimet.2005.10.001>
- [5] Altelaar A.F.M., Klinkert I., Jalink K., de Lange R.P.J., Adan R.A.H., Heeren R.M.A., Piersma S.R. Gold-Enhanced Biomolecular Surface Imaging of Cells and Tissue by SIMS and MALDI Mass Spectrometry. 2006. *Analytical Chemistry*. V. 78. N. 3. P. 734–742. DOI: 10.1021/ac0513111
- [6] Besinger M.C., Miller D.J., Harbottle R.R., Possmayer F., McIntyre N.S., Petersen N.O. Imaging lipid distributions in model monolayers by ToF-SIMS with selectively deuterated components and principal component analysis. 2006. *Applied Surface Science*. V. 252. N. 19. P. 6957–6965. DOI: 10.1016/j.apsusc.2006.02.121
- [7] Thiel V., Toporski J., Schumann G., Sjövall P., Lausmaa J. Analysis of archaeal core ether lipids using Time of Flight–Secondary Ion Mass Spectrometry (ToF-SIMS): Exploring a new prospect for the study of biomarkers in geobiology. *Geobiology*. 2006. V. 5. N. 1. P. 75–83. DOI: 10.1111/j.1472-4669.2006.00093.x
- [8] Leefmann T., Heim C., Kryvenda A., Siljeström S., Sjövall P., Thiel V. Biomarker imaging of single diatom cells in a microbial mat using time-of-flight secondary ion mass spectrometry (ToF-SIMS). *Organic Geochemistry*. 2013. V. 57. P. 23–33. DOI: 10.1016/j.orggeochem.2013.01.005
- [9] Stephan T., Jessberger E.K., Heiss C.H., Rost D. TOF-SIMS analysis of polycyclic aromatic hydrocarbons in Allan Hills 84001. *Meteoritics & Planetary Science*. V. 38. N. 1. P. 109–116. DOI: 10.1111/j.1945-5100.2003.tb01049.x
- [10] Thiel V., Sjövall P. Using Time-of-Flight Secondary Ion Mass Spectrometry to Study Biomarkers. *Annual Review of Earth & Planetary Sciences*. 2011. V. 39. P. 125–156. <https://doi.org/10.1146/annurev-earth-040610-133525>
- [11] Tsakonas N., Chatzitheodoridis E., Kiliass S.P., Lyon I. How to increase the credibility and ease the investigation of biosignatures in TOF-SIMS mass spectra. The 14th European Astrobiology Conference (EANA 2014), Edinburgh 2014.

ASTROCHEMISTRY: SYNTHESIS OF THE BASIC 'BUILDING BLOCKS' OF LIFE

S. Jheeta

Network of Researchers on Chemical Evolution of Life (NoR CEL)

sohan @sohanjheeta.com

Keywords:

Astrobiology, space chemistry, astrochemistry, molecules, origin of life,

The necessary molecules for the basic 'building blocks' of life – i.e. molecules – can be made by the action of charged particles and UV light, especially at the boundaries of denser and less dense atmospheric layers; during electrical discharge (i.e. lightning strikes) in the primordial planetary atmosphere; at the hydrothermal vents after the formation of earth's crust; on the shores of primordial seas and oceans when the tides were huge and more frequent and in the small puddles of water at the foot hills of volcanoes due to gas from the magma being percolated through the water. However, these places are insignificant compared to the vastness of space where molecules were being formed via the processes of astrochemistry.

It is believed that some of the necessary organic molecules may have been formed in specific areas of space (namely dark molecular clouds, e.g. Horsehead nebula) and delivered on to the Earth during the heavy bombardment period of its history, approximately 4.3–4.0 billion years ago. These organic molecules may have played a pivotal role in the formation of life on Earth. In addition, it is believed that life on Earth was formed within a very short geological time frame of only 200–300 million years. So, it is not unreasonable to suppose that these molecules were initially made in space which in effect could be, metaphorically speaking, a huge chemical laboratory.

To date no less than 190 molecules have been discovered in dark molecular clouds; the formation of molecules under a variety of simulated space conditions (e.g. different temperatures, levels of radiation energies and different types of impinging radiations) compares well with what is found in these huge structures. Such molecules are then eventually delivered on the surface of a planet by impactors. Collectively, the molecules made in the vastness of space and those other places mentioned at the beginning of this abstract form the inventory of molecules from which life on Earth emerged.

ORIGIN OF LIFE THROUGH THE EFFICIENT REACTION OF PREBIOTIC SYSTEMS TO EXTERNAL OSCILLATIONS: APPLICATION TO MARS, EUROPA, AND ENCELADUS

V.N. Kompanichenko

Institute for Complex Analysis of Regional Problems FEB RAS, 4 Sholom Aleyhem Street, Birobidzhan 679016, Russia; kompanv@yandex.ru

Keywords:

origin of life, prebiotic microsystem, living cell, planet, satellite, hydrothermal environment, oscillation, organic compound, laboratory testing, computational testing

Introduction

The origin of life on Earth and other planets is usually understood as a step-by-step chemical complication of organic macromolecules and microsystems. However, plenty of laboratory experiments in this direction have resulted in obtaining protocells and artificial cells, but not actually living cells. Therefore, there exists a certain principal gap between non-living and living types of natural systems. In a context of physics, E. Schrödinger defined it as a gap between the primary "order from chaos" to the secondary "order from order" [1]. However, he did not explain how the secondary order (i.e. life proper) may arise from the primary one. Some other researchers indicated the gap as "Mysterious Evolution Jump", or the "Missing Link", that should be examined in framework of the origin of life problem [2]. Till now nature of this gap is not satisfactory explained by the three existing approaches to evolution of cells: compositional (or metabolism-first), RNA-world (or genes-first) and cellular (last universal common ancestor). The author's inversion concept examines nature of the difference between these types of natural systems from the thermodynamic point of view [3, 4].

Thermodynamic difference between living and non-living systems

Entropy, free energy, and information are basic thermodynamic notions. Owing to their universality, they can be used for a fundamental comparison of living and nonliving systems. It is well known that biological evolution paradoxically proceeds with accumulation of free energy (that is, its contribution prevails over the contribution of entropy). In contrast, non-biological systems evolve with the tendency of entropy growth, in accordance with the 2nd law of thermodynamics (in particular, stars or magmatic systems continuously dissipate free energy into the environment, i.e., lose it). There is no generally accepted explanation for this difference. But it is obvious that the emergence of the first living microorganisms from non-living organic microsystems implies a reversal of the thermodynamic tendency (as on the Earth as on another planet). The tendency to increase of entropy (in non-living prebiotic systems) must be replaced with the opposite tendency to increase of free energy (in the simplest living cells) through some intermediate state (neutral or zero "point", where the contributions of free energy and entropy are approximately equal). The author calls this turn 'thermodynamic inversion' [3].

The transition of prebiotic microsystems to life.

According to the elaborated inversion concept, the conversion of prebiotic microsystems into the simplest forms of life occurs under conditions far from equilibrium in the presence of multilevel oscillations of physico-chemical parameters in the maternal hydrothermal environment. Those nonequilibrium conditions sustain self-organization investigated by Ilya Prigogine and his colleagues [5], and correspond with the "order of chaos" by Schrödinger [1]. Self-organization under nonequilibrium (far from equilibrium) conditions is considered by the abstract's author as a necessary preliminary stage for the transition to life. The actual turn to life is carried out during the following stage - thermodynamic inversion in the prebiotic organic microsys-

tems, when they perform effective (enhanced) response to external oscillating influences. The scheme of the transition is shown on Fig. 1. The author correlates the described thermodynamic inversion with the secondary “order from order” by Schrödinger [1].

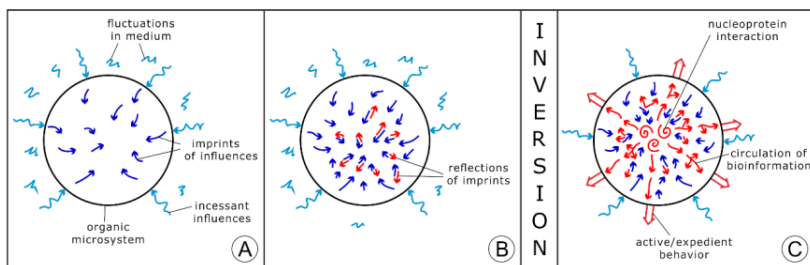


Fig. 1. The scheme of conversion of a nonequilibrium prebiotic microsystem into the primary form of life under oscillating conditions [4]. (A) The rise (self-assembly) of an organic prebiotic microsystem within the oscillating medium; the penetration of continuous external influences into the microsystem and the transformation of the network of chemical reactions (blue arrows); (B) the initiation of the system’s response to continuous external stress, arising of the chemical reactions counteracting the stress and partially compensating it; (C) the conversion of the prebiotic microsystem in the initial form of life when its activity (counteraction) exceeds the pressing from the oscillating environment. The conversion corresponds to the thermodynamic inversion.

Four required conditions for the origin of life

According to the widely accepted opinion, the origin of life demands three required conditions: the availability of organic matter, a liquid medium, and a source of energy. The inversion concept adds one more required condition to this set: multilevel oscillations of physico-chemical parameters (temperature, pressure, pH, redox potential, etc.) in the maternal hydrothermal environment. Such oscillations are necessary for incessant “pumping” of prebiotic microsystems as shown on Fig. 1. The approach to laboratory and computational testing of this approach is formulated in [4]. According to the preliminary evaluation, the regular constituent of the oscillations should be within the interval between split second and 30 min.

Application of the elaborated concept to the solar planets and satellites.

Let’s evaluate the possibility of life origin on some solar bodies basing on the four required conditions listed above. Availability of water (and/or ice, vapor), that is the 1st required condition, is verified on all bodies under consideration – Mars, Europa, and Enceladus. Some observations indicate availability of a source of thermal and chemical energy (the 2nd condition) on them: diapirs of warm ice within the cold Europa’s ice crust [6], geysers (water/ice vents) on Enceladus [7], traces of hydrothermal discharges on Mars [8]. Simple organic compounds (the 3rd condition) are detected on Mars (methane) and Enceladus (methane, methanol, possibly amino acids) [7, 9]; however, they have not found on the Europa’s surface yet. Oscillations of physico-chemical parameters (the 4th condition) are continuously generated by active tectonics along with the subsurface or submarine hydrothermal process; signs of these processes are also found on the solar bodies under consideration.

Conclusion

According to the inversion concept, life might originate at least on three solar bodies: early Mars, Europa, and Enceladus. Other planets and satellites of the solar system need a special consideration in this context.

References:

1. Schrödinger E. What is Life? The Physical Aspect of the Living Cell. Lectures at the Trinity College, Dublin. 1944.
2. Sugawara T., Kurihara K., Suzuki K. Constructive approach toward protocells // Mikhailov A. (ed) Engineering of chemical complexity. World Sci. Rev. 2012. January 23. P. 1–17.
3. Kompanichenko V.N. Thermodynamic Inversion: Origin of Living Systems. Springer International Publishing. Cham (Switzerland). 2017. P. 275

4. Kompanichenko V. The Rise of A Habitable Planet: Four Required Conditions for the Origin of Life in the Universe. *Geosciences*. 2019. V. 9. № 92.
5. Prigogine I., Stengers I. *Order out of chaos*. Bantam. New York. 1984.
6. Rathbun J., Musser Jr., Squyres S. Ice Diapirs on Europa: Implications for Liquid Water. *Geophysical Research Letters*. 1998. V. 25 (22). P. 4157–4160.
7. Drabek–Maunder E., Greaves J., Fraser H.J., Clements D.L. Ground-based detection of a cloud of methanol from Enceladus: when is a biomarker not a biomarker? *International Journal of Astrobiology*. 2019. V. 18. Iss. 1 February. P. 25–32
8. Carlton C. Allen, Dorothy Z. Oehler. A Case for Ancient Springs in Arabia Terra, Mars. *Astrobiology*. 2008. V. 8. No 6. P. 1093–1112.
9. Guzman M., Lorenz R., Hurley D., Farrell W.. Collecting amino acids in the Enceladus plume *International Journal of Astrobiology*. 2019. V. 18. Iss. 1. P. 47-59.

SORPTION THEORY OF THE ORIGIN OF LIFE

V.V. Matveev¹, A.V. Malygin²

¹ *Institute of Cytology, Russian Academy of Sciences, Tikhoretsky Ave 4, St. Petersburg 194064, Russia, vladimir.matveev@gmail.com;*

² *Pavlov Institute of Physiology, Russian Academy of Sciences, nab.*

Makarova 6, St. Petersburg 199034, Russia, malygin.av@gmail.com

Keywords:

adsorption, biophase, origin of life, peptide, physics, physiology, protocell, semipermeability, water.

Adsorption is regarded as a key physical phenomenon for the origin of the first living cell, and, consequently, of life itself. Due to the sorption properties of primary short peptides formed abiogenously, special physical conditions arise around them, different from the physical properties of a medium and favorable for processes and interactions necessary for life.

The following fundamental interactions of such peptides that are necessary for the emergence of a living cell can be distinguished.

1. Multilayer adsorption of water on the molecular surface of the peptide. Due to adsorption of water, an aqueous shell with a more regular structure (than the structure of bulk water) and with reduced molecular dynamics is formed around the peptide. These changes in the properties of the water occur because, under influence of fixed peptide charges (polar groups of peptide bonds, carboxyl groups of dicarboxylic amino acid residues), water dipoles become more polarized and so hydrogen bonds that they form with the peptide and with each other become stronger. Strengthening of hydrogen bonds stabilizes the water shell around the peptide and a phase of adsorbed water originates, which does not mix with bulk water, like a drop of oil in an aqueous environment. Stronger hydrogen bonds in the aqueous cocoon around the peptide reduce solvent potency of adsorbed water, which leads to excluding of all substances from this phase into the environment. This is how compartmentalization arises, the separation of the internal environment from the external one. Concentration gradients of neutral and charged substances, including inorganic ions, arise.
2. The concentration gradients of the solutes will increase if the peptide selectively adsorbs some of them. For example, if a peptide selectively adsorbs K^+ in the presence of Na^+ , then this process will lead to accumulation of K^+ , cation necessary for life, while Na^+ will be excluded into the environment by the phase of adsorbed water. If a peptide enclosed in an aqueous shell selectively adsorb also organic molecules necessary for life (amino acids, nucleic acids, sugars), this will create necessary prerequisites for the emergence of a biochemical reactor. In such a reactor, more complex peptides, polynucleotides can be synthesized, and systems for synthesis and degradation of organic substances can be formed. Self-condensation of the peptides and merger of their aqueous shells will lead to the appearance of a biophase, a membraneless protocell.
3. The cell shape biophase (protocell) has the same fundamental physical properties as a living cell: (i) semipermeability (due to the phase of adsorbed water); (ii) the ability to selectively accumulate some substances and exclude others (also due to the phase of adsorbed water and the ability of the peptide to adsorb other substances not just water); (iii) the ability to generate electrical potentials; (iv) osmotic stability due to the stability of the adsorbed water phase.
4. With adequate exposure to physical factors (temperature, hydrostatic and osmotic pressure) and various ligands (H^+ , Ca^{2+} , inorganic anions), the peptide can reversibly change its sorption properties. In this case, the water shell is destroyed, Na^+ and other substances that are outside the biophase will begin their movement inside the biophase. Na^+ will displace K^+ from binding sites on the peptide and efflux of K^+ from the biophase to external

environment will begin. Destruction of the gradients of the main physiologically important cations (K^+ and Na^+) will lead to a release of energy that was accumulated in their gradients when the biophase was at the resting state (transition of the biophase from resting state into active one). This energy will have a significant effect on conformation of the peptides, on peptide-peptide and peptide-ligand interactions. In this way, the work necessary for functionally significant structural transformations of the protocell will be done, without which the emergence of life would be impossible. Binding of ATP (or its precursors) to activated peptides will return biophase into a resting state (model of two states). The protocell protometabolism (matter and energy flows) thus formed is a fundamental basis for the formation of living cell metabolism. It is clear that all the considered properties of the biophase (1–4) have one cause-sorption properties of peptides. Thus, a study of the sorption properties of peptides is an urgent problem for the science of the origin of life.

Described sorption approach to the origin of life [1, 2] is based on the fundamental achievements of the Russian [3] and American [4] schools of cell physiology.

References:

- [1] Matveev V.V. 2017. Comparison of fundamental physical properties of the model cells (protocells) and the living cells reveals the need in protophysiology // *Int. J. Astrobiol.* 2017. V. 16. No. 1. P. 97–104.
- [2] Matveev, V.V. 2019. Cell theory, intrinsically disordered proteins, and the physics of the origin of life // *Prog. Biophys. Mol. Biol.* 2019. DOI: 10.1016/j.pbiomolbio.2019.04.001.
- [3] Troshin A.S. *Problems of Cell Permeability*. Pergamon Press, 1966. P. 549
- [4] Ling G.N. *Life at the Cell and Below-Cell Level: The Hidden History of a Fundamental Revolution in Biology*. Pacific Press, 2001. P. 373 (The Russian translation was published in 2008).

THE MOST LIKELY PLACES TO DETECT TRACES OF EXTRATERRESTRIAL LIFE IN THE SOLAR SYSTEM

V.N. Snytnikov

Bereskov Institute of Catalysis SB RAS, Novosibirsk, Russia, snyt@catalysis.ru;

Keywords:

Astrocatylisis, Venera missions, astrobiology, Origin of Life

According to the astrocatylisis hypothesis [1], life arises in circumstellar disks at the stage of the formation of planets. Meteorites such as carbonaceous chondrites and another bodies of the Solar system can bear traces of the Origin of Life. The report discusses the question of which objects in the Solar system are the most promising for detecting extraterrestrial life, including Venus [2].

References:

- [1] Snytnikov V.N. Astrocatylisis—Abiogenic Synthesis and Chemical Evolution At Pregeological Stages of the Earth's Formation // *Paleontological Journal*. 2010. V. 44. No. 7. P. 761–777.
- [2] Ksanfomality L.V., Zelenyi L.M., Parmon V.N. Snytnikov V.N. Hypothetical signs of life on Venus: revising results of 1975–1982 TV experiments // *Physics Uspekhi*. 2019. V. 62. No. 4. P. 378–404.

EXOPLANETS: NATURAL LABORATORIES OF CHEMICAL EVOLUTION AND ORIGIN OF LIFE

Martin Ferus

J. Heyrovsky Institute of Physical Chemistry, Czech Academy of Sciences, Dolejškova 3, CZ18223 Prague 8. Czech Republic, martin.ferus@jh-inst.cas.cz

Keywords:

Exoplanets, Ariel, origin of life, impacts

Introduction:

The chemical environments of young planets are assumed to be largely influenced by impacts of bodies lingering on unstable trajectories after the dissolution of the protoplanetary disk [1, 2]. We explore the chemical consequences of impacts within the contexts of several model planetary atmospheres. A terawatt high-power laser was used in order to simulate the airglow plasma and blast wave surrounding the impactor. The chemical results of these experiments were then applied to a theoretical atmospheric model. We predict that acetylene absorption bands are observable on exoplanets with reducing atmospheres that have recently undergone their own. Heavy Bombardments, with prominent features at 3.05 μm and 10.50 μm . Furthermore, we demonstrate that impact reprocessing of volcanic atmospheres leads to a formation of carbonyl sulfide (OCS) and carbon disulfide (CS₂). These results show that impact plasma is the driving force of atmospheric chemistry on young planets and can lead to the formation of marker molecules that can be predicted through laboratory experiments and observed by space telescopes such as James Webb or Ariel [3].

References:

- [1] Ferus M. et al. Formation of nucleobases in a Miller–Urey reducing atmosphere // PNAS. 2017. V. 114 No. 17. P. 4306–4311.
- [2] Ferus M. et al. High-energy chemistry of formamide: A unified mechanism of nucleobase formation // PNAS. 2015. V. 112. No. 3. P. 657–662.
- [3] Tinetti G. et al. A chemical survey of exoplanets with ARIEL, 2018. V. 46 No. 1. P. 35–209.

BIG DATA AND MACHINE LEARNING FOR EXOPLANETS AND ASTROBIOLOGY: RESULTS FROM NASA FRONTIER DEVELOPMENT LAB

Daniel Angerhausen^{1,2}, and the NASA Frontier Development Lab Exoplanet and Astrobiology Teams

¹ Center for Space and Habitability, University of Bern, Switzerland

² Blue Marble Space Institute of Science, USA

Keywords:

Exoplanets, Astrobiology, biosignature detection, transit detection, exoplanet spectroscopy, machine learning, data science

Summary

We present results from NASA's Frontier Development Lab 2018, an Artificial Intelligence/Machine Learning incubator tackling challenges in various fields of space sciences. Here we focus on the results of the Exoplanet and Astrobiology teams: a project on planet candidate classification in TESS data and modeling and retrieval of exoplanet atmospheres and spectra in the context of life detection. A particular focus will be on two data sets produced at FDL 2018: a set of 3 million exoplanet spectra calculated with the GSFC Planetary Spectrum Generator (PSG) and a set of 150 000 exoplanet atmospheres computed with the ATMOS code.

Context

For the third time since 2016 machine learning researchers and space science domain experts spent the summer 2018 in Silicon Valley to work on some of humanity's most important present day challenges in space research and exploration. The 8 week long program developed in partnership with NASA's Ames Research Center — NASA frontier development lab (FDL, <https://www.frontierdevelopmentlab.org/>) — at the SETI institute faced problems ranging from predicting solar storms and localization on the moon to finding life in space.

The FDL program aims to apply AI technologies to challenges in space exploration by pairing machine learning expertise with space science and exploration researchers from academia and industry. These interdisciplinary teams address tightly defined problems and the format encourages rapid iteration and prototyping to create outputs with meaningful application to the space program and humanity. What makes FDL unique is its close collaboration with industry stakeholders like such as Intel, Google Cloud, Kx Systems, IBM and NVIDIA and key players in private spacesuch as Space Resources Lu, Lockheed Martin, KBRWyle and XPRIZE.

Exoplanet Challenge

The Exoplanet team used state-of-the-art deep learning models to automatically classify Kepler transit signals as either exoplanets or false positives. Their Astronet code expanded upon work of Shallue and Vanderburg (SV18) by including additional scientificdomain knowledge into the network architecture andinput representations to significantly increase overall model performance. Notably, they achieved 15–20 % gains in recall for the low-est signalto-noise transits that can correspond to rocky planets in the habitable zone. They input CCD pixel centroid time-series information derived from Kepler data and key stellar parameters taken from the catalogueinto the network and also implement data augmentation techniques to alleviate model over-fitting. These improvements allowed them to drastically reduce the size of the model, while still maintaining improved performance. These smaller models are better for generalization, for example from Kepler to TESS data. Their work illustrates the importance of including expert domain knowledge in even state-of-the-art deep learning models when applying them to scientific research problems that seek to identify weak signals in noisy data. This classification tool will be especially useful for current

and upcoming space-based photometry missions focused on finding small planets, such as TESS and PLATO. A first application to TESS data was published in Osborn et al. 2019.

Astrobiology challenges

The Astrobiology team 1 project demonstrated how cloud computing capabilities can accelerate existing technologies and map out previously neglected parameter spaces (Bell et al., 2019; Chopra et al., in prep). They succeeded in modelling tens-of-thousands of potential atmospheres over a few days, using software (ATMOS) that was originally intended for use in single run applications. The full atmospheric composition data set that was generated will become a useful resource for the community to understand distributions of habitability parameters and will enable better interpretations of future observations of exoplanet atmospheres and potential biosignatures. The software product created during FDL has the potential to significantly improve the accessibility of ATMOS for a wide community of researchers. The parameter search approach, can be adopted to simulate more atmospheres and/or modified to rapidly iterate on other problems that utilize ATMOS. In Soboczenski et al., 2018 and Cobb/Himes et al., 2019 the Astrobiology 2 team presented a Machine-Learning-based retrieval framework called Intelligent exoplaNet Atmospheric Retrieval (INARA) that consists of a Bayesian deep learning model for retrieval and a data set of 3 000 000 synthetic rocky exoplanetary spectra generated using the NASA Goddard Planetary Spectrum Generator (PSG). This work represents the first ML retrieval model for rocky, terrestrial exoplanets and the first synthetic data set of terrestrial spectra generated at this scale (Zorzan et al., in prep.; O’Beirne et al., in prep.).

Conclusions

We present results from the NASA FDL Exoplanet and Astrobiology challenges 2018: an improved method to classify Exoplanet candidates from photometric surveys, a new deep learning approach for spectral retrieval of Exoplanet atmospheres and containerized software of Astrobiology legacy codes, which we used to provide large data sets for the community. We demonstrate that the NASA frontier development lab format is a successful blueprint for other potential industry/academia collaborations in the future.

Acknowledgements

The work presented here, are the result of the 2018 NASA Frontier Development Lab (FDL) exoplanet and astrobiology challenges. The teams want to thank the organisers, mentors, and sponsors for providing this opportunity. The results are based on work supported by Google Cloud, Nvidia and Kx Systems.

References:

- [1] Bell, A., et al. 2018, NIPS. 2018. CiML workshop, ciml.chalearn.org
- [2] Soboczenski, F., et al. 2018. NeurIPS Workshop on Bayesian Deep Learning, [arXiv:1811.03390](https://arxiv.org/abs/1811.03390)
- [3] Ansdell, M., et al. 2018. *ApJL*, V. L7. P. 869 (1),
- [4] Shallue, C.J., & Vanderburg, A. 2018, *V. AJ*, P. 155, 94
- [5] Cobb A., Himes M. et al. 2019, *V. AJ*, V. 158, 1
- [6] Osborne H. et al. 2019, *A&A*, accepted, [arXiv:1902.08544](https://arxiv.org/abs/1902.08544)

STUDY OF EXOPLANET HABITABILITY: POTENTIAL ATMOSPHERIC BIOMARKERS O_2/O_3 IN ULTRAVIOLET

V.I. Shematovich, M.E. Sachkov

*Institute of Astronomy of the Russian Academy of Sciences, Moscow, Russia;
shematov@inasan.ru*

Keywords:

extrasolar planets, space telescopes, UV observations, potential habitability zones, astrobiology.

Introduction:

At present time, the strongest remotely detectable sign of life in the Earth's atmosphere is the molecular oxygen (O_2) produced in the photosynthesis processes. However, recent studies of geochemical features on exoplanets like Earth suggest that, for most of them, atmospheric O_2 would not be detectable to a remote observer except during the last ~500 million years of evolution. During a long period in the Earth's history (2.0–0.7 billion years ago), O_3 was probably present in the atmosphere, but with low concentrations estimated at ~0.1–1% of the today's level. Although the spectral manifestations of O_2 are weak at such low levels, however, ozone molecules O_3 are in photochemical equilibrium with such low O_2 concentrations and will cause noticeable spectral features in the Hartley-Huggins UV band (~0.25 μm), with a weaker manifestation in the mid-IR region of about 9.7 μm [1]. Thus, taking the history of the Earth as an informative proxy, it can be concluded that there may be a category of exoplanets for which conventional atmospheric biomarkers can be identified only in the UV radiation range.

The report emphasizes the importance of UV observations in the design of future space telescopes for direct observations of exoplanets and their atmospheres, such as the World Space Observatory–UV (WSO–UV), the Habitable Exoplanet Observatory (HabEx) or The Large UV/Optical/Infrared Surveyor (LUVOR), for the detection of ozone O_3 in the planetary atmospheres with intermediate oxidation states [2]. Strategies to mitigate the so-called “false positive detections”, i.e. the detection of O_3 created in abiotic processes, are also discussed. The importance and broad implications of studying the history of the Earth as a window to understanding potential biomarkers for exoplanet atmospheres, and the importance of ultraviolet observations for the identification of habitable exoplanets by the next-generation space telescopes are discussed.

This study was supported by the Russian Foundation for Basic Research (project 18-02-00721) and the program of fundamental research of the Presidium of the Russian Academy of Sciences (KP 19-270).

References:

- [1] Meadows V.S., Reinhard C.T., Arney G.N., Parenteau M.N., Schwieterman E.W., Domagal-Goldman S.D., Lincowski A.P., Stapelfeldt K.R., Rauer H., DasSarma S., Hegde S., Narita N., Deitrick R., Lustig-Yaeger J., Lyons T.W., Siegler N., Grenfe J.L. Exoplanet Biosignatures: Understanding Oxygen as a Biosignature in the Context of Its Environment // *Astrobiology*. 2018. V. 18. P. 630–662.
- [2] Sachkov M.E., Shematovich V.I. Study of exoplanet habitability: potential O_2/O_3 biomarkers in ultraviolet // *Sol. Syst. Res.* 2019. V. 53. No. 5 (in press).

EMERGENCE OF PHOTOAUTOTROPHIC ASSIMILATIVE MECHANISMS IN AN IRRADIATED STERILIZED AQUEOUS MIXTURE OF SOME INORGANIC AND ORGANIC SUBSTANCES INDUCED BY ELECTROMAGNETIC RADIATION OF SUN

V.K. Gupta

Department of Zoology, C.M.D. Post Graduate College, Bilaspur - 495 001, Chhattisgarh, India

Irradiated sterilized aqueous mixture of ammonium molybdate, di ammonium hydrogen phosphate, biological minerals and formaldehyde shows photochemical formation of supramolecular protocell-like assemblies, "Jeevanu" shows abiogenesis of various biochemicals (1) and can catalyse photolytic decomposition of water. It was observed that hydrogen thus released is utilized in photochemical fixation of molecular Carbon di oxide and molecular nitrogen (2, 3). Energy transduction through non-linear, photo synergistic collaborative processes at mesoscopic level in the mixture leads to emergence of molecular associations capable of showing various functional properties of biological order. The energy metabolism based on coupled redox processes in Jeevanu mixture results into sustainable assimilative pathway similar to universal common ancestors.

References

- [1] Bahadur, K. and Ranganayaki, S. 1970 J. British Interplanetary Soc., 23, 813
- [2] Rao, K.K., Adams, M.W.W., Morris, P., Hall, D.O., Ranganayaki, S. and Bahadur, K. 1978. Presented at the BASE Symposium, Madurai, Dec., India.
- [3] Smith, A. Folsome, C. and Bahadur, K. 1981. *Experientia* 37, 357–359.

COMETS, CARBONACEOUS CHONDRITES AND EXTRATERRESTIAL LIFE

N.C. Wickramasinghe¹, R.B. Hoover²

¹ *Buckingham Centre for Astrobiology, University of Buckingham, UK.
ncwick@gmail.com;*

² *U.S. Space and Rocket Center, One Tranquility Base, Huntsville, Alabama
35805, USA, RichardBHoover@icloud.com*

Keywords:

Comets, Water, Carbonaceous Chondrites, Microfossils, Ceres, 67P/G-C, Organics, Extraterrestrial Life, Panspermia

Introduction:

It is now well established that water is absolutely essential for all known forms of life. Living organisms require water in liquid state for growth, replication, locomotion and the transport of life-critical ions and biomolecules. Microorganisms of diverse ecological and morphological groups can remain viable while frozen deep within polar ice caps [1, 2] or permafrost for thousands to millions of years [3]. Space missions and ground based observations show water is the dominant volatile of the nuclei of comets [4] and water-bearing asteroids [5]. The asteroid Ceres has been observed to eject water vapour plumes ($\sim 10^{26}$ molecules/sec) from localized mid-latitude sources due to sublimation of water ice or cryo-volcanism [6]. The gamma ray and neutron detector on board NASA's Dawn Spacecraft revealed vast quantities of water ice across the surface and shallow subsurface [7] of Ceres. The hydrogen content of the non-icy portion of the Carbon-bearing regolith was similar to the aqueously altered CI and CM carbonaceous chondrites. Localized bright areas of Ceres were attributed to hydrated magnesium sulfate [8], which is a dominant mineral in the Orgueil meteorite.

The Deep Impact mission obtained images of the nucleus of comet Temple 1 with regions where exposed deposits of water ice were detected on the surface of the comet nucleus. The temperature of the sunlit region of the nucleus comet P/Temple was found to be 330 K (57 C) at 1.5 AU and other regions of the crust were at 280K [9]. Prior to impact the ambient, the outgassing of water from comet 9P/Temple 1 was $\sim 6 \times 10^{27}$ molecules/s. This is far above the calculated value for the free sublimation of ice calculated ($\sim 4.5 \times 10^{21}$ molecules/m²/s) indicating that the ambient outgassing had significant subsurface sources. The Deep Impact spacecraft also observed numerous events of flaring of the nucleus and eruption of geyser-like jets as the comet was approached and before the collision of the impactor. These results indicate the black crust impedes the flow of sublimation gas from interior ices, and therefore may allow pressure to develop within veins, pores, pockets and cavities beneath the crust. In regimes where the pressure exceeds 6 mbar and the temperature exceeds 273 K, liquid water can exist and remain in liquid state as long as these conditions co-exist.

These pockets could provide microniches with pools of liquid water and rock fragments trapped within pockets similar to the cryoconite and ice bubble ecosystems that exist in the polar ice caps and glaciers of Earth. Cryoconite communities in polar ice are typically dominated by cyanobacteria, bacteria, eukaryotic algae, fungi and protists [10]. The minerals of the CI and CM carbonaceous provide clear and convincing evidence of extensive aqueous alteration by a brine with elevated levels of organic and inorganic soluble components in the parent body [11]. The Orgueil CI1 and Murchison CM2 carbonaceous chondrites have been found to contain a host of complex biomolecules along with a great diversity of exceptionally well-preserved carbonized or permineralized remains of cyanobacteria, prasinophytes and other aquatic microalgae [12, 13]. Although it was previously thought that diatoms might be abundant in carbonaceous meteorites [14], they are rare but have recently been discovered in Orgueil [15]. The nitrogen levels of the microfossils below the detection limit of the Energy Dispersive Spectrometer

of the Field Emission Scanning Electron Microscope shows they are not modern biological contaminants and hence are indigenous to the stones and provide strong support for the Panspermia hypothesis.

From the convergence of a wide range of data, derived from many different fields of study, the commonly held view that comets and small bodies of the solar system are necessarily unsustainable as microbial habitats has been seriously challenged [16]. Domains of liquid water, no matter how limited in extent, or transient in time, that are required for microbial sustenance appear to be widespread. Organic molecules that are fully consistent with microbial nutrients as well as metabolites and their degradation products are also widely present in comets [14, 18].

Theoretical arguments for comets as biological habitats go back over several decades. Hoyle and Wickramasinghe first developed the theory of cometary panspermia, arguing that comets were incubators and distributors of microbiology in the cosmos [19, 20]. It has been shown that with the expected inclusion of ^{232}Th , ^{238}U and ^{40}K in the cometary regolith, liquid water domains would be maintained for upward of 10^9 years [22–24]. Furthermore, in comets approaching perihelion (as for instance in the case of Comet Hale-Bopp) biological activity could be triggered by solar heating near the surface, thus leading to the generation of high-pressure pockets of gaseous metabolites that in turn trigger the release of jets of gas [25]. Evidence for such processes has recently been reported in the case of Comet 67P/C-G [17]. Jets of water and organics issuing from and vents in the frozen surface of the comet are fully consistent with biological activity occurring within sub-surface liquid pools generating gaseous metabolites that sporadically rupture overlying ice. The report of O_2 along with evidence for the occurrence of water and organics in the same comet provides further evidence of ongoing biological activity [18]. Similar microbial habitats are likely to exist in subsurface “lakes or oceans” in solar system planetary bodies including Europa and Enceladus [26].

References:

- [1] Abyzov, S.S. Microorganisms in the Antarctic ice // in Antarctic Microbiology, ed. E.I. Friedman. New York, NY: Wiley-Liss Press. 1993. P. 265–295.
- [2] Abyzov, S.S., Hoover, R.B., Imura, S. et al. Use of different methods for discovery of ice-entrapped microorganisms in ancient layers of the Antarctic glacier // *Advances in Space Research*. 2004. V. 33. P. 1222–1230.
- [3] Gilichinsky, D.A. et al. Long-term preservation of microbial ecosystems in permafrost // *Advances in Space Research*. 1992. V. 12. No. 4. P. 255–263.
- [4] Delsemme, A.H. The deuterium enrichment observed in recent comets is consistent with the cometary origin of seawater // *Planetary and Space Science*. 1998. V. 47. No. 1–2. P. 125–131.
- [5] Nittler, L.R. The Provenances of Asteroids, and Their Contributions to the Volatile Inventories of the Terrestrial Planets // *Science*. 2012. V. 337. P. 721–723.
- [6] Küppers, M. et al. Localized sources of water vapour on the dwarf planet (1) Ceres // *Nature*. 2014. V. 505. P. 525–528.
- [7] Prettyman, T.H. et al. Extensive water ice within Ceres’ aqueously altered regolith: Evidence from nuclear spectroscopy // *Science*. 2017. V. 355. No. 6320. P. 55–59.
- [8] Nathues, A., et al. Sublimation in Bright Spots on (1) Ceres. // *Nature*. 2015. V. 528. P. 237–240.
- [9] Sunshine, J.M., et al. Exposed water ice deposits on the surface of comet 9P/Tempel 1 // *Science*. 2006. V. 5766. P. 1453–1455.
- [10] Mueller, D.R., et al. Glacial Cryoconite ecosystems: a biplolar comparison of algal communities and habitats // *Nova Hedwigia*. 2001. V. 123. P. 173–197.
- [11] Le Guillou, C., Bernard, S., Brearly, A.J., Remusat, L. Evolution of organic matter in Orgueil, Murchison and Renazzo during parent body aqueous alteration: In situ investigations // *Geochemica et Cosmochemica Acta*. 2014. V. 131, P. 268–392.
- [12] Hoover, R.B. Comets, Carbonaceous Meteorites and the Origin of the Biosphere // *Biosphere Origin and Evolution*. 2008. Springer, Boston, MA P. 55–65.
- [13] Hoover, R.B. Fossils of cyanobacteria in C1 carbonaceous meteorites: Implications to life on comets, Europa and Enceladus // *Journal of Cosmology*. 2010. V. 11. P. 3500–3549.
- [14] Hoover, R.B., Hoyle, F., Wickramasinghe, N.C. et al. Diatoms on Earth, Comets, Europa and in interstellar space // *Earth Moon and Planets*. 1986. V. 35. P. 19–45.

- [15] Hoover, R.B., Rozanov, A.Yu., Krasavin, E.A., Ryumin, A.K., Kapralov, M.I. Diatoms in the Orgueil Meteorite // *Paleontological Journal*. 2018. V. 52. No. 13. P. 1647–1650.
- [16] Wickramasinghe, J.T., Wickramasinghe, N.C., Wallis, M.K., Liquid water and organics in comets: implications for exobiology // *International Journal of Astrobiology*. 2009. V. 8. No. 4. P. 281–299.
- [17] Agarwal, J., et.al. Evidence of sub-surface energy storage in comet 67P from the outburst of 2016 July 03 // *MNRAS* 2017 V. 469, P. S606–S625.
- [18] Wallis, M.K., Wickramasinghe, N.C. Rosetta Images of Comet 67P/ Churyumov-Gerasimenko: Inferences from its Terrain and Structure // *Astrobiology Outreach*. 2015. V. 3. P. 12.
- [19] Hoyle, F. and Wickramasinghe, N.C. Comets – a vehicle for panspermia // in *Comets and the Origin of Life 1981*. (ed. C. Ponnampertuma) D. Reidel, reprinted as *Astrophysics and Space Science*. 1999. V. 268, 333–341.
- [20] Hoyle, F., Wickramasinghe, N.C., *Living Comets* // Cardiff, Univ. College Press.
- [22] Wallis, M.K., 1980. Radiogenic melting of primordial comet interior. // *Nature*. 1980. V. 284. P. 431–434.
- [23] Yabushita, S. Thermal evolution of cometary nuclei by radioactive heating and possible formation of organic chemicals // *Mon. Not. RAS*. 1993. V. 260, P. 819–825.
- [24] Mark, R., Prialnik, D. Early thermal and structural evolution of small bodies in the Trans-Neptunian zone // *Earth, Moon and Planets*. 2003. V. 92. P. 359–374.
- [25] Wickramasinghe, N.C., Hoyle, F. and Lloyd, D., Eruptions from comet Hale-Bopp at 6.5AU // *Astrophysics and Space Science*. 1996. V. 240. P. 161–165.
- [26] Wickramasinghe, N.C., Wickramasinghe, D.T., Steele, E.J., 2018. Comets, Enceladus and panspermia // *Astrophysics and Space Science*. V. 363. P. 244.

MICROBIAL LIFE UNDER THICK GLACIER SHEETS: LESSONS FROM THE SUBGLACIAL ANTARCTIC LAKE VOSTOK EXPLORATION

Sergey Bulat¹, Maxim Doronin¹, Elizabeth Rudaya¹, Danyl Sumbatyan¹, Dominique Marie²

¹ NRC 'Kurchatov Institute' — Petersburg Nuclear Physics Institute, St. Petersburg-Gatchina, Russia

² Station Biologique de Roscoff, Roscoff Cedex, France, bulat@omrb.pnpi.spb.ru

Keywords:

Antarctica, subglacial Lake Vostok, lake unsealing, ice cores, life, extremophiles, bacteria, 16S rRNA genes, contamination, astrobiology

Introduction:

The objective was to search for microbial life in the subglacial Antarctic Lake Vostok by analyzing the uppermost water layer entered the borehole and shortly got frozen within following three lake unsealing (February 5, 2012; January 25, 2015, and February 03, 2015). The samples included the drillbit frozen and re-cored borehole-frozen water ice.

All the lake water frozen samples proved to be contaminated to a different extent with the kerosene-based drill fluid. The cell concentrations measured by flow cytometry varied from 167 (drillbit frozen water) until 5.5–38 cells per ml in different borehole-frozen samples. The comprehensive DNA analyses came up with total 53 bacterial phylotypes discovered by sequencing of different regions of 16S rRNA genes. Of them, only 3 phylotypes successfully passed all contamination criteria. Two phylotypes detected after the 1st lake unsealing were reported before [1] — hitherto-unknown and phylogenetically unclassified phylotype w123–10 showing less than 86% similarity with known taxa and likely belonging to *Parcubacteria Candidatus Adlerbacteria* featured by unusual biology and 3429v3-4 showing 93.5% similarity with *Herminiimonas glaciei* of *Oxalobacteraceae* (*Beta-Proteobacteria*) — water-inhabited ultra micro bacterium isolated from deep Greenland GISP2 ice core. The borehole-frozen water samples after the 2nd lake unsealing gave nothing of confident while the new finding just recently came from the samples after the 3rd lake unsealing. The phylotype 3698v46-27 proved to be conspecific with several species of *Marinilactobacillus* of *Carnobacteriaceae* (*Firmicutes*) sharing very similar 16S rRNA genes. Among them is *M. piezotolerans* isolated from 4.15 m deep sub-seafloor sediment core collected at 4790.7 m deep Nankai Trough. No archaea were detected in any samples.

Thus, 3 discovered bacterial phylotypes might represent ingenious cell populations in the subglacial Lake Vostok. New samples (new horizons) of the Vostok Lake water are under the study now.

References:

- [1] Bulat S.A. Microbiology of the subglacial Lake Vostok: first results of borehole-frozen lake water analysis and prospects for searching for lake inhabitants // Philosophical Transactions of The Royal Society A Mathematical Physical and Engineering Sciences. 2016. V. 374(2059)20140292.

ADVANCES IN ASTROBIOLOGY: LIFE IN ICE

R.B. Hoover¹ E.V. Pikuta²

¹ U.S. Space and Rocket Center, One Tranquility Base, Huntsville, Alabama 35805, USA, RichardBHoover@ICloud.Com

² Athens State University, 300 N. Beaty St., Athens, AL 35811, USA

Keywords:

Astrobiology, Extremophiles, Ice, Moon, Europa, Enceladus, Cyanobacteria, Carbonaceous Chondrites

Introduction:

The vast majority of the small bodies of our Solar System (e.g., comets, water-bearing asteroids and icy moons) as well as the outer planets are frozen worlds in which water ice is the dominant volatile. All known life forms require the co-existence of water, a source of energy and a small group (~20) of life-critical bioelements (mainly C, H, O, N, P, S). Since water in liquid state appears to be absolutely necessary for the delicate chemistry that makes life possible, it has become almost a paradigm that life and ice are incompatible. It has long been known that water ice is abundant on comets, the polar caps of Mars, and the icy moons and outer planets of the Solar System. However, it was not until the Galileo and Cassini spacecraft detected evidence for liquid water oceans beneath the frozen crusts of icy moons of Jupiter (Europa, Callisto, Ganymede) and Saturn (Titan, Enceladus) that these bodies became prime Astrobiology targets [1–4]. The Viking 1 (7/20/1976) and Viking 2 (9/3/1976) landings on Mars spurred interest in the cold desert ecosystems of Antarctica resulting in the discovery of cryptoendolithic cyanobacteria in thin films of liquid water in rocks [5]. Sabit Abyzov (INMI, RAS) discovered life in deep ice cores from Vostok Station, Antarctica including cryopreserved and viable cells of bacteria, actinomycetes, cyanobacteria, yeasts, fungi and diatoms [6–9]. Cyanobacteria are dominant life of Earth's cryosphere [10]. Diatoms, ice worms [11] and other organism produce proteins and enzymes that allow them to locally melt the ice allowing them to live in these frozen regimes.

Lunar samples returned by the Apollo missions half a century ago led to the conclusion that water did not exist on the Moon. In 1980, Markov et.al. [12] reported IR spectroscopy data showing evidence for valence bands and vibrations of the water molecule in lunar soil returned by Luna 24. However, these results were largely ignored. Recent reflectance spectra acquired by the Moon Mineralogy Mapper [M(3)] instrument revealed diagnostic near-infrared absorption features of water ice [13], confirming prior observations for water ice trapped in permanently shadowed regions of deep craters at the lunar poles. The water may have been deposited or transported to the moon by large water-bearing asteroids like Ceres or cometary nuclei. Water is essential for human life and it can be easily converted to fuel for liquid hydrogen and liquid oxygen rocket engines. These facts, combined with the 1/6 g and absence of atmospheric drag makes the South Pole of the Moon an attractive site for a Lunar Outpost and launching missions to Mars or other Solar System bodies. The possibility of cryopreserved extraterrestrial life forms make the polar craters of the Moon prime targets for Astrobiology.

Materials and Methods:

Samples of deep ice cores isolated using sterile techniques from just above Lake Vostok were provided by Sabit Abyzov, Institute of Microbiology (RAS) Moscow. The Orgueil C11 carbonaceous chondrite samples were provided the Planetary Studies Foundation, Galena, Illinois, USA. Miocene ice from the Beacon Valley Glacier of Antarctica was provided by Prof. Elena Vorobyova, Moscow State University. Pleistocene Ice samples from the Fox Permafrost Tunnel in Alaska and Vatnajökull Ice Cave of Iceland and the Whistler Ice Cave of Canada were collected by Hoover using sterilized stainless steel core tubes. Kemmerer bottles were used to collect water samples from the anoxic trough from deep beneath the perennial ice cover of Lake Untersee in Antarctica. Microorganisms contained within these samples were isolated, cultured and described by E.V. Pikuta with colleagues and their morphology and

motility was investigated with high resolution Optical and Video Microscopy methods and Field Emission Scanning Electron Microscopy with EDS at the NASA/Marshall Space Flight Center

Results:

Studies we have conducted on deep Vostok ice cores and samples from permafrost tunnels, ice caves, ancient glaciers and ice sculptures have resulted on the discovery of cryopreserved and complete cells of diatoms that living bacteria, protists, and other viable microorganisms, many of which were observed to exhibit active motility just after thawing from the ice [14].



Fig. 1.

Figure 1 provides FESEM images of astonishingly well-preserved diatoms, complete frustules of diatoms. The C and N content of the diatoms from **a**. 2827 m layer of Vostok ice core; **b**. the cell from the Miocene (8.1 mya) ice of Beacon Valley Glacier are like living cells indicating the organic matter was cryopreserved, The diatoms **c**. from the Orgueil CI1 carbonaceous chondrite have lack nitrogen and are infused with magnesium sulfate indicating they are ancient fossils rather than modern contaminants [15]. The tip of the ice sculpture **d**. yielded the new species *Sanguibacter gelidistatuariae* [14]. The Whistler Ice Cave **e**. of Canada contained **f**. ice worms *Mesenchytraeus solifugus* imaged in-situ while exhibiting motility within the glacial ice.

Conclusion:

Water is essential for all known forms of life. However, many organisms are cryopreserved and even viable in deep cores above Lake Vostok or in ice sculptures and caves of Antarctica, Canada and other frozen regimes of Earth. The discovery of water ice renders the permanently shaded deep craters at the lunar poles the Moon profoundly important for Astrobiology research and for future missions to Mars and other Solar System bodies.

References:

- [1] Khurana, K.K. et.al. Induced magnetic fields as evidence for subsurface oceans in Europa and Callisto // Nature. 1998. V. 395. P. 777–780.
- [2] McCord, T.B. et al. Hydrated Salt Minerals on Ganymede's Surface: Evidence of an Ocean Below // Science, 2001. V. 25. P. 1523–1525.
- [3] Lorenz, R.D. et al. Titan's Rotation Reveals an Internal Ocean and Changing Zonal Winds // Science. 2008. V. 21. P. 1649–1651.
- [4] Porco, C.C. et al. Cassini Observes the Active South Pole of Enceladus // Science. 2006. V. 311, P. 1393–1401.
- [5] Friedmann E.I., Ocampo R. (Endolithic blue-green algae in the dry valleys: primary producers in the Antarctic desert ecosystem // Science. 1976. V. 193. P. 1247–1249.
- [6] Abyzov, S.S., Bobin, N.E. and Koudryashov, B.B. Microbiological flora as a function of ice depth in central Antarctica // in Life Sciences and Space Research, Oxford, 1979. P. 99–103.

- [7] Abyzov, S.S. Microorganisms in the Antarctic Ice // Antarctic Microbiology, 1993. Willey-Liss Inc., New York. P. 265–295.
- [8] Hoover, R.B., Abyzov, S.S. and Ivanov, M.V. Environmental Scanning Electron Microscopy Investigations of Ancient Microorganisms from Deep Ice above Lake Vostok // Proc. SPIE. 1999. V. 3755, P. 187-198.
- [9] Abyzov, S.S., Hoover, R.B. et al. Comparative Results of Using Different Methods for Discovery of Microorganisms in Very Ancient Layers of the Central Antarctic Glacier above Lake Vostok // Advances in Space Research, Cospar, 2004. V. 33, P. 1222–1230.
- [10] Quesada, A. and Vincent, W.F. Cyanobacteria in the Cryosphere: Snow, Ice and Extreme Cold // in Ecology of Cyanobacteria II: Their Diversity in Space and Time. Springer-Science. P. 387–399.
- [11] Shain, D.H. Mason, T.A. et al. Distribution and behavior of ice worms (*Mesenchytraeus solifugus*) in south-central Alaska // Canadian Journal of Zoology. 2001. V. 79. No. 10. P. 1813–1821.
- [12] Markov, M.N., Petrov, V.S., Akhmanova, M.V., Dementjev, B.V. Infrared Reflection Spectra of the Moon and Lunar Soil // COSPAR Colloquia Series. 1980. P. 189–192.
- [13] Li, S., Lucey, P.G. et al. Direct evidence of surface exposed water ice in the lunar polar regions // Proceedings of the National Academy of Sciences. 2018. 201802345.
- [14] Pikuta, E.V. et al. *Sanguibacter gelidistatuariae* sp. nov., a novel psychrotolerant anaerobe from an ice sculpture in Antarctica, and emendation of descriptions of the family Sanguibacteraceae, the genus *Sanguibacter* and species *S. antarcticus*, *S. inulinus*, *S. kedieii*, *S. marinus*, *S. soli* and *S. suarezii* // International Journal of Systematic and Evolutionary Microbiology. 2017. V, 67. P. 1442-1450.
- [15] Hoover, R.B., Rozanov, A.Yu., Krasavin, E.A., Ryumin, A.K., Kapralov, M.I. Diatoms in the Orgueil Meteorite // Paleontological Journal. 2018. V. 52. No. 13. P. 1647–1650.

METHANOGENIC ARCHAEA AS MODEL MICROORGANISMS FOR ASTROBIOLOGY

O.R. Kotsyurbenko

Yugra State University, 16, Chekhova str., Khanty-Mansiysk, Russian Federation, 628012, kotsor@hotmail.com

Keywords:

Methanogenic archaea, methanogenesis, origin of life, panspermia

Methane is recognized to be the important biomarker in the concept of searching for life in the universe. Cosmic bodies in Solar System where methane was detected and subsurface water reservoirs are presumed are potential habitats for methanogenic microorganisms.

Methane is produced by methanogens that are strict anaerobic archaea reducing CO₂, some one-carbon compounds and acetate.

Evolutionary, methanogenesis seem to be one of the most archaic pathways to get energy for organisms on Earth. The hypothesis of chemolithoautotrophic origin of life states that life started from hydrothermal vent systems with metal sulfide surfaces or compartments acting as catalysts. In this scenario, the reductive acetyl-CoA or Ljungdahl-Wood pathway and hydrogenotrophic methanogens fixing CO₂ via this pathway are considered to be an ancestral pathway and primordial microbial living forms. In contrast to most other microbes, methanogens are generally unable to assimilate sulfate; instead, all known methanogens can use sulfide as the sole sulfur source, which may have been abundant on the early anoxic Earth.

Methanogens drive exotic metabolism and can live in habitats with environmental extremes such as anaerobiosis, high salt, high temperature, high pressure, or combinations of these. For this reason methanogenic archaea are good model organisms for astrobiologists to understand environmental limits for life and possible life outside of earth.

Methanogens are important terminal microbial group of the methanogenic microbial community, a complex trophically connected biological system. It composes of different microbial groups degrading organic matter step by step and sharing energy available from various metabolic processes. The occurrence of these processes is driven by thermodynamic laws. Methanogens depend on substrates provided by other microorganisms in the trophic chain and in turn regulates microbial processes by feedback.

Methanogenic microbial community could be a model biological system for the astrobiological experiment testing the hypothesis of panspermia including return space missions. The community should be enclosed in soil being a matrix that is suggested to protect microorganisms and increase their survival.

ASTROBIOLOGICAL STUDIES IN DUBNA

A.K Ryumin, M.I. Kapralov

Astrobiology Sector, Laboratory of Radiation Biology, Joint Institute for Nuclear Research, Dubna, Russia, 141980, arjumin@mail.ru

Keywords:

Astrobiology, meteorites, carbonaceous chondrites, microfossils, prebiotic chemistry, formamide, cosmic dust

Introduction:

Astrobiology is an actively developing area in modern science, located at the junction of many scientific disciplines, such as: cell and molecular biology, biophysics, chemistry, ecology, paleontology, astronomy, geology, planetology, climatology, etc. Astrobiological studies allow us to come closer to the problem of the origin of life and to clarify the question of the habitability of other celestial bodies.

In the astrobiology sector of the Laboratory of Radiation Biology (JINR), research is being conducted in the following main areas:

Study of microfossils and organic compounds in meteorites and in ancient terrestrial rocks

Microfossils are fossilized microorganisms and their metabolic products. They are important evidence of the prevalence of life in the universe. Microfossils are present in almost all sedimentary and sedimentary-volcanogenic rocks of the earth's crust, beginning with 3.9 billion years. The experience of bacterial paleontology made it possible to confidently distinguish microfossils in meteorites such as carbonaceous chondrites. The study of microfossils and organic compounds in meteorites and ancient terrestrial rocks will provide data on the forms of ancient terrestrial and extraterrestrial life and shed light on the problem of the origin of life.

In the astrobiology sector, more than 20 samples of meteorites (first of all, Orgueil and Murchison carbonaceous chondrites) and terrestrial rocks were studied using a Tescan Vega 3 electron scanning microscope. Several hundreds of images of fossil microorganisms were obtained and analyzed: coccoidal forms, filamentous forms similar to cyanobacteria and actinomycetes, prazynophytes, testate amoebae, alveolates, etc. Pennate diatoms were discovered for the first time in the Orgueil meteorite [1]

The study of the elemental and mineral composition of meteorites and terrestrial rocks is carried out by the method of x-ray energy dispersive microanalysis. When we study meteorites, we must be able to distinguish between ancient microfossils, which differ from terrestrial contaminants and abiogenic structures. Terrestrial contamination is detected using a microanalyzer, since we are dealing with pseudomorphs, which don't differ in chemical composition from their native meteorite. Abiogenic structures, as a rule, differ sharply from abiogenic morphologically.

Studies of the synthesis of complex prebiotic compounds from formamide under the action of radiation involving meteorites as catalysts

As is known, meteorites have inside a significant amount of organic substances, many of which are necessary for the origination of life. It is assumed that they were synthesized during the gas phase and then were integrated into minerals.

In particular, formamide (FA) (HCONH_2) — one of the simplest chemical compounds which is common both in the interstellar and interplanetary media — might have been such "initial material". The research performed at the Astrobiology Sector in cooperation with scientists of the University of Tuscia (Viterbo, Italy) has shown that more complex organic molecules can form from FA, including amino acids, carboxylic acids, sugars, nucleic bases, and even nucleosides. This diverse synthesis takes place when a mixture of FA and meteorite matter is exposed to ionizing radiation. After irradiation, a GC/MS method was used to identify the organic compounds in a complex mixture. Some important results on this field were published [2,3].

Biogeochemical studies of cosmic dust; study of cosmic matter using nuclear physics techniques

Cosmic dust (CD) research allows obtaining data on the regularities of the time distribution of the cosmic dust falling on the Earth surface, which is important for the reconstruction of the Earth's geological history and paleoclimate evaluation. Research on the CD structure, chemical and isotope composition, and biological properties helps solving fundamental problems like the nature of interplanetary matter and its role in the origin of life.

M.V. Frontasyeva et al. (Laboratory of Neutron Physics, JINR) have performed at the IBR-2 reactor neutron activation analysis of cosmic dust particles [4,5]. Samples were collected in Belarus, Georgia, Russia, the U.S., and more.

Most of the particles, when passing through the atmosphere, are subject to melting. It is especially typical of larger particles. Cosmic spherules have been observed; these particles are relatively easy to identify. They are the background magnetic component of cosmic dust. In the latter, Fe, Fe-Ni, and Fe-Cr minerals have been found most often.

Compared with Arctic ice, Antarctic ice contains much less terrestrial and no anthropogenic dust. S.A. Bulat et al. [6,7] performed in 2018 a cycle of studies to search for cosmic dust particles in Antarctic ice. Found were iron-stone micrometeorites, but no carbonaceous chondrites.

References:

- [1] Hoover R.B., Rozanov A.Yu., Krasavin E.A., Ryumin A.K., Kapralov M.I. Diatoms in the Orgueil Meteorite // *Paleontological Journal*. 2018. V. 52, No. 13. P. 1647–1650.
- [2] Saladino R., Carota E., Botta G., Kapralov M.I., Timoshenko G.N., Rozanov A.Yu., Krasavin E.A., Di Mauro E. First Evidence on the Role of Heavy Ion Irradiation of Meteorites and Formamide in the Origin of Biomolecules // *Origins of Life and Evolution of Biospheres*. 2016. V. 46. No. 4. P.515–521.
- [3] Saladino R., Bizzarri B.M., Botta L., Šponer J., Šponer J.E., Georgelin T., Jaber M., Rigaud B., Kapralov M., Timoshenko G.N., Rozanov A.Yu., Krasavin E.A., Timperio A., Di Mauro E. Proton irradiation: a key to the challenge of N-glycosidic bond formation in a prebiotic context, *Scientific Reports*. 2017. V. 7. No. 1. P. 1–7.
- [4] Frontasyeva M.V., Tselmovich V.A., Steinnes E. Atmospheric Deposition of Cosmic Dust Studied by Moss Analysis // *LPI Contributions*. 2018. V. 2067. P. 37–45.
- [5] Shetekauri S., Chaligava O., Shetekauri T., Kvlivdze A., Kalabegishvili T., Kirkesali E., Frontasyeva M.V., Chepurchenko O.E., Tselmovich V.A. Biomonitoring air pollution using moss in Georgia // *Polish Journal of Environmental Studies*, 2018. V. 27. No. 5. P. 2259–2266.
- [6] Bulat S.A., Ezhov V.F., Tselmovich V.A. The first observation of iron-nickel micrometeorites near the snow surface of the Central East Antarctic, Vostok Station // *Proceedings of the 19th International Conference “Physico-Chemical and Petrophysical Research as Part of Earth Sciences.”* Moscow. 2018. P. 45–48 (in Russian)
- [7] Bulat S.A., Bulat E.S., Grokhovsky V.I., Muftakhedinova R.F., Kolunin R.N., Tselmovich V.A., Sekatski S.K., Smirnov A.A., Ekaykin A.A., Petit J.R. Search for Antarctic Micrometeorites in Blue Ice Field, Lomonosov Mountains, Voltat Massive, Queen Maud Land, East Antarctica // *LPI Contributions*. 2018. No. 2067.

PINGOS ON SPITSBERGEN AND ON MARS AS ASTROBIOLOGICAL TARGET

N.E. Demidov¹, V.E. Demidov¹, Gunar A.Yu.², E.S. Karaevskaya¹, S.S. Krasilnikov³, S. Liebner⁴,

¹ Arctic and Antarctic research institute, St.-Petersburg, Russia, nikdemidov@mail.ru;

² Moscow State University, geological department, Moscow, Russia

³ Vernadsky Institute of Geochemistry and Analytical Chemistry RAS, Moscow, Russia

⁴ GFZ German Research Centre for Geosciences, Section 3.7 Geomicrobiology, Helmholtz Centre Potsdam, Postdam, Germany

Keywords:

pingo, bulgunyakh, Mars, Spitsbergen, astrobiology

Introduction:

Low temperature and pressure on the surface of modern Mars complicate presence of liquid water and life forms based on it. At the same time, microorganisms which could originate during warm and wet Noachian time potentially still exist in deep aquifers under permafrost. Deep biosphere of Earth colonized by chemolithotrophs may be considered as analog of this ecotone. This is the only ecotone where life could survive all history of Mars regardless to changing conditions on the surface [1]. However, great depth of burial makes them inaccessible for investigation. Young volcanism was considered as a possible way to transport biomarkers from the depth [2]. Another geological process which may result in transport of material from the depth to the surface is ground water seepage with formation of frost mound called pingo (in English literature) or bulgunyakh (in Russian).

Pingos on Earth, Spitsbergen:

Two pingo types are commonly distinguished on Earth, which are closed system and open system pingos. Closed system pingos usually form after drainage of lakes and following freezing of underlaketalik. Open system pingos, unlike closed system pingos, gravitate toward mountain relief and do not need presence of standing bodies of water on the surface. They form when freezing from the surface is accomplished by inflow of pressurized water from within or below permafrost. Both processes result in a massive ice body that heaves the surface and form conical elevations. Using logistic facilities of Russian scientific center on Spitsbergen we studied group of seven pingos in Grondalen valley in the vicinity of Barentsburg settlement on island Western Spitsbergen (Fig. 1). Pingos Fili and Noriwere entirely drilled through ice body to underlying permafrost; upper boundary of ice was sampled in Kilipingo. Hydrochemical measurements of ions Cl, SO₄, HCO₃, Na, Ca, Mg, K and measurements of isotopes δD and $\delta 18O$ in ice body showed composition similar to nearby spring [3]. This data allows us to reconstruct history of pingo formation in Grondalen as follows: after retreat of the sea from Grondalen freezing from the surface took place and open system pingos grew on tectonic fissure controlling seepage of groundwater fed by subglacial melt. Ground based georadar and noncontact electrical survey were performed on pingos to test geophysical methods for mapping underground ice bodies. Georadar with low frequency antennas (40 MHz) was unable to detect ice on Nori and Kilipingo (upper ice boundary according to drilling is located at depth 4,5 and 13 m, respectively) and all other pingos expect Fili, where due to degradational crater upper ice boundary is located at 1,5 m. Near-field transient electromagnetic sounding (NTES method) with square antenna (25, 50 and 100 m quarter) showed valid data only on Kili, Oin and Gloipingo. On geoelectrical crosse ctions (fig. 2) taliks with ground water are seen but, unfortunately, ice was indistinguishable from permafrost. On other pingos measurements were non-liquid due to absence of conductors in the section and polarization effect.

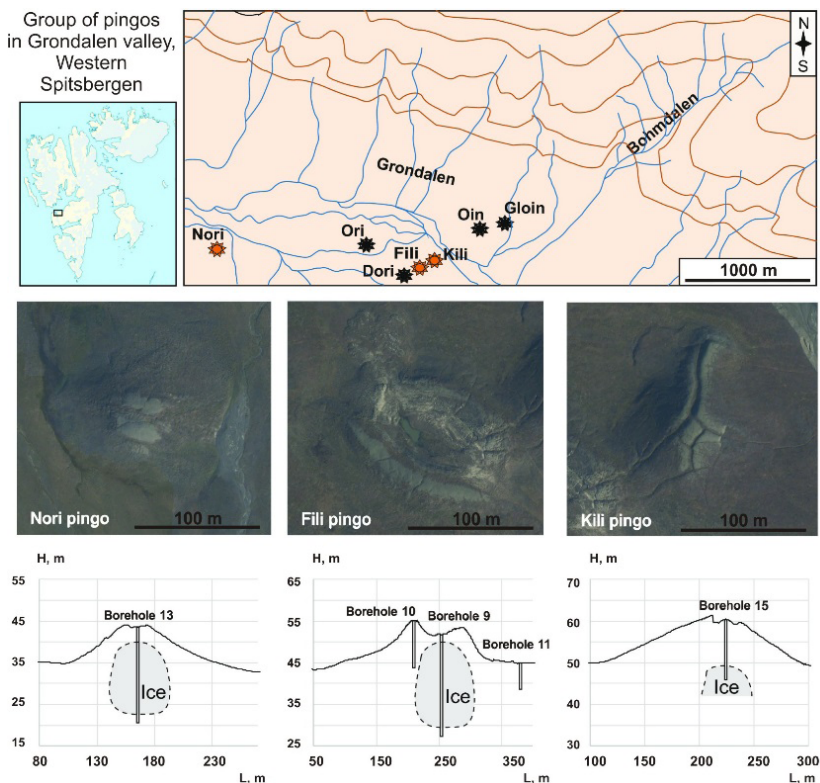


Fig. 1. Location, space images and crosssections of pingos in Grondalen, Western Spitsbergen.

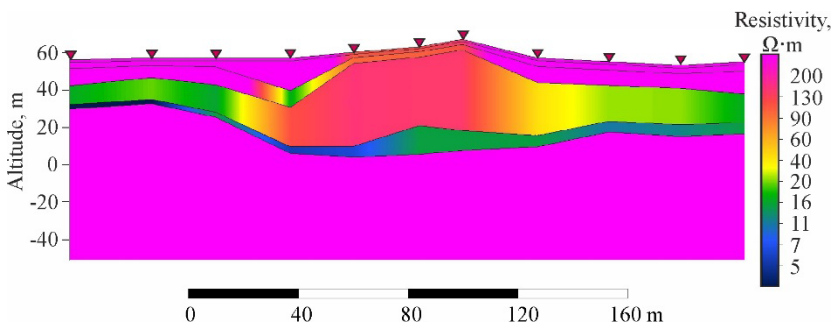


Fig. 2. Goelectrical crosssection of Gloipingo.

Pingos on Mars:

Discussion about presence of pingos on Mars has a long history. Mechanism of formation of frost mounds on Mars may be quite different from what we know on Earth. At the same time, it was proposed [4] that there should be no systematic difference between pingo heights and diameters on Earth and Mars. Using HiRISE images, we found several locations on Mars (fig. 3) with mounds having identical morphometry to open system pingos studied in Grondalen, Western Spitsbergen. Next step was to understand how Martian mounds comply with geomorphological diagnostic characters of Spitsbergen pingos, which are: correlation with glacier-like ice bodies, negative relief forms and tectonic faults, the source of pressurized ground water flow, presence of degradational crater and cracks on the top of mound.

Discussion:

Presence of mounds on Mars that match geomorphological criteria's for being pingo-like frost mounds drums up interest to potential presence of liquid water under the surface. Near surface massive pingo ice may be consid-

ered as the best resource of water for human exploration of Mars. It must be taken into account, that even on Earth detection of ice body and its geometry under pingo cone is complicated when using only geophysical survey without drilling. In next expeditions we plan to test detailed gravimetric measurements in combination with laser altimetry for mapping of pingos' massive ice. Spits Bergen pingos allow us to investigate processes of microbial life transport from deep biosphere to the surface and preservation of viable forms in ice. Results of microbiological studies of pingo ice, permafrost and spring water available for the conference date are going to be presented in the talk. Terrestrial pingo life refuge model may be useful for choosing candidate targets for astrobiological missions to Mars with shallow drilling and search for water and biomarkers.

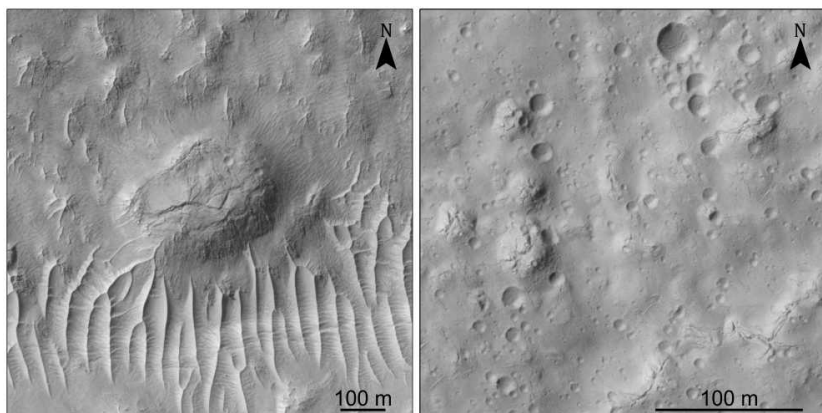


Fig. 3. HiRISE images of Mars' pingos-like features on the bottom of mid-latitudes craters. Left - 37°S 203°E (PSP_001578_1425), right - 33°S 131°E (PSP_002135_1460).

Acknowledgement:

This work is supported by a grant of Russian Science Foundation 19-77-10066.

References:

- [1] Demidov N.E. Martian econiches and perspectives of life search in them // Chapter 23 in "Life and Universe", Moscow: MVM. 2017. P. 253–263 (in Russian).
- [2] Gilichinsky M., Demidov N. and Rivkina E. Morphometry of volcanic cones on Mars in perspective of Astrobiological Research // International journal of astrobiology. 2015. V. 14. № 4. P. 537–545.
- [3] Demidov, N., Wetterich, S., Verkulich, S., Ekaykin, A., Meyer, H., Anisimov, M., Schirmeister, L., Demidov, V., and Hodson, A. J.: Pingo development in Grøndalen, West Spitsbergen // The Cryosphere Discuss., 2019, <https://doi.org/10.5194/tc-2019-76> (<https://www.the-cryosphere-discuss.net/tc-2019-76/tc-2019-76.pdf>)
- [4] Burr, D.M., Soare, R.J., Wan Bun Tseung, J.-M., Emery, J.P., 2005. Young (late Amazonian), near-surface, ground ice features near the equator, AthabascaValles, Mars // Icarus 178, P. 56–73.

TESTING THE EFFECTIVENESS OF IMPACT BOMBARDMENT ON EARLY MARS LANDSCAPE DEGRADATION

Benjamin D. Boatwright and James W. Head

Brown University, Providence, RI USA

benjamin_boatwright@brown.edu

Keywords:

Mars, impact cratering, landscape degradation, atmospheres, climate

Introduction:

Impact cratering is a major geomorphic agent on all planetary bodies, particularly on those where atmospheres are tenuous or absent. Emplacement of impact craters and ejecta resulting in net downslope transport of regolith is generally accepted as the primary agent of landscape degradation on the Moon [1-2]. At relatively low slopes, this process can be approximated by topographic diffusion, in which the volumetric flux of material being redistributed is a function of the slope [3-4]. Landform evolution modeling supports existing interpretations that landscape degradation on early Mars proceeded incrementally through a combination of advective fluvial sediment transport and diffusive mass wasting in a warm and arid climate over hundreds of millions of years [5-7]. The mechanism of diffusive degradation on early Mars remains poorly understood; since fluvial sediment transport has traditionally been linked to runoff from precipitation, rainsplash has been proposed as the primary diffusive mechanism [e.g. 8].

Diffusive degradation through impact bombardment as observed on the Moon has not been applied in the context of early Mars. The contribution to degradation of a given impactor population will be a function of the emplacement of each individual crater and also the size-frequency distribution of the population as a whole, both of which can be expressed as power law functions of the crater diameter D . In this context, the relative importance of large vs. small craters to the degradation of the surface can be explored. This is important for bodies with atmospheres such as Mars, since the atmosphere will filter out impactors below a certain size as a function of atmospheric pressure. We first explore a range of crater emplacement and production scenarios to determine which combination of these parameters is most conducive to impact degradation in general. Second, we compare these estimates to determine under what conditions atmospheric filtering may have been most efficient in removing small impactors from the population of degrading craters on early Mars.

Methods:

The net downslope volume flux due to crater emplacement is proportional to the topographic slope, which results in diffusive motion when mass is conserved [1,3]:

$$\bar{q} = -k\nabla h \quad (1)$$

The diffusivity k is a scaling factor that reflects the integrated effect of crater emplacement over the size and temporal range of cratering being considered.

Diffusive degradation has been defined using a time-integrated degradation state $K = kt$, which allows the uncertainty in the absolute diffusivity over time to be removed, and only depends on the observable (current) degradation state of the feature in question [3-4]. In simplest terms, the degradation state K can be expressed as a power law function of the crater diameter D :

$$K = cD^\alpha \quad (2)$$

The constant c will depend on empirical scaling relations, but the exponent will reflect a scale-independent property of the cratering process itself. The constant can be canceled by expressing the degradation state K as a ratio

to some initial state K_0 , which can be defined in the case of early Mars as the degradation state of the surface with no atmosphere.

According to Minton et al. [4], the exponent of D will depend on 1) an emplacement function for each individual crater, and 2) the production function for all craters in the population. They define the exponents as $\psi + 2$ for the emplacement function and η for the production function; thus, from Eq. 2:

$$\alpha = \alpha = \psi - \eta + 2 \quad (3)$$

The case of $\psi = 1$ indicates a simple volumetric (D^3) relation between D and the emplacement function and is the minimum physically plausible value. Minton et al. [4] suggest that $\psi = 2$, which satisfies the condition of geometric similarity identified in the equilibrium SFD of small lunar craters. Therefore, some value of $1 < \psi < 2$ on Mars is most likely. The Mars crater production function contains separate power law branches according to size [9]; therefore, the relevant value of η may change depending on what size range of craters are considered in the degrading population. For craters $D < \sim 64$ km, $\eta = 2.2$, and for craters $D > \sim 64$ km, $\eta = 1.8$ [9]. For craters $D > \sim 1.4$ km, the production function is much steeper, $\eta = 3.8$ [9]. The steeper production function at small sizes may be due to the emplacement of secondaries, but we will consider these, since the effects of secondary crater emplacement will be the same as primaries for the purpose of landscape degradation.

Logically, the size of the degrading crater must be smaller than the size of the feature being degraded. Thus, the landscape scale in question will implicitly determine the maximum crater size D_{\max} to be considered in the degrading population. We consider a range of D_{\max} from the meter to kilometer scale. The minimum crater size D_{\min} will depend on the introduction of atmospheric drag, which will curtail the impactor population according to the atmospheric pressure, gravity, and physical properties of the impacting body [10]:

$$L = \frac{0.001 \times 0.15P}{\rho g \sin\theta} \quad (4)$$

L is the minimum diameter impactor (km) that survives atmospheric entry for a given atmospheric pressure P (pascals, or 10^{-5} bar); ρ is the impactor density, taken to be 3000 kg/m^3 ; g is the acceleration due to gravity on Mars, 3.74 m/s^2 ; and θ is the average impact angle, taken to be 45° , or $\pi/4$; and v (used below) is the average impact velocity, taken to be 9.6 km/s . The value D_{\min} can be determined by substituting L into the Schmidt-Housen scaling law [11]:

$$D_{\min} = 1.16L^{0.78} (v \sin\theta)^{0.43} g^{-0.22} \quad (5)$$

Results:

We first compare a range of ψ and η values to determine which combination of these parameters is 1) most conducive to impact degradation in general, and 2) most conducive to efficient atmospheric filtering of small impactors. The results are illustrated in Fig. 1. For the likely range of $1 < \psi < 2$, the slope of the production function for craters larger than $D > \sim 1.4$ km results in $0.8 < \psi < 2.2$, which is positive in all cases. This means the largest craters in the population will dominate the degradation state K , and atmospheric filtering, which only affects the smallest size range, will have a minimal effect. For craters $D < \sim 1.4$ km, so smaller craters dominate the degradation state if $\eta < 3.8$. For $\eta = 3.8$, there is a slight bias toward larger craters, similar to the case for $D > \sim 1.4$ km. The much greater value of α overall means that atmospheric filtering will be more efficient, since small craters are much more numerous than large ones.

The exact effect of atmospheric filtering will depend on the choice of D_{\max} and the D_{\min} as determined by Eq. 5. In Fig. 2, we plot a range of atmospheric pressures from 0.01 to 10 bar against the ratio K/K_0 , showing the relative effects of atmospheric filtering on the degradation state K over a case with

no atmospheric filtering, K_0 , for different choices of D_{\max} for 0.01 to 5 km. As the atmospheric pressure increases, D_{\min} also increases, eventually leading to complete removal of impacts over the size range of degradation being considered. For the same atmospheric pressure, a choice of larger D_{\max} will allow larger craters to contribute to degradation, lessening the effect of atmospheric filtering overall. In Fig. 2a, we set to an average value of 1.5 and for craters km, and in Fig. 2b we do the same for craters km, and . As expected from Fig. 1, the effect of atmospheric filtering under conditions where there are much more substantial thanfor , and subsequently the change in D_{\max} is less important since larger craters are relatively sparse in the distribution.

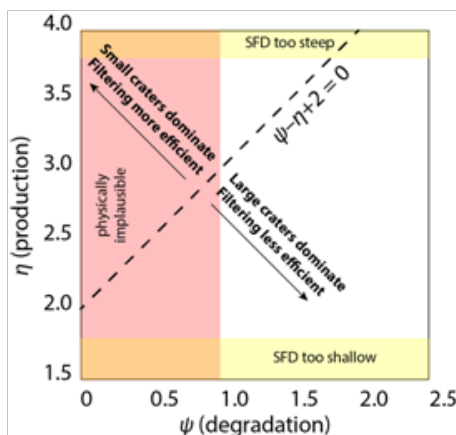


Fig. 1. Plot of two exponents determining the scaling of the degradation state K . The line divides the plot between cases of positive and negative. For , large craters will dominate the degradation state; for , small craters will dominate. is unlikely for physical reasons. For craters km, , which falls well below the line. This means the largest craters will dominate the degradation state and atmospheric filtering will have little effect. For km, , the smallest craters will dominate as long as , and atmospheric filtering will remove a significant portion of the population that contributes to landscape degradation.

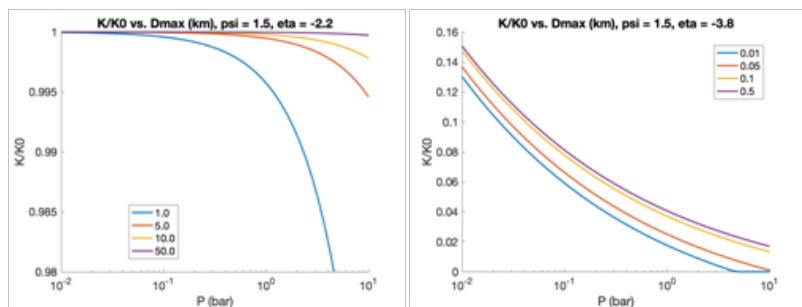


Fig. 2. (left) Plot of K/K_0 as a function of atmospheric pressure P for a range of D_{\max} for craters km, . (right) Same plot but for , typical of craters km.

Conclusions:

We have tested a range of conditions for crater emplacement and production on early Mars to determine the effects of impact degradation on the surface. The results are different depending on the size of the craters being considered. For craters km, the production function is relatively shallow, such that for a range of likely exponents for the emplacement function, landscape degradation caused by these craters will be dominated by the largest craters in the distribution, and atmospheric filtering of smaller impactors has little effect. This also means that, at sufficiently large spatial scales, landscape degradation by impacts could have played a significant role on early Mars even if the atmosphere was denser by up to several bars. In contrast, we have found that the degradation of the surface by small impacts (km) is significantly

more sensitive to atmospheric filtering. Even at pressures on the order of 10^{-2} bar, for D_{max} up to 0.5 km, suggesting that the smallest size range of craters is only an effective contributor to landscape degradation if atmospheric pressures are very low.

Landscape degradation by impact cratering on the Moon has been modeled as a diffusive process, where the absolute value of K is calculated using a priori assumptions of the initial topography. While we have not undertaken such an analysis here, similar steps could be taken to calculate the degradation state of various geomorphic features on the surface of Mars, particularly ancient craters that are thought to have undergone the majority of their degradation in the Noachian or Early Hesperian. Such an analysis would be complicated by the addition of other transport processes – namely fluvial erosion – that have also contributed to landscape degradation on Mars. One possibility is to use measurements of crater wall slopes, which have been minimally affected by fluvial processes, as a proxy for the amount of diffusive degradation that has occurred. If diffusive degradation on Mars could be simulated successfully, then the role of impact bombardment on the surface could be quantified in terms of the different emplacement and production scenarios explored here. Additional comparisons to atmospheric filtering profiles could also provide an independent estimate of the martian paleopressure and early climate conditions.

References:

- [1] Soderblom L.A. (1970) JGR 75;
- [2] Craddock R.A., Howard A.D. (2000) JGR 105;
- [3] Fassett C.I., Thomson B.J. (2014) JGR 119;
- [4] Minton D.A. et al. (2019) Icarus 326;
- [5] Craddock R.A., Howard A.D. (2002) JGR 107;
- [6] Forsberg-Taylor N.K. et al. (2004) JGR 109;
- [7] Mastubara Y. et al. (2018) JGR 123;
- [8] Craddock R.A., Lorenz R.D. (2017) Icarus 293;
- [9] Hartmann W.K. (2005) Icarus 174;
- [10] Melosh H.J. (1989);
- [11] Schmidt R.M., Housen K.R. (1987) Intl. J. Impact Eng. 5.

RAINFALL ON NOACHIAN MARS: NATURE, TIMING, AND INFLUENCE ON GEOLOGIC PROCESSES AND CLIMATE HISTORY

A.M. Palumbo and J.W. Head

Dept Earth, Environmental & Planetary Sciences, Brown University, Providence RI 02912 USA, Ashley_Palumbo@brown.edu

Keywords:

rainfall; climate; Noachian; erosion; rain splash; runoff

Introduction. Widespread valley networks (VNs) [1, 2] and lakes [3–5], indicate that overland flow occurred on Mars in the Late Noachian–Early Hesperian (LN–EH) [1], possibly related to abundant rainfall [8, 9]. This implies that the LN–EH climate and erosive regime were different than both earlier in the Noachian and later in the Hesperian and Amazonian [6, 7]. However, overland flow, a form of advective erosion, is not the only signature of liquid water on early Mars: Noachian-aged craters have degraded rims, shallow floors, and lack ejecta, features that cannot be explained without the dominant influence of diffusive erosion [8]. Researchers have postulated that rain splash, a form of diffusive erosion through which sediment transport is initiated by the collision of raindrops with the surface, was responsible for crater degradation [8]. Thus, the previously proposed paradigm for Noachian erosion follows [8, 10]: diffusive erosion from rain splash was dominant throughout most of the Noachian, causing crater degradation, and advective erosion from rainfall and runoff was dominant in the LN–EH, leading to formation of VNs and lakes. In this paradigm, in the Hesperian and Amazonian, temperatures are interpreted to have been too cold to permit rainfall, thereby explaining the absence of degraded craters, VNs, and lakes on younger terrains [8].

Analysis of the predicted nature and persistence of these two Noachian erosional regimes may provide insight into the early climate: was it “cold and icy” (with periods of punctuated heating to permit fluvial activity, as predicted by climate models) [11–13], or “warm and wet” (with continuous rainfall varying in rate and intensity as a function of time, suggested by the geology) [8, 9, 14].

Constraining the potential for a paradigm shift in erosional regime.

What approach can be undertaken in order to reconcile the geologic signature of rainfall with climate models that apparently cannot reproduce conditions with abundant rainfall? Recent work utilized measurements of fossilized raindrop imprints and mathematical relationships in order to estimate the atmospheric pressure on early Earth [15]. Craddock and Lorenz [10] called upon these methods to provide insight into the evolution of the early martian atmosphere and the process that could be responsible for the changing nature of rainfall. Based on their analysis, the authors suggested that the long-lived Noachian climate was “warm and wet” and that the rainfall erosional regime could have shifted from rain splash- to runoff-dominated as a function of decreasing atmospheric pressure through time [10]. This hypothesis is consistent with evidence for both diffusive and advective Noachian erosional regimes.

We revisit these mathematical relationships (following [10, 15]) in order to test the hypothesis that different erosional regimes could have existed under different atmospheric pressure regimes. This test provides insight into the plausibility that the long-lived Noachian climate was “warm and wet” with continuous rainfall of varying intensity [10]. By improving our understanding of the role that atmospheric evolution has on rainfall intensity and erosional regime, we strive to place tighter constraints on the predicted conditions that climate models must reproduce.

In order to estimate possible rainfall regimes that could exist as a function of atmospheric pressure, we employ a parameterized approximation of rainfall intensity as a function of median raindrop size. To do this, we must first introduce mathematical relationships for (1) the energy transfer from raindrops colliding with the martian surface and (2) the maximum raindrop size capable of passing through the martian atmosphere (following [10]).

The maximum amount of energy transferred as a raindrop collides with the surface is equal to the kinetic energy (KE) of the falling raindrop, which depends on the mass and terminal velocity of the raindrop as it passes through the atmosphere. Raindrop mass depends on raindrop size and can be approximated by assuming that the raindrop is spherical (

$m = V_{raindrop} \rho_{water} = \frac{4}{3} \pi \left(\frac{d}{2}\right)^3 \rho_{water}$, where d is drop diameter). The terminal

velocity of the raindrop depends on raindrop mass (m), gravity (g), atmospheric drag coefficient (C_d), atmospheric density (ρ_α), and cross-sectional area of the raindrop ($A = \pi \left(\frac{d}{2}\right)^2$), and is represented by the equation (eq. 1 from [10]):

$$v_t = \left(\frac{2mg}{C_d \rho_\alpha A} \right)^{\frac{1}{2}}$$

By using terminal velocity to estimate KE of the falling raindrop, we can estimate the energy transferred through the collision of a falling raindrop with the martian surface (following [10]):

$$KE = \frac{1}{2} m v_t^2 = \frac{m^2 g}{C_d \rho_\alpha A} = \frac{16}{9} \pi \frac{\rho_{water}^2 g}{C_d \rho_\alpha} \left(\frac{d}{2}\right)^4$$

Larger raindrops transfer more energy upon collision and the amount of energy transferred depends on atmospheric drag and density, gravity, and raindrop diameter. We find that rain splash is possible for a wide range of atmospheric pressure values.

Next, we estimate the maximum raindrop size that can pass through the martian atmosphere and reach the surface without breaking up, or the "fragmentation diameter" (FD) [10]. We review the derivation of the FD equation because previous studies made mathematical errors at this step. Fragmentation of raindrops begins when (eq. 3 from [10]):

$$v_t^2 d = \frac{8\gamma}{n \rho_\alpha C_d}$$

Where d is raindrop diameter, γ is surface tension on the raindrop, n is related to radius of curvature of the raindrop, and $n C_d$ is approximated as 1 due to the simplifying assumption of spherical raindrop shape (following [10]). To find a relationship for FD, we substitute for v_t , then substitute for raindrop mass (m) and cross-sectional area (A), and finally solve for d :

$$d = \left(6 \frac{\gamma}{\rho_{water} n g} \right)^{\frac{1}{2}}$$

FD depends only on raindrop surface tension (γ), the constant n , and gravity (g). Raindrop surface tension (γ) depends on temperature but not atmospheric density. The value is approximately constant for a reasonable temperature range; we implement a value of 0.0728 N/m (following [10]). The constant n is approximated as 1 [10]. Gravity (g) on Mars is 3.71 m/s².

FD does not depend on atmospheric density; the maximum raindrop size that could pass through the atmosphere has been approximately the same throughout history, regardless of decreasing atmospheric density (in contrast with [10]). For Mars, raindrop FD is 10.85 mm.

From FD, we can finally estimate rainfall intensity. Rainfall intensity is useful for estimating regimes where rainfall exceeds infiltration capacity, permitting surface runoff. A parameterized relationship for rainfall intensity follows:

$$D_{50} = \alpha I^\beta$$

Where D_{50} is the median drop size, approximated to be half the maximum drop size (or FD) [10], I is rainfall intensity, and α and β are coefficients that have been approximated from empirical measurements of terrestrial rain-

falls. This equation shows that larger drop sizes cause more intense rainfall. Importantly, because FD does not depend on atmospheric density, rainfall intensity also does not depend on atmospheric density, in contrast to the findings of Craddock and Lorenz [10]. Thus, we find that a change in rainfall intensity as a function of time is not predicted to occur naturally with decreasing atmospheric pressure. Recall that such a change in rainfall intensity is required to explain the shift from a diffusive to advective erosional regime in a long-lived “warm and wet” climate [10]. Our results suggest that either (1) the long-lived climate was “warm and wet” and a mechanism other than decreasing atmospheric pressure was responsible for the shift in rainfall intensity and erosional regime, or (2) the long-lived climate was “cold and icy” and the peak in fluvial activity and advective erosion in the LN-EH was due to punctuated heating, ice melting, and runoff, not rainfall.

Discussion and Conclusions.

We tested the hypothesis that two Noachian erosional regimes can be reconciled by a “warm and wet” climate with continuous rainfall and rainfall intensity that changed as a function of decreasing atmospheric pressure [10]. Testing work is critical for our understanding of the evolution of the hydrological cycle and for placing constraints on rainfall characteristics that GCMs must reproduce. We find that:

Raindrops on Mars are capable of transferring sufficient energy to initiate sediment transport regardless of atmospheric pressure.

Maximum raindrop size, or fragmentation diameter, does not depend on atmospheric pressure. This is in contrast to the findings of Craddock and Lorenz [10] due to a mathematical error in the earlier work.

Rainfall intensity does not vary as a function of atmospheric pressure.

There would not have been a transition between rain splash- and runoff-dominated erosion related to decreasing atmospheric pressure through time. This finding is inconsistent with the canonical view that the long-lived Noachian climate was “warm and wet” with continuous rainfall and that the rainfall intensity changed as atmospheric pressure declined.

Many outstanding questions remain, including:

If the long-lived Noachian climate was “warm and wet”, what mechanism can explain the apparent shift in rainfall intensity and erosional regime?

If the long-lived Noachian climate was “cold and icy”, what mechanism is responsible for producing a period of intense fluvial activity in the LN-EH?

Is melting of surface snow/ice and runoff capable of producing sufficient advective erosion to explain the VNs and lakes, or is rainfall required?

How can continuous diffusive erosion throughout the Noachian be reconciled with a “cold and icy” climate in the absence of rainfall?

Acknowledgments:

This work was supported by NASA Headquarters under NESSF to AMP; Grant 90NSSC170487.

References:

- [1] Fassett&Head 2008. Icarus.
- [2] Hynes et al. 2010. JGR Planets.
- [3] Cabrol& Grin 1999. Icarus.
- [4] Fassett& Head 2008. Icarus.
- [5] Goudge et al. 2015. Icarus.
- [6] Howard et al. 2005. JGR Planets.
- [7] Irwin et al. 2005. JGR Planets.
- [8] Craddock& Howard. 2002. JGR Planets.
- [9] Ramirez& Craddock. 2018. Nat. Geosci. Perspect.
- [10] Craddock& Lorenz. 2017. Icarus.
- [11] Wordsworth et al. 2013. Icarus.
- [12] Forget et al. 2013. Icarus.
- [13] Head& Marchant. 2014. Antarct. Sci.
- [14] Ramirez. 2017. Icarus.
- [15] Som et al. 2012. Nature.

O₂ NIGHTGLOW OBSERVATIONS IN THE MARTIAN ATMOSPHERE BY SPICAM/MEX

M. Zharikova^{1,2}, A. Fedorova¹, F. Lefèvre², F. Montmessin², O. Korabev¹,
G. Lacombe², J-L. Bertaux²

¹ Space Research Institute (IKI), 84/32 Profsoyuznaya, 117810 Moscow, Russia, mariyazharikova96@yandex.ru

² LATMOS du CNRS/IPSL, Guyancourt, France; ³ MIPT, Dolgoprudny

³ Moscow Institute of Physics and Technology, 9 Institutskiy per., Dolgoprudny, Moscow Region, 141701, Russian Federation

Keywords:

Mars, atmosphere, spectroscopy, the O₂ nightglow

Introduction:

Nightglow is a good indicator of circulation in the middle atmosphere of Mars in polar regions. In contrast with dayglow O₂(a1Δg) caused by photolysis of ozon on Mars, the O₂(a1Δg) nightglow is a product of recombination of O atoms formed by the CO₂ photolysis on the dayside at altitudes higher than 80 km and transported on the nightside through the meridional circulation of the Hadley cell: $O + O + CO_2 \rightarrow O_2^* + CO_2$.

The first observations of the emission on the night side have been obtained by OMEGA onboard of Mars-Express in 2010 [1] and later confirmed and studied by CRISM on Mars-Reconnaissance-Orbiter [2] and SPICAM on Mars-Express [3].

Infrared AOTF spectrometer SPICAM IR sounds the Martian atmosphere in the near-IR range (1-1.7 μm) with the spectral resolution of 3.5 cm⁻¹ in nadir, limb, solar and star occultation modes since January 2004 [4]. It allows to perform measurements of the O₂ emission with a good spectral power (~2200). FOV of the spectrometer at nadir and limb is 1° which corresponds to vertical resolution varied from 20 to 100 km.

In this work we will present a seasonal map of the O₂ nightglow in polar regions for several Martian years starting from MY30.

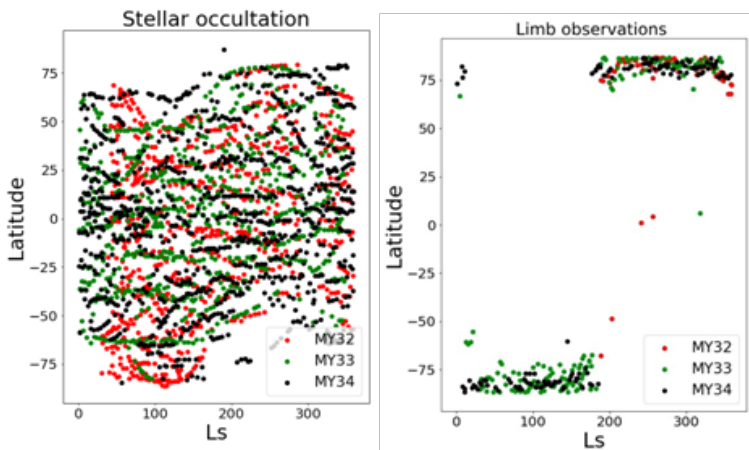


Fig.1. Distribution of limb observations and stellar occultations for MY32-34

References:

- [1] Bertaux J.L., et al. (2012), J. Geophys. Res., 117, E00J04;
- [2] Clancy R.T., et al. (2012), J. Geophys. Res., 117, E00J10
- [3] Fedorova A.A. et al. (2012), Icarus, Volume 219, Issue 2, p. 596-608
- [4] Korabev O. et al. (2006), J. Geophys. Res., 111, E09S03

FIRST MEASUREMENTS OF CARBON MONOXIDE IN MARTIAN ATMOSPHERE FROM ACS-TIRVIM SOLAR OCCULTATION OBSERVATIONS ONBOARD EXOMARS TGO

N. Savelyeva¹, N. Ignatiev¹, A. Grigoriev¹, A. Trokhimovskiy¹, A. Shakun¹, O. Korablev¹, F. Montmessin²

¹ *Institute for Space Research, Russian Academy of Sciences, ul.*

Profsoyuznaya 84/32, Moscow, 117997 Russia, korab@iki.rssi.ru

² *LATMOS/IPSL, UVSQ Université Paris-Saclay, UPMC Univ. Paris 06, CNRS, Guyancourt, France*

Keywords:

TGO ACS TIRVIM CO vertical profiles CO mixing ratio

The atmospheric chemistry suite (ACS) package is a part of the ExoMars space mission of ESA and Roscosmos. The ACS experiment is led by IKI Space Research Institute in Moscow.

ACS is installed onboard of the trace gas orbiter (TGO) satellite. ACS consists of three separate infrared spectrometers, including the thermal infrared channel (TIRVIM) is a 2-inch double pendulum Fourier-transform spectrometer for the spectral range of 1.7–17 μm with apodized resolution varying from 0.2 to 1.6 cm^{-1} [1].

TIRVIM is primarily dedicated to the monitoring of atmospheric temperatures and aerosol states in nadir. Besides of that, TIRVIM is used for solar occultation spectroscopy of minor gas species, including CO.

Processing of L1 data gathered by TIRVIM in solar occultation mode can be divided into the following steps, (1) retrieval of slant path optical thickness of the Martian atmosphere by transmitted solar radiation; (2) calculation of optical thickness of the separate atmosphere layers by “Onion Peeling” technique, (3) spectral separation of CO absorption from continuum extinction, wing absorption, etc., and (4) retrieval of vertical profiles of CO mixing ratio.

This paper describes the results of processing L1 data, gathered by TIRVIM instrument operating in solar occultation mode [2]. Besides the standard regularization and noise reduction techniques [3, 4], consideration of TIRVIM instrument function is required to avoid extra errors. Proper calibration and preprocessing of TIRVIM L0 data gathered in solar occultation mode provide for stable and reliable L1 data. Based on L1 data, the first vertical profiles of CO mixing ratio were calculated.

The project acknowledges funding by Roscosmos and CNES. Science operations of ACS are funded by Roscosmos and ESA. Science support in IKI is funded by Federal agency of science organizations (FANO).

References:

- [1] Korablev O., Trokhimovsky A., Grigoriev A.V., et al. Three infrared spectrometers, an atmospheric chemistry suite for the ExoMars 2016 trace gas orbiter. // *Journal of Applied Remote Sensing*. 2014. V. 8(1). No. 084983
- [2] Korablev, O., Montmessin, F., Trokhimovskiy A. et al. The Atmospheric Chemistry Suite (ACS) of three spectrometers for the ExoMars 2016 Trace Gas Orbiter. // *Space Sci. Rev.*, 2018, V. 214, No. 7
- [3] Moroz, V.I. Spectra and spacecraft. // *Planet. Space Science*. 2001, No. 49, pp. 173–190
- [4] Timofeev Yu. M. Vasil'ev, A.V. *Theoretical Foundations of Atmospheric Optics*. Nauka, St. Petersburg, 2003 143 p.

GRAVITY WAVES IN MARTIAN ATMOSPHERE FROM ACS/TGO SOLAR OCCULTATIONS: PRELIMINARY RESULTS

E.D. Starichenko^{1,2}, D.A. Belyaev^{1,2}, A.A. Fedorova^{1,2}, A.S. Medvedev^{3,4}, O.I. Korablev^{1,2}, F. Montmessin⁵, A.Trokhimovskiy¹

¹ Space Research Institute of the Russian Academy of Sciences, Moscow, Russia

² Moscow Institute of Physics and Technology, Dolgoprudnyi, Russia

³ Max Planck Institute for Solar System Research, Göttingen, Germany

⁴ Institute of Astrophysics, Georg-August University, Göttingen, Germany

⁵ LATMOS/IPSL, UVSQ Université Paris-Saclay, UPMC Univ. Paris 06, CNRS, Guyancourt, France

Keywords:

Martian atmosphere, gravity waves, Brunt-Väisälä frequency, solar occultation, Atmospheric Chemistry Suite, Trace Gas Orbiter

Introduction:

Gravity waves (GW) in the planetary atmospheres appear with periodic oscillations of the air mass, and, as a result, with fluctuations of density, temperature and pressure. Measuring vertical distribution of density and temperature, one can characterize altitude propagation of the atmospheric GWs. In this case the main parameters of GW – amplitude, vertical wave number (in $[\text{km}^{-1}]$), and Brunt-Väisälä frequency – can be estimated. The third value is the frequency, at which a displaced air parcel will oscillate when displaced vertically within a statically stable environment.

In this paper, we present preliminary results of the GWs retrievals in the atmosphere of Mars on a basis of solar occultation experiment being performed by the Atmospheric chemistry Suite (ACS) onboard ExoMars/TGO [1]. The ACS is a set of infrared spectrometers operating at the orbit of Mars since April 2018. The MIR channel ACS is a cross-dispersion spectrometer working in the 2.3–4.2 μm spectral range with resolving power reaching $\sim 30\,000$. In the solar occultation mode the spectrometer can observe thin layers of the Martian thermosphere and lower atmosphere in strong (e.g. 2.7 and 4.3 μm) and weak (about 3 μm) CO_2 absorption bands. The NIR channel is a combination of an echelle spectrometer and an acousto-optic tunable filter (AOTF) working in 0.73–1.6 μm spectral range with the resolving power $\sim 25\,000$. With high resolution infrared CO_2 spectroscopy these instruments give us an opportunity to thoroughly study the density, temperature and pressure of the Martian low atmosphere and the thermosphere. We characterize the atmospheric GW by analyzing the fluctuations of the vertical profiles of density and temperature.

References:

- [1] Korablev O., Montmessin F., and ACS Team. "The Atmospheric Chemistry Suite (ACS) of three spectrometers for the ExoMars 2016 Trace Gas Orbiter", SpaceSci. Rev., 214:7, 2018.

INVESTIGATION OF THE MARTIAN DUST DYNAMICS WITH DUST COMPLEX: INSTRUMENT DEVELOPMENT AND CALIBRATION

G. Dolnikov¹, A. Zakharov¹, I. Kuznetsov¹, A. Lyash¹,
I. Shashkova¹, V. Gotlib¹, E. Seran², M. Godefroy², F. Esposito³,
C. Molfese³, F. Cozzolino³, F. Cortecchia⁴, D. Scaccabarozzi⁵,
B. Saggin⁵, A. Martin Ortega Rico⁶

¹ IKI RAN, Moscow, Russia, kia@iki.rssi.ru;

² LATMOS, Paris, France;

³ INAF — Osservatorio Astronomico di Capodimonte, Napoli, Italy

⁴ INAF — Osservatorio Astronomico di Bologna, Bologna, Italy;

⁵ Politecnico di Milano, Milano, Italy;

⁶ INTA, Madrid, Spain

Keywords:

mars, dust, in-situ measurements, dust instrument, dust suit, dust complex

The load of suspended dust in the Martian atmosphere varies dramatically but never drops entirely to zero. Effects of airborne dust contribute to the dynamic and thermodynamic evolution of the atmosphere and its large-scale circulation processes on diurnal, seasonal and annual timescales. Suspended dust plays a key role in determining the present climate of Mars and probably influenced the past climatic conditions and surface evolution. Atmosphere dust and windblown dust are responsible for erosion, redistribution of dust on the surface, and surface weathering.

The mechanisms for dust entrainment in the atmosphere are not completely understood, as the current data available so far do not allow us to identify the efficiency of the various processes. Dust-grain transport on the surface of Mars has never been directly measured despite great interest in and high scientific and technological ramifications of the associated phenomena. This paper describes planned, future investigations of the Martian dust environment made possible by the scientific payload Dust Complex (DC) of the ExoMars-2020 mission's landing platform.

The Dust Complex is a suite of sensors devoted to the study of Aeolian processes on Mars. It includes four units: an Impact Sensor, the MicroMED sensor, Conductive sensor and a Mast. The Impact Sensor contains the main electronics of the DC and two different elements: a piezoelectric based sensor, for the detection of the saltating sand grain flux and momentum, and a Charge-Sensitive Grid for the measurement of the grains' electric charges. MicroMED is an optical-particle counter for the measurement of airborne dust size distribution and number density. The Mast accommodates the following sensors: 1) a second Impact Sensor, with the same sensors of the first one, 2) two Electric Probes for the measurement of the atmospheric electric field, 3) a Conductive Sensor, for the measurement of the electric conductivity of the Martian atmosphere and 4) an EM Sensor (antenna), which scans the atmosphere at frequencies up to 1 MHz to monitor electric discharges in the atmosphere.

The Dust Suit primary scientific goal is to monitor the dust cycle by direct measurements of dust flux at the surface of Mars. This has never been performed on Mars. Indeed, the dust cycle and the resulting feedback on atmospheric circulation are still poorly known for Mars. The unpredictability of the global dust storms on Mars is one of the most evident consequences of this lack of understanding.

ExoMars 2020 mission will offer a unique opportunity to study these processes by monitoring dust dynamics for one Martian year. This will allow spanning from periods of relatively clear sky to more dusty periods, where an important load of dust is expected to be injected into the atmosphere.

The presentation reviews outlining design and characteristics of DC, various dust effects and dust phenomena that are anticipated to occur in the near-sur-

face environment on Mars and that are possible to observe by DC as well as the instrument developing status.

Scientific outcomes of DC have future meteorological and environmental applications on Mars, for example, for the study of the evolution dynamics of the atmospheric aerosols and near-ground stratification.

PERFORMANCE OF A MINIATURE MARTIAN 3D WIND SENSOR IN THE DUST DEVIL SCALE

M. Dominguez-Pumar¹, L. Kowalski¹, V. Jimenez¹, S. Bermejo¹,
I. Rodríguez², M. Soria²

¹ MNT-Group. UPC-Campus Nord, Ed. C4. Jordi Girona 1–3. 08034 Barcelona, SPAIN;

² TUAREG-Group, UPC, Colom 11, Terrassa (Barcelona) 08222, Spain, manuel.dominguez@upc.edu

Keywords:

Wind sensor, mars atmosphere, anemometer, Navier-Stokes, Large-eddy simulations, extreme Martian winds.

Introduction:

The objective of this paper is to explore the performance of a miniature 3D spherical wind sensor for Mars atmosphere, [1-3], working under extreme wind speeds, up to the Dust Devil scale. The experimental campaign has been made for winds in the range Reynolds 1000–2000, which for typical Mars conditions and the dimensions of the sensor, represent 65–130 m/s wind velocities. The experimental results further confirm high-fidelity numerical simulations of the fluid dynamics and heat transfer from a sphere for Reynolds 1000–104 and Prandtl 0.7, recently published in [4], which indicate that it is possible to measure in this regime.

Sensor description:

The sensor is composed of 4 equally shaped sectors, conforming a 10 mm diameter sphere, that are placed on two superimposed PCBs, which act as supporting structure and provide signal routing (see Fig. 1), [1–3]. A customized silicon die which includes a Pt resistor is attached to each sector in order to sense temperature and provide heating power. The sensor is operated at the same constant temperature in the core and in all sectors. From the heating powers injected on the 4 resistors in the sectors and the air temperature, the thermal conductance of each sector is calculated. From these 4 signals 3D wind speed recovery can be made.

Main result:

The paper presents experimental results obtained under conditions representative of extreme wind velocities in Mars atmosphere. Reynolds numbers in the range 1000–2000 have been attained by controlling pressure and wind speed in a wind tunnel inside a dry-air hypobaric chamber at room temperature. These Renumbers represent wind speeds of 65 m/s–130 m/s for typical Mars conditions (CO_2 , 210 K, 630 Pa), for the sensor diameter.

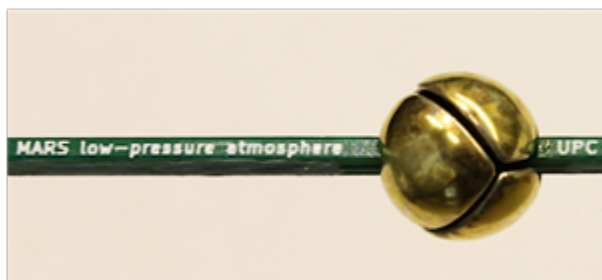


Fig. 1. Photograph of the 4-sector spherical sensor (10 mm diameter).

Simulation results:

High-fidelity simulations have been published in [4]. Direct numerical simulations (DNS) have been made for $\text{Re}1000$ and large-eddy simulations (LES) for $\text{Re}10^4$. As an example, a snapshot of the temperature field in the wake of the sphere at $\text{Re}10^4$ is shown in Fig. 2. The scalar represented is the normalized temperature where T_{sph} is the temperature on the surface of the sphere and T_{in} is the temperature of the fluid at the inlet.

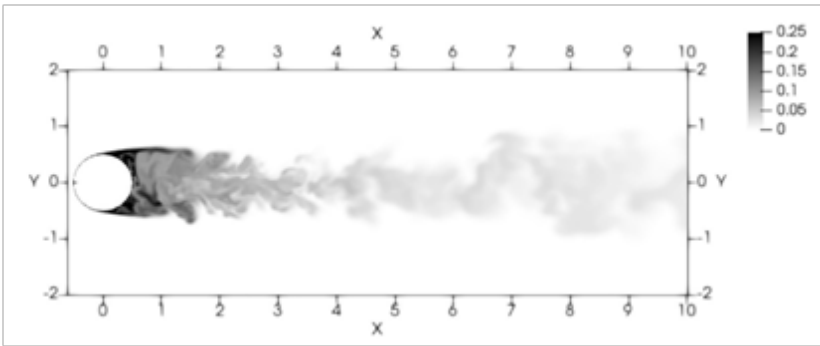


Fig 2: Figure from [4] showing a snapshot of the temperature field in the wake of the sphere for Re_{10^4} obtained from Large Eddy Simulations of the incompressible Navier-Stokes and energy equations.

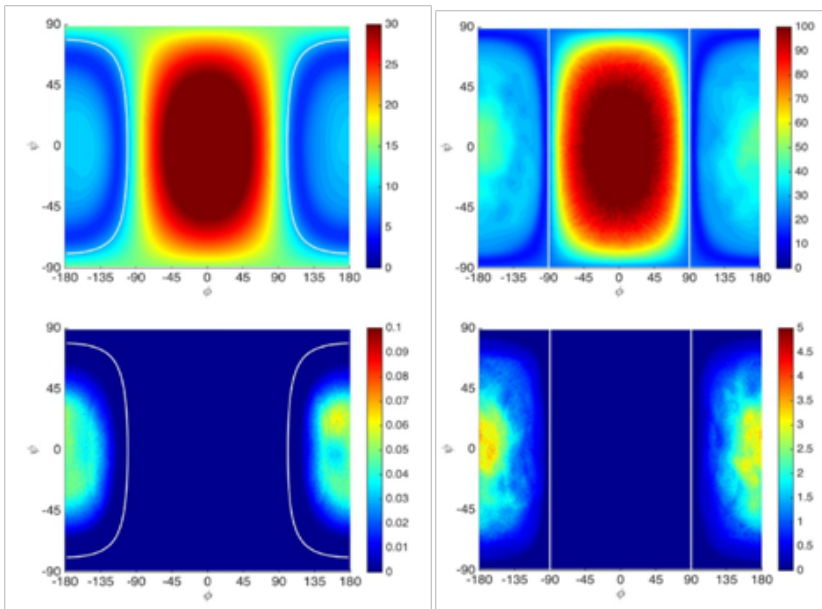


Fig. 3 — left shows the average local Nusselt number at Re_{1000} on the sphere. Fig. 3-right shows a section of Fig. 3 — left corresponding to a triangular sector (a first approximation to the sectors of the sensor).

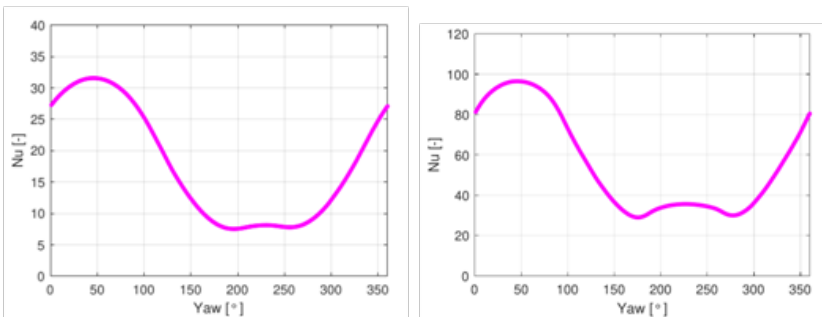


Fig. 4. Average Nu number for (left) Re_{1000} , (right) Re_{10^4} on a triangular sector of the sphere, as a function of yaw angle.

Fig. 3 — top graphs show the average Nusselt number on the sphere: (left) for Re_{1000} and (right) for Re_{10^4} . Fig. 3 — bottom graphs show the fluctuation rms values of the local Nu numbers. There are two stagnation

points: one in the front and another one in rear, in the wake of the sphere. The average Nu number in region near the rear stagnation points increase for increasing Re.

The simulations indicate that the average Nusselt of the sector as a function of the incident wind yaw angle presents a second maximum when the sector is near the rear stagnation point, which widens for increasing Re numbers. This represents a signature of the expected behavior of the sensor.

Experimental results:

Fig. 6 and 7 present the experimental curves obtained with the sensor in a wind tunnel inside a vacuum chamber at room temperature:

- Re1000: Equivalent UMars-flow of 65m/s (under typical Mars conditions). Udryair-flow in the chamber 6.5–7 m/s, $T_{\text{air}}=22.9\text{C}$, $T_{\text{sph}}=35.6\text{C}$.
- Re2000: Equivalent UMars-flow 130 m/s. Udryair-flow in the chamber 6.5-7 m/s, 500 mbar, $T_{\text{air}}=23.9\text{C}$, $T_{\text{sph}}=34.4\text{C}$.

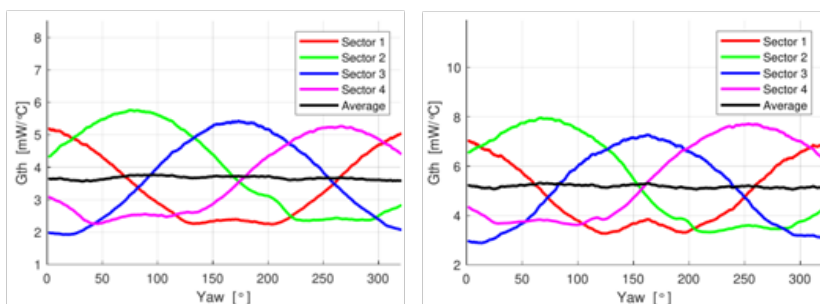


Fig. 6. Thermal conductances of each sector, and average value, as a function of Yaw angle for (left) Re1000. Equivalent UMars-flow velocity under typical Mars conditions of 65m/s. (right) idem for Re2000 (UMars-flow = 130m/s).

The thermal conductance of sectors follows the trend predicted by the simulations: for yaw angles leaving the sector in the wake of the sphere and for increasing Re numbers, the Gth presents widening minima and the maximum between them tends to increase. These preliminary results indicate that 3D wind speed inference can be made in this extreme regime.

References:

- [1] L. Kowalski, et al.. 2016. IEEE Sensors Journal, 16, P. 1887–1897.
- [2] M.T. Atienza, et al.. 2017. Sens. and Act. A, V. 267, P. 342–350.
- [3] M. Dominguez-Pumar et al. 2016. IEEE Trans. Ind. Electr., V. 64 (1), P. 664–673.
- [4] I. Rodriguez, et al.. V. 2019, Int. J. Heat and Fluid Flow, V. 76, P. 141–153.

HYDRODYNAMIC SIMILARITY OF DUST DEVILS ON EARTH AND MARS

Y.N. Izvekova^{1,2}, S.I. Popel^{1, 2}, O.Y. Izvekov²

¹ Space Research Institute, Russian Academy of Sciences, ul. Profsoyuznaya 84/32, Moscow, 117997 Russia

² Moscow Institute of Physics and Technology, 9 Institutskiy Pereulok, Dolgoprudnii, 141700 Russia

Keywords:

Dust devils, similarity theory, similarity criterion, planetary atmospheres, convective processes.

Introduction:

Convective processes resulting from the presence of vertical temperature gradients play an important role in planetary atmospheres. Particularly convection is the main cause of dust vortices (dust devils) on Earth and on Mars. This phenomenon is being actively investigated [1], but the final generally accepted model is not currently constructed. Dust vortices can lift and carry large amounts of dust from the surface which is especially important in the rarefied atmosphere of Mars.

Hydrodynamic similarity of convective near-surface vortices:

An important tool for studying processes in the atmospheres of planets is the theory of similarity. For example there is the well-known similarity theory for the circulation of planetary atmospheres [2]. In this work the hydrodynamic similarity of convective near-surface vortices is considered.

Phenomena are called similar if physical parameters differ in magnitude, but dimensionless complexes (similarity criterion) are the same [3]. It is also obvious that the physical essence of the phenomena must be the same. Analysis of free convective flows [4] shows that in our case flow velocity \mathbf{v} is as follows

$$\mathbf{v} = \frac{a}{L} f\left(\frac{\mathbf{x}}{L}, Gr \cdot Pr^2\right)$$

Where L is characteristic scale, \mathbf{x} is position in space, a is thermal conductivity, Gr (Grashof criterion) is a measure of the ratio of the Archimedean force and the viscosity forces, Pr (Prandtl criterion) is the ratio between the intensities of molecular momentum transfer and heat transfer by thermal conductivity.

Assuming for similar vortices that $Gr Pr^2$ is the same on Mars and on the Earth we obtain the ratio between the characteristic scales is about 17 (scales on Mars larger than on the Earth). Further, from the equality of dimensionless velocities for the Earth and Mars we obtain the characteristic flow velocity on Mars is about 2.6 times greater than the one on the Earth. The values obtained do not contradict the available data [5].

Here should be noted the possibility of the development of plasma processes in the atmospheres of the planets such as the generation of electric fields and charging of dust particles [6–7]. At the same time the dynamics of vortices are determined by hydrodynamic processes due to the prevailing role of the neutral component in the near-surface atmosphere. This fact makes possible to construct a theory of hydrodynamic similarity of convective vortices.

Conclusions:

The analysis showed that there is the similarity of dust vortices on the Earth and on Mars. This conclusion may be useful in the study of Martian vortices due to difficulties of direct measurements.

Acknowledgements:

The work is supported by the Russian Foundation for Basic Research (project No 18-02-00341).

References:

- [1] Barth E.L., Farrell W.M., Rafkin S.C.R. Electric field generation in Martian dust devils // *Icarus*. 2016. V. 268. P. 253-265.

- [2] Golitsyn G.S. A similarity approach to the general circulation of planetary atmospheres // *Icarus*. 1970. Vo. 1. No 1. P. 1-24.
- [3] Guhman A.A. Introduction to similarity theory. Vysshaya Shkola, Moscow, 1973. [in Russian].
- [4] Izvekova Y.N., Popel S.I., Izvekov O.Y. On calculation of vortex parameters in near-surface atmosphere of Mars // *Solar System Research*. 2019. V. 53 No. 5. [in press].
- [5] Ryan J.A., Lucich R.D. Possible dust devils, vortices on Mars // *Journal of Geophysical Research: Oceans*. 1983. V. 88. No. C15. P.11005–11011.
- [6] Izvekova Yu.N. and Popel S.I. Charged Dust Motion in Dust Devils on Earth and Mars // *Contrib. Plasma Phys.* 2016. V. 56. No. 3–4. P. 263–269.
- [7] Izvekova Y.N., Popel S.I. Plasma effects in dust devils near the martian surface // *Plasma Physics Reports*. 2017. V. 43. No. 12. P. 1172 – 1178.

COMPARISON OF LIULIN–MO DOSIMETER RADIATION MEASUREMENTS DURING EXOMARS 2016 TGO MARS' A CIRCULAR ORBIT WITH DOSE ESTIMATIONS BASED ON GALACTIC COSMIC RAY MODELS

Benghin V. ¹, Semkova J. ², Dachev Ts. ², Mitrofanov I. ³, Zelenyi L. ³, Malakhov A. ³, Shurshakov V. ¹, Maltchev St. ², Tomov B. ², Matviichuk Yu. ², Dimitrov P. ², Koleva R. ², Kanev K. ², Mokrousov M. ³, Sanin A. ³, Litvak M. ³, Kozyrev A. ³, Tretyakov V. ³, Golovin D. ³, Nikiforov S. ³, Drobyshev S. ¹

¹ *Institute of Biomedical Problems, Russian Academy of Sciences, v_benghin@mail.ru*

² *Space Research and Technologies Institute-BAS; jordankasemkova@gmail.com*

³ *Space Research Institute, Russian Academy of Science; malakhov@np.cosmos.ru*

Keywords:

ExoMars, Mars, radiation dose, FRENDO device, Lyulin-MO dosimeter

This presentation continues a series of publications devoted to the analysis of the results obtained with the Lyulin-MO dosimeter, which is a part of the FRENDO device, on board the ExoMars 2016 TGO interplanetary probe. From April 2018 to present, the spacecraft operates in a circular orbit around Mars at an altitude of about 400 km.

There are presented the results of a comparison of the measurements obtained with the Lyulin-MO dosimeter for this period of time with calculated estimates based on the galactic cosmic rays model. The effect of "shading" the particles flux by Mars, the albedo particles effect on the measured values and the effect of the detectors orientation are taken into account. Satisfactory agreement between measured values of radiation dose rate and calculated values is shown.

These results are important for manned mission to Mars radiation risk estimations.

THE ADRON-RM INSTRUMENT ONBOARD THE EXOMARS ROVER

**S.Y. Nikiforov, I.G. Mitrofanov, M.L. Litvak, A.A. Anikin, D.V. Golovin,
M.V. Djachkova, A.S. Kozyrev, D.I. Lisov, A.V. Malakhov, M.I. Mokrousov,
A.S. Sanin, V.I. Tretyakov**

*Space Research Institute of the Russian Academy of Sciences (IKI), 117997,
84/32 ProfsoyuznayaSt., Moscow, Russia, nikiforov@np.cosmos.ru.*

Keywords:

Mars exploration, Surface, NeutronSpectroscopy, Water, ExoMars

Introduction:

ExoMars is a joint Russian-European mission to study Mars. After the launch in 2020, the European rover and the Russian landing platform will be delivered to the surface of Mars.

The Adron-RM is a neutron detector, which is installed onboard the European rover [1]. This instrument will allow to analyze the hydrogen component (represented as bound water, water ice or OH (H₂O) molecules in hydrated minerals) in the upper subsurface of Mars using the method which was applied with the DAN instrument [1, 2]. A full description of the objectives and method of water equivalent hydrogen (WEH) estimation will be presented.

Neutron sounding of the Martian surface was first successfully carried out by the DAN experiment installed onboard the NASA Mars Laboratory. Based on the latest results obtained from the instrument, there is a serious correlation between the data obtained by means of the galactic cosmic-ray neutron flux and measurement using the neutron generator installed onboard the rover.

Adron-RM consists of two proportional counters filled with ³He, one of which has cadmium protection to eliminate the low-energy neutron flux. A parallel measurement of the neutron flux in the thermal and epithermal ranges allows us to estimate the subsurface structure of the martian subsurface in the area of ³He the rover traverse. Estimates the hydrogen component at different points of movement, made it possible to estimate a percentage value of the WEH content in the traversed area. Another important goal is to work in close synergy with the other instruments installed on the rover, in order to choose the most optimal place for the drilling experiment of the martian subsurface.

References:

- [1] Mitrofanov I.G. et al. 2017. *Astrobiology*, 17, 585–594.
- [2] Mitrofanov I.G. et al. 2014. *JGRE*, 119, 1579–1596.
- [3] Livak M.L. et al. 2014. *JGRE*, 119, 1259–1275.

LARA (LANDER RADIOSCIENCE) ON THE EXOMARS 2020 KAZACHOK LANDER

**A. Kosov¹, V. Dehant², S. Le Maistre², M. Yseboodt², R.M. Baland²,
Ö. Karatekin², M.J. Péters², A. Rivoldini², T. Van Hoolst², B. Van Hove²
and the LaRa team³**

¹ IKI — Space Research Institute of Russian Academy of Sciences, Moscow,
Russia, akosov@iki.rssi.ru;

² Royal Observatory of Belgium, Brussels, Belgium, lara@oma.be;

³ <http://lara.oma.be/team>

Keywords:

Radioscience, Mars rotation, precession, nutation, ExoMars.

The LaRa (Lander Radioscience) experiment is designed to obtain coherent two-way Doppler measurements from the radio link between the 2020 ExoMars lander (the Kazachok surface platform) and Earth during at least one Martian year. The Doppler shifts are measured by comparing the frequency of the radio signal received from LaRa with the known frequency of a ground-based reference signal. Transmitting signals from Earth to Mars and back again is called two-way communication and greatly enhances the accuracy of the radio experiment. The Doppler measurements are used to determine the orientation and rotation of Mars in space (precession, nutations, and length-of-day variations), as well as polar motion, more accurately than ever before. The LaRa transponder is designed to maintain the phase coherency of the signal, and the global precision on the Doppler measurements is expected to be better than 0.1 mm/s for a 60-second integration time (compared to instrument precision requirements at the level of 0.02 mm/s for a 60-second integration time). The final objective is to obtain new information and constraints on the interior of Mars, and on the sublimation and condensation cycle of atmospheric CO₂. Rotational variations will allow us to constrain the moments of inertia of the whole planet, including its mantle and core, moments of inertia of the core only, and seasonal mass transfer between the atmosphere and ice caps. The LaRa experiment will be combined with other ExoMars experiments in order to retrieve a maximum amount of information. We will also combine LaRa's Doppler measurements with similar data from the Viking landers, Mars Pathfinder, Mars Exploration Rovers, and the ongoing InSight/RISE mission, will provide information on the interior of Mars with unprecedented accuracy, improving our understanding of the formation and evolution of the Red Planet.

AMR INSTRUMENT FOR EXOMARS 2020: SCIENTIFIC PAYLOAD FOR STATIONARY MAGNETIC MEASUREMENTS ON THE SURFACE OF MARS

D. Rodríguez Díaz¹, J. Vicente López¹, J. García-Martínez¹,
R. Sanz González¹, C. Pérez García¹, R. Kilian², M.A. Rivero Rodríguez¹,
E. De Diego Custodio¹, A. Aspas Venegas¹, M.C. Parrondo Sempere¹,
J. De Frutos Hernansanz¹, J. Pazos Peces¹, M. Díaz Michelena¹

¹ INTA, National Institute for Aerospace Technology, Crta. Torrejón-Ajalvir km 4, 28850 Torrejón de Ardoz, Madrid, Spain;

² Geology Department, University of Trier, Behringstrasse, 54286 Trier, Germany.

Keywords:

AMR magnetometer, ExoMars 2020, Oxia Planum, COTS, deployment system, magnetic contamination, magnetic crust signatures.

Introduction:

AMR instrument is a magnetometer, part of the scientific payload on board the Rosalind Franklin Surface Platform for the ExoMars 2020 mission. The instrument has been through many different changes during the development of the early stages of the mission, including several reallocations within the surface platform for the mission, always searching for the most optimal position in terms of magnetic cleanliness.

The main scientific goals of the instrument are the determination of local magnetic crust signatures at the landing site, the Oxia Planum region, through measurements during the descent phase, and the monitoring of the magnetic field on the surface.

AMR magnetometer integrates two magnetometric units:

- the E-Box, allocated in the surface platform, is the physical and electrical interface with METEO. It deals with control, communications, magnetic sensing and power distribution tasks, and
- the S-Box, which is the main sensor unit including an ad-hoc deployment system that will allow the unit to be ejected up to a 2-meter distance from its ramp solar panel location in order to avoid the magnetic contamination from the platform.

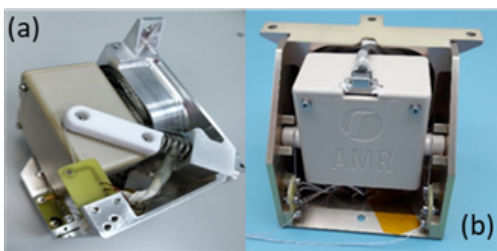


Fig. 1. a) S-BOX Thermal Model side view, b) S-BOX Deployment Assembly Unit Qualification Model.

The main sensing devices included in both units are COTS sensors whose working principle is the Anisotropic Magneto-resistive Effect. These sensors have been extensively screened, tested in low temperatures (as expected in the surface of Mars) and calibrated.

The AMR instrument has been completely designed, developed, manufactured, qualified and calibrated at INTA facilities. Of special attention is the qualification of the innovative deployment system and the calibration performed at the magnetic singular facility of INTA.

In this work the team will describe the instrument, its evolution and the most important technological and scientific results to the date after its delivery in Moscow for its acceptance and subsequent integration within the Rosalind Franklin Surface Platform before the launch of the mission in 2020.

Acknowledgements:

This project has received funding from the Spanish Programme of Research, Development and Innovation oriented to the challenges of the society under grant ESP2017-88930-R.

References:

- [1] M. Díaz Michelena, R. Kilian, R. Sanz, F. Ríos, O. Baeza. Mars MOURA magnetometer demonstration for high-resolution mapping on terrestrial analogues. *Geosci. Instrum. Method. Data Syst.*, 5. P. 127–142. 2016.
- [2] M. Díaz Michelena, R. Sanz, A.B. Fernández, V. De Manuel, M.F. Cerdán, V. Apéstigue, I. Arruego, J. Azcue, J.A. Domínguez, M. González, H. Guerrero, M.D. Sabau, R. Kilian, O. Baeza, F. Ríos, M. Herráiz, L. Vázquez, J.M. Tordesillas, P. Covisa, J. Aguado. MOURA magnetometer for Mars MetNet Precursor Mission. Its potential for an in situ magnetic environment and surface characterization. *Física de la Tierra*. 2016. V. 28. P. 65–82.

M-DLS EXPERIMENT FOR THE EXOMARS-2020 MISSION STATIONERY LANDING PLATFORM: INSTRUMENT DESIGN, FABRICATION AND CALIBRATION RESULTS

I.I. Vinogradov¹, V.V. Barke¹, I.Sh. Gazizov^{2,1}, I.V. Golovnin^{4,1}, V.A. Kazakov¹, T.O. Kozlova¹, Yu.V. Lebedev¹, C.V. Malashevich^{2,1}, V.V. Mescherinov^{2,1}, A.V. Nosov¹, A.V. Rodin^{2,1}, O.Z. Roste¹, M.V. Spiridonov^{3,1}, A.A. Venkstern¹, S.G. Zenevich^{2,1}, J. Cousin⁵, G. Durr⁵, M. Ghysels-Dubois⁵

¹ Space Research Institute of the Russian Academy of Sciences (IKI RAS), 117997, 84/32 Profsoyuznaya Str., Moscow, Russia, imant@iki.rssi.ru

² Moscow Institute of Physics and Technology (MIPT), 141701, Institutsky Dr. 9, Dolgoprudny, Moscow Region, Russia, alexander.rodin@phystech.edu

³ Prokhorov General Physics Institute of the Russian Academy of Sciences (GPI RAS), 119991, Vavilov Str., 38, Moscow, Russia;

⁴ Lomonosov Moscow State University, Faculty of Physics, 119991, GSP-1, 1-2 Leninskiye Gory, Moscow, Russia;

⁵ GSMA, UMR CNRS 7331, Université de Reims, BP 1039, 51687 Reims, Cedex 2, France.

Keywords:

ExoMars-2020; Martian atmosphere; chemical and isotopic composition variations; tunable diode laser absorption spectroscopy; integrated cavity output spectroscopy.

Introduction:

An application of tunable diode laser absorption spectroscopy (TDLAS) in combination with integrated cavity output spectroscopy (ICOS) was proposed for Martian atmosphere study as a Martian multichannel diode laser spectrometer, or M-DLS experiment. M-DLS instrument has been designed and fabricated as a compact and lightweight device for continuous in situ study of chemical and isotopic composition variations of atmosphere near the Martian surface at the ExoMars-2020 mission stationery Landing Platform.

Measurement method:

In the M-DLS experiment, Martian atmosphere will be studied by optical measurements of molecular absorption spectrum of ambient gas sample, taken from a close location, ahead of the stationery Landing Platform. Flexibility of TDLAS and radical optical path enhancement of ICOS are combined in the M-DLS instrument for fine measurements of weak absorption at low pressure of the Martian atmosphere sample. H₂O and CO₂ molecular content and isotopic ratio variations for D/H, ¹⁸O/¹⁷O/¹⁶O, ¹³C/¹²C will be retrieved from absorption data during one Martian year.

Instrument fabrication and calibration:

Following the M-DLS experiment idea, industrial design and fabrication of QM and FM units of the M-DLS instrument have been completed, in compliance with the M-DLS definite location on board of the ExoMars-2020 Landing Platform and of its interfacing with the LP scientific payload microprocessor control unit BIP and with other LP systems. Calibration of the M-DLS instrument parameters have been carried out in IKI RAS. For each of the two M-DLS units, there have been tested and verified mechanical, thermal, electrical, gas sampling, command and data interfaces, instrument functions and metrological parameters. Basic results of the tests and calibrations are shown in the presentation.

Summary:

The idea of M-DLS experiment, combining TDLAS and ICOS methods, was proposed for continuous study of atmosphere near the Martian surface. Compact and lightweight M-DLS instrument, aiming for in situ measurements of H₂O and CO₂ content and of D/H, ¹⁸O/¹⁷O/¹⁶O, ¹³C/¹²C isotopic ratio variations have been designed, fabricated, tested and calibrated for the scientific payload of the coming soon ExoMars-2020 mission.

References:

- [1] Vinogradov I., Klimchuk A., Alexandrov K., Barke V., Benderov O., Fedorova A., Gerasimov M., Ignatiev N., Kazakov V., Kozlova T., Lebedev Yu., Patsaeva M., Rodin A., Roste O., Sapgir A., Semenov V., Spiridonov M., Venkstern A., A multichannel diode laser spectrometer for in situ study of atmosphere near the Martian surface for the ExoMars-2020 mission Landing Platform // European Planetary Science Congress (EPSC 2017) Abstracts, Vol. 11, EPSC2017-23, Riga, Latvia, 17–22 September 2017.
- [2] Vinogradov I.I., Barke V.V., Kazakov V.A., Lebedev Yu.V., Rodin A.V., Roste O.Z., Venkstern A.A., Klimchuk A.Yu., Semenov V.M., Spiridonov V.V., Cousin J., Durrý G., Ghysels-Dubois M., Joly L., Diode laser spectroscopy instrument design for in situ study of atmosphere near the Martian surface // 18th International Conference on Laser Optics (ICLO 2018), DOI: 10.1109/LO.2018.8435269, St. Petersburg, Russia, 4–8 June, 2018.
- [2] Vinogradov I.I., Barke V.V., Kazakov V.A., Klimchuk A.Yu., Kozlova T.O., Lebedev Yu.V., Rodin A.V., Roste O.Z., Spiridonov M.V., Venkstern A.A., Zenevich S.G., Cousin J., Durrý G., Ghysels-Dubois M., Joly L., M-DLS experiment for the ExoMars-2020 stationery landing platform // The Ninth Moscow Solar System Symposium (9M-S3), 9MS3-PS-11, IKI RAS, Moscow, 8–12 October, 2018.

CHARACTERIZATION OF SPACE RADIATION MONITOR BASED ON DIAMOND SENSITIVE ELEMENTS FOR FUTURE INTERPLANETARY MISSIONS

K.V. Zakharchenko¹, A.A. Altukhov¹, R.F. Ibragimov², V.A. Kolyubin¹, S.A. Lvov¹, E.M. Tyurin²

¹ *Industrial Technological Center "UralAlmazInvest", Ltd. 121108, 4, Ivana Franko str., Moscow, Russia;*

² *National Research Nuclear University "MEPhI". 115409, 31, Kashirskoe sh., Moscow, Russia;*

Keywords:

Space radiation, electrons, protons, diamond, detector, calibration.

Introduction:

Radiation and temperature hardness of diamond detectors makes them perspective for applications in space radiation registration instrumentation for long-term space missions or for spacecrafts orbiting in radiation belts [1, 2]. To recover space radiation spectra the instrumentation must be calibrated. The absence of standard sources representing space radiation makes computing methods of calibration necessary.

The aim of this work is the calibration of the energy scale of diamond-based radiation monitor. To minimize the effect of device construction the calibration has been carried out using neutron radiation. The interaction of neutron radiation with the diamond is well investigated [3, 4] and the energy transmitted to the diamond by the neutrons is quite independent on the device construction so the calibration of completed device is possible.

Calibration method and results:

Brief description of the instrumentation.

The instrumentation includes a set of registration channels based on the diamond detectors. Registration of space particles in one channel is carried out as described in Figure 1.

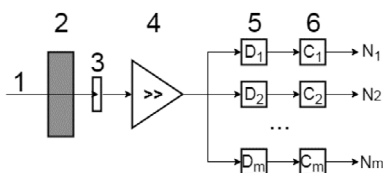


Fig. 1. Operation principle of one registration channel of radiation monitor. 1 — radiation; 2 — filter; 3 — diamond detector; 4 — amplifier; 5 — discriminators; 6 — particle counters; N_1 — N_m — output of m particle counters.

Cosmic particle 1 passes the filter 2 and hits the diamond sensitive element (DSE) 3. The output of DSE 3 is proportional to the energy transmitted to the diamond. After amplification in 4 the signal is sent to the discriminators 5 connected to the particle counters 6. The particle counter is actuated provided the energy transmitted by the particle to DSE exceeds the energy threshold of the discriminator. Processing of all counters readings is carried out to recover the radiation energy spectra.

The calibration of the instrumentation is conducted as follows: (1) the energy thresholds of counters activation are obtained using neutron radiation; (2) the spectra of the energy transmitted by different components of space radiation to DSE are computed and (3) the responses of counters to the action of space radiation are determined.

Energy thresholds determination.

To obtain the energy thresholds of counters activation the response of the instrumentation to neutron radiation has been measured [4]. The spectrum

of energy transmitted to DSE by neutron radiation has been recorded using 2048 channel spectrometer. The comparison of monitor's counters readings and spectrometer output allowed obtaining the energy thresholds of counters activation. Verification of energy thresholds has been carried out using beta radiation of a standard 90Sr:90Y source. The output of the spectrometer above the thresholds obtained has been compared to that of the counters of the instrumentation. The relative difference didn't exceed 6% [4].

To extend the method to other registration channels including different DSE we normalized the output of the spectrometer and that of the counters to be calibrated. The energy has also been normalized by the charge collection efficiencies of DSE. Verification of energy thresholds has been carried out as it has been described above. The spectrum of energy transmitted to DSE by beta particles has been computed using Geant4 platform.

The energy transmitted to diamond detectors and the counter responses.

An important part of calibration is the determination of the spectra of energy transmitted to DSE by different components of space radiation. We have computed these spectra using Geant 4 platform. The spectra $g_{e,p}(E, W)$ of the energy W transmitted to DSE of one registration channel by electrons and protons with different initial energies E are presented at Figure 2.

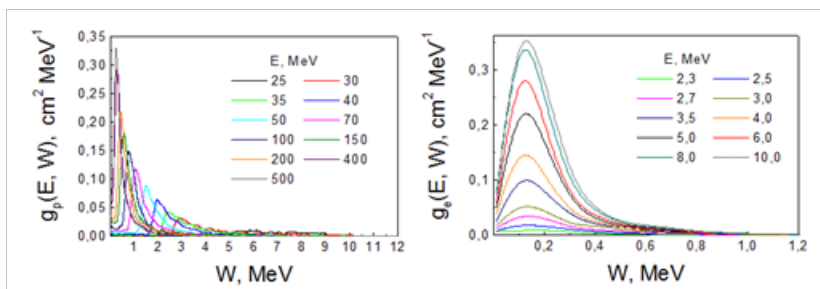


Fig. 2. Spectra of energy W transmitted to DSE by protons (left) and electrons (right) with initial energy E .

The electrons and protons of different energies are registered simultaneously so the counting rate of one counter C is the superposition of the responses to the action of monochromatic particles:

$$C = \int f_e(E) \cdot \sigma_e(E) dE + \int f_p(E) \cdot \sigma_p(E) dE \quad (1)$$

where $f_e(E)$ and $f_p(E)$ are the energy spectra of electrons and protons, respectively, determining their fluxes $\phi_{e,p}$ outside the instrumentation:

$$\phi_{e,p} = \int f_{e,p}(E) dF \quad (2)$$

$\sigma_e(E)$ and $\sigma_p(E)$ are the discrete efficiencies of electron and proton registration by the particle counter, E is the energy of cosmic particles outside the instrumentation.

The output of a set of particle counters is described by a system of equations similar to equation (1). To calculate electron and proton spectra the discrete efficiencies σ_e and σ_p must be measured. The values of σ_e and σ_p are calculated on the base of the spectra of the energy transmitted to DSE:

$$\sigma_{e,p}(E) = \int_{E_{tr}}^E g_{e,p}(E, W) dW \quad (3)$$

where E_{tr} is the threshold of counter activation. The dependences of discrete efficiencies of registration on the energy of the particles outside the radiation monitor are presented at the Figure 3.

Conclusions:

The method of calibrating the radiation registration instrumentation using neutron radiation has been developed and tested. Discrete efficiencies of electrons and protons registration of radiation monitor particle counters have been determined. The data obtained allow solving the equations

describing the outputs of the particle counters to determine the radiation spectra outside the instrumentation.

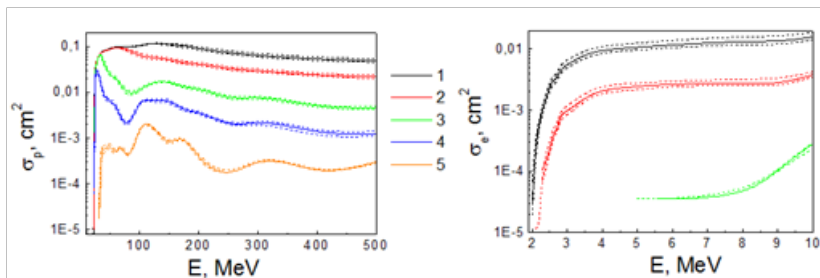


Fig. 3. The dependencies of discrete efficiencies of proton (left) and electron (right) registration on the energy of the particles. Curves 1–5 correspond to different particle counters of one registration channel (the energy threshold increases with the number of the counter). Dashed lines demonstrate lower and upper limits of the confidence intervals obtained from the uncertainties of energy thresholds.

References:

- [1] Kania D.R, Landstrass M.I., Plano M.A., Pan L.S., Han S. Diamond radiation detectors // *Diamond and Related Materials*. 1993. V. 2. P. 1012–1019.
- [2] Gladchenkov E.V., Zakharchenko K.V., Ibragimovich R.F., Kaperko A.F., Kolyubin V.A., Kulagin V.P., Nedosekin P.G., Tyurin E.M. Experimental Investigations and Mathematical Simulation of the Operation of Ionizing-Radiation Diamond Detectors // *Instruments and Experimental Techniques*. 2017. V. 60. No. 3. P. 339-344
- [3] Shimaoka T., Kaneko J.H., Ochiai K., Tsubota M., Shimmyo H., Chayahara A., Umezawa H., Watanabe H., Shikata Sh., Isobe M., Osakabe M. A diamond 14 MeV neutron energy spectrometer with high energy resolution // *Rev. Sci. Instrum.* 2016. No. 87. P. 023503
- [4] Altukhov A.A., Zakharchenko K.V., Ibragimov R.F., Kolyubin V.A., Lvov S.A., Tyurin E.M. Calibration of energy scale of the instrumentation of cosmic particles registration based on diamond sensitive elements using neutron radiation // *Proceedings of 22th all-Russian science and technology conference "Stoykost'-2019"*. Lytkarino. Russia. 2019. P. 79–80.

WARM AND WET MARTIAN PERIOD IN COMPARISON WITH MANTLE HEATING IN OTHER ROCKY PLANETS AND THE MOON

G.G. Kochemasov

*IGEM of the Russian Academy of Sciences, 35 Staromonetny, 119017
Moscow, RF, kochem.36@mail.ru*

Keywords:

Mars, warm period, wet period, Earth, Moon, mantle heating

Introduction:

The Earth-Moon system widens with time that is increases its angular momentum. A natural reaction to this is slowing the system's both bodies rotation diminishing the angular momentum (action – anti-action). The diminishing momenta are compensated by melting and uplifting to the surface of dense basaltic material [3-5]. But on the Moon this happens early (3-4.5 billion years ago) because of diminished inertia of the small satellite mass (Fig). Essentially “postponed” by time this process was on much more massive and inert Earth (the Jurassic-Cenozoic). Earth is 81 times more massive than its satellite. (3-4.5 b.y.) : 81 = 37-55 mln. y. According to these calculations the “peak” of the “basaltic” reaction of Earth, filling in oceanic basins gets into the boundary of the Mz-Cz. One more peculiarity of basaltic infillings of terrestrial oceans and lunar basins is in relatively high Fe content of the latter. This peculiarity speaks on smaller temperatures of basalt melting out of the lunar mantle and the higher their density. This correlates with a notion of relatively low temperatures in the mantle at the initial periods of transformation of the mechanical energy of moving to the heat energy for the mantle melting –creating asthenosphere.

Despite of enormous age differences between lunar and terrestrial basaltic covers (billions of years!) some common chemical shift of their compositions is notable and significant. Let us compare Procellarum Basin and Pacific Ocean basalts. The oldest parts of their covers occur in the W of Procellarum (KREEP) and SW of the Pacific (Ontong Java Plateau – the largest LIP of Earth). Potassium, phosphorus, rare earths, thorium enrich the older lunar KREEP basalts. The older terrestrial oceanic Ontong Java basalts (Cretaceous age-about 122 mln. y) also show “KREEP trend”. They belong to E-MORBs and have elevated values of potassium, lithium, chlorine, REE, thorium. Elevated Fe/Mg (and siderophile platinum group elements) also is in Ontong Java basalts [1, 2]. All these chemical peculiarities distinguish them from the younger N-MORBs of other parts of the Pacific Ocean (EPR, for example). As all considered basalt melts of both bodies originate in asthenospheres, the older parts of these melts derive from relatively earlier “cool” asthenosphere. It means that only easily melted alkali and iron rich parts were involved in the process. Later on, significantly heated asthenospheres produced enormous volumes of chemically different (less alkaline and more magnesian) basalts. In this sense, rather impressive is a comparison of the lunar iron and thorium geochemical maps stressing coincidence of their anomalies in the Procellarum KREEP terrain area.

The considered time development of basaltic magmatism could be paralleled with the development of alkaline terrestrial magmatism [6]. Its earlier older parts often are more alkaline than later Cenozoic parts. Famous large agpaitic massifs are mainly Proterozoic-Paleozoic in age. Again, early “cold” asthenosphere produces more easily melted relatively small alkaline parts than the later “hot” asthenosphere making large volumes of deeply melted more magnesian less alkaline ones.

Mars is intermediate by mass between Earth and the Moon (Fig). It is ten times less massive than Earth and 11 times more massive than the Moon. Moving in the wider orbit with its own peculiarities, small Mars, nevertheless, also fills in its dichotomous Northern Basin (Vastitas Borealis) by relatively ferruginous basalts. Beginning of the effusions is considered, by impact

(?) crater counts, to be in the end of the Hesperian, that is about 3 b.y. ago. The last ages of crater infillings in the giant volcanoes are determined as 3 b.-500-200 m. y. [7-9]. Counting age of massive effusions by the mass relations of Earth (Moon) and Mars (understanding difference in orbits influencing warming mantle and melting basalts) one gets ages 400-270 m. y. The rejuvenation of melting out intervals and their widening in Mars is evident, what resembles terrestrial processes. The martian mantle melting and its warm and wet period occur in agreement. According to sequence of masses and inertia of above three celestial bodies (not considering difference of their orbits) their planetary basaltic “explosions” form up a regular age row – from the oldest of some billion years to the Mz-Cz. The massive Venus also is regularly inscribed in this row with its vast Mg-rich basaltic cover. Giving up a little to the Earth by mass (but superior to it by the frequency of orbiting), it gives up a little to Earth in age of the basaltic “explosion”. Counting impact (?) craters gives age about 500 mln.y. It is older than calculated (4.5-3 b.y.: 66=68-45 mln.y.) but is not absolutely determined – the “explosion” could last some prolonged time.

Two inner planets – Venus and Mercury are united by big orbiting frequencies, slow rotations, abundant degassing (atmosphere is preserved on Venus and is “swept” away on Mercury), and abundant Mg-rich magmatism.

So, the terrestrial group planets and the Moon have various masses and a common significant geomorphologic peculiarity: their negative surface forms – depressions of various scales (oceans, basins, and seas) are filled with dark dense basaltic material. It is explained by that the loss by bodies of rotation rate, that means angular momentum, must be compensated by transfer to surface of relatively dense basaltic material. To prepare basaltic melts, in the mantle depths temperature must be raised to a certain level, and in bodies significantly differing by mass and rather impoverished in heat-generating radioactive elements. A plausible process for this is transition of the mechanical energy of orbital movement into the heat energy. This process is connected with a mass or inertia bodies. If the mantle of the smallest body – the Moon is warmed up quickly and the absolute ages of the surface basalts are 3-4.5 b. y. , then oceans of the massive and inert Earth are filled with basalts aged some tens of million years and even modern. Other three planets with intermediate masses show intermediate ages of basaltic “explosions”.

Wide basaltic covers are characteristic for the rocky planets and the Moon. However, ages of basaltic effusions are significantly different. Small Moon develops asthenosphere for making melts very earlier- 3-4 billion y. ago. 81 times more massive Earth develops its asthenosphere much later- in the MZ-Cz. These age differences are proportional to their masses. In both bodies the earlier basaltic melts are richer in alkalis and iron reflecting a “cool” state of the earlier asthenospheres. Later, the “warmer” mature asthenospheres produce large volumes of less alkalic more magnesian basalts.

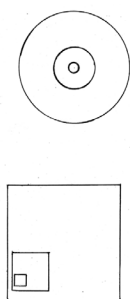


Fig. 1. Comparison of Earth (big circle or square), Moon (smallest circle or square) and Mars masses

References:

- [1] Ely J.C. and Neal C.R. Using platinum-group elements to investigate the origin of the Ontong Java Plateau, SW Pacific // *Chemical Geology*, v. 196, 2003, 235-257.

- [2] Hiesinger H., and J.W. Head III. (2016) Ages of Oceanus Procellarum basalts and other nearside mare basalts // Workshop on New Views of the Moon II, 2016, abs.8030.
- [3] Kochemasov G.G. (2014) Earth and Moon: similar structures – common origin // NCGT Journal, 2014, v. 2, # 2, 28-38.
- [4] Kochemasov G.G. (2015) A lunar “mould” of the Earth’s tectonics: four terrestrial Oceans and four lunar Basins are derivative of one wave tectonic process // NCGT Journal, v. 3, # 1, 2015, 29-33.
- [5] Kochemasov G.G. New planetology and geology: tectonic identity and principal difference of terrestrial oceans and lunar basins // New Concepts in Global Tectonics (NCGT) Journal, 2017, V. 5, # 1, p 131-133.
- [6] Kogarko L.N. and Khain V.E. Alkaline magmatism in the Earth’s history: geodynamical interpretation // Doklady of the Academy of Sciences. 2001. vol. 377 Iss. 5 pp. 677-679 (in Russian).
- [7] Martel, Linda M.V. (2005-01-31). “Recent Activity on Mars; Fire and Ice”. Planetary Science Research Discoveries. Retrieved 2006-07-11.
- [8] Neukum G. et al. Surface age of martian shield volcanoes and channels // Abstracts X Lunar and Planetary Science Conference, March 19-23 1979, part 2, p. 907-909.
- [9] Neukum G., et al. (2004) “Recent and Episodic Volcanic and Glacial Activity on Mars Revealed by the High Resolution Stereo Camera”. Nature, v. 432, 971- 979. doi:
- [10] 1038/nature03231. PMID 15616551..

MULTISCALE HIPSOMETRIC WEB-MAP OF MARS

O.S. Tretyukhina

Vernadsky Institute, Moscow, Kosygina street 19, 119334, lekanosova@gmail.com;

Keywords:

Mars, GIS, MOLA, TileMill, DEM, multiscale map, web mapping.

Introduction:

The project is relevant in view of the active development of the space industry and geoinformation technologies on the Web. It helps to visualise the survey data of the surface of Mars using modern Internet technologies together with traditional methods of hypsometric map design.

The process of the map creation:

Using ArcGis.

Five digital models of MOLA (The Mars Orbiter Laser Altimeter) [1] were used in the work: CB (29.6 km/pixel), EB (7.41 km/pixel), FB (3.7 km/pixel), GB (1.8 km/pixel), HB (0.92 km/pixel). Depending on the spatial resolution of the digital models, they were used to create maps different scales. The most detailed digital models were used in the maps of the large scale.

Three stages were followed to create a scale of height with various height levels for different zooms (Tab. 1): allocation of height levels depending on the distribution of heights, averaging DEM heights for generalization on smaller scales (focal statistical with different cell size) and contour drawing. For each of the scales its own hillshade was created: the larger the scale, the higher the resolution of the DEM on which the hillshade was made.

Table 1. Parameters of the scale of heights

Scale inTileMill	Scale inArcGis	Using DEM	Cell size	Contours
1	1:160 000 000	CB	15	-7; -5; -3; -1; 0; 1; 3; 5; 7; 10; 15; 21; 22
2	1:80 000 000	EB	25	-7; -5; -3; -1; -2; 0; 1; 2; 3; 5; 7; 10; 15; 21; 22
3	1:40 000 000	FB	10	-7; -5; -3; -4; -2; -1; 0; 1; 2; 3; 4; 5; 7; 10; 13; 15; 19; 21; 22
4	1:20 000 000	GB	20	-7; -6; -5; 4; -3; -2; -1; 0; 1; 2; 3; 4; 5; 6; 7; 8; 9; 10; 11; 13; 15; 17; 19; 21; 22
5	1:10 000 000	GB	10	-7; -6; -5; 4; -3; -3,5; -2; -2,5; -1; 0; 1; 2; 2,5; 3; 3,5; 4; 5; 6; 7; 8; 9; 10; 11; 13; 15; 17; 19; 20; 21; 22
6				-7; -6; -5; 4; -3,5; -3; -2,5; -2; -1; 0; 1; 2; 2,5; 3; 3,5; 4; 5; 6; 7; 8; 9; 10; 11; 12; 13; 14; 15; 16; 17; 18; 19; 20; 21; 22
7	1:5 000 000	HB	10	
	1:2 500 000	HB	—	At500-meters intervals

A table of Mars forms of relief contains 1767 objects with coordinates, types, and physical characteristics. It was downloaded from the site Planetary Names [2]. At each zoom there is a special set of objects and there is a special font for each type.

UsingTileMill.

Each layer – polygons, lines, points, etc. – is processed separately using the language Carto (Fig. 1). Colour of the height scale and signatures of contours are the main steps of the map design.

Hillshade is the lowest layer. The next is the colour with transparency for better visibility of hillshade layer and readability.

The colours of layer colouring should provide relief to the map readers, increase visibility and readability of maps.

```
.places[zoom>0]{
  [name!='Mars-2'][name!='Mars-3'][name!='Mars-6'][name!='Beagle-2']{
    marker-file:url('C:\Users\Olya\diploma\text\flags\_ _48_ .png');
    marker-transform:"scale(0.05)";
    text-size:13;
    text-face-name:"Book Antiqua Bold Italic";
    text-name:[name];
    text-dx:10;
    text-dy:10;
    text-placement-type:simple;
    text-placements:"SE,WN,NE,SW";
    text-avoid-edges:true;
    [zoom>3]{text-size:15;}
    [zoom>5]{text-size:17;marker-transform:"scale(0.4)";text-dx:15;text-dy:15;}
    [name='Beagle-2']{text-placements:"SE,E,NE";}
  }
}
```

Fig. 1. Example of the code in TileMill.

The project is based on the principles of hypsometric scales design developed by Austrian cartographer Karl Peiker: use light and bright shades for the upper levels of the relief, and dark and cold shades for the bottom levels to achieve a better relief of a map [3]. As the basis of the color scale the shades of orange, red and brown were taken to create an associative image. The shades become lighter at the top (Fig. 2).

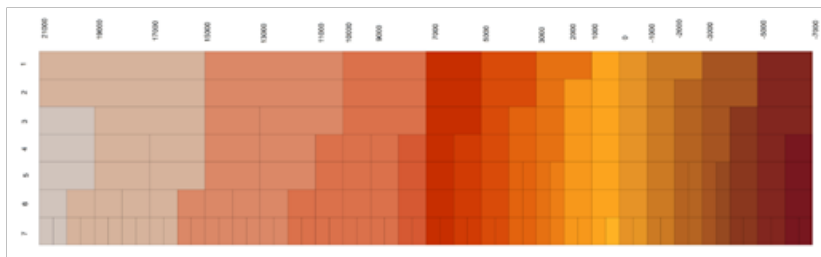


Fig. 2. Colour scale.

The final step is export map of or mat Mbtiles, which allows to save map stiles, and uploading to Mapbox for public access (Fig. 3).

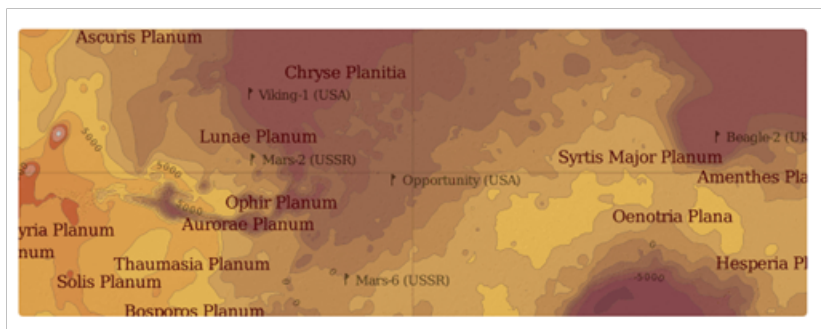


Fig. 3. Map fragment in zoom 4.

References:

- [1] <https://ode.rsl.wustl.edu/mars/>
- [2] <http://planetarynames.wr.usgs.gov>
- [3] Haliulina A.R., Samsonov T.E. Multiscale hypsometric map of Russia // Publisher MSU, 2013. URL: http://istina.msu.ru/media/publications/article/07e/9a1/4616970/Haliullina_Samsonov_2013.pdf

POSSIBLE ELECTROMAGNETIC EMISSIONS ABOVE THE MAGNETIC ANOMALIES: PHOBOS-2 OBSERVATIONS

S.V. Kulikov¹, S.I. Klimov¹, S.P. Savin¹, V.A. Styazhkin², A.A. Skalsky¹, O. Santolik³, I. Kolvasova³

¹ IKI RAS, 84/32 Profsovnaya, Moscow, Russia, kulikov@rx24.ru

² IZMIRAN, Troitsk, Russia

³ IAF, Prague, Czechia

Keywords:

Phobos 2, waves, electromagnetic emissions, magnetic anomalies, plasma.

Introduction:

The Plasma Wave System (PWS) and MAGMA instruments onboard the Phobos2 spacecraft carry out electric and magnetic field measurements in the plasma environment of Mars in 1989. It is shown that some of the observed waves can be tentatively interpreted as emissions originated in the Martian ionosphere near the boundaries of the magnetic anomalies.

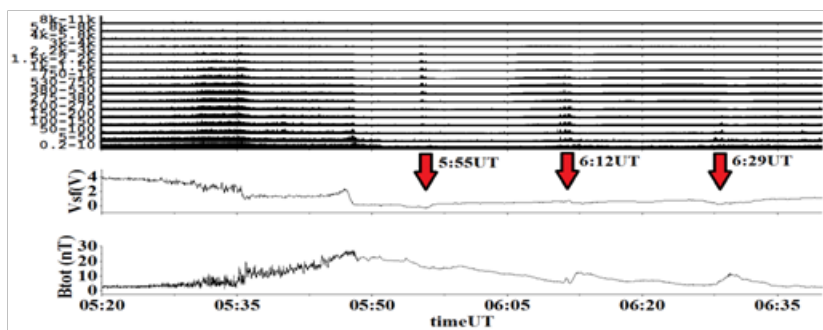


Fig. 1. The data obtained on February 8, 1989 by the Phobos-2 in an elliptical orbit around Mars. The signals delivered by 17 elements of the PWS filter bank, spacecraft potential and total magnetic field are shown from top to bottom.

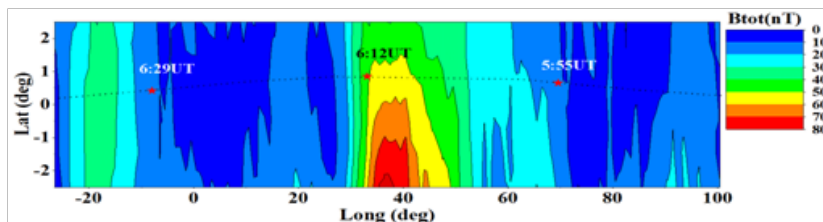


Fig. 2. The Phobos-2 trajectory is represented by the dotted line on the magnetic field map. The red stars show the places where emissions were detected.

Acknowledgments:

We wish to remember and to thank A. Pedersen, R. Gvard and D. Klinge from SSD ESA who developed the PWS instrument and makes PWS data available.

PHYSICAL, MECHANICAL, HYDROPHYSICAL, AND MICROBIOLOGICAL PROPERTIES OF MARTIAN SOIL SIMULANT

E.A. Grishakina¹, V.Yu. Makovchuk¹, Z.S. Ezhelev², V.S. Cheptsov^{2,3}, A.A. Belov², J.L. Vázquez-Poletti⁴, I.M. Llorente⁴, M. Ruiz-Ramos⁵, A. Sanz-Cobena⁵, A. Rodríguez^{5,6}

¹ Vernadsky Institute of Geochemistry and Analytical Chemistry, RAS, Moscow, Russian Federation.

² Lomonosov Moscow State University, Moscow, Russian Federation.

³ Space Research Institute, RAS, Moscow, Russian Federation.

⁴ Universidad Complutense de Madrid (UCM), Spain.

⁵ Universidad Politécnica de Madrid (UPM), Spain.

⁶ Universidad de Castilla La Mancha (UCLM), Spain.

Keywords

Mars; Martian soil simulant; crop simulation; physical and mechanical soil properties; hydrophysical and microbiological soil characteristics.

Introduction

In this study we tested the hydrophysical and microbiological properties of Martian soil analogue for the ExoMars mission [1], imitating the main physical and mechanical properties of the Martian soil in the surface layer that determine its aptitude for growing crops like corn, wheat or potatoes in different climatic conditions and supporting missions to explore Mars.

Material and Methods: Laboratory experiments

Table 1a. Grain-size distribution in Martian soil simulant in weight %

	Cobble		Pebble		Sand					Dust		
Grain-size (mm)	>10	10-5	5-2	2-1	1-0.5	0.5-0.25	0.25-0.1	0.1-0.05	0.05-0.01	0.01-0.005	0.005-0.002	<0.002
Percentage (%)	0.0	0.0	0.2	7.4	21.2	4.6	16.9	12.5	35.1	1.0	1.0	0.0

Table 1b. Physical and mechanical properties of Martian soil simulant

Moisture content, %	Particle density, g/cm ³		Dry bulk density, g/cm ³	Cohesion, MPa	Angle of internal friction, degree	Stiffness modulus (in stress range 0.1-0.2 MPa), MPa	Elastic modulus, MPa	Bearing capacity, MPa	Dynamic elastic modulus, MPa	Frictional coefficient	Dynamic modulus, MPa
	Compact	Loose									
W	ρ_s	ρ_d max	ρ_d min	c	φ	E	E_y	E_{bc}	E_d	tg(φ)	E_{vd}
0.4	2.48	1.55	1.30	0.007	25	5.6	57.3	0.332	248.9	0.458	55.3

In this work, we continue the laboratory studies of the Martian soil analogue, originally created for the drop tests of the ExoMars landing module. For the analogue soil, the components that were cheap and available in a volume of several tons were selected: crushed quartz sand 0.5–1.2 mm — 25%, rounded quartz sand 0.19–0.23 mm — 15%, fly-ash — 30%, ash-slag waste — 30%. After mixing the components in the required proportions, a soil-analogue was obtained, according to the grain composition, referring to silty sand, having a density of 1.30 g/cm³ in loose composition and 1.55 g/cm³ in dense composition, with a moisture content of less than 1% and a value of cohesion within the first ten kilopascals (Tables 1a, 1b). Mechanical properties of soil analogue were obtained in triaxial and direct shear tests.

Based on the similarity of the analogue soil to the Martian soil on the physical and mechanical properties [1], we conducted a series of laboratory tests of the analogue soil to determine the hydrophysical (coefficient of filtration, water retention curve, liquid limit) and microbiological properties (total number of prokaryotic cells in situ, number of culturable bacteria, multisubstrate testing of the microbial community as described in [2]).

Results

Conducted experiments of hydrophysical parameters show coefficient of filtration of our Martian soil analogue in range of 25–28.6 cm/day (med 25.7 cm/day), which corresponds to average level of filtration [3].

In the course of microbiological analyzes, the total number of prokaryotic cells was found at a level of $1.14 \pm 0.35 \times 10^7$ per gram of model soil, and about 2×10^3 colony forming units per gram were found on rich nutrient media. Cultivated bacteria are predominantly Gram-positive and belong to the genera *Arthrobacter*, *Bacillus*, *Micrococcus*, *Staphylococcus* and *Streptomyces*. During multisubstrate testing, potential metabolic activity was found close to the sensitivity limit of the method: out of 47 substrates studied, only peptone consumption is recorded.

Thus, analogue soil is characterized by a low number and variety of prokaryotes, as well as low functional diversity and potential metabolic activity.

Discussion and further work

In further vegetative experiments, we are planning to add plant growth-promotion bacteria, various functional groups of bacteria to provide mineral nutrition of plants, as well as natural microbial communities of extreme ecosystems, characterized by conditions similar to those of the Martian regolith. The low biological activity of analogue soil necessitates the introduction of microorganisms, and at the same time, the native microflora of analog soil will not hinder the development of introduced microorganisms.

To refine hydrophysical growth conditions of plants, we are planning to determine water retention curve of our analogue (saturation, field capacity and wilting point) as well as liquid limit, plastic limit and plasticity index of soil (according to ASTM D 4318 standart). Some of these features are required inputs for crop model simulations. Crop modelling will allow to extend the scope of the experimental set-up and testing a wide variety of genetic x management x environmental (GME) interactions. Therefore, in future, data obtained during this and future research on this topic will be used crop model simulation on a Martian soil [4].

References:

- [1] Grishakina E.A., Dmitrovskii A.A., Ivanov M.A., Makovchuk V.Y., Sorokin E.M., Uvarova A.V., Voznesensky E.A., Nikitin M.S., Slyuta E.N. 2018. Martian soil simulant for large-scale field experimental research. Proc. 9th Moscow Solar System Symposium, Moscow: IKI RAS, 240–242.
- [2] Belov A.A., Cheptsov V. S., Vorobyova E.A., Manucharova N.A., & Ezhelev Z.S. 2019. Stress-Tolerance and Taxonomy of Culturable Bacterial Communities Isolated from a Central Mojave Desert Soil Sample. *Geosciences*, 9(4), 166.
- [3] Shein E.V. Course of soil physics. MSU, Moscow. 2005
- [4] J.L. Vázquez-Poletti, I.M. Llorente, M. Ruiz-Ramos, P.J. Pascual, M. Ramírez-Nicolás, A. Sanz-Cobena, S. Jiménez, A. Rodríguez, D. Usero, L. Vázquez, V.Yu. Makovchuk, E.A. Grishakina, A.A. Belov, V.S. Cheptsov, Z.S. Ezhelev. Serverless computing for Mars exploration and colonization applications. 2019

MEASURING OF VOLUME AND THICKNESSES OF REMNANT MASSIFS OF LAYERED DEPOSITS ON MARS, USING ALTIMETRY DATA AND MATH APPROXIMATION

S.S. Krasilnikov¹, A.V. Zarnodnyuk², M.A. Ivanov¹, R.O. Kuzmin^{1,3}

¹ Vernadsky Institute of Geochemistry and Analytical Chemistry RAS, Moscow, Russia, krasilnikovruss@gmail.com;

² Lomonosov Moscow State University, Moscow, Russia;

³ Space Research Institute RAS, Moscow, Russia

Keywords

Mars, polar region, ice, layered deposits, remnant massifs.

In the high northern latitudes of Mars, around the polar cap, the remnant massifs of layered deposits can be found. These massifs could be remnants of polar layered deposits (PLD) of northern polar cap. In our research, we used the MOLA topography data to assess the shape of ice massifs both on the flat surface and within larger impact craters. For the ice deposits in the craters, we used an empirical relationship between the craters depth and diameter, original program for measuring of average elevation and math approximation approach to estimate volume of ice.

Introduction

Around the north polar cap of Mars, ice layered deposits can be found. There is a hypothesis that boundaries of the northern polar cap advanced to the lower latitudes in previous climatic epochs [1, 2]. The last such advance could happen in previous ice age in period 0.4–2.1 Myr ago [3, 4]. In this period, the polar cap could reach $\sim 75^\circ\text{N}$ [2] and overlap such regions as Olympia Undae and Scandia Cavi. Currently, around the polar cap we can find residual massifs of the ice layered deposits in a zone between $70\text{--}85^\circ\text{N}$ on northern plain and within of impact craters [2]. Study of these features provide important information about evolution of climate and the polar caps on Mars. The remnant ice massifs contain a large volume of water, which is an important resource for the future human exploration of the planet.

Measuring of ice massifs using altimetry data

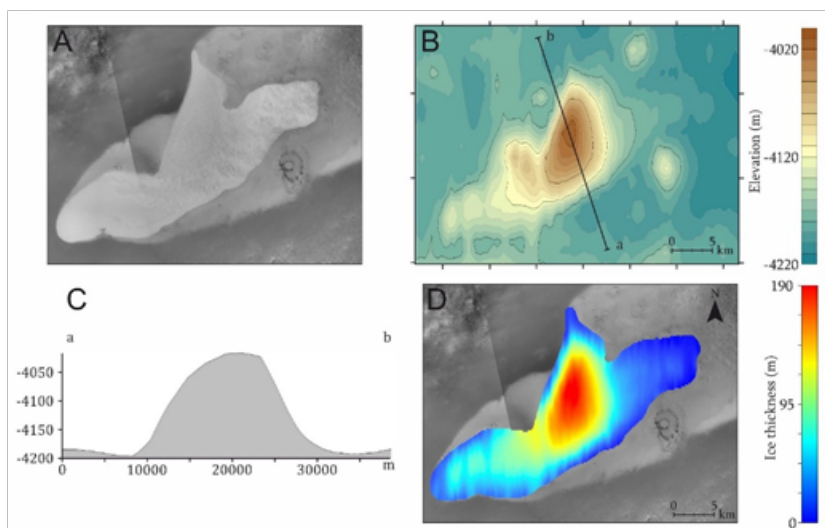


Fig. 1. Analysis of MOLA altimetry data. A—CTX images mosaic of an ice massif at 105°E , $73^\circ 40'\text{N}$; B — elevation map with a topographic profile (C); D — thickness of ice massif.

In our study, we firstly analyzed morphometric parameters of several topographically positive features on the flat surface of the northern plains. Their thicknesses and volumes can be calculated by an elevation difference between their elevation model and the surrounding surface. This approach gives reasonably accurate estimates only for relatively small objects, located on a flat surface (Fig. 1).

The results of the measurements are compared to the radar SHARAD data in Table 1. For each measurement, we have a systematic difference of 50–100 m between the altimetry and SHARAD data. We ascribe it to the lower spatial (3–6 km) and vertical (~15 m) resolution of the SHARAD data. Density of the radar profiles is also relatively low and the profiles can miss the thickest portions of the ice massifs.

Measuring of ice massifs in craters using math approximation

If an ice massif is on a rough surface or inside a crater, determination of the massif thickness and volume is more complicated. In this situation measurements should be done using either the SHARAD data or an empirical dependence between the depth and diameter of craters on Mars [5] and additional math approximation approach.

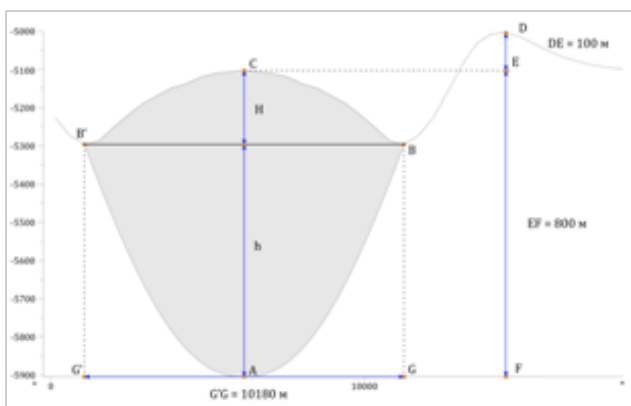


Fig. 2. Measuring of ice massif volume in craters using the empirical model for the shape of the Mars craters and approximation of the ice massif profile by two parabolas.

For ice massifs, located in impact craters, analysis of crater morphology and applying of math approximation, can be alternative approach in calculation of ice volume. According to this model, the characteristic relationship between diameter (D) and depth (d) of the fresher craters is described by the following formula $d=(0.19D)^{0.55}$ [5]:

In order to apply this relationship for estimates of the thickness of the ice massifs in craters, we used an original computer program [6], which calculates an average elevation in a series of concentric zones extending from the center of a crater to three crater radii from the center. The difference between the model depth of a crater [5] and its actual averaged profile gives an estimate of the thickness of an ice massif located within the crater.

The next step was a calculation of volume of ice massif. The maximum possible volume of the ice massifs were estimated under an assumption that craters have bowl-like shape, and positive ice massif on the bottom of it have a “hill” shape, below we will make some approximation to calculate volume of ice using math approximation. We assume, that central profile of massif can be sufficiently accurate approximated by two parabolas (B', A, C and B', C, B). Sought-for volume is the volume of axisymmetric body — solid of revolution. Let's locate coordinate axis x through B' and B points, and axis y through points A and C . In this approximation, if we know coordinates of points B', A, B and C in axis x and y , equations of parabolas can be calculated. These equations will describe upper and lower part of central profile. Using this approach, volume of ice massif can be described as sum of volumes of two bodies, formed by rotation of arcs of lower and upper parabolas related to vertical axis y .

Table 1. Morphometrical parameters of the ice massifs on the plains and in craters.

№	Locality	Coordinates		Area and Diameter	Volume, km ³	Maximum thicknesses, km	Radar
		Longitude	Latitude				
1a	Plain	95°	74°10′	404.1 km ²	41.3	0.35	0.27
1b	Plain	98°	74°30′	1535.5 km ²	115.5	0.42	0.33
2	Plain	102°	74°30′	18.1 km ²	0.9	0.12	-
3	Plain	103°40′	74°40′	4.7 km ²	0.12	0.03	-
4	Plain	105°	73°40′	291.3 km ²	27.8	0.17	0.12
5	Plain	107°30′	74°50′	11.5 km ²	0.3	0.02	-
5	Plain	110°30′	74°44′	113.4 km ²	26.1	0.12	0.09
6	Crater	319°10′	73°14′	16.9 km	32.7	0.8	-
7	Crater	164°30′	72°40′	83.9 km	2169.3	1.48	1.48
8	Crater	240°10′	78°06′	15.8 km	3.3	0.4	-
9	Crater	103°10′	70°11′	37.3 km	3.6	0.1	0.15
10	Crater	159°40′	79°20′	6.3 km	7.4	0.48	-
11	Crater	1°40′	78°	4.5 km	0.1	0.4	-
12	Crater	151°20′	76°23′	4 km	0.5	0.4	-
13	Crater	190°10′	81°	19.5 km	26.2	0.8	-
14	Crater	60°50′	79°08′	24 km	12.2	0.4	0.3
15	Crater	89°10′	77°06′	31.4 km	148.5	1.1	0.38

Results:

MOLA data can be used on the plain surface for measuring of thickness and volume of surface ice massif deposits. Using [5] model, our average profiling of craters and math approximation, volume and thickness of ice massifs in part of craters can be calculated. For others cases, when we have deposition of ice massif in territory with rough relief, or when massif cover huge area, SHARAD data should be used.

References:

- [1] Forget F., Byrne S., Head J.W., et al. Recent Climate Variations. In: The Atmosphere and Climate of Mars // Cambridge University Press, Cambridge. 2017. P. 497–525.
- [2] Krasilnikov S.S., Kuzmin R.O., Evdokimova N.A. Remnant Massifs of Layered Deposits at High Northern Latitudes of Mars. // Solar System Research. 2018. V. 52. P. 32–42.
- [3] Head J.W., Mustard J.F., Kreslavsky M.A., et al. Recent ice ages on Mars. // Nature. 2003. 426:797–802.
- [4] Schorghofer N. Dynamics of ice ages on Mars // Nature. 2007. V. 449. P. 192–194.
- [5] Garvin J.B., Frawley J.J. Geometric properties of Martian impact craters: Preliminary results from the Mars Orbiter Laser Altimeter // Geophys. Res. Lett. 1998. V. 25. P. 4405–4408.
- [6] Guseva E.N., Ivanov M.A. Topographic configuration of coronae on Venus: supporting evidence for time-dependent styles of resurfacing // Solar System Research. 2019 (in press).

CONTROLLING ELECTROMAGNETIC WAVES WITH ALL DIELECTRIC METAMATERIALS

S. Bermejo, S. Perera, M. Domínguez, B. Veliz, M. Cedeño

Micro and Nanotechnologies Group (MNT), Universitat Politècnica de Catalunya (UPC), Campus Nord, C/Jordi Girona 1-3, 08034 Barcelona, Spain, sandra.bermejo@upc.edu

Keywords:

Metamaterial, electrospray, colloidal dispersion, nanospheres

Introduction:

Controlling electromagnetic waves is a challenge that may open a broad field of disruptive applications. Photonic integrated devices [1], optical filters [2], photonic crystals [3], smart optical coatings [4] and optical detectors in general [5], among others, are of paramount importance in optoelectronic instrumentation and, most specifically, in optical space instrumentation. Besides, the new trend of nanoparticles-based biosensors that may be driven by optical biomarkers can be of especial interest in astrobiology applications [6]. In this context, metamaterials have paved the way to the development of very attractive applications, such as negative refractive index materials for invisible cloaks [7] or super lenses [8]. All these devices have in common that they are usually able to accurately tune the electromagnetic wave spectra. However, optical metamaterials require a three-dimensional sculpting of the material at the nanoscale, which is still challenging nowadays. In this work we show a technology [9] to develop all dielectric metamaterials suitable for the optical range. The technology may be potentially easily extended to any frequency range. It consists on a bottom-up approach that uses dielectric nanoparticles as composite building blocks. Besides the use of all dielectric materials in general, may exhibit an enhanced mechanical hardness against radiation, a key issue in space applications.

In this work a setup based on electrospray technique to build the metamaterials is shown. Electrospray consists on applying a high electrical field between two terminals, one of them onto a colloidal suspension, causing the creation of a fine aerosol. The electrical field drives the created droplets containing the nanospheres onto a substrate, thus forming the desired nanostructured devices. Controlling the main parameters of the deposition, different topographies are achieved. With this technology we are able to make totally disordered, semi-ordered and completely ordered nanostructures. This will allow us to effectively control the electromagnetic waves for energy harvesting or smart sensing in space applications.

Experimental

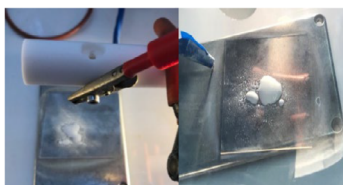
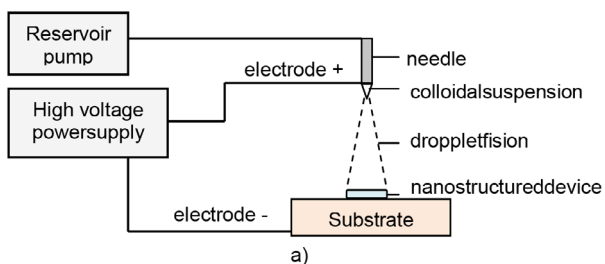


Fig. 1. Electrospray setup: a) schematics, b) reservoir pump, c) top and bottom electrodes.

The developed electro spray technology needs a specific setup to achieve the required conditions. Mainly, an infusion pump, a syringe and a needle containing the colloidal suspension, and a high-voltage bipolar source, ranging from -15 kV to 15 kV . The deposition takes place inside a glove box. The technique is easily scalable and nowadays allows deposition areas from 1 cm^2 to 60 cm^2 [10]. Fig. 1 shows the schematics and pictures of part of the setup of the electro spray technique. The usual applied voltages range from -3 kV to 6 kV , the pumping rates range from 0.4 ml/h to 0.6 ml/h and the volume fraction disperse solid is 5% . Typical nanosphere diameters range from 295 nm to 836 nm .

Results

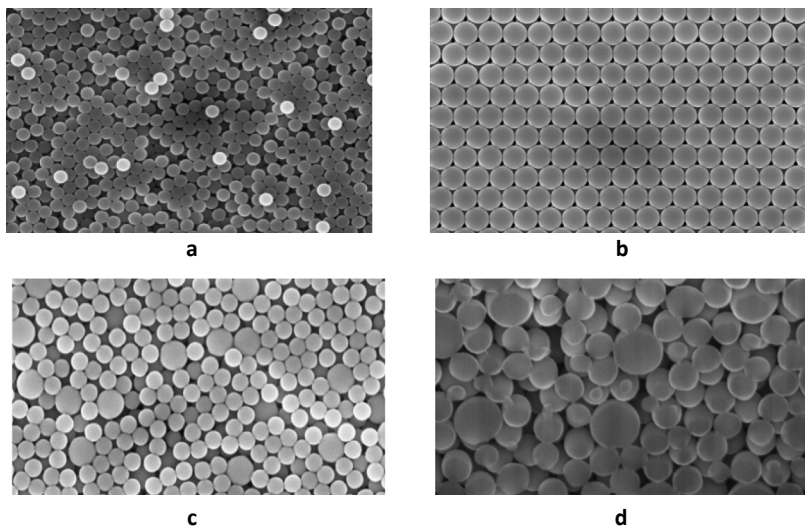


Fig. 2. FIB pictures of polystyrene nanospheres: **a)** 295 nm nanosphere diameter **b)** 522 nm nanosphere diameter, **c)** top view picture of the mixture of 295 nm and 522 nm nanospheres **d)** close view of the 295 nm and 522 nm mixture.

Figure 3 shows reflectance values measured with a spectrophotometer. Case examples have been measured, mixing different configurations of 295 nm , 522 nm and 836 nm . The technology allows to have different and very controllable reflectance spectra, allowing the use of these metamaterials in smart space sensing applications, among others.

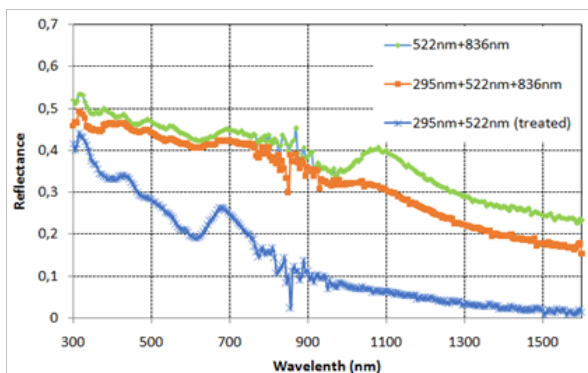


Fig. 4. Reflectance measurements for different nanosphere diameter mixtures. The $295+522\text{ nm}$ mixture have been treated with isopropyl alcohol.

Scanning electron microscopy (SEM), focused ion beam (FIB), and reflectance measurements have been made onto different nanostructured devices. Fig. 2 shows SEM and FIB pictures of samples with polystyrene nanospheres of 295 nm and 522 nm diameter. Semi-order is achieved for the 295 nm nano-

spheres whereas an almost complete order, arranged in large area dislocations, appears for the 522 nm structure. A mixture of both diameters is also shown, modifying the order and the topography of the nanostructures.

References:

- [1] D. Marpaung, J. Yao, and J. Capmany, "Integrated microwave photonics," *Nat. Photonics*, vol. 13, no. 2, pp. 80–90, 2019.
- [2] H.S. Song et al., "Reflective color filter with precise control of the color coordinate achieved by stacking silicon nanowire arrays onto ultrathin optical coatings," *Sci. Rep.*, vol. 9, no. 1, p. 3350, 2019.
- [3] M.I. Shalaev, W. Walasik, A. Tsukernik, Y. Xu, and N.M. Litchinitser, "Robust topologically protected transport in photonic crystals at telecommunication wavelengths," *Nat. Nanotechnol.*, vol. 14, no. 1, pp. 31–34, 2019.
- [4] G. Abadias et al., "Review Article: Stress in thin films and coatings: Current status, challenges, and prospects," *J. Vac. Sci. Technol. A Vacuum, Surfaces, Film.*, vol. 36, no. 2, p. 020801, 2018.
- [5] L.J. Deutsch, S.M. Lichten, D.J. Hoppe, A.J. Russo, and D.M. Cornwell, "Toward a NASA Deep Space Optical Communications System," in *2018 SpaceOps Conference*, 2018, no. June.
- [6] Y. Blanco et al., "Effects of Gamma and Electron Radiation on the Structural Integrity of Organic Molecules and Macromolecular Biomarkers Measured by Microarray Immunoassays and Their Astrobiological Implications," *Astrobiology*, vol. 18, no. 12, pp. 1497–1516, 2018.
- [7] G. Klotz, N. Malléjac, S. Guenneau, and S. Enoch, "Controlling frequency dispersion in electromagnetic invisibility cloaks," *Sci. Rep.*, vol. 9, no. 1, pp. 1–7, 2019.
- [8] B. Jia, F. Wang, H. Chan, G. Zhang, and W.J. Li, "In situ printing of liquid superlenses for subdiffraction-limited color imaging of nanobiostructures in nature," *Microsystems Nanoeng.*, vol. 5, no. 1, pp. 1–13, 2019.
- [9] A. Coll, S. Bermejo, D. Hernández, and L. Castañer, "Colloidal crystals by electrospaying polystyrene nanofluids," *Nanoscale Res. Lett.*, vol. 8, no. 1, pp. 1–8, 2013.
- [10] B. Véliz, S. Bermejo, J. Vives, and L. Castañer, "Large area deposition of ordered nanoparticle layers by electrospray," *Colloids Interface Sci. Commun.*, vol. 25, no. February, pp. 16–21, 2018.

ESTIMATES OF STRESSES BENEATH ELYSIUM PLANITIA ON MARS

A.V. Batov^{1,2}, **T.V. Gudkova**¹, **V.N. Zharkov**¹

¹ *Schmidt Institute of Physics of the Earth RAS, B. Gruzinskaya, 10, Moscow, Russia, batov@ipu.ru;*

² *V.A. Trapeznikov Institute of Control Sciences RAS, 65 Profsoyuznaya street, Moscow, Russia.*

Keywords:

Extension-compression stresses, shear stresses, gravity and topography data, interior structure, Mars

Introduction:

The seismic experiment of the InSight mission (Interior Exploration using Seismic Investigations Geodesy and Heat Transport) [1] is going on Mars. As only one seismometer is operating on Mars, the information on stress state of the interiors could give an additional information on the source location. Joint analysis of gravity and topography data in a frame of the static method let us some know ledge on stress field in the crust and in the lithosphere of Mars [2, 3]. At present detailed data on topography [4] and gravity field [5, 6] are available.

Method:

The static method that uses Green's functions technique (or the load coefficients method) is applied [7–9]. Numerical model considers only nonhydrostatic stresses arising due to the deviation of Mars from the state of hydrostatic equilibrium [10]. The detailed description of the method is given in [3]. Within the static approach, the planet is simulated as an elastic body with density, compression modulus K and shear modulus μ depending on the radius. Deformation and stresses obeyed Hooke's law are caused by the pressure of topographic structures on the planet's surface and by density anomalies distributed in some manner in the crust and mantle. To calculate the stresses, the set of equations is solved that includes the elastic equilibrium equation, and the Poisson equation that relates the anomalous gravitational potential to the density distribution.

Data:

Currently, there are detailed data about the Martian topography obtained by the MOLA instrument onboard the Mars Global Surveyor spacecraft [3]. Using the data obtained by the Mars Global Surveyor (MGS), Mars Odyssey, and Mars Reconnaissance Orbiter spacecrafts in 2016, two independent teams of scientists have simultaneously published papers on studies of the Martian gravitational field expansion in normalized spherical harmonics up to the degree and order of 120, model MRO120D [5] and model GMM-3 [6]. Model MRO120D [5] is used in this study.

Results:

Calculations of tension–compression and maximum shear stresses are carried out for a test model of Martian internal structure, which satisfies all today's geophysical and geochemical data, with a step of $1^\circ \times 1^\circ$ over latitude and longitude down to the depth of 1000 km. We take the distribution of density, gravity acceleration, compression modulus K and shear modulus μ for Mars' interior structure model M_50 [3]. The results of our numerical experiments are shown in Figure 1. As it is seen from the figure, the areas of maximum extensional stresses along with high shear stresses are located to the East from the landing site.

Acknowledgements:

This work is partly financially supported by Budget funding of Schmidt Institute of Physics of the Earth and partial support for Program 28 of the Presidium of the Russian Academy of Sciences.

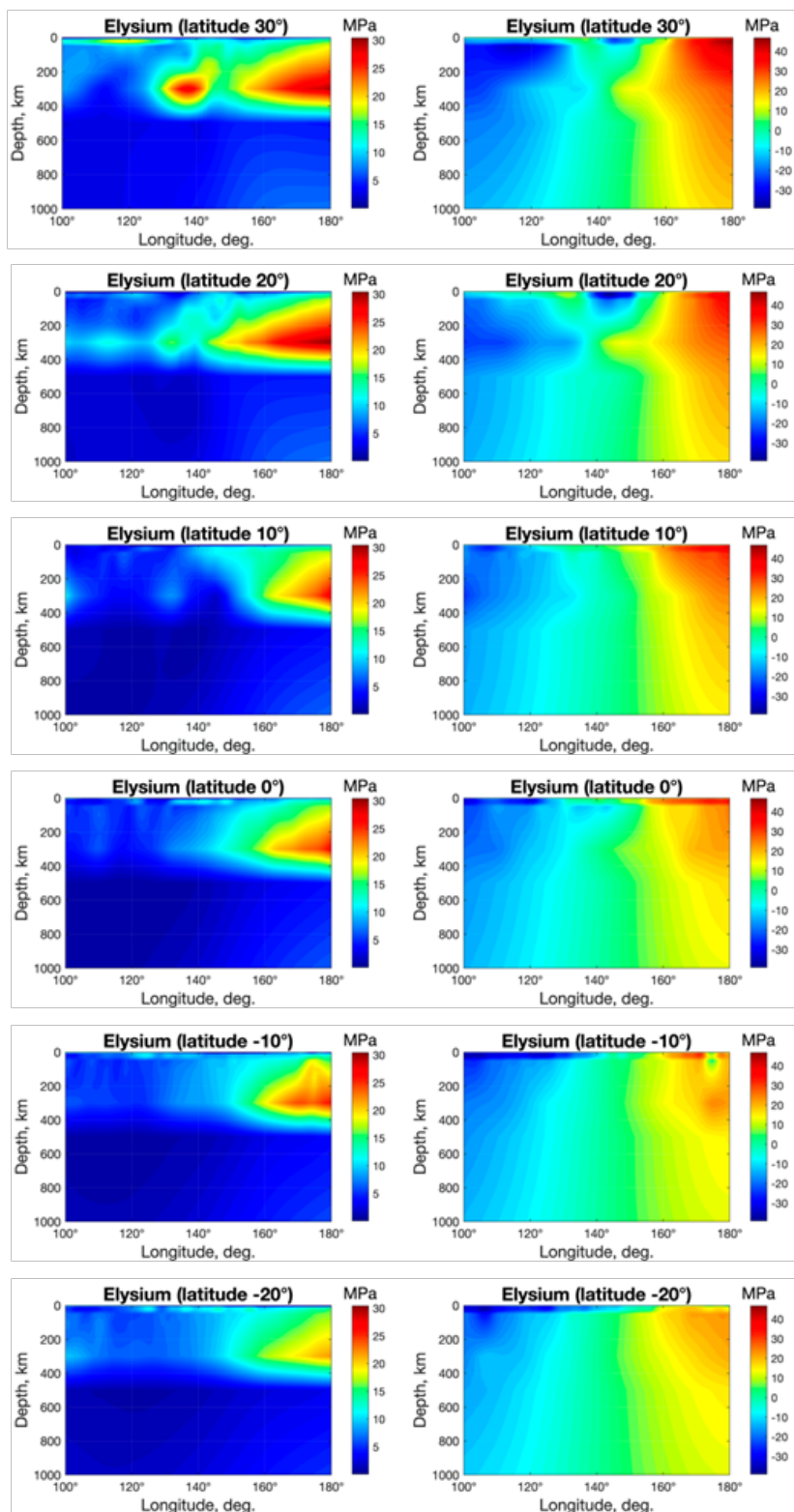


Fig. 1. Stress state map for the Elysium region on Mars : shear stresses (left) extension-compression stresses (right) (in MPa) for the longitude interval (100–180 deg.) at different latitudes (from top (30 North) till bottom (20 South) with 10 deg. step). Extension — positive, compression — negative.

References:

- [1] Banerdt W.B., Smrekar S., Hoffman T., Spath S., Lognonne P., Spohn T., et al. The InSight mission for 2018 // 48th Lunar and Planetary Science Conference. 2017. The Woodlands, Texas.
- [2] Zharkov V.N., Koshlyakov E.M., Marchenkov K.I. Composition, structure and gravitational field of Mars // Sol. Syst. Res. 1991. V. 25. P. 515–547).
- [3] Gudkova T.V., Batov A.V., Zharkov V.N.. Model estimates of non-hydrostatic stresses in the Martian crust and mantle: 1. Two-level model // Solar System Research. 2017. V. 51 (6), P. 490–511.
- [4] Smith D.E., Zuber M.T., Frey H.V. et al. Mars Orbiter Laser Altimeter: Experimental summary after the first year of global mapping of Mars // J. Geophys. Res. 2001. V. 106 (E10). P. 23689–23722.
- [5] Konopliv A.S., Park R.S., Folkner W.M. An improved JPL Mars gravity field and orientation from Mars orbiter and lander tracking data // Icarus. 2016. V. 274. P. 253–260.
- [6] Genova A., Goossens S., Lemoine F.G., et al. Seasonal and static gravity field of Mars from MGS, Mars Odyssey and MRO radio science // Icarus. 2016. V. 272. P. 228–245.
- [7] Marchenkov K.I., Lyubimov V.M., Zharkov V.N. Calculation of load factors for deeply buried density anomalies // Doklady Earth Science Sections. V. 279. 1984. P. 14–16.
- [8] Zharkov V.N., Marchenkov K.I., Lyubimov V.M. On long-waves shear stresses in the lithosphere and the mantle of Venus // Sol. Syst. Res. 1986. V. 20. P. 202–211.
- [9] Marchenkov K.I., Zharkov V.N. Stresses in the Venus crust and the topography of the mantle boundary // Sol. Astron. Lett. 1989. T. 16. № 1. P. 77–81.
- [10] Zharkov V.N., Gudkova T.V. On model structure of gravity field of Mars // Sol. Syst. Res. 2016. V. 50. P. 250–267.

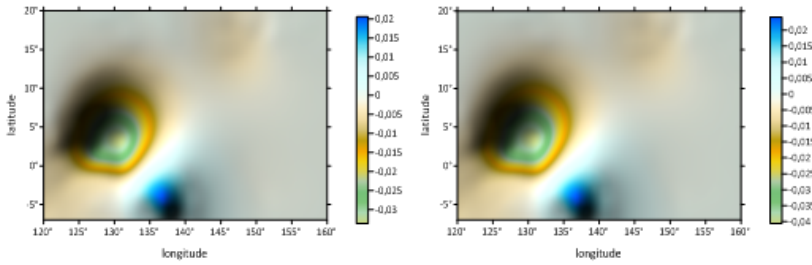


Fig. 2. Model anomalous density distribution in the Elysium Planitia region. Model 1, two planes. Depths: 0.5 km (left), 0.5 (right).

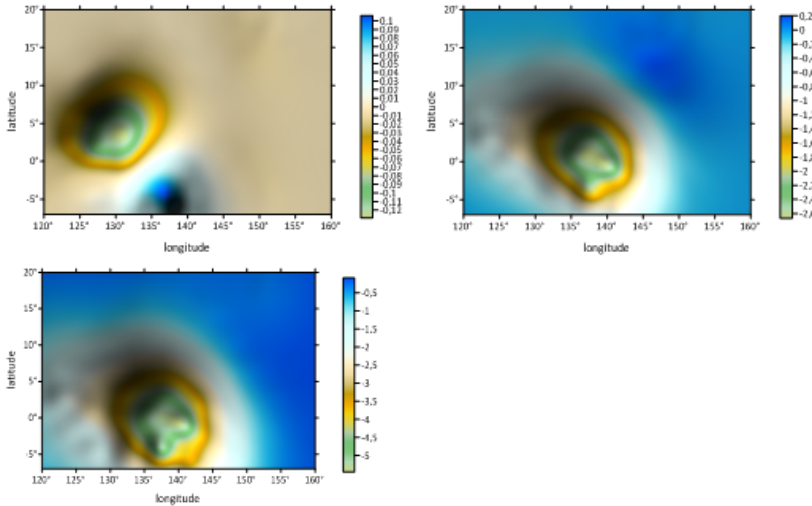


Fig. 3. Model anomalous density distribution in the Elysium Planitia region. One plane models. Upper panel — Model 2, depth 0 km (left); Model 3, depth -2.0 km (right), bottom — Model 4, depth -4.0 km.

Acknowledgements:

This work is partly financially supported by Budget funding of Schmidt Institute of Physics of the Earth and partial support for Program 28 of the Presidium of the Russian Academy of Sciences.

References:

- [1] Banerdt W.B., Smrekar S., Hoffman T., Spath S., Lognonne P., Spohn T., et al. The InSight mission for 2018 // 48th Lunar and Planetary Science Conference, 2017. The Woodlands, Texas.
- [2] Stepanova I. On the S-approximation of the Earth's gravity field // Inverse Problems in Science and Engineering. 2008. V. 16 (5). P. 547–566.
- [3] Stepanova I., Raevsky D. The modified method of S-approximation. Regional version // Izvestiya Physics of the Solid Earth. 2015;. V. 51 (2). P. 197–206.
- [4] Smith D.E., Zuber M.T., Frey H.V. et al. Mars Orbiter Laser Altimeter: Experimental summary after the first year of global mapping of Mars // J.Geophys.Res. 2001. V. 106. (E10). P. 23689–23722.
- [5] Konopliv A.S., Park R.S., Folkner W.M. An improved JPL Mars gravity field and orientation from Mars orbiter and lander tracking data // Icarus. 2016. V. 274. P. 253–260.
- [6] Genova A., Goossens S., Lemoine F.G., et al. Seasonal and static gravity field of Mars from MGS, Mars Odyssey and MRO radio science // Icarus. 2016. V. 272. P. 228–245.

METHOD OF S-, AND R-APPROXIMATIONS IN SOLVING THE PROBLEMS OF GEOPHYSICS: APPLICATION FOR MARS

I.E. Stepanova¹, T.V. Gudkova¹, A.V. Batov^{1,2}

¹ *Schmidt Institute of Physics of the Earth RAS, B.Gruzinskaya, 10, Moscow, Russia, tet@ifz.ru;*

² *V.A. Trapeznikov Institute of Control Sciences of RAS, 65 Profsoyuznaya street, Moscow, Russia,*

Keywords:

regularization, integral, representation, modified, optimal, gravity anomalies, topography, Mars

Introduction:

Different modifications of the method of linear integral representation are studied. Solutions of the related inverse problems based upon a “gibrid version of two approximations” of the topography and geopotential fields enable more refined tuning of the method in solving the inverse problems of geophysics and geomorphology and more complete allowance for the a priori information about the surface elevation data and elements of anomalous fields. The technique for finding a stable approximate solution for the inverse problem of determining the mass distributions equivalent by the external gravitational (or any other potential) field is presented. The method is applied to study anomalous densities beneath one of the highest elevation Elysium Mons and deep Hellas basin on Mars. The results of the mathematical experiment are discussed.

Method:

As it was stressed in [1–3], the problem of linear approximation of the gravity field (potential) may be reduced to the linear algebraic system:

$$Ax = f_{\delta} = f + \delta f \quad (1)$$

where, in general, the design matrix A is a full $M \times N$ matrix with real coefficients a_{ij} , $1 \leq i \leq M$, $1 \leq j \leq N$, x is the N -vector to be determined; f is the M -vector describing the signal, denotes the given vector of the observed gravitational functional that contains errors, characterizes the M -vector of the noise, resp. of the errors. The main problem of gravity field modeling is to obtain stable approximate solutions of linear algebraic equation systems, Eq. 1.

In the method of S -approximations, the known component of the gravitational field is approximated by the sum of a simple and double layers, which are distributed on a certain areas. In the local case (R -approximation), these areas are horizontal planes and edges of a dihedral angle, and in the regional version these are spheres or spheroids. The solution obtained by the methods of S -approximations (and R -approximations as well) allows efficient construction of the linear transforms of the field and can be used as zero approximation for solving the nonlinear inverse problem on localizing the sources (anomalous bodies). We present the results of constructing analytical approximations of the anomalous gravitational field of Mars in the local version with the use of rectangular Cartesian coordinates.

Data:

We apply our method for two regions on Mars: one of the large uplifts Elysium Mons and for the deepest depression Hellas Planitia. The Elysium Mons is the second largest volcanic province after Tharsis (about 12 km of relief). This zone is located immediately on the boundary between the southern highlands with thicker crust, and the northern lowlands with thinner crust (the dichotomy boundary). The Hellas Planitia is the deepest depression on Mars, it is stretching for 2.3 thousand km, its surface is 9 km below the surrounding highland, while positive gravity anomaly are being observed in this region [4]. On the whole Hellas is isostatically compensated impact basin, some overcompensation may be related to the accumulation of erosion

products on the bottom of the basin, which leads to the formation of a mascon type structure.

Data about the Martian topography are obtained by the MOLA instrument onboard the Mars Global Surveyor spacecraft [5]. In Figure 1, the map of the Martian relief heights after expansion in series up to the degree and order of 90 is presented for Elysium Mons and Hellas impact basin. The Martian gravitational field has been expanded in normalized spherical harmonics up to the degree and order of 120. In this study we use the model MRO120D [6] up to 90th degree and order, as for higher harmonics data correlation of gravitational field and topography is noticeably worse. The gravity anomalies are shown in Fig. 2.

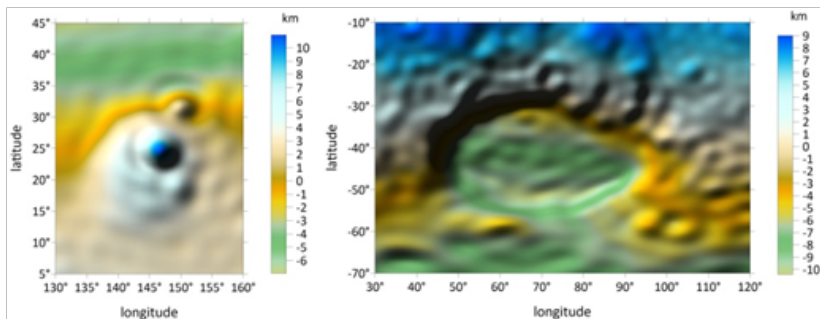


Fig. 1. The map of Martian relief heights after the expansion in spherical harmonics complete to the degree and order of 90: Elysium Mons (left), Hellas impact basin (right).

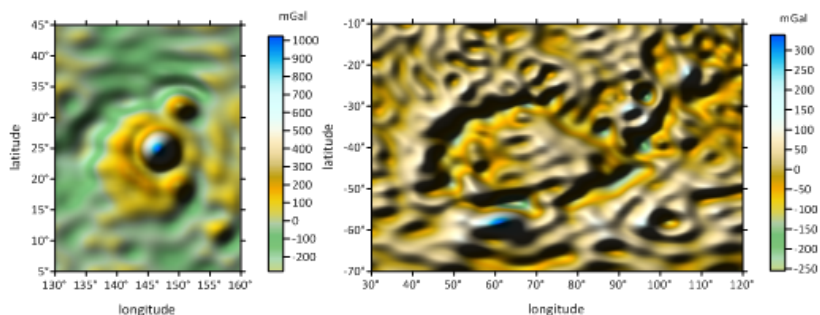


Fig. 2. The map of gravity anomalies δg on the Martian surface for harmonics of degree 7 through 90 Elysium Mons (left), Hellas impact basin (right).

Results:

We have performed calculations for 6 different models for Elysium Mons and Hellas Basin. Calculations are performed with spatial resolution a 1×1 arc-deg spherical grid. We have 1271 points for Elysium Mons area and 5551 points for Hellas impact basin. The minimum relief height of chosen Elysium Mons area is -6.97 km and the minimum point of Hellas impact basin is -10.42 km. The planes for approximation are situated close to these minimum relief heights. Model 1 for each chosen area is the model with 2 planes spaced relatively close to each other. In models 2–6 we choose one plane, situated at different depths. The results obtained for Model 1 are shown in Fig. 3 and 4.

Figure 3 presents the results for model 1 for Elysium Mons. The field of gravity anomalies correlates “quite well” (in comparison with Hellas basin region) with the topography of the Elysium Mons region. “The roots” are clearly seen beneath the Elysium Mons. For the Hellas basin region the gravity anomalies are distributed much more complicated. As mentioned above, positive gravity anomalies are observed in this region, and it is considered as a mascon type structure. Such a complex subsurface structure of Hellas basin region may be the cause for the result anomalous density distribution shown in Figure 4.

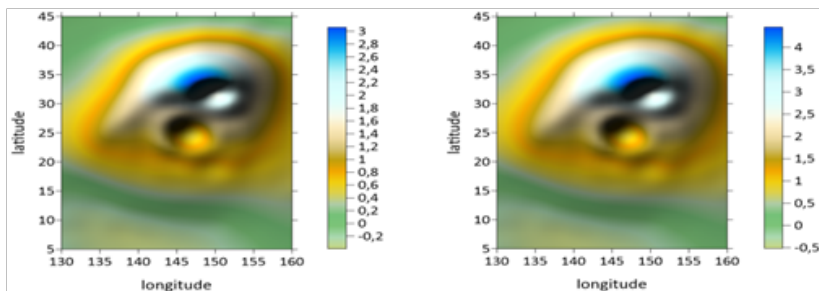


Fig. 3. Model anomalous density distribution in the Elysium Mons region, Model 1, two planes. Depths: -7.5 km (left), -9.5 (right).

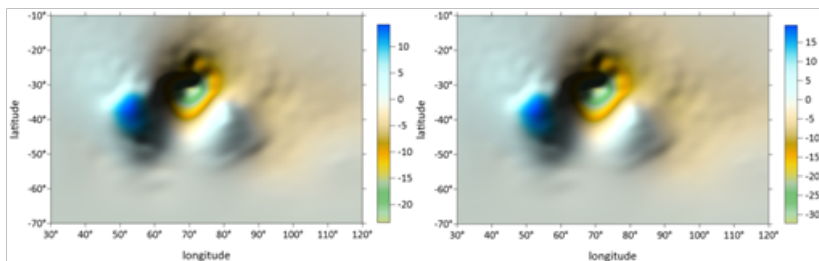


Fig. 4. Model anomalous density distribution in the Hellas impact basin, Model 1, two planes. Depths: -11.5 km (left), -14 km (right).

Acknowledgements:

This work is partly financially supported by Budget funding of Schmidt Institute of Physics of the Earth and partial support for Program 28 of the Presidium of the Russian Academy of Sciences.

References:

- [1] Stepanova I. On the S-approximation of the Earth's gravity field // Inverse Problems in Science and Engineering. 2008. V.16 (5). P.547–566.
- [2] Stepanova I. On the S-approximation of the Earth's gravity field. Regional version // Inverse Problems in Science and Engineering. 2009. V.17 (8). P.1095–1111.
- [3] Stepanova I.E., Kerimov I.A., Raevskiy D.N. and Shchepetilov, A.V. Combined method of F-, S-, and R-approximations in solving the problems of geophysics and geomorphology // Izvestiya, Physics of the Solid Earth. 2018. V. 54(1). P.91–105.
- [4] Zharkov V.N., Gudkova T.V. On model structure of gravity field of Mars // Solar Syst. Res. 2016. V. 50. P. 250–267.
- [5] Smith D.E., Zuber M.T., Frey H.V. et al. Mars Orbiter Laser Altimeter: Experimental summary after the first year of global mapping of Mars // J.Geophys.Res. 2001. V. 106 (E10). P. 23689–23722.
- [5] Konopliv A.S., Park R.S., Folkner W.M. An improved JPL Mars gravity field and orientation from Mars orbiter and lander tracking data // Icarus. 2016. V. 274. P. 253-260.

DEVELOPMENT OF THE VENERA-D SPACECRAFT DESIGN

A.B. Martynov, A.V. Kosenkova, P.D. Pisarenko, A.S. Feofanov

Lavochkin Association, Russia, Khimki, Leningradskaya 24, 141402, alexey.martynov@laspace.ru

Keywords:

Venus, Spacecraft, Atmosphere, Surface, Design.

Introduction:

Building on the results of the highly successful Soviet Venera and VEGA missions [1], along with the Pioneer, Magellan [2, 3], and more recent Venus Express and Akatsuki missions [4, 5], a joint NASA Roscosmos/IKI Science Definition Team (JSDT) was established in 2015. Within the overarching goal of understanding why Venus and the Earth took divergent evolutionary paths, the JSDT has the task of defining the science and architecture of a comprehensive Venera-D (Venera-Dolgozhivuschaya (long-lasting)) mission. The baseline Venera-D concept includes two elements, Orbiter and a Lander, with payload for distance and contact analysis, including detachable elements such as aerial platforms that can flow in the atmosphere, small long-lived surface stations, small satellite(s). In January 2017, the JSDT completed the first phase and generated a report to NASA - Roscosmos/IKI of its findings [6]. The second phase was completed in January 2019 with a focus on refining the science investigations, undertaking a compressive development of the core Orbiter and Lander mission architecture, a detailed examination of contributed elements and aerial platforms that could address key Venus science [7, 8, 9]. Current activities are focused on more precise definition of the payload, landing sites, orbits and landing, including variations of a maneuverable landers.

Lavochkin Association is creating the spacecraft design. This work includes:

- 1) development of the general design and configuration for the spacecraft;
- 2) accommodation of systems and standalone devices within the spacecraft;
- 3) assessment of orbit options along with the strategy for descent and landing and long term observation long-lived stations;
- 4) forming the radio communications between Earth, spacecraft, surface stations, satellites.

Launch dates between 2026 and 2031 have been evaluated.

References:

- [1] Sagdeev, R.V., et. al. 1986. *Science*. 231, 1407–1408.
- [2] Colin, L., et.al. 1980. *JGR*, 85, A13.
- [3] Saunders, R.S. et al. 1992. *JGR*, 97, 13067.
- [4] Svedhem, H. et al. 2009. *JGR*, 114, E00B33.
- [5] Nakamura, M. et al. 2011. *Earth, Planets and Space*, 63, 443.
- [6] Venera-D JSDT, 2017. http://iki.rssi.ru/events/2017/venera_d.pdf
- [7] Venera-D JSDT, 2019. <http://www.iki.rssi.ru/events/2019/Venera-DPhaseIIFinal-Report.pdf>
- [8] Cutts, J. et al. 2017. *Planetary Science Vision 2050 Workshop*, 1989.
- [9] Cutts, J. 2017. 15th Meeting of the Venus Exploration Analysis Group (VEXAG), 8015.

WATER VAPOUR DISTRIBUTION IN THE VENUS DEEP ATMOSPHERE BY THE SPICAV-IR/VEX NIGHT OBSERVATIONS

D.G. Evdokimova^{1,2}, A.A. Fedorova¹, D.A. Belyaev¹, O.I. Korablev¹,
E. Marq², J.-L. Bertaux^{1,2}

¹ Space Research Institute of the RAS (IKI), 84/32 Profsoyuznaya Str.,
Moscow 117997, Russia. evd.dar@yandex.ru

² LATMOS, CNRS/UVSQ/IPSL, 11 Boulevard d'Alembert, Guyancourt 78280,
France.

Keywords:

Venus, H₂O, transparency windows, clouds, SPICAV IR.

Introduction:

A thick cloud layer at altitudes of 47–70 km obstructs remote sensing of the Venus lower atmosphere and surface. Thermal IR emission forming below clouds escapes to outer space only within several transparency windows. They were discovered in the beginning of 1980s as narrow spectral intervals between strong CO₂ absorption bands [1]. Intensity of the windows is defined by CO₂ and minor gases absorption and scattering within the cloud layer. The emission can be observed at the night side of Venus where sunlight is absent and, thus, a composition of deep atmospheric layers as well as clouds variations can be studied.

Two windows at 1.10 and 1.18 μm coincide an absorption band of H₂O molecule at 1.10–1.20 μm. Their emission originates from the surface and the first scale height of the atmosphere (5–15 km) allowing to study the water vapour mixing ratio at altitudes of 10–20 km. The Venus atmosphere is enormously dry in comparison with the Earth one. The major amount of water is condensed to the clouds droplets consisting of concentrated aqueous solution of H₂SO₄. The recent ground-based observations and data obtained by SPICAV-IR and VIRTIS on Venus Express showed a H₂O volume mixing ratio varying about 30 ppmv below clouds [2–4]. A gradient was observed by Ignatiev et al. only below 5 km where the H₂O mixing ratio increases up to 50–70 ppm [5]. However, the water vapour distribution is nearly uniform below clouds and temporal and spatial variations have not been studied in detail yet. Global investigation of H₂O distribution in the lower troposphere should make a significant impact on understanding the evolution of the Venus atmosphere.

Retrieving the H₂O volume mixing ratio in the deep atmosphere:

The current work is aimed to study the water vapour abundance in the lower atmosphere and its temporal and spatial distributions based on the whole dataset of SPICAV observations. The IR channel of the spectrometer on board the Venus-Express spacecraft was operating in 2006–2014. It measured night emission spectra with a good spectral and spatial resolution and the accumulated dataset covered almost the whole globe. The instrument spectral range allows studying transparency windows at 1, 1.1, 1.18, 1.28 and 1.31 μm. Three of them at 1.1, 1.18 and 1.28 μm were chosen for the analysis. The 1-μm window was not constantly observed by the instrument to decrease one spectrum exposition time. Moreover, we also not consider the 1.31-μm window which intensity is low.

The theoretical spectrum of the infrared emission is built by a radiative transfer model considering a multiple scattering [3, 6]. It is computed using the SHDOMPP program which releases aspherical harmonic discrete ordinate method for plane parallel geometry [7]. Vertical profiles of CO₂ concentration, temperature and pressure is set according to the VIRA database for the Venus atmosphere. The clouds structure is defined by the model of Haus et al. 2016. [8]. The aerosol particles composition is assumed the 75% sulfuric acid solution. We take an assumption that aerosol droplets are spherical to calculate an optical depth, a single scattering albedo and an asymmetry parameter using the Mie theory. The water vapor mixing ratio is set constant. Absorption

lines of the H₂O molecule are taken from the BT2 linelist [9]. The variations of the night IR emission intensity are defined by changings of water vapor mixing ratio, cloud opacity and surface emissivity. Therefore, the transparency windows model has three parameters varied to describe experimental data.

The analysis of the whole dataset of SPICAV observations displays that the water vapour in the deep atmosphere is distributed uniformly with the volume mixing ratio of 25–27 ppmv. The instrument properties do not allow to make a conclusion about vertical gradient of the H₂O mixing ratio profile.

Acknowledgements:

D.G. Evdokimova, A.A. Fedorova, D.A. Belyaev, O.I. Korablev and J.-L. Bertaux acknowledge the support from the Ministry of Science of Russian Federation grant #14.W03.31.0017.

References:

- [1] Allen D. A., Crawford J.W. Cloud structure on the dark side of Venus. // *Nature*, 1984. V. 307. P. 222–224.
- [2] Haus R. et al. Lower atmosphere minor gas abundances as retrieved from Venus Express VIRTIS-M-IR data at 2.3 μm // *Planetary and Space Science*, 2015. V. 105. P. 159–174
- [3] Bezard B. et al. The 1.10- and 1.18-μm nightside windows of Venus observed by SPICAV-IR aboard Venus Express. // *Icarus*, 2011. V. 216. P. 173-183.
- [4] Arney G. et al. Spatially resolved measurements of H₂O, HCl, CO, OCS, SO₂, cloud opacity, and acid concentration in the Venus near-infrared spectral windows. // *J. Geophys. Res.* V. 119. Pp. 1860-1891.
- [5] Ignatiev N.I. et al. Water vapour in the lower atmosphere of Venus: a new analysis of optical spectra measured by entry probes. // *Planet. Space Sci.*, 1997. V. 45. P. 427-438
- [6] Fedorova A. et al. The CO₂ continuum absorption in the 1.10- and 1.18-μm windows on Venus from Maxwell Montes transits by SPICAV IR onboard Venus Express. // *Planet. Space Sci.*, 2014. V.113-114. P. 66-77.
- [7] Evans K. F. The spherical harmonic discrete ordinate method for three-dimensional atmospheric radiative transfer. // *J. Atmos. Sci.* 1998. V. 55. P. 429–446.
- [8] Haus R. et al. Radiative energy balance of Venus based on improved models of the middle and lower atmosphere. // *Icarus*. 2016. V. 272. P. 178–205.
- [9] Barber R.J., et al. A high-accuracy computed water line list. // *Mon. Not. R. Astron. Soc.*, 2006. V. 368. P. 1087–1094.

RADIO OCCULTATION OF VENUSIAN IONOSPHERE

A.L. Gavrik

*Kotel'nikov Institute of Radio Engineering and Electronics, Russian Academy of Sciences, Fryazino branch, V.A. Vvedensky sq, 1, Fryazino, Russia
alg248@ire216.msk.su*

Keywords:

Radio wave, occultation, Venus, ionosphere, wave-like structure.

Introduction:

Radio occultation technique is applied for the atmospheric and ionospheric investigations since interplanetary missions to Mars [1] and Venus [2]. Quite soon the general formulae for the radio occultation data inversion, based on the geometrical optics approximation and the local spherical symmetry assumption, have been derived [3]. During further progress in this field, new sophisticated approaches for investigations of the fine ionospheric structure have been proposed [4]. The report outlines the measurement technique and the new mathematical model underlying the data processing, providing for their possible implementation in the Venera-D mission.

The results of the analysis of occultation data:

Numeric modeling of experiments revealed the nature of influence of various disturbances on the reliability of determination of multilayer plasma structures in Venusian ionosphere observed in radio occultation data. It was shown that precision of interpretation of occultation data depends on the selections of equipment and experiment parameters. Quality of obtained information depends on the interrelations between radio physical effects, determined by the studied medium, and the hindering factors. How informative the radio science occultation experiments are depending on the energy ratios along the signal path and on the stability of the transceiver using coherent monochromatic radio waves. Proper selection of frequencies is an important task in the planning of the occultation experiments for the coming Venus-D mission. Under optimal conditions there appears a possibility to acquire information about the atmosphere and ionosphere of the planet, not obtainable before, which is important for the study of anomalous properties of the gaseous atmosphere on Venus and a study of propagation of gravity waves from the atmosphere into the ionosphere.

Acknowledgment:

The work was carried out within the framework of a state task and partially was supported by the RAS Presidium Program.

References:

- [1] Kliore A., Cain D.L., Levy G.S., Eshleman V.R., Fjeldbo G., Drake F.D. Occultation experiment: Results of the first direct measurement of Mars's atmosphere and ionosphere // *Science*. 1965. V. 149, No. 3689, P. 1243.
- [2] Mariner Stanford Group. Venus: ionosphere and atmosphere as measured by dual-frequency radio occultation of Mariner V // *Science*. 1967. V. 158, No. 3809, P. 1678.
- [3] Phinney R.A., Anderson D.L. On the radio occultation method for studying planetary atmospheres // *J. Geophys. Res.* 1968. V. 73. P. 1819.
- [4] Gavrik A.L., Gavrik Y.A., Kopnina T.F., Samoznaev L.N. Amplitude and frequency variations of coherent radio signals during probing of the daytime Venusian ionosphere // *Journal of Communications Technology and Electronics*. 2010. V. 55. No. 3. P. 256.

DEPENDENCE OF CLOUD TOP CIRCULATION ABOVE APHRODITE TERRA ON SOLAR-RELATED EFFECTS AND TOPOGRAPHY. VARIATIONS IN THE BEHAVIOR OF ZONAL WIND OVER MISSION TIME FROM VMC/VENUS EXPRESS WIND FIELDS

M.V. Patsaeva¹, I.V. Khatuntsev¹, L.V. Zasova¹, A. Hauchecorne², D.V. Titov³, J.-L. Bertaux^{1,2}

¹ Space Research Institute RAS, Profsoyuznaya 84/32, Moscow, 117997, Russia, Contact: marina@irn.iki.rssi.ru;

² LATMOS/INSU/CNRS, UVSQ, 11 bdd'Alembert, 78280 Guyancourt, France;

³ ESA/ESTEC, 2200AG Noordwijk, The Netherlands

Keywords:

Venus, mesosphere, dynamics, local time, topography.

Introduction:

UV (365 nm) images obtained by Venus Monitoring Camera [1] onboard Venus Express spacecraft from 2006 to 2013 were used to study the mesosphere dynamics. More than 44,000 wind vectors (received during processing 262 orbits) derived by digital cloud tracking [2, 3] were analyzed in the latitude band 0-30°S. Due to a big data set, the dependence of zonal and meridional winds was studied not only on longitude and latitude, but also on local time. The behavior of the zonal wind in the first and second half of the mission was also investigated.

Results:

Detailed analysis of the cloud top zonal wind deceleration, found in [4], showed [5] that the braking of the zonal wind at 13.4 ± 4.4 m/s is observed above Aphrodite Terra, which is the highest region in equatorial latitudes. The surface topography also affects the meridional wind component. The influence of topography on the cloud top winds was found as a function of local solar time. A study of slowest wind positions in the latitude band $10 \pm 5^\circ$ S above Aphrodite Terra as a function of longitude shows that the wind velocity minimum (in module) is reached above Ovda Regio (the highest region, $90 \pm 5^\circ$ E) at noon local time. The amplitude of the wind deceleration decreases and shifts downstream when moving south from Aphrodite Terra. The horizontal flow at the cloud top level in the equatorial region is perturbed at 13-14 h. A solar tide can be an explanation of the perturbation of both zonal and meridional wind components.

Results obtained from Akatsuki images [5] confirm the deceleration of the zonal wind connected with the solar tide, but don't confirm the deceleration above Aphrodite Terra. Venus Express observed Venus from 2006 to 2014. Akatsuki began to operate in 2015 continuing in time the observations started by Venus Express. Comparison of the zonal wind behavior in the first and second half of the Venus Express mission in the latitude band $10 \pm 5^\circ$ S shows that the zonal wind minimum, connected with Aphrodite Terra, is observed over mission time, but changes its location. It is less noticeable at a higher speed observed in the second half of the mission, and displaced downstream from Aphrodite Terra. The number of orbits available in the second half of the Venus Express mission is two times less than in the first half. Smaller number of orbits and poorer quality of the images in the second half of the mission leads to sparser spatial coverage especially in equatorial regions above Aphrodite Terra, and this may distort the result. A longer observation series is required to investigate the influence of topography on the atmosphere circulation.

Acknowledgements:

L.V. Zasova would like to thank the program #AAAA-A18-118052890092-7 of the Ministry of Science and Higher Education of the Russian Federation for the support. I.V. Kha-

tuntsev, M.V. Patsaeva would like to thank the program #AAAA-A18-118052890092-7 of the Ministry of Science and Higher Education of the Russian Federation for the support in the study of the zonal wind behavior over mission time. J.-L. Bertaux, I.V. Khatuntsev and M.V. Patsaeva were supported by the Ministry of Science and Higher Education of the Russian Federation grant 14.W03.31.0017 to study the dependence of the cloud top circulation on topography and solar-related effects.

References:

- [1] Markiewicz, W.J., Titov, D.V., Ignatiev, N., Keller, H.U., Crisp, D., Limaye, S.S., et al. Venus Monitoring Camera for VenusExpress // *Planetary and Space Science*. 2007. V. 55(12). P. 1701–1711.
- [2] Khatuntsev, I.V., Patsaeva, M.V., Titov, D.V., Ignatiev, N.I., Turin, A.V., Limaye, S.S., et al. Cloud level winds from the VenusExpress Monitoring Camera imaging // *Icarus*. 2013.V. 226(1), P. 140–158.
- [3] Patsaeva, M.V., Khatuntsev, I.V., Patsaev, D.V., Titov, D.V., Ignatiev, N.I., Markiewicz, W.J., Rodin, A.V. The relationship between mesoscale circulation and cloud morphology at the upper cloud level of Venus from VMC/Venus Express // *Planetary and Space Science*. 2015.V. 113–114(08) .P. 100–108.
- [4] Patsaeva, M. V., Khatuntsev, I. V., Zasova, L. V., Hauchecorne, A., Titov, D. V., Bertaux, J.-L. Solar-related variations of the cloud top circulation above Aphrodite Terra from VMC/Venus Express wind fields // *Journal of Geophysical Research: Planets*. 2019. V. 124. P. 1864–1879.
- [5] Horinouchi, T., Kouyama, T., Lee, Y. J., Murakami, S., Ogohara, K., Takagi, M., et al. Mean winds at the cloud top of Venus obtained from two-wavelength UV imaging by Akatsuki // *Earth, Planets and Space*. 2018. 70:10.

AUTONOMOUS AERODYNAMIC REPEATING DIVER FOR VENUS ATMOSPHERIC RESEARCH OF CLOUDS

Jacob Benheim¹, Jim Head¹, Madeleine Gaw¹, Neha Sajja², Rick Fleeter¹

¹ Brown University

² Rhode Island School of Design, Nsajja@risd.edu

Keywords:

Venus atmosphere in-situ, lightweight inflatable airplane, diving communications infrastructure, solar-powered, long-term.

Introduction:

Past Venus missions did little to clarify the true complexity of Venus' Atmosphere because they did not have the ability to collect and transmit continuous data over a significant period of time. The AARDVARC mission will collect and relay atmospheric data from a wide range of latitudes throughout a Venusian year using a deployable and inflatable electrically powered aircraft at 65 to 45 km above the surface.

Mission details:

The AARDVARC mission, Autonomous Aerodynamic Repeating Diver For Venus Atmospheric Research Of Clouds, is composed of three main components — the Relay Satellite, the Deployment Mechanism, and the Inflatable Aircraft.

Modeled after the Mars Reconnaissance Orbiter, the Venus Orbiting Communication Satellite (VOCS) should continue to be operational well after the end of the AARDVARC mission providing communications infrastructure for later missions.

The Deployment Mechanism is deployed from the VOCS. The mechanism releases the inflatable airplane at 50 km above the surface and then the Deployment Mechanism burns up in the lower atmosphere.

The Diving Atmospheric Research Aircraft (DARA) then stabilizes its flight at 65 km above the surface. The plane will dive into the clouds for 15 min approximately once every 24 hours. During that time it will collect meteorological data including wind speed and direction, temperature, humidity, and pressure. It will also collect data on atmospheric chemical composition, cloud particle density, particle size, and cloud composition. When not performing periodic dives the aircraft will collect, at a lower sampling rate, the same data for the upper atmosphere of Venus.

The Diving Atmospheric Research Aircraft (DARA) will operate for a mission time of 116 Earth days. After deployment and stabilization, it will navigate to Venus's equator, staying at constant solar noon. To maintain this position DARA will compensate for winds and Venus' rotation by maintaining a velocity of 335 km/hr above the clouds and a Velocity of 190 km/hr at the low points of its dives. This means that Venus will rotate beneath the plane like a treadmill. Because one full rotation of Venus is 116 Earth days, this treadmill effect allows DARA to sample the equatorial atmosphere of the entire planet during its planned mission lifetime.

The optimal Launch date for AARDVARC is Friday November 16, 2029, which would result in an estimated arrival on Sunday February 9, 2031 (450 days en-route). The orbit insertion is as follows. The VCOS approaches Venus with its initial Type IV trajectory before performing a down transfer to reach the optimal location for releasing the deployment mechanism. The VCOS then performs an up transfer to a High

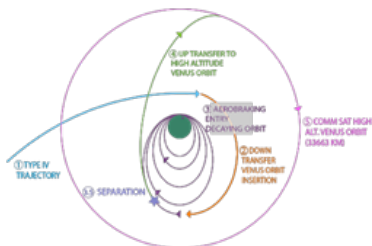


Fig. 1

Altitude Venus orbit at 33,663 km (Fig 1). After being released the deployment mechanism is in an Aerobraking Decaying Entry Orbit. Once the Deployment Mechanism reaches 2 000 km the orbit becomes unstable and the mechanism formally enters the Venesian atmosphere (Fig 2)

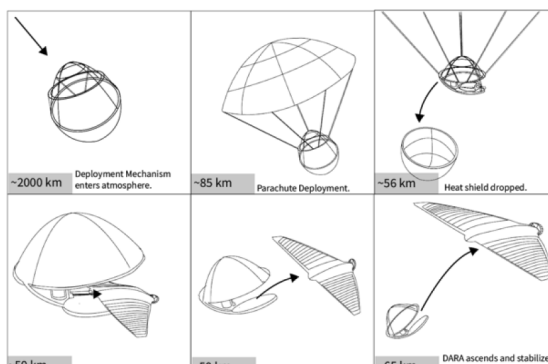


Fig. 2

AARDVARC's strategy for exploring Venus allows a long mission duration and global data collection. The plane will avoid the thermal degradation experienced by past probes by loitering at a high altitude. At its cruising altitude of 65 km the temperature is -43°C and during its dives it will encounter only 15 min at 100°C . DARA will also remain at noon solar time for the duration of its mission. This allows for the maximum collection of solar energy while cruising. Additionally, because DARA is an inflatable structure, buoyancy will keep the aircraft aloft so there is no need to create lift during cruise. This reduces the power requirement for the plane. The inflatable structure also allows for a large surface area at low mass commensurate which lowers both launch vehicle constraints and aircraft power consumption.

With an array size of 304 m^2 , the power provided by the photovoltaic array integrated into the wing's upper surface is 155 kW. Considering 20% losses for regulation, power conversion and storage, total power available for propulsion and avionics is 124 kW, providing an end-of-life power margin of 19%. Of this power 100 kW are used to maintain the speed of the plane. The remaining power is used for the science instruments and avionics including computers, radios and controls.

The attitude control of DARA is unique because of its inflatable design (Fig 3). DARA has four control modes — charging cruise, diving, data collection cruise, and rising. These modes are controlled by an Automatic Flight Control System and a Stability Augmentation System. Both of these systems also work to counteract the effects of unpredicted wind gusting and debris. The ADCS hardware consists of inflatable ailerons, various sensors and a propeller/motor.

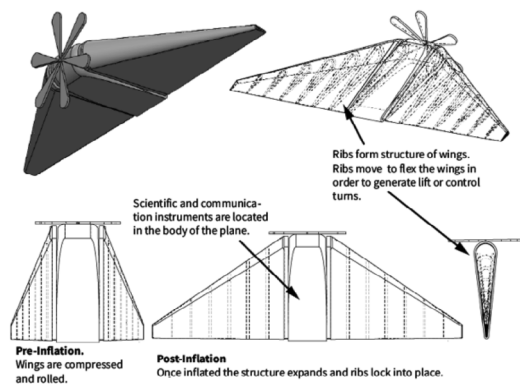


Fig. 3

The uplink from DARA to the VOCS is the critical element of the communication systems design. The main parameters driving the design are the data rate and the time available for the DARA to transmit that data to the VOCS. Total daily data collection is 140 Mbit. The VOCS has an orbital period of 24 hours allowing it to connect to the DARA daily for about 8 hours, resulting in a data rate requirement of 5kbps. With 10 Wt of transmitter power, a 1 m diameter antenna on the VOCS, and an antenna gain of 3 dB on the DARA the achieved link margin is 7.54 dB for 10^{-6} bit error rate. The frequency of the transmission is 928 Ghz which is the same frequency that was successfully used on the Venera—9, 10, and 11 Venus decent missions. Modulation is BPSK and QPSK with $R^{1/2}$ Viterbi Decoding.

The downlink from the Relay Satellite to Earth is a similar, but less powerful, variation of the connection for the Mars Reconnaissance Orbiter. The VOCS will connect to the DSN at duty cycle 14% (e.g. 24 hours of contact per week for the 17 week mission) with a data rate of 11.4 kbps. In order to close the link from the VOCS to the 70m DSN dishes over the Earth–Venus distance of 40 000 000 km, the Satellite will be fitted with a 2m diameter parabolic antenna providing 29 dB gain. This antenna will use gimbals for antenna pointing, similar to those used for solar panel orientation. Transmission is at Xband, 12 GHZ with 15 watts of power. Overall this connection has a link margin of 7.7 dB, sufficient to accommodate changes in distance between Venus and Earth during the duration of the mission.

AARDVARC's unique mission design makes it possible to have a long-term mission on Venus. This will provide consistent and comprehensive data that will allow scientists to gain a more complete understanding of Venus' atmosphere.

References:

- [1] James R. Wertz, Wiley J. Larson, Space Mission Analysis and Design // Microcosm. Edition. 1999. P. 3.
- [2] David A. Senske, James A. Cutts, Jeffery L. Hall, Mark Bullock, Rick Grammier. Venus Flagship Mission Study // Venus Science & Technology Definition Team, NASA, JPL. 2009.
- [3] Rick Fleeter. The Logic of Microspace. Microcosm, 2000.

ACTIVITY OF SMALL-SCALE INTERNAL WAVES IN THE VENUS'S NORTHERN POLAR ATMOSPHERE BY USING RADIO OCCULTATION MEASUREMENTS OF SIGNAL INTENSITY ($\lambda=32$ cm) FROM THE VENERA-15 AND -16 SATELLITES

V.N. Gubenko, I.A. Kirillovich, D.V. Gubenko, V.E. Andreev, T.V. Gubenko
Kotel'nikov Institute of Radio Engineering and Electronics RAS, Vvedenskii Square 1, Fryazino, Moscow Region, 141190, vngubenko@gmail.com;

Keywords:

Radio occultation measurements, signal intensity fluctuations, Venera-15 and -16 satellites, Venus's polar atmosphere, small-scale internal waves, model of radiative damping.

Introduction:

Radio occultation (RO) measurements of signal intensity ($\lambda=32$ cm) from the Venera-15 and -16 satellites provide complementary information about small-scale structure of internal waves in the Venus's polar atmosphere. Our method of analysis is similar in many respects to that used in previous studies [1, 2]. Authors of above indicated works suggested that radiative damping is the principal process to dissipate internal atmospheric waves having vertical wavelengths <4 km, which have been observed by radio occultation experiments. Figure 1 shows the basic signal intensity measurements. The RO signal intensity remains nearly constant until the occultation by neutral polar atmosphere begins at a relative time of about ~ 0 sec. From that time onward the RO signal exhibits rapid fluctuations (scintillations) superimposed on a gradually decreasing trend. Figure 1 clearly shows the signal intensity responses (see selected fragments on the right) when radio waves pass through the Venus's daytime (solar zenith angles Z_{\odot} are correspondingly equal 85.8° and 87.2° for sessions 24 and 30) and nighttime ($Z_{\odot}=95.4^{\circ}$ for session 42) ionosphere near terminator. It is known that the signal intensity minima correspond to electron density maxima in the ionospheric layers [3]. Taking into account that the apparent ray velocity normal to the radio path was equal here ~ 4.3 km/s [4], one can find that the ionospheric electron density maxima near terminator both for the day and for the night sides of Venus are located at altitude of ~ 150 km.

It is convenient to represent the RO signal intensity data as a function of the instantaneous ray path height (ray perigee height). The ray path height (h) as a function of time is obtained as a natural byproduct of the steps of data analysis that yield atmospheric density, pressure and temperature profiles [5]. We applied a high-pass spatial filter to the signal intensity data to isolate the scintillations. This is filter operates as follows:

$$i(h) \equiv \frac{l(h) - \langle l(h) \rangle}{\langle l(h) \rangle} \quad (1)$$

Here, $l(h)$ is the measured signal intensity and h is the ray perigee height. Angle brackets denote the local mean computed by fitting a quadratic polynomial to $l(h)$ over a 4-km interval centered on height h . By definition $l(h) > 0$, so that $i(h) > -1$. However, the value $i(h)$ can exceed $+1$ by a significant margin as a result of large spikes in signal intensity, which are commonly observed in the RO experiments of Venera-15 and -16 satellites.

In the case of weak scattering when $|i(h)| \ll 1$, the RO signal intensity fluctuations $i(h)$ are proportional to variations $p'(h)$ in atmospheric density [6]. According to the internal gravity wave (IGW) theory, the following expression can be written [1]:

$$i(h) \propto \rho'(h) \propto G_p(h) \exp \left[j \int^h m(h) dh \right], \quad (2)$$

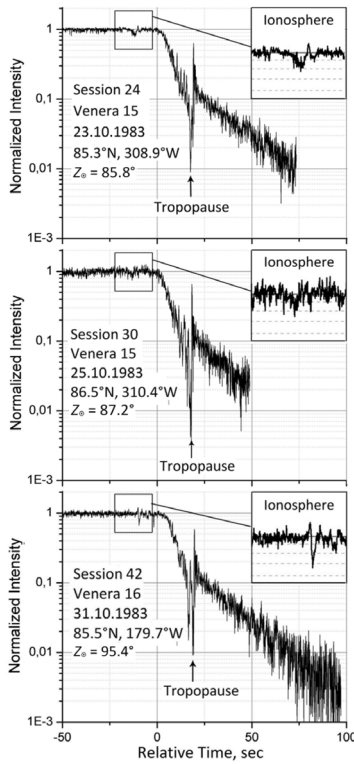


Fig. 1. Measurements of signal intensity ($\lambda=32$ cm) versus time in the Venus's polar atmosphere for three radio occultation sessions: 24, 30 and 42 (ingresses) of the Venera-15 and -16 spacecrafts. Time $t=0$ sec corresponds to a ray path height of ~ 100 km (Venus's mean radius is 6051 km). Tropopause of the probed atmospheric regions is located at altitude: ~ 57.6 km (sessions 24, 30) and ~ 59.0 km (session 42) [5].

where $m=2\pi/\lambda_z$ is the vertical wave number, λ_z is vertical wavelength, j is imaginary unit. Amplitude function G_p here is described by the formula (3):

$$G_p(h) \equiv (\rho_b N_b^3)^{1/2} \exp \left[- \int^h \frac{dh}{L_r(h)} \right], \quad (3)$$

where ρ_b and N_b are the background values of atmospheric density and Brunt-Vaisala frequency, respectively; L_r is the radiative damping length scale. In the absence of wave energy dissipation, $\rho'(h)$ will generally decrease with altitude as $\sqrt{\rho_b(h)}$, but with additional modulation due to the vertical variation of $N_b^{3/2}(h)$. The radiative damping is described by the radiative damping length scale L_r , given by [1]:

$$L_r \equiv 2 \left| \frac{\omega}{m} \right| \tau_r, \quad (4)$$

where τ_r is the radiative relaxation time [7], and ω is the IGW intrinsic frequency, which means the wave frequency relative to an observer moving with the background wind speed [8–12]. The radiative relaxation time τ_r (Figure 2) is estimated from the model result $\lambda_z = 7$ km given in the work [13] by assuming that the damping time is proportional to the vertical wavelength.

The altitude dependence $\tau_r(h)$ for the $\lambda_z=1$ km was determined by us for the analysis of signal intensity fluctuations $i(h)$, and the graphs $\tau_r(h)$ for verti-

cal wavelengths of 5 and 2.5 km, obtained earlier in the work [14, see Fig. 7], are shown in Figure 2 for comparison.

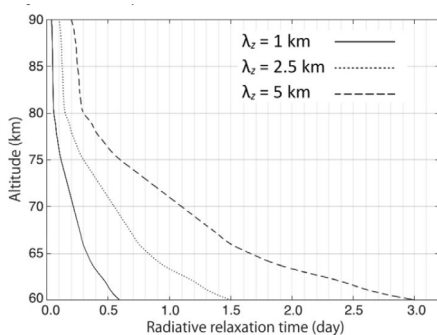


Fig. 2. Altitude profiles of the radiative relaxation time $\tau_r(h)$ in the Venus's atmosphere for vertical wavelengths of 5 km (dashed), 2.5 km (dotted), and 1 km (solid) obtained by extrapolating the model prediction [13].

Figure 3 shows examples of the signal intensity fluctuations profiles $i(h)$ observed in RO sessions 24, 30, and 42 (jagged lines). The ray path height is measured here from the level of the Venus's average surface with a radius of 6051 km. The rapid intensity fluctuations represent diffraction effects due to small-scale inhomogeneities in the Venus's atmosphere. As follows from results of the work [4], the diffraction pattern of the RO signal intensity scintillations at tropopause level in the Venus's polar atmosphere is produced by the small-scale refractive index inhomogeneities with a vertical size of <0.32 km (radius of the first Fresnel zone). Inhomogeneities with larger vertical sizes, observed in the RO experiments, do not contribute to the diffraction pattern and may be due to the influence of thin regular layers or internal atmospheric waves. Early, thin stable layers in the Venus's polar clouds were found at altitudes of 59.0–61.5 km [4]. At altitudes above ~ 61.5 km, where the effects of radiative attenuation are significant, the fluctuations $i(h)$ are probably caused by internal atmospheric waves, and we have found that their dominant vertical size is of ~ 1 km. The dashed curves in Figure 3 show the wave envelope, $G_r(h)$, computed with aid of Eq. (3) and profiles $\rho_b(h)$ and $N_b(h)$ appropriate to each RO occultation.

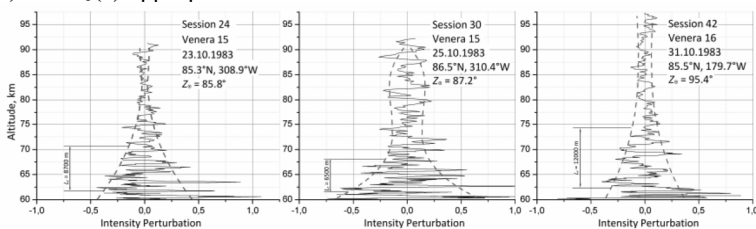


Fig. 3. Signal intensity fluctuations, $i(h)$, observed during three RO sessions 24, 30 and 42 (jagged lines). Altitude refers to the ray path height above Venus's mean radius 6051 km. Smooth lines show how magnitude of fluctuations varies with height according to wave theory (including effect of radiative damping). Vertical length scale for radiative damping (L_r) in the Venus's atmosphere is equal $L_r = 8700$ m (reference altitude below is $h_{ref} = 61.8$ km) for session 24; $L_r = 6500$ m ($h_{ref} = 61.5$ km) for session 30; $L_r = 12000$ m ($h_{ref} = 62.3$ km) for session 42.

The key IGW characteristics in the Venus's polar atmosphere, obtained from the analysis of seven RO sessions of signal intensity ($\lambda = 32$ cm) measurements from Venus-15 and -16 satellites are given in Table. 1. The formula (4) is used when calculating the wave parameters. First, analyzing the vertical profile of the signal intensity fluctuations, the vertical scale of the radiative attenuation (L_r) is determined for a given measurement session. At the next stage, the radiative relaxation time (τ_r) in the Venus's atmosphere is calcu-

lated for the analyzed intensity fluctuations with $\lambda_z=1$ km, localized in a given altitude interval (see Figure 2). Then, using the formula (4), the intrinsic frequency (ω) of the identified internal wave is determined. Further, on the basis of the dispersion equation, $\omega/N_b = |k_h|/|m| = \lambda_z/\lambda_h$, for internal waves in the interval of intermediate intrinsic frequencies ($f^2 \ll \omega^2 \ll N_b^2$) and the background estimate of Brunt-Vaisala frequency $N_b=0.02$ rad/s, the horizontal wavelength (λ_h) was calculated. At the last stage, the intrinsic horizontal ($|c_{ph}^{in}| = \omega/|k_h|$) and vertical ($|c_{pz}^{in}| = \omega/|m|$) phase speeds are determined, as well as the intrinsic period for IGWs [3, 8–12]. The vertical wavelength of these fluctuations is about 1 km at the altitude of >61.5 km. The developed model for radiative damping implies that the intrinsic frequencies of identified IGWs vary from $3.5 \cdot 10^{-4}$ rad/s to $9.5 \cdot 10^{-4}$ rad/s, and their horizontal wavelengths are confined in the interval from 21 to 57 km.

Table 1. Internal gravity wave characteristics in the Venus's atmosphere inferred from the radio occultation signal intensity ($\lambda=32$ cm) measurements of Venera-15 and -16 satellites

Session Number	h_{ref} , km	L_r , m	τ_r , sec	$L_r/(2\tau_r)$, m/s	ω , rad/s	τ_{tr} , hrs	N_b , rad/s	λ_z , m	λ_h , m	$ c_{ph}^{in} $, m/s	$ c_{pz}^{in} $, m/s
10	62.2	$4.6 \cdot 10^3$	$41.0 \cdot 10^3$	0.056	$3.5 \cdot 10^{-4}$	5.0	$2.0 \cdot 10^{-2}$	$\sim 10^3$	$57 \cdot 10^3$	3.2	$5.6 \cdot 10^{-2}$
12	63.0	$5.2 \cdot 10^3$	$36.7 \cdot 10^3$	0.071	$4.5 \cdot 10^{-4}$	3.9	$2.0 \cdot 10^{-2}$	$\sim 10^3$	$44 \cdot 10^3$	3.2	$7.3 \cdot 10^{-2}$
20	62.4	$8.4 \cdot 10^3$	$39.8 \cdot 10^3$	0.105	$6.6 \cdot 10^{-4}$	2.6	$2.0 \cdot 10^{-2}$	$\sim 10^3$	$30 \cdot 10^3$	3.2	$11 \cdot 10^{-2}$
24	61.8	$8.7 \cdot 10^3$	$43.2 \cdot 10^3$	0.100	$6.3 \cdot 10^{-4}$	2.8	$2.0 \cdot 10^{-2}$	$\sim 10^3$	$32 \cdot 10^3$	3.2	$10 \cdot 10^{-2}$
30	61.5	$6.5 \cdot 10^3$	$44.3 \cdot 10^3$	0.073	$4.6 \cdot 10^{-4}$	3.8	$2.0 \cdot 10^{-2}$	$\sim 10^3$	$43 \cdot 10^3$	3.2	$7.4 \cdot 10^{-2}$
32	62.3	$12.2 \cdot 10^3$	$40.1 \cdot 10^3$	0.152	$9.5 \cdot 10^{-4}$	1.8	$2.0 \cdot 10^{-2}$	$\sim 10^3$	$21 \cdot 10^3$	3.2	$15 \cdot 10^{-2}$
42	62.3	$12.0 \cdot 10^3$	$40.1 \cdot 10^3$	0.150	$9.4 \cdot 10^{-4}$	1.9	$2.0 \cdot 10^{-2}$	$\sim 10^3$	$21 \cdot 10^3$	3.2	$15 \cdot 10^{-2}$

Acknowledgements:

This work was carried out within the framework of the state task and partially was supported by the Russian Foundation for Basic Research (project No. 19-02-00083 A) and Program 12 of RAS Presidium.

References:

- [1] Hinson D.P., Jenkins J.M. Magellan radio occultation measurements of atmospheric waves on Venus // *Icarus*. 1995. V. 114. P. 310–327.
- [2] Tellmann S., Hausler B., Hinson D.P., Tyler G.L., Andert T.P., Bird M.K., Imamura T., Patzold M., Remus S. Small-scale temperature fluctuations seen by the VeRa Radio Science Experiment on Venus Express // *Icarus*. 2012. V. 221. P. 471–480.
- [3] Gubenko V.N., Pavelyev A.G., Kirillovich I.A., Liou Y.-A. Case study of inclined sporadic E layers in the Earth's ionosphere observed by CHAMP/GPS radio occultations: Coupling between the tilted plasma layers and internal waves // *Adv. Space Res.* 2018. V. 61. No. 7. P. 1702–1716. DOI: 10.1016/j.asr.2017.10.001.
- [4] Gubenko V.N., Andreev V.E., Pavelyev A.G. Detection of layering in the upper cloud layer of Venus northern polar atmosphere observed from radio occultation data // *J. Geophys. Res.* 2008. V. 113. No. E03001. DOI: 10.1029/2007JE002940.
- [5] Yakovlev O.I., Matyugov S.S., Gubenko V.N. Venera-15 and -16 middle atmosphere profiles from radio occultations: Polar and near-polar atmosphere of Venus // *Icarus*. 1991. V. 94. No. 2. P. 493–510. DOI: 10.1016/0019-1035(91)90243-M.
- [6] Hinson D.P., Tyler G.L. Internal gravity waves in Titan's atmosphere observed by Voyager radio occultation // *Icarus*. 1983. V. 54. P. 337–352.

- [7] Fels S.B. A parameterization of scale-dependent radiative damping grace in the middle atmosphere // *J Atmos. Sci.* 1982. V. 39. P. 1141–1152.
- [8] Gubenko V.N., Pavelyev A.G., Andreev V.E. Determination of the intrinsic frequency and other wave parameters from a single vertical temperature or density profile measurement // *J. Geophys. Res.* 2008. V. 113. No. D08109. DOI: 10.1029/2007JD008920.
- [9] Gubenko V.N., Pavelyev A.G., Salimzyanov R.R., Pavelyev A.A. Reconstruction of internal gravity wave parameters from radio occultation retrievals of vertical temperature profiles in the Earth's atmosphere // *Atmos. Meas. Tech.* 2011. V. 4. No. 10. P. 2153–2162. DOI: 10.5194/amt-4-2153-2011.
- [10] Gubenko V.N., Pavelyev A.G., Salimzyanov R.R., Andreev V.E. A method for determination of internal gravity wave parameters from a vertical temperature or density profile measurement in the Earth's atmosphere // *Cosmic Res.* 2012. V. 50. No. 1. P. 21–31. DOI: 10.1134/S0010952512010029.
- [11] Gubenko V.N., Kirillovich I.A., Pavelyev A.G. Characteristics of internal waves in the Martian atmosphere obtained on the basis of an analysis of vertical temperature profiles of the Mars Global Surveyor mission // *Cosmic Res.* 2015. V. 53. No. 2. P. 133–142. DOI: 10.1134/S0010952515020021.
- [12] Gubenko V.N., Kirillovich I.A. Diagnostics of internal atmospheric wave saturation and determination of their characteristics in Earth's stratosphere from radiosonde measurements // *Sol.-Terr. Phys.* 2018. V. 4. No. 2. P. 41–48. DOI: 10.12737/stp-42201807.
- [13] Crisp D. Radiative forcing of the Venus mesosphere. II. Thermal fluxes, cooling rates, and radiative equilibrium temperatures // *Icarus.* 1989. V. 77. P. 391–413.
- [14] Ando H., Imamura T., Tsuda T., Tellmann S., Patzold M., Hausler B. Vertical wave-number spectra of gravity waves in the Venus atmosphere obtained from Venus Express radio occultation data: Evidence for saturation // *J. Atmos. Sci.* 2015. V. 72. P. 2318–2329. DOI: 10.1175/JAS-D-14-0315.1.

CORRECTIONS TO MODEL LOVE NUMBER k_2 DUE TO INELASTICITY OF THE INTERIORS OF VENUS

T.V. Gudkova, V.N. Zharkov,

Schmidt Institute of Physics of the Earth RAS, B.Gruzinskaya, 10, Moscow, Russia, gudkova@ifz.ru

Keywords:

Venus, inelasticity, Love number, interior structure

Introduction:

Interior structure models of Venus are based on the topography and gravity field data: mass, mean radius, moment of inertia and tidal Love number k_2 , which is a functional of the distributions of elastic moduli K and μ and density. The value of k_2 was obtained from KA Magellan and Pioneer Venus Orbiter, but it has significant error bar ($k_2=0.295\pm 0.066$) [1]. The value k_2 depends on the inelasticity of the interiors at a tidal period of 58.4 days. The interior structure models of the Venus are elastic, while k_2 contains both elastic and inelastic components. When constructing an interior structure model, the elastic component is calculated. It is necessary to introduce the correction to the elastic value due to the inelasticity of the interior.

Effects of inelasticity:

The problem of partitioning of the Love number k_2 into elastic and inelastic components for Mars was examined in detail in [2]. In this study we assume that Venus is similar to the Earth by mechanical parameters (radius and density), therefore for a $Q_\mu(l)$ distribution in the silicate envelope of Venus we use $Q_\mu(l)$ distribution in the interiors of the Earth – four-layer piecewise-constant QML9 model [3] (see Table): (0–80 km), $Q_\mu=600$; (80–220 km), $Q_\mu=80$; (220–400 km), $Q_\mu=143$ and (400–670 km), $Q_\mu=276$.

In a dissipative medium, as in the interiors of Venus, the dissipative function $Q(l)$, the shear modulus $\mu_0(r)$ and tidal Love number k_2 are functions of frequency. Frequency dependence of dissipative factor Q_μ for the interiors of the Earth is based on seismic data and laboratory data [4]. The review on recent study of dissipative properties of Earth' interiors one can find in [5].

In the reference Earth model PREM in the period interval from ~ 1 still ~ 1 h (3.6×10^3 s), which corresponds to Earth seismology, Q_μ is constant. This case corresponds to the logarithmic creep function (Lomnitz rheology model) [4], and the shear moduli ratio $\mu_0(\sigma)$ at frequencies σ_1 and σ_2 is expressed in the following form [6]

$$\frac{\mu_0(\sigma_2)}{\mu_0(\sigma_1)} = 1 - \frac{2}{\pi Q_\mu} \ln \frac{\sigma_1}{\sigma_2}. \quad (1)$$

In the interval of long periods Q_μ weakly depends on frequency, which refers to the stage of transient (unsteady) creep [7, 8, 9]. In this case we have [4, 6]

$$\frac{\mu_0(\sigma_2)}{\mu_0(\sigma_1)} = 1 - \frac{1}{Q_\mu(\sigma_1)} \left[\left(\frac{\sigma_1}{\sigma_2} \right)^n - 1 \right] \operatorname{ctg} \frac{n\pi}{2}. \quad (2)$$

$$Q_\mu(\sigma_2) = Q_\mu(\sigma_1) \left(\frac{\sigma_2}{\sigma_1} \right)^n. \quad (3)$$

The value of n in (2–3) is in the interval $n \sim 0.1-0.2$.

In this study, in the interval of periods from 1 s to 1h we use the Lomnitz rheological model, formula (1) for the ratio of shear modulus $\mu_0(\sigma)$. In the interval of periods from 1 h to 58.4 days we use formulas (2). Let σ_1 be the frequency corresponding to the period of 1 s, σ_2 – the frequency corresponding to the period of 1 h = 3.6×10^3 s, σ_3 – the frequency corresponding to the period of Solar-induced tide of about 58.4 days = 5×10^6 s. Formulas (1) and (2) allow

us to estimate the decrease in the shear modulus at the transition from frequency σ_1 to σ_2 (Table 1).

The numerical results of transformation of $Q_\mu(l)$ distribution at transition from seismic band to the period of 1 h and 58.4 days, corresponding changes of shear modulus in four layers in silicate envelope of Venus and total change of shear modulus are given in the Table. Based on the laboratory data and the experience of studying this problem for the Earth, we take n in the interval of 0.15–0.2.

Due to inelasticity, $\mu(5 \times 10^6 \text{ s})$ is lower than $\mu(1 \text{ s})$ by 5, 35, 23 and 11% in four layers, respectively. The Love number k_2 is approximately proportional to the shear modulus, and inelasticity leads to the increase of Love number k_2 in comparison with the value for an elastic model. Numerical modeling shows that at n in the interval of 0.15–0.2, Love number k_2 increases by 8–12 percent. By this estimate the difference between $k_2(5 \times 10^6 \text{ s})$ and $k_2(1 \text{ s})$ is about 0.02–0.03, respectively, and is within the error bars of k_2 .

The values of Love number k_2 for the interior structure models of Venus with solid and liquid cores are noticeably different. For the models with solid core k_2 is about 0.17, while for the liquid core being about 0.25–0.27. The authors of paper [10] came to the conclusion that because of inelasticity one cannot conclude if the core of Venus is liquid or solid. The estimates of corrections due to inelasticity depend on the choice of dissipative factor in the interiors of the planet and the value n in the creep function. If $n=0.25-0.3$ we also cannot exclude the presence of a solid core. The clue to the solution of this problem is in decreasing the uncertainty of k_2 , that also could accurate the radius of the core and the content of iron in the mantle.

Table. Values of the dissipative factor $Q_m(l)$ and the decrease ratio of shear modulus in four silicate layers of Venus at the transition from 1 s to 58.4 days and values of $n = 0.15$ and 0.2 in formulas (1) and (2).

n	0.15				0.2			
Глубина (km)	0-80	80-220	220-400	400-670	0-80	80-220	220-400	400-670
$Q(\sigma_1)$	600	80	143	276	600	80	143	276
$Q(\sigma_2)$	202	27	48	93	140	20	35	65
$\mu(\sigma_2)/\mu(\sigma_1)$	0.991	0.935	0.964	0.981	0.991	0.935	0.964	0.981
$\mu(\sigma_3)/\mu(\sigma_2)$	0.96	0.7	0.903	0.91	0.93	0.5	0.71	0.85
$\mu(\sigma_3)/\mu(\sigma_1)$	0.95	0.65	0.77	0.89	0.92	0.47	0.68	0.83

Conclusion:

It is demonstrated that in order to put restriction on the interior structure model of Venus it is worth taking into account the effects of inelasticity on Love number k_2 . Numerical modeling shows that inelasticity of venusian interiors leads to the increase of k_2 by several hundredths. The value of k_2 observed at the period of solar tide on Venus (the period 58.4 days), should be decrease, at least, by 0.02–0.03, when comparing with model values. This correction is still within the error bars of k_2 determination.

Acknowledgements:

This work is partly financially supported by Budget funding of Schmidt Institute of Physics of the Earth and partial support for Program 28 of the Presidium of the Russian Academy of Sciences.

References:

- [1] Konopliv, A.S., Yoder, C.F. Venusian k_2 tidal Love number from Magellan and PVO tracking data // Geophys. Res. Lett. 1996. V. 23. P. 1857–1860.
- [2] Zharkov V.N., Gudkova T.V. Construction of Martian Interior Model // Sol. Syst. Res. 2005. V. 39. № 5. P. 343–373.
- [3] Lawrence J.F., Wyession M.E. QLM9: A new radial quality factor (Q_μ) model for the lower mantle // Earth Planet. Sci. Lett. 2006. V. 241. P. 962–971.
- [4] Zharkov, V.N., Fizika zemnykh nedr (Physics of the Earth's Interior, Moscow: Nauka i Obrazovanie, 2012).

- [5] Zharkov V.N., Gudkova T.V., Batov A.V. On estimating the dissipative factor of the Martian Interior // *Sol. Syst. Res.* 2017. V. 51. № 6. P. 512–523.
- [6] Akopyan S.Ts., Zharkov V.N., Lubimov V.M. Theory of attenuation of torsional oscillations of the Earth // *Phys. Solid Earth*. 1977. V. 8. P. 3–11.
- [7] Zharkov, V.N. and Molodensky, S.M., Corrections To Love Numbers and Chandler Period for Anelastic Earth's Models // *Phys. Solid Earth*, 1979, V. 6. P. 88–89.
- [8] Anderson, D.L. and Minster, J.B., The Frequency Dependence of Q in the Earth and Implications for Mantle Rheology and Chandler Wobble // *Geophys. J.R. Astron. Soc.* 1979. V. 58. P. 431–440.
- [9] Smith, M.L. and Dahlen, F.A., The Period and Q of the Chandler Wobble // *Geophys. J.R. Astron. Soc.* 1981. V. 64. P. 223–284.
- [10] Dumoulin, C., Tobie, G., Verhoeven, O., Rambaux, N. Tidal constraints on the interior of Venus // *J. Geophys. Res. Planets.* 2017. V. 122 (6). P. 1338–1352. doi:10.1002/2016JE005249.

TOPOGRAPHIC CONFIGURATION OF CORONAE ON VENUS: SUPPORTING EVIDENCE FOR TIME-DEPENDENT STYLES OF RESURFACING

E.N. Guseva, M.A. Ivanov

Vernadsky Inst., RAS, Moscow, Russia, guseva-evgeniya@ya.ru

Keywords:

Venus, coronae, topographic configuration, stages of the coronae evolution

Introduction:

Coronae on Venus represent circular and often axisymmetric landforms that are characterized by an annulus of densely packed grooves and, in some cases, ridges [1–3]. The annulus encircles corona interior where volcanic features dominate [3]; at some coronae, distinct lava flows extend from the annulus into the corona surroundings [4]. The circular shape of coronae, their non-random spatial distribution, and prominent volcanic and tectonic components indicate that these volcano-tectonic complexes are the surface manifestations of mantle diapirs [5–7]. In this interpretation of coronae, their topographic configuration is important because it should reflect different stages of the coronae evolution [8]. Numerical simulations of a mantle diapir evolution on Venus suggest a sequence of characteristic topographic profiles ranging from a dome-shaped uplift during a progressive stage of the diapir development (diapir impinging against lithosphere and warps it up) to a topographic depression at the final stage of diapir evolution (loss of extra heat, relaxation and sinking). In our study, we investigated topographic configuration of all coronae and corona-like features in order to classify them by their characteristic topographic profiles and assess a possible stage of mantle diapirs evolution that the profiles may illustrate.

Data and methods:

In this study, we used published catalogues of coronae on Venus [3, 9] to collect a population of features for the topographic analysis. We inspected these catalogues to exclude repetitions and combined the catalogues together into one list of structures. We examined morphology of each coronae from this list to determine their lateral extent using mosaics of the Magellan C1-MIDR images (resolution 225 m/px). Then we mapped each feature as a polygon in an ArcGIS project and defined its area from an equal-area projection (Mollweide). The area was a key parameter to calculate an effective radius (r) of each feature ($r = \sqrt{\text{Area}/\pi}$). When coordinates of the centers and radii of the mapped coronae have been determined, we constructed their average topographic profiles. For this, we used gridded Magellan topographic data presented as a topographic map with resolution ~ 5 km/px. Each point of an average profile represents a mean elevation value in a circular zone, which is concentric relative to the corona geographic center. Width of each zone is equal to the spatial resolution of the topographic map.

Results and discussion:

In our work, we investigated 551 corona and corona-like features and analyzed their topographic profiles. By this characteristic, all studied features can be divided into five categories. (1) Dome-shaped coronae, the interior of which is uplifted and occurs at higher elevations than the annulus and the broader corona surroundings (Fig. 1a). We counted 99 such coronae that make $\sim 18\%$ of the entire analyzed population. (2) W-shaped coronae. For these features, the interior is characterized by a central dome-like structure surrounded by a circular, moat-like depression (Fig. 1b). We identified 189 such coronae ($\sim 34\%$ of the population). (3) W-W-shaped coronae that are mostly correspond to the double-rim coronae [3]. The interior of such structures represent a broad depression surrounded by an additional interior rim (Fig 1c). In our study, we have found only 18 such features ($\sim 3\%$ of the population). (4) W-V-shaped coronae, the interior of which represents a topographic depressions surrounded by a topographically prominent rim (Fig. 1d); there are 59 such coronae ($\sim 11\%$ of the population). (5) Coronae

the interior of which represents a broad U-shaped topographic depression (Fig. 1e). The annulus of such coronae is topographically indistinctive feature. There are 186 such coronae (~34% of the population).

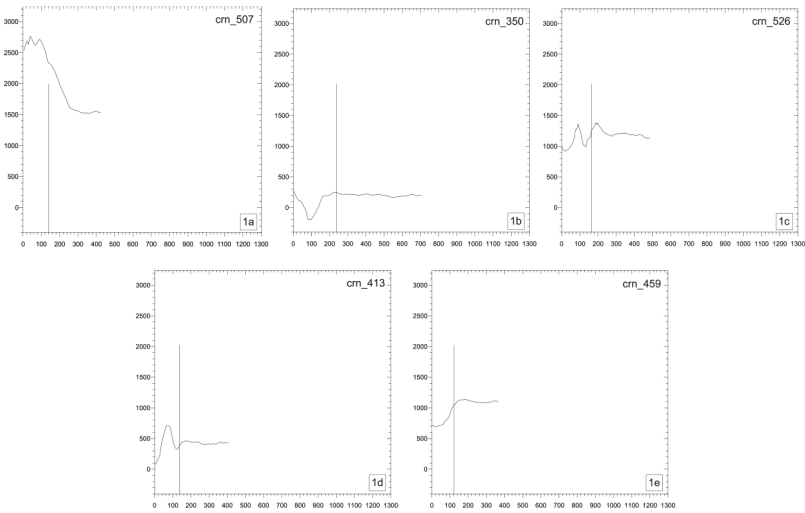


Fig. 1. Five categories of topographic profiles of coronae on Venus.

A series of model topographic profiles illustrates different phases of the progressive and regressive stages of evolution of the corona parent diapirs (Fig. 2). The initial phases of the progressive stage are characterized by growth of a dome-shaped structure above a diapir that impinges against the bottom of a lithospheric rheological barrier (Fig. 2a–c). This characteristic topographic profile corresponds to the dome-shaped coronae (Fig. 1a). According to the model results [8], these coronae represent a stage of corona evolution when the parent diapir still possesses sufficient positive buoyancy to be able to displace the lithospheric barrier upward. About one fifth of the entire population of coronae and corona-like features belong to this category. These coronae are strongly concentrated within the Beta-Atla-Themis (BAT) region outlined by the major branches of rift zones and showing abundant fields of lobate plains. Both rifts and lobate plains are characteristic features of the later network rifting-volcanism regime of resurfacing [10]. Close spatial association of the dome-shaped coronae with the BAT region suggests that about 20% of coronae on Venus formed during the network rifting-volcanism regime.

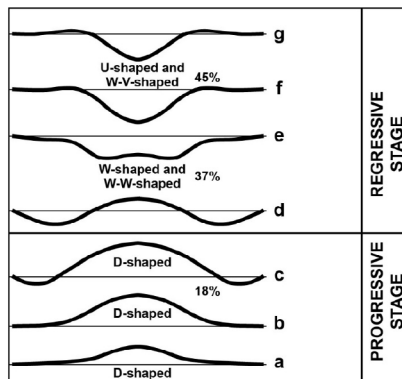


Fig. 2. Topographic profiles of a corona at different stages of its evolution (modified from [8]).

For all other coronae, the principal feature of their topographic configuration is a longer-wavelength depression within the corona interior, which is compli-

cated by shorter-wavelength positive topographic features. According to the model results [8], the presence of the subsided interior indicates that these coronae are at their regressive stage of evolution when the parent diapir lost positive buoyancy due to melt escape and cooling. The W- and W-W-shaped coronae, which form ~ 37% of the entire corona population, may correspond to the earlier phases of the regressive stage (Fig. 2d,e).

About half (45%) of the analyzed coronae represents either rimmed or rimless topographic depressions (categories W-V and U, Fig. 1d,e) that may correspond to the late phases of the regression stage of the diapirs evolution [8]. Our results indicate that the majority of coronae on Venus manifest the later stage of evolution of the mantle diapirs when the diapir bodies gained negative buoyancy. The absolute majority of these coronae are spatially associated with groove belts and characterize the later episodes of the tectonic regime of resurfacing [10]. Numbers of coronae that may manifest the earlier and later phases of the regressive stage are about the same (37% and 45%, respectively). This suggests that the corona parent diapirs formed during a broader time interval by the end of the tectonic regime but this activity ceased before the emplacement of vast lava plains (shield and regional plains) that have embayed the tectonic components of most coronae during the volcanic regime of resurfacing.

References:

- [1] Barsukov V.L., Basilevsky A.T., Burba G.A. et al (27 others) The geology and geomorphology of the Venus surface as revealed by the radar images obtained by Venera 15 and 16 // *J. Geophys. Res.* 1986. v. 91. NB4. p. D399–D411.
- [2] Pronin A.A. and Stofan E.R. Coronae on Venus: Morphology and distribution // *Icarus*. 1990. v. 87. p.452–474.
- [3] Stofan E.R., Sharpton V.L., Schubert G., Baer G., Bindschadler D.L., Janes D.M., and Squyres S.W. Global distribution and characteristics of coronae and related features on Venus: Implications for origin and relation to mantle processes // *J. Geophys. Res.* 1992. v. 97. N. E8. p. 13347–13378.
- [4] Ivanov M.A. and Head J.W. Geology of Venus: Mapping of a global geotraverse at 30N latitude // *J. Geophys. Res.* 2001. v. 106. N.E8. p. 17515–17566.
- [5] Janes D.M., Squyres S.W., Bindschadler D.L., Baer G., Schubert G., Sharpton V.L., and Stofan E.R. Geophysical models for the formation and evolution of coronae on Venus // *J. Geophys. Res.* 1992. v. 97. N. E10. p. 16055–16068.
- [6] Jellinek A.M., Lenardic A. and Manga M. The influence of interior mantle temperature on the structure of plumes: Heads for Venus, tails for the Earth // *Geophys. Res. Lett.* 2002. v. 29. N. 11. p. 27-1-27-4.
- [7] Johnson C.L. and Richards M.A. A conceptual model for the relationship between coronae and large-scale mantle dynamics on Venus // *J. Geophys. Res.* 2003. v. 108. NO. E6. 5058.
- [8] Smrekar S.E. and Stofan E.R. Corona formation and heat loss on Venus by coupled upwelling and delamination // *Science*. 1997. v. 277. p. 1289–1294.
- [9] Crumpler L. S. and Aubele J. Volcanism on Venus // in: *Encyclopedia of Volcanoes*. Bruce Houghton, Hazel Rymer, John Stix, Steve McNutt, and Haraldur Sigurdson eds., Acad. Press, San Diego, San Francisco, New York, Boston, London, Sydney, Toronto. 2000. p. 727–770.
- [10] Ivanov M.A. and Head J.W. The history of tectonism on Venus: A stratigraphic analysis // *Planetary and Space Science*. 2015. v. 113–114. p. 10–32.

INA IRREGULAR MARE PATCH (IMP): NEW INSIGHTS FROM OBSERVATIONS OF SUPERPOSED IMPACT CRATERS

J.W. Head¹, B.A. Ivanov²

¹ Brown University, Providence, RI 02912 USA, james_head@brown.edu;

² Institute for Dynamics of Geospheres, Russian Academy of Science, Leninsky Prospect 38-1, Moscow, Russia, 119334. baivanov@idg.chph.ras.ru

Keywords:

The Moon, impact craters, cratering chronology.

Introduction:

Irregular Mare Patches (IMPs) [1–3] are an unusual and distinctive manifestation of lunar volcanism [4–6]. Initial age estimates for the largest IMPs using Neukum's impact crater chronology model ages resulted in very young age interpretations for large IMP extrusive basaltic lava flow activity (<100 Ma) [3], while others [4–8] expressed concern about these estimates on the basis of the close association of these IMPs with ancient (~3.5 Ga) edifices and structures. It was proposed instead that the IMP mounds were formed by ancient extrusion of porous highly vesicular magmatic foams predicted theoretically [4] to form in lava shield summit pit craters, and that the young ages were caused by substrate effects with superposed impacts smaller by a factor of ~3 due to their formation in compressible magmatic foam [7–8]. In a previous contribution [9] we assessed the nature of laboratory experimental data for impacts into highly porous materials, outlining several key points about target cohesion, small crater degradation target layering, and scaling to high impact velocity. The recent intensive multidisciplinary characterization and analysis of the major IMP Ina [10] provides a basis for further IMP assessment. The goal of this work is to help distinguish among theories for the formation of IMPs by assessing the nature, physical properties, stratigraphic relationships, and ages of the two major units in Ina using the common theme of impact cratering.

1) What is the predicted regolith thickness on Ina units?: For an impact-generated regolith developed on lava flows emplaced on the floor of Ina at ~59 Ma [3], a regolith thickness of less than a meter would be expected; however, regolith thicknesses on Ina mounds are of the order of 3–5 m (Fig. 1 and [10]), although regolith thickness on surrounding hummocky terrain appears to be less. An impact-generated regolith developed on an ~3.5 Ga age extrusive basalt lava flow unit emplaced contemporaneously with the surrounding volcanic shield would be expected to be >5 m. The situation is much more complex for a 3.5 Ga summit pit crater lava lake model [4]: in this case, 1) the hummocky unit represents the macro-porous lava lake floor (thus, regolith thickness development is retarded by drainage into the macro-porous substrate and may be very uneven); 2) mounds are interpreted to be magmatic foams extruded out from the lava lake below onto the lava lake floor (foams on top of solidified lava lake): the process of emplacement of foams into the lunar vacuum produces a fragmental layer on top of the foam, creating an initial "auto-regolith" layer [11], and a three-layer substrate ("auto-regolith" layer, magmatic foam layer, underlying basalt lava lake floor) on which the impact generated regolith is developed. More specific models for the physical properties of each of these units need to be developed to compare to experimental data.

2) What are the stratigraphic relationships of the Ina units?: Most of the recent (<100 Ma) volcanic activity models call on extrusion of solid basalts onto the surface (mounds) and in some cases, the hummocky floor is younger material extruded from inflated flows and embaying the mounds and is thus younger (see review in [10]). The lava lake model [4] predicts magmatic foam flowing out over the solidified lava lake floor; the mound would thus currently underlie meters-thick fragmental "auto-regolith" and impact generated regolith [4]. We analyze an ~75 m diameter,

12–14 m deep crater on the floor of Ina (Figs. 2–3) that impacted the contact between the mound and hummocky floor units; the crater has penetrated through the mound unit and into a blocky substrate that we interpret to be an extension of the adjacent hummocky floor unit underneath the mound, thus supporting an extrusive foam model. The crater has excavated a large number of solid blocks and scattered them on the crater rim on top of the surrounding mound and hummocky units: the mound to the SE appears at first glance to embay (and thus postdate) the crater, but the presence of boulders on top of this mound, and images from different illumination geometries (Fig. 2–3), clearly show that this apparent relationship is caused by post-event mass wasting of fragmental mound material down the crater wall. The fragmental nature of the upper half of the crater wall in the mound areas is clearly seen, consistent with an ancient age and/or unusual target properties.

3) What are the implications of Ina target properties for crater formation, degradation and retention?: Our analyses clearly show that the hummocky and mound materials have different physical properties (Figs. 1–3), and thus these differences must be taken into account in interpreting the impact crater size-frequency distributions and ages. The convex-up topographic profile of the mounds has been shown to affect the distribution of superposed craters, with fewer on the steeper marginal areas [10]. Still to be determined is the energy partitioning in impacts into targets consisting of magmatic foams, foam “auto-regolith”, foam-derived impact regolith, and macro-porous lava lake floor material. These differences could affect their initial depth and diameter in substrates where crushing may be relatively more important than fragmentation and ejection; these factors could also influence crater degradation as a function of time, potentially making fresh craters appear degraded, or not easily recognizable.

Conclusions:

Detailed analysis of the Ina IMP reveals important new information about target characteristics and stratigraphy. More sophisticated models need to be constructed and more specific laboratory experiments need to be undertaken to explore this improved parameter space.

Acknowledgements:

B.A. I is supported with the Russian Academy of Science project “Origin and evolution of Space studied with telescopic observations and space missions” (the former Program 28 and Program 12).

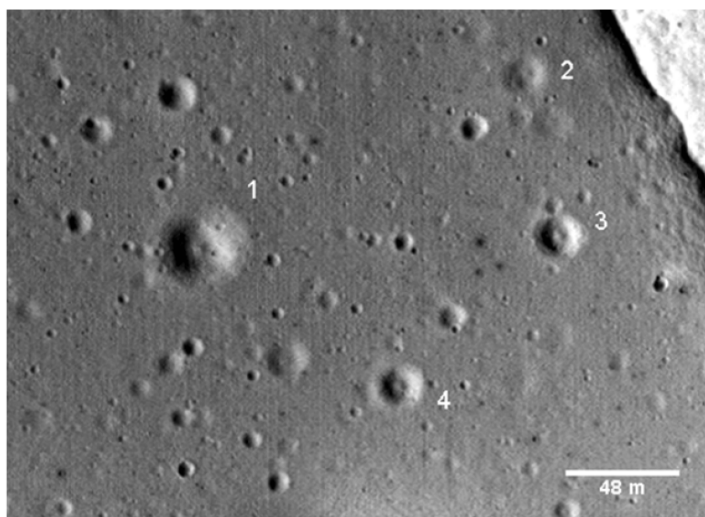


Fig. 1. Four craters in an Ina Mound with central floor mounds, $D=20$ to 32 m. DTM estimated depth for $D=32$ m is about 3 m ($d/D\sim 0.1$). The ratio of the substrate depth T to the crater diameter is $T/D\sim 1/6$ to $1/4$ —the proper range for central mound formation (a layer at 3 to 5 m depth?).

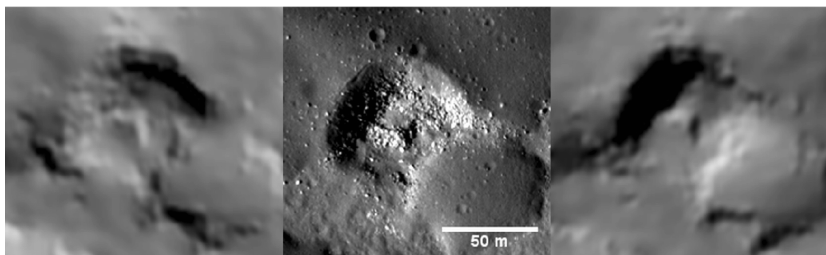


Fig. 2. A flat floor crater with $D=75$ m (Ina) penetrated the mound material of ~ 8 m thickness. Left and right shadowed DTM-based images illustrate the crater perception at various illumination.

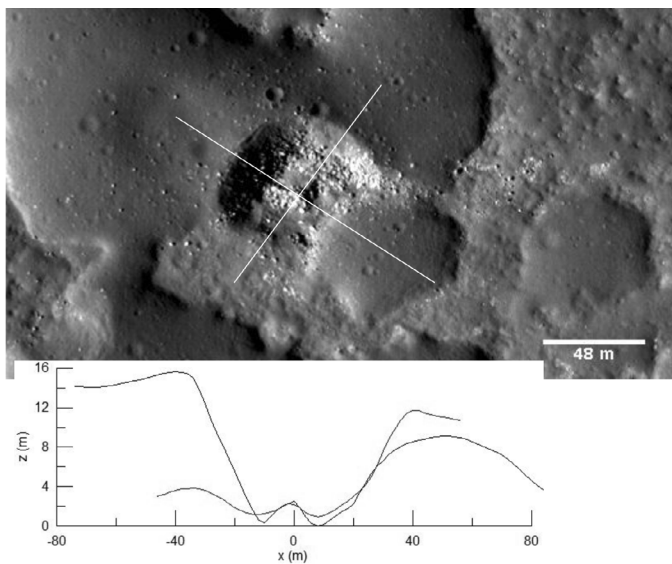


Fig. 3. ~ 75 m-diameter fresh blocky impact crater superposed on the border between Ina floor mounds and hummocky floor material, showing topographic profiles.

References:

- [1] Whitaker. 1972. NASA SP-289, P. 25–84.
- [2] Stooke. 2012. LPSC XLIII, Abstract #1011.
- [3] Braden S. E, et al. 2014. Nature Geoscience7, 787–791.
- [4] Wilson L. & Head J. W. 2017. Jour. Vol. Geotherm. Res. 335, 113–127.
- [5] Wilson L. & Head J. W. 2107. Icarus283, 146–175.
- [6] Head J. W. & Wilson L. 2017. Icarus 283, 176–223.
- [7] Qiao, L., et al. 2017. Geology45, 455–458.
- [8] Qiao, L., et al. 2017. Meteor. Planet. Science 53, 455–458.
- [9] Ivanov, B.A. & Head, J. W. 2019. LPSC 50, Abstract #1243.
- [10] Qiao, L., et al 2019. JGR-Planets, doi: 10.1029/2018JE005841.
- [11] Head, J W. & Wilson, L. 2019. LPSC 50, Abstract 253

VOLCANICALLY-INDUCED TRANSIENT ATMOSPHERES ON THE MOON: ASSESSMENT OF DURATION AND SIGNIFICANCE

James W. Head¹, Lionel Wilson^{1,2}, and Ariel N. Deutsch¹

¹ Department of Earth, Environmental and Planetary Sciences, Brown University, Providence, RI 02912 USA, James_Head@brown.edu

² Lancaster Environment Centre, Lancaster University, Lancaster, LA1 4YQ, UK, l.wilson@lancaster.ac.uk

Keywords:

lunar transient atmosphere, volcanic flux, polar deposits, volatile content, basalts, lava thickness.

Background:

Needham and Kring [1] have proposed that a transient, more prominent atmosphere may have been present on the Moon at several times during its geologic history as a result of gases released in volcanic eruptions. On the basis of their analysis of the volumes and dates of lunar mare basalt eruptions, assumptions about the buried structure of mare-filled lunar impact basins, and volatile release patterns of erupted magmas, they conclude that during an interpreted peak volcanic and volatile release flux at ~ 3.5 Ga, "maximum atmospheric pressure at the lunar surface could have reached ~ 1 kPa" (~ 1.5 x Mars' current atmospheric surface pressure) and that the atmosphere "may have taken ~ 70 million years to fully dissipate." Schulze-Makuch and Crawford [2] explored the possibility of transient niches in which life could have evolved accompanying such an atmosphere. Needham and Kring [1] further explored the possibility that this transient atmosphere may have been a source for the hydrogen, presumably present as water, located in cold traps at the lunar poles, and conclude that "even if only 1% of the mare water vented during these eruptions remains in the polar regions...volcanically derived volatiles could account for all hydrogen deposits" currently observed in the lunar PSRs.

On the basis of recent work in assessing the generation, ascent and eruption of lunar basaltic magma [3, 4], we adopt a more detailed approach and forward-model the production of volatiles in individual eruptions [5, 6], and compare these with the results from the Needham and Kring approach [1]. We utilize our treatments [3–5] to forward-model magma emplacement and volatile release patterns and abundances, and then proceed to assess the likelihood of sufficiently abundant eruptions occurring to produce a transient atmosphere similar to that found by Needham and Kring [1].

The issues requiring examination are 1) the range (and mean value) of magma volumes in individual eruptions, 2) the masses, and hence volumes, of the various gases released in any one eruption, 3) the duration of the eruption and hence the gas release rate (possibly varying significantly as the eruption progresses), 4) the typical time intervals between volcanic eruptions on the Moon as a function of geologic time and 5) the timescale for the dissipation of an atmosphere once one is emplaced.

Input data:

Eruption volumes: Individual eruption volumes, V , of typical visible and therefore most recent lava flow deposits [3], are at least ~ 200 – 300 km³, with some potentially up to 1000 – 2000 km³ (Table 1) and we can estimate the minimum volumes of lava, ~ 100 km³, needed to thermo-mechanically erode the preserved sinuous rille channels [7].

Total mare basalt erupted volumes: Using mare basins lava fill depth estimates, we have a reasonable value for the total volume, V_t , of all volcanic products erupted on the Moon over its lifetime, close to $\sim 10^7$ km³ [8]. We do not know the absolute dates of specific eruptions but we can use crater size-frequency distribution-derived dates of units mapped from orbit, and stratigraphic relationships, to estimate the overall time span, τ_v , ~ 2 Ga, of the vast majority of the Moon's volcanic activity [9,3].

Number of eruptions, average rates and estimated repose periods: Using the 100–300 km³ average eruption volume, the total erupted volume of mare basalts, and the duration, we calculate a total of ~30,000 to 100,000 eruptions in the 4–2 Ga period, and an average repose time of 20,000 to 60,000 years. Accounting for lunar thermal evolution in terms of mare mantle production rates and the evolving state and magnitude of stress in the lithosphere [3] we would predict greater volumes generated and released in earlier periods than later. Assuming that three times as much magma was erupted in the 4–3 Ga period than in the 3–2 Ga period, this suggests that the earlier eruptions could have occurred every 13,000 to 40,000 years.

Volatiles and release patterns: What volatile components were released, in what order, quantity, and in what relative abundance? We have good estimates of the mass fractions, n , a few hundred to perhaps 1500 ppm, and species, dominated by CO, water and sulfur compounds, of volatiles released from lavas and pyroclastics sampled by the Apollo missions [5, 10].

Eruption durations: Analyses of the dynamics of lunar eruptions allow us to estimate the volume fluxes, F_v , of lava forming surface flows and sinuous rilles [4–6]; coupled with the erupted volumes, these give values for the typical durations, τ_e , of these eruptions.

Volatile input to the atmosphere: Multiplying the dense-rock-equivalent erupted volume V by the typical density of lunar basaltic magma, $\rho_m = \sim 3000$ kg m⁻³, yields the magma mass erupted, and multiplying that by the released gas mass fraction n gives the total gas mass released, G . Finally dividing G by τ_e yields the gas mass input rate to the atmosphere, F_g . Table 1 summarizes these values.

Analysis: For each of the released gas masses in Table 1 we can find the properties of the lunar atmosphere that would be created if the gas release rate from the erupted magma was much greater than the total loss rate of the atmosphere into space by whatever mechanisms were relevant (which we shall show shortly is the case). Based on [5] we assume that the volcanic gas consists of CO, H₂O, sulfur compounds and traces of halogens [10] such that the mean molecular mass is $m \sim 25$ kg/kmol. We then find the scale height of the resulting atmosphere, $H = (QT) / (mg)$ where Q is the universal gas constant, 8.314 kJ kmol⁻¹ K⁻¹, T is the mean lunar surface temperature, ~ 235 K, and g is the acceleration due to gravity at the lunar surface, 1.62 m s⁻². These values give $H = 48$ km. The surface density of the atmosphere, τ_s , is equal to its mass, M , from Table 1, divided by the volume equivalent to the surface area of the Moon multiplied by the scale height, i.e. $\tau_s = M / (4 \pi R^2 H)$ where R is the lunar radius, 1738 km. Finally the surface pressure is $P_s = \rho_s g H$. Table 2 lists the values of ρ_s and P_s corresponding to eruption types in Table 1.

Table 1. Parameters of various types of lunar eruption. Cobra Head is the source of VallisSchroeteri [3] and FFC is a typical floor-fractured crater [11–12]. Released volatiles assumed to be dominated by CO and to form $n = 1000$ ppm by mass of a magma that has a liquid density $\rho_m = 3000$ kg m⁻³. V = lava volume; F_v = lava volume eruption rate; τ_e = eruption duration; M = total gas mass released; F_g = gas mass release rate. Typical values for parameters are quoted but individual eruption values may vary by a factor of at least 2 to 3.

Feature	V/km^3	$F_v/(\text{m}^3 \text{s}^{-1})$	τ_e/days	M/kg	$F_g/(\text{kg s}^{-1})$
Cobra Head	2000	1.4×10^5	165	6×10^{12}	4×10^5
FFC	1000	$\sim 10^5$	115	3×10^{12}	3×10^5
long flow	30	30	9×10^1	3×10^6	3×10^6
small flow	200	$10^5 - 10^3$	100	6×10^{11}	3×10^5
sinuous rille	100	1.6×10^{-7}	50	3×10^{11}	10^5
sinuous rille		1.3×10^{-2}	950	10^5	

Discussion: The implied atmospheric gas masses due to typical types of lunar volcanic activity (see Table 1) are of order a few times 10^{11} to a few times 10^{12} kg. As part of an extensive review of three possible types of lunar atmo-

sphere, Stern [13, his section 5.2.2] treats a hypothetical volcanically-induced atmosphere, and with some prescience chooses a total gas mass of 10^{14} g, i.e., 10^{11} kg, for his illustration, the same order of magnitude as the smallest value that we predict. We therefore follow his arguments about the rate at which such a collisionally dominated atmosphere would be lost to space, and like him we adopt the loss rate calculated by Vondrak [14] of 10^4 g s⁻¹, i.e., 10 kg s⁻¹. This leads to the timescales for atmospheric decay, τ_d , shown in Table 2, between $\sim 1,000$ and $\sim 20,000$ years. These are likely maximum atmosphere durations because as the density becomes very small, other loss mechanisms come into play. These values need to be compared with the likely intervals between eruptions on the Moon. With a total volume of volcanics of $V_t = 10^7$ km³ [1, 5], a typical erupted volume of 200 ± 100 km³ (Table 1), and a total duration of volcanism of $\tau_v \sim 2$ Ga, the average interval is 20,000 to 60,000 years. Assigning higher eruptions fluxes to the early part of the mare volcanism era does not change this conclusion greatly.

Table 2. Initial values of the surface density, ρ_s , and surface pressure, P_s , in a transient atmosphere produced by the five types of volcanic activity listed in Table 1. The maximum duration of the atmosphere, τ_d , is indicated.

Feature	ρ_s /(kg m ⁻³)	P_s /Pa		τ_d /years
Cobra Head	3.3×10^{-6}	3.3×10^{-6}	0.26	19,000
FFC	1.6×10^{-6}	1.6×10^{-6}	0.13	9,500
long flow	4.9×10^{-7}	4.9×10^{-7}	3.8×10^{-2}	2,900
long flow	3.3×10^{-7}	3.3×10^{-7}	2.6×10^{-2}	1,900
sinuous rille	1.6×10^{-7}	1.6×10^{-7}	1.3×10^{-2}	950

Conclusions:

The implied intervals between typical lunar eruptions, $\sim 20,000$ to 60,000 years, are an order of magnitude greater than the likely durations of the vast majority of individual transient atmospheres, between $\sim 1,000$ and 3,000 years, though for some floor-fractured crater events and the extreme example of Schroeter's Valley the time scales are comparable. Otherwise, only if all of the Moon's $\sim 10^7$ km³ of basaltic volcanism were to have taken place within a 200 Ma interval would the time scales be comparable. We therefore think it unlikely that the Moon had a semi-permanent (as long as ~ 70 Ma) volcanically-driven atmosphere as proposed by Needham and Kring [1]. We attribute the differences between our estimates and those of Needham and Kring [1] to their use of maximum impact basin depths as average depths, and assignment of all excess volumes below datable units to one age (e.g., 5.9×10^6 km³ assigned to 3.5 Ga in the case of Imbrium).

References:

- [1] Needham D.H. & Kring D. A. 2017. *EPSL*, 478, 175–178.
- [2] Schulze-Makuch D. & Crawford I. A. (2018) *Astrobiol.*, 18, 985–988.
- [3] Head J.W. & Wilson L. 2017. *Icarus*, 283, 176–223.
- [4] Wilson L. and Head J. W. 2017. *Icarus*, 283, 146–175.
- [5] Rutherford M. J. et al. 2017. *Amer. Mineralogist*, 102, 2045–2053.
- [6] Wilson L. & Head J.W. 2018. *GRL*, 45, 5852–5859.
- [7] Head J.W. & Wilson L. 1981. *LPS*, XII, 427–429.
- [8] Head J. W. & Wilson L. 1992. *GCA*, 56, 2155–2175.
- [9] Hiesinger H. et al. 2011. *GSA Sp. Paper* 477, 1–51
- [10] Renggli C. J. et al. 2018. *GCA*, 206, 296–311.
- [11] Jozwiak, L. et al., 2015. *Icarus* 248, 424–447.
- [12] Wilson L. & Head J. W. 2018. *Icarus* 305, 105–122.
- [13] Stern S. A. 1999. *Rev. Geophys.*, 37, 453–491.
- [14] Vondrak R. R. 1974. *Nature*, 248, 657–659.

PROJECT ORPHEUS: LUNAR LABORATORY

A. Cherian¹, C. McKie¹, J. Pensler¹, R. Fleeter¹, J. Head², M. Bowler¹

¹ School of Engineering, Brown University, Providence RI, 02912, USA

² Department of Earth, Environmental and Planetary Sciences, Brown University, Providence RI 02912, USA.

Keywords:

Space, Laboratory, Regolith, Seismometer, Moon, Seismology.

Introduction:

Growing global interest in human and robotic lunar and extraterrestrial exploration is creating new opportunities for lunar transportation. We present a modular autonomous instrumentation host suitable for research at any location on the lunar surface. The system provides power, communications, thermal control and instrument control and data collection buffering with the capability to sustain operations throughout a two week lunar night time. Up to 1 kg of scientific payload is supported on the lunar surface for up to three years at a total mission cost including integration, transportation and operations less than \$10M. This new capability will enable more experiments to be conducted allowing for rapid expansion of knowledge of the Moon.

Orpheus Overview:

Orpheus is a small lunar laboratory in a 20 cm×20 cm×20cm (comparable to an 8U cubesat) enclosure, equipped with its own communication, deployment and power systems. Orpheus houses a 1 kg payload that is deployed onto the lunar regolith (seen in Fig. 1A). The user can configure any experiment or mix of instruments compatible with the mass and volume envelope for extended operation anywhere on the lunar surface. A detachable lid on the box forms as a high gain communication antenna, compatible with one or more low cost ground stations on earth. The parabolic antenna is supported on linear actuators that point the antenna towards the Earth (Fig.1B). Orpheus' onboard systems provide power to the science payload as well as communications of experiment data and control commands with Earth. Deployable solar panels on each face of the box provide power for operations in sun illuminated periods, and recharge of internal batteries (Fig. 1C) for operation during lunar night time

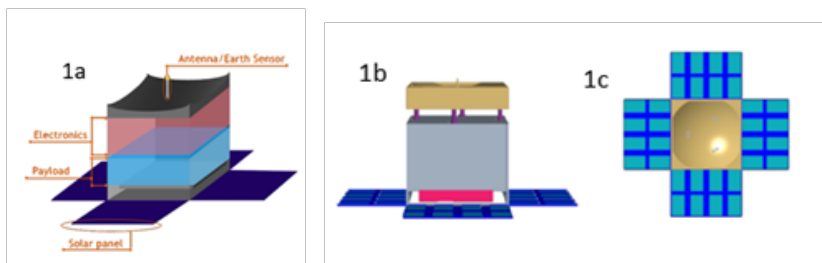


Fig. 1: Orpheus overview (A) basic overview of Orpheus structure, including general payload and electronics placement. (B) 3D model of Orpheus. The communication array lid (gold) is tilted towards the Earth by vertical actuators (purple) to transmit data from the deployed payload (pink). (C) Top view of Orpheus, showing deployed solar panels

Methods:

Orpheus operates in four primary modes: deployment; alignment; transmission and nighttime.

Deployment:

In deployment, Orpheus is ejected from the lunar lander onto the lunar regolith. Initial operations such as satellite lid release and solar panel deployment will occur in this phase (Fig. 2). While different methods of deployment (launching straight from the lander, using a rover, using a robotic arm etc.) have been discussed, the exact method of implementation will be determined based on the lunar lander used.



Fig. 2: After landing on the lunar regolith, solar panels will be deployed to beginning powering Orpheus systems.

Alignment and Transmission:

A defining feature of Orpheus is its transmission of experimental data towards the Earth. The lid (which acts as the communications array) is placed on four linear actuators. During the alignment phase, linear actuator deployment will allow for alignment of the antenna with the ground station (Fig. 3). An Earth sensor on the lid will be used to direct alignment. Once aligned with the Earth, experimental data can be continuously transmitted to the ground station while it is within range. Alignment will be repeated as necessary to maintain contact.

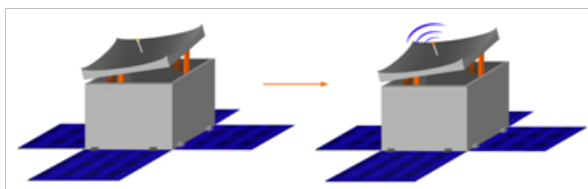


Fig. 3: Using an Earth sensor, vertical actuators attached to the lid will tilt towards the Earth, before beginning transmission of data.

Nighttime:

Due to extended day and night cycles on the Moon (14 Earth days with sunlight, 14 Earth days without), Orpheus will be powered solely by its batteries during nighttime. To allow for payload operations while minimizing battery weight, only essential Orpheus systems (processors and memory boards) will be run, while payload operations will be run at the minimum possible power and duty cycle (Fig. 4). Data transmission will not occur during this phase, and data will be stored and transmitted in bulk at the beginning of the next transmission phase. Dependant on client needs however, payloads can also be run at higher operational levels at the cost of decreasing mass of the payload (which will be taken up by the batteries needed to support increased power draw).

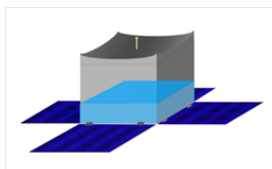


Fig. 4: In nighttime mode, Orpheus shuts down all non-critical processes to maximize battery power, leaving only the payload (light blue) running.

Systems:

Communication:

Onboard Orpheus will be a mechanically steered 24 db gain parabolic dish and an omnidirectional 3 db antenna. In normal operation (at a bit rate of 300 baud) the 24 db dish has a healthy link margin with a 1.8 m diameter ground station dish. In the unlikely circumstance the dish does not respond or is misaligned, an 8m ground station (assumed rented for a short period of time) dish can issue reboot protocol to Orpheus via the 3db antenna. This setup was chosen for availability of smaller ground station dishes, and relative cost of a high gain spacecraft antenna versus a large ground dish. This keeps both budget down and potential markets open.

Power:

For alignment and transmission modes, power will be provided by solar panels. One solar panel will be placed on each face of the box, and the panels will open up during the deployment phase. With an area of 400 cm² on each face, a total area of 1600cm² available for solar panel use. The nighttime phase will last 14 days, and must be battery powered. To reduce battery weight on Orpheus, all non-essential systems will be shut off during this mode, and the only thing being consistently run will be the payload and the payload interface board. The duty cycle of the payload will also be kept as low as possible to reduce power consumption. As mentioned above however, there is flexibility to increase payload operation during this phase at the cost of reducing payload mass, and we are willing to work with the clients on this aspect.

Thermal:

Given the aim of trying to land on the equator of the Moon as the main challenge of Orpheus, this leads to a very difficult thermal problem. Between the lunar day and night, the surface can fluctuate in temperature from 95 K to 350 K [1]. Hence, not only does Orpheus need to be insulated from the surface, but also the payload; which is touching the surface. The shell is in direct sunlight and will also fluctuate in temperature. The outside of Orpheus will be heavily insulated with MLI, and painted to ensure minimum heat transfer to the electronic components and batteries inside. The solution to this problem is to isolate the electronic components (the 'insides') from the structure (the 'shell'). On the lunar surface, as Orpheus is stationary, the insides will be suspended on 4 Kevlar fibers. More than strong enough to hold the equipment and batteries the Kevlar fibers also have small enough surface area to not impact the thermal transfer to the electronic components. On takeoff, all electronics will be bolted into the shell, which will purposefully and slowly outgas once on the lunar surface. In our thermal models, if 1 % of the incident radiation on Orpheus is transferred to the insides, the temperature range of all temperature sensitive equipment can be kept within $\pm 20\text{C}$.

Model:

We completed a prototype of the deployable high gain antenna to demonstrate the capabilities of the communication system and thermal protection (seen in Figure 5).

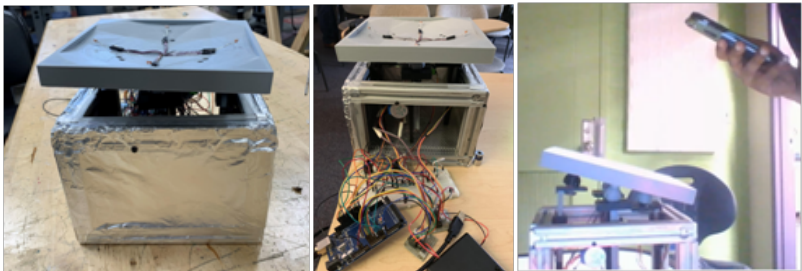


Fig. 5: Left and Middle: Orpheus prototype system, modeling the communications array (the parabolic lid) and the insulation (the aluminum foil). Input from the photoresistors attached to the lid is processed by the Arduino, which then powers the stepper motor and custom actuation system to angle the lid towards the light source. Right: The lid is angled towards a cell phone flashlight acting as a light source. To model the Alignment phase of the mission (where the high gain antenna is directed towards the Earth using an Earth sensor), we used four photoresistors to detect a specific light source. The angle needed to tilt the dish was calculated based on the distance from the light source calculated by each photoresistor using an Arduino microprocessor. To physically angle the dish, we custom designed, 3D printed, and built a low-cost vertical actuation system, using stepper motors to provide torque to raise and lower the system, as seen in Figure 5.

References:

- [1] Williams, J., Paige, D., Greenhagen, B., & Sefton-Nash, E. (2017). The global surface temperatures of the Moon as measured by the Diviner Lunar Radiometer Experiment. *Icarus*, 283, 300-325. doi:10.1016/j.icarus.2016.08.012

INVESTIGATING DIURNAL CHANGES IN THE NORMAL ALBEDO OF THE LUNAR SURFACE AT 1064 nm: A NEW ANALYSIS WITH THE LUNAR ORBITER LASER ALTIMETER

Ariel N. Deutsch¹, Gregory A. Neumann², James W. Head¹, Paul G. Lucey³

¹ Department of Earth, Environmental and Planetary Sciences, Brown University, Providence, RI 02912, USA(ariel_deutsch@brown.edu);

² NASA Goddard Space Flight Center, Greenbelt, MD 20771, USA;

³ Hawaii Institute of Geophysics and Planetology, University of Hawaii at Manoa, Honolulu, HI, 96822, USA.

Keywords:

Moon; Altimetry; Reflectance; Albedo; Temperature; Composition; Diurnal.

Introduction:

The thermal environment of the lunar surface is extreme. At the equator, temperatures drop ~ 300 K between local noon and night [1]. Here we are interested in how this drastic thermal environment may affect the reflectance of the lunar surface. A variety of laboratory studies have demonstrated that minerals common to the lunar surface (e.g., pyroxene, olivine) show spectral changes with respect to temperature in near infrared wavelengths [e.g., 2–4]. Specifically, an increase in reflectance is observed with decreasing temperatures at key wavelengths [2–4]. Over temperature changes equivalent to the lunar thermal environment ($\Delta T \approx 300$ K), the reflectance of pure pyroxene samples can vary by a factor of two [4].

For almost a decade, the Lunar Orbiter Laser Altimeter (LOLA) onboard the Lunar Reconnaissance Orbiter (LRO) [5,6] has been acquiring measurements of the Moon's surface reflectance by measuring the strength of the returned altimetric laser pulse. Measurements are acquired at a wavelength of 1064 nm, which is coincident with a diagnostic absorption feature of pyroxene (centered near $1 \mu\text{m}$) due to the presence of Fe^{2+} in the M2 site of the crystal [7]. At LOLA's wavelength, this iron absorption feature has been observed in laboratory studies to reveal temperature-dependent spectral changes [2–4]. Here we are interested in how the surface reflectance of the Moon as measured from orbit by LOLA changes during the extreme temperature fluctuations experienced by the surface over the course of a lunar day.

Methods:

We analyze the normal albedo of the lunar surface using the highest quality calibrated LOLA data, which was acquired by Detector 3 on Laser 1 [8]. The normal albedo is the reflectance of the lunar surface measured at zero phase angle relative to a Lambertian surface illuminated at normal incidence angle and the same phase. During the nine years of still ongoing operations, LOLA has nominally collected data throughout the lunar day, although returns are minimal when the LRO spacecraft crosses the terminator due to instrument cooling and contraction [5]. Here we analyze the LOLA data for differences in mean normal albedo during the cycle of the lunar day by sorting the data into two groups based on the local time at which the data were acquired: mid-day (11:00–13:00) and morning/evening (06:00–07:00 and 16:00–17:00). These two groups are chosen to represent times at which surface temperatures are at a maximum and minimum, respectively, and times for which LOLA data exist.

We target regions of interest (ROIs) within the mare and highlands between 65°S and 65°N , latitudes between which temperature fluctuations are greatest. Each ROI is only $1^\circ \times 1^\circ$ in spatial extent, representing surface areas that are ~ 30 km \times 30 km depending on the specific location. The individual ROIs are binned to this size so that there are enough returns within each ROI for statistical analyses, yet compositional variations are minimized within each ROI. For example, latitude-dependent variations in reflectance have been observed with LOLA [6, 8, 9], and thus, larger ROIs may include latitudinal reflectance artifacts. Data that were acquired when the received energy

was $< 0.14 f$, when the spacecraft was pointing off-nadir, or when the range was > 70 km, are excluded as well, due to cited reflectance anomalies [8]. To date, our analysis includes 65 ROIs located within the maria and 383 ROIs located within the highlands.

Discussion:

The ROIs that show lower mean albedos during mid-day are consistent with laboratory studies that observe a temperature-dependent spectral change for common lunar minerals [2–4]. Of particular interest are previous laboratory measurements of returned lunar soils, which revealed a change in relative reflectance with temperature of $\sim 1\%$ or less per 100 K near-IR wavelengths [4]. This is similar to what we observe in the majority of mare ROIs.

It is possible that we do not detect a clear temperature-dependent albedo change in the highlands due to a variety of factors. For example, surfaces that are low in iron will show a weaker change because iron is responsible for the temperature-dependent absorption near 1064 nm, the wavelength at which LOLA observes the surface [4]. In addition, mature soils show less contrast due to the attenuating effect of submicroscopic iron that has accumulated through time [10, 11]. The reflectance may also be affected by grain size effects, where particularly fine-grained regions have a decreased reflectance in comparison to a region of similar composition with larger grains [12, 13].

Conclusions:

Here we provide the preliminary results of a new analysis investigating diurnal changes in the normal albedo of the lunar surface. Our statistical analysis, incorporating over 200,000 individual LOLA shots, suggests that temperature variations do have a measurable effect on the normal albedo of the surface at 1064 nm wavelength in the maria, and this may be due to temperature-induced spectral changes. However, the diurnal differences discussed here are only on the order of a few % change in normal albedo, indicating that temperature changes do not have a large effect on measurements of the lunar surface at the sensitivity of the LOLA instrument. An ability to understand how the lunar surface varies with temperature will provide important constraints for future remote sensing observations of the Moon [e.g., 14, 15]. Such observations can help constrain the relative abundance of particular minerals (here, pyroxene) that exhibit a change in spectral reflectance with temperature independent of spectroscopic methods.

References:

- [1] Williams J.-P. et al. (2017) *Icarus*, 283, 300–325.
- [2] Singer R.B. and Roush T.L. (1985) *JGR*, 90, 12434–12444.
- [3] Roush T.L. and Singer R.B. (1986) *JGR*, 91, 10301–10308.
- [4] Hinrichs J.L. and Lucey P.G. (2002) *Icarus*, 155, 169–180.
- [5] Smith D.E. et al. (2010) *SSR*, 150, 209–241.
- [6] Smith D.E. et al. (2017) *Icarus*, 283, 70–91.
- [7] Adams J.B. (1974) *JGR*, 79, 4829–4836.
- [8] Lemelin M. et al. (2016) *Icarus*, 273, 315–328.
- [9] Lucey P.G. et al. (2014) *JGRP*, 119, 1665–1679.
- [10] Hapke B. (2001) *JGR*, 106, 10039–10074.
- [11] Pieters C.M. (2000) *MAPS*, 35, 1101–1107.
- [12] Hapke, B. (1993). Cambridge University Press, NY.
- [13] Clark R.N. and Roush T.L. (1984). *JGR*, 89, 6329–6340.
- [14] Cohen B.A. et al. (2015) LEAG, Abstract #2008.
- [15] Lucey P.G. et al. (2017) LEAG, Abstract #5048.

DISTRIBUTION OF SURFACE WATER ICE ON THE MOON: AN ANALYSIS OF HOST CRATER AGES PROVIDES INSIGHTS INTO THE AGES AND SOURCES OF ICE AT THE LUNAR SOUTH POLE

Ariel N. Deutsch¹, James W. Head¹, Gregory A. Neumann²

¹ Department of Earth, Environmental and Planetary Sciences, Brown University, Providence, RI 02912, USA(ariel_deutsch@brown.edu);

² NASA Goddard Space Flight Center, Greenbelt, MD 20771

Keywords:

Moon; ice; impact craters; ages

Introduction:

Over the last several decades, ground- and spacecraft-based observations have provided data to support the presence of water ice at the poles of the Moon [e.g., 1–5]. The polar ice appears to be spatially heterogeneous in distribution. For example, mapping of UV albedo spectra and surface temperature measurements reveal a highly spatially heterogeneous distribution of water frost within PSRs [3]. Enhanced surface albedo suggestive of water frost [4] and detections of exposed water ice [5] also indicate a patchy distribution of surface water ice.

Impact gardening can produce spatial heterogeneities in ice distribution because these processes cause loss and redistribution of volatiles [6, 7]. Impacts remove volatiles via vaporization and also preserve volatiles through the emplacement of ejecta, with a net effect of breaking up and burying the ice [6, 7]. Because these processes take time, the spatial heterogeneity is highly likely to be related to the exposure age of the ice.

Objective:

Here we assess the distribution of surface water ice [5] at the south polar region of the Moon (80°S–90°S). We estimate ages for host craters to provide upper limits for any ice contained within the craters, and examine the relationship between the patchiness of the ice within each crater and the age of each host crater. Finally, we discuss possible sources for the ice, given the results of our age analyses.

Methods:

Age estimates for lunar cold traps. From crater-counting statistics, we estimate ages of 20 south polar lunar craters that are located between 80°S and 90°S. In combination with previous estimates of south polar crater ages [8, 9], our catalogue represents 24 large polar craters, capturing all permanently shadowed craters in this region that have at least 100 km² of flat-floored regions (<10°) for counting statistics. The count areas are in permanent shadow, so we create artificially illuminated hillshade maps (pixel resolution of 20 m) at various azimuth angles from a gridded digital elevation model that was derived from Lunar Orbiter Laser Altimeter data. For each host crater, superposed craters with diameters >200 m are catalogued. Obvious secondary craters (those that appear elongated in form, or in chains or clusters) are systematically excluded from the counts. CSFDs are produced and fit to models of the production function [10] in order to estimate ages using CraterStatsII [11]. The ages of the host craters provide a maximum age of any surface ice contained within each crater.

For age analyses, we require count areas to be ≥100 km² and have slopes <10°, and thus not all south polar impact craters (particularly impact craters <20 km) are analyzed. Some smaller impact craters also host surface water ice, and here we identify all simple craters that have crisp-looking rims, but are too small in size to accurately date with from crater counting statistics. From this dataset, we determine what population of small (<100 km²) craters with morphologically fresh characteristics host surface ice.

Patchiness of lunar surface ice. The patchiness of surface water ice within each of the 24 south polar craters analyzed here is quantified as the percent of the current cold trap surface area that is occupied by surface water ice. Cold traps are defined as surface areas with maximum surface temperatures ≤ 110 K, as measured by the Diviner Lunar Radiometer Experiment [12], representing temperatures at which surface water ice is stable. Direct detections of exposed surface water ice [5] are used as surface ice detections. These surface water ice detections were made using NIR data acquired by the Moon Mineralogy Mapper (M3) instrument, specifically from diagnostic overtone and combination mode vibrations of water ice that occur near 1.3, 1.5, and 2.0 μm [5].

Results:

The majority of surface water ice at the lunar south pole [5] is found in large, old (~ 3.5 Gyr) craters, which comprise the majority of the cold-trapping area available. We also identify 301 small (< 15 km in diameter) impact craters that are likely to be relatively young, given sharp crater rim morphologies. We find that $\sim 5\%$ of these craters, which are too small for crater counting analyses, have at least one pixel with a positive ice detection [5]. Thus, while surface ice is predominantly located in ancient craters (Fig. 1), it is found in relatively young craters as well. Furthermore, given that the footprint size of the M3-derived surface ice detections [5] is $\sim 280 \text{ m} \times 280 \text{ m}$, it is possible that many additional surface ice deposits are cold-trapped below this resolution [13, 14], both in ancient and young craters.

There are also some ancient craters that are present-day cold traps, but do not host surface water ice (Fig. 1). Our age-dating analysis strengthens the interpretation [5] that the retention of volatiles within cold traps may have been affected by the stability of these cold traps on long timescales, related to true polar wander (TPW). Under predicted paleo-conditions [15], the thermal surface environments of these craters would not have been stable for the survival of surface water ice. Thus, our results suggest that the patchy distribution of surface ice observed at the lunar poles today may be controlled by ice supply rate, impact destruction rate, and an additional factor that affects the long-term stability of volatiles in individual cold traps, such as TPW.

Discussion:

Patchiness of lunar ice. No more than $\sim 11.5\%$ of the surface areas of the polar craters in this study are occupied by water ice. The precise surface areas of cold traps occupied by water ice may be even less given that an M3 spectrum of only $\sim 30\%$ water ice is classified as a positive ice detection, resulting in a single detection at the spatial scale of a M3 pixel ($\sim 280 \text{ m} \times 280 \text{ m}$) in resolution. Overall, the very patchy surface distribution of lunar ice suggests that the rates of destructive processes (regolith gardening) exceed the rates of ice emplacement through time.

Possible sources of ice. The majority of detected surface water ice [5] is confined to large, ancient (> 3.5 Gyr) cold traps and appears to be re-worked, given its very patchy spatial distribution within individual cold traps. Ancient ice may have been delivered by impactors [e.g., 16] or volcanically outgassed volatiles [e.g., 17]. Early in the Moon's history, the flux of impactors was much higher than present-day rates [16], and these early impactors were likely to be delivering ice to the lunar poles, in addition to breaking up and covering the ice [6, 7], consistent with the patchy surface distribution observed today. Because we also identify a population of small (< 15 km) impact craters that appear to be young, it is possible that some surface water ice has been delivered to the south pole recently. The presence of ice in fresh craters suggests that ice delivery rates to these cold traps are greater than the ongoing destructive and burial processes at these cold traps. Candidates for recent delivery of surface ice include solar wind interactions with the lunar regolith [e.g., 18] as well as micrometeorite delivery.

Differences between ice on the Moon and Mercury. The low percentages of cold trap surface areas that host surface water ice on the Moon are in stark contrast to the host craters on Mercury that are interpreted to be occupied

by laterally contiguous ice deposits [19–21]. If ice deposits on Mercury are relatively young [e.g., 14, 19–22], then they have not been exposed to extensive regolith gardening that would break up, destroy, or bury the ice [22]. The same impact bombardment and space weathering processes operate on Mercury and the Moon, and Mercury's regolith may be overturned even more frequently than the lunar regolith due to higher impact rates and speeds [23]. Thus, it is possible that relatively ancient, degraded ice deposits exist below the extensive, pure deposits observed on Mercury's surface today. The lunar polar deposits therefore provide an important opportunity to inform us about the ultimate fate of mercurian polar deposits, as well as ices on other airless bodies.

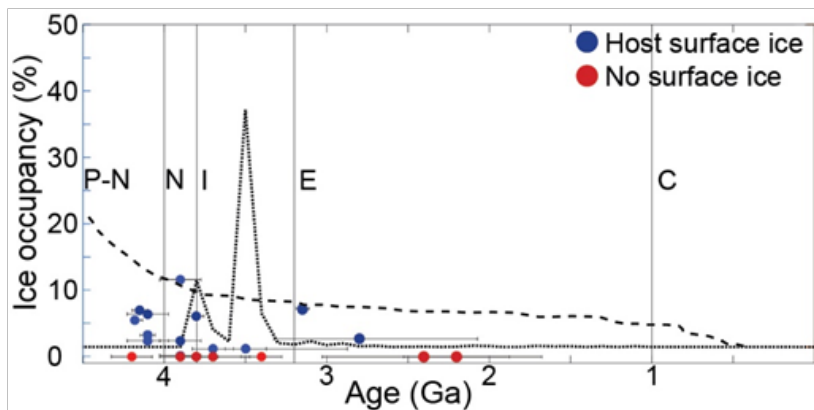


Fig. 1. The percentage of specific cold traps occupied by water ice is plotted with respect to the estimated model ages of the host craters. The modeled impact flux for the Moon [16] is plotted in the thick dashed line, and estimated effusive volcanic flux [17] is plotted in the thin dashed line. Lunar geologic eras are separated by vertical lines.

References:

- [1] Lawrence D. J. et al. (2006) *JGR*, 111, E08001.
- [2] Colaprete A. et al. (2010) *Science*, 330, 463–468.
- [3] Hayne P. O. et al. (2015) *Icarus*, 255, 58–69.
- [4] Fisher E. A. et al. (2017) *Icarus*, 292, 74–85.
- [5] Li S. et al. (2018) *PNAS*, 115, 8907–8912.
- [6] Crider D. H. and Vondrak R. R. (2003) *JGR*, 108, 5079.
- [7] Hurley D. M. et al. (2012) *GRL*, 39, L09203.
- [8] Tye A. R. et al. (2015) *Icarus*, 255, 70–77.
- [9] Zuber M. T. et al. (2012) *Nature*, 486, 378–381.
- [10] Neukum G. et al. (2001) *SSR*, 96, 55–86.
- [11] Michael G. G. and Neukum G. (2010) *EPSL*, 294, 223–229.
- [12] Paige D. A. et al. (2010) *Science*, 330, 479–482.
- [13] Hayne P. et al. (2018) *DPS* 50, Abstract 116.05.
- [14] Rubanen-ko L. et al. (2018) *JGRP*, 123, 2178–2191.
- [15] Siegler M. A. et al. (2016) *Nature*, 531, 480–484.
- [16] Nesvorný D. et al. (2017) *AJ*, 152, 103.
- [17] Needham D. H. and Kring D. A. (2017) *EPSL*, 478, 175–178.
- [18] Crider D. H. and Vondrak R. R. (2000) *JGR*, 105, 26773–26782.
- [19] Neumann G. A. et al. (2013) *Science*, 339, 296–300.
- [20] Chabot N. L. et al. (2014) *Geology*, 42, 1051–1054.
- [21] Chabot N. L. et al. (2016) *GRL*, 43, 9461–9468.
- [22] Deutsch A. N. et al. (2018) *AGU* 100, Abstract #P22B-06.
- [23] Domingue D. L. et al. (2014) *SSR*, 181, 121–214.

³HE-RICH POTENTIAL LANDING SITES ON THE MOON

A.A. Berezhnoy¹, K.J. Kim², C. Wöhler³, M. Bhatt⁴, A. Grumpe³

¹ Sternberg Astronomical Institute, Moscow State University, Universitetskij pr., 13, 119234 Moscow, Russia

² Korea Institute of Geoscience and Mineral Resources, 124, Gwahangro, Yuseong-gu, Daejeon, Korea

³ TU Dortmund University, Image Analysis Group, Otto-Hahn Str. 4, Dortmund 44227, Germany

⁴ Physical Research Laboratory, Ahmedabad 380009, India

Keywords:

³He, TiO₂, landing sites, slope, Grimaldi, Riccioli

Introduction:

The ³He content in returned lunar samples increases with increasing soil maturity degree and TiO₂ content [1]. For a set of 25 Apollo samples, the correlation coefficient was found to be 0.938 [1]. Based on this very high empirical correlation, global maps of the ³He distribution on the surface of the Moon have been constructed in [1, 2]. In this study, we constructed a global ³He map as well as ³He maps of candidate landing sites on the Moon based on an alternative technique for TiO₂ abundance estimation.

Methods:

Our ³He abundance maps were constructed using TiO₂ abundance data derived from data of the Moon Mineralogy Mapper (M³) instrument [3] in combination with maps of the OMAT parameter [4]. TiO₂ abundance maps of the regions under study were constructed using the method of [5]. The M³ data were corrected for the effect of topography using [6, 7], the thermal emission component was removed from the M³ level 1B radiance spectra based on [8]. For the regions under study, we computed maps of the ³He abundance and the monthly average solar wind flux according to [1].

The study of the distribution of surface slopes is an important component during selection of candidate landing sites [9]. The surface slope maps on spatial scales of 140 m were derived from topographic maps constructed using the shape from shading based framework of [6, 7]. For selected areas of interest we provide slope maps of 2 m resolution obtained by shape from shading analysis of LRO NAC images [10] using the technique of [11].

Results:

A nearly global map of the calculated ³He content on the Moon has been constructed. The ³He content is higher in the maria (especially high-Ti maria) than in the highlands. The obtained ³He map shows good agreement with previously published ³He maps [1, 2]. Our main focus is to find sites with high ³He content, low slopes and good illumination conditions, in order to propose ³He-rich landing sites. A moderately high ³He content of 10–15 ppb is predicted in western Oceanus Procellarum, the craters Grimaldi, Riccioli and Tsiolkovsky, the Apollo basin, Mare Orientale, Mare Fecunditatis, Mare Crisium, Mare Moscoviense, and Mare Marginis. The highest ³He concentrations of up to about 24 ppb are predicted for parts of the lava-flooded floors of the craters Grimaldi and Riccioli, in the south-western part of Oceanus Procellarum, the north-eastern part of Mare Fecunditatis, the north-western part of Mare Tranquillitatis, the southern part of Mare Moscoviense, the eastern part of Mare Crisium, and in Mare Marginis.

It is shown that the first six abovementioned sites fulfill the following criteria for landing site selection: (1) high ³He content (20–25 ppb), (2) local slopes on 2 m scale less than 10 degrees, (3) located such that they are illuminated and can be continuously in contact with an orbiter or facilities on the Earth. Based on the technical requirements for soft landing, the craters Riccioli and Grimaldi were selected as first priority potential landing sites.

Regions with high ³He content in the crater Riccioli usually have a low albedo and a high FeO and TiO₂ content. The largest ³He-rich region is

located on the partially lava-flooded floor of crater Riccioli (2.63 S, 73.95 W). It is an approximately rectangular area of about 20x40 km² size oriented in northeast-southwest direction. In this region, slopes at 2 m resolution are usually less than 2 degrees. The required landing accuracy is about 5 km.

The second-best candidate landing site is within crater Grimaldi. The region with the highest ³He, FeO, and TiO₂ content is located in the south-western part of crater Grimaldi (7° S, 69° W). The required landing accuracy in the crater Grimaldi is about 15 km. For the proposed landing site in the crater Grimaldi, the typical slopes are lower than 3 degrees at 2 m spatial resolution.

Conclusions:

The global distribution of the ³He content on the surface of the Moon has been mapped with a modified method of TiO₂ abundance estimation and has been applied to M³ high-resolution observations for the first time. Regions of highest ³He content and, respectively, highest TiO₂ content on the Moon are located mainly near the edges of nearside maria. The craters Riccioli and Grimaldi were selected as the most promising candidate landing sites. Detailed high-resolution studies of topography and slope distribution favor the possibility of safe soft landing in these regions. The obtained ³He and TiO₂ content at these candidate landing sites can be verified by in situ measurements from lunar rovers. The proposed most promising sites of highest ³He content can be further studied by the LUTI camera of the upcoming Korean Pathfinder Lunar Orbiter (KPLO)[12].

References:

- [1] Fa, W., Jin, Y.-Q. Quantitative estimation of helium-3 spatial distribution in the lunar regolith layer // *Icarus*. 2007. V. 190. No. 1. P. 15–23.
- [2] Shkuratov, Yu.G. et al. ³He distribution over the lunar visible hemisphere // *Solar System Research* 1999. V. 33. P. 409–420.
- [3] Pieters, C.M. et al. The Moon Mineralogy Mapper (M³) on Chandrayaan-1. *Current Science*. 2009. V. 96. P. 500–505.
- [4] Lucey, P.G., Blewett, D.T., Jolliff, B.L. Lunar iron and titanium abundance algorithms based on final processing of Clementine ultraviolet–visible images // *J. Geophys. Res.* 2000. V. 105. P. 20297–20306.
- [5] Bhatt, M. et al. A comparative study of iron abundance estimation methods: Application to the western nearside of the Moon // *Icarus*. 2015. V. 248. P. 72–88.
- [6] Grumpe, A., Wöhler, C. Recovery of elevation from estimated gradient fields constrained by digital elevation maps of lower lateral resolution // *ISPRS Journal of Photogrammetry and Remote Sensing*. 2014. V. 94. P. 37–54.
- [7] Grumpe, A., Belkhir, F., Wöhler, C., Construction of lunar DEMs based on reflectance modelling // *Adv. Space Res.* 2014. V. 53. No. 12. P. 1735–1767.
- [8] Wöhler, C. et al. Time-of-day-dependent global distribution of lunar surficial water/hydroxyl. *Science Advances* 2017. V. 3. No. 9. P. e1701286.
- [9] Ivanov, M.A. et al. Geological characterization of the three high-priority landing sites for the Luna-Glob mission // *Planetary and Space Science*. 2018. V. 162. P. 190–206.
- [10] Robinson, M.S. et al. Lunar Reconnaissance Orbiter Camera (LROC) instrument overview // *Space Science Reviews*. 2010. V. 150. No. 1–4. P. 81–124.
- [11] Grumpe, A. et al. Elemental and topographic mapping of lava flow structures in Mare Serenitatis on the Moon. In: Wu B. et al. (eds.), *Planetary Remote Sensing and Mapping*, CRC Press, 2018. 350 p.
- [12] Ju, G. H. Korean Pathfinder Lunar Orbiter (KPLO) Status Update. *Proc. Ann. Meeting Lunar Exploration Analysis Group*, Columbia, Maryland, 2017.

SELECTION OF LANDING SITE FOR POTENTIAL LUNAR BASE ON MONS MALAPERT

S.S. Krasilnikov¹, A.T. Basilevsky^{1,2}, M.A. Ivanov¹

¹ Vernadsky Institute of Geochemistry and Analytical Chemistry RAS
Moscow, Russia, krasilnikovruss@gmail.com;

² Planetary Sciences and Remote Sensing, Institute of Geological Sciences,
Freie Universitaet Berlin, Berlin, Germany

Keywords:

Moon, south pole, landing site, Mons Malapert, lunar base

Introduction:

Polar areas of the Moon are one of the most perspective regions of exploration of this body including building there a lunar base(s). Presence of water ice in regolith of many polar localities is important both as a resource for needs of lunar base(s) and as a subject of scientific studies. The mountain Mons Malapert near the South pole (about 86°S 0°E) was mentioned as a perspective place for potential lunar base [1, 2, 3]. Malapert mountain rises above the surrounding surface by ~5 km, has reliable visibility from and to Earth and long periods of sunlight (87 to 91% of the year). Its 5×15 km top at the base of hundreds of meters is almost flat (<5°) although most slopes are relatively steep (20–25°). The Mons Malapert mountain massif was interpreted by [4] as a part of the South Pole – Aitken (SPA) basin rim. This abstract considers issue of selection of potential landing sites for the Mons Malapert base, while issues of topography, geology and trafficability of this locality are discussed in [5]. In the following consideration we suggest that top of Malapert Mons is the locality of potential base or locality of some its parts (radio antenna, solar batteries, instruments for distant observations).

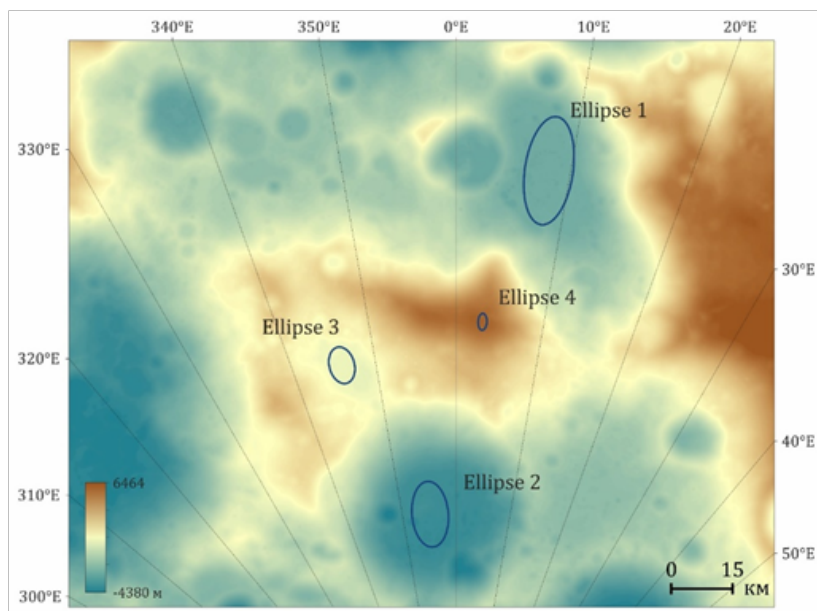


Fig. 1 Potential ellipses of landing sites in the vicinities of Mons Malapert.

Selection of landing sites.

The main problem of selection of landing site(s) in this region is deficit of large enough flat areas to be possible landing ellipses. Four nearly flat places in the vicinity of the mountain were initially considered as possible landing sites (ellipse 1 — north-east, ellipse 2 — south (crater Haworth) and ellipse 3 — south-west of region) and one — ellipse 4 on the top of mountain (fig. 1). These ellipses have the following sizes: ellipse 1 — 12×26 km; 2 — 9×16 km; 3 — 6×9 km; 4 — 2×4 km. Ellipses 1–3 are not included in the subsequent

analysis, because their location is too far (several tens of kilometers) from the mountain, steep slopes of which make difficult the rovers' drive and logistics between the landing site and the base [5]. As an alternative option can be construction of base in the footnote of the mountain and location of radio antenna, solar batteries and other facilities on the top/slope. However, this task, no matter needs a transportation of goods to the tens of kilometers and then, lifting of the antenna and other issues to the mountain top.

We have chosen the ellipse 4 as the main landing site, if base construction going to be located on the top of the mountain. For slope analysis LOLA-based GDR DTM with 20 m/pix resolution was used. Using this DTM, five classes of slopes for ellipse 4 were calculated ($<7^\circ$ – 28%; 7° - 10° – 21%; 10° - 15° – 39%; 15° - 20° – 10% and $>20^\circ$ - 2%). Allowable slopes for safe landing ($<10^\circ$) compose only 49% of the ellipse, that undoubtedly, brings certain risks in landing processes. However, measuring the surface roughness at the latest stages of landing combined with possibility for horizontal maneuver like it was done in the case of NASA Curiosity and Chinese Yutu 1 and 2 should decrease the risk of robotic landing. Landing the piloted spacecraft showed its relative safe as early as in the Apollo era.

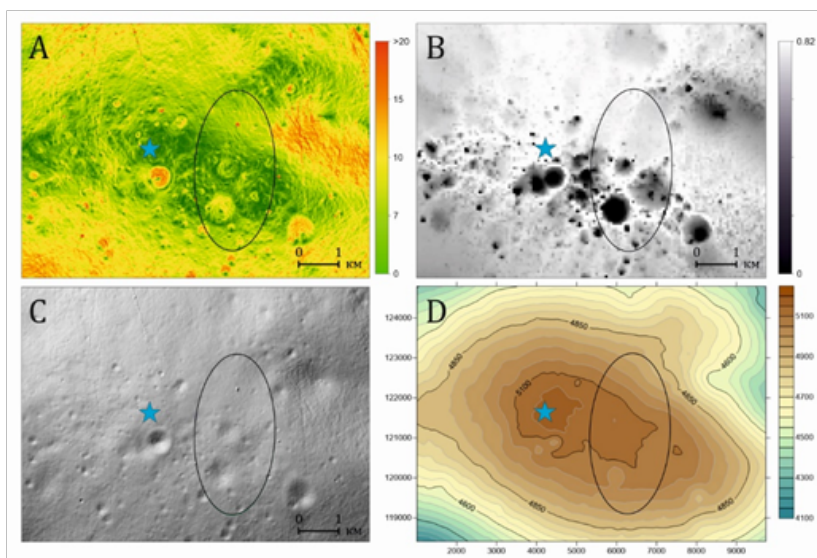


Fig. 2. Eastern top of the Mons Malapert with landing ellipse 4 (4x2 km in size) and potential base place (blue star). A – slopes; B – solar illumination; C – hillshade relief (270° azimuth and 45° sunlight angle); D – topographic map.

In the future research, the preflight estimating of the slopes' steepness at this landing ellipse on the baseline of the lander's pads may be done by different techniques including by measuring the shaded area percentage in the LROC NAC images taken at different Sun elevation [6, 7]. Rock boulders' presence was explored by radar Mini-RF data [8, 9] and showed reasonably good, acceptable for landing, values for this region.

Suggested location of lunar base disposed on the top of eastern site of the mountain with coordinates $2^\circ\text{E } 85^\circ 59' 15''\text{S}$. Distance between potential base and suggested landing site is more than one kilometer, that provides comfortable distance for logistic and protection from regolith dust, lifted by the landers.

Results and discussion.

As it was shown above, Mons Malapert is a perspective place to construct lunar base at its top. Although most slopes are significantly steep ~ 20 to 25 and 30° [5], on the top of mountain there is nearly flat surface (less than 5° at the baseline of hundreds meters) 5×15 km in size. Within this flat area we suggest to put the base and at some distance from it the landing area: 2×4 km ellipse centered at $2^\circ 59' 34''\text{E } 86^\circ 0' 9''\text{S}$. More studies are needed to measure topographic and soil-mechanics characteristics of this and adjacent areas.

Acknowledgments:

This work was partly supported by Russian Science Foundation, project #17-17-01149.

References:

- [1] Sharpe B.L. and Schrunk D.G. Malapert mountain: Gateway to the Moon // *Advances in Space Research*. 2003. V. 31. No 11. P. 2467–2472.
- [2] Cooper B.L. and Simon T. ISRU production of life support consumables for a lunar base // *SAE Technical Report 2007-01-3106*. 2007. 7 p.
- [3] Schrunk D., Sharpe B., Cooper B.L., and Thangavelu M. The first lunar base. In: *The Moon* // Springer Praxis Books. Praxis. 2008. P. 83-95.
- [4] Wilhelms, D.E., Howard, K.A., Wilshire, H.G. Geologic map of the South Side of the Moon. US Geological Survey Map I-1192.1979.
- [5] Basilevsky A.T., Krasilnikov S.S., Ivanov M.A. et al. Potential lunar base on Mons Malapert: Topographic, geologic and trafficability considerations // *Solar System Research*. 2019 (in press).
- [6] Abdrakhimov, A.M., Basilevsky, A.T., Ivanov, M.A. et al. Occurrence probability of slopes on the lunar surface: estimate by the shaded area percentage in the LROC NAC images // *Solar System Research*. 2015. V. 49. no. 5. P. 285–294.
- [7] Krasilnikov S.S., Basilevsky A.T., Ivanov M.A., et al. Steepness of Slopes at the Luna-Glob Landing Sites: Estimating by the Shaded Area Percentage in the LROC NAC Images // *Solar System Research*. 2018. Vol. 52. No. 2. P. 87–97.
- [8] Bussey, D.B.J., McGovern, J.A., Spudis, P.D., et al. Illumination conditions of the south pole of the Moon derived using Kaguya topography // *Icarus*. 2010. V. 208. P. 558–564.
- [9] Nozette, S., Spudis, P., Bussey, B., et al. The Lunar Reconnaissance Orbiter miniature radio frequency (Mini-RF) technology demonstration // *Space Sci. Rev*. 2010. 150 (1–4), 285–302.

LUNAR RESOURCES TO ADDRESS ENERGY AND CLIMATE PROBLEMS ON EARTH

G.A. Sizentsev¹, V.V. Sinyavskiy², B.A. Sokolov³

¹ *S.P. Korolev Rocket and Space Public Corporation Energia (RSC Energia)*

^{4A} *Lenin str., Korolev, Moscow region, 141070, Russian Federation, e-mail: Sizentsev37@mail.ru*

² *S.P. Korolev Rocket and Space Public Corporation Energia (RSC Energia)*

^{4A} *Lenin str., Korolev, Moscow region, 141070, Russian Federation, e-mail: Viktor.Sinyavsky@rsce.ru*

³ *S.P. Korolev Rocket and Space Public Corporation Energia (RSC Energia)*

⁴ *A Lenin str., Korolev, Moscow region, 141070, Russian Federation,*

Keywords:

global climate, lunar exploration, renewable energy sources, lunar rare-earth materials, space technology, lunar industrial infrastructure. Solar Sail Vehicles

In view of the need to prevent a sudden warming of the Earth global climate, it is proposed to consider lunar exploration for the purpose of using its resources to address energy and climate problems on Earth [1].

Lunar exploration effort, to be carried out in a phased manner, is to be spread over three phases, each of which is supposed to achieve a certain milestone.

The first milestone is to establish a sustainable lunar outpost capable of conducting scientific research and developing industrial infrastructure technologies for in-situ resource utilization, to support both the outpost itself and the efforts to achieve further milestones in lunar exploration. The funding for this milestone is to be provided through international investment and credit.

The second milestone is to start mining, processing and delivering to Earth the rare-earth metals recently prospected on the Moon. Selling them back on Earth may help to solve the problem of funding the efforts to prevent the global threat and adapt to it. To achieve this milestone it will be required to build up a significant infrastructure for power-generation, mining, processing, manufacturing and other industries, as well as a transportation system to support traffic between the Moon and Earth. The funding for this milestone is to come from payments under international investments and credits, self-financing of this and the next milestones.

Achieving the third milestone consists in further expanding the industrial infrastructure in order to utilize a wider range of lunar in-situ resources and develop a circumlunar orbital assembly facility for large-scale space structures, including Solar Sail Vehicles (SSV). Stationing a fleet of SSVs in the vicinity of the linear Lagrange point L1 of the photogravitational Sun-Earth field would make it possible to reduce the flux of solar energy toward Earth, and, accordingly, its global temperature.

At present, it is possible to build a small-scale SSV and run a math simulation of the proposed concept to confirm its feasibility.

References:

- [1] Sizentsev G.A., Sinyavskiy V.V., Sokolov B.A. A concept of an energy-and-climate control facility in space to counter global overheating // *Kosmicheskaya tekhnika i tekhnologii*, 2019. no. 1, pp. 107–119.
- [2] Shevchenko V.V. Utilizatsiya privnesennogo na Lunu asteroidnogo veshchestva kak bolee ekonomichnyy put' k polucheniyu kosmicheskikh resursov vysokoy tsennosti [Utilization of the asteroid subject on the Moon — a more economic way to obtain cosmic resources of high value] // *Kosmicheskaya tekhnika i tekhnologii*, 2018, no. 1, pp. 5–22.

THEY ARE AHEAD OF TIME: THE INFLUENCE OF THE SOVIET AND AMERICAN LUNAR ROVERS ON MODERN PLANETARY RESEARCH

M.I. Malenkov¹, R.A. Creel², V.G. Dovgan¹, D.R. Scott^{4*}, A.T. Basilevsky⁵, J.W. Head⁴

¹ Space Research Inst. RAS. 117997, Profsoyuznaya 84/32, GSP-7, Moscow, Russia, e-mail: m.i.malenkov@gmail.com

² Apollo Lunar Roving Vehicle Team Member for Thermal Control

³ Member of the crew of remote driving Lunokhod 1 and 2 on the surface of the Moon

^{4*} Commander, Apollo 15 Mission, Brown Univer., USA

⁴ Brown Univer., Providence, RI 02912 USA

⁵ Vernadsky Inst. RAS, 119991, Kosygin St. 19, Moscow, Russia;

Keywords:

Lunar Rover (Lunokhod), Lunar Roving Vehicle (LRV), locomotion system, hard wheel, flexible wheel, rim, tire, suspension, self-propelled chassis.

Introduction:

World Space Week (WSW) will be celebrated on October 4–10, 2019 under the motto “Moon: Gates to the Stars” in recognition of the 50th anniversary of the first human landing on the Moon. We propose to celebrate WSW 2020 under the motto “Space robots for humans.” This will be a recognition of the 50th anniversary of the first return of the lunar soil by the automatic station Luna-16 and the first lunar track laid by Lunokhod-1 (Fig. 1). On August 7, 1971, when Lunokhod-1 “woke up” after the 10th lunar night, the Lunar Module of the Apollo-15 landed and brought to the lunar surface Lunar Roving Vehicle (LRV) (Fig 1), actively used by the Commander David Scott and Pilot James Irwin. Our report considers results of the work of robotic and manned LRVs from the standpoint of modern technologies and the tasks for Moon and Mars exploration.

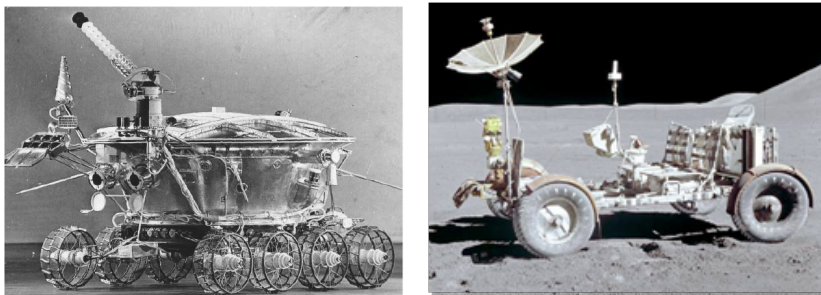


Fig. 1. Lunokhod-1 (left) and Lunar Roving Vehicle (right)

1. Robotic and Manned Lunar Rovers: Similarities and differences — what is still relevant?

The initiative to create the Soviet lunar rover was born in OKB-1 almost immediately after the successful flight on October 4, 1957 of the first artificial satellite of the Earth. The head of that team, Sergey Korolev, after several years of searching, had chosen the main partners: VNII-100 (1963) and the Lavochkin Association (1965). The design, testing and production of flight models of the self-propelled chassis (chief designer Alexander Kemurdzhan, VNII-100) as well as the Luna-17 station and the Lunokhod-1 with this chassis (chief designer Georgy Babakin, Lavochkin Association) were completed in 1968 [1].

In the USA, the first impulse to the lunar program was given personally by President John F. Kennedy. In 1961, he set a national task for the country: to carry out a manned flight to the Moon before 1970. To create the LRV, an open competition was held, in which the leading high-tech companies in the country took part. Already at this stage, the head of the lunar program Vernher von Braun participated in the testing of running models [2].

The state order was won by the tandem of Boeing Co — General Motors Co. Key to ultimate success of the Apollo lunar rovers was the ability to fold them up and store those vehicles in an unused quadrant of the Lunar Module lander, and the decision to have 4 individual electrically powered motors and drive systems for the USA lunar rovers.

In the USSR, the task of performing a manned flight to the moon using an N-1 rocket was first set forth in a government decree of August 3, 1964. However, launches of four missiles in 1969 -1971 failed and the N-1 program was closed. At the same time, flights to the Moon of the lighter automatic spacecraft (SC) could be performed using the Proton rocket. The design of moon rovers in the USSR and the USA was carried out completely independently of each other. Interesting that in both countries common theoretical and experimental approaches to the creation of new machines for unprepared terrain prevailed. This became clear to Soviet scientists and engineers after the publication in the USSR of the Russian edition of a generalizing monograph by M.G. Becker [3]. There are some general technical solutions that are still relevant today. This is the choice of all-wheel drive scheme, including a self-propelled chassis with independent hinge suspension, elastic wheel suspension with built-in electromechanical traction drives, as well as brake and parking brakes. With a certain difference in suspension schemes (with longitudinal rotation of the levers in the USSR and transverse rotation of the levers in the USA), both designs ensured optimal plane-parallel trajectories of vertical wheel movements on an uneven surface. For elastic suspension elements were selected torsion bars.

The differences were associated only with the different purposes of the new machines. In both the USSR and the USA, the advantages of elastic wheels of sufficiently large diameter were revealed when tested on terrestrial analogs of loose lunar regolith. At a relatively high LRV speed (up to 13 km/h), elastic tires of such wheels, to some extent, increased the smoothness on uneven terrain and allowed the driver to maneuver with the help of steering gears. With a lower speed of movement of the Soviet lunar rovers (up to 2 km/h), turning on the spot and maneuvering on the move were easily accomplished by only adjusting the traction drives. But it was necessary to increase the number of motor-wheels, at least up to six and have wheels with a hard rim. In one of the key problems — the choice of the type of contact surface of the wheels, the developers of the two countries were surprisingly unanimous! Both the hard wheel rim of Lunokhod-1 and the elastic tire LRV wheels are made of wire mesh, albeit with different characteristics.

2. Critical moments of operation of Moon rovers through the eyes of drivers, researchers and engineers

The only failure of the self-propelled chassis occurred on the first lunar day of Lunokhod-1 (Fig. 1). At the 104th communication session, when turning in motion by 20°, the flight engineer recorded increased values of the motor-wheel motor current. After analysis of telemetry data, the failure of the control electromagnets of the parking brakes of all 8 motor-wheels was detected. So all subsequent drive was undertaken at the first speed of movement (about 0,85 km/h), and maneuvering was carried out only by turning in place. Movement at the second speed, and turns during movement were excluded, to protect the electric motors against overcurrent triggers. The reasons for the termination of Lunokhod-1 operation on the 12th lunar day were the development of a resource of an isotopic heat source and a decrease in the charge of the backup battery. Its total path for 11 lunar days was 10540 m.

At Lunokhod-2, a significant anomaly developed during the flight — the local vertical sensor failed. This greatly complicated the remote control of Lunokhod-2: drivers lost instrumental ability to determine the angle of inclination of the mobile spacecraft relative to the longitudinal and transverse axes. Visually, they could estimate the spatial position of the vehicle approximately only if the horizon was in the field of view of the navigation cameras. This navigational anomaly led to the fact that the head of the control group on the fourth lunar day made not the best decision: to leave the class B crater with a diameter of about 6 meters in reverse.

At this exit, Lunokhod-2 hooked the regolith with the open solar battery lid that became clear due to a decrease in the battery charge current. On the fourth night the lid was closed, that put the soil on an isotopic heat source radiator. On the 5th lunar day, a temperature increase in the container and a decrease in the charging current were observed. Nevertheless, Lunokhod-2 crossed 880 m on this day, but on May 10, 1973, it stopped communicating [4]. The length of its entire route was about 40 km. Nevertheless, the assigned scientific and applied tasks for both lunar rovers were carried out. A large territory was surveyed where high-quality panoramas were obtained, hundreds of measurements of the mechanical properties of the soil and analyzes of its chemical composition were carried out. Both moon rovers overcame routes with difficult terrain and loose soil without loss of mobility.

LRVs were used in the Apollo J-missions 15, 16, and 17 to significantly expand the surface area of the moon, which was studied by astronauts, and to expand lunar science, which was carried out in these missions. In the Apollo 15 expedition, LRV made 3 voyages with a total length of 27.9 km in 3 hours and 8 minutes. During the first trip, the front wheel steering wheel did not work, but on two subsequent trips, both front and rear wheel roles worked. However, the turns of both axles were more dangerous. LRV was superb. But on the steep slopes, the LRV might slip off if both crew members left it. More dangerous was the movement on steep slopes with one driver. As soon as the team checked the LRV transmission at hand, it was not difficult [5]. The trip to Rovers significantly reduced the heart rate and the use of consumables for oxygen and water for these astronauts and allowed them to collect 291 kg of lunar regolith material using 3 Rovers compared to 97.6 kg for the 3 previous missions. The main problems included changes in slope and grip, which may be major local obstacles to driving, as well as the direction of sun light and the angle of the sun, which may restrict the hemisphere to optimal or acceptable driving conditions. An important factor in all missions was an attempt to cope with moon dust on thermal radiators and other equipment. The inability to adequately clean the radiators in combination with the accidental loss of wing extensions created a problem with dust and even caused the batteries to exceed their design temperatures and the need to turn them off from time to time, but there were no battery failures.

3. Thermal control system of future Moon rovers — a prototype of a smart climate in the premises of the lunar base Lunokhod-1 was designed to operate for 3 Earth months. At the same time, research was not foreseen during lunar nights; it was only necessary to maintain the efficiency of all service systems and instruments during daytime operation. The LRV resource on Apollo expeditions 15, 16, and 17 was about 3 Earth days each, and no overnight stays were planned. These circumstances, as well as the formation of strong dust when the LRV moves at high speeds on the Moon, determined the fundamental differences in the thermal control systems of the manned and robotic lunar rovers.

Plans for future Apollo missions after the third LRV, included the concept of a Dual-Mode Lunar Roving Vehicle (DMLRV) in which the Astronauts would outfit the LRV with an instrument trailer at the end of their mission, and the two vehicles would traverse from one site to the next landing site (hundreds of km away) by remote operation, obtaining important scientific information to allow interpolation between the sites.

Nuclear energy for supplying heat is presently the only near term solution, as was accomplished on previous surviving Russian and USA Moon experiment systems. Other kinds of non-nuclear heating systems are presently low on needed "technology readiness levels" for implementation.

Coping with Lunar Dust is an equal challenge for extended Moon exploration. Experience has shown that dust behavior on the Moon is very much different than simulation on the Earth can provide. System designers are encouraged to develop systems that provide isolation from exposure to lunar dust, and avoid attempts to remove the lunar dust.

The report also discusses some areas of development of new generation planetary rovers, which are based on the experience of exploiting moon rovers of the twentieth century and modern American rovers. This applies primarily to the systems of locomotion, navigation, thermal control, and automatic locomotion control algorithms.

References:

- [1] Malenkov M. Self-propelled automatic chassis of Lunokhod-1: History of creation in episodes. *Front. Of Mech. Eng.* 2016. # 11(1). P. 60–86.
- [2] Burkhalter B.B. and Sharpe M.R.. LRV: Historical Origins Development and Deployment. *Jour. of The British Interplanetary Society.* 1995. V. 48. P. 199–212
- [3] Bekker M.G.. *Terrain-Vehicle Syst. Cop. by Un. Of Michigan.*1969. (Moscow, 1973)
- [4] Dovgan V.G.. *The Moon Odyssey of the domestics Astronautics. From Dreams to the Moon Rovers.* SF University, Rostov-on-Don. 2015. P.169–257. (Rus.)
- [5] Skott et. al. D.R. *Robotics and Manned Lunar Rovers of the XX Century: The View from XXI Century.* Proc. LPSC 50. 2019.

PROBLEMS OF STUDYING THE PHYSICO-MECHANICAL PROPERTIES OF LUNAR SOIL IN THE TERMO-LR EXPERIMENT FOR THE LUNA-RESOURCE-1 PROJECT

I.A. Agapkin, E.N. Slyuta

Vernadsky Institute of Geochemistry and Analytical Chemistry, Moscow, Kosygina str. 19, Russia, agapkinia@gmail.com

Keywords:

Moon, physico-mechanical properties of lunar soil, cohesion, friction angle

Introduction:

For the TERMO-LR experiment, a deep logging probe is created for geophysical contact studies to study the electromagnetic and physicommechanical properties of regolith and the temperature distribution in the Phobos soil to a depth of 2 m with a resolution over the regolith layers ≥ 2 cm.

The optomechanical mechanism on the coil, consisting of an LED, a photoresistor, and a shutter, measures with high accuracy the speed of rotation of the coil, unwinding of the tape and, accordingly, the depth of the hammer, which depends on the physico-mechanical properties of each soil layer. The well-known geometric parameters of the hammer cone, impact energy, and penetration rate of the embedder will allow the distribution of physical (density), mechanical (angle of internal friction, cohesion, and shear strength) and deformation (general deformation modulus) soil properties in depth and for each regolith layer.

Data and area of research:

It is planned to obtain data on the layering of the regolith at Phobos and the distribution of the physical and mechanical properties of the soil (density, etc.) to a depth of two meters..

References:

- [1] Bazilevsky A.T., Grebennik N.N., Gromov V.V. et al. (1984) Dependence of Physicalland Mechanical Properties of the Lunar Soil upon Specific Reliefand Processesin Operation Sites of Lunokhod-2', *Kosm. Issled.*, V. 22, N°2.
- [2] Sluta E.N. (2014) Physical and mechanical properties of the lunar soil. *Solar System Research* V. 5, P. 330–353.

PRELIMINARY DATA ON MAPPING AND OUTLINING OF VARIOUS CONCENTRATIONS OF ILMENITE IN LUNAR ROCKS ON THE VISIBLE SIDE OF THE MOON

O.I. Turchinskaya, E.N. Slyuta

Vernadsky Institute of Geochemistry and Analytical Chemistry, Moscow, Kosygina str. 19, Russia, olgaturch@yandex.ru.

Keywords:

Moon, lunar mare basalts, high titanium basalts, TiO_2 , ilmenite, spectral survey.

Introduction:

The concentration of implanted solar wind gases in the particles and minerals of lunar regolith depends on the chemical and mineral composition of the particles, on the degree of maturity of the regolith (the degree of radiation imperfection of the mineral crystal lattice) and on the particle size, and can vary in a very wide range — up to three orders of magnitude and more [1]. The lowest concentrations of noble gases are observed in impact and volcanic glasses. Similar low concentrations of implanted helium in the crystalline minerals of lunar regolith are observed only in plagioclase (bitovnite). The highest concentrations of implanted helium are observed in ilmenite, which is the main ore mineral in marine lunar basalts. Selective enrichment depending on the mineral composition leads to an inhomogeneous regional distribution of the concentration of helium isotopes and other implanted gases in the lunar regolith. The distribution areas of the increased content of Ti oxides (5–10%) according to spectral data [2–4] actually reflect the ilmenite content in the regolith and the distribution of high-titanium marine basalts.

The objective of this work is to identify and outline several main categories of ilmenite content from low-titanic to high-titanic lunar rocks on the basis of mapping the distribution of TiO_2 according to the spectral data of the Clementine spacecraft.

Results of mapping:

High-titanium marine basalts are common in the Sea of Tranquility, in Sea of Vapors, in the Sea of Rains, in the Ocean of Storms and in a subordinate meaning in the Sea of Humidity and in the Sea of Clouds (Fig. 1).

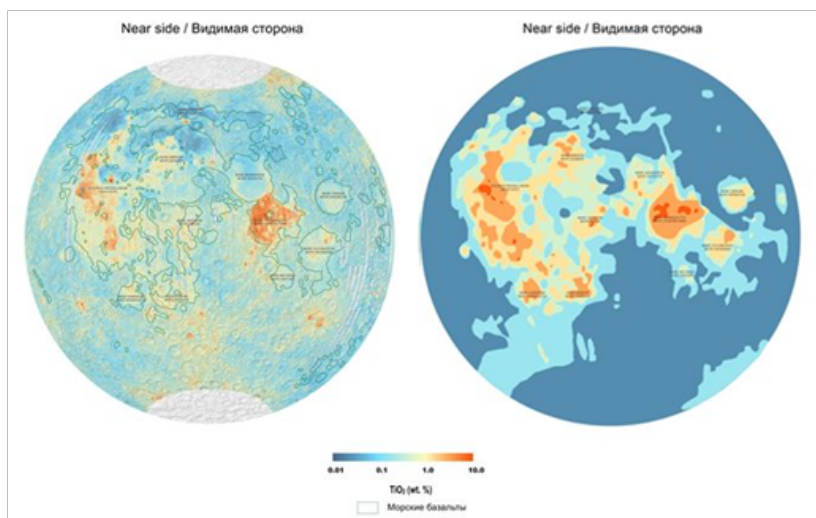


Fig. 1. Map of the distribution of TiO_2 content (wt.%) according to Clementine spacecraft data (left) on the Near side of the Moon, and the selected and contoured categories of TiO_2 content (right).

Maps of distribution of the content of TiO_2 on the lunar surface were obtained according to the spectral survey. The base represents the Clementine Ultraviolet/Visible (UVVIS) warped color-ratio mineral map. This was generated from the UVVIS mosaics using three spectral filters (415, 750, and 1000 nm) and which were previously warped (spatially adjusted) to the ULCN2005 control network. The mosaic is a composite in which the ratio of the 750/415 nm bands is used for the red-channel brightness, 415/750 nm for the blue channel, and the 750/1000nm ratio controls the green channel [2–4].

The distribution of TiO_2 content varies from 0.01 to 10 % (Fig. 1). Depending on the TiO_2 content (wt.%), six main categories were isolated and outlined on the Near side of the Moon: VI — 0.01–0.1, V — 0.1–0.5, IV — 0.5–1.0, III — 1.0–5.0, II — 5.0–8.0 and I — 8.0–10.0 wt.% respectively (Fig. 1).

References:

- [1] Slyuta E.N., Yakovlev O.I., Voropaev S.A., and Dubrovskii A.V. He implantation and concentrations in minerals and lunar regolith particles // *Geochemistry International*. 2013. Vol. 51, No. 12. P. 959–967.
- [2] Blewett D.T., Lucey P.G., Hawke B.R., Jollif B.L. Clementine images of the lunar sample-return stations: Refinement of FeO and TiO_2 mapping techniques // *J. Geophys. Res.* 1997. Vol. 102, E7, P. 16319–16326.
- [3] Lucey P.G., Blewett D.T., Hawke B.R. Mapping the FeO and TiO_2 content of the lunar surface with multispectral imagery // *Journal of Geophysical Research Atmospheres*, 1998 vol. 103, No. E2, P. 3679–3699.
- [4] Lucey P.G., Blewett D.T., Taylor G.J, Hawke B.R. Imaging of lunar surface maturity // *J. Geophys. Res.* 2000. V. 105. No. E8, P. 20377–20387.

STRUCTURE OF THE ELECTROSTATIC POTENTIAL ABOVE ION-SCALE LUNAR MAGNETIC ANOMALIES

A.V. Divin¹, I.F. Shaikhislamov², J. Deca³, R. Beliaev¹, I. Zaitsev¹, V. Semenov¹

¹ St. Petersburg State University, St. Petersburg, Russia;

² Institute of Laser Physics SB RAS Novosibirsk, Russia;

³ Laboratory for Atmospheric and Space Physics (LASP), University of Colorado Boulder, 80303, USA;

Keywords:

Lunar magnetic anomalies; Moon; Particle-in-cell simulations; mini-magnetospheres

Introduction:

High-resolution observations of the solar wind interaction with crustal magnetic fields of the Moon (known as Lunar Magnetic Anomalies, LMA) indicate the presence of ion-scale mini-magnetospheres. One of the most interesting features of LMAs, given their spatial scales, is the possibility to reflect and deflect ions impinging on the magnetic structure away from the lunar surface. LMAs typically possess a non-dipolar magnetic topology [1], but for simplicity a magnetic dipole or a combination of magnetic dipoles [2] is often used as a modeling approximation [3].

Due to its small scales a full kinetic approach is required to model the near-surface plasma environment. We use Particle-in-Cell code iPIC3D [4] to investigate the distribution of self-consistent electromagnetic field and solar wind ion demagnetization effects. Decoupling of ion and electron components close to LMA is possible because the electrons move with the solar wind magnetic field and hence cannot access the core of anomaly, where $|B|$ is large [5]. Strong “vertical” Hall electric field is formed due to this decoupling. The effect of this antioomward electric field can be quantitatively measured by introducing the electrostatic potential. It is important to notice that this electrostatic potential does not consider the effect of the Lunar surface charging and photoemission which might be responsible for generation of the potential drop of the order of the first few hundred electronvolts [6] at strong anomalies.

In order to avoid the effect of the solar wind motional electric field, we approximate the electrostatic potential by integrating this vertical electric field along the solar wind direction (but not along ion streamlines as in [7]). Our results can be summarized as follows: (1) The potential goes from zero (far from the LMA, just unperturbed solar wind flow) up to the value comparable to the upstream solar wind kinetic energy. (2) For solar wind slow enough, the potential is biased by temperature. (3) Magnetic pressure is just $\sim 1\%$ of the dynamic pressure upstream, but the structure of magnetic connectivity influences electron fluid distribution which in turn pulls ion component. Therefore, the effectiveness of ion reflection depends crucially on the interplanetary magnetic field direction and strength.

References:

- [1] Tsunakawa, H., Takahashi, F., Shimizu, H., Shibuya, H. & Matsushima, M. Surface vector mapping of magnetic anomalies over the Moon using Kaguya and Lunar Prospector observations // *J. Geophys. Res.* 2015, 120, 1160–1185.
- [2] Kurata, M. et al. Mini-magnetosphere over the Reiner Gamma magnetic anomaly region on the Moon // *Geophys. Res. Lett.* 2005, Vol. 32, 24205.
- [3] Poppe, A.R., Fatemi, S., Garrick-Bethell, I., Hemingway, D. & Holmström, M. Solar wind interaction with the reiner gamma crustal magnetic anomaly: connecting source magnetization to surface weathering // *Icarus* 2016, Vol. 266, 261–266.
- [4] Markidis, S., Lapenta, G., Rizwan-uddin. Multi-scale simulations of plasma with ipic3d // *Math. Comput. Simul.* 2010, 80, 1509–1519.
- [5] Deca, J. et al. Electromagnetic particle-in-cell simulations of the solar wind interaction with lunar magnetic anomalies // *Phys. Rev. Lett.* 2014, 112, 151102.
- [6] Poppe, A.R., Halekas, J.S., Delory, G.T. & Farrell, W.M. Particle-in-cell simulations of the solar wind interaction with lunar crustal magnetic anomalies: magnetic cusp regions // *J. Geophys. Res.* 2012, Vol. 117, 9105.
- [7] Jarvinen, R. et al. On vertical electric fields at lunar magnetic anomalies // *Geophys. Res. Lett.* 2014, Vol. 41, 2243–2249.

ROLLING BOULDERS AND THEIR TRACKS ON LUNAR SLOPES

A.T. Basilevsky^{1,2}, U. Mall², D. Kloskowski², H. Schmidt², S.S. Krasilnikov^{1,2} and E.N. Guseva¹

¹ Vernadsky Institute of Geochemistry and Analytical Chemistry, Russian Academy of Sciences, Moscow, 119991, Russia

² Max-Planck Institute for Solar System Research, Goettingen, 37077 Germany

Keywords:

Lunar rock boulders, boulder tracks, slope

Introduction:

Lunar rock boulders were the subject of intense studies since the 1960–70's as obstacles for safe landing and indicators of thickness of the regolith layer [e.g. 1, 2, 3, 4]. New possibilities to study them appeared since the Lunar Reconnaissance Orbiter Narrow Angle Cameras (LROC NAC) started to provide to the scientific community images of the lunar surface with a resolution of ~ 1 m and locally even higher [5]. Combined with other scientific information this led, in particular, to estimations of the lifetime of lunar boulders exposed on the surface of the Moon [e.g., 6, 7]. This fact provided again, a possibility to estimate the absolute ages of small craters based on the measured spatial densities of boulders in their ejecta, and to use these ages to estimate the times of formation of other lunar landforms [e.g., 8]. Characteristics of tracks formed by boulders bouncing on slopes allowed one to estimate bearing capacities of surface materials in some usual and specific geologic environments [9]. In the present work we consider rock boulders and their tracks on lunar slopes as a tool to understand episodes of recent geologic history in the studied areas. We consider LROC NAC images and LOLA-based topographic information for the NW inner slopes of the 320 km crater Schrodinger and the NE part of the South massif in the Taurus-Littrow valley.

The crater Schrodinger NW inner slope:

Under study was the 13×10 km area which included the Schrodinger inner slope, as well as the sub-horizontal surfaces above and below it (Fig. 1).

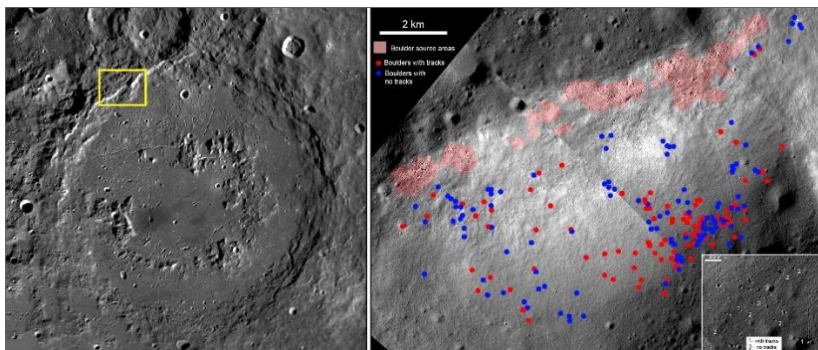


Fig. 1. Left is LROC WAC mosaic showing a position of the study area in the NW rim of crater Schrodinger. Right is the mosaic of LROC NAC images showing boulders with (red) and without (blue) associated tracks.

We analyzed a mosaic of LROC NAC images with resolution 2 m per pixel using the Photoshop program and measured the vertical (a) and horizontal (b) dimensions of the illuminated parts of the boulders and selected for further study those which had 5 pixels at least in one dimension. The total lengths of the illumination parts $l = \sqrt{(a^2 + b^2)}$ were calculated and presented in meters. Outlines of selected boulders were marked and thus mapped. This procedure led to the mapping of 211 boulders. The length of the illu-

minated part of the boulders ranges from 13 to 80 m, with a median size of 17 m, the average size is 20 m. Ninety-eight (46%) boulders are associated with tracks whose width is about the boulder size, and 113 (54%) are without tracks. Most mapped boulders are located on the slopes whose inclinations are in the range of 20 to 25°. In the upper part of the slope there are areas with numerous no-track boulders (pink-colored areas in Fig. 1). These areas seem to be source regions of the boulders we observed on the slope below.

Taurus-Littrow — NE slope of South massif:

This study area is 7.4×9.2 km² and includes parts of the South massif, its NE slope, and a small portion of the Taurus-Littrow valley floor (Fig. 2).

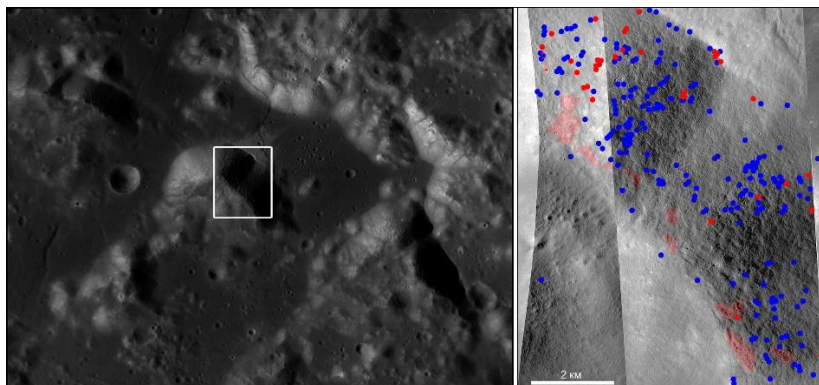


Fig. 2. Left is LROC WAC mosaic of Taurus-Littrow valley; Right is the mosaic of LROC NAC images showing boulders with (red) and without (blue) associated tracks.

Here we analyzed mosaics of the LROC NAC images with resolution 0.43 m per pixel performing all of the procedures as described in the above section of the paper. This led to a mapping of 249 boulders. The length of the illuminated part of the boulders ranges from 4 to 23 m, with a median size of 7 m, and an average size of 8 m. Thirty-two (13%) boulders have associated tracks whose width is about the boulder size, and 217 (87%) are without tracks. Most mapped boulders are located on slopes of 20 to 25°. In the upper part of the slope there are areas with numerous no-track boulders (pink-colored in Fig. 2). As in the Schrodinger study area, these seem to be source regions of the boulders observed on the slope below.

Discussion and conclusions:

The above considered study areas are on the slopes of pre-mare landforms which evolved for 3–3.9 Ga. During this time period the slopes represented an area where the slope retreat via down-slope material movements, including a supply of boulders from the mentioned source regions, was accompanied by destruction of the boulders by meteorite impacts and thermal fatigue. The lifetime of the meter-sized rock boulders (T) was estimated as 200–300 Ma, with half of the new-formed ones being destroyed within a time of ~ 50 Ma [e.g., 6–8]. New boulders appeared on the surface of the above shown slopes and produced tracks consisting of chains of crater-like pits. The track lifetime can be roughly estimated as the lifetime of a crater with a diameter equal to the track width; in our cases this is on average ~ 10 – 20 m. For craters of this size the lifetime was found to be $t = 2.5D$, where t is in Ma and D is in meters [10]. In our cases t could be 25 to 50 Ma. But this is an estimate for craters on sub-horizontal surfaces. On slopes as steep as 20–25° the crater lifetime is by an order of magnitude shorter [10]; in our case $t = 2.5$ to 5 Ma, that is by an order of magnitude shorter than the boulder lifetime T . If on some slope the rate of the boulders' appearance (per unit of time) is close to constant, then the ratio R of the number of boulders with tracks (N_t) to the total number of boulders (N_T) should be proportional to t/T , in our case ~ 0.1 .

In the above considered cases, R was found to be $98/211 = 0.46$ for the Schrodinger study area and $32/249 = 0.13$ for the Taurus-Littrow area. This prob-

ably means that in the Taurus-Littrow area for the latest geologic time period (probably ~ 100 Ma [11]) the interaction between the appearance of new boulders and their destruction by surface processes was close to equilibrium, while in the Schrodinger study area some catastrophic event which provoked the appearance of many new boulders occurred recently (moonquake, meteorite impact).

Acknowledgements:

We acknowledge the referencing of the NAC images with ISIS by Valentin Bickel and discussion with Yuri Skorov.

References:

- [1] Rennilson J.J. et al. In Surveyor I mission report, part II: Scientific data and results. NASA JPL Technical Report №32–1023. P. 7–44.
- [2] Shoemaker E.M. and Morris E.C. 1969. Thickness of the regolith. In Surveyor: Program results. NASA Special Paper №184. Washington, D.C. P. 96–98.
- [3] Florensky K.P. et al. Geomorphological analysis of the area of Mare Imbrium explored by the automatic roving vehicle Lunokhod 1. Space Research XII, AkademieVerlag, Berlin. 1972. P. 107–121
- [4] Wilcox B.B. et al. Constraints on the depth and variability of the lunar regolith. Meteoritics & Planetary Science 2005. V. 40, Nr 5. P. 695–710.
- [5] Robinson M.S, Brylow S.M., Tschimmel M. Lunar Reconnaissance Orbiter Camera (LROC) Instrument Overview. Space Sci. Rev. 2010. V.150. P. 81–124.
- [6] Basilevsky A.T., Head J.W., Horz F. Survival times of meter-sized boulders on the surface of the Moon. Planetary & Space Science. 2013. V. 89. P. 118–126.
- [7] Basilevsky A.T., Head J.W., Horz F., Ramsley K. Survival times of meter-sized rock boulders on the surface of airless bodies. Planetary & Space Science. 2015. V. 117, P. 312–328.
- [8] Lu Yu et al. Young wrinkle ridges in Mare Imbrium: Evidence for very recent compressional tectonism. Icarus. 2019. V. 329. P. 24–33.
- [9] Bickel V.T. et al. Analysis of lunar boulder tracks: Implications for trafficability of pyroclastic deposits. Journ. Of Geophys. Res.: Planets. 2019. V. 124. P. 1296–1314.
- [10] Basilevsky A.T. On the evolution rate of small lunar craters. Proc. Lunar Sci. Conf. 7th, Pergamon Press, 1976, 1005–1020.
- [11] Schmitt H.H. et al. Revisiting the field geology of Taurus–Littrow. Icarus. 2017. V. 298. P. 2–33.

THE STRUCTURE, COMPOSITION AND TEMPERATURE IN THE MOON BASED ON THE JOINT INVERSION OF GEOPHYSICAL AND GEOCHEMICAL DATA FOR A LINEAR TEMPERATURE PROFILE IN THE MANTLE

E. Kronrod¹, K. Matsumoto², R. Yamada³, O. Kuskov¹, V. Kronrod¹

¹ Vernadsky Institute of Geochemistry and Analytical Chemistry (GEOKHI RAS), e.kronrod@gmail.com

² RISE Project, National Astronomical Observatory of Japan,

³ The University of Aizu, Research Center for Advanced Information

Keywords:

Moon, numerical simulation, inversion, internal structure, seismic, thermodynamic properties, chemical composition.

We used Markov chain Monte Carlo method MCMC for inversion of seismological and seismic data together with thermodynamic approach (to calculate physical properties in mantle layers). Bulk FeO and Al₂O₃ concentrations and magma ocean condition were considered as geochemical constraints. Internal structure models which are consistent with both geochemical and geophysical constraints were obtained including probable temperature distribution in the lunar mantle is calculated.

The model of the Moon:

We apply viscoelastic, spherically symmetric model of the Moon consisting of nine layers: megaregolith, core, four mantle layers, low-viscosity (LVZ) layer, liquid outer core and solid inner core. The physical properties in each zone are assumed to be constant (for the mantle they are calculated in the middle of the layers). The division of the mantle into layers was carried out in accordance with the model [1]: the boundaries between the layers are located at depths of 250, 500 and 750 km.

The concentrations of the main oxides were set equal in the four upper layers of the mantle, the magma ocean model was used to calculate the concentrations in the lower mantle (the concentration of oxides in the lower mantle is equal to the average concentration in the upper mantle and crust and equal to the bulk concentration in the Moon [2]). The models of the magma ocean in such a formulation were considered in our previous study [3]. Parameters in the crust (thickness, density, shear and bulk modulus) were fixed.

We considered linear temperature distribution in the lunar mantle:

$$T(H) = Ta \cdot H + Tb \quad (1)$$

where H – depth (km); T – temperature (°C) at the depth H ; Ta , Tb - dimensionless coefficients.

Ta and Tb are model parameters.

Geochemical models of bulk composition in the mantle:

Models of the lunar composition can be conventionally divided into two groups: 1 – bulk Al₂O₃ content is close to Earth's value, 2 – bulk Al₂O₃ concentration is higher than 4,5 wt.% [2]. The analysis of majority of current Moon's composition models [5] revealed that Al₂O₃ = 4,05 ± 0,36 wt.% for group 1 and Al₂O₃ = 5,91 ± 0,39 wt.% for group 2, FeO = 12,25 ± 1,33 wt.% for both groups. Concentrations of main oxides were equal in first 3 upper mantle layers and we applied the model of magma ocean to calculate oxide concentrations in fourth lower mantle layer.

Inversion:

A Bayesian inversion approach is an effective method to solve for a non-linear problem such as planetary internal structure modeling ([4, 5] et al.). This study utilizes Markov chain Monte Carlo (MCMC) algorithm to infer the parameters of the lunar internal structure. The solutions of the parameters and their uncertainties are obtained from the posterior distribution

which is sampled by the MCMC algorithm. Then the likelihood function $L(m)$, which is a measure of misfit between the model predictions and the observations, is calculated. [2] Bulk chemical composition of the Moon is considered as observed data and is included into $L(m)$. Bulk Al_2O_3 and FeO concentrations are included into $L(m)$ as observed data.

Thermodynamic modeling of phase relations and physical properties in the multicomponent mineral system CFMAS was used for mantle physical properties calculation [2].

Results and conclusions:

Seismic velocities, main oxides (Al_2O_3 , FeO, MgO, SiO_2) concentrations and temperature distribution in the mantle, core sizes (for inner and outer core), viscosity exponent in LVZ for two types of bulk chemical composition models were calculated from the inversion.

The results of inversion for some calculated parameters are shown in fig. 1 and fig. 2: in fig. 1 - seismic velocities V_p , V_s and temperature distribution and in fig. 2 - distribution of main oxides Al_2O_3 , FeO and MgO.

The results indicate that for both types of models in a wide temperature range it is possible to obtain solutions that are consistent with geochemical and geophysical constraints. Calculated distributions of concentrations and seismic velocities are in a good agreement with the results obtained by other authors.

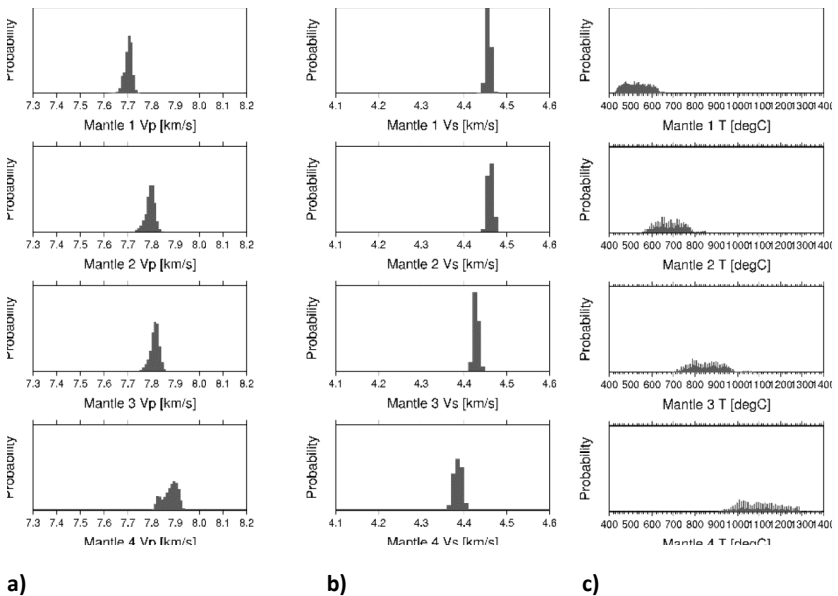


Fig. 1 Probable distribution of seismic velocities V_p (a), V_s (b) and temperature (c) in the lunar mantle for type-1 models (bulk Al_2O_3 similar to Earth)

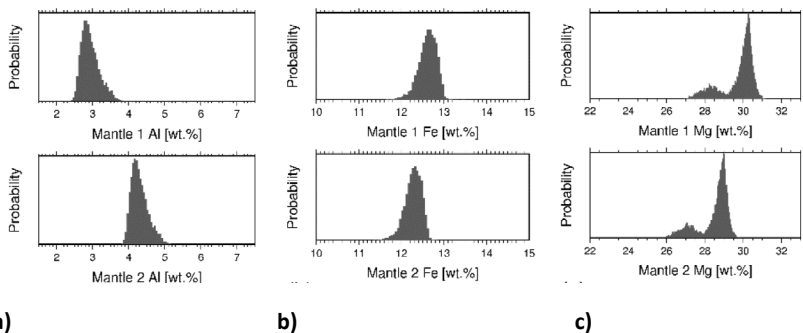


Fig. 2. Probable distribution of oxides Al_2O_3 (a), FeO (b) and MgO (c) in the lunar mantle for type-1 models (bulk Al_2O_3 similar to Earth)

Acknowledgments:

This work was supported by JSPS KAKENHI grant 17K05643, the RFBR grant18-05-00225 and Russian Academy of Sciences under Program 17.

References:

- [1] Gagnepain-Beyneix J., Lognonné P., Chenet H., Lombardi D., Spohn T. A seismic model of the lunar mantle and constraints on temperature and mineralogy // *Phys. Earth and Planet Int.* 2006. V. 159, P. 140–166.
- [2] Kuskov O.L., Kronrod E.V., Kronrod V.A. Thermo-chemical constraints on the lunar bulk composition and the structure of a three-layer mantle // *Phys. Earth Planet.Int.* 2019. V. 286. P. 1-12 <https://doi.org/10.1016/j.pepi.2018.10.011>
- [3] Kronrod E.V., Matsumoto K., Kuskov O.L., Kronrod V.A., Yamada R., Kamata S. Adjustment of geophysical and geochemical models of the Moon // 49th Lunar and Planetary Science Conference 2018 (LPI Contrib. No. 2083) 1667.pdf
- [4] Matsumoto K., Yamada R., Kikuchi F., Kamata S., Ishihara Y., Iwata T., Hanada H., Sasaki S. Internal structure of the Moon inferred from Apollo seismic data and selenodetic data from GRAIL and LLR // *Geophysical Research Letters*. 2015. V. 42, 18. P. 7351–7358. doi: 10.1002/2015GL065335
- [5] Khan A., Connolly J.A.D., MacLennan J., Mosegaard K. Joint inversion of seismic and gravity data for lunar composition and thermal state // *Geophys. J. Int.* 2007. V. 168. P. 243–258.

IMPLEMENTATION OF LUNAR CRATER CATALOGUE FOR MORPHOMETRIC STUDIES OF THE CRATERS (DIAMETER 1-10 KM)

I.Yu. Zavyalov, N.A. Kozlova, M.M. Kolenkina, I.P. Karachevtseva
*Moscow State University of Geodesy and Cartography (MIIGAik), MIIGAik
Extraterrestrial Laboratory (MExLab), Russia (n_kozlova@miigaik.ru)*

Keywords:

The Moon, Craters, Morphometry, Depth, Slopes, Crater catalogue

Introduction:

The Lunar Reconnaissance Orbiter mission (LRO) opens to us new possibilities to achieve knowledge about morphology of Lunar craters of smaller diameters than studied before. Global coverage and high resolution of the new images and digital elevation models (DEM) with GIS technologies make it possible to compute morphometric characteristics of craters and calculate some statistics. Our work at this stage focuses on creation of a global catalogue of Lunar craters with their main morphometric parameters to provide data for further analyses.

Crater Catalogue:

Although there are some methods and tools for image analysis in order to recognize craters automatically, in this study we preferred manual crater identification for our catalogization, as it is still the most easy and reliable way. For this purpose we used LRO WAC Global Morphologic Map (http://wms.lroc.asu.edu/lroc/view_rdr/WAC_GLOBAL) with pixel size of 100 m, which confidentially shows most of the craters more than 1 km in size. During two years we were thoroughly looking through the parts of global orthomosaic and digitizing visible craters using ArcMapCraterTools module (Kneissl et al., 2011). We managed to catalog about 350 000 craters more than 1 km — determine their center coordinates and size.

Moreover, due to stereo imaging and laser altimeter measurements we now have digital elevation models (DEMs) for the whole surface of the Moon. This makes possible determination of crater depth and other morphometric parameters, such as steepness of slopes, height of the rim, form of crater depression (e.g., bowl-shaped, conical, with flat floor). However, automatic calculation of crater morphometry is complicated because of irregular craters shape — different stages of their degradation and destruction by superimposed craters — as well as due to different surrounding surface. Therefore, special algorithms have to be used to reduce the influence of all these factors on the resulting value.

In our study for morphometric calculations of crater depth we used special program CRaMo (Kokhanov et al., 2015) and DEM GLD100 (Scholten et al., 2012). However, because of the problems mentioned above, automatic determinations of crater depth are possible not for all craters.

Maximal value of inner slopes for each crater was determined using zonal statistic function in ArcGIS based on raster of slopes calculated from GLD100, so the accuracy of the steepness determination mostly depends on the DEM and its correlation with orthomosaic used for crater identification.

The determined parameters (slopes and depth to diameter ratio) can be of great importance for estimations of crater degradation rates and their dependence on crater age and diameter (Basilevsky et al., 2018).

The resulted catalogue will be available via MExLab Planetary data Geoportal <http://carsrv.mexlab.ru/geoport/>.

Conclusions:

In the future, we plan to consider the ways to deal with the complications to make automatic morphometric determinations more accurate and reliable. Also we plan to investigate the obtained results in order to find principal similarities of differences in crater morphology in different Lunar regions,

or between craters of different age. Another big work is creation of a morphometric crater catalogues on other solid planetary bodies (e.g. Mercury) and their comparative studies.

Acknowledgements:

The work on creation of a morphometric lunar catalogue was supported by Russian Foundation for Basic Research (RFBR), project № 16-37-00323.

References:

- [1] Basilevsky A.T., Kozlova N.A., Zavyalov I.Y., Karachevtseva I.P., Kreslavsky M.A. 2018. Morphometric studies of the Copernicus and Tycho secondary craters on the Moon: Dependence of crater degradation rate on crater size. *Planetary and Space Science*, 162, DOI: 10.1016/j.pss.2017.06.001.
- [2] Kneissl T., van Gasselt S., Neukum G., Map-projection-independent crater size-frequency determination in GIS environments — New software tool for ArcGIS, *Planetary and Space Science*, 59, 1243–1254.
- [3] Kokhanov A.A., Kreslavsky M.A., Karachevtseva I.P. 2015. Small impact craters in the polar regions of the Moon: peculiarities of morphometric characteristics. *Solar System Research*. 49 (5): 295–302. doi:10.1134/S0038094615050068.

THERMAL REGIME AND REGOLITH PARAMETERS OF LANDING SITE OF PROBE CHANG'E

D.V. Petrov¹, S.G. Pugacheva², E.A. Feoktistova², V.V. Shevchenko²

¹ Crimean Astrophysical Observatory of Russian Academy of Science (CrAO RAS), Nauchnyj, Russia

² Sternberg Astronomical Institute, Moscow State University, Moscow, Russia

Keywords:

Moon, impact crater, landing site.

Introduction:

China's Chang'e — 4 lunar probe landed in the south part of the far side of the Moon in the Von Karman crater (44,3° S, 176,2° E) on the floor of the South Pole-Aitken basin. The probe delivered to the Von Carman crater the automatic lunar rover Yutu — 2, which began its movement across the bottom of the crater.

Von Carman is a lunar crater with a diameter 186 km and a maximal depth is about 3 km. It lies in the largest lunar impact basin — South Pole — Aiken basin. In this paper we investigated the thermal regime, Chemical composition and characteristics of the regolith in the area of the landing site of the Chang'e — 4 probe.

We studied such mechanical properties of lunar soil as a density, porosity, strength and other at the floor of Von Carman crater. Based on the obvious idea that the denser the regolith, the stronger the multiple scattering developed among its constituent particles, we conducted a computer simulation of single and double scattering particles. For computer simulation, we used the Sh-matrix method [1–3]. Using this method, we estimated the effect of multiple scattering among olivine particles on the photometric and polarimetric scattering characteristics, such as the photometric color, the degree of linear polarization P , and the color of polarization $CP = P_{\text{red}} - P_{\text{blue}}$. It is known that multiple scattering at phase angles less than 100° leads to an increase in color. Thus, the areas inside the crater with the maximum photometric color are the most dense and the most suitable for landing spacecraft.

We also investigated the chemical composition of rocks in the Von Karman crater area. There are no signs of active volcanic processes in this area, no tectonic faults. The data from the Lunar Prospector [4] probe show that in the area of the crater there is an increased content of Fe, Th, as in the whole South Pole — Aitken basin. The Ti content in the crater area is insignificant.

We used the data from altimeter LOLA [5] onboard probe LRO to study the temperature regime in the Von Carman crater area. To do this we used the model, described in [6]. At nighttime temperatures decrease to about 100 K in this area.

References:

- [1] Petrov D.V., Synelnyk E., Shkuratov Y.G., Videen G. The T-matrix technique for calculations of scattering properties of ensembles of randomly oriented particles with different size // *Journal of Quantitative Spectroscopy and Radiative Transfer*. 2006. V. 102, № 1. P. 85–110.
- [2] Petrov D.V., Shkuratov Y.G., Kaydash M.V., Videen G. Analytic T-matrix solution of light scattering from capsule and bi-sphere particles: applications to spore detection // *Journal of Quantitative Spectroscopy and Radiative Transfer*. 2007. V. 102, № 1. P. 81–105.
- [3] Petrov D.V., Shkuratov Y.G., Videen G. Light scattering by arbitrary shaped particles with rough surfaces: Sh-matrices approach // *Journal of Quantitative Spectroscopy and Radiative Transfer*. 2012. V. 113, № 18. P. 2406–2418.
- [4] Prettyman T.H., Hagerty J.J., Elphic R.C., Feldman W.C., Lawrence D.J., McKinney G.W., Vaniman D.T. Elemental composition of the lunar surface: Analysis of gamma ray spectroscopy data from Lunar Prospector // *Journal of Geophys. Res.* 2006. Res. V. 111. Issue E12
- [5] <https://ode.rsl.wustl.edu/moon/>
- [6] Feoktistova, E.A., Pugacheva, S.G., Shevchenko, V.V. On the possibility of the existence of volatile compounds in the region of the Scott craters on the Moon // *Cosmic Research*. 2018. V. 56. P. 169–179.

RESEARCH OF THE LUNAR SOUTH POLAR AREA

S.G. Pugacheva, E.A. Feoktistova, V.V. Shevchenko

*Astronomical Institute, Moscow State University,
Universitetsky 13, Moscow 119992, Russia, sve-pugacheva@yandex.ru*

Keywords:

The Moon, South Pole of the Moon, peaks of eternal light, projects of lunar bases on the Moon

Introduction:

Exploration of the Moon is the main direction in the development of astronautics in the world. The Moon is the closest and human-accessible source of extraterrestrial matter, natural resources, minerals, volatile compounds, water, a natural testing ground for technological research and testing of new space technology. According to research results, the polar areas of the moon are of special interest. Temperature differences in the regions of polar areas are minimum; the average temperature is 223.15 °K. Darkness and permafrost reigns in the craters of a kilometer depth. Nevertheless, the peaks of eternal light are observed on the north and south Poles of the Moon. So, at the north pole a small area of the north pole is illuminated by the sun during the whole lunation. This area is called the Peak of Eternal Light; this phenomenon is associated with the inclination of the Moon rotation axis by 1.5 degree relative to the earth's orbit plane around the Sun [1, 2]. As a result, there are little distinguishable seasons and efficient illumination of the poles on the Moon. In the Northern Hemisphere, sunlight illuminates the shaft of the Piri crater. There are also areas of eternal light in the Southern Hemisphere. These are the peaks of the mountains surrounding the crater of Malapert, as well as the peaks and slopes of the high crater shafts. The mountains around the crater of Malapert are illuminated by sunlight for 78% of the time. Sunlight illuminates the crater shafts located around the South Pole over 80% of the lunar day time (Fig. 1). The bottom of most craters of the South Pole of the Moon is in constant shadow.

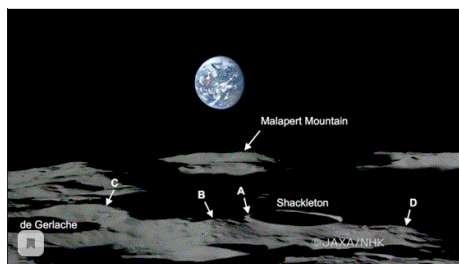


Fig. 1. The hills of ever-shaded craters are almost always lit by sunlight.

Craters of the lunar South polar area.

In a lot of constantly shaded craters of the South Pole of the Moon, there are the areas containing relic ice. The craters of the south pole of the Moon are of unique nature since the sunlight never illuminates their bottom. Our calculations of the illumination and temperature of crater soil demonstrate that the areas of some craters being in constant shade, the soil temperature is about 25 °K, such craters are called "cold traps". Water ice on the Moon surface can be located only in the places where the surface is heated below 373.15 °K and all the ice evaporates at a higher temperature under vacuum conditions. In addition to water, these lowlands may contain the simplest organic compounds of non-biological origin (for example, methane) brought to the Moon by comets. Substance of the crater soil may contain records about the early stage of the Solar system existence. In this article, we explore the craters of the lunar South polar area, the bottom soil of which is in constant shadow, and the crater shafts are illuminated by sunlight for a long time. According to satellite imagery, the soil surface temperature in areas constantly illuminated by sun can reach more than 300°K [Fig.2].

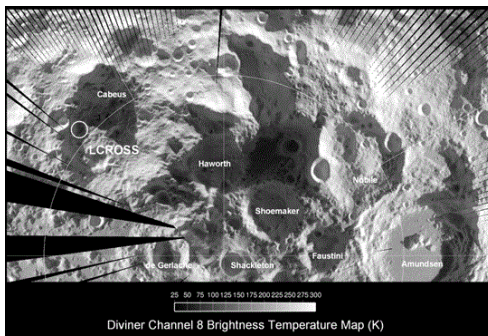


Fig. 2. Photo of the South pole in the infrared range (photo by KA LRO).

Constantly shaded craters of the South Pole of the Moon: De Gerlache, Shackleton, Sverdrup, Haword, Shoemaker, Faustini, Cabeus the craters are located near the South Pole of the Moon. The report shows the graphs of distribution of the listed craters according to their diameter and geological age, the height profiles of the crater shafts are built. According to the data of the Lunar Prospector spacecraft, the chemical composition of the craters soil surface is determined.

Conclusions:

The South Pole of the Moon was explored by the spacecrafts of many countries. The USA launched a series of 5 automatic spacecrafts Lunarorbiter in 1996-1997 to map the lunar surface at the South Pole of the Moon. The Clementine spacecraft (USA, 1994) is the first scientific explorer confirming the hypothesis of the presence of water at the Moon poles. Lunar Prospector (USA, 1995), investigated the gravitational and magnetic field, made a global survey of the elemental composition of the Moon surface. The LRO spacecraft (Lunar Reconnaissance Orbiter, USA, 2009) performed surface surveys and studies of the Moon lunar topography. A Russian scientific instrument LEND (Lunar Exploration Neutron Detector) was installed on the LRO spacecraft to build a global map of hydrogen content in the lunar soil. The Kaguya spacecraft (India, 2007) received a high-definition video from the Moon's orbit, and also discovered the last landing site for American astronauts. In 2009, the Indian Chandrayaan-1 spacecraft and the NASA LROSS unit discovered a large supply of ice in the craters of Shakleton and Cabeo. In 2019, China landed the Chang'e-4 lunar probe near the South Pole of the Moon near the Aitken South Pole basin (crater Von Karman).

References:

- [1] Pugacheva S.G., Feoktistova E.A., Shevchenko V.V. On the possibility of the existence of volatile compounds in the region of the Scott craters on the Moon// Cosmic Research. 2018. V. 56. № 3. P. 169–179
- [2] Mitrofanov, I.G., Sanin, A.B., Boynton, W.V., Chin G., Garvin J.B. and et al. Hydrogen mapping of the lunar South Pole using the LRO neutron detector experiment LEND, Science. 2010. V. 330. P. 483–486.

STRATIGRAPHIC SCALE AS PROOF OF CYCLICITY BOMBARDMENTS OF SOLAR SYSTEM BY GALACTIC COMETS

A.A. Barenbaum

Oil and Gas Research Institute RAS (Moscow), azary@mail.ru

Keywords:

Galactic comets, cometary bombardments, stratigraphic scale.

Introduction:

Currently, there is no doubt that geological processes on the Earth are cyclical. The most complete information about these cycles is systematized in a Stratigraphic (geochronological) scale, built in the form of a hierarchical system of geological cycles of various duration nested in each other.

In connection with the discovery of the phenomena jet outflow of gas and dust from the nuclear disk of our Galaxy [1, 2], the author discovered that the Stratigraphic scale serves as a unique indicator of powerful quasi-periodic cosmic impacts that the Earth has experienced since formation. Throughout the entire history of the Earth, these impacts have not changed and in fact boiled down to the bombardments of our planet by galactic comets, as well as the fall of large interplanetary bodies on it.

Therefore this scale can be considered [3] as empirical classification of aggregate response individual Earth's subsystems (biosphere, tectonosphere, atmosphere and hydrosphere) to falls of large cosmic bodies, is ranked by three parameters: 1) amount of highlighted energy, 2) of prevailing type of falling bodies (comets or asteroids) and 3) character of their falls (single or mass).

Nomenclature of the subdivisions of the stratigraphic (geochronological) scale of with indication of the possible energy of cosmic impacts at borders of this scale is given in Table 1 [3].

Table 1. Reflection of cosmic events by boundaries of the stratigraphic scale

Cosmic impact (event cause)	Subdivision of Scale	Repetition period of events	Impact energy, J *
1. Numerous falls of large interplanetary bodies	Eonothem, Eon	1 billion years	$\sim 10^{28} \div 10^{31}$
2. Bombardments by galactic comets:			
in Galaxy arms at distance of corotation radius from Galaxy center	Erathem, Era	250 mln years	$\sim 10^{29}$
of jet streams in gas-condensation zones of Galaxy arms	System, Period	20÷80 mln years	$\sim 10^{28} \div 10^{29}$
of jet streams outside Galaxy arms	Departments, Epoch	19÷37 mln years	$\sim 10^{26} \div 10^{27}$
3. Falls of interplanetary bodies with a diameter of:			
> 3.5 km	Stages, Age	2.9±0.2 mln years	$\sim 10^{22} \div 10^{23}$
~1-2 km	Zone, Section	~0.01÷1 mln years	<10 ²²

* Energy estimates are obtained from the Earth geology data [1].

Table 1 shows that cosmic cyclicity is a phenomenon inherent in the entire Solar System, and the Earth is just a planet where this phenomenon is studied incommensurably better than on others planets.

The author developed a theoretical model [2], which with an accuracy not inferior to accuracy of empirical construction of the Stratigraphic scale itself

according to geology data, made it possible to calculate the moments of cometary bombardments, corresponding to the scale boundaries, starting from the rank of departments (epochs) and higher.

Subject matter:

Many natural sciences adhere to outdated notions. Therefore, they face problems that are easily solved by the Galactocentric paradigm. Consider two such problems: one in stratigraphy, and the other in comparative planetology.

Stratigraphy. In our country, it is recommended to use two stratigraphic scales: the General Stratigraphic Scale (GSS) of Russia [4] and International Stratigraphic Scale (ISS) [5]. Both scales are based on a unified system of geological data; however, they differ in the age of same borders (Table 2).

In Table 2, estimated times of cometary bombardments (Table 1) are compared with the SNR-1993 and MSS-2019 scales borders.

Table 2. Times of borders of the Phanerozoic scale according to our calculations and GSS-1993 and ISS-2019 data

	Calculation	GSS-1993	ISS-2019	Systems	Eras
0	3	1.6	2.58	Q	K z
	24	24.6	23.03	N	
	45	38.0	33.9	P	
	69	54.9	56.0		
	94	65	66.0		
100	122	97.5	100.5	K	M z
	156	144	145.0		
	187	163	163.5	J	
	213	188	174.1		
	233	213	201.3	T	
200	253	248	237		P z
	274	258	251.9	P	
	295	286	272.95		
	319	300	298.9	C	
	344	320	323.2		
300	372	360	358.9		P z
	387	374	382.7	D	
	403	387	393.3		
	437	408	419.2	S	
	462	421	443.8		
400	483	438	458.4	O	P z
	503	448	470.0		
	524	478	485.4	G	
	545	505	497		
	569	523	509		
500	594	540	541.0		R f
				V	
600		570			

Solid and dashed lines in columns 1 and 2 show the borders of systems and departments, respectively, and the thin dotted lines in column 3 are the stages borders. Age of same-name borders in the GSS and ISS scales as a rule is different, that is a serious unsolved problem in stratigraphy [4, 5].

In essence this problem is a consequence of two modern approaches to construction of the Phanerozoic stratigraphic scale [6] which are considered alternative however they are not quite the same. The ISS scale is based on fixing the moments of large interplanetary bodies fall, and the GSS scale is on identifying epochs of mass extinction of living organisms caused by cyclic bombardments of Earth by galactic comets, what geologists don't know about. Therefore this problem is automatically eliminated by a transition in geology to the Galactocentric paradigm representations [2].

Comparative planetology. Due to ignoring the galactic comets falls and in this science there are also serious problems. The main difficulties are related to the explanation of the origin of water, as well as large craters and mascons on the Moon, Mars and Mercury. What cannot be explained [7, 8] by the fall of cosmic bodies with the same size distribution as in the asteroid belt.

These problems are also fundamentally solved [9, 10, 11] with the participation of galactic comets. However, unlike the Earth, on Moon, Mars, Mercury, as well as in the Solar System as a whole, there is reliable evidence of only the latest cometary bombardment on the N-Q boundary (Table 2).

Along with formation of craters, mascons and mascons on Moon, Mars and Mercury the consequences of this bombardment also are: modern “peculiar-ity” of the Sun [12]; strong turbulence of giant planets atmospheres [13]; excited state of asteroid belt bodies [14]; significant “dustiness” of the inter-planetary space [15], as well as presence in it of a large number of comets, meteorites and asteroids with dynamically short ($\sim 10^6$ years) lifetime [16].

It was concluded [1] that these facts are a complex of interrelated residual phenomena caused by the presence of the Sun from 5 to 0.7 million years ago in a stream of galactic comets of the Orion-Cygnus branch.

References:

- [1] Barenbaum A.A. Galaxy, Solar System, Earth. Subordinated Processes and Evolution (Moscow, PH: GEOS) 2002.
- [2] Barenbaum A.A. Galactocentric Paradigm in Geology and Astronomy (Moscow, PH: LIBROKOM) 2010.
- [3] Barenbaum A.A., Gladenkov Yu.B., Yasamanov N.A. Geochronological scales and astronomical time // Stratigrafiya. Geol. Korrelyatsiya. 2002. V. 10, № 2. P. 3–14.
- [4] Zhamoyda A.I. General stratigraphic scale adopted in USSR – Russia. Its meaning, purpose and improvement (St. Petersburg, PH: VSEGEI) 2013.
- [5] Alekseev A.S. The international stratigraphic scale and its current status // Geologiya i geofizika. 2015. V. 56, № 4, P. 671–681.
- [6] Harland W., Armstrong R., Cox A. et. al. A geologic Time scale 1989. Cambridge, Univ. Press, 1990. 263 p.
- [7] Woronow A. Crater saturation and equilibrium: Monte Carlo simulation // J. Geophys. Res. 1977. V. 82. P. 2447–2456, doi: 10.1029/JB082i017p02447
- [8] Neumann G.A., Zuber M.T., Wieczorek M.A. et al. Lunar impact basins revealed by Gravity Recovery and Interior Laboratory measurements // Science Advances, 1, 2015, e1500852, doi:10.1126/sciadv.1500852.
- [9] Barenbaum A.A. Shpekin M.I. About age of the lunar surface // Vestnik ONZ RAS, V.3, NZ6011, 2011, doi:10.2205/2011NZ000141.
- [10] Barenbaum A.A., Shpekin M.I. Problem of lunar mascons: An alternative approach // J. of Physics: Conf. Ser. 2018, 946, 012079, doi:10.1088/1742-6596/946/1/012079.
- [11] Barenbaum A.A., Shpekin M.I. Origin and formation mechanism of craters, seas and mascons on the Moon // J. of Physics: Conf. Ser. 2019, 1147, 012057, doi:10.1088/1742-6596/1147/1/012057.
- [12] Glushneva I.N. Synthetic indicators of color and energy distribution in the spectra of solar-type stars // Astronomicheskij zhurnal. 1994. V. 71, № 4, P. 652–656.
- [13] Marov M.Ya. Planets of the Solar System (Moscow, PH: Nauka) 1981.
- [14] Ruskol E.L. Natural satellites of planets // Itogi nauki i tekhniki. Astronomiya. (PH: VINITI). 1986. V. 28, P. 3–116.
- [15] Brounlee D.E. Interplanetary dust – its physical nature and entrance to atmosphere of terrestrial planets // Comets and Origin of Life. Ed.: Ponnmpuruma C., Reidel D. Dordrecht: Holland /Boston: U.S.A. London: England. 1981.
- [16] Simonenko A.N. Asteroids (Moscow, PH: Nauka,) 1985.

PROBLEMS OF INTERPRETATION CRATER DATA IN THE SOLAR SYSTEM

A.A. Barenbaum¹, M.I. Shpekin²

¹ Oil and Gas Research Institute RAS, Gubkin str. 3, Moscow, 119333, Russia, azary@mail.ru;

² Kazan Federal University, Kremlyovskaya 18. Kazan, Tatarstan 420008, Russia, michaelis1@yandex.ru

Keywords:

galactic comets, origin craters, mares and mascons.

Introduction

The study of the Solar System planets and their satellites in recent years has put a number of fundamental problems before the comparative planetology. The first is the discovery water on Moon, Mars, Mercury, as well as satellites of giant planets and large asteroids. The second problem is the presence of large craters and mares on Moon, Mars and Mercury. In the lunar mares with $D > 218$ km under a layer of basaltic lava, clusters of mantle matter – mascons, creating positive Bouguer gravity anomalies have been revealed [1–3]. It is believed [4, 5] that most of craters and mares on Moon, Mars and Mercury were created by interplanetary bodies, which fell from 4.1 to 3.8 billion years ago during so-called “late heavy meteorite bombardment” [6].

The problem of interpretation crater data

These views however face serious difficulties caused by explaining the size-distribution of craters. These difficulties apply both to “continental” craters on upland areas of surface (Fig. 1), and “marine” craters in mares (Fig. 2). Density of continental craters is 1–2 orders of magnitude greater than craters in mares, and at this their size distribution is equally complex for different planets. The authors of [2, 7] believe that it is impossible to explain the origin of continental craters by the falls of cosmic bodies with size distribution, as in the modern asteroid belt.

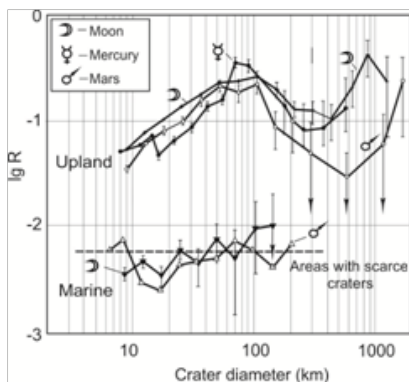


Fig. 1. Craters density in upland portions of Moon, Mars and Mercury (upper graph) and in mares (lower graph) [8]

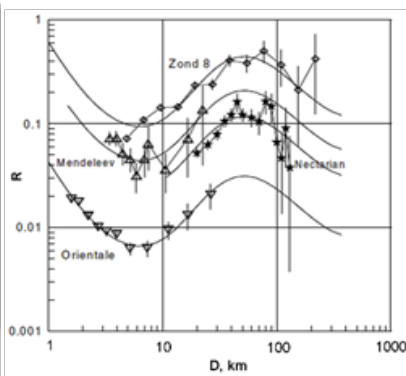


Fig. 2. Craters density with a diameter from 0.01 to 200 km in mares on Moon. Curves – theoretical craters description [5]

It is equally difficult to explain the origin of marine craters (Fig. 2). The authors of [5] approximate their distribution by a polynomial of 12 members, which is then used in estimating the age of a planetary surface from the density of craters existing on it. This relationship is expressed by the formula:

$$N(1) = 5.44 \times 10^{-14} (\exp(6.93T) - 1) + 8.38 \times 10^{-4} T,$$

Where: $N(1)$ is the number of craters with $D > 1$ km on an area of 1 km^2 ; T is the time of accumulation of craters in billion years.

When deriving the formula, it is assumed [5] that: 1) the density of craters on Moon is determined by the age of rock samples brought to Earth from

the Apollo landing sites; 2) the size distribution of crater-forming bodies and their frequency of falls have been relatively stable over the past 4 billion years; 3) the size distribution of crater-forming bodies in the first approximation is similar to modern distribution of bodies in the asteroid belt, and 4) with an increase in the craters density, the age of the surface increases.

This theoretical model is very far from reality.

New approach to interpretation of craters data

As a result of the discovery in astronomy of the phenomenon of jet outflow of matter from the center of spiral galaxies [9] and the creation on its basis of the Galactocentric paradigm [10], it has now been established that the Solar System is cyclically subjected to powerful bombardments by high-speed galactic comets. The fall of galactic comets is the main relief-forming factor for the planets, as well as the supplier of water to the planets [11].

The last comet bombardment occurred from 5 to 0.7 million years ago. The comets are moved relative to the Sun at a speed of about 450 km/s, consisted mainly of water ice, had mass of $\sim 10^{12}$ – 10^{17} g and energy of $\sim 10^{20}$ – 10^{25} J, and their size distribution was exponential. During this bombardment, an area of the surface of the planet with an area of 100×100 km² could fall ~ 13 comets of all sizes [12].

The study of the mechanisms of interaction of galactic comets with planets [9–16] shows that such a density of comet fallings leads to different effects on areas of planets with “thick” and “thin” lithosphere. In the first case (Fig. 3), comets repeatedly “plow up” the surface, which leads to its full saturation with comet craters. And in the second (Fig. 4), the imposition of craters is accompanied by melting of rocks with formation of larger mares.

We explain the lower density of cometary craters on Mars (Fig. 3) by the presence of a rarefied atmosphere in it [10], and the differences of the size-distribution of mares on Fig. 4 by the greater thickness of lunar crust on back side of Moon [14].

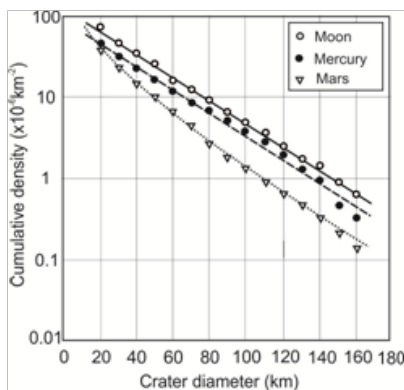


Fig. 3. Cumulative size-distribution of “upland” craters on the Moon, Mercury and Mars [10]

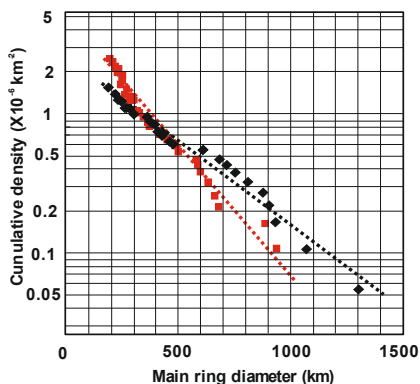


Fig. 4. Cumulative size-distribution of mares on near (red icons) and back (black icons) sides of the Moon [2]

Our other findings are as follows:

- Craters and mares on Moon, Mars and Mercury (Fig. 1) arose during the last comet bombardment 5–0.7 million years ago.
- The continents of Moon, Mars and Mercury (Fig. 3) are completely saturated with cometary craters with diameter $D \approx 10 \div 180$ km, outside this range, comet craters are absent. Craters with $D < 7$ – 10 km are “leveled” by later falls of comets, and with $D > 180$ km, these structures qualify as mares.
- Mares arise as a result of the imposition of crater funnels from the fall of many ($k > 1$) comets. With an increase in k , the diameter of the mares and the volume of magmatic melts accompanying their formation grow. Starting from $D > 218$ km [3], heating and melting of rocks reaches the man-

tle depths, which causes formation of mantle diapirs, creating Bouguer anomalies.

- Craters with $D < 7$ km on mares (Fig. 2) are created when interplanetary bodies fall. The size distribution of these craters follows the inverse quadratic dependence inherent in the asteroid belt bodies. These craters have an age of not more than 700 thousand years; they arose after the end of the last cometary bombardment and continue to arise today.

References:

- [1] Melosh H.J., Freed A.M., Johnson B.C. et al. The origin of lunar mascon basins // *Science*. 2013. V.340, Issue 6140, P. 1552-1555, doi: 10.1126/science.1235768.
- [2] Neumann G.A., Zuber M.T., Wieczorek M.A. et al. Lunar impact basins revealed by Gravity Recovery and Interior Laboratory measurements // *Sci. Adv.*, 1, 2015, e1500852, doi: 10.1126/sciadv.1500852.
- [3] Soderblom J.M., Evans A.J. Johnson B.C. et al. The fractured Moon: Production and saturation of porosity in the lunar highlands from impact cratering // *Geophys. Res. Lett.*, 2015, 42, 6939–6944, doi: 10.1002/2015GL065022.
- [4] Holsapple K.A. The scaling of impact processes in planetary sciences // *Annu. Rev. Earth Planet. Sci.* 1993, V.21, P. 333-373.
- [5] Neukum G., Ivanov B.A., Hartmann W.K. Cratering records in the inner Solar System in relation to the lunar reference system // *Space Sci. Rev.*, 2001. V. 96. 1–4, P. 55–86. doi: 10.1023/A:1011989004263.
- [6] Gomes R., Levison H.F., Tsiganis K., Morbidelli A. Origin of the cataclysmic Late Heavy Bombardment period of the terrestrial planets // *Nature*, 2005, V.435, Issue 7041. P. 466–469, doi:10.1038/nature 03676.
- [7] Woronow A. Crater saturation and equilibrium: Monte Carlo simulation // *J. Geophys. Res.* 1977. V. 82. P. 2447–2456, doi: 10.1029/JB082i017p02447
- [8] Woronow A., Strom R.G., Garkis M. Interpretation of the crater chronicle: from Mercury to Ganymede and Callisto // *Satellites of Jupiter*, ed. D. Morrison, (PH: Mir, Moscow) 1986, V. 2. P. 5–48.
- [9] Barenbaum A.A. *Galaxy, Solar system, Earth. Subordinated processes and evolution* (Moscow, PH:GEOS), 2002
- [10] Barenbaum A.A. *Galactocentric Paradigm in Geology and Astronomy* (Moscow, PH: LIBROKOM), 2010.
- [11] Barenbaum A.A. Shpekin M.I. About age of the lunar surface // *Vestnik ONZ RAS*, V.3, NZ6011, doi: 10.2205/2011NZ000141.
- [12] Barenbaum A.A., Shpekin M.I. Origin and formation mechanism of craters, seas and mascons on the Moon // *J. of Physics: Conf. Ser.* 2019, 1147, 012057, doi: 10.1088/1742-6596/1147/1/012057.
- [13] Barenbaum A.A. On the mechanism of energy dissipation of galactic comets bombarding terrestrial planets // *J. of Physics: Conf. Ser.* 2015, 653, 012073, doi: 10.1088/1742-6596/653/1/012073.
- [14] Barenbaum A.A. Shpekin M.I. To the development of the mechanism of interaction of galactic comets with the terrestrial planets // *J. of Physics: Conf. Ser.* 2016, 774, 012096, doi: 10.1088/1742-6596/774/1/012096.
- [15] Barenbaum A.A., Shpekin M.I. Problem of lunar mascons: An alternative approach // *J. of Physics: Conf. Ser.* 2018, 946, 012079, doi: 10.1088/1742-6596/946/1/012079.
- [16] Barenbaum A.A., Shpekin M.I. Origin of craters, mares and mascons on the Moon in the light of Galactocentric paradigm // *Proc. of Rus. Ann. Seminar on Experimental Mineralogy, Petrology and Geochemistry (RASEMPG-2019)*, (in press).

DETERMINATION OF GLOBAL DENSITY INHOMOGENEITIES AND STRESSES INSIDE THE MOON

N.A. Chujkova, L.P. Nasonova, T.G. Maksimova

Sternberg Astronomical Institute, Moscow State University, Universitetskii pr. 13, Moscow, 119991 Russia; chujkova@sai.msu.ru; nason@sai.msu.ru

Keywords:

Moon, internal structure, density anomalies, stresses, isostatic compensation depths, incorrect gravimetry problem, quadratic approximation

In [1], some preliminary results were obtained on the density structure of the lunar crust. In the present work, on the basis of the theory developed by us and the complex of programs for solving the inverse problem of gravimetry [2], the possible distribution of density and stresses in the depths of the Moon is determined. For this purpose, applied a new solution to the incorrect inverse problem of gravimetry, we have tested for the Earth and Mars [2, 3]. Its essence lies in the fact that the possible depths of isostatic compensation are determined for the harmonics of the decomposition of the relief heights with respect to the equilibrium ellipsoid for various degrees and orders of harmonics. Since each relief heterogeneity is characterized by a certain set of harmonics, the maximum compensation concentration of this set in a limited depth range may indicate the most probable compensation depths for the relief heterogeneity under consideration. The compensation depths obtained in this way will make it possible to solve the problem posed: to find the lateral distribution of the compensating masses at the selected depths.

Before calculating the internal anomalous structures of the moon, the contribution of the relief in the quadratic approximation was subtracted from the gravitational field of the moon. Formulas and programs to solve this problem were obtained by us in earlier works by mathematical modeling of symbolic calculations in computer algebra systems [4].

The study of the solution for both Earth and Mars [3] showed that compensation of the relief masses at one level is possible only for a certain set of harmonics. For the remaining harmonics, two compensation options were chosen, which to the least extent lead to deviations of the internal structure from the equilibrium one: 1) compensation is carried out at two levels, the first of which is the boundary the crust, the possible depths for the second level were determined from the analysis of the results obtained for the harmonics for which a solution exists. In this case, the final choice was made taking into account the weight function, inversely proportional to the deviation of the interior structure from the equilibrium one; 2) uncompensated harmonics of the relief lead to stresses in the lithosphere, provided that the stresses do not exceed the tensile strength of the lithosphere.

The final result of the work was the distribution of density anomalies in different layers of the moon (up to the lower boundary at a depth of 528 km), as well as the distribution of vertical compressive and tensile stresses. Figure 1 shows a histogram of the distribution of depths for compensating the harmonics of the relief based on the isostatic compensation hypothesis.

The histograms and average compensation depths were calculated taking into account weights corresponding to the contribution of the considered harmonics to the gravitational field (in%). From Fig. 1 it can be seen that the main compensation of the relief is carried out in the crust and in the tops of the mantle (up to a depth of 280 km), as well as on the border of the upper and middle mantle (at a depth of 528 km). The main layers of compensation are clearly traced (0 ÷ 10 km, 20 ÷ 30 km, 90 ÷ 110 km, 160 ÷ 70 km, 190 ÷ 280 km, 520 ÷ 530 km). At medium depths for each layer (3.0 km, 24.6 km, 100.3 km, 161.1 km, 238.3 km, 528.2 km), maps of lateral density anomalies for simple layers were constructed, taking into account all three compensation options, as well as a map of possible stresses in the lithosphere. The analysis of the maps shows that the main den-

sity anomalies correspond to the upper layer of the crust (to a depth of 10 km), for which the range of density variations of a simple layer is $(-11.0 \div 18.1) \cdot 10^6 \text{ kg/m}^2$). The maxima of positive density correspond to lunar mascons (Sea of Rains, Clarity, Crises, Nectar, Smith, Humboldt - on the visible side of the moon), and some of them are surrounded by a ring of negative anomalies (East Sea, Rydberg, Moscow Sea — on the back side). The map for the tops of the crust (to a depth of 10 km) also shows that the visible hemisphere of the crust corresponds mainly to positive density anomalies, and the opposite hemisphere — to negative anomalies, which apparently causes a shift in the center of mass of the moon toward the Earth. At the same time, the maximum depth variations relative to the average depth can reach $-4.3 \div 7.1 \text{ km}$ (with an average crust density of $2.55 \times 10^3 \text{ kg/m}^3$). As for maps at depths of 24.6 km, 100.3 km, 161.1 km, 238.3 km, there the density anomalies do not exceed $5.4 \times 10^6 \text{ kg/m}^2$. This leads, with variations in density at these depths of the order of $0.1 \times 10^3 \text{ kg/m}^3$ [5], to maximum variations in depths of 25–50 km, which may indicate significant heterogeneity in the upper mantle. The maximum variations in the boundary between the middle and lower mantles at a depth of 528 km reach $-32.4 \div 10.3 \text{ km}$ at latitudes of $\pm 2.5^\circ$, $\pm 32.5^\circ$, $\pm 37.5^\circ$ with an average density variation of $0.2 \times 10^3 \text{ kg/m}^3$ [5]. In the circumpolar regions, the elevation of the relief with respect to the middle sphere is determined mainly by the second zonal harmonic and reaches 40 km.

The resulting stress maps, caused by the pressure of uncompensated relief masses, recalculated to the depths of the upper crust, lead to a range of stress changes of $-14.88 \div 14.90 \text{ MPa}$, while the compression stress maxima correspond to the lunar mascons (maximum — to the Sea of Crises), and the maximum tensile stresses correspond to the lunar craters (maximum — Korolev crater). It can be noted that almost all mascons with positive compression stresses are surrounded by a ring of negative anomalies of tensile stress, especially characteristic of some seas surrounded by mountainous areas (for example, Sea of Rains, Clarity, East, Humboldt, Nectar, Smith). And areas with negative anomalies of stretching are most common on the reverse side and in the southern region and are surrounded by rings of positive compression anomalies (for example, Birkhof, Korolev, Gershprung, Bayi, Dualsky, Schrödinger, Mendeleev, Moscow Sea).

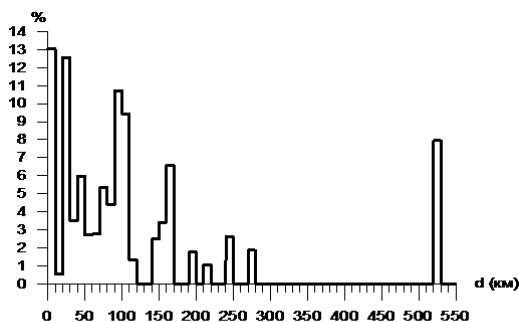


Fig. 1. Histogram of the distribution of the compensation depths for the relief harmonics with step of 10 km.

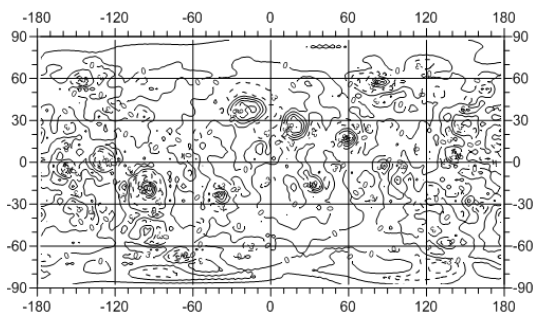


Fig. 2. Anomalies of the vertical stresses in the crust, the cross section of isolines is 3 MPa.

References:

- [1] Chuikova N.A., Rodionova Zh.F., Maksimova T.G., and Grishakina E.A. Analysis of Lunar Terrain Altitudes and Correlation Links between the Terrain and Gravitational Field; Preliminary Conclusions on the Global Density Inhomogeneities of the Lunar Crust // ISSN 0038-0946, Solar System Research, 2019, V. 53, No. 3, P. 161–171, published in *Astronomicheskii Vestnik*, 2019, V. 53, No. 3, P. 174–184.
- [2] Chujkova N.A., Nasonova L.P., Maximova T.G. The New Method to Find the Anomalous Internal Structure of Terrestrial Planets and Its Test on the Earth // 2014, IAG Symposia Series, V.144, chapter 195, P. 209-219. proceedings of the 3rd International Gravity Field Service (IGFS), Shanghai, China, June 30–July 6, 2014.
- [3] Chujkova N.A., Nasonova L.P., Maximova T.G. Density, Stress, and Gravity Anomalies in the Interiors of the Earth and Mars and the Probable Geodynamical Implications: Comparative Analysis // ISSN 1069_3513, *Izvestiya, Physics of the Solid Earth*, 2014, V. 50, No. 3, P. 427–443
- [4] Nasonova L.P., Chujkova N.A. The External and Internal Gravitational Fields of the Earth's Isostatically Balanced Crust in the Quadratic Approximation // MOSCOW UNIVERSITY PHYSICS BULLETINE, 2007, V. 62, No. 6, P. 397–405.
- [5] Gusev A., Hanada H., Petrova N., Kosov A., Kuskov O., Kronrod E. Rotation, physical librations and interior structure of the active and multi-layer Moon Monograph Kazan University Publishing Co., 2015, Kazan. 328 p, (Russian+English)

PATTERNS IN MORPHOMETRY OF MERCURY AND THE MOON: MORPHOLOGICAL MAPPING AT THE GLOBAL LEVEL

M.M. Kolenkina¹, A.Yu. Zharkova^{1,2}, I.P. Karachevtseva¹

¹ *Moscow State University of Geodesy and Cartography (MIIGAik), MIIGAik Extraterrestrial Laboratory, Moscow, 105064, Russia, maria_kolenkina@list.ru*

² *Sternberg Astronomical Institute, Moscow State University, Moscow, 119234, Russia, a_zharkova@miigaik.ru*

Keywords:

Mercury, The moon, relief features, morphometric parameters, comparative planetological analysis, morphological mapping.

Introduction:

Classification of values of relief characteristics are widely used for descriptions and explanation of Earth's geomorphology. Such parameters as interquartile range of the second derivative of heights (IQR) and relative topographic position (RTP) can help us not only to distinguish and classify geological features automatically but also to identify patterns in relief at the global level. However, methods that are usually applied to our planet can be effective for other celestial bodies with solid surface. In our work we not only calculate morphometric parameters and classify them to create morphological maps. Besides this we study distribution of parameters' values for Mercury and the Moon and compare the obtained preliminary results.

Data:

For Mercury we use high resolution MESSENGER DEMs: 1. The first global Mercury DEM with resolution 665 m/pixel (Becker et al., 2016); 2. DEMs on four Mercury quadrants with resolution ~222 m/pixel [1]. For the Moon we choose the global DEM GLD100 with a resolution of 118 m/pixel [2].

All DEMs listed above are obtained as result of photogrammetric image processing, not altimetry data. Because maps based on processing of photogrammetric DEM have better isotropy than maps developed using altimeter data, which characterize the surface roughness in the main direction along meridional-oriented orbits. For this reason photogrammetric DEMs have some advantage in calculation of morphometric parameters.

Methods:

Depending on the tasks we calculate different morphometric parameters. For example, we use interquartile range of the second derivative of heights (IQR), when we want to obtain the distribution of smooth and rough areas – plains and regions heavily covered with craters (Fig. 1a). To calculate this parameter we use a previously developed tool integrated into the ArcGIS software [3].

On the other hand, relative topographic position (RTP) applies when, when we want to select elevations (rims of craters and ridges) and depressions (bottoms of craters) automatically (Fig. 1b). RTP is almost identical to the topographic position index (TPI), but its values are normalized (converted to the range from 0 to 1) for ease of use.

The choice of these parameters is justified by the fact that they are quickly calculated by ArcGIS and clearly show the macrorelief forms (such as smooth volcanic plains, rough intercrater plains, rims of craters, relief depressions and tops of hills) without difficulties in interpretation of results. Furthermore, both parameters have already been used for transition from numerical values of morphometric parameters to morphological classes on Earth [4] and development of the Moon maps [5], which confirms the correctness of the chosen approach.

After calculating morphometric parameters, we classified their values, in other words, we determined ranges of numerical values associated with

particular types of planetary relief and made the transition from morphometry to morphology (Fig. 1c).

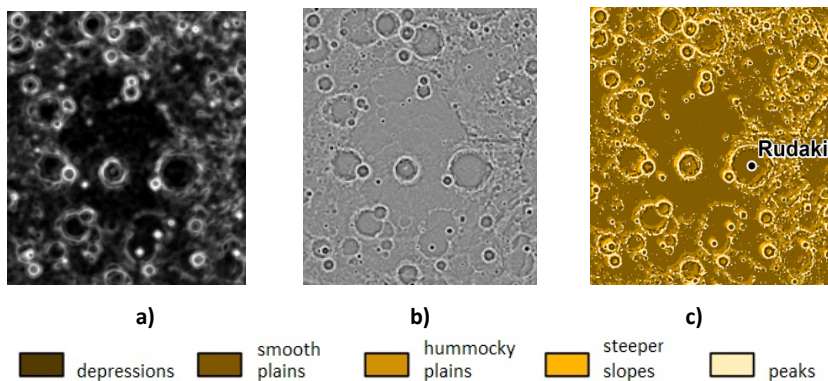


Fig. 1. Sihtu Planitia – small smooth plain on Mercury: **a)** with IQR values (dark areas – smooth plains, light – rough features); **b)** RTP values (dark areas – depressions, light – peaks); **c)** fragment of the global morphological map of Mercury with combined and classified IQR and RTP values.

We used areas of Mercury and the Moon surfaces – regions of interest with typical landforms – as training data for experiments with supervised classification technique.

Main results:

We distributed the most common large landforms among the parameters that best distinguish them and determined the ranges of numerical values that express each selected type of macrorelief (Table 1).

Table 1. Forms of macrorelief, morphometric parameters and values correspond to them.

Class on map	Parameter	Approximate range of values
Depression	RTP	0 – 0,15
Smooth plains	IQR	0,15 – 0,3
Hummocky plains	IQR	0,3 – 0,5
Slopes of highland	IQR	0,5 – 0,8
Peaks	RTP	0,8 – 1

All steps divided by morphological classes range from 0 to 1, where 0 is the minimum display of the morphometric parameter and 1 is the maximum. In addition, we worked on comparative analysis of the IQR and RTP values for Mercury and the Moon. We carry it out on the basis of comparing the distribution of areas occupied by the most common forms of macrorelief. Primarily, surfaces of celestial bodies were divided into five parts by latitudes: two polar belts (from 90° to 60°), two temperate belts (from 60° to 20°) and one equatorial belt (from 20° N to 20° S). After that, a comparison of the percentage ratio of the areas occupied by certain forms of macrorelief to the total area of a particular latitudinal belt was made.

Statistical calculations for Mercury showed that area of plains decreases from the North Pole of the planet to the south. The largest percentage of smooth plains on Mercury is observed within the northern polar belt (73.2%), where the Borealis Planitia is located. However, on the Moon the presence of the plains near the North Pole is not so significant (16.87% versus 45.03% within the northern temperate belt).

Conclusions:

In the future, we plan to use a larger number of morphometric parameters to simplify detection of more specific relief features (grooves on the Moon and scarps on Mercury) and create more detailed maps.

Such results can be used to perform comparative planetological analysis at deeper level and process data of European mission to Mercury – BepiColombo – successfully launched in 2018.

Acknowledgements:

A.Yu. Zharkova and M.M. Kolenkina were supported by Russian Foundation for Basic Research (RFBR), project № 18-35-00334.

References:

- [1] Preusker, F., Oberst, J., Stark, A., Matz, K.-D., Gwinner, K., Roatsch, T., 2017. High-Resolution Topography from MESSENGER Orbital Stereo Imaging – The Southern hemisphere, EPSC Abstracts, 11, EPSC2017-591;
- [2] Scholten F., Oberst J., Matz K.-D., Roatsch T., Wählisch M., Speyerer E.J., Robinson M.S., 2012. GLD100: The near-global lunar 100 m raster DTM from LROC WAC stereo image data. *J Geophys Res*, 117, E00H17. doi.org/10.1029/2011JE003926;
- [3] Kokhanov, A.A., Bystrov, A.Y., Kreslavsky, M.A., Matveev, E.V., Karachevtseva, I.P., 2016. Automation of morphometric measurements for planetary surface analysis and cartography. In *Int. Arch. Photogramm. Remote Sens. Spatial Inf. Sci.*, XLI-B4, 431-433. doi.org/10.5194/isprs-archives-XLI-B4-431-2016;
- [4] Jenness, J., 2006. Topographic Position Index (TPI) v. 1.3a, Jenness Enterprises. url: <http://www.jennessent.com/arcview/tpi.htm> (accessed 2 June 2019);
- [5] Kreslavsky, M.A., Head, J.W., Neumann, G.A., Rosenburg, M.A., Aharonson, O., Smith, D.E., Zuber, M.T., 2013. Lunar topographic roughness maps from Lunar Orbiter Laser Altimeter (LOLA) data: Scale dependence and correlation with geologic features and units. *Icarus*, 226, 52-66. doi.org/10.1016/j.icarus.2013.04.027.

CREATING A MUSEUM COLLECTION OF ARCHIVE DATA OF PLANET RESEARCH WITH THE HELP OF MODERN TECHNOLOGIES

M.M. Kolenkina, A.S. Garov, N.A. Kozlova, I.P. Karachevtseva

Moscow State University of Geodesy and Cartography (MIIGAIK), MIIGAIK Extraterrestrial laboratory, Moscow, Russia, maria_kolenkina@list.ru

Keywords:

The Moon, Lunokhod-1-2, Maps, Geoportal, Archive, Digital museum of planetary data.

Modern technologies make it possible to work not only with fresh data, but also involve archival information obtained during historical missions. So, following the example of NASA Regional Planetary Image Facility (RPIF), where photographic and digital data are included (<https://www.lpi.usra.edu/library/RPIF>) we have started to collect information (mostly analog) available at MIIGAIK and results of processing into an Archive of planetary data. Further plans are to represent the Archive as an open-access electronic museum, to preserve historical heritage in Space Research.

Nowadays, there is a strong breakthrough in digital technology: analog sources of information are rapidly replaced with digital format. At the same time, a large number of archival materials remain in analog form. To provide their safety and accessibility to potential users it is essential to convert the data into modern formats. So, the work on the creation of an electronic museum collection of planetary data has been started at MIIGAIK [1].

To provide access to the data we use MIIGAIK Planetary DataGeoportal (<http://cartsrv.mexlab.ru/geoportal>), where we publish results of the works of our Laboratory. However, we try to show not only new results but also archival materials for the same region of interest, so one could make a comparison or assess the quality of archival data. Practically all planetary data is so unique that it nearly never can become obsolete. For example, Lunokhods panoramic images obtained in 1970s became relevant again (after forty years!) when Lunar Reconnaissance Orbiter spacecraft (LRO) captured the Lunokhods landing sites and routes. At the Geoportal we have tried to fully provide Lunokhod data — both new (LRO NAC DEMs, orthomosaics, refined tracks) and historic (old schemas, scanned panoramas [2]) — as well as complement them with supplementary materials, such as the names of craters along the tracks, photos of crew members, in whose honor the names were given to the craters, etc. It is important to notice that GIS technologies allow us to unite such heterogeneous data in a single spatial context. Thus, it is possible to trace how the form of data presentation has changed from the era of the USSR to the present.

It is important to note that our archive contains data not only on the Moon, but also on Mercury, Mars, Phobos, Io, Ganymede, Callisto, Enceladus.

Thus, the creation of an electronic museum of planetary data solves several problems at once:

- Save archive data.
- Structuring of various information on one portal, from morphometric relief parameters to historical maps.
- Visualize all data in chronological order.
- Ability to work with data remotely from anywhere in the world.
- Wide public access to the data: the Geoportal can be used not only by scientific community, but also at schools and universities at Astronomy classes.
- Popularization of planetary research.

It is worth noting the convenience of using a geoportal in the educational process. On the basis of the electronic museum of planetary data, you can

create educational games, tests, quests of various levels of complexity and orientation, to facilitate studying.

In the future, it is planned to expand the archive with such data as thematic articles, teaching materials, interactive maps of the Moon and other planets. And also to develop a series of tasks for high school students in the framework of the curriculum of the subject Astronomy.

Acknowledgements:

The work is carried out together with the MIIGAik Educational and Historical Center (<http://www.miigaik.ru/sveden/unique/muzeum/>).

We are grateful to the Russian State Archive of Scientific and Technical Documentation which provided lunar panoramas for the research. Processing of Lunokhod panoramic images received funding from the European Community's Seventh Framework Programme (FP7/2007-2013) under grant agreement № 312377 PRoViDE.

References:

- [1] Kolenkina M., Kozlova N., Garov A., Karachevtseva I. Digital museum collection to maintain heritage in planetary research RPIF // European Planetary Science Congress 2018. EPSC2018-959.16-21 September 2018, Berlin. <https://meetingorganizer.copernicus.org/EPSC2018/EPSC2018-959.pdf>
- [2] Karachevtseva I., Kozlova N., Kokhanov A., Zubarev A., Patratiy V., Konopikhin A., Basilevsky A., Oberst J., Haase I., Joliff B., Plescia J., Robinson M., 2016. Cartography of the Luna-21 landing site and Lunokhod-2 traverse area based on Lunar Reconnaissance Orbiter Camera images and surface archive TV-panoramas. // *Icarus* 2017, Vol. 283, pp. 104–121. (Doi: 10.1016/j.icarus.2016.05.021).

USING RELIEF APPROXIMATION METHODS TO STUDY THE SURFACE OF THE MOON

M.M. Kolenkina, V.B. Nepoklonov, N.A. Kozlova

Moscow State University of Geodesy and Cartography (MIIGAIK), 105064, Gorokhovskiy per, 4, Moscow, Russia, maria_kolenkina@list.ru

Keywords:

The moon, craters, crater catalogue, morphometry, approximation methods.

Nowadays, one of the main directions in space research is the study of lunar topography and its implementation for geodetic support of the proposed lunar missions. A well-known approach to solving this problem is based on mathematical modeling. Taking into account growing requirements for the hypsometric and morphometric characteristics of the lunar relief (in terms of resolution and accuracy), we propose to use along with traditional digital elevation models, topographic models of a new class — based on the analytical approximation of the topographic surface [1].

Models of this class describe the relief using a linear combination of given analytical basic functions and numerical coefficients. These coefficients are calculated from the given relief heights under certain restrictions regarding the properties of the approximating surface. The task is reduced to solving an appropriately compiled system of linear equations. The variation of the basis functions will allow one to obtain high accuracy characteristics of the approximation in areas of almost any level of complexity. Analytical approximation methods based on integral representations (in particular, the S-approximation method [1]) provide wide possibilities of adaptation to the initial data and for increasing the accuracy of topography description. To date, there are such algorithms for solving systems of algebraic equations that can be efficiently used in the numerical implementation of these methods [2].

The prerequisites for the use of analytical approximation methods for studying the surface of the Moon can also be attributed to the fact that analytical models are convenient for studying and refining the main morphometric parameters of lunar craters, such as depth to diameter ratio, rim shape, slope steepness [3].

Another advantage of analytical approximation methods is that they can be used to simulate not only the topography field, but also other physical fields of the Moon, for example, the gravitational field [4]. The S-approximation method can reveal and clarify the depth of the anomalous substance under the surface of the lunar crust. Together with the morphometric characteristics, refined using the analytical approximation methods, this will expand our understanding of the internal structure of the Moon and the history of its formation.

References:

- [1] Strahov V.N. Linejnye analiticheskie approksimacii rel'efa poverhnosti Zemli // V.N. Strahov, I.A. Kerimov, A.V. Strahov // Geofizika i matematika: materialy 1-j Vseross. konf. M.: OIFZ RAN, 1999. P. 199–212 (in Russian).
- [2] Raevskij D.N. Razrabotka novyh effektivnyh iteracionnyh metodov resheniya sistem algebraicheskikh uravnenij obratnyh zadach geofiziki na osnove metoda integral'nyh predstavlenij // Dissertaciya http://www.ifz.ru/fileadmin/user_upload/autoreferats/2016/Raevskij/Dissertation_Raevskij.pdf (in Russian).
- [3] Kolenkina M., Kozlova N., Zavyalov I., Basilevsky A. Morphometry of lunar craters having 1–10 km in diameter // The Ninth Moscow Solar System Symposium, Space Research Institute, 9MS3-PS-80.
- [4] Strahov V.N., Strahov A.V. Approksimacionnyj podhod k resheniyu zadach gravimetrii i magnitometrii. Ch. 1. // Rossijskij zhurnal nauk o Zemle. 1999. V. 1. No 4. P. 271–299 (in Russian).

INTERACTIVE GLOBE OF THE DIGITAL ELEVATION MODEL OF MOON RELIEF

O.S. Tretyukhina, E.N. Slyuta

Vernadsky Institute, Moscow, Kosygina street 19, 119334, lekanosova@gmail.com;

Keywords:

Globe, DEM, Moon relief, GIS, LRO, LOLA

Introduction:

For illustrative purposes of the simulation of the navigation situation while approaching the moon, an interactive globe was created using DEM in Arc-Gis(ArgGlobe).

The process of globe building:

First 10 DEM were downloaded from the site of NASA [1]: 8 parts 90×60 degrees, covering the all surface of the Moon up to 60 parallel and 2 DEM on the Poles. To facilitate the process all the data were combined into one common model, which was done by the Mosaic tool (data management tools). By the tool Hillshade (special analyst tools) white black map was create in rectangle projection on the scale of 1:40 000 000, where black colour means minimal height and white – maximum height (Fig. 1). And 2 similar maps of the Poles in stereographic projection on the scale of 1:10 000 000 (Fig. 2).

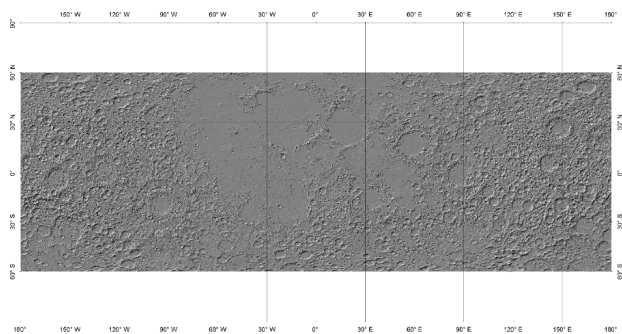


Fig. 1. White-black relief map of the all Moon surface.

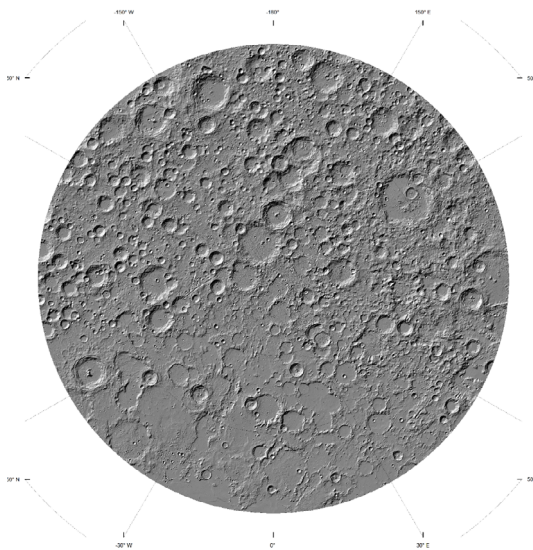


Fig. 2. White-black relief map of the Moon North Pole.

ArcGlobe allows to reproject the data on the sphere. There life maps were added as draped layers, which use other layers as an elevation data source. The interactive globe can be rotate and zoomed. Also, you can get coordinates of any place within 0,0001 degree by clicking on it (Fig. 3). There solution of the globe is the same as data source – from 100 to 128 meters/pixel.

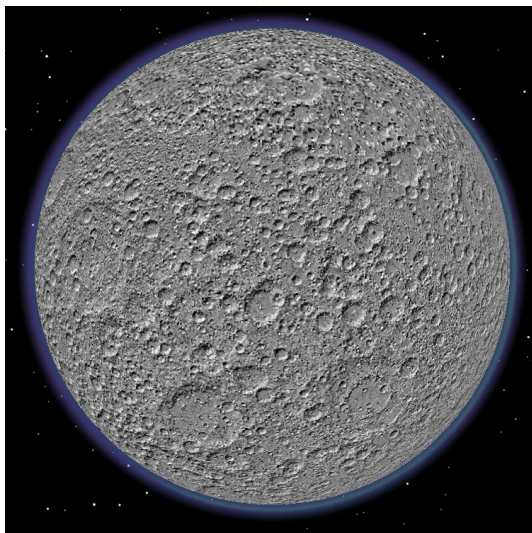


Fig. 3. Screenshot of the globe.

Results:

Eventually it was created some small-scale maps:

- small-scale DEM with resolution 100 meters of middle latitudes by 60° on the scale of 1:40 000 000;
- small-scale DEM with resolution 128 meters of the Poles from 60° to 90° on the scale of 1:10 000 000;
- interactive globe of the all Moon surface based on these small-scale maps.

References:

- [1] <https://pds-geosciences.wustl.edu/>

ANGULAR MOMENTA OF COLLIDING RAREFIED CONDENSATIONS AND FORMATION OF THE EARTH-MOON SYSTEM

S.I. Ipatov

Vernadsky Institute of Geochemistry and Analytical Chemistry of Russian Academy of Sciences, Moscow, Russia, siipatov@hotmail.com

Keywords:

Rarefied condensations, angular momentum, satellite systems, the Earth-Moon system

Introduction:

It is considered that there was a stage of rarefied condensations during evolution of the Solar System. Masses of the condensations could exceed masses of the largest asteroids. Condensations that formed at collisions of condensations could acquire the angular momenta which are needed for formation of satellite systems as a result of compression of condensations [1]. Ipatov studied formation of trans-Neptunian satellite systems [1–2] and embryos of the Earth-Moon system [3] at the stage of condensations. The previous studies were based on the model of the collision of two condensations that moved in circular heliocentric orbits at the moment of the collision. Below we consider also eccentric orbits of collided condensations.

Angular momentum acquired at a collision of two condensations moved in circular orbits at the moment of the collision:

The angular momentum at a collision of two condensations (with radii r_1 and r_2 and masses m_1 and m_2) moved before the collision in circular heliocentric orbits is equal to $K_s = k_o \cdot (G \cdot M_s)^{1/2} \cdot (r_1 + r_2)^2 \cdot m_1 \cdot m_2 \cdot (m_1 + m_2)^{-1} \cdot a^{-3/2}$, where G is the gravitational constant, M_s is the mass of the Sun, and the difference in semi-major axes a of condensations equals $\Theta \cdot (r_1 + r_2)$ [4]. At $r = (r_1 + r_2)/a \ll \Theta$ and $r_a \ll 1$, one can obtain $k_o \approx (1 - 1.5 \cdot \Theta^2)$. The mean value of $|k_o|$ equals 0.6. Below I present estimates for the model for which two collided condensations form a new condensation with mass $m = m_1 + m_2$ and radius $r = (r_1^3 + r_2^3)^{1/3}$. The angular velocity of such condensation equals $\omega_c = K_s / J_s = 2.5 \cdot k_o \cdot \chi^{-1} \cdot (r_1 + r_2)^2 \cdot r^{-2} \cdot m_1 \cdot m_2 \cdot (m_1 + m_2)^{-2} \Omega$, where $\Omega = (G \cdot M_s)^{1/2} a^{-3/2}$ is the angular velocity of the motion of the condensation around the Sun. $J_s = 0.4 \cdot \chi \cdot m \cdot r^2$ is the momentum of inertia of the condensation, and $\chi = 1$ for a homogeneous sphere. Nesvorny et al. [5] made computer simulations of compression of condensations in the trans-Neptunian belt for initial angular velocities of condensations equal to $\omega_o = k_w \Omega_o$, where $\Omega_o = (G \cdot m)^{1/2} r^{-3/2}$ is the angular velocity of the motion in a circular orbit of radius r around the gravity center of mass m . Nesvorny et al. [5] obtained binaries and triples only at k_w equal to 0.5 or 0.75. For most their runs $r = 0.6 r_H$, where r_H is the Hill radius for mass m . Note that $\Omega_o / \Omega = 3^{1/2} (r_H / r)^{3/2} \approx 1.73 (r_H / r)^{3/2}$, e.g., $\Omega_o \approx 1.73 \Omega$ at $r = r_H$. So $\omega_o = k_w \Omega_o \approx 1.73 k_w \Omega_H^{-3/2}$, where $k_H = r / r_H$. Galimov & Krivtsov [6] made calculations of compression of condensations which masses were equal to the mass of the Earth-Moon system, and which radii exceeded by a factor of 5.5 the radius of the body of Earth's density which mass equaled to the mass of this system (i.e., the radius of the condensation was smaller by a factor of 40 than the Hill radius). In their 3D model, satellite systems formed at $1 \leq \omega_o / \Omega_o \leq 1.5$. These values of ω_o / Ω_o exceeded by a factor of about 2 the values 0.5 and 0.75, at which formation of satellites was obtained in [5]. We can suppose that formation of satellites is possible at smaller ratios of radii of preplanetesimals to their Hill radii (for not smaller values of ω_o / Ω_o) than in [5].

At $r_1 = r_2$, $r^3 = 2r_1^3$, $m = m_2 = m/2$ and $\chi = 1$, we have $\omega_c \approx 1.575 k_o \cdot \Omega$. Considering $\omega_c = \omega_o \approx 1.73 k_w \Omega_H^{-3/2}$, one can get $k_H \approx (1.1 k_w / k_o)^{2/3}$, e.g. $k_H \approx (1.83 k_w)^{2/3}$ at $k_o = 0.6$. For $k_w = 0.5$ and $k_o = 1$, $k_H \approx 0.67$. For greater k_w and smaller k_o , k_H is greater than 0.67. The above estimates show that initial angular velocities at which satellite systems formed in simulations presented in [5] could be acquired at collisions of condensations that formed the parental condensation. The radii of collided condensations should not differ much from their Hill radii.

The values of k_H could be smaller than those for the above estimates, if we take into account the eccentricities of heliocentric orbits of colliding condensations. A small increase of the estimates of the angular momentum could be due to initial rotation of condensations. If the value of ω_c would be greater (mainly due to consideration of eccentric orbits) by a factor of k_e than that for the model considered above (at the beginning of this paragraph), then the estimates of k_H would be smaller by a factor of $k_e^{2/3}$.

Let us consider a collision of two condensations with masses $k_m \cdot m$ and $(1-k_m) \cdot m$ (where $0 < k_m < 1$), with initial angular velocity equal to 0.2Ω , and with the same χ and initial density ρ . In this case, the component of the angular momentum K_s of the formed condensation caused by initial rotation equals to $K_{si} = 0.2\Omega(0.4\chi \cdot m \cdot r_{in}^2)[(1-k_m)^{5/3} + k_m^{5/3}]$, where r_{in} is the radius of a condensation of mass m and initial density ρ . The component of K_s of the formed planetesimal with a radius r_{col} which is caused by the collision equals $K_{sc} = k_{col} \cdot \Omega \cdot m \cdot r_{col}^2 \cdot k_m \cdot (1-k_m) \cdot [(1-k_m)^{1/3} + k_m^{1/3}]^2$. $K_{si} > K_{sc}$ at $r_{in}/r_{col} > 2.7$, $\chi=1$ and $k_{col}=0.6$. This suggests that collisions produced the dominant contribution to angular momentum only when the sizes of homogeneous preplanetesimals did not differ significantly (by not more than a factor of 3) from the initial sizes. At $k_{col}=\chi=1$ and $r_{col}=r_{in}$ the ratio K_{sc}/K_{si} equals 12.5, 3 and 0.8 at k_m equal to 2^{-1} , 9^{-1} and 28^{-1} (i.e., at the ratio k_{col} of radii of collided condensations equal to 1, 2 and 3), respectively. It means that for the considered model at the ratio k_{col} of radii of collided uniform condensations of different masses greater than 3, the role of initial rotation in the angular momentum K_s of the formed condensation is greater than that of the collision.

Angular momentum acquired at a collision of two condensations moved in eccentric orbits:

As one of the model implementations, a disk with a width of 0.4 AU was considered, consisting of 100 identical condensations with masses equaled to $0.01m_E$ (where m_E is the Earth's mass). At $a=1$ AU, the Hill radius r_H of such condensation is about 0.002 AU. Let us consider a model for which a condensation moves under the gravitational influence of the Sun and one another condensation. For initially circular heliocentric orbits of condensations and not large time elapsed before the collision, two condensations with radii of Hill spheres could collide if the difference $d = a \cdot k$ between initial values of a of their orbits is less than about $3.5r_H$ [8–9]. If the initial angle with vertex in the Sun between directions to two condensations is greater than 60° , then condensations with $d < r_H$ will not collide. For such a model, if the difference between semi-major axes $a \approx 1$ AU of close orbits is about $0.004 a$, then each condensation has about $5 \times 0.002 / 0.004 \approx 2$ candidates for collisions (1 with greater, and 1 with smaller semi-major axis). So such estimate of the time elapsed before a collision would be similar to that for consideration of only two condensations. Actually all condensations did not form at the same time and could be smaller than r_H . If there were only two condensations with masses of $0.01m_E$ which could collide, then the mean value of the angular distance ϕ between two condensations is about π rad. As the period of a revolution around the Sun is proportional to $a^{3/2}$, then during one revolution around the Sun, the angle ϕ decreases by about $2\pi(3k_a/2) = 3\pi k_a$. So about $\pi / (3\pi k_a) = (3k_a)^{-1}$ revolutions are needed to reach $\phi=0$. At $a k_a = 2r_H$ and $r_H = 0.002a$, we have $k_a = 0.004$ and the condensations could collide after about 100 revolutions. As discussed above, the diameters of these condensations must not change considerably during this time.

If an aphelion distance of an orbit of a "first" condensation is $a + a \cdot k_a = a + r_{H_a} \cdot k_{H_a}$ and this condensation collides with a "second" condensation, which has a semi-major axis a and circular velocity v_c , then its eccentricity can be about $k_a = k_{H_a} \cdot (r_{H_a}/a)$. At a collision of the condensations, the tangential component v_{te} of the collision velocity can be about $e \cdot v_c$, e.g. about $k_{H_a} \cdot v_c \cdot r_{H_a}/a$. At a collision of two condensations that moved before the collision in circular heliocentric orbits, the tangential velocity of the collision equals to $v_{tc} = k_{col} \cdot v_c \cdot (r_1 + r_2)/a$. At $k_{col}=0.6$ and $r_{col}=r_2$, $v_{tc} = 1.2 \cdot v_c \cdot r_{H_a}/a$. At $k_{H_a}=2.4$ the above value of $v_{te} = k_{H_a} \cdot v_c \cdot r_{H_a}/a$ is greater by a factor 2 than the above value of v_{tc} . So the tangential velocity and the angular momentum of such collided condensations could be greater

by a factor of 2 than those for circular orbits. Due to gravitational influence of other objects in the forming Solar System, the eccentricities of condensations could be greater than those for the model considered above. For a greater tangential velocity, the formation of a satellite system can take place at a greater difference in masses of collided condensations and/or at smaller sizes of condensations. However, the greater is the velocity of a collision of condensations, the less material can be left in the condensation formed as a result of collision, and more material can be left in the forming condensation.

Conclusions:

The angular momenta K_s of rarefied condensations that are needed for formation of satellite systems as a result of contraction of the condensations could be acquired at collisions of condensations. The angular momentum could be greater for eccentric than for circular heliocentric orbits of colliding condensations. At a greater K_s , collided condensations, that produce the condensation parental for a satellite system, could be smaller in sizes and differ more in masses. A time between formation of two condensations and their collision that produce the condensation which was parental for the embryos of the Earth-Moon system could be of the order of 100 years.

Acknowledgements:

The work was supported in part by the grant of Russian Foundation for Basic Research № 17-02-00507 A.

References:

- [1] Ipatov S.I. Formation of trans-Neptunian satellite systems at the stage of condensations // *Solar System Research*. 2017. V. 51, N 4, P. 294–314. <https://arxiv.org/abs/1801.05217>.
- [2] Ipatov S.I. Origin of orbits of secondaries in the discovered trans-Neptunian binaries // *Solar System Research*. 2017.V. 51, N 5, 409-416. <https://arxiv.org/abs/1801.05254>.
- [3] Ipatov S.I. Formation of embryos of the Earth and the Moon from the common rarefied condensation and their subsequent growth // *Solar System Research*. 2018. V. 52. N 5, P. 401-416.
- [4] Ipatov S.I. The angular momentum of two collided rarefied preplanetesimals and the formation of binaries // *Mon. Not. R. Astron. Soc.* 2010. V. 403. P. 405–414. <http://arxiv.org/abs/0904.3529>.
- [5] Nesvorny D., Youdin A.N., Richardson D.C. Formation of Kuiper belt binaries by gravitational collapse // *Astron. J.* 2010. V. 140. P. 785–793.
- [6] Galimov E.M., Krivtsov A.M. Origin of the Moon. New concept. De Gruyter. Berlin. 2012. 168 p.
- [7] Safronov V.S. Evolution of the protoplanetary cloud and formation of the Earth and the planets. NASA TTF-677. 1972. 212 p.
- [8] Ipatov S.I. Migration of celestial bodies in the solar system. Editorial URSS Publishing Company, Moscow. 2000. 320 p., in Russian. http://www.rfbr.ru/rffi/ru/books/o_29239.
- [9] Ipatov S.I. Gravitational interaction of two planetesimals moving in close orbits, *Solar System Research*. 1994. V. 28. N 6. P. 494–512.

THE FOCUSING EFFECT OF P-WAVE IN THE MOON'S AND EARTH'S LOW-VELOCITY CORE. ANALYTICAL SOLUTION

A.G. Fatyanov¹, V.Yu. Burmin²

¹ *Russian Academy of Sciences Novosibirsk Scientific Centre Institute of Computational Mathematics and Mathematical Geophysics, Akademika Lavrentjeva 6, Novosibirsk 630090, Russia, fat@nmsf.sccc.ru*

² *Schmidt Institute of Physics of the Earth, Russian Academy of Sciences, Bolshaya Gruzinskaya 10 Moscow 123995, Russia. burmin@ifz.ru*

Keywords:

Analytical solution. Inhomogeneous sphere. Wave field. Moon. Earth. Liquid core. Collecting lens. Focus effect.

Introduction:

The important aspect in the study of the structure of the interiors of planets is the question of the presence and state of cores inside them. While for the Earth this task was solved long ago, the question of whether the core of the Moon is in a liquid or solid state up to the present is debatable up to present. If the core of the Moon is liquid, then the velocity of longitudinal waves in it should be lower than in the surrounding mantle. If the core is solid, then most likely, the velocity of longitudinal waves in it is higher than in the mantle. Numerical calculations of the wave field allow us to identify the criteria for drawing conclusions about the state of the lunar core.

In this report we consider the problem of constructing a stable analytic solution for wave fields in a layered sphere of arbitrary size. After the Fourier-Legendre transformations, the statement of the problem reduces to the consideration of a two-parameter family of boundary-value problems for ordinary differential equations. The solution of the latter problem in each spherical layer is in the form of a linear combination of Bessel functions [1]. The unknown coefficients are determined from known conjugation conditions on the boundary of spherical layers. As a result, a matrix system of linear equations is obtained for their determination. For a small number of layers, its solution can be obtained in explicit form. Since Bessel functions of different types tend to zero and infinity rapidly, uncertainty arises in the solution. And the more the radius of the sphere in relative values (wavelengths), the faster it arises. In this situation, computer calculations become unstable. To construct a stable solution, it is proposed to use the classic asymptotic of Bessel functions [2]. In the article [3] it is shown that the classical asymptotic behavior of Bessel functions gives an error in the solution. To construct the solution, we use the new asymptotes of cylindrical functions obtained in the article [3]. This gives a stable analytical solution for wave fields in an inhomogeneous sphere of arbitrary size.

Formulation of the problem:

The mathematical statement of the problem of modeling the P-wave is formulated in a spherical coordinate system ($0 \leq r \leq R_1$, $0 \leq \theta \leq \pi$, $0 \leq \phi \leq 2\pi$) as follows: define a function from equation

$$\frac{1}{v^2(r)} \frac{\partial^2 u}{\partial t^2} = \frac{1}{r^2} \frac{\partial}{\partial r} \left(r^2 \frac{\partial u}{\partial r} \right) + \frac{1}{r^2 \sin \theta} \frac{\partial}{\partial \theta} \left(\sin \theta \frac{\partial u}{\partial \theta} \right) + \frac{1}{r^2 \sin^2 \theta} \frac{\partial^2 u}{\partial \phi^2} + f_r \times f(t) \quad (1)$$

with initial conditions and boundary data

$$u = \frac{\partial u}{\partial t} \Big|_{t=0} = 0, \quad \frac{\partial u}{\partial r} \Big|_{r=R_1} = 0. \quad (2)$$

In (1), (2) R_1 – the radius of the sphere, f_r – is the source function over space, is the source function with respect to time t .

At boundaries $r=R_1$ where the velocity of longitudinal waves $v(r)$ suffers a discontinuity, known conjugation conditions are introduced [1]:

$$[u] = \left[\frac{\partial u}{\partial r} \right] \Big|_{r=R} = 0.$$

Analytical Solution Results:

Figure 1 shows the result of calculating P-waves for a simplified model of the Moon, consisting of a mantle and a low-velocity core. The velocity of longitudinal waves in the mantle is 7.8 km/s, in the low-velocity core is 5.81 km/s. The radius of the Moon is 1,737 km. The radius of the low-velocity core is 380 km. Time source function $f(t)$ is taken in the form of a Gauss-Puzzyrev pulse [3]:

To clarify this effect, figure 2 shows the drawing of rays. The rays exit the source at a uniform pitch. Figure 2 clearly shows that the low-velocity core has the properties of a collecting lens. There is a focus area around 180 degrees. We can see a strong expansion of the amplitude of the amplitude around 180 degrees on this figure. This increase in the amplitude is denoted by L (Lens). This fully corresponds to the ray pattern shown in Figure 2. The low-velocity core on the Moon has the properties of a collecting lens. A focus area appears. This leads to the formation of a powerful wave.

Figure 3 shows the result of calculating P-waves for a simplified model of the Moon consisting of a mantle and a high-velocity core. The velocity of longitudinal waves in the mantle is 7.8 km/s, in the high-velocity core — 10.0 km/s. The radius of the high-velocity core is also taken equal to 400 km. Here the arrow indicates the beginning of the shadow zone for the direct wave P propagating in the mantle of the Moon. And Figure 4 shows the drawing of rays. It can be seen from Figures 3 and 4 that the high-velocity core of the Moon does not possess the properties of a collecting lens.

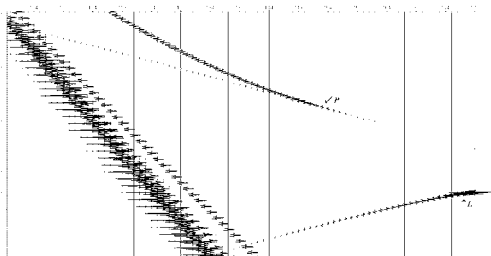


Fig. 1. Fragment of the wave field of P-wave for the Moon model with a low-velocity core. The arrow marks the beginning of the shadow zone for the refracted wave. L - a focusing effect of the low-speed core of the Moon

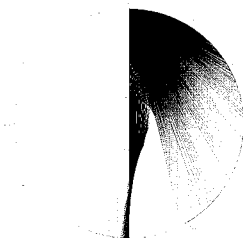


Fig. 2. The pattern rays for the Moon model with a low-velocity core.

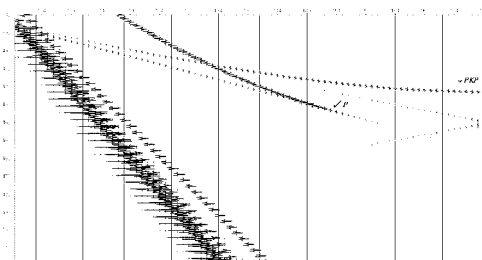


Fig. 3. Fragment of the wave field of P-waves for the Moon model with a high-velocity core with the first arrival of PKP-waves. The arrow marks the beginning of the shadow zone for the refracted wave.

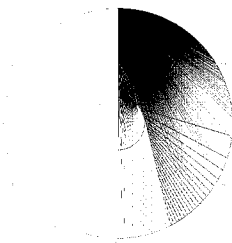


Fig. 4. The pattern rays for the Moon model with a high-velocity core.

Conclusions:

We obtained a stable analytical solution for the wave fields of longitudinal waves in a two- and three-layer sphere of arbitrary size. This made it possible to calculate the total wave fields for simplified models of the Moon and the Earth with real parameters. The results of mathematical modeling and ray pattern showed that the low-velocity cores of the Moon and the Earth possess the properties of collecting lenses.

As a result of focusing, waves of considerable amplitude appear on the surface of the Moon and the Earth. And on the surface of the Earth they come before the first entry of the PKP-wave. These are so-called “precursors” which continue in the subsequent arrivals of waves.

We also note that the detection of the effect of focusing region appearance of the oscillations emerging on the surface in the first arrivals is extremely important in elucidating the question of the state of the core not only for the Earth and the Moon, but also for other planets. If it were possible to detect the above oscillations on lunar seismograms, the question of the state and size of the core, as well as the velocity of longitudinal waves in the lunar core, would be decided unambiguously. For the currently considered models of the inner structure of the Moon, the oscillations generated by focusing inside the core must reach the surface of the Moon at distances of 180–220 degrees, or in the opposite direction in the range of 140–180 degrees. Unfortunately, at present no such oscillations are detected in the indicated range of angles [5].

References:

- [1] Tikhonov A.N. and Samarskii A. A. Equations of mathematical physics [in Russian]. Nauka, Moscow, 1997.
- [2] Korneev V.A. and Johnson L.R. // *Geophys. J. Int* 1993. No. 115. P. 230–250.
- [3] Fatyanov A.G. The stable analytical solution for the wave fields in the sphere [in Russian], *Mat. Zamet. SVFU*, 2016, 23, No. 3, P. 91–103.
- [4] Burmin V.Yu Seismic wave velocities in the Earth's core // *Izvestiya. Physics of the Solid Earth*. 2004. T. 40. No. 6. P. 477–490.
- [5] Lognonné P., Gagnepain-Beyneix J., Chenet H. *Earth and Planetary Science Letters*. 2003. Vol. 211. P. 27–44.

MODULATED LUNAR ORBITING FREQUENCIES AND CORRESPONDING THEM STRUCTURES (CHANG'E 3 & 4)

G.G. Kochemasov

IGEM of the Russian Academy of Sciences, 35 Staromonetny, 119017 Moscow, Russia, kochem.36@mail.ru

Keywords:

Moon, orbital frequencies, modulation, Solar system, Galaxy, fine rippling

Introduction:

Intersecting ripples of certain wavelengths and produced them tectonic granules are inversely proportional to the satellite main orbital frequencies (1/1 month — $\pi R/4$ and 1/1 year- $\pi R/60$ for the Moon) and calculated side frequencies (division and multiplication of the higher frequency by the lower one- $\pi R/15$ and $\pi R/240$) (Fig. 3) [4]. The granules can be observed on the lunar surface more or less pronounced. Often they are confused with impact craters but their even sizes and regular shoulder-to-shoulder disposition in lines and grids normally solve the problem.

Rare chances present the landings of the Chinese probes Chang'E 3 & 4 on the Mare Imbrium and SPA areas. Landing surface possibly cleaned by thruster jets of landing device revealed clear crossing lineation of a few centimeters spacing and produced them granules. This very fine granulation fortunately can be calculated comparing it with a track of the Yutu' rover wheel. (about 10 cm wide) (Fig.1, 2). An explanation of the granule size should be done with the above modulation procedure using two frequencies as was done for some celestial bodies earlier [4–7]. The Moon main frequencies are 1/1 year and 1/1 month, the modulating Galaxy frequency is about 1/200 000 000 years. A scale is the Earth's orbiting period 1 year with the corresponding tectonic granule size $\pi R/4$ [6–7].

Calculations for the Moon:

(1y. : 200 000 000y) $\pi R = (1 : 200 000 000) 3.14 \times 1738 \text{ km} = 5.46 \text{ cm}$ wave length for the circumsolar orbiting (or 0.46 cm wavelength for the around Earth orbiting). By the same galactic frequency modulation one obtains enigmatic metric radio waves for the Sun and decametric waves for Jupiter [5–7]. Amalthea has 4.88cm (for the circumsolar fr.), 0.0028 mm (circumjovian fr.), the Moon 5.46 cm (circumsolar fr.), 0.46 cm (circumterrestrial fr.) [5–7]. It is interesting that an enigmatic extra heat emission of Amalthea and its pronounced red color could relate to these calculated microwave and infrared emissions. Radio emission of the Moon at 2.5 cm wavelength was described in Berezhnoi et al., 2001 [1]. It is worth to note that well known radio wave and gamma-ray background observations are added by soft X-rays emitting from various celestial bodies – from cold comets to the hot Sun and measured by the Chandra X-ray Observatory [2].

The Chinese Chang'E-1 orbiter was equipped with a passive microwave radiometer (MRM) to measure the natural microwave emission from the lunar surface. The microwave emission, characterized by a frequency-dependent brightness temperature (TB), is related to the physical temperature and dielectric properties of the lunar surface. By measuring the brightness temperatures at different frequencies, detailed thermal behavior and properties of the lunar surface can be retrieved. The resulting maps show fine structures unseen in previous microwave maps that disregarded the local time effect. The new features revealed and their possible connections with the lunar geology were discussed. Daytime brightness temperatures are found to correlate well with TiO₂ abundance by numerical analysis [8].

In an earlier publication Chan et al. [3] indicated that resulting maps from the high frequency microwave channel show lunar topographic signatures with close similarity to those seen in Clementine's lunar topographic maps, while the low frequency channels reveal intriguing lunar surface properties

not previously observed. Two characteristics displayed by the filtered brightness temperature maps are discussed: in the high frequency maps the existence of an anti-correlation between daytime and nighttime brightness temperature deviations in certain regions (especially in the lunar maria), and in the low frequency maps the appearance of cold spots which correspond with the hot spots observed in the infrared during lunar eclipses.

Thus, some relationship between lunar microwave emission and the geological background was discussed earlier [1, 3, 8]. In the present work we show existence of the fine crossing rippling of the lunar surface at the microwave lengths and its origin indicating at galactic structuring trace.

Similar fine cm-size crossing rippling is clear in images of the Chang'E-4 (Fig. 2). Thus, this modulation process, involving orbital frequencies of the Moon and Galaxy, is observed at the northern and southern lunar hemispheres as well as in the near and far lunar sides. Now, one might speak about the whole Moon modulation event. It is worth to note that the same approach is applied to calculating frequencies of the martian global dust storms (joint consideration of the rotation and orbiting of Mars-spin-orbit coupling) [9, 10].



Fig. 1. Yutu's rover wheel track on Mare Imbrium surface clearly showing fine inter-crossing lineation (centimeters spacing). A portion of Chang'E 3 image 00.



Fig. 2. Chang'E 4 image. DwEFLgUwAEMFq-1.jpg .

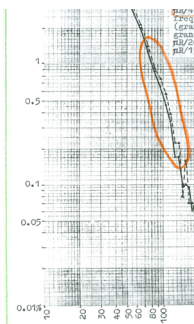


Fig. 3. Frequency-lunar crater size curve. Main and side lunar frequencies and corresponding them crater sizes.

References:

- [1] Berezhnoi A.A., Bervalds E., Khavroshkin O.B., Ozolins G., Shevchenko V.V, Tsyplakov V.V. (2001) Radio emission of seismic origin from the Moon at 25 mm during the Leonid 2000 meteor shower // First Convention of Lunar Explorers, 8th to 10th March, 2001, Programme and Contributed Abstracts, Palais de la Découverte, Paris, France, p. 2.
- [2] Bhardwaj A. , Gladstone G. R. , Elsner R. F. et al.(2002) Soft X-Ray emissions from planets and moons // ESLAB 36: Earth-like planets and moons, Programme and abstract book, ESTEC, Noordwijk, The Netherlands, 3-8 June 2002, Abstract # 23.
- [3] Chan K.L., Tsang K.T., Kong B., Zheng Y-C. (2010) Lunar regolith thermal behavior revealed by Chang'E-1 microwave brightness temperature data // EPSL, v. 295, (1-2), 2010, 287-291.
- [4] Kochemasov G.G. (2001) On one condition of further progress in lunar studies // First Convention of Lunar Explorers, 8th to 10th March, 2001, Programme and Contributed Abstracts, Palais de la Découverte, Paris, France, p. 26
- [5] Kochemasov G.G. (2003) Universe of oscillations: sound-radiowaves-gamma-rays-ether // Geophysical Research Abstracts, Vol. 5, 02159, 2003;
- [6] Kochemasov G.G. (2008) Wave modulations in the Solar system bodies and their radio emissions // Geophysical Research Abstracts, Vol. 10, EGU2008-A-01272, 2008. SRef-ID: 1607-7962/gra/EGU2008-A-01272, EGU General Assembly 2008.
- [7] Kochemasov G.G. (2002) Radiowaves and tectonic dichotomy: two sides of one coin // Geophysical Research Abstracts, Vol. 4, 2002, European Geophysical Society XXVII General Assembly, Nice, France, 21-26 April 2002.
- [8] Zheng Y.C., Tsang K.T., Chan K.L., Zou Y.L., Zhang F., Ouyang Z.Y. (2012) First microwave map of the Moon with Chang'E-1 data: the role of local time in global imaging // Icarus, 2012, v. 219, issue 1, 194-210.
- [9] Shirley J.H. (2017) Orbit-spin coupling and the circulation of the Marian atmosphere // Plan. Space Sci., 141, 1-16. 10.1016/j.pss.2017.04.006.
- [10] Kochemasov G.G. Modulated wave frequencies in the Solar system and Universe // Universal Journal of Physics and Application 12(4): 68-75, 2018. Doi: 10.13189/ujpa.2018.120402

THE NEUTRAL GAS MASS SPECTROMETER FOR THE LUNA-RESURS MISSION

R.G. Fausch¹, P. Wurz¹, M. Tulej¹, D. Lasi¹, L. Hofer¹, A. Buch², M. Cabane³, P. Coll⁴, D. Coscia³, S. Aseev⁵, M. Zaitsev⁵, M. Gerasimov⁵, A. Sapgir⁵, C. Szopa³

¹ Physics Institute, University of Bern, Sidlerstrasse 5, 3012 Bern, Switzerland, rico.fausch@space.unibe.ch

² LGPM, Ecole Centrale Paris, 92295 Châtenay-Malabry, France

³ LATMOS, Université Pierre et Marie Curie, 75252 Paris, France

⁴ LISA, Université Paris-Est Créteil, Université Denis Diderot & CNRS, 94010 Créteil, France

⁵ Space Research Institute IKI, 117997 Moscow, Russia

Keywords:

In situ mass spectrometry; Gas chromatography mass spectrometry; Luna-Resurs; Lunar volatiles; Lunar regolith analysis

Introduction:

Analysing the chemical composition of lunar polar volatile materials will give insight to the origin and evolution of solar system bodies. Additionally, if they are found in sufficient quantities, they will be a valuable resource for future exploration missions, particularly of manned missions. The Russian Luna-Resurs mission (Luna 27) is a lunar landing mission designed to land in a polar region. Our Gas Chromatograph (GC) — Neutral Gas Mass Spectrometer (NGMS) [1] will analyse volatile materials trapped in the icy lunar surface when in GC-mode. An additional measurement mode will analyse the tenuous lunar exosphere (exosphere mode).

Instrumentation and operation:

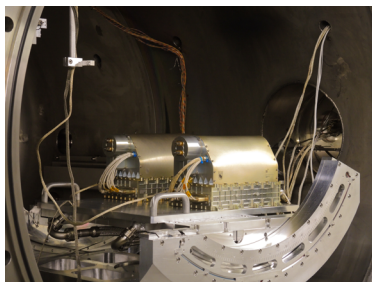


Fig. 1. The NGMS flight model and the flight spare unit during preparation for calibration tests. Each unit consumes < 25 W when in GC-mode, at a mass of < 3.5 kg and size of 18 x 26 x 15 cm.

The Gas Analytical Package (GAP) consists of a pyrolysis cell to thermally release the volatile material of the collected sample, a GC with Thermal Differential Analyzer (TDA) for chemical pre-separation and the NGMS instrument. In this measurement mode (GC-mode), the NGMS instrument will quantitatively analyse the content and identity of volatile species of the lunar regolith. This time-of-flight instrument includes an ion storage source [2], which allows for an analysis of the continuous output of the GC. It is therefore capable of analysing the chemical composition including CHON elements and noble gases, their isotopes, organics and their molecular structure and water fraction.

Results and discussion:

Measurements with calibration gas mixtures (exosphere-mode) showed that both flight units meet the scientific requirements of analysing the exosphere. Calibration measurements of the flight units indicated that their performance in GC-mode is comparable to the prototype GC-NGMS instrument [3] where sensitivities of hydrocarbons of about $2 \cdot 10^{-10}$ by mass and of about $2 \cdot 10^{-9}$ by mass for noble gases are demonstrated. Performance parameters

included a dynamic range of up to 10^6 within 1 second integration time and mass resolution $M/\Delta M$ up to 1200. Given this performance, the flight unit is capable to detect and quantify even traces of species in the lunar regolith and exosphere.

References:

- [1] Wurz P., Abplanalp D., Tulej M., Lammer H. A Neutral Gas Mass Spectrometer for the Investigation of Lunar Volatiles, *Planet. Space Sci.* 2012. V. 74. 264–269.
- [2] Abplanalp D., Wurz P., Huber L., Leya I. An optimised compact electron impact ion storage source for a time-of-flight mass spectrometer, *Int. J. Mass Spectrom.* 2010. V. 294. 33–39.
- [3] Hofer L., Wurz P., Buch A., Cabane M., Coll P., Coscia D., Gerasimov M., Lasi D., Sapgir A., Szopa C., Tulej M. Prototype of the gas chromatograph–mass spectrometer to investigate volatile species in the lunar soil for the Luna-Resurs mission, *Planet. Space Sci.* 2015. V. 111. 126–133.

EXPERIMENTAL STUDY OF DEGASSING OF THE EARLY EARTH AND MOON DURING ACCRETION

V. Fedulov, N. Dushenko, S. Voropaev

GEOKHI RAS, Moscow, Kosygina str. 19. fedulov_vs@geokhi.ru

Keywords:

Moon, Earth, meteorites, volatiles, impact, accretion

Introduction:

The process of formation of impact craters on the Earth and the moon not only led to local high temperatures and pressures, but also to the evaporation of volatile, such as H_2O , CO_2 , etc [1]. Also, a large amount of dust was emitted into space together with gases in the formation of craters. Therefore, the surface of the growing planet, very likely, were covered with rock fragments and impact melt with a captured fugitive. It is well known that CO_2 and H_2O , one of the most common separable volatiles, have intense absorption bands in the infrared region [2]. Therefore, at the origin of such a primary atmosphere, the energy released on the surface could not immediately go into space. Taking into account this "shielding" effect, it can be expected that the surface temperature of the early Earth has increased dramatically and began melting rocks

The aim of this study is an experimental quantitative assessment of volatiles contained in large groups of ordinary chondrites — H, L and LL. This class of meteorites is one of the main building blocks of the early Earth and the moon. This will allow us to clarify the physical parameters of the secondary (in relation to the gases of the protoplanetary nebula) atmosphere of the Earth and build a correct numerical model of the cooling of its surface.

Analytical procedure:

For experimental quantitative determination of volatile compounds composition in the laboratory of Carbon Geochemistry of GEOKHI RAS, a special installation was developed and created, the schematic diagram of which is shown in Fig. 1.

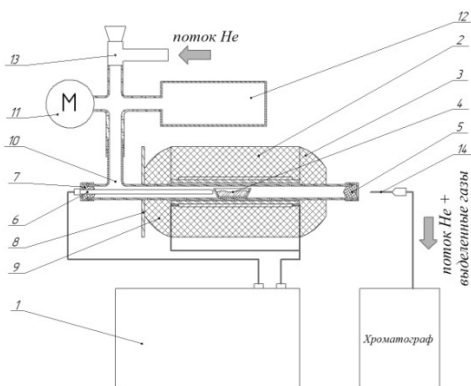


Fig. 1. Schematic diagram of the installation: 1 — electronic control unit; 2 — induction heater (furnace); 3,9 — protective disc of thermal insulation wool; 4 — quartz boat with a loaded sample; 5,7 — a tube of special rubber for gas extraction; 6 — thermocouple; 8 — heat-reflecting screen; 10 — quartz glass reactor; 11 — pressure gauge; 12 — pressure equalization tank in a closed circuit with a piston; 13 — gas leak; 14 — needle of a gas-tight syringe

This unit is designed as an attachment to the gas chromatograph for degassing solid and liquid samples at temperatures up to 1200°C in the carrier gas flow, to create the necessary atmosphere. Helium was chosen as a carrier gas for our experiments. The attachment of the crushed meteorite sample in a quartz boat (4) is placed in a quartz glass reactor in the center

of the heater (2), then the system is locked with a special heat-resistant vacuum rubber stopper (5) and fixed by a press sleeve. The plug made of special rubber allows the needle of a gas-tight syringe to be inserted without breaking the tightness (14).

After that, the reactor with the sample placed in it is purged with helium and heated at a temperature of 100°C , the helium pressure inside the system is 1.0 ± 0.1 bar. The flow of helium is regulated with a gas leak (13) accurate to 0.05 bar and controlled by a pressure gauge (11). The outflow of helium, through the needle of a gas-tight syringe, through a fluoroplastic tube is connected to the chromatograph and periodically analyzed until there are no traces of atmospheric gases. This process takes about three hours. After the reactor and sample are cleaned of atmospheric gases, the system is disconnected from the chromatograph and the helium flow is blocked.

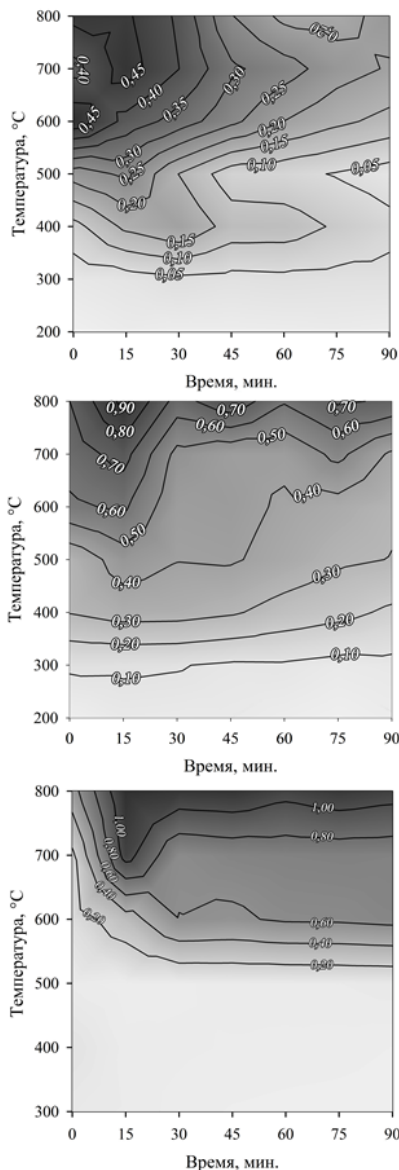


Fig. 2. Contours of H_2 content in meteorites of different classes (from top to bottom — Chelyabinsk LL5, Aba Panu L3, NWA 12370 H5). Figures indicate concentration in $\mu\text{g/g}$

The electronic control unit (1) sets the required temperature and heats the sample. Sample heating rate $4.5^{\circ}\text{C}/\text{sec}$. The temperature inside the system is determined by a thermocouple of high-temperature oxidation-resistant alloy Microbell D (6) alloy in close proximity to the quartz boat. Due to the high heating rate, the system was brought to the required temperature in no more than 5 minutes. During heating, the pressure is controlled (1.0 ± 0.1 bar.) inside the system as the gas expands when heated. The excess pressure is equalized by the tank (12) with a variable volume in a closed circuit to avoid the beginning of the process of diffusion of light gases through a quartz glass reactor.

Degassing experiments:

During the experiment, the dependences of changes in the concentration of the main gas components (CO_2 , CO , CH_4 , H_2 , H_2O , H_2S , N_2) on time and temperature were obtained. The quantitative composition of gases determined by us is not complete. Products such degassing, as the noble gases had not been determined because the measurement method did not allow to perform the calibration used by us. Depending on the type of meteorite (as well as on the content of Fe and FeO), we have a natural change in the content of the components we define. Due to the composition of the meteorite NWA 12730 (H5), we did not degass at 200°C , as this temperature was not enough to heat the entire sample matrix. We also came across difficulties in determining the so-called reducing components (CH_4 , H_2 , H_2S) at temperatures below 500°C : due to the high content of iron acting

as a catalyst. Carbon dioxide (CO₂) was detected in all meteorites in amounts ranging from 0.004 to 10 ng/g.

As example of the obtained results, we submit here data concerning H₂ (see Fig. 2). Already on the example of hydrogen, we see an increase in its content in the LL-L-H series twice. On all contours it is visible that the maximum of its allocation is at the initial stage of degassing. As an active reducing agent, it immediately interacts with other gas components and the meteorite matrix, as evidenced by the decrease in concentration over time, which is seen on the contours of LL and L. On the contour H hydrogen is active for the first time, then its concentration goes to the plateau, i.e. its content becomes equilibrium. The amount of hydrogen depends on the content of CO and CH₄, as will be discussed extra. Under experimental conditions, hydrogen can recover metals from their oxides, but this requires a sufficiently large amount of time. When comparing hydrogen and water circuits, it cannot be said that the maximum hydrogen content will account for the maximum water content that should be formed during the reduction of these metals. Although under impact events a sharp spike in temperature and pressure will provide flow of this process. The hydrogen content in all studied classes of ordinary chondrites varies from 0.10 to 1.20 µg/g. The average value of juvenile hydrogen is 0.65 µg/g.

Conclusions:

H₂O, CO₂ and N₂ contribute greatly to the formation of the proto-atmosphere [3]. But the presence of other volatile and thermal processes in the impact of meteorites on the proto-planet provides the process of evolution of the atmosphere. At very high temperatures, associated degassing from the melt is possible. We define components make up 10–15% of the total composition of volatile in the rest of the number consists of heavy noble gases and sulfur gases. In the future, it is necessary to carry out thermodynamic and kinetic calculations to compare the experimental data with different computational models.

Acknowledgments

This work was supported by the Russian Science Foundation, project no. 17-17-01279.

References:

1. Matsui T., Abe Y. Impact-induced atmospheres and oceans on Earth and Venus // *Nature*. 1986. V. 322. P. 526–528.
2. Buckvic D.S. Outgassing of chondritic planets. M.S. thesis. 1976. MIT. P. 80
3. Abe Y., Matsui T. The formation of an impact-generated H₂O atmosphere and its implications for the early thermal history of the Earth // *J. Geophys. Res.* 1985. № 90 (Suppl.). P. 545–559.

DEPENDENCE OF ACCURACY OF ELEMENTAL AND ISOTOPIC COMPOSITION MEASUREMENT ON THE VOLUME OF THE SPECTRA ARRAY FOR THE LASMA-LR INSTRUMENT ONBOARD LUNA-GLOB AND LUNA-RESOURCE MISSIONS

V.S. Cheptsov^{1,2}, A.E. Chumikov¹, N.G. Managadze¹

¹ Space Research Institute of Russian Academy of Sciences (117997, Russian Federation, Moscow, Profsoyuznaya Street, 84/32, cheptcov.vladimir@gmail.com);

² Lomonosov Moscow State University (119991, Russian Federation, Moscow, Leninskie Gory, 1)

Keywords:

Laser ionization mass spectrometry; LASMA; Luna-Glob; Luna-Resource; elemental and isotopic composition.

Introduction:

Investigation of the molecular, elemental, and isotopic composition of the regolith and dust is an integral part of almost all landing space missions. Such assays are crucial to understand the past and future evolution of cosmic bodies, to study a number of their physicochemical characteristics, to forecast the prospects for their exploration and to solve many other fundamental and applied issues. One of the most attractive methods for analyzing the elemental and isotopic composition of solids in space experiments is laser ionization mass spectrometry (LIMS), due to it offers simplicity of operation, absence of necessity of sample preparation, high spatial resolution, and robustness of the instruments construction [1–3]. LIMS for space applications has been developing rapidly over the past decades, and several LIMS prototypes as well as flight instruments are constructed to date [2, 4, 5]. One of them, LASMA instrument, was onboard Phobos-Grunt spacecraft, and its modification, LASMA-LR instrument, is accepted for Luna-Resource and Luna-Glob missions [4, 6].

The measurement technique by LASMA-LR is as follows: after installing a sample of regolith on a rotating disk at a given distance corresponding to the focal length of the laser emission, it is pulsed by Nd:YAG laser at 1.064 μm wavelength with 7 ns pulse duration and with a power density of $\sim 10^9$ W/cm². Such an effect causes complete atomization and ionization of the sample substance, severe overheating, and emission of the formed ions as a plasma torch. High-speed ions in the free expansion mode fall into the time-of-flight mass analyzer, where they are separated by the time of flight. The ions separated in time, after their reflection in the retarding field of the electrostatic reflector, are registered by a secondary electron multiplier. Further the signal goes to a high-speed analog-to-digital converter and is stored in the device's memory as a single spectrum. By the time of flight of ions and signal intensity, it is possible to determine ions mass and relative concentrations with high accuracy [4, 5] (Figure 1).

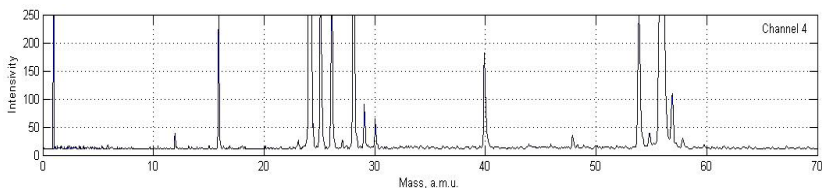


Fig. 1. An example of the spectrum of enstatite (only the most sensitive registration channel is shown; only the spectrum fragment is shown).

It is important that the accuracy of measurements substantially depends on the size of the statistical sample of the spectra array. Due to its purpose of this

work was to study dependence of accuracy of elemental and isotopic composition measurement on the volume of statistical sample of the spectra array for the LASMA-LR instrument as well as to determine accumulation times of the spectra during the Luna-Glob and Luna-Resource missions, which are stipulated by the required measurement accuracy.

Materials and Methods:

The object of the study was enstatite. This mineral is part of the lunar regolith and some meteorites [7,8]. A sample of enstatite taken in Norway was obtained from the Museum of Natural History in Berlin, where it was characterized using a JEOL 8500-F field emission scanning electron microscope. The sample contained oxides Al_2O_3 , Na_2O , TiO_2 , Cr_2O_3 , SiO_2 , MgO , MnO , CaO , and FeO in concentrations of 0.09, 0.02, 0.04, 0.01, 57.15, 32.54, 0.04, 0.29, and 9.91%, respectively. Microscopic studies have shown that the sample is homogeneous, which eliminates the effects of the heterogeneity of the target on the results and allows to define namely instrument accuracy.

Studies of the accuracy characteristics of elemental and isotopic analysis were carried out using LASMA instrument of the Phobos-Grunt project, which is a complete analog of the LASMA-LR instrument (of the Luna-Resource and Luna-Glob projects) in the analytical part of the instrument. The device was placed in a vacuum chamber, where it was pumped to a working pressure of 5×10^{-6} Torr. Then a series of spectra of enstatite was registered. The registration of the spectra was carried out in the normal mode of operation of the instrument. Frequency of obtaining spectra was determined by the frequency of the laser and was 0.1 Hz.

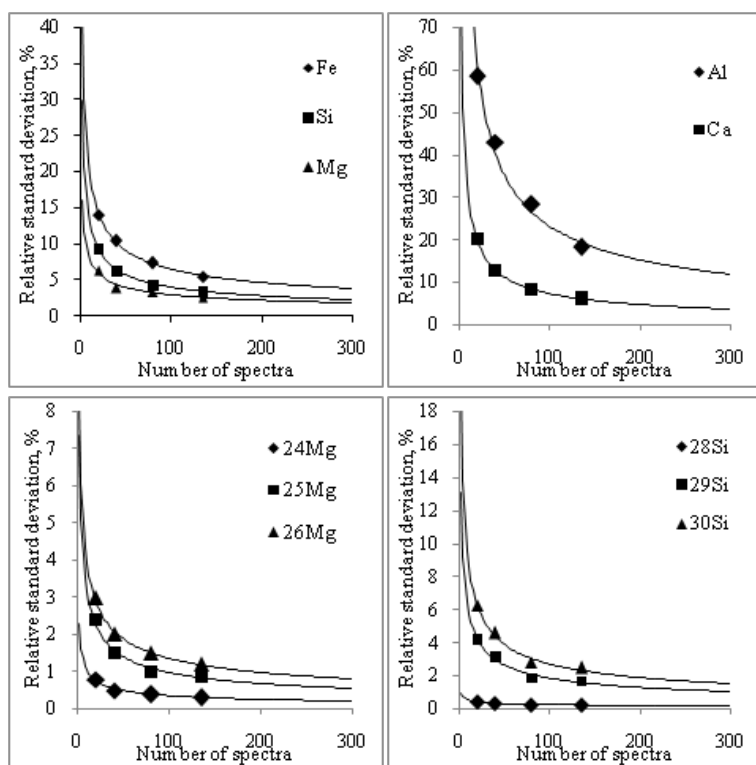


Fig. 2. The dependencies of the accuracy of the elemental and isotopic composition measurement on the volume of spectra array obtained.

Results and Conclusions:

The dependencies (for some elements and isotopes) of the accuracy of the elemental and isotopic composition determination on the number of spectra obtained are shown in Figure 2. Experimental studies to determine the magnitude of the spectra array and the time of analysis of a single sample, to

achieve an accuracy of measurements of the elemental and isotopic composition of 10% and 1%, respectively, showed:

- 1) this accuracy of elemental analysis is ensured by obtaining and processing an array of 300 spectra, which corresponds to the 4 h of continuous operation of the LASMA-LR instrument;
- 2) the accuracy of isotopic distributions determining depends not only on the number of observations, but also on the concentrations of isotopes;
- 3) for the same 4 h time interval, 1% accuracy of measurement of isotopic distributions is achieved only for intense isotopes that are in a ratio of not more than 10;
- 4) measurement of low-intensity isotopes with 1% accuracy is possible, but requires an unjustified increase in analysis time.

Based on the conclusions made, and assuming a small variability in the isotopic composition of different samples of the Moon's regolith taken from one landing site, it is proposed to use at least a 4 h observation interval for a single sample, and to measure isotopic distributions with usage of all the statistics obtained during the experiment, to avoid the restrictions associated with the concentrations of isotopes.

References:

- [1] Tulej M. et al. On applicability of a miniaturised laser ablation time of flight mass spectrometer for trace elements measurements // *International Journal of Spectroscopy*. 2012. Article ID 234949.
- [2] Tulej M. et al. Chemical composition of micrometer-sized filaments in an aragonite host by a miniature laser ablation/ionization mass spectrometer // *Astrobiology*. 2015. V. 15. № 8. P. 669-682.
- [3] Riedo A. et al. Performance evaluation of a miniature laser ablation time-of-flight mass spectrometer designed for in situ investigations in planetary space research // *Journal of mass spectrometry*. 2013. V. 48. № 1. P. 1–15.
- [4] Managadze G.G. et al. Study of the main geochemical characteristics of Phobos' regolith using laser time-of-flight mass spectrometry // *Solar System Research*. 2010. V. 44. № 5. P. 376–384.
- [5] Managadze G.G. et al. A new method and mass-spectrometric instrument for extraterrestrial microbial life detection using the elemental composition analyses of Martian regolith and permafrost/ice // *Astrobiology*. 2017. V. 17. № 5. P. 448-458.
- [6] Mitrofanov I.G. et al. Science program of Lunar Landers of "Luna-Glob" and "Luna-Resource" missions // *Lunar and Planetary Science Conference*. 2011. V. 42. P. 1798.
- [7] Reid A.M. et al. Luna 20 soil: abundance and composition of phases in the 45–125 micron fraction // *Geochimica et Cosmochimica Acta*. 1973. V. 37. № 4. P. 1011-1030.
- [8] Rubin A.E. The Hadley Rille enstatite chondrite and its agglutinate-like rim: Impact melting during accretion to the Moon // *Meteoritics & Planetary Science*. 1997. V. 32. № 1. P. 135–141.

PRECISE ORBIT DETERMINATION OF CHANG'E 4 LANDER BASED ON DOPPLER MEASUREMENT

JianfengCao, Lue Chen, Yu Zhang

¹ Beijing Aerospace Control Center, *jfcao@foxmail.com*, *chenlue@xao.ac.cn*, *zackzy@163.com*

Keywords:

Chang'E-4 Mission; Doppler; UXB; VLBI; Orbit Determination; Accuracy analysis;

Introduction:

China's lunar exploration project utilizes ground-based USB/UXB (Chang'e-1 and Chang'e-4 relay satellites use S-band, the rest of the lunar exploration missions use X-band), and astronomical VLBI measurements to accomplish the tracking of Spacecraft^[1-3]. Limited by the accuracy of measurement data, the orbit calculation of Chang'e-1 mission mainly depended on USB ranging and VLBI delay and delay-rate measurement, and the orbital accuracy was better than 50m in the circumlunar phase. During Chang'e-2 mission, deep-space phase measurement experiments were carried out, and Doppler data with accuracy of about 0.1 mm/s were obtained. In Chang'E 3 mission, the accuracy of Doppler measurement in X-band was 0.2–0.4 mm/s (10 s integration period), and that of three-way Doppler measurement was about 0.3–0.5 mm/s (10 s integration period). Chang'E-4 lander adopts X-band measurement system. Thanks to the modification of the tracking equipment, the Doppler measurement accuracy has been further improved^[4]. In this paper, the orbit of Chang'E-4 during the lunar flight phase is calculated, and the orbital accuracy is analyzed.

During the circumlunar flight phase, Chang'E-4 carried out attitude control jet about every ten minutes and directional bias setting every day to provide Transponder with proper pointing direction. The acceleration induced by attitude control is estimated during orbit determination. A constant-acceleration motion model in orbital coordinate system is adopted to model the attitude control.

The performance of Doppler tracking data of Chinese Deep Space network has been significantly improved over the last ten years. To access the orbital accuracy obtained by Doppler-only solution, orbit determination is done with the time span of 00:00:00.000-1T:04:00:00.000, and the 4 hour arcs at the end is used to compare the overlap.

Fig. 1 shows the overlap comparison. The overlap statistics is better than 35m for most cases. While for case 8–12 and 18–19, the accuracy slightly decreased because of the orbit maneuver.

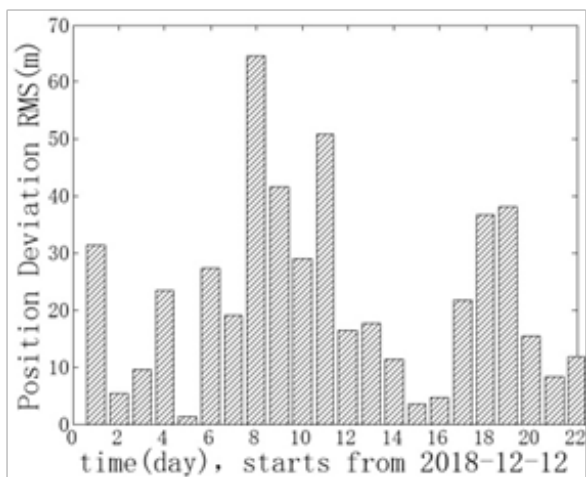


Fig. 1. Overlap Comparison for Chang'E-4 during circumlunar flight phase

The attitude control jets are performed more frequently in the 100 km×15 km stage. And the inaccuracy of gravity force acting on the spacecraft is more significant [5]. Fig. 2 shows the post fit residuals of Doppler. The ignorance of acceleration induced by attitude control will increase the post-fit residual significantly. The residuals have distinct periodic terms, which is consistent with orbital period. Comparing the orbit solutions, the unmodeled attitude control force only changes the orbit by less than 20 m.

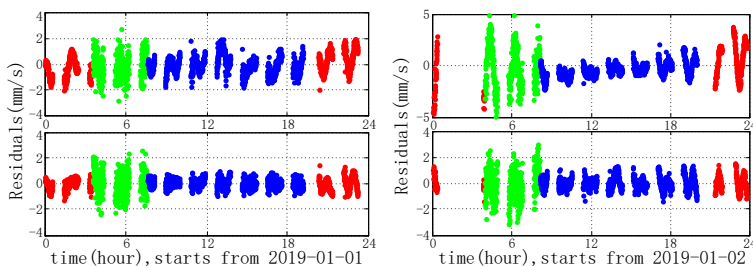


Fig. 2. Post fit residuals

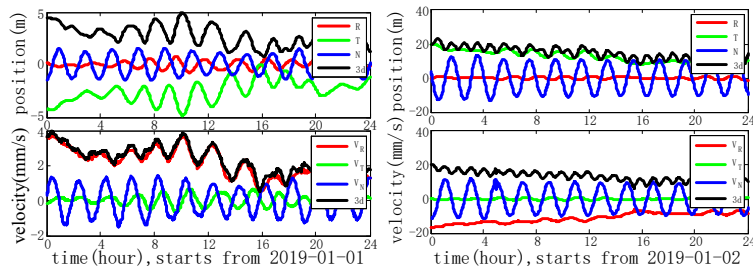


Fig. 3.

The accuracy of the orbit determined using USB combined with VLBI has been verified to be stabilized at 10-50m in previous lunar exploration missions. Fig. 4 shows the difference between the orbits obtained with different tracking data. The results show that the two data sources are highly consistent, and the difference between them is less than 45 m.

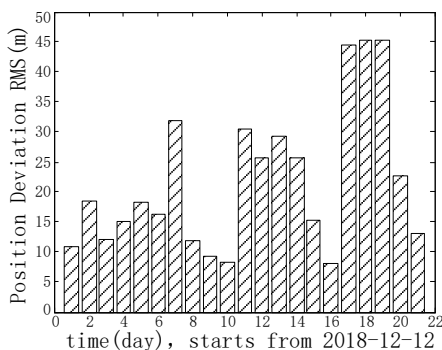


Fig. 4.

The Doppler measurements of Chang'E 4 lander are processed. The accuracy level of Doppler measurements of Jiamusi Deep Space Network in China is similar to that of South America. The RMS of orbital determination residual is about 0.3 mm/s–0.8 mm/s (1s integration period). The data accuracy level of Kashi station is slightly worse, about 0.6–1.2 mm/s. Frequent attitude control jets and sun-directional offset have a slight acceleration effect on the lander and a 20–50m impact on orbit calculation. By overlap comparison, the three-dimensional accuracy of the independent solution based on Doppler

data is 5–50m. The accuracies of orbits calculated by ranging and VLBI data are relative, and their difference is less than 50 m.

References:

- [1] CHEN M, TANG G, CAO J, et al. Precision orbit determination of CE-1 lunar satellite[J]. *Geomatics and Information Science of Wuhan University*, 2011, 36(2): 212-217.
- [2] CHEN M, ZHANG Y, CAO J, et al. Orbit determination and tracking technology of CE-2 satellite[J]. *Chinese Science Bulletin*, 2012, 57(9): 689-696.
- [3] HUANG Y, CHANG S, LI P, et al. Orbit determination of Chang'E-3 and positioning of the lander and the rover[J]. *Chin Sci Bull*, 2014, 59(23): 3858-3867.
- [4] DONG G, LI H, HAO M, et al. Development and future of China's deep space tt&c system[J]. *Journal of Deep Space Exploration*, 2018, 5(2): 99-114.
- [5] ZHANG Y, CAO J, DUAN J, et al. Orbit dynamics model compensation and implementation for continuous attitude control of Chang'E-3 probe[J]. *Journal of Astronautics*, 2015, 36(5): 489-495.

PRECISE OPEN-LOOP DOPPLER MEASUREMENT OF CHANG'E-4 PROBE BASED ON CHINA'S DEEP SPACE INTERFEROMETRY SYSTEM

Lue Chen¹, Jianfeng Cao², Jinsong Ping³, Songtao Han⁴, Weitao Lu⁵

¹ Beijing Aerospace Control Center, chenlue@xao.ac.cn

² Beijing Aerospace Control Center, jfcao@foxmail.com

³ National Astronomical Observatories, the Chinese Academy of Sciences, jsping@bao.ac.cn

⁴ Beijing Aerospace Control Center (justdoit_doing@126.com);

⁵ Beijing Aerospace Control Center, looweitao@126.com

Keywords:

Chang'e-4 probe; open-loop measurement; Doppler; Orbit Determination; Accuracy

Introduction:

Chang'e-4 probe successfully landed in South Pole-Aitken (SPA) basin on the far side on 3 January 2019 [1], [2]. High accuracy orbit measurement strongly supported this lunar mission based on China's Deep Space Network (CDSN) and astronomical VLBI system, provided tracking observations for probe orbit determination on probe's Earth-Lunar transfer phase and circumlunar phase. A new Doppler signal processing technology and open-loop measurement experiment were introduced for Chang'e-4 probe orbit measurement based on China's Deep Space Interferometry System (CDSIS) which belongs to CDSN. Firstly, Chang'e-4 probe's carrier downlink signal was received by deep space telescope, and the carrier signal was sampled and recorded by deep space interferometry sample and record terminal system. The signal was recorded in VLBI Science Receiver (VSR) format, the frequency spectrum of carrier signal is shown in Figure 1.

Secondly, VSR signal was transformed to Beijing Interferometry Mission Center (BIMC) for signal processing to obtain high accuracy Doppler observation and VLBI observation. The mixed signal processing method of frequency and phase domain was utilized to process Chang'e-4 carrier signal to estimate high accuracy Doppler frequency, the random noise level of the Doppler results was about 5 mHz, which was smaller than deep space station velocity baseband's Doppler noise level. Figure 2 shows the different Doppler results obtained by different signal processing systems, in this figure, DTE means data terminal equipment's results, which is obtained from the station's baseband measurement equipment. Phase means accumulation carrier phase measurement equipment's results. IMC means interferometry mission center's results. Figure 3 shows the different residual Doppler results obtained by different signal processing systems. It is obviously shown that IMC's Doppler noise level is smaller than DTE and Phase's Doppler noise level.

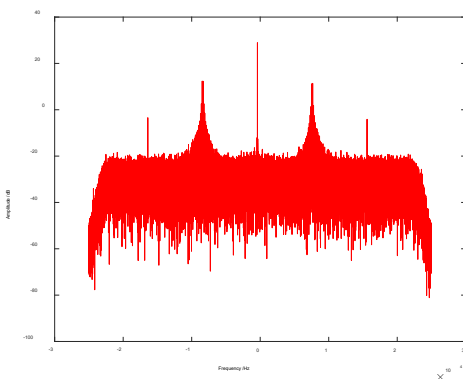


Fig. 1. Chang'e-4 probe carrier signal frequency spectrum

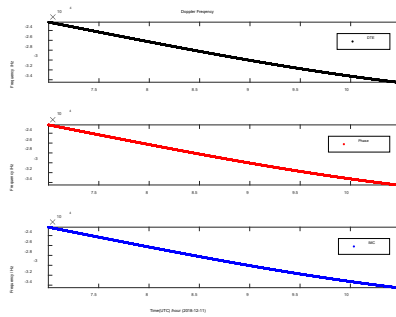


Fig. 2. Doppler results obtained by different systems

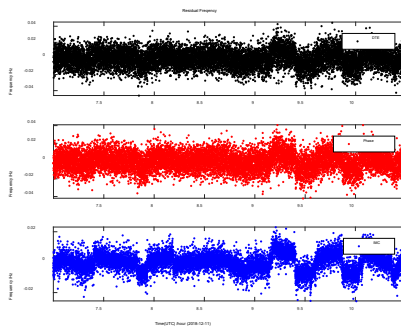


Fig. 3. Residual Doppler results obtained by different systems

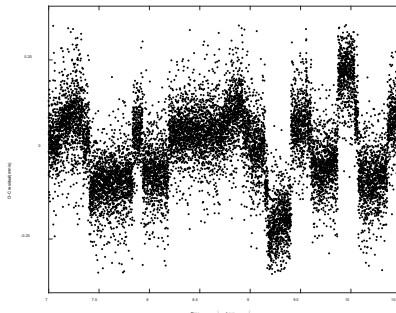


Fig. 4. Orbit determination residual based on open-loop Doppler observation

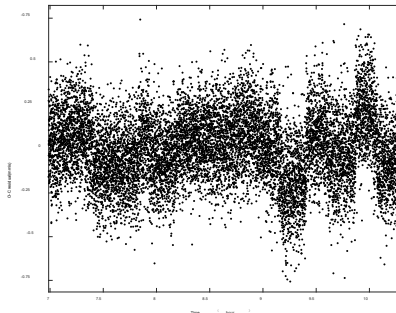


Fig. 5. Orbit determination residual based on two-way Doppler observation

Finally, the open-loop Doppler observation results were provided for Chang'e-4 precise orbit determination. The orbit determination accuracy analysis shows that Chang'e-4 open loop Doppler measurement accuracy is 0.1 mm/s on Earth-Lunar transfer phase, and 0.3 mm/s on circumlunar phase. This accuracy was better than deep space station velocity baseband's Doppler measurement accuracy, which were shown in Figure 4 and Figure 5.

This paper's high accuracy Doppler tracking technology and software could be effectively utilized in future deep space probe mission and planet radio science application.

References:

- [1] Weiren Wu, Chunlai Li, Wei Zuo, et al. Lunar farside to be explored by Chang'e-4 // *Nature Geoscience*.2019. V. 12. P.222–223.
- [2] Chunlai Li, Dawei Liu, Bin Liu, et al. Chang'E-4 initial spectroscopic identification of lunar far-side mantle-derived materials // *Nature*.2019. V. 569. P. 378–393.

COMPARISON OF THE JUPITER'S CURRENT DISC MODEL WITH THE MAGNETIC FIELD OBSERVATIONS FROM JUNO AND GALILEO

I.A. Pensionerov, E.S. Belenkaya, I.I. Alexeev

Lomonosov Moscow State University, Skobeltsyn Institute of Nuclear Physics (SINP MSU), 1(2), Leninskie gory, GSP-1, Moscow 119991, Russian Federation

Keywords:

Planetary magnetospheres, magnetodisc, Jupiter, Juno, Galileo

Introduction:

Jupiter's magnetosphere contains gigantic disc-shaped current system, placed near the magnetic equator of the planet. There are many models, describing its magnetic field and structure. Models developed in [1] and significantly improved in [2] and [3] solve a force balance equation, that takes into account plasma pressure, electromagnetic and centrifugal forces. These models allow to obtain the most detailed picture of the processes in the current disc.

A different kind of model was developed in [4]. It specifies the current density a-priori and calculates the magnetic field of it. While this empirical model does not yield the same amount of detail as the dynamic ones, it is very useful as a tool for computing magnetic field of the magnetodiscs. Model [4] was extensively used in many studies concerned with the structure of the Jovian magnetosphere and was adopted for using in the Saturn's magnetosphere as well. Other empirical models of the current disc were presented in e.g. [5, 6].

In [7] we introduced an improved version of the [4] model. It employed different current density dependence on radial distance and took into account lagging of the current sheet from magnetic equator, according to [5, 8]. Models [7], [4], [5] and [6] were compared with the Juno Perijove-01 magnetic field data and the new model showed the lowest root-mean-square deviation.

Here we present an improved version of the model [7] tested extensively using Juno and Galileo magnetic field observations.

Acknowledgements.

The MAG data was obtained from Planetary Data System (PDS). Instrument scientist of FGM — J. E. P. Connerney. Principal investigator of Juno mission — Scott J. Bolton.

Work was partially supported by the Ministry of Education and Science of the Russian Federation (grant RFMEFI61617X0084).

References:

- [1] Caudal, G.: A self-consistent model of Jupiter's magnetodisc including the effects of centrifugal force and pressure // *Journal of Geophysical Research*. 1986. 91, 4201
- [2] Nichols J. D.: Magnetosphere-ionosphere coupling in Jupiter's middle magnetosphere: Computations including a self-consistent current sheet magnetic field model // *Journal of Geophysical Research: Space Physics*. 2011.
- [3] Nichols, J. D., Achilleos, N., and Cowley, S. W. H.: A model of force balance in Jupiter's magnetodisc including hot plasma pressure anisotropy, *Journal of Geophysical Research: Space Physics*. 2015. 120, 10,185–10,206
- [4] Connerney, J.E.P., Acuña, M.H., and Ness, N.F.: Modeling the Jovian current sheet and inner magnetosphere // *Journal of Geophysical Research: Space Physics*. 1981. 86, 8370–8384
- [5] Alexeev, I.I. and Belenkaya, E.S.: Modeling of the Jovian Magnetosphere // *Annales Geophysicae*. 2005. 23, 809–826
- [6] Khurana, K.K.: Euler potential models of Jupiter's magnetospheric field // *Journal of Geophysical Research: Space Physics*. 1997. 102, 11 295–11 306
- [7] Pensionerov, I.A., Alexeev, I.I., Belenkaya, E.S., Connerney, J. E. P., & Cowley, S. W. H.: Model of Jupiter's current sheet with apiecewise current density. // *Journal of Geophysical Research: Space Physics*. 2019. 124, 1843–1854.
- [8] Khurana, K.K.: A generalized hinged-magnetodisc model of Jupiter's nightside current sheet // *J. Geophys. Res.* 1992. 97, 6269

JUPITER'S AURORAS ASSOCIATED WITH GALILEAN MOONS AND THE MAIN OVALS

E.S. Belenkaya

¹Federal State Budget Educational Institution of Higher Education M.V. Lomonosov Moscow State University, Skobeltsyn Institute of Nuclear Physics (SINP MSU), 1(2), Leninskie gory, GSP-1, Moscow 119991, Russian Federation

Keywords:

Jupiter, Callisto, magnetic field, aurora, alfvénic wings.

Introduction:

Galilean moons play significant role in investigation of the Jupiter's magnetosphere, because their field-aligned projections to the Jovian atmosphere are marked by bright emissions [1–3]. If the UV emissions in the footprints of Io, Europa, and Ganymede are often seen, the observation of Callisto's trace is rather hard. One of the reasons is that the ionospheric field-aligned projection of Callisto is located very close to (or even inside) the main auroral oval. The other cause is that Callisto is not always located in the subalfvénic flow of the Jovian magnetospheric plasma. The third circumstance is that the Callisto's trace occurred to be rather weak. For these reasons, the Callisto's footprint was observed only in 2018 for the first time using the special technique [4]. The problem of Callisto's interaction with the Jupiter's magnetospheric plasma flow is very significant and widely discussed in the literature. Its understanding highlights the key features of the Jupiter's system.

References:

- [1] Clarke J.T., Ballester G.E., Trauger J., Evans R., Connerney J.E.P., Stapelfeldt K., Crisp D., Feldman P.D., Burrows C.J., Casertano S., Gallagher III J.S., Griffiths R.E., Hester J.J., Hoessel J.G., Holtzman J.A., Krist J.E., Meadows V., Mould J.R., Scowen P.A., Watson A.M., Westphal J.A. Far-ultraviolet imaging of Jupiter's aurora and the Io "footprint" // *Science*. 1996. V. 274, No 5286. P. 404–409.
- [2] Clarke J.T., Ajello J., Ballester G., Ben Jaffel L., Connerney J., Gérard J.C., Gladstone J.R., Grodent D., Trauger P.W., Waite J.H. Ultraviolet emissions from the magnetic footprints of Io, Ganymede, and Europa on Jupiter // *Nature*. 2002. V. 415. No. 6875. P. 997–1000.
- [3] Prange R., Rego D., Southwood D., Zarka P., Miller S., Ip W. Rapid energy dissipation and variability of the Io-Jupiter electrodynamic circuit // *Nature*. 1996. V. 379. No. 6563. P. 323–325.
- [4] Bhattacharyya D., Clarke J.T., Montgomery J., Bonfond B., Gerard J.-C., Grodent D. Evidence for auroral emissions from Callisto's footprint in HST UV images. *J. Geophys. Res. Space Physics*. 2018. V. 123. P. 364–373.

ZONAL FEATURES OF THE WEAK AMMONIA ABSORPTION BANDS BEHAVIOR ON JUPITER

V.D. Vdovichenko, G.A. Kirienko, A.M. Karimov, P.G. Lysenko, V.G. Tejfel, V.A. Filippov, G.A. Kharitonova, A.P. Khozhenetz
Fesenkov Astrophysical Institute, Almaty, Kazakhstan

Keywords:

Jupiter, atmosphere, clouds, spectrophotometry, ammonia, methane, absorption bands

Introduction:

The gaseous NH_3 absorption bands' intensities depend on the local abundance of ammonia at different latitudes of the planet. In the main, the radiation-convective regime of the atmosphere and the equilibrium between the gas and condensed phases of ammonia governs absorption, but its behavior and space-time variations are still very poorly studied. The condensation of ammonia in the upper troposphere whereupon there is a sharp decrease in its abundance in the gas phase, affects the horizontal and vertical distribution of ammonia.

The authors of [1] show that global depletion and its band-zonal variations one can explain with using a simple model of the interaction of wet convection with circulation inside Jupiter's stratus clouds. In the atmosphere with such powerful dynamics, which is Jupiter's one, ammonia should undergo horizontal variations. Optical observations from the Voyager-1 satellite [2] and those with using the Hubble space telescope, as well as radio astronomy observations [3], revealed a difference in the latitudinal absorption of ammonia on the Jupiter disk.

Observations and processing

We performed a large cycle of spectral observations of Jupiter in March-June 2018. We paid a main attention to scanning the Jovian disk from the south pole to the north one to obtain spectrograms of the entire sequence of latitudinal belts (up to 60 or more zonal spectrograms in the same scan). The spectra of the central meridian of the planet were also recorded.

The vertical structure of clouds, their optical density and the position of the upper boundary of the cloud cover at different latitudes of the planet influence the behavior of the absorption bands of both ammonia and methane (which have different intensity) along the central meridian. But if we talk about ammonia, then its absorption bands intensities depend on the local content of gaseous ammonia at different latitudes of the planet. As mentioned above, the absorption is determined by the radiation-convective regime of the atmosphere and the equilibrium between the gas and condensed phases.

However, our task becomes more complicated because of that in the near-infrared spectral region (600–1100 nm) that is accessible to our devices, almost all ammonia absorption bands are blended by stronger methane absorption bands. So, our main aim was to separate these bands, i.e., make them "clean" ones.

Due to the large difference in the intensities of the studied absorption bands, it is difficult to compare the variations of both their depths and equivalent widths. A more demonstrative picture, in our opinion, is a comparison of variations in the central residual intensities of the absorption bands (B_λ), that we regard as $B_\lambda = I_\lambda / I_c \sim \exp(-\tau_\lambda^*)$, where τ_λ^* can be represented as a certain function of the wavelength. In the chosen model B_λ is proportional to the average number of molecules of the absorbing gas in the thickness of the investigated area of the Jovian atmosphere.

Asymmetry in the ammonia absorption processes in the northern and southern hemispheres of Jupiter

Figure 1 (left) presents a comparison of the effective optical paths forming ammonia absorption bands ($\tau_\lambda^* \text{NH}_3$) for two spectral regions - 645 and 790 nm. For clarity, here is an image of Jupiter on the same date 09/05/2018. [4]. On the right, we give a comparison of the latitudinal absorption variations

of ammonia and methane, expressed using equivalent widths of the bands normalized to their values in the equatorial zone. Each point on the graphs corresponds to a separate zonal spectrogram obtained by scanning the Jupiter disk.

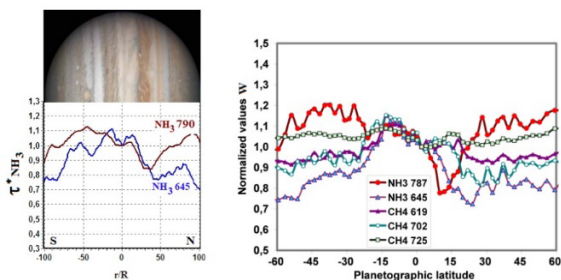


Fig. 1. The ammonia absorption meridional variations at two wavelengths of 645 and 790 nm (left) and a comparison of the ammonia and methane absorption latitudinal variations presented by comparison of their equivalent widths normalized to their values in the equatorial zone (right).

Clearly noticeable ammonia deficiency in the northern hemisphere in a region of the Northern Equatorial Belt (NEB), as we have already mentioned in our earlier works [5, 6], is particularly pronounced in the 790 nm band. However, more interesting results are observed from a comparison of ammonia and methane absorption along the central meridian of Jupiter. We conducted a pair-wise comparison of the absorption intensity variations over the Jupiter disk of ammonia and methane in two neighboring and close in intensity absorption bands, and also compared the absorption variations across the Jupiter disk in two ammonia bands 645 and 790 nm. Figure 2 shows variations of the meridional absorption of ammonia in two wavelengths with respect to methane.

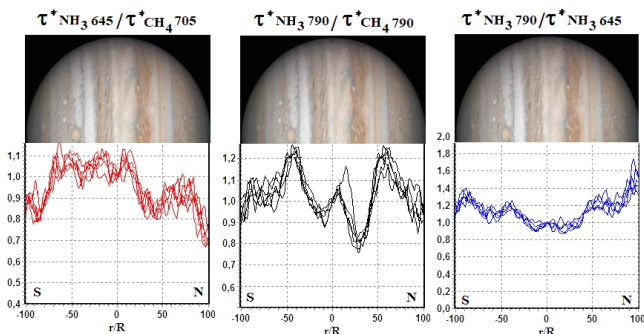


Fig. 2. Latitudinal (meridional) variations of the ratios of NH_3 645 / CH_4 705 (left), NH_3 790 / CH_4 790 (middle) and NH_3 790 / NH_3 645 (right).

One can see from the figures that at low and middle latitudes there is an excess of ammonia ($\approx 10\%$), while at high latitudes and near the poles there is a 10% deficiency. The influence of the structure of Jovian cloud bands is clearly visible.

In the 645 nm ammonia band, a particularly low (by 15%) ammonia abundances observed in the northern hemisphere in a region of the broad dark NEB, capturing the transition region between NEB and NTrZ.

In the 790 nm ammonia band, absorption variations during movement along the central meridian of Jupiter are much more noticeable. This band's absorption is very clearly correlated with the zonal structure of the cloud layers of the planet: the light zones correspond to the increased ammonia abundance, the dark bands (belts) – to the lowered one. The decline profile of the ammonia absorption during the NEB is more narrow in width (i.e., the NH_3 deficiency-

takes up a small latitudinal interval) and it is deeper at the maximum (20%), pointing to the maximum NH_3 deficiency against a well-pronounced excess of the same ammonia in the light zones of STRZ (20%) and NTRZ (10%).

The ratio of the two ammonia absorption bands to each other (Figure 2 on the right) shows for the stronger absorption band at 790 nm, when moving through a weakly pronounced zonal structure, the tendency to increase the ammonia absorption to high latitudes. One can consider it as evidence of an extended, cloudless, purely gaseous atmospheric layer under the upper visible cloud cover of Jupiter.

The course of the ammonia and methane absorption along the equator of Jupiter

It is noteworthy that if the brightness distribution in the continuous spectrum at 630 nm and in the deep absorption band of methane at 889 nm in the west-east direction is fairly symmetric, then in the smaller absorption bands of methane and ammonia some asymmetry is observed. It is especially well pronounced in the absorption band of 645 nm, which is formed at a great depth (according to some estimates, of the order of 10–20 bar). Recall that observations were made during the period of Jupiter's opposition on May 9, 2018 at the zero phase, which in the case of horizontal homogeneity of the cloud cover also implies a symmetric absorption distribution.

Acknowledgements

This research was carried out in accordance with the grants of MES RK 0073 / GF4 and AP05131266

References

- [1] Showman A.P., de Pater I. Dynamical implications of Jupiter's tropospheric ammonia abundance // *Icarus*. 2005, V.174. P. 192–204.
- [2] Gierasch P.J., Conrath B.J., Magalhaes J.A. Zonal mean properties of Jupiter's upper troposphere from Voyager infrared observations // *Icarus*. 1986. V. 67. P. 456-483.
- [3] Pater I., Sault R.J., Wong M.H., Fletcher L.N., Boer D., Butler B. Jupiter's ammonia distribution derived from VLA maps at 3 – 37 GHz. // arXiv: 1902.07294v1 [astro-ph.EP] 19 Feb 2019.
- [4] <http://alpo-j.asahikawa-med.ac.jp/indexE.htm>
- [5] Tejfel' V.G., Karimov A.M., Vdovichenko V.D. Strange latitudinal variations of the ammonia absorption on Jupiter, // *Bulletin of the American Astronomical Society*. 2005.V. 37(3): P.682.
- [6] Tejfel' V.G., Vdovichenko V.D., Lysenko P.G., Karimov A.M., Kirienko G.A., Bondarenko N.N., Filippov V.A., Kharitonova G.A., Khozhenets A.P. Ammonia in Jupiter's atmosphere: spatial and temporal variations of the NH_3 absorption bands at 645 and 787 nm, // *Solar System Research*. 2018. V. 52: P. 480-494.

THEORETICAL COMPOSITION OF THE TITAN'S OCEAN DERIVED FROM THE TIDAL LOVE NUMBERS

A.N. Dunaeva¹, V.A. Kronrod¹, T.V. Gudkova², O.L. Kuskov¹

¹ V.I. Vernadsky Institute of Geochemistry and Analytical Chemistry RAS, Moscow, dunaeva.an@gmail.com

² Schmidt Institute of Physics of the Earth RAS, Moscow

Keywords:

Titan, Love numbers, internal ocean.

Introduction:

The existence of an internal ocean in Titan interiors was predicted in the early cosmochemical and evolutionary satellite's models and has been further confirmed by experimental measurements realized during Cassini spacecraft. The main evidence for the large water reservoir presence in the satellite depths is the Titan's tidal Love number, k_2 , calculated from Cassini space observations. The obtained k_2 values are equal to 0.589 ± 0.150 , 0.637 ± 0.224 [1] and 0.616 ± 0.067 — refined data from [2]. These k_2 values reflect the dynamic tidal response of the satellite's gravity field on tidal perturbation caused by Saturn, and it is such large k_2 values which indicate a global ocean existence at satellite's depth. The volumes of the internal ocean, as well as its component composition remain uncertain. In this paper, theoretical assumptions about ocean composition agreed with the satellite's gravity field measurements were viewed.

Main results:

We consider the model of partially differentiated Titan which includes the outer water-ice shell (outermost 1h-icy crust + water ocean), rock-ice mantle and the central silicate core [3]. For this model k_2 values were calculated using special program code. Obtained results in comparison with k_2 data derived from another models [4–6] are shown in Fig. 1. The satellite's surface heat fluxes (F) and their corresponding thicknesses of 1h-crust are shown as well. Maximum value of the total heat flux in Titan which calculated as the sum of L/LL-chondritic rock radiogenic heat, satellite tidal heating and latent heat of ice crystallization (ocean solidification) does not exceed 6 mW/m^2 . Taking into account potential hydration of chondritic substance and/or possible presence of Cl-chondritic material in the satellite rocky component, the probable value of Titan heat flux can be estimated as $5\text{--}6 \text{ mW/m}^2$.

In general, k_2 value depends mainly on the density and thickness of outer icy shell, on the ocean density, and to a lower extent on the other parameters, including model of satellite's internal structure [4, 6]. Fig. 1 shows that in the range of F values $5\text{--}6 \text{ mW/m}^2$ all satellite's models with pure water ocean lie within two sigma measured values of k_2 (0.589 ± 0.075) but no model meet improved experimental k_2 values 0.616 ± 0.067 (shown by hatching).

According to computed Love numbers [4, 5] k_2 values tends to rise with increasing of subsurface ocean density and thinner outer ice shell. In order to harmonize all experimental and theoretical k_2 data some Titan models with salt oceans were tested (Fig. 2). Reviewed models include the salt oceans of most likely compositions: water-ammonium, water-methanol, water-ammonium sulfate and seawater.

Line with a points and hyphens — ammonium sulfate $(\text{NH}_4)_2\text{SO}_4$ solution, solid line — sea water, dashed line — water-methanol solution (10%), dotted line — water-ammonia solution (10%).

As can be seen from the Fig.2, Titan models with pure water-ammonium (10%) and pure water-methanol (10%) oceans do not satisfy any experimental k_2 within a wide range of satellite's heat fluxes. So, such kinds of oceans are unlikely to occur in Titan. Only solutions with a very low NH_3 and CH_4 concentrations (<5%) can meet lowest k_2 values.

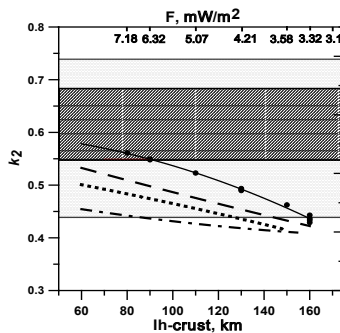


Fig. 1. Tidal Love number k_2 as a function of the l_h -ice shell thickness (Titan model with pure water ocean).

The gray area — experimental k_2 interval 0.589 ± 0.150 , hatching — k_2 interval 0.616 ± 0.067 .

Solid line — this study, dashed line — [4], dotted line — [5], line with a points and hyphens — [6].

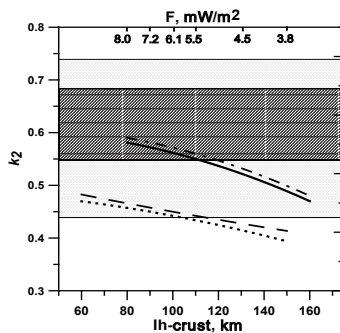


Fig. 2. Tidal Love number k_2 as a function of the l_h -ice shell thickness (Titan model with salt ocean).

Models with seawater or water-ammonium sulfate solutions lie within one sigma measured values of k_2 at the satellite heat fluxes 5.5–6 mW/m^2 . Thus, the most likely composition for the satellite's underlying ocean could be modeled by the sea water, water ammonium sulfate or another salt solution of a total density $1.13 \text{ g}/\text{cm}^3$ at least.

Another way to reconcile the calculated and experimental Love numbers is to consider the possibility of substituting K^+ , Na^+ and Ca^{2+} ions in mineral phases of Titan rock component with NH_4^+ ions in a contact with aqueous solution. Such exchange reactions lead to the leaching of salt ions into solution, that increases its density and, therefore, increases k_2 . To develop such models, additional thermodynamic calculations of water-salts-minerals systems under high-pressure should be done.

Acknowledgements:

This research was supported by the RFBR grant (№ 18-05-00685)

References:

- [1] Iess L., Jacobson R.A., Ducci M., Stevenson D.J., Lunine J.I., Armstrong J.W., Asmar S.W., Racioppa P., Rappaport N.J., Tortora P. (2012) The tides of Titan. *Science* 337(6093), 457-459.
- [2] Durante D., Hemingway, P., Racioppa, L. Iess, and D. J. Stevenson. Titan's gravity field and interior structure after Cassini. *Icarus*, V. 326, p.123-132.
- [3] Dunaeva A.N., Kronrod V.A., & Kuskov O.L. (2016). Physico-chemical models of the internal structure of partially differentiated Titan. *Geochemistry International*, 54(1), 27-47.
- [4] Baland R.M., Tobie G., Lefèvre A., Van Hoolst T. (2014) Titan's internal structure inferred from its gravity field, shape, and rotation state. *Icarus* 237, 29-41.

- [5] Sohl F., Solomonidou A., Wagner F.W., Coustenis A., Hussmann H., Schulze-Makuch D. (2014) Structural and tidal models of Titan and inferences on cryovolcanism. *Journal of Geophysical Research: Planets* 119(5), 1013-1036.
- [6] Beuthe, M. (2015). Tidal Love numbers of membrane worlds: Europa, Titan, and Co. *Icarus*, 258, 239-266.

ADJUSTMENT OF MODELS OF THE INTERNAL STRUCTURE OF TITAN WITH LOVE NUMBERS DATA

V.A. Kronrod¹, A.N. Dunaeva¹, T.V. Gudkova², O.L. Kuskov¹

¹ V.I. Vernadsky Institute of Geochemistry and Analytical Chemistry RAS, Moscow, va_kronrod@mail.ru;

² O.Y. Schmidt Institute of Physics of the Earth RAS, Moscow

Keywords:

Titan, internal structure, moment of inertia, Love numbers, composition.

The problem of matching the models of the internal structure of a partially differentiated Titan with the refined Love numbers, $k_2 = 0.616 \pm 0.067$, obtained by studying the gravitational field of Titan based on nine spans of the Cassini spacecraft (Cassini) is discussed. We obtained constraints on the heat flux and the structure of the ice-water shell, that lead to the calculated Love numbers which exceed the lower limit of the confidence interval $k_2 \geq 0.549$: surface heat flow $\geq \sim 6.3 \text{ mWm}^{-2}$, ice I_h - crust $\sim 90 \text{ km}$, depth of the ocean $\geq \sim 310 \text{ km}$. The contribution of the crystallization energy released during freezing over time of the internal ocean is $\sim 6.3 \cdot 10^{10} \text{ W}$, and the corresponding contribution to the surface heat flux is determined to be $\sim 0.76 \text{ mWm}^{-2}$. Estimates of possible maximum surface heat flow in Titan $\sim 5.8 \text{ mWm}^{-2}$ and the corresponding model parameters were obtained: the estimated Love number $k_2 \sim 0.539 \text{ mWm}^{-2}$, the thickness of the I_h -crust $\sim 100 \text{ km}$, the depth of the water ocean $\sim 290 \text{ km}$. The insertion of corrections to k_2 (an increase of $\sim 5\%$) due to simplifications made in the rheology of Titan will make it possible to consider these models consistent with the experimental Love numbers.

Introduction:

In a recent paper [1], based on the processing of new gravitational data, the updated value of the Love number $k_2 = 0.616 \pm 0.067$ was published, which differs significantly from the previously determined values of $k_2 = 0.589 \pm 0.15$ [2], primarily due to the narrowing of the determination error.

The k_2 data definitely indicate the presence of large masses of fluid, causing powerful tidal stresses and strains in the bowels of Titan [3]. However, reliable experimental data on the thickness of the proposed inland ocean and ice crust have not yet been obtained.

This paper presents the results of estimates of Love numbers k_2 , h_2 for a wide range of models of partially differentiated Titan. The limitations on the internal structure, the composition of the satellite and the ocean, following from the modern estimates of the values of k_2 [1], are discussed. Particular attention is paid to the outer ice-water shell.

Problem definition and solution method:

The satellite consists of three shells of different composition [4]: 1) the outer ice-water shell (ice crust from ice I_h + underlying water layer (ocean) + high-pressure ice). 2) an intermediate stone-ice shell (mantle) consisting of a homogeneous mixture of high-pressure ices and iron-stone material (substance L / LL chondrites [5, 6]). 3) the central core of iron-stone material. The formulation of the problem and the solution method are described in detail in [7]. As a result of the solution, there are: distribution of the density of high-pressure ice over the mantle depth and their phase boundaries; mass concentrations of ice in the mantle; the location of the boundary of the ice-water shell - stone-ice mantle; sizes of iron core; water (ice) / rock ratio in the mantle of Titan and in the satellite as a whole.

For estimates of Love numbers, Titan is considered as an elastic inhomogeneous gravitating sphere. Love numbers are found by integrating linearized equations for small elastic deformations in a spherically symmetric incompressible self-gravitating body, taking into account the boundary conditions and continuity of the medium [8].

Results and discussion:

Love numbers were determined for a series of models of partially differentiated Titan that satisfy all the constraints imposed. As shown by calculations, the surface heat flux (F) from the depths of the satellite in all models actually determines the structure of the ice-water shell and Love numbers. Therefore, the flow F was used as the main parameter of the models. At heat flux $F < F_0$ ($F_0 \approx 3.1 \text{ mWm}^{-2}$), Titan's water-ice shell is represented only by ice, while at $F > F_0$ an internal ocean forms at the satellite, the depth of which at $F = 5 \text{ mWm}^{-2}$ reaches 250 km. The calculation results show a close to linear dependence of the model values of the Love numbers k_2 on the thickness of the ice crust (H_{ih}) and of the F , Fig. 1.

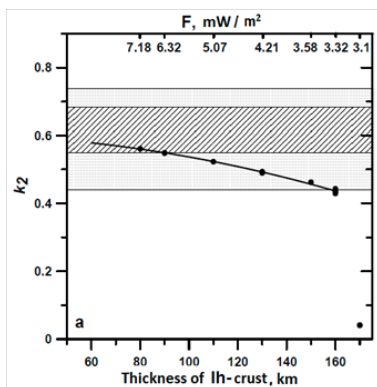


Fig. 1. The dependence of the Titan Love numbers k_2 on the thickness of the Ih - crust and flow F . The gray hatching shows Love numbers k_2 according to [2], dark hatching — according to [1].

Model Love numbers should satisfy the conditions $k_2 > \sim 0.549$, which corresponds to the restrictions on heat fluxes $F > \sim 6.3 \text{ mWm}^{-2}$, thickness of the ice crust $H_{ih} \geq \sim 90 \text{ km}$, depth of the ocean $H_w \geq \sim 300 \text{ km}$.

The surface flow can be written: $F = F_R + F_T + F_C$,

where F_R is the radiogenic energy flow, F_T is the dissipation energy flow, F_C is the phase transition (crystallization) energy flow. We estimated the maximum possible heat flows F .

We obtained the radiogenic heat release in Titan, $F_R \approx 4.15 \text{ mWm}^{-2}$ from the heat decay of the chondritic substance for time t from the creation of the solar system and the rock / water ratio (50%) in the satellite.

Based on the results of [9–11], we approximately take the value of tidal energy: $QT \approx 7.6 \cdot 10^{10} \text{ W}$; the corresponding contribution to the surface flow $F_T \approx 0.9 \text{ mWm}^{-2}$.

To estimate the contribution of crystallization energy, an approximate balance equation for surface flows was solved. Two quasistationary identical Titan models for two time values are considered. The estimated energy of crystallization processes $Q_C \approx 6.3 \cdot 10^{10} \text{ W}$ and the contribution of crystallization to the surface flow $F_C \approx 7.6 \text{ mWm}^{-2}$. Summing up all the components of the heat flux, we got $F \approx 5.8 \text{ mWm}^{-2}$, which leads to the following values: $k_2 \approx 0.539$, ice crust thickness $H_{ih} \approx 100 \text{ km}$, depth of the ocean $H_w \approx 290 \text{ km}$. Love numbers k_2 are obtained in the present work for the Titan rheological model, which does not take into account the viscosity of its bowels. There is reason to believe that the value of the Love number, calculated for the real values of the shear modulus, can probably be increased by five percent and $k_2 \approx 0.57$. The introduction of corrections to k_2 will make it possible to make models with heat flow $F = 5.8 \text{ mWm}^{-2}$ consistent with the experimental Love numbers.

Acknowledgments:

This research was supported by the RFBR grant № 18-05-00685, Program of the Presidium of the Russian Academy of Sciences No. 17.

References:

- [1] Durante D., Hemingway D. J., Racioppa P., Iess L., & Stevenson D. J. (2019). Titan's gravity field and interior structure after Cassini. *Icarus*, 326, 123–132.
- [2] Iess L., Jacobson R.A., Ducci M., Stevenson D.J., Lunine J.I., Armstrong J.W., Asmar S.W., Racioppa P., Rappaport N.J., Tortora P. (2012). The tides of Titan. *Science* 337(6093), 457-459.
- [3] Baland R.M., Tobie G., Lefevre A., Van Hoolst T. (2014) Titan's internal structure inferred from its gravity field, shape, and rotation state. *Icarus*. 237, 29-41.
- [4] Dunaeva A. N., Kronrod V. A., Kuskov O. L. (2014). Models of Titan with Water–Ice Shell, Rock–Ice Mantle, and Constraints on the Rock–Iron Component Composition. *Doklady Earth Sciences*, Vol. 454, Part 1, pp. 89–93.
- [5] Kuskov O.L., Kronrod V.A. (2001). Core sizes and internal structure of the Earth's and Jupiter's satellites // *Icarus*. V. 151. P. 204-227.
- [6] Kuskov O.L., Kronrod V.A. (2005). Internal structure of Europa and Callisto // *Icarus*. V. 177. P.550–569.
- [7] Dunaeva A.N., Kronrod V.A., & Kuskov O.L. (2016). Physico-chemical models of the internal structure of partially differentiated Titan. *Geochemistry International*, 54(1), 27-47.
- [8] Raevskiy S.N., Gudkova T.V., Kuskov O.L., Kronrod V.A. (2015). On Reconciling the Models of the Interior Structure of the Moon with Gravity Data. *Izvestiya, Physics of the Solid Earth*. Vol. 51, No. 1, pp. 134–142.
- [9] Sohl F., Sears W.D., Lorenz R.D. (1995). Tidal dissipation on Titan. 1995. *Icarus* 115(2), 278_294.
- [10] Chen E., Nimmo F., Glatzmaier G.(2014). Tidal heating in icy satellite oceans. *Icarus*. 229, 11–30.
- [11] Hay H. C. & Matsuyama I. (2019). Nonlinear tidal dissipation in the subsurface oceans of Enceladus and other icy satellites. 2019. *Icarus*, 319, 68-85.

PLUTO GRANULES AND X-RAY EMISSION CALCULATED BY MODULATED ORBITAL FREQUENCIES (COMPARISON WITH SATURN AND JUPITER)

G.G. Kochemasov

IGEM of the Russian Academy of Sciences, 35 Staromonetny, 119017 Moscow, RF, kochem.36@mail.ru

Keywords:

Pluto, tectonic granulation, X-ray emission, frequency modulation, Saturn, Jupiter

Introduction:

“Orbits make structures”. As all cosmic bodies in Universe rotate and move in several orbits with very different orbiting frequencies they are affected by modulated waves. They appear as predicted by the radio wave physics. The modulation is division and multiplication of the higher frequency by the lower one. As a result along with main frequencies appear two side frequencies with corresponding them tectonic granules. The wave born tectonic granules normally are evenly sized, shoulder-to-shoulder disposed in lines, crossing lines, grids and lattices. Examples are below (Fig. 1, 2, 3, 4). Very effective “leopard skin” structure of the saturnian atmosphere with regularly spaced storms about 400 km across (Fig. 1) can be calculated by the modulation of rapidly rotating atmosphere (1/0.45 days, 60000 km radius) by slowly orbiting Saturn around Sun (1/30 years). To modulated side frequencies correspond smaller granules ($1/3421 \times 7.5$) $3.14 \times 60000 = 7.3$ km and larger granules ($1/3421 : 7.5$) $3.14 \times 60000 = 413.5$ km. The smaller granules are not yet observed (maybe they show themselves in kilometric radio emissions), but the larger granules are ubiquitous on the Saturn’s surface as the “leopard skin” spots. Waiting for Juno detailed images we analyzed the famous Voyager image with the Red Spot (Fig. 2). This image reveals various wave forms and penetrating them weak and fine tissue made of granules ~ 200 to 400 km across. This size is explained by modulation by 1/12 y.fr. Of 1/10 h.fr. giving modulated size ~ 191 km. The Juno Red Spot image (Fig. 2) confirms this very fine modulated granulation clearly seen at the lower part of the image (south of the Spot).

Pluto’ rotation and orbiting with frequency 1/6.39 days around the barycenter of the Pluto-Charon system gives granule size 16.3 km ($\pi R/228$) according to the relation between orbiting frequencies and tectonic granules sizes (Kochemasov, 1986 – 2016). These granules as polygons about 20 km across are visible especially on the brightest and highest sector of Sputnik Planum. Another widespread granule size is about 0.25 km (Fig. 3 — “lake” ~ 30 km across peppered with fine granules ~ 0.25 km and Fig. 4). It is calculated by modulation of fr. 1/6.39 days by orbital fr. 1/248 years = 1/90465 days to obtain side frequency 1/14157 and corresponding to it granule size 0.263 km.

The first detection of Pluto in X-rays has been made using NASA’ Chandra X-ray Observatory. Chandra obtained data during four separate observations. During each observation Chandra detected low energy X-rays from the planet (Fig. 5). X-rays from Pluto are somewhat surprising result given that Pluto — a cold, ice-rocky world without a moon with magnetic field — has no natural mechanism for emitting X-rays. However, it is known that comets can create X-rays by the interaction between their gases and the solar wind. The immediate mystery is that Chandra’s readings on the brightness of the X-rays are much higher than expected from the solar wind interacting with Pluto’s atmosphere. Some inadequate explanations were proposed. But modulation of orbiting frequencies of Pluto was not considered. In the solar system it is 1/248y., in Galaxy it is approx. 1/200000000 y. Division of the first by the second gives 1/806452 y. To this fr. corresponds wave long ~ 10 -8 M (proportion with 16.3 km corresponding to the rotation fr. 1/6.39 d. [1, 2] or soft X-rays.

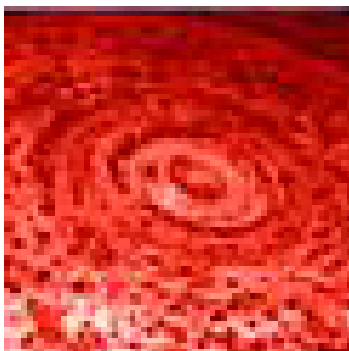


Fig. 1



Fig. 2

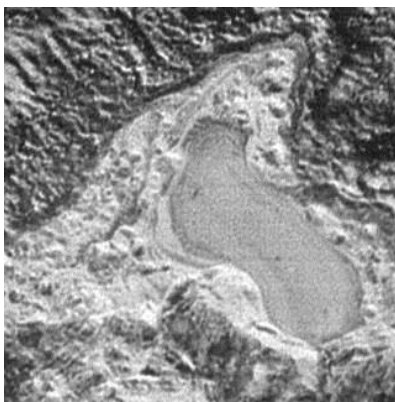


Fig. 3



Fig. 4. Fig. 1. Saturn, PIA08333-“Leopard skin spots”. Fig. 2. Jupiter, Juno image PIA21772 Fine granulation south of the Red spot. Fig. 3, Pluto, “Lake” ~ 30 km across covered by fine granules. Fig.4. Detail_lorri_rider, Pluto.

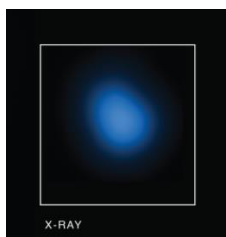


Fig. 5. Pluto_Main-Chandra1, X-ray.

References:

- [1] Kochemasov G.G. Wave modulation in planetology: a new way of planetary thinking // The seventh Moscow Solar System symposium, 10-14 October 2016, Space Research Institute (IKI), Moscow, Abstracts, 7MS3-PS-67, p. 283-284.
- [2] Kochemasov G.G. Gamma-ray emission in the Universe — a possible explanation by the wave modulation // The eighth Huntsville gamma-ray burst symposium, 2016, Abstract №4107.

SATURNIAN HEXAGON IS NOT ALONE

G.G. Kochemasov

*IGEM of the Russian Academy of Sciences, 35 Staromonetny, 119017
Moscow, Russia, kochem.36@mail.ru*

Keywords:

Hexagon, Saturn, Mimas, Tethys, Dione, Rhea, Iapetus, tetrahedron, octahedron, wave structures.

Introduction:

Saturn's polar dichotomy was observed as color hues: gold south and azure north. Now infrared images of NASA/JPL/University of Arizona allow seeing substantial structural differences of two polar regions. First was observed a large centered on the south pole hurricane 8000 km across with a central eye about 1500 km across (PIA08333). Then on the northern night hemisphere was observed a huge centered on the pole hexagon about 25000 km across (PIA09186)(Fig. 1). The dichotomous structure of celestial bodies is their first characteristic feature marked as Theorem 1 of the wave plane-tology [1 & others]. Origin of this ubiquitous feature is due to an interference of warping waves 1 of four directions appearing in any rotating body (but all bodies rotate!) moving in elliptical orbit with periodically changing accelerations (I. Kepler has shown that all planetary bodies move in such orbits) [1]. The fundamental warping inertia-gravity wave 1 has overtones of which wave 2 — the first overtone is most prominent in structures of celestial bodies as traces of an octahedron. It makes tectonic sectors superimposed on tectonic dichotomy (e.g., continents and secondary oceans of Earth; the Pacific basin is the primary ocean — one of the dichotomous segments of Earth).

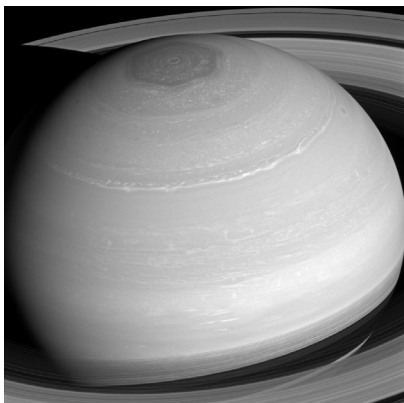


Fig. 1 Saturn, PIA18280, R=60000 km

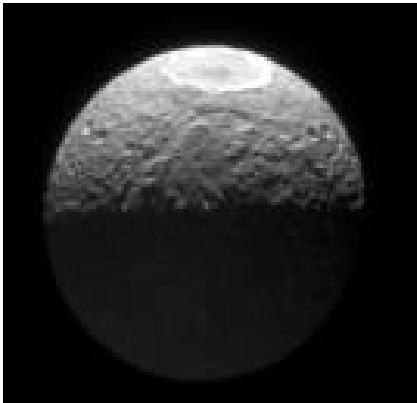


Fig. 2. Mimas, PIA09811, R=197 km

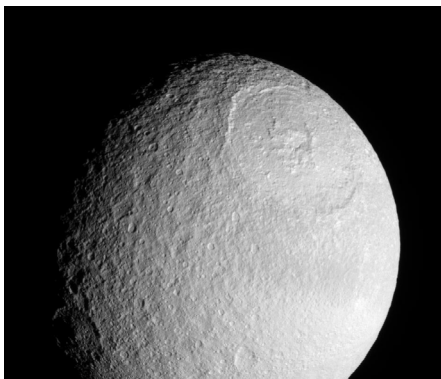


Fig. 3. Tethys, PIA09017

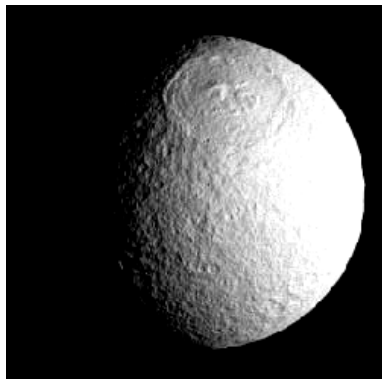


Fig. 4. Tethys, PIA10438, R = 524 km

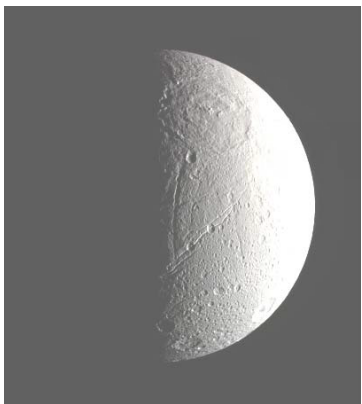


Fig. 5. Dione PIA08938, R = 559 km

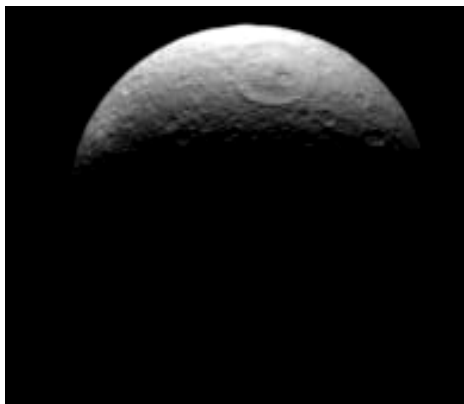


Fig. 6. Rhea, PIA08909, R = 765 km

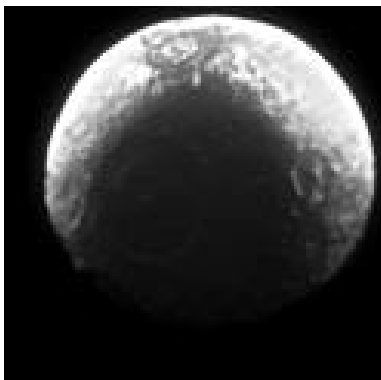


Fig. 7. Iapetus, PIA08273, R = 718 km

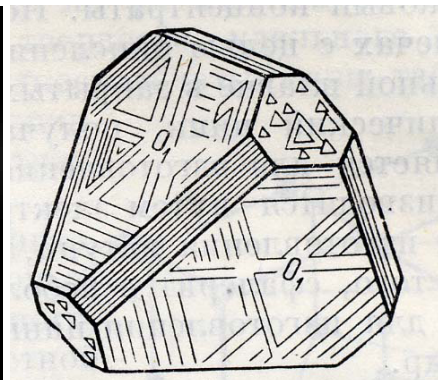


Fig. 8. Tetrahedron crystal (sphalerite) with lineations of three directions reflecting orientation of faces.

Interfering waves tend to produce in globes geometrical figures according to their lengths. Thus, wave 1 makes tetrahedron, wave 2 octahedron, wave 4 cube. Naturally, mighty gravity of relatively large bodies (more than 400 to 500 km across) “smashes” this superimposed figures in favor of a sphere. What is left, it is axes and planes of symmetry of this figures and perching but obliterated vertices (e.g., the Pamirs-Hindukush and antipodean to it the Easter Island). A tetrahedron — the simplest polyhedron of Plato — has three faces narrowing to a vertex and widening to a fourth face. Thus, tetrahedron is a basically dichotomous body because cut amidst any of its 4 axes of symmetry it always has an opposition of a vertex (contraction) to a face (expansion) (Fig. 8). Traces (projection) of three tetrahedron faces combined with an octahedron are typically seen on surfaces of planetary spheres as hexagons, for an example, on many of the saturnian satellites icy surfaces (Fig. 2–7) and in total shapes of some small bodies. Now a hexagon shows itself on the northern polar region of Saturn where it is rather stable as it was observed even by the Voyagers about 30 years ago. This stability of planetary structural features (even in a gaseous media!) is explained by producing them standing waves that for larger waves have rather long periods of phase change. So, at Saturn now is the expanded northern hemisphere with well developed wide structural lines and the contracted southern hemisphere with smashed squeezed structures twisted in hurricane. Strikingly, hexagons of icy saturnian satellites (Fig. 2–7) mimic not only shape but relative size of the big saturnian hexagon. This similarity betrays their common wave origin.

The saturnian hexagon is not flat but volumetric as it continues deep into the atmosphere for at least 100 km and projects up into the stratosphere for 300 km [2].

References:

- [1] Kochemasov G.G. 1998. Tectonic dichotomy, sectoring and granulation of Earth and other celestial bodies. Proceedings of the International Symposium on New Concepts in Global Tectonics, "NCGT-98 TSUKUBA", Geological Survey of Japan, Tsukuba, Nov 20–23, 1998, p. 144–147.
- [2] Fletcher L.N., Orton G.S., Sinclair J.A. et al. 2018. A hexagon in Saturn's northern stratosphere surrounding the emerging summertime polar vortex // Nature, Nature communications, 03 Sept. 2018, article №: 3564

POLARIZATION OF COMET 46P/WIRTANEN

M. Zheltobryukhov¹, E. Chornaya^{2,1,3}, E. Zubko⁴,
 O.V. Ivanova^{5,6,7}, A. Kochergin^{2,1}, G. Kornienko¹, I. Luk'yanyk⁶, A. Matkin¹,
 I.E. Molotov³, S.S. Kim⁴, and G. Videen^{8,9}

¹ Institute of Applied Astronomy of RAS, 10 Kutuzova Emb., Saint-Petersburg 191187, Russia

² Far Eastern Federal University, 8 Sukhanova St., Vladivostok 690950, Russia, ekaterina.d.chornaya@gmail.com

³ Keldysh Institute of Applied Mathematics, Russian Academy of Sciences, 4 Miusskaya sq., Moscow 125047, Russia

⁴ Humanitas College, KyungHeeUniversity, 1732 Deogyong-daero, Yongin-si, Gyeonggi-do17104, Republic of Korea

⁵ Astronomical Institute of the Slovak Academy of Sciences, SK-05960 TatranskáLomnica, Slovak Republic

⁶ Astronomical Observatory, TarasShevchenkoNationalUniversity of Kyiv, 3 Observatorna St., 04053, Kyiv, Ukraine

⁷ Main Astronomical Observatory of National Academy of Sciences, 27 AkademikaZabolotnoho St., Kyiv, 03143, Ukraine

⁸ Space Science Institute, 4750 Walnut Street, Boulder Suite 205, CO 80301, USA

⁹ Department of Astronomy and Space Science, KyungHeeUniversity, 1732, Deogyong-daero, Giheung-gu, Yongin-si, Gyeonggi-do17104, Republic of Korea

Keywords:

Comet 46P/Wirtanen; polarization; low- P_{\max} comets; observations.

Introduction:

Comet 46P/Wirtanen is a Jupiter-family comet whose orbital period is of approximately 5.44 years and perihelion lying at about 1.06 au. The comet is known for being a primary target of the Rosetta space mission prior to it being rescheduled to 67P/Churyumov–Gerasimenko. Although 46P experienced a number of perihelion passages since discovery in 1948, polarization of its coma remains largely unknown. In its 2018 apparition, comet 46P approached Earth within ~ 0.08 au, which made possible its study with relatively small telescopes. We used this rare opportunity to conduct a comprehensive study of the 46P polarization.

Observations:

We started our polarimetric observations of comet 46P on November 16, 2018, about a month prior to its perihelion passage December 12, and continued until January 17, 2019. Over this two-month time period, weather conditions were favorable on 13 nights. Observations were made with the 22-cm telescope located at the Ussuriysk Astrophysical Observatory (code C15), which operates within the International Scientific Optical Network (ISON). We used CCD detector FLI ProLine PL4301E that has a resolution of 2084 x 2084 pixels and pixel size of 24 μm . The field of view of the CCD detector is 326 x 326 arcmin with angular resolution of 9.39 x 9.39 arcsec per pixel. The Johnson V filter was used for polarimetric observations of the comet. We use a dichroic polarization filter (analyzer), which rotated sequentially through three fixed position angles 0°, +60°, and +120°. Using the images obtained at three evenly distributed orientations of the analyzer, we compute the corresponding fluxes from the inner coma within two aperture radii, 5,000 km and 10,000 km. The obtained magnitudes can be translated into the I, Q, and U Stokes parameters using the Fesenkov formulae [1] and, thus, one can compute the degree of linear polarization $P = -Q/I$, that often is expressed in percent.

On twelve of the epochs, we repeated polarimetric observations of 46P 12 times; whereas, on one epoch observations were repeated 10 times. Every sequence of measurements yielded similar values of polarization in the 46P coma.

Results and Discussion:

Fig. 1. shows the shape and size of the 46P coma on December 12 of 2018, during its perihelion passage. The inner part of the coma (radius of $\sim 5,000$ km)

is shown here overexposed. As one can see, the comet had a very much rounded coma, with no apparent tail. The coma extends beyond 15,000 km from the 46P photometric center.

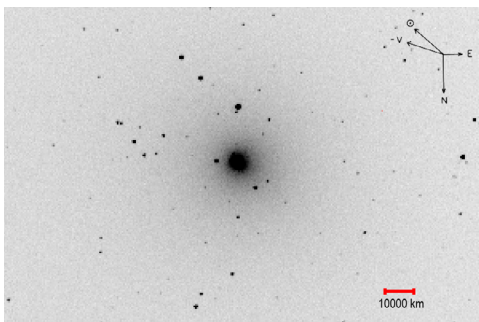


Fig. 1. Image of comet 46P taken on December 12 of 2018, date of perihelion passage.

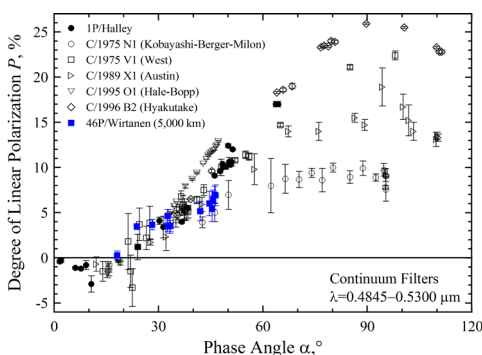


Fig. 2. Degree of linear polarization as a function α , of phase angle in comet 46P versus six other comets.

In Fig. 2, we compare the polarization measured in 46P with the V Johnson filter through the aperture of radius $\sim 5,000$ km (blue squares) versus six other comets measured with the continuum filters in the blue-green part of the spectrum. Data on these comets are taken from the compilation presented in [2], where more details and references to the observations are given. Fig. 2 demonstrates significant dispersion of the positive polarization maximum P_{\max} in comets, which was first noted in [3] and, later, investigated in [2]. As one can see, our observations suggest that 46P may belong to a group of comets with low P_{\max} . This conclusion, however, requires further investigation as it is difficult to constrain unambiguously P_{\max} in a comet observed at $\alpha \leq 46^\circ$. Nevertheless, it is worth noting that low- P_{\max} comets have very long orbital periods, except for 23P/Brorsen–Metcalf (~ 70 years). Comet 46P may turn out to be the first Jupiter-family comet with low P_{\max} .

Finally, we address the mechanism governing the dispersion of P_{\max} in comets. In the literature (e.g., [3]), it is believed to result from the depolarizing effect of resonant emission from complex gaseous molecules. The solid line in Fig. 3 demonstrates the angular profile of polarization of the C_2 emission, whose $P_{\max} \approx 7.7\%$ [4]. Although such emission could formally affect our polarimetric measurements of 46P with the broadband V filter, in practice, it is very difficult to obtain a significant contribution of the C_2 emission to the response from the inner coma.

Indeed, there is no C_2 ice in comets. The fact that we, nevertheless, observe the C_2 emission in a cometary coma suggests that these molecules are a product of photodissociation of some parent molecule(s) and/or carbonaceous dust. This is a long lasting process. During that time, parent molecules/particles depart from the nucleus by a considerable distance that is referred as scale length. It is significant that, at a heliocentric distance of

about 1 au, the scale length of the C_2 parents is estimated to be a minimum 16,000 km; whereas, some estimations suggest a much larger scale length, up to 58,000 km [5]. It implies observations of 46P with the 5,000-km aperture cannot be significantly affected by the C_2 emission.

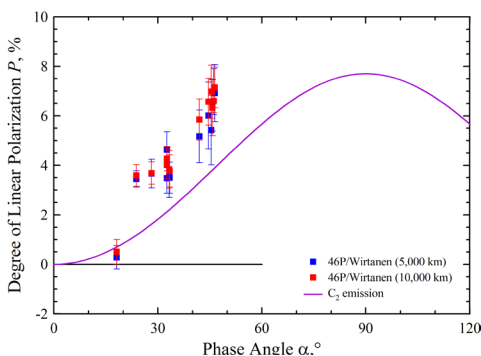


Fig. 3. Degree of linear polarization as a function of phase angle in comet 46P inferred with apertures of two different radii, 5,000 km and 10,000 km. The solid line shows the angular profile of polarization of the C_2 gaseous emission computed based on [4].

Interestingly, an increase of the aperture radius to 10,000 km should enhance the relative contribution of the C_2 emission, which must decrease the polarization. However, we observe the opposite trend in 46P (see Fig. 3). This observation provides supports the conclusion of weak C_2 contamination of our measurements.

References:

- [1] Hines D.C., et al. Hubble Space Telescope pre-perihelion ACS/WFC imaging polarimetry of comet Ison (C/2012 S1) at 3.81 au // *Astroph. J. Lett.* 2014. V. 780. Article number L32.
- [2] Zubko E., et al. The positive-polarization of cometary comae // *Planet. Space Sci.* 2016. V. 123. P. 63–76.
- [3] Chernova G.P., et al. Polarimetric characteristics of dust particles as observed in 13 comets – Comparisons with asteroids // *Icarus*. 1993. V. 103. P. 144–158.
- [4] Le Borgne J.F., et al. Polarimetry of visible and near-UV molecular bands – Comets P/Halley and Hartley-Good // *Astron. Astrophys.* 1987. V. 173. P. 180–182.
- [5] Fink U., Combi M.R. The effect of using different scale lengths on the production rates of Comet 46P/Wirtanen // *Planet. Space Sci.* 2004. V. 52. P. 573–580.

FAST VARIATIONS OF COMPOSITION IN THE 21P/GIACOBINI-ZINNER COMA

E. Chornaya^{1,2,7}, E. Zubko³, I. Luk'yanyk⁴, A. Kochergin^{1,2},
M. Zheltobryukhov², O.V. Ivanova^{5,4,6}, G. Kornienko², A. Matkin²,
A. Baransky⁴, I.E. Molotov⁷, V.S. Sharoshchenko¹, and G. Videen^{8,9}

¹ Far Eastern Federal University, 8 Sukhanova St., Vladivostok 690950, Russia, ekaterina.d.chornaya@gmail.com

² Institute of Applied Astronomy of RAS, 10 Kutuzova Emb., Saint-Petersburg 191187, Russia

³ Humanitas College, Kyung Hee University, 1732 Deogyong-daero, Yongin-si, Gyeonggi-do 17104, Republic of Korea

⁴ Astronomical Observatory, Taras Shevchenko National University of Kyiv, 3 Observatorna St., 04053, Kyiv, Ukraine

⁵ Astronomical Institute of the Slovak Academy of Sciences, SK-05960 Tatranská Lomnica, Slovak Republic

⁶ Main Astronomical Observatory of National Academy of Sciences, 27 Akademika Zabolotnoho St., Kyiv, 03143, Ukraine

⁷ Keldysh Institute of Applied Mathematics, Russian Academy of Sciences, 4 Miusskaya sq., Moscow 125047, Russia

⁸ Space Science Institute, 4750 Walnut Street, Boulder Suite 205, CO 80301, USA

⁹ Department of Astronomy and Space Science, Kyung Hee University, 1732, Deogyong-daero, Giheung-gu, Yongin-si, Gyeonggi-do 17104, Republic of Korea

Keywords:

Comet 21P/Giacobini-Zinner; polarization; color; modeling; agglomerated debris particles.

Introduction:

Comet 21P/Giacobini-Zinner (hereafter 21P/G-Z) is a short-period comet with orbital period of approximately 6.6 years. Its perihelion lies at about 1 au, making ground-based observations at large phase angles possible. The comet has a long history of investigation, including polarimetric observations, which were first accomplished in 1959 [1]. Polarimetric studies were also conducted in the apparitions of 1985 [2, 3] and 1998–1999 [4]. Here we report results of our polarimetric and photometric observations of comet 21P/G-Z in its apparition of 2018.

Observation and data reduction:

Imaging polarimetry.

On September 10, 12, 16, and 17 of 2018, we conducted polarimetric observations of comet 21P/G-Z at the prime focus of the 22-cm telescope of the Ussuriysk Astrophysical Observatory (observatory code C15), which operates within the International Scientific Optical Network (ISON). The telescope was equipped with a commercially available CCD detector SBIG STX-16803 that has a resolution of 4096×4096 pixels and pixel size of 9 μm. The field of view of the CCD detector is 251×251 arcmin with angular resolution of 3.68×3.68 arcsec per pixel. The comet was observed through the V filter of the Johnson-Cousins photometric system. In addition, we used a dichroic polarization filter (analyzer). The analyzer was rotated sequentially through three fixed position angles 0°, +60°, and +120°. These observations allow computation of the degree of linear polarization $P_Q = (I_{\lambda} - I_{\perp\lambda}) / (I_{\lambda} + I_{\perp\lambda})$ of 21P/G-Z [5]. Note, P_Q is measured in per cent. A detailed log of the polarimetric observations of comet 21P/G-Z is presented in Table 1.

Photometry.

Photometric observations of comet 21P/G-Z were carried out at the observation station Lisnyky of the Astronomical Observatory of Taras Shevchenko National University of Kyiv (Ukraine) with the AZT-8 telescope (D=0.7 m, F=2.8 m, observatory code — 585) on September 16, 2018. The CCD PL47-10 FLI camera with 1×1 binning was used as a detector with an image size of 1027×1056 pixels and a scale of 0.95"/pix, which corresponds to a full field

of $16' 15'' \times 16' 43''$. We obtained images through the Johnson-Cousins broadband V and R filters. A detailed log of the observations of comet 21P/G-Z is presented in Table 1.

Table 1. Log of observations of the inner coma (radius of aperture ~ 6000 km) in comet 21P/G-Z

Date, UT	Exp, sec	F	r_h , au	Δ , au	α , °	m	P_Q , %
10.7310 [*]	30	V	1.01	0.392	78.0	10.46 ± 0.03	22.52 ± 0.49
12.7267	30	V	1.01	0.392	77.8	10.11 ± 0.03	22.51 ± 0.49
16.6875	60	V	1.01	0.398	77.0	10.47 ± 0.03	20.46 ± 0.50
16.9894	20	V, R	1.01	0.398	76.9	10.08 ± 0.06 (V), 9.58 ± 0.05 (R)	-----
17.7125	30	V	1.01	0.400	76.7	10.49 ± 0.04	18.77 ± 0.39

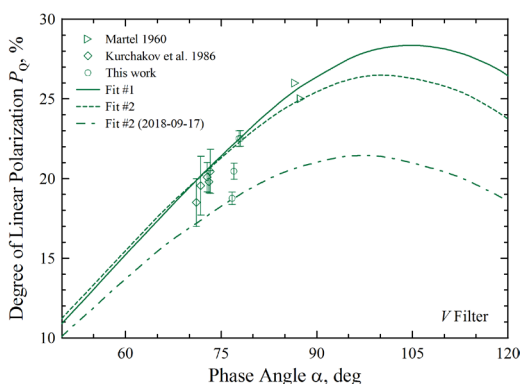


Fig. 1. Aperture-averaged degree of linear polarization P in the blue-green portion of the spectrum as a function of the phase angle α . Open symbols show data for comet 21P/G-Z obtained by different teams on different epochs; whereas, solid and dashed lines correspond to modeling with the agglomerated debris particles.

Results and Discussion:

In Fig. 1 we plot the degree of linear polarization P in comet 21P/G-Z as a function of phase angle α that was measured by three different teams. All these observations correspond to the inner coma, whose radius was about 5000–6000 km. Analysis of this entire set of observational data reveals that they can be satisfactorily reproduced within a two-component model of the cometary coma that has been successful in other comets [e.g., 6]. The model realistically reproduces highly irregular shape of cometary dust with the agglomerated debris particles (see Fig. 2).

The modeling reveals that the 21P/G-Z coma predominantly consists of Mg-rich silicate particles, whose complex refractive index m is characterized with $\text{Re}(m)=1.6\text{--}1.7$ and $\text{Im}(m)=0\text{--}0.02$ [7], and amorphous-carbon particles with $m=2.43+0.59i$ [8]. Both components obey the same power-law size distribution r^{-n} with the power index ranging from $n=1.5$ to 2.3. It is worth noting that such chemical composition and size distribution of dust in 21P/G-Z appears in good accordance with what was previously detected in situ in comet 1P/Halley [9, 10].

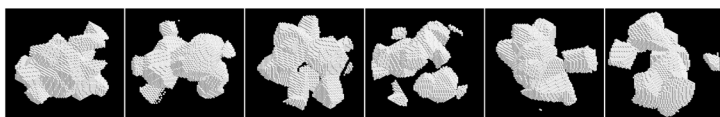


Fig. 2. Six examples of the agglomerated debris particles; see [6, 7] for more details on their generation and characteristics.

Solid line in Fig. 1, corresponding to Fit #1, shows results obtained with a mixture of 22.5% (by volume) of agglomerated debris particles with $m=1.6+0.01i$ and 77.5% of the agglomerated debris particles with $m=2.43+0.59i$. The dashed line (Fit #2) corresponds to 33% of particles with $m=1.6+0.02i$ and 67% of particles with $m = 2.43+0.59i$. As one can see, both fits satisfactorily reproduce the vast majority of available polarimetric observations of 21P/G-Z with the broadband V filter. This suggests no dramatic change in population of dust emanated from 21P/G-Z over the last 59 years.

We also notice some day-to-day variations of polarization in comet 21P/G-Z. One such variation was detected on 2018-09-17. We adjust Fit #2 to this epoch (dash-dot line) and find a somewhat greater relative volume abundance of the silicate particles, 45 % vs. 33 % on the other epochs. Temporal variations in the relative abundance of constituent materials in the 21P/G-Z coma could be indicative of changes in its jet activity. This makes comet 21P/G-Z an interesting target for further study in its future apparitions.

References:

- [1] Martel M.-T. Observations polarimétriques de la comète Giacobini-Zinner (1959b) // *Annales d'Astrophysique*. 1960. V. 23, P. 498. [In French].
- [2] Chernova G.P., et al. Polarimetric characteristics of dust particles as observed in 13 comets – Comparisons with asteroids // *Icarus*. 1993. V. 103. P. 144–158.
- [3] Kurchakov A.V., et al. Observations of polarization of comet Giacobini-Zinner (1984e) // *Komet. Tsir*. 1986. No. 350. P. 4. [In Russian].
- [4] Kiselev N.N. et al. Anomalous wavelength dependence of polarization of Comet 21P/Giacobini-Zinner. // *Planet. Space Sci*. 2000. V. 48. P. 1005–1009.
- [5] Zubko E., Chornaya E. On the ambiguous definition of the degree of linear polarization // *Res. Notes of the AAS*. 2019. V. 3, Article number 45.
- [6] Zubko E., et al. The positive-polarization of cometary comae // *Planet. Space Sci*. 2016. V. 123. P. 63–76.
- [7] Dorschner J., et al. Steps toward interstellar silicate mineralogy. II. Study of Mg-Fe-silicate glasses of variable composition // *Astron. Astroph*. 1995. V. 300. P. 503–520.
- [8] Duley W.W. Refractive indices for amorphous carbon // *Astroph. J*. 1984. V. 287. P. 694–696.
- [9] Fomenkova M.N., et al. Compositional trends in rock-forming elements of comet Halley dust // *Science*. 1992. V. 258, P. 266–269.
- [10] Mazets E.P., et al. Comet Halley dust environment from SP-2 detector measurements // *Nature*. 1986. V. 321. P. 276–278.

PECULIAR POLARIZATION OF COMET C/2018 V1 (MACHHOLZ-FUJIKAWA-IWAMOTO)

E. Zubko¹, E. Chornaya^{2,3,4}, M. Zheltobryukhov³, A. Matkin³,
O.V. Ivanova^{5,6,7}, D. Bodewits⁸, A. Kochergin^{2,3}, G. Kornienko³, I. Luk'yanyk⁵,
D.C. Hines⁹, G. Videen^{10,11}

¹ *Humanitas College, Kyung Hee University, 1732 Deogyong-daero, Yongin-si, Gyeonggi-do 17104, Republic of Korea; evgenij.s.zubko@gmail.com*

² *Far Eastern Federal University, 8 Sukhanova St., Vladivostok 690950, Russia*

³ *Institute of Applied Astronomy of RAS, 10 Kutuzova Emb., Saint-Petersburg 191187, Russia*

⁴ *Keldysh Institute of Applied Mathematics, Russian Academy of Sciences, 4 Miusskaya sq., Moscow 125047, Russia*

⁵ *Astronomical Institute of the Slovak Academy of Sciences, SK-05960 Tatranská Lomnica, Slovak Republic*

⁶ *Astronomical Observatory, Taras Shevchenko National University of Kyiv, 3 Observatorna St., 04053, Kyiv, Ukraine*

⁷ *Main Astronomical Observatory of National Academy of Sciences, 27 Akademika Zabolotnoho St., Kyiv, 03143, Ukraine*

⁸ *Auburn University, Physics Department, Auburn, AL 36849-5319, USA*

⁹ *Space Telescope Science Institute, 3700 San Martin Drive, Baltimore, MD 21218, USA*

¹⁰ *Space Science Institute, 4750 Walnut Street, Boulder Suite 205, CO 80301, USA*

¹¹ *Department of Astronomy and Space Science, Kyung Hee University, 1732, Deogyong-daero, Giheung-gu, Yongin-si, Gyeonggi-do 17104, Republic of Korea*

Keywords:

Comet C/2018 V1 (Machholz-Fujikawa-Iwamoto); polarization; low- P_{\max} comets; modeling; agglomerated debris particles.

Introduction:

Twenty six years ago, Chernova et al. [1] reported results of their polarimetric survey of thirteen different comets, where they unambiguously demonstrated significant dispersion of polarization in comets at large phase angles ($\alpha \sim 90^\circ$). This can be seen in Fig. 1 (adapted from [2]) demonstrating the degree of linear polarization P as a function of phase angle α in various comets. However, there exists a disparity between the numbers of comets with high and low maximum of polarization P_{\max} . Namely, there are well over a dozen comets whose $P_{\max} > 20\%$ is detected with confidence; whereas, only three comets with $P_{\max} < 10\%$ are known to date. In mid-November of 2018, we conducted a polarimetric study of a newly discovered comet C/2018 V1 (Machholz-Fujikawa-Iwamoto) that appeared to be a fourth member of the low- P_{\max} family. This comet, in fact, has the lowest P_{\max} yet observed.

Observations:

We conducted polarimetric observations of comet C/2018 V1 shortly after its discovery on November 7, 2018. The comet passed perihelion at 0.387 au on December 3, 2018. Weather conditions were favorable on three dates, November 16, 17, and 18. It is significant that the results obtained on all three epochs appear in very good accordance with one another. Observations were made with the 22-cm telescope located at the Ussuriysk Astrophysical Observatory (code C15), which operates within the International Scientific Optical Network (ISON). We used CCD detector FLI ProLine PL4301E that has a resolution of 2084×2084 pixels and pixel size of 24 μm . The field of view of the CCD detector is 326×326 arcmin with angular resolution of 9.39×9.39 arcsec per pixel. The Johnson V filter was used for polarimetric observation of the comet. We use a dichroic polarization filter (analyzer), which rotated sequentially through three fixed position angles 0° , $+60^\circ$, and $+120^\circ$. Using the images obtained at three evenly distributed orientations

of the analyzer, we compute the corresponding fluxes from the inner coma within the aperture radius of 17,000 km. These values can be translated into the I, Q, and U Stokes parameters using the Fesenkov formulae (e.g., [3, 4]). In what follows, the degree of linear polarization is computed as $P = -Q/I$ that often is measured in percent.

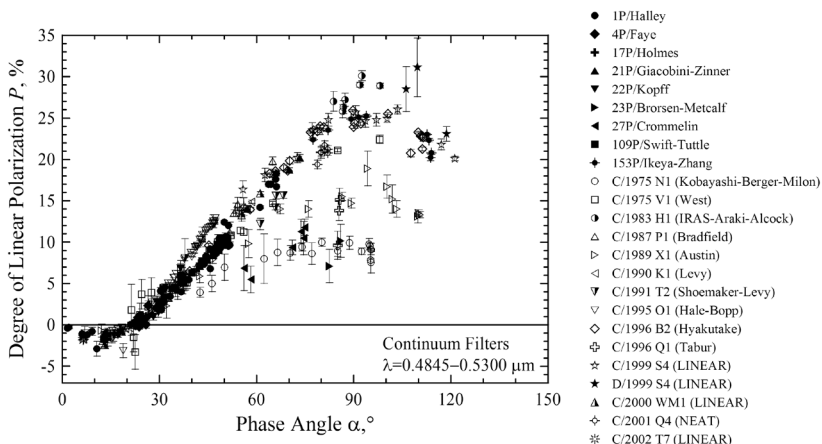


Fig. 1. Aperture-averaged degree of linear polarization P in the blue-green portion of the spectrum as a function of the phase angle α in various comets. Compilation is adapted from [2].

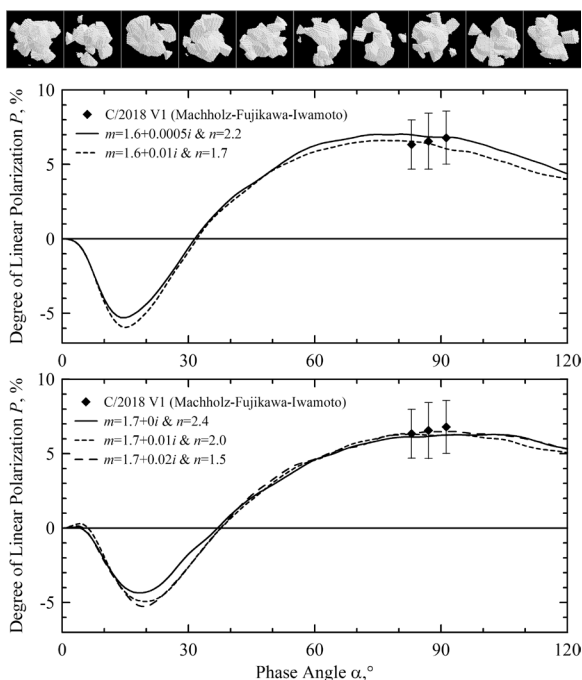


Fig. 2. Top: Ten examples of the agglomerated debris particles. Middle and bottom: Best fits to polarization in comet C/2018 V1 (black diamonds) obtained with agglomerated debris particles at different values of their refractive index m and index n in power-law size distribution r^{-n} . See legend for specific values of m and n corresponding to each curve.

Results and modeling:

Our observations of the inner coma in C/2018 V1 reveal $P=(6.34\pm 1.65)\%$ on November 16.829 at phase angle $a=83.0^\circ$, $P=(6.56\pm 1.88)\%$ on November 17.840 at $a=87.0^\circ$, and $P=(6.80\pm 1.78)\%$ on November 18.833 at $a=91.2^\circ$. When comparing these values with what is shown in Fig. 1, one can see that

comet C/2018 V1 reveals one of the lowest polarimetric responses at side scattering.

Using the agglomerated debris particles (see ten examples on top in Fig. 2), we search for complex refractive index m and power-law size distribution r^{-n} that can satisfactorily reproduce the polarization of comet C/2018 V1. We refer Reader to [2] for more details on the generation algorithm and micro-physical characteristics of the agglomerated debris particles, and on the discrete-dipole approximation (DDA) used to calculate their light scattering.

The middle and bottom panels in Fig. 2 demonstrate the best fits (lines) to the observations of comet C/2018 V1 (black diamonds) obtained with the agglomerated debris particles. It was previously noticed that the low positive polarization of a comet unambiguously constrains the imaginary part of the refractive index in its refractory material (dust) [5]. In application to C/2018 V1 we find that $\text{Im}(m) \leq 0.01$ at $\text{Re}(m)=1.6$; and $\text{Im}(m) \leq 0.02$ at $\text{Re}(m)=1.7$. These refractive indices appear in good quantitative accordance with Mg-rich silicates [6]. Such particles have long been known to be present in comets in considerable quantities [7].

Finally, it is worth noting that a reasonably good fit to observations C/2018 V1 can be formally obtained at $\text{Im}(m)$ slightly greater than those displayed in Fig. 2. However, it occurs at power index $n < 1.5$ that does not conform with the in situ findings in submicron- and micron-sized cometary dust particles, $1.5 \leq n \leq 3$ [8].

References:

- [1] Chernova G.P., et al. Polarimetric characteristics of dust particles as observed in 13 comets – Comparisons with asteroids // *Icarus*. 1993. V. 103. P. 144–158.
- [2] Zubko E., et al. The positive-polarization of cometary comae // *Planet. Space Sci.* 2016. V. 123. P. 63–76.
- [3] Fessenkoff B. Détermination de la polarisation de la couronne solaire // *Astron. J. Sov. Union*. 1935. V. 12, P. 309–323 [In French].
- [4] Hines D.C., et al. Hubble Space Telescope pre-perihelion ACS/WFC imaging polarimetry of comet Ison (C/2012 S1) at 3.81 au // *Astroph. J. Lett.* 2014. V. 780. Article number L32.
- [5] Zubko E., et al. Characteristics of cometary dust in the innermost coma derived from polarimetry by Giotto // *Mon. Not. Roy. Astron. Soc.* 2013. V. 430. P. 1118–1124.
- [6] Dorschner J., et al. Steps toward interstellar silicate mineralogy. II. Study of Mg-Fe-silicate glasses of variable composition // *Astron. Astroph.* 1995. V. 300. P. 503–520.
- [7] Fomenkova M.N., et al. Compositional trends in rock-forming elements of comet Halley dust // *Science*. 1992. V. 258, P. 266–269.
- [8] Mazets E.P., et al. Comet Halley dust environment from SP-2 detector measurements // *Nature*. 1986. V. 321. P. 276–278.

SMALL FRAGMENTS OF ASTEROIDS AND COMETARY NUCLEI ORBITING EARTH: NUMERICAL SIMULATION

T. Nozdrachev¹, A. Kochergin^{1,2}, E. Zubko³, G. Videen^{4,5}

¹ FarEasternFederalUniversity, 8 Sukhanova St., Vladivostok 690950, Russia; nozdrachev.ta@mail.ru

² Institute of Applied Astronomy of RAS, 10 Kutuzova Emb., Saint-Petersburg 191187, Russia

³ Humanitas College, Kyung Hee University, 1732 Deogyong-daero, Yongin-si, Gyeonggi-do 17104, Republic of Korea; evgenij.s.zubko@gmail.com

⁴ Space Science Institute, 4750 Walnut Street, Boulder Suite 205, CO 80301, USA

⁵ Department of Astronomy and Space Science, Kyung Hee University, 1732, Deogyong-daero, Giheung-gu, Yongin-si, Gyeonggi-do 17104, Republic of Korea

Keywords:

Asteroids; cometary nuclei; gravitational capture; orbit; Earth; the Moon.

Introduction:

A fundamental problem that arises in planetary science concerns collecting samples of materials of other Solar-system objects and returning them back to Earth safely. In particular, the leading space agencies are currently paying significant attention to the problem of sampling small bodies in the Solar system, like asteroids and comets. These efforts require long-lasting space missions to those objects; in practice, being always longer than 5 years. The length of such missions drives their total cost because long journeys necessitate multiple safeguards of the space-probe systems, stronger facilities of radio communication, and a support team. In addition, flight maneuvers needed for target rendezvous consume significant fuel that further increases the gross mass of the spacecraft. As a consequence, such spacecraft launches could be accomplished only with expensive heavy carrier rockets. Thus, total cost of mission typically exceed US\$1 billion. Small fragments of asteroids or cometary nuclei also get captured by Earth gravity on a stable orbit over its long existence, ~5 billion years. Such small moons were difficult to discover in the past due to the low-efficiency of telescopes and detectors. However, significant progress in astronomical facilities achieved over the last twenty years would make this possible now in principle. In this short paper we investigate the possibility of a small-body capture by the system Earth-Moon.

Model:

We model the motion of a small body having mass of 3500 kg (diameter ~ 1 m) in the vicinity of the Earth-Moon system using an iterative time-domain approach. Such an approach makes it possible to account rigorously for all three gravitational forces acting on the small body: gravity of the Sun, Earth, and the Moon.

We suppose that the small body approaches the Earth-Moon system from some initial point characterized with the position vector S_0 with initial velocity V_0 at the initial time $t_0 = 0$. At $t_0 = 0$, we calculate the resultant of all three gravitational forces acting on the small body. During the next increment of time Dt , the resultant force is assumed to remain constant, implying also a constant acceleration of the small body a_0 . This assumption significantly simplifies the numerical simulation of projectile motion during the increment Dt . In the end of this increment, we update all three forces and their resultant for the current location of the small body, the Moon, and Earth, and repeat the entire procedure. As $Dt \rightarrow 0$, the model trajectory converges to its exact profile. We experimentally examine different values of Dt and find that $Dt = 1$ s yields a very much converged trajectory of the projectile.

Results and modeling:

In this work we investigate numerous scenarios for a close encounter of the projectile with the Earth-Moon system. The studied orbits of the small body resemble what is typical for the Aten asteroids (e.g., [1]), a dynamical group whose perihelion is somewhat smaller than 1 au; whereas, aphelion lies slightly beyond Earth orbit. A famous current member of this group is the asteroid (99942) Apophis [2].

Our modeling reveals that the minor body may get captured if it first approaches the Moon ($< 25,000$ km) with a relative velocity ranging from 1. km/s to 2.4 km/s. Fig. 1 demonstrates two examples of the small body being captured by the Earth-Moon system. Here, Earth placed at the coordinate origin, lunar orbit is shown with a cyan solid line, and distances are scaled to the radius of the Earth. The pink line shows the trajectory of the small body passing through the Earth-Moon system. We use a solid line to mark part of the orbit that is gravitationally bound with Earth.

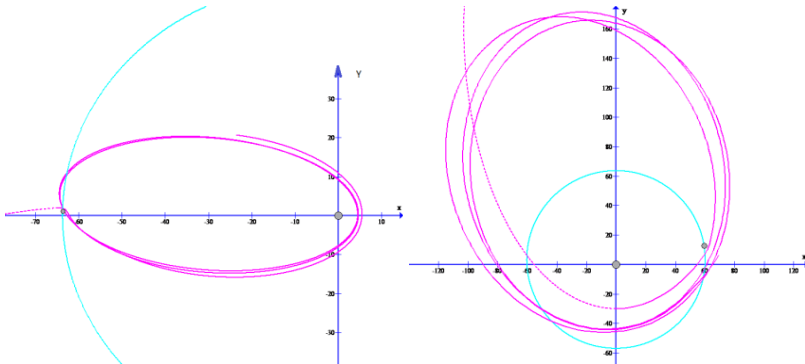


Fig. 1. Two examples of trajectories of a small body that could be captured by the gravitation of the Earth.

Thus, our modeling suggests that the Earth-Moon system, in principle, is capable of gravitational capture of a small fragment (~ 1 m) of asteroid or cometary nucleus. However, when orbiting around Earth, this small body will cross the lunar orbit, which makes it unstable. In a very short time period (< 2 year), a close approach with the Moon will dramatically affect the small-body orbit, making it most likely leaving the Earth-Moon system. However, searching for a more stable orbit of the captured small bodies is a subject of our further study.

References:

- [1] Zausaev A.F., Pushkarev A.N. On the probability of asteroids colliding with the Earth // *Solar Sys. Res.* 1994. V. 27. P. 465–468.
- [2] Shuvalov V.V., et al. Asteroid Apophis: Evaluating the impact hazards of such bodies // *Solar Sys. Res.* 2017. V. 51. P. 44–58.

ESTIMATION OF THE FRACTION OF ICE DELIVERED TO THE MAIN ASTEROID BELT IN THE EARLY SOLAR SYSTEM

V.V. Busarev¹, S.I. Ipatov²

¹ *Lomonosov Moscow State University, Sternberg Astronomical Institute, (SAI MSU), 13 Universitetskij av., Moscow 119992, Russian Federation (RF), e-mail: busarev@sai.msu.ru;*

² *Vernadsky Institute of Geochemistry and Analytical Chemistry of RAS, Moscow, RF, siipatov@hotmail.com*

Keywords:

spectrophotometry of asteroids, sublimation of ices, ice content in asteroid matter, origin and dynamical evolution of asteroids.

Introduction:

Simultaneous sublimation activity of four main-belt primitive asteroids (145 Adeona, 704 Interamnia, 779 Nina and 1474 Beira having considerable eccentricity of the orbits and passing near perihelion was discovered in 2012 [1]. The process was confirmed on three of the bodies (Adeona, Interamnia and Nina) in 2016-2018 [2]. It points likely to a widespread character of the phenomenon among primitive-type asteroids in the Main asteroid belt (MAB). Very probably, this is a sign of the presence of a considerable fraction of ices (predominately water ice) in the matter of such bodies [3]. To investigate dynamical reasons of ice matter delivery to the MAB from behind of the "snow line" in the early Solar system, we modeled the migration of planetesimals and pre-planetary bodies from the feeding zones of Jupiter, Saturn, Uranus and Neptune to the MAB and calculated the probability of a collision of a planetesimal with icy content (probably about 1/3) with a parent asteroid body (PAB) moving in the MAB. It was made by the same methods as in our previous publications [4-6]. The aim of the work is to estimate a relative quantity of ice materials delivered to the MAB at such collisions. Such delivery from the feeding zone of Jupiter and Saturn was within a few first million years, but main migration of bodies from the feeding zones of Uranus and Neptune to the MAB could be later, depending on when Uranus and Neptune acquired considerable fractions of their masses.

Results of modeling and conclusions:

We define as p_a the probability of a collision of one planetesimal (during its dynamical lifetime) with a PAB. Results of the calculations are presented in Table. Each value of p_a in the Table was obtained based on calculations made for an asteroid orbit with a semi-major axis equal to a_o and 500 planetesimals with initial semi-major axes a_o from $a_{o\min}$ to $a_{o\min} + 2.5$ AU. A diameter of an asteroid equaled to 1000 km, and a density equaled to that of Ceres (2.16 kg dm^{-3}). The eccentricity and inclination of the orbit of an asteroid were close to those for Ceres: 0.1 and 10° , respectively. The diameter of an asteroid was considered to be greater than that of a planetesimal. Initial eccentricities of planetesimals were equal to $e_o = 0.3$ and their initial inclinations $i_o = 0.15$ rad. But the values of eccentricities and inclinations of the migrating bodies could take any values (for example, eccentricity almost from 0 to 1, and the inclination from 0 to 90 degrees and above). For planetesimals which got orbits with aphelia inside the orbit of Jupiter, the more typical eccentricities and the sine of inclination of such orbits were perhaps about 0.6-0.8 and 0.2-0.3, respectively, but they could take any other values.

Several series of calculations of migration of planetesimals under the gravitational influence of planets (from Venus to Neptune) have been made. The symplectic code from the Swift integration package [7] was used. Integrations were made until planetesimals reached 2000 AU or collided with the Sun.

Table. Values of $10^8 p_a$, where p_a is the probability of a collision of one planetesimal (during its dynamical lifetime) with an asteroid with a semi-major axis a_{ast} equal to 2.3, 2.5, 2.8, or 3.1 AU for the runs with 500 planetesimals with

initial semi-major axes from a_{omin} to $a_{\text{omin}} + 2.5$ AU, initial eccentricity $e_0 = 0.3$, initial inclination $i_0 = 0.15$ rad.

$a_{\text{ast}} \backslash a_{\text{omin}}$	5.	7.5	10.	15.	20.	25.	30.
2.3	1.29	0.26	0.85	0.72	0.32	0.08	0.14
2.5	1.40	0.64	1.23	0.90	0.65	0.11	0.14
2.8	2.94	0.94	1.18	0.77	0.66	0.12	0.13
3.1	2.06	0.74	1.55	2.36	0.76	0.19	0.14

The Table and results presented in [6] show that the probability of a collision of planetesimals from Jupiter's and Saturn's feeding zones with an asteroid (PAB) having a diameter of 1000 km (of Ceres' size), semi-major axes of the orbit in the range from 2.3 to 3.1 AU was estimated to be of the order 10^{-8} . For such value of the probability, with a total mass of planetesimals in the feeding zones of Jupiter and Saturn equal to 100 Earth masses (m_E), the total mass of planetesimals colliding with a PAB of Ceres' size (when planetesimals were smaller than PABs) is $10^{-6}m_E$, that is, about 50 times less than the mass of this asteroid ($1.9 \times 10^{-4}m_E$). For a model in which the planetesimals are smaller than the PABs, for 100-km PABs of the same total mass as a 1000-km PAB, the total mass of planetesimals colliding with them is 10 times greater than in previous case. It means that the relative quantity of ice material delivered to the MAB in the first and second cases changes from 2 to 20%, respectively.

Thus, for three Ceres (the common mass of the present MAB) the total mass of planetesimals colliding with asteroids is of the order of $3 \times 10^{-6}m_E$, and for 300 Ceres, it is of the order of $3 \times 10^{-4}m_E$. The last number is comparable to the mass of the present asteroid belt. However, due to approximately the same ejection from the MAB of old and new asteroids, the estimates of the fraction of delivered matter in the MAB depend mainly on the above-mentioned ratio of the total mass of asteroids to the total mass of colliding planetesimals (see first and second estimates in the previous paragraph), and not on the total mass of bodies in the MAB.

An increase the radius of PABs by 10 times (while maintaining the total mass) leads to a decrease in the total delivered mass of planetesimals colliding with the PABs by 10 times (proportional to the radius) [6]. If we consider planetesimals with a diameter n times greater than 1000 km and PABs with a diameter of 1000 km, the total mass of planetesimals colliding with asteroids will be approximately smaller by a factor of n than in the case when diameters of all planetesimals are no more than 1000 km (the size of PABs). The capture of the matter of planetesimals can be even less than these estimates, since when a massive planetesimal collides with a PAB, fragments of the planetesimal can be ejected out of the MAB. That is, the inflow of matter from the Jupiter's zone in the case of massive planetesimals will be less than 2% of the mass of the asteroid belt.

If we consider PABs smaller than 1000 km and planetesimals of a larger size, it is difficult to estimate the inflow without calculating the results of collisions. The smaller are asteroids (with the same total mass), the more is the number of their collisions with planetesimals. But the smaller are the asteroids, the less they can damage the planetesimals.

The probability of collisions of dust particles with asteroids can be much greater than for bodies [8]. However, it is not known what part of the mass of matter in the Jupiter zone was in dust particles. Dust particles fell possibly on local asteroids, and did not form new asteroids.

Thus, according to our modeling, probable relative (to the mass of the MAB) quantity of icy planetesimals' matter delivered from the formation zones of Jupiter, Saturn, Uranus, and Neptune to the MAB may be in the range from 2 to 20%.

References:

- [1] Busarev V.V. et al. *Icarus*. 2015. V. 262. P. 44-57.
- [2] Busarev V.V. et al. The Ninth Moscow Solar System Symposium (9MS3). Moscow, Space Research Inst., 2018. Abstract #9MS3-SB-08.
- [3] Busarev V.V. et al. *Sol. Sys. Res.* 2016. V. 50. P. 281-293.
- [4] Ipatov S.I., Mather J.C. *Adv. Space Res.* 2004. V. 33. P. 1524-1533. (<http://arXiv.org/format/astro-ph/0212177>).
- [5] Ipatov S.I., Mather J.C. *Ann. N.Y. Acad. Sci.* 2004. V. 1017. P. 46-65. (<http://arXiv.org/format/astro-ph/0308448>).
- [6] Busarev V.V., Ipatov S.I. The Ninth Moscow Solar System Symposium (9MS3). Moscow, Space Research Inst., 2018. Abstract #9MS3-PS-48.
- [7] Levison H. F., Duncan M.J. *Icarus*. 1994. V. 108. P. 18-36.
- [8] Ipatov S.I. *Proc. of the International Astronomical Union, IAU vol. 5, Symposium S263, "Icy bodies in the Solar System"*, ed. by J.A. Fernandez, D. Lazzaro, D. Pralnik, R. Schulz, Cambridge University Press, 2010. P. 41-44. (<http://arxiv.org/abs/0910.3017>).

MODELING OF ASTEROID REFLECTANCE WITH LABORATORY DATABASES OF ANALOG SAMPLES

A.A. Rezaeva, M.P. Shcherbina, V.V. Busarev

Lomonosov Moscow State University, Sternberg Astronomical Institute (SAI MSU), University Av., 13, Moscow, 119992, RF), aa.rezaeva@physics.msu.ru;

Keywords:

Asteroids, reflectance spectra of asteroids, spectral databases of minerals and meteorites, modeling reflectance spectra of asteroids.

Introduction:

Asteroids are among the oldest objects in the Solar system, the composition of which has been minimally changed since their formation. This fact was established according to the results of studies of numerous meteorites that have fallen to Earth, which are fragments of these bodies. Knowledge of the characteristics of asteroids makes it possible to evaluate the correctness of the solution of cosmogonic problems. In particular, statistical analysis of the characteristics of a large number of small bodies allows test any theory of the formation and evolution of the Solar system [1].

Asteroids, as bodies that, as a rule, do not have an atmosphere, are traditionally studied by the spectrophotometric method in the visible and near IR ranges, because of a spectral "window" of the earth's atmosphere [2],[3]. In this work, we used reflectance spectra of asteroids obtained by the authors at observatories "PikTerskol" (INASAN) and the Crimean laboratory SAI MSU in 2013-2019 [4]. Then, a quantitative interpretation of the reflectance spectra of asteroids was carried out using the program written in the Matlab software and data on reflectance spectra of minerals and meteorites.

Some new in the algorithm:

In comparison with previous works [4], the algorithm of the program and the database of minerals were changed. The database was added new reflectance spectra (RS) of terrestrial minerals corresponding to those indicated in the article by Rubin [5]. According to some estimates, only about 30% of all the minerals that make up the asteroids are known [6]. Since unknown minerals probably formed under conditions far from the terrestrial, it was decided not to include in our database terrestrial minerals that are not similar to found in meteorites. Secondly, only those RS of minerals and meteorites are included in our database which spectral range at least partially overlaps with the spectral range used by us in observations (0.4-1 μm), where the Earth's atmosphere is the most transparent.

Besides, in the specified range are the strongest and well studied absorption bands of minerals. These features allow us identify the main rock-forming minerals and in more detail establish the composition of the substance. For example, in the visible range are the wings of the two strongest absorption bands. The band centered at 0.2 μm characterizes the intensity of electron-oxygen-metal charge transfer. The second band with the center at 1 μm , caused by the spin-allowed Fe^{2+} absorption band in the crystal structure of minerals, shows the content of olivine, pyroxene, or their mixture. The wings of the absorption bands at 0.2 and 1 μm form the general shape of asteroid reflectance in the visible and near-IR ranges. In addition, there are also weaker absorption bands, for example, bands with centers at 0.506 μm and 0.55 μm , corresponding to forbidden electronic transitions in Fe^{2+} ions [2,7].

In addition, the minerals in our database were divided into sub-groups according to the temperature and other conditions in which they were formed, into low-temperature, high-temperature, and mixtures [8].

Conclusion:

Using a modified program and an updated database of minerals, new quantitative estimates of the surface composition of asteroids were obtained. The results are in good agreement with the established spectral type and

assumed mineralogy of asteroids, for some objects a mixed composition was found. Some our results will be shown in our presentation.

References:

- [1] Safronov V.S. Evolution of the preplanetary cloud and the formation of the Earth and planets. Science, 1969 [in Russian]
- [2] Busarev V.V. Spectrophotometry of Atmospheric Solids of the Solar System // *Astronomicheskyy Vestnik*. 1999. V. 33. No. 2. P. 140-150. [in Russian]
- [3] Busarev V.V. Spectrophotometry of asteroids and its applications // LAP LAMBERT Acad. Publish., ISBN: 978-3-8465-3704-6, 2011, 250 p. [in Russian]
- [4] Shcherbina M. P., Rezaeva A. A. Quality and quantitative interpretation of the reflection spectra of the Main Belt asteroids and NEA // *Fundamental and applied space research. Abstracts of the XIV Conference of Young Scientists. - Mechanics, control and computer science*. 2017. P. 104-104. [in Russian]
- [5] Rubin A.E. Mineralogy of meteorite groups // *Meteoritics & Planetary Science*. 1997. V. 32. P. 231-247.
- [6] Vernazza P., Marsset M., Beck P. et al. Interplanetary dust particles as samples of icy asteroids // *Astrophys. J.* 2015. V. 806. P. 204-213.
- [7] Shestopalov D.I., Golubeva L.F. The composition of the substance of asteroids by their reflection spectra // LAP LAMBERT Academic Publishing. 2018. [in Russian]
- [8] Betekhtin, A.G. Mineralogy Course. Book House, 2014. 542 p. [in Russian]

SURFACE GRAIN SIZE AND STRUCTURE FROM POLARIMETRIC PROPERTIES OF ASTEROID 3200 PHAETHON

L.F. Golubeva, D.I. Shestopalov

Shemakha Astrophysical Observatory, Shemakha AZ-3243, Azerbaijan, lara_golubeva@mail.ru

Keywords:

asteroids, 3200 Phaethon, polarimetry, polarization phase curves, surface, particle size.

The 3200 Phaethon is the largest body among known potentially hazardous asteroids. Moving in a very elongated orbit, Phaethon approaches the Sun at a distance of approximately 2 times less than the perihelion of Mercury. The asteroid is probably a parent body of the Geminids meteor shower and can be an inactive cometary nucleus with a depleted stock of volatile fractions.

Several teams of observers [1–4] carried out the high-precision polarimetric observations of Phaethon at the approaches to the Earth in 2004, 2016, 2017 and 2017. In these datasets, the phase angle coverage (23–117°) proved to be insufficient to estimate the main parameters of Phaethon's polarimetric curves that, in turn, leads to a high degree of uncertainty in the interpretation of the polarimetric properties of the asteroid surface. We aimed to retrieve all possible information from the available polarimetric measurements of Phaethon in order to improve our understanding of the asteroid surface properties. Such a tasking takes a sense as the spacecraft DESTINY+, which is planned to be launched to asteroid Phaethon in 2022, is not intended for polarimetric measurements. Thus the first step in this line is approximation of the polarimetric curves of Phaethon by continuous functions according to the known set of discrete data. We applied a simple approximate formula [5], which proved itself well in analyzing asteroid, comet and lunar polarimetric data [6, 7].

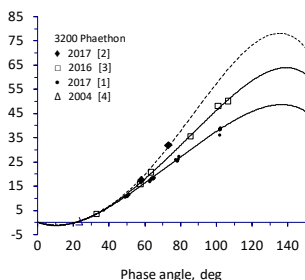


Fig.1

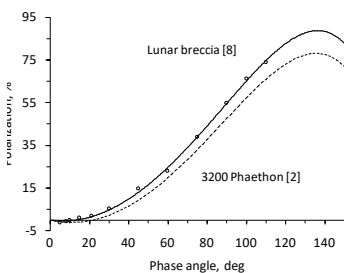


Fig. 2

Figure 1 gives an example of the phase-dependent polarimetric measurements of Phaethon performed by the various groups of investigators and the best fitting of the observations by the approximate formula [5].

Error bars are comparable to the size of symbols on the plot; the accuracy of the approximation is comparable to measurements errors. These datasets were obtained in different epochs and at different wavelengths, but the differences in the curves do not correlate with different spectral ranges. The negative polarization branch is actually the same for these observations, ($P_{min} \approx 1.35\%$ at $\alpha_{min} \approx 10^\circ$ and the polarimetric slope $h \approx 0.015\%/^\circ$ at the inversion angle $\alpha_i \approx 21^\circ$), but the positive polarization branch ($P_{max} \approx 78\%$, 64% , and 47% at $\alpha_{max} \approx 135^\circ$) depends on the observation time. Of course, the derived estimate of 78% should be considered as a preliminary since we have only two measurements [2] and three roots of approximate equation [5] at $\alpha = 0^\circ$, 180° , and $\alpha_i = 21.9^\circ$ to construct this polarimetric curve (dashed line in Fig. 1). At the same time, we found a suitable pattern in the polarimetric catalog [8]: the maximum polarization degree for the lunar breccia with slagged surface (the Luna-16 collection) reaches even 88.7% at $\alpha_{max} = 136.4^\circ$ (see Fig. 2).

The authors [2] notice that their polarimetric observations at $\alpha = 73.2^\circ$ concur with a minimum of the asteroid brightness variation, and suggest about a large-scale heterogeneity of Phaethon's surface. The new observation data that have been published in 2019 apparently support authors' suggestion, since the spectral and radar observations [9, 10] carried out in the same time as the polarimetric ones sense together a spacious low-albedo region on Phaethon's surface. Bearing in mind the result in Fig. 2, we can also add that the idea of Phaethon's surface burned by solar insolation [11, 12] receives a further support.

Such parameters as the maximum polarization degree P_{max} and albedo A are believed to be linked to the particle size of particulate surface. This question in relation to Phaethon was studied in [2, 3] not so much on a quantitative as qualitative level because of the uncertainty in the position of Phaethon on the $A - P_{max}$ diagram. We use the diagram (both parameters A and P_{max} are measured in the V bandpass) designed in [13] where regions occupied by the lunar and powdered terrestrial samples are shown by straight regression lines. They are almost parallel, but their position on the diagram depends on the grain size of the powdered and separated samples. When the grain size increases, these regression lines are offset with respect to each other. The farthest region from the lunar fines is occupied by solid terrestrial rocks in their natural state with dusty and dust-free surfaces.

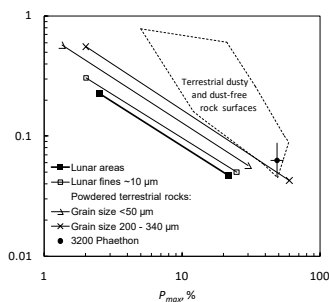


Fig. 3.

Note, that albedo A was reduced to the phase angle of 5° in the referred telescopic and laboratory datasets [13]. To put correctly Phaethon in its place on this $A - P_{max}$ diagram we used the correlation between A and polarimetric slope h [13]: $\log A = -1.026 \log h - 1.873$. For Phaethon, we have $A = 0.062$ that corresponds its polarimetric slope $h = 0.222$ in the V band. As shown in Fig. 3, the A, P_{max} parameters of Phaethon fall into the region occupied by the nonseparated natural terrestrial rocks with solid surfaces sometimes powdered with a dust. Therefore, we can imagine Phaethon's surface as a mixture of pebble-stone and coarse sand with grains of at least 300 microns in size. On the whole, polarimetric properties of the asteroid surface correspond, to a structure of thermally altered regolith particles mixed with larger rock fragments like a coarse pebble.

References:

- [1] Devogèle M., Cellino A., Borisov G., et al. The phase-polarization curve of asteroid (3200) Phaethon // *MNRAS* 2018. V. 479. P. 3498–3508.
- [2] Zhebtobryukhov M., Chornaya E., Kochergin A., et al. Umov effect in asteroid (3200) Phaethon // *Astron. Astroph.* 2018. V. 620. id. A179. P. 1–6.
- [3] Ito T., Ishiguro M., Arai T., et al. Extremely strong polarization of an active asteroid (3200) Phaethon // *Nature Comm.* 2018. V. 9. id. 2486. P. 1–8.
- [4] Fornasier S., Belskaya I. N., Shkuratov Yu. G., et al. Polarimetric survey of asteroids with the Asiago telescope // *Astron. Astroph.* 2006. V. 455. P. 371–377.
- [5] Shestopalov D. Approximation formula for polarization of the light scattered by particulate surfaces: an application to asteroids // *J. Quant. Spectrosc. Radiat. Transfer* 2004. V. 88. P. 351–356.
- [6] Shestopalov D. I., Golubeva L. F. Polarimetric properties of asteroids // *Adv. Space Res.* 2015. V. 56. P. 2254–2274.
- [7] Shestopalov D. I., Golubeva L. F. About a linear polarization of comets: The phase-angle dependences of polarization degree // *Adv. Space Res.* 2017. V. 59. P. 2658–2678.
- [8] Kvaratskheliya O.I. Spectropolarimetry of the lunar surface and samples of the lunar soil // *Bull. Abastuman. Astrophys. Obs.* 1988. V. 64. P. 1–312.
- [9] Lazzarin M., Petropoulou V., Bertini I., et al. Phaethon variability during December 2017 closest approach to Earth // *Planet. Space Sci.* 2019. V. 165. P. 115–123.
- [10] Taylor P. A., Rivera-Valentin E. G., Benner L. A. M., et al. Arecibo radar observations of near-earth asteroid (3200) Phaethon during the 2017 apparition // *Planet. Space. Sci.* 2019. V. 167. P. 1–8.
- [11] Ohtsuka K., Nakato A., Nakamura T., et al. Solar-Radiation Heating Effects on 3200 Phaethon // *Publ. Astron. Soc. of Japan* 2009. V. 61 P. 1375–1387.
- [12] Hanuš J., Delbó M., Vokrouhlický D., et al. Near-Earth asteroid (3200) Phaethon: Characterization of its orbit, spin state, and thermophysical parameters // *Astron. Astroph.* 2016. V. 592. id.A34. P. 1–15.
- [13] Geake J.E., Dollfus A. Planetary surface texture and albedo from parameter plots of optical polarization data // *MNRAS* 1986. V. 218. P. 75–91.

NUMERIC MODELING OF ASTEROID ORBITS CLOSE TO 3:1 RESONANCE

A.E. Rosaev

GAUK YO Center named after V.V. Tereshkova, 150000, Yaroslavl, Chaikovskogo, 3, hegem@mail.ru

Keywords:

Mean motion resonance, numeric integration, orbital evolution, perihelion argument rate, chaotic notion

Introduction:

As it is well known, the dynamical evolution of all test particles in 3:1 resonance is characterized by very rapid increasing of their eccentricity. This phenomenon is predicted by the works of Wisdom [1]. Moreover, 50% particles becomes Earth-crosser in 1Myr due secular resonance overlapping inside 3:1 resonance (Moon, Morbidelli 1995). [2]

Evidently, it is interesting to reconstruct dynamical history of real asteroids near 3:1J resonance in the past. First of all, we perform backward integrations of orbits of some 3:1J resonant asteroids and have found great increasing of eccentricity most of them in the last million year.

To study motion near 3:1 resonance in most straightforward form, we repeat our integrations with only Jupiter perturbations. We use orbital elements of 887 Alinda as basic (table 1, where orbital elements of Jupiter are given in last line) and integrate orbits of some clones with different initial semimajor axis, inclinations, eccentricity and mean anomaly. The values of initial angles node longitude and perihelion argument was fixed in this series of integrations.

The equations of the motion were numerically integrated 800 kyrs into the past, using the N-body integrator Mercury (Chambers, 1999) [3] and the Everhart integration method (Everhart, 1985). The initial epoch of our integrations was $T_0=1998\text{-Jul-06}$ (JD2451000.5).

Table 1 Osculating orbital elements of the some 3:1 resonance asteroids at epoch 1998-Jul-06 (JD2451000.5)

Object	ω	Ω	i	e	a	M
887 Alinda	350.054565	110.7167828	9.30331	0.5627231	2.48549841	77.4
Jupiter	275.190830	100.4726265	1.304674	0.0485423	5.20300974	333.5

Theoretic background

We will look for evolution of orbital elements as:

$$E = E_{sec} + E_{res}$$

Secular equation for eccentricity has the solution (with assumption accepted by Murray and Dermott) [4]:

$$e = e_0 + \frac{n\alpha}{\bar{\omega}} (m_p / m_s) C_3 e_p (\cos \bar{\omega} t - \cos \bar{\omega}_0) \quad (4)$$

We can write the proper frequencies in according (Murray, Dermott,1999):

$$g = \bar{\omega} = 2n\alpha(m_p / m_s) C_1 \quad (5)$$

$$\hat{\Omega} = s = n\alpha(m_p / m_s) C_2 / 2$$

Perihelion rate has a key value in a simple secular theory. There are 6 variables, completely determined motion of the infinitesimal particle in RTBP: $a, e, i, \bar{\omega}, \Omega$ and t . a is assumed constant. It is possible to show, that always $2C_1 = -C_2 / 2$ and by this way to exclude Ω . Node longitude Ω related with inclination. Expression (4) allows us to set relation between g and eccentricity. If we not interest position particle on orbit, knowledge of the dependence $g(t)$ allows us to construct approximate evolution of orbit in time.

Semimajor axis has no secular variations. We can note that mean semimajor axis as well as resonance variations of eccentricity is simple depends on resonant argument. As a result of Lagrange linear theory, we can expect large increase of amplitudes of perturbations with the period tends to infinity. It is in contradiction with numeric integration results.

Numeric integration results

At the large $e=0.5$ and initial semimajor axis far from resonance $a=2.45$ AU we have small oscillations a and e . After move close to resonance $a=2.465$ AU we have large variations a in range 2.47-2.53 AU around resonance value and quasi-periodic variations e in range=0.4-0.56. At the small $e\sim 0.1$ semimajor axis changes in range $a=2.48$ -2.49 around initial value, smaller than resonant. In close vicinity to resonance $a=2.485$ AU we have large variations a in range 2.49-2.51 AU around resonance value and quasi-periodic variations e in range=0.4-0.84. The main period of the eccentricity variations becomes about six times longer than period of the semimajor axis and is about 100 kyrs. The short period of eccentricity holds resonance value and variations of the eccentricity and semimajor axis are in opposite phase. At the same time mean semimajor axis lose dependence on initial value and become very close to resonant value for all a_0 in range 2.48-2.52 (Fig.1). The exact resonance position is expected at $a=2.50135$ AU.

For small initial eccentricity we have no such effect. Moreover, clear dependence on initial mean anomaly (i.e. on resonant argument) is present. The effect of capture semimajor axis into resonance takes place close to Alinda-like initial anomaly $M\sim 77^\circ$. It is according start for resonant argument $s=90^\circ$. Additionally, we have detected some chaotic regimes at large resonance perturbations.

Other series of integration with fixed initial semimajor axis and varying eccentricity show that at initial eccentricity $e=0.3$ -0.5 we have increasing of secular perturbations in the eccentricity amplitude up to 0.27, when at $e<0.2$ amplitudes are 0.02-0.03. In the boundary case $e=0.25$ we have giant eccentricity variations predicted by Wisdom (fig.3). In all cases short periodic resonance perturbations are small.

Our conclusion about key role of perihelion argument is still true. But we cannot use expression (5). However, we can estimate g from our numeric integrations. We approximate eccentricity by expression:

$$e = e_0 + e_{\text{ampl}} \cos(f_e t + \varphi_c) \quad (6)$$

and assume $\omega_0=350^\circ$, $\Omega_0=110^\circ$, $e_0=0.5$, $i_0=1.0$, $M_0=77.4$ and varying initial semimajor axis a_0 . The main observed eccentricity perturbation frequency is equal perihelion rate with very good accuracy. It means that we can continue use expression (4). Perihelion rate nonlinearly depends on initial semimajor axis, i.e. on distance from exact resonance or resonant argument (Fig 2) and we can write:

$$\begin{aligned} \dot{\omega} &= \dot{\omega}_{\text{sec}} + \dot{\omega}_{\text{res}}(|\sigma|) \\ e &= e_{\text{sec}}(\dot{\omega}_{\text{sec}}) + e_{\text{res}}(\sigma) \\ a &= a_{\text{res}}(\sigma) \\ \dot{\Omega} &= \dot{\Omega}_{\text{sec}}(\dot{\omega}_{\text{sec}}) + \dot{\Omega}_{\text{res}}(\sigma) \\ i &= i_{\text{sec}}(\dot{\Omega}_{\text{sec}}) + i_{\text{res}}(\sigma) \end{aligned} \quad (7)$$

We have only two independent variables: $\dot{\omega}_{\text{sec}}$ and σ . Finally we can conclude that number of variables, required for resonance motion description may be reduced and for planar case one dimensional pendulum model is sufficient. In the non-resonance case we have no parameter like σ and cannot bound short periodic variations (e and a for example). In spite presented simple model cannot describe chaotic motion at resonance like Wisdom-predicted giant eccentricity variations (fig.3), it give the way to quantitative description motion at resonance. In particular, we note that expressions for eccentricity and semimajor axis (mean motion n) through resonance argument in the pendulum model of resonance (Murray, Dermott,1999) are more

adequate, than Lagrange linear equations solutions. The observed dependence $\dot{\omega}_{res}(|\sigma|)$ is required more detailed theoretic analyses, as well as the behavior of the secular eccentricity amplitude.

Conclusions

On base our numeric integrations, we have shown that orbital evolution in 3:1J resonance can be described in general by two independent parameters — resonant argument and perihelion rate. This simple model gives way to quantitative description motion at resonance in the regular (nonchaotic) case. Perihelion rate has determine secular eccentricity variations, node precession and inclination behavior. Resonant argument has determines resonance eccentricity, semimajor axis and inclination variations

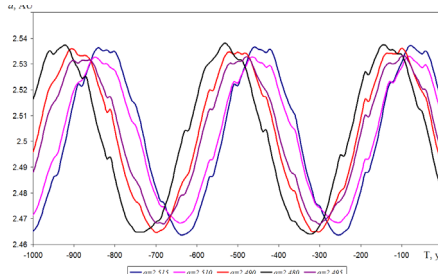


Fig. 1. Evolution semimajor axis with different initial values (initial $e=0.5, i=9$)

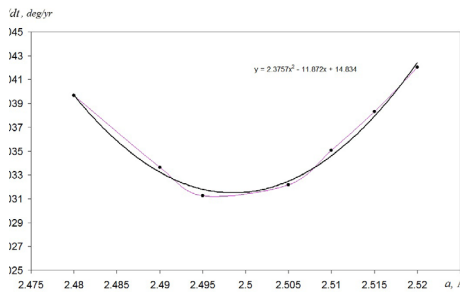


Fig. 2. Rate of the perihelion argument in semimajor axis dependence.

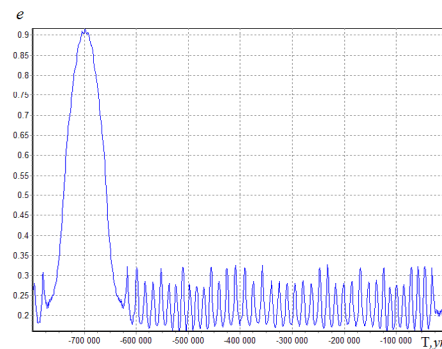


Fig. 3. Eccentricity evolution of orbit with initial $a=2.485$ AU, $i=9^\circ, e=0.25$.

References:

- [1] Wisdom J. Chaotic Behavior and the Origin of the 3/1 Kirkwood Gap. // *Icarus*, 1983, 56, 51-74
- [2] Moons, M., Morbidelli, A.: Secular resonance in mean motion commensurabilities: the 4/1, 3/1, 5/2, and 7/3 cases. // *Icarus*., 1995, 114, 33- 50.
- [3] Chambers, J.E.. A hybrid symplectic integrator that permits close encounters between massive bodies. *Monthly Notices of the Royal Astronomical Society*, 1999,, 304, 793-799.

SPACE IRON OXIDE MICROSPHERES: ORIGIN AND TYPOMORPHIC FEATURES

A.V. Gusev¹, A.I. Bakhtin¹, R.Kh. Sungatullin¹, V.A. Tselmovich²

¹ Kazan Federal University, 420008, Kazan, 18, Kremlevskaya str., Russia, agusev33@gmail.com

² Geophysical Observatory "Borok" – a branch of the Federal State Budgetary Institution of Science Institute of Earth Physics. O.Yu. Schmidt of the Russian Academy of Sciences, 152742, Yaroslavl region, Borok, 142, Russia.

Keywords:

meteoroids, Earth's atmosphere, iron oxide microspheres, typomorphic features, cosmic origin.

Introduction: In the sedimentary rocks of the Earth, metal spherical particles (microsphere) are often found, ranging in size from the first to several hundred micrometers across [1]. They are composed of native iron, wustite, magnetite, have magnetism and therefore are relatively easy to extract from finely dispersed terrigenous and carbonate rocks. It is believed [2] that the majority of metallic microspheres are of cosmic origin and are ubiquitous in the rocks of the Earth, mainly in the form of iron oxide (magnetite) microspheres. This implies the possibility of using such objects for the purposes of global stratigraphic correlation of sedimentary strata. To date, the typomorphic features of iron oxide microspheres remain underexplored. In this paper, we attempted to identify the typomorphic features of cosmic iron oxide microspheres, depending on the conditions of their formation.

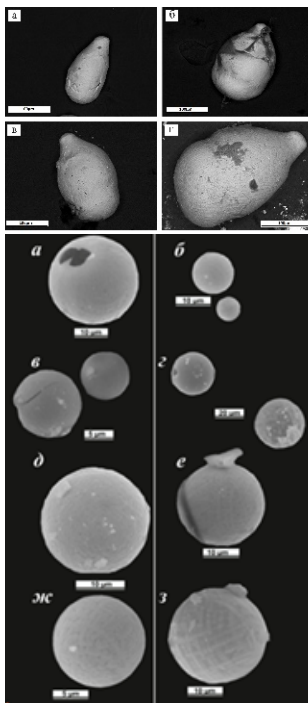


Fig. 1.

Objects and methods of research: Space bodies entering the atmosphere of the Earth are called meteoroids [3]. Braking in the atmosphere, they experience heating, melting, evaporation. Large meteoroids do not evaporate completely, but only fuming from the surface, they fall out in the form of meteorites. In this case, the melt film is blown away by the oncoming air flow (ablation). Small meteoroids (from 0.01 micron to 3 cm) can completely melt and evaporate. Melt particles arising during deceleration of meteoroids in the Earth's atmosphere have the form of droplets (Fig. 1). As the rate of fall of a melt falls off, the melt particle decreases its elongation (drop-likeness) and it becomes more spherical (Fig. 2). The main factors that determine its shape and size are gravity force, surface tension and rotational moment.

To identify the conditions for formation of metal (iron oxide) microsphere, which determine the formation of their typomorphic features, we carried out theoretical calculations of the deceleration of meteoroids of various sizes in the Earth's atmosphere. For this purpose, the theory of deceleration of meteoroids in the Earth's atmosphere was used [3].

Results and discussion: Our calculations of the deceleration of native iron meteoric particles show that all microsphere with a radius of 0.1 to 250 μm (without taking into account energy losses due to radiation) experience melting when they are decelerated in the Earth's atmosphere. Accounting for energy losses due to radiation according to [4] shows that the critical radius for our conditions is 7 μm , that is, particles with a radius less than 7 μm do not melt, while larger ones melt. This predeter-

mines a possibility of spherical forms formation for cosmic particles of native iron in **two scenarios**.

The first of them occurs when a meteor particle during deceleration almost completely dampens its cosmic velocity along the flight path in the Earth's atmosphere. The drop-shaped particles of iron's melts formed in atmosphere, when the cosmic velocity is extinguished, ones lose a rotational impulse and become spherical. If during the rotation (tens - the first hundreds of seconds) the melt cools down, hardening at least from the periphery, then there are Fe microspheres with sizes ranging from 0.1 to 500 microns in diameter. The formation of a spherical shape of Fe melt particles less than 150 microns in size is additionally stimulated by an increased value of the surface tension values for the Fe melt, which, however, decreases with increasing oxygen content in the melt. The latter leads to the fragmentation and reduction of the size of Fe microspheres formed in the more dense layers of the atmosphere closer to the surface of the Earth, and with a higher oxygen content. Iron in them becomes more oxidized to wustite and magnetite.

Another scenario of the spherical shapes formation for metal particles under the conditions of the Earth's atmosphere is associated with an increased surface tension of the ferrous melt, which arose as a result of deceleration of meteoric particles in the atmosphere and fully extinguishing its velocity v at height H ($v = 0$). It is known that small particles of melts of various substances under weightless conditions take the form of a sphere, since it corresponds to the minimum surface energy of these particles. The calculations show that the size of the maximum radius of spherical particles of the Fe melt (having quenched their speed at height H ($v = 0$)) depends on the specific energy of the melt surface tension σ and the magnitude of the acceleration of gravity g [7]. The value of g from the ground to a height of 100 km decreases slightly (from 9.81 m/s² to 9.51 m/s²). However, it is necessary to take into account that the specific energy of the Fe melt surface tension σ decreases with increasing oxygen in it. At the same time, the oxygen content in the Earth's atmosphere increases with decreasing altitude.

The degree of oxidation and the cooling rate of Fe melt microsphere are determined by the height of their formation above the Earth's surface and the mass (size) of the particle. This facilitates the formation of typomorphic features (size, structure, oxygen content, presence of magnetite, wustite, degree of sphericity) in "cosmic" Fe microsphere. In the case of a moderate rate for Fe melt cooling at medium altitudes (50-80 km) the microsphere, falling and cooling down, has time to oxidize outside, becomes covered with a crust of magnetite crystals ("shield"), in which a liquid Fe melt is often mixed with nickel. This residual high-temperature melt is capable of melting the outer crust of the microsphere along the boundaries of magnetite crystals.

Leaking out and freezing, the melt forms various aggregates-growths of native Fe, and if it has time to oxidize, then garlands of magnetite, wustite dendrites appear. Typomorphic features of Fe microspheres formed at a small height from the Earth's surface during impact processes are their small size (up to 20-60 μm in diameter), high oxidation (high O/Fe) and abundance of magnetite. The obtained results show that with an increase in the oxygen content in the Fe melt, the maximum possible radius of the microsphere capable of maintaining their sphericity in the Earth's atmosphere decreases. Hence the conclusion: with the approach to the Earth's surface, the radius of the microsphere decreases several times, and the iron in them becomes more oxidized. Practically all the microsphere of the Fe melt formed in impact processes on the Earth included into this group.

The fate of the Fe melt microsphere formed in the earth's atmosphere during the deceleration of meteor particles may vary depending on environmental conditions. With a high rate of cooling of the melt, its structure will be fine, hidden grained, the substance is undifferentiated and homogeneous. The surface of such drops and microsphere turns out to be smooth and weakly oxidized; it consists more often of wustite, less often of magnetite [5]. On surface of the Earth, in sedimentary rocks and in peat, metallic Fe particles are often encountered that have not passed the melt stage, and therefore

have a wide variety of forms, sometimes they can be spherical. Their origin should be attributed to the low cosmic velocity of entry of some meteoric particles into the Earth's atmosphere, which is confirmed by our calculations [7]. Meteoric bodies entering the Earth's atmosphere at low speeds (of the order of 5 km/s) are apparently due to the impact processes on the Moon and on objects from the asteroid belt [6]. From there can fly and ready-made metal balls. Their characteristic typomorphic sign is the minimum value of Fe oxidation, i.e., a low (down to zero) O/Fe ratio.

Conclusions: In order to identify the typomorphic features of the cosmogenic iron oxide microspheres, which are found in sedimentary rocks of the Earth, theoretical calculations of the deceleration in Earth's atmosphere of various sizes meteoroids were carried out. The most important typomorphic features of such microspheres are the size, the structure with different precipitates of metals (native iron, nickel) and intermetallides, the presence / absence of wustite, the oxygen content, the degree of sphericity. Calculations show that particles of native iron with a radius of more than 7 μm slow down and experience melting in the Earth's atmosphere at an initial velocity of their fall of 15 km/s, and the larger their size, the closer to the surface of the Earth they melt. With an initial fall rate of 5 km / s, Fe particles of all studied sizes (0.1–250 μm) do not melt during deceleration in the Earth's atmosphere and therefore retain their shape and composition that meet the conditions of their formation as a result of impact processes on asteroids and the Moon. At the same time, they contain no magnetite, wustite, a low O / Fe ratio, and the size can reach several hundred micrometers in diameter.

Acknowledgments:

The work was done at the expense of subsidies allocated to the Kazan (Volga Region) Federal University as part of state support in order to increase its competitiveness among the world's leading scientific and educational centers and to carry out the project part of the state task in the field of scientific activity, as part of the state task "Spatio-temporal structure of the ancient geomagnetic field and petrophysics of magnetic minerals as indicators of geological and geophysical processes", state number registration AAAA-A17-117040610183-6, microprobe studies - with the support of the RFBR project No. 16-05-00703.

References:

- [1] Korchagin O.A., The Presence of Metallic Microspheres and Microparticles in the Early Cenomanian of the Crimea - "Cosmic Dust Event". // Dokl. RAS, 2010, V. 431 N.6, P. 783-787.
- [2] Pechersky D. M., Kuzina D. M., Nurgaliev D. K., Tselmovich V. A. The unified nature of native iron in terrestrial rocks and meteorites Results of microprobe and thermomagnetic analyzes // FizikaZemli, 2015, No. 5, p. 140–155
- [3] Bronshten V. A. Meteors, meteorites, meteoroids. M.: Science, 1987. 176 p.
- [4] Brandt D.S., Hodge P.W. Astrophysics of the Solar System. M.: MIR, 1967. 488 p.
- [5] Sungatullin R. H., Bakhtin A. Io., Sungatullina G. M., Tsel'movich V. A., Glukhov M. S., Osin Yu. N. and Vorobiev V. V. Composition And Morphology Of Metal Microparticles In Paleozoic Sediments Of Caspian Depression // International Journal of Applied Engineering Research, 2015, v. 10 (24), p. 45372-45382.
- [6] Flynn G. J. Atmospheric entry heating of micrometeorites // Proc. 19-th Lunar and Planet. Sci. Conf. Houston, 1989. p. 673-682.
- [7] Bakhtin A.I., Sungatullin R.Kh., Sonin G.V., Gusev A.V., Kuzina D.M., Sungatullina G.M. Braking of Meteor Particles in the Atmosphere of the Earth and Creation of Magnetic Microspheres // Meteoritics & Planetary Science. 2018. Vol. 53, Is. S1. P. 6296.

THE PROJECT OF MULTIBAND PHOTOMETRY OF SMALL BODIES OF THE SOLAR SYSTEM WITH ROBOPHOT

A.E. Potoskuev¹, V.V. Busarev², V.V. Krushinsky¹, E.D. Kuznetsov¹,
A.A. Popov¹, A.M. Sobolev¹

¹ Kourvka Astronomical Observatory, Ural Federal University, Lenina Avenue, 51, Yekaterinburg, 620000, Russian Federation (RF), alexander.potoskuev@gmail.com, krussh@gmail.com, eduard.kuznetsov@urfu.ru, apopov66@gmail.com, andrej.sobolev@urfu.ru

² Lomonosov Moscow State University, Sternberg Astronomical Institute, University Av., 13, Moscow, 119992, RF, busarev@sai.msu.ru

Keywords:

Multichannel photometer, light curve, asteroids, taxonomical classification, color index

Asteroids have diverse spectral features representing distinct compositions, and, therefore, various taxonomical classifications have been implemented over the last decades [1]. Multiband photometry of asteroids enables their spectral analysis in order to define their taxonomic classes, even for faint objects and using telescopes of moderate sizes (e.g., [2]). Directly measured flux over a substantial period of time (at least rotational period) may be used for light curve plotting to obtain geometrical and rotational parameters of the objects [3]. Surface color irregularities, for instance, due to the presence of young facets characteristic of recently formed asteroids, might be detected with the light curve multiband photometry.

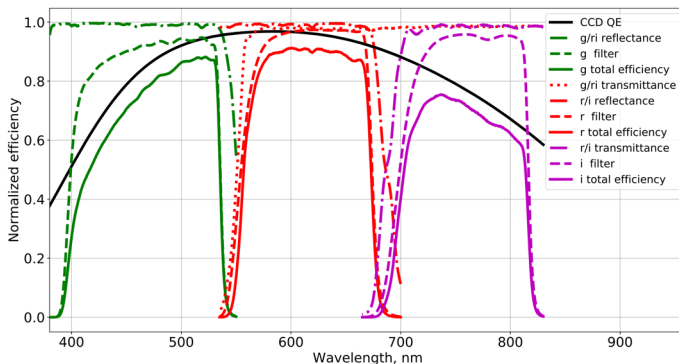


Fig. 1. The efficiency of the components and total efficiency (provided by the manufacturer [7]).

Ordinary detectors with replaceable photometric filters (e.g., a filter wheel) do not allow deriving color images simultaneously, what is desirable for studying rapid rotating objects, such as some near-Earth asteroids. Longer exposures, which are required for faint objects but taken sequentially, will lead to a phase shift in the measured light curves. For this reason, a three-channel CCD photometer equipped with the Sloan g' , r' , i' filters (the effective wavelengths are 4775, 6130 and 7485 Å, respectively (Fig. 1)) was developed for studies of asteroids at Kourvka Astronomical Observatory (KAO) of Ural Federal University. It is designed for telescopes with a focal ratio $F/D > 7$ with a field of view of about $20'$. The photometer was installed on the "Robophot" telescope of KAO, which is a modified Dall-Kirkham telescope with a diameter of the main mirror of 0.6 m and a focal length of 4.2 m. Test observations showed that FWHM of the PSF was about $2.8''$ being dependent primarily on the atmospheric quality. The instrument is operated through an open source RTS2 package [4] for remote control, allowing fully autonomous running of the facility.

One of the advantages of the SDSS colors is that $r' - i'$ vs. $g' - r'$ color-color diagram enables easy separation of C-type asteroids from S-types [5] and correction of their albedo [6]. Three-color simultaneous observations should allow significant progress in the study of the surface layers of asteroids as well as the rotational dynamics, shape, and multiplicity.

The study was funded by RFBR (the research project no. 18-02-00015), the Ministry of Science and Higher Education of the Russian Federation (the basic part of the State assignment, RK no. AAAA-A17-117030310283-7) and the Government of the Russian Federation (Act 211, contract no. 02.A03.21.0006).

Acknowledgments:

The study was funded by RFBR (the research project no. 18-02-00015), the Ministry of Science and Higher Education of the Russian Federation (the basic part of the State assignment, RK no. AAAA-A17-117030310283-7) and the Government of the Russian Federation (Act 211, contract no. 02.A03.21.0006).

References:

- [1] Binzel R.P., DeMeo F.E., Turtelboom E.V. et. al. Compositional distributions and evolutionary processes for the near-Earth object population: Results from the MIT-Hawaii Near-Earth Object Spectroscopic Survey (MITHNEOS) // *Icarus*. 2019. V. 324. P. 41–76.
- [2] DeMeo F.E., Carry B. The taxonomic distribution of asteroids from multi-filter all-sky photometric surveys // *Icarus*. 2013. V. 226. P. 723–741.
- [3] Pravec P., Fatka P., Vokrouhlický D. et. al. Asteroid pairs: A complex picture // *Icarus*. <https://doi.org/10.1016/j.icarus.2019.05.014>.
- [4] Kubánek P., Jelinek M., Nekola M. et. al. RTS2 — Remote Telescope System, 2nd Version // *AIP Conference Proceedings*. 2004. V. 727. No. 1. P. 753–756.
- [5] Ivezić Z., Tabachnik S., Rafikov R. et al. Solar System Objects Observed in the Sloan Digital Sky Survey Commissioning Data // *Astronomical Journal*. 2001. V. 122. P. 2749–2784.
- [6] Mainzer A., Masiero J., Grav T. et al. NEOWISE studies of asteroids with Sloan photometry: preliminary results // *Astrophysical Journal*. 2012. V. 745. Id. 7. P. 9
- [7] Asahi Spectra // <https://www.asahi-spectra.com/>

EXPERIMENTAL INVESTIGATION OF MECHANICAL PROPERTIES OF METEORITES

A.P. Krivenko¹, N.V. Dushenko¹, S.A. Voropaev¹, I.I. Nugmanov²

¹ GEOKHI RAS, Moscow, Kosygina str. 19. Voropaev@geokhi.ru

² Kazan Federal University, Kazan, Russia

Keywords:

Moon, Earth, stress, strain, meteorites, asteroids.

Introduction:

Usually, meteorites are fragments of their parent bodies surface. So, their properties provide important information about the composition and evolution of asteroids and small bodies of the Solar system [1]. But frequently the body of the fallen meteorite is broken with the cracks and splits, like Chelyabinsk. In order to identify the different failure mechanisms, we have to experimentally investigate the strength properties of the small part of meteorite. Most industrial facilities for researching mechanical properties of materials don't allow provide the estimation of such meteorites, because it need dimensions of sample at least 25 mm diameter and 50 mm length [2]. To avoid these constraints, we have designed special installation for evaluation such elastic mechanical values as Poisson's ratio, Young's modulus, and ultimate tensile and compression strengths.

Methods:

Design of the developed installation for estimation of mechanical properties comprises sensors, electronic unit, personal computer (see Fig. 1). The cylindrical samples with dimensions starting from 5 mm in diameter and 10 mm length can be studied on it. The only limited factor is size of chondrules, main components of chondrites. The study of so small samples can be performed by tiny foil strength sensors with nominal impedance from 300 Ohms to 1000 Ohms, with different base size. Electronic unit has 4 channels. 2 channels intended for signals from sensors of relative longitudinal and transverse deformation. The third channel used for force sensor, which measure the force applying to sample. The fourth channel can be used for external temperature sensor in case when sample is only one. Usage sensors of relative longitudinal and transverse deformation in pair increase accuracy by 2 times per channel. Each pair of sensors connects to 32-bit analog to digital converter. All analog to digital convertors send digital data to controller, which proceed it and send on personal computer. The electronic unit has power station unit to stabilize supply current. The schematics of electronic unit optimize out signal and increase accuracy of evaluation. Installation can compensate the fluctuation of signal from temperature and added impedance of wires

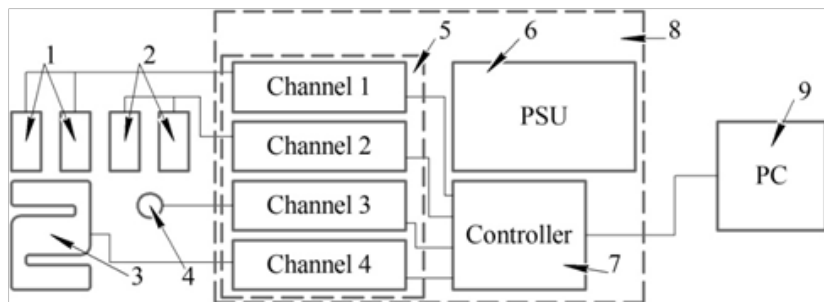


Fig. 1. Block-scheme of installation. 1,2 — foil sensors, 3 — force sensor, 4 — temperatures sensor, 5 — ADC group, 6 — power station unit, 7 — controller, 8 — electronic unit, 9 — personal computer

Results:

Developed setup allowed us to perform measurement of mechanical properties of small samples of meteorites in according to standard GOST 28985-

91 Rocks. Method for determination of deformation characteristics is uniaxial compression. The calculation of the characteristics can be carry out according to the following formulas: Young`s modulus:

$$E_y = \frac{\sigma_K - \sigma_H}{\varepsilon'_{1K} - \varepsilon'_{1H}} \quad (1)$$

Poisson`s ratio:

$$\mu = \frac{\varepsilon'_{2K} - \varepsilon'_{2H}}{\varepsilon'_{1K} - \varepsilon'_{1H}} \quad (2)$$

where σ_K, σ_H — tension at finish and at start of loading and unloading range of sample, $\varepsilon_{1K}, \varepsilon_{1H}$ — relative longitudinal deformation of sample at finish and at start of range on loading, $\varepsilon_{2K}, \varepsilon_{2H}$ — relative transverse deformation of sample at finish and at start of range on loading, $\varepsilon'_{1K}, \varepsilon'_{1H}$ — relative longitudinal deformation of sample at finish and at start of range on unloading, $\varepsilon'_{2K}, \varepsilon'_{2H}$ — relative transverse deformation of sample at finish and at start of range on un-loading.

Dynamical and Brazilian test:

Further, we will modify this installation to perform the Brazilian test. The great advantage of the Brazilian test is determination of the elastic modulus, tensile strength and fracture toughness of rock materials in one test [3]. For calibration, it is planned to use the equipment of mining mechanics of the Geological Institute of Kazan Federal State University: Installation for testing rocks in crust conditions GTAN.441179.050 (see Fig. 2a) is an automated system for comprehensive testing of rocks at normal and elevated temperature and pressure parameters that simulate crust conditions.

Determination of tensile strength during splitting by applying a compressive load along the diameter of the sample in the form of a disk is performed according to the requirements of standard ASTM D3967-08 (see Fig.2b). The tests are carried out on specimens in the form of a disc with a thickness-to-diameter ratio (t/D) of 0.2 to 0.75. The diameter of the sample should be at least 10 times the linear size of the grains (inhomogeneities) composing the rock. Cylindrical samples were obtained by taking a meteorite from the initial sample delivered to the laboratory.

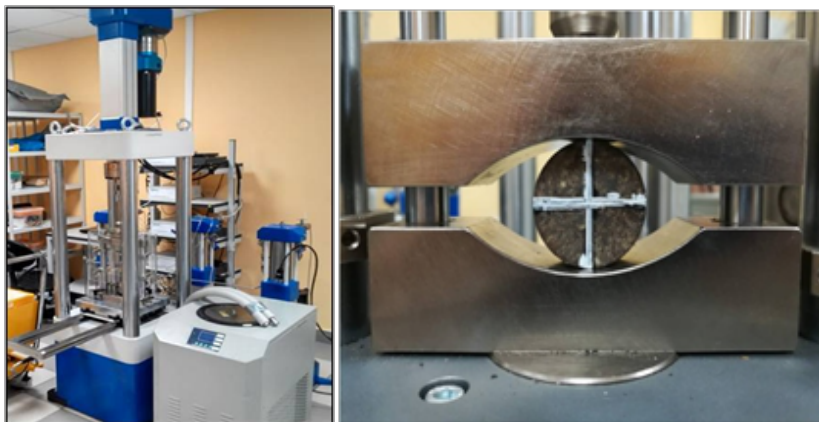


Fig. 2. a) Setup GTAN.441179.050; b) Brazilian test

Sample preparation of samples for testing was to bring to the required length on the cutting machine and grinding the end surfaces with an accuracy of 0.01 mm. Tests were carried out in a state of natural saturation. The diameter and thickness of each sample was determined using a caliper, with at least 4 measurements for each parameter and an average. The calculation for determining the tensile strength at splitting (Brazilian test) is carried out according to the following formula:

$$\sigma_t = \frac{2P}{\pi LD} \quad (3)$$

where σ_t – limit of tensile strength when splitting, in MPa; P is the maximum applied load, fixed by the force sensor of the test machine, in N; L – sample thickness, in mm; D – sample diameter, in mm.

Measurement of the velocity of the longitudinal and transverse ultrasonic wave is performed at the additional setup PIC-ULTRASONIC-EP installation. The system consists of two ultrasonic sensors, a signal source, an oscilloscope, an RLC device and a relay system. The source generates a signal with a frequency of 1 MHz. The signal is received by one of the sensors, which excites the pulses of S and P waves. The waves pass through the sample installed in the core holder and are detected by a second ultrasonic measurement sensor. Then the signal is received by the oscilloscope. The oscilloscope is connected to a PC to analyze and record the received signal. The source has three outputs: S wave, P wave and synchronization signal of the source with the oscilloscope.

When measuring the elastic properties of the sample on the PC monitor is synchronized with the oscilloscope display graphs S and P waves. Graphs are displayed in time-amplitude coordinates. Using the program of processing of the PIC-ULTRASONIC-EP installation, the performer interactively gives the entry time of each wave. Using the values of the samples height, automatically calculation of the speed of P and S waves is deduced. The calculation of the dynamic elastic modules (Young's and Poisson's ratio) was carried out according to the following formulas:

$$R = \frac{V_p}{V_s} = \frac{\sqrt{2}(1-\mu)}{(1-2\mu)}, \quad (4)$$

$$E = V_p^2 \cdot \rho \cdot \frac{(1+\mu)(1-2\mu)}{(1-\mu)}, \quad (5)$$

where R – ratio of longitudinal and transverse waves, V_p – velocity of longitudinal waves, V_s – velocity of transverse waves, μ – dynamic Poisson's ratio, E – dynamic young's modulus, ρ – density of rocks.

Acknowledgments

This work was supported by the Russian Science Foundation, project no. 17-17-01279.

References:

- [1] Petrovic J.J. // Journal of Materials Science. 2001. V. 36. P. 1579–1583.
- [2] Voropaev S. et al. // Doklady Physics. 2017. V. 62. No. 10. P. 486–487.
- [3] Wung Q.Z. et. al. // International Journal of Rock Mechanics and Mining Sciences. 2004. V. 41. P. 245–253.

INTERSTELLAR METEORIDS SORTING IN THE SOLAR SYSTEM

N.I. Perov^{1,2}, V.E. Pakhomycheva²

¹ State Autonomous Organization of Culture and Education named after V.V. Tereshkova, ul. Chaikovskogo, 3, Yaroslavl, 150000, Russia, perov@yarplaneta.ru

² Yaroslavl's State Pedagogical University named after K.D. Ushinskii, ul. Respublikanskaya, 108, Yaroslavl, 150000, Russia, pahomycheva.vika@mail.ru

Keywords:

Galactic meteors, size, distances from the Sun, velocities, transearth flight time, distributions, Pointing–Robertson effect, light pressure, gravitation.

Introduction:

Particles arrived in the Solar System from interstellar medium are found but their nature is not cleared [1, 2]. Discovering of such particle fluxes and working out the criteria of galactic meteors identification is a problem of the modern astronomy [2]. It is usually supposed that interstellar meteoroids' particles velocities near the Earth's orbit may vary from dozens to hundreds kilometers per second [1, 2]. Below it is stated the heliocentric velocities of meteoric particles near the orbit of the Earth may be equal almost zero if light pressure and effect of Pointing–Robertson as well as gravitational force acting on the particle from the Sun are taken into account. Moreover in the frame of suggested model we try to find the distributions of these particles on transearth flight time, heliocentric velocities and maximal distances from the Sun for the fixed time motion depended upon density and radii of the considered meteoroids.

Fundamental equations:

The model equation of particle motion we put in the form (1) [3]

$$\frac{d^2\mathbf{r}}{dt^2} = -\frac{GM'\mathbf{r}}{r^3} - 2b'v \cdot \cos(u) \frac{\mathbf{e}_r}{r^2} - b'v \cdot \sin(u) \frac{\mathbf{e}_t}{r^2}. \quad (1)$$

Here, v is a heliocentric velocity of the considered particle, u is an angle between the vector of the velocity v and the heliocentric radius-vector r of the particle, \mathbf{e}_r and \mathbf{e}_t are units' orts of radial and tangent directions of the particle vector acceleration,

$$b' = \pi R^2 \frac{qr_{se}^2}{Mc^2}, \quad M' = M_S - \pi R^2 \frac{qr_{SE}^2}{GMc},$$

G is the gravitational constant, c is the velocity of light, R is a radius of the particle, q is the solar constant, M' is reduced mass of the Sun, M_S is the real mass of the Sun, M is mass of the particle, r_{se} is the averaged distance between the Earth and the Sun.

Using the density ρ of the spherical black particle we have

$$b' = \frac{3}{4} \cdot \frac{qr_{SE}^2}{\rho R c^2}, \quad M' = M_S - \frac{3}{4} \cdot \frac{qr_{SE}^2}{\rho R G c}.$$

If the particle moves along the straight line in the gravitational field of the Sun (light pressure and effect of Pointing–Robertson are also taken into account), then equation (1) is simplified ($u = \pi$) and we have $v = v(r)$. After integrating the in this case the differential equation (1) $v(r)$ may be found from the expression

Here, LambertW(x) is the function of Lambert and v_0 is the initial velocity of the particle, r_0 is the initial positions of the particle, the final distance of the particle from the Sun is equal to $r = r_{SE}$. It should be noted $v(r)$ is expressed in evidence form with help of Lambert function.

$$v = \frac{1}{2} \cdot \frac{GM'}{b'} \left(\text{LamberW} \left(-\frac{(-2b'v_0 + GM')}{GM'} \times \right. \right. \\ \left. \left. \times \exp \left(-\frac{2b'rr_0v_0 + GM'rr_0 - 4b'^2r_0 + 4b'r}{GM'rr_0} \right) \right) + 1 \right) \quad (2)$$

Examples:

Graphs of $v(v_0, \rho \cdot R)$ functions, presented in figures (Fig. 1–3), are plotted for values: $q = 1360 \text{ Wt/m}^2$, $r_{SF} = 1.49597 \cdot 10^{11} \text{ m}$, $M_S = 2 \cdot 10^{30} \text{ kg}$, $r_0 = 100 \text{ 000 AU}$, $G = 6.672 \cdot 10^{-11} \text{ m}^3/\text{kg} \cdot \text{s}^2$, $c = 3 \cdot 10^8 \text{ m/s}$; $0 < v_0 < 100 \text{ 000 m/s}$, $0 < \rho \cdot R < 10^6 \text{ kg/m}^2$.

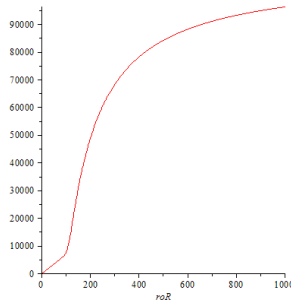


Fig. 1. Dependence of interstellar meteoroid velocity v near the Earth's orbit on $\rho \cdot R$ for $v_0 = 100 \text{ 000 m/s}$ and $r_0 = 10^5 \text{ AU}$

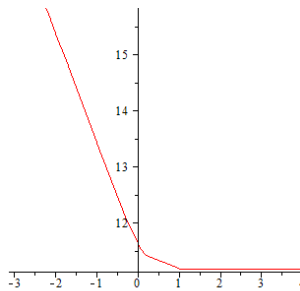


Fig. 2. Time t (s) particles motion from $r_0 = 100 \text{ 000 AU}$ to $r = 1 \text{ AU}$ depended upon ρR (kg/m^2) in logarithm scales; $v_0 = 100 \text{ km/s}$

In figures (Fig. 1.–3.) for the case of equality of the light wave length λ and the radius R of the particle effects of diffraction are not taken into account [3]. It should be noted [2] the middle mass of the detected interstellar particles is equal to $8 \cdot 10^{-16} \text{ kg}$ and the corresponding flux equals $1.5 \cdot 10^{-4} \text{ m}^{-2}\text{c}^{-1}$ in accordance with the data of "Galileo" probe.

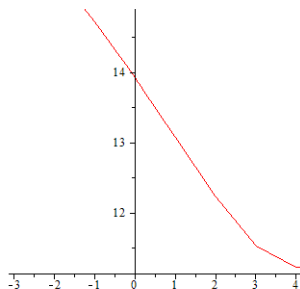


Fig. 3. Distances (in meters) of particles from the Sun for the time equals $1.4959411979004 \cdot 10^{11} \text{ (s)}$ for the different values of $\rho \cdot R$ (kg/m^2). Etalon time (distance) the particle passes for $\rho \cdot R = 10^6 \text{ kg/m}^2$. Logarithmical scales are used $v_0 = 100 \text{ 000 m/s}$, $r_0 = 100 \text{ 000 AU}$.

Conclusion:

The small values of the radii R and the low density ρ of the particles make the velocities of interstellar meteoroids near the Earth's orbit tend to zero even for the large initial velocities of these meteoroids (Fig. 1.).

The large values of the radii R and the great density ρ of the particles make the velocities of interstellar meteoroids tend to parabolic (hyperbolic) ones near the Earth's orbit even for the small initial velocities of these meteoroids (Fig. 1.).

For the small values of product of $\rho \cdot R$ and the small values of the initial meteoroids velocity v_0 the final velocity of the meteoroid (near the orbit of the Earth) tends to zero (Fig. 1.).

So, the interstellar meteoroids in some cases have almost zero velocities near the Earth's orbit and majority of them may be lost for their searching in accordance with the method [4], using only the criterion of high velocities of interstellar meteoroids.

For the small values of products of ρR and the distance from the Sun equaled $r_k = 1$ AU, – heliocentrically velocities of meteoroids have been decreasing, and time of motion t has been increasing (for the parameters: $v_0 = 100$ km/s, $r_0 = 10^5$ AU, $\rho R = 0.00075$ kg/m²; we have $v_k = 0.0426$ m/s, $t = 2.2057843 \cdot 10^{17}$ s). (Fig. 1–3).

The meteoroid for which $\rho \cdot R = 10^6$ kg/m², $v_0 = 100$ km/s, $r_0 = 10^5$ AU, $r_k = 1$ AU has motion time $t = 1.4959 \cdot 10^{11}$ s, while the meteoroid, for which $\rho \cdot R = 0.00075$ kg/m², $v_0 = 100$ km/s, $r_0 = 10^5$ AU, $t = 1.4959 \cdot 10^{11}$ s, will be placed from the Sun at the distance only equals $r_k = 95430.14 \cdot 10^{11}$ m.

So, in the given model the small soft particles of interstellar meteoroids may localize in the “pipes” of length, compared with the size of the Solar system (Fig. 3).

References:

- [1] Hajdukov'a M., Paulech Jr., Paulech T. Hyperbolic and interstellar meteors in the IAU MDC radar data // Contrib. Astron. Obs. Skalnat'e Pleso. 2007. V. 37. P. 18–30. (<http://www.ta3.sk/caosp/Eedition/FullTexts/vol37no1/pp18-30.pdf>).
- [2] Kramer E.N., Smirnov V.A. Interstellar Meteors: A Reality? // Solar System Research. 1999. V. 33. P. 77.
- [3] Radzievskii V.V. Photogravitational Celestial Mechanics / Ed. Chief Yu.A. Nikolaev. Nijnii Novgorod, 2003. 196 pp. (In Russian).
- [4] Slivinskii A.P., Bushuev F.I., Kalyujnyi N.A., Shulga A.V. The possibility of observations of interstellar meteors with using broadcast wave // Science and Technics. 2013. V. 92. No 2. P. 28–34.

POSSIBLE MODELS OF THE PLANETARY SYSTEMS FORMATION

T.V. Salnikova^{1,2}, E.I. Kugushev¹, S.Ya. Stepanov³

¹ *Lomonosov Moscow State University (GSP-1, Leninskie Gory, Moscow, 119991, Russian Federation);*

² *RUDN University (Moscow Miklukho-Maklaya str.6, Moscow, 117198, Russian Federation);*

³ *Dorodnicyn Computing Centre, RAS (Vavilov str.40, Moscow, 119333, Russian Federation).*

Keywords:

Celestial mechanics, cosmology, mathematical simulation

We discuss "widened" model of planetary system formation. Gravitational collapse of protoplanets leads to the formation of planets and their satellite systems. We consider the hypothesis of a two-stage mechanism of formation of satellite system. Small satellites are formed from the remnants of a collapsing protoplanetary cloud, and large satellites are formed by capturing other relatively small protoplanets [1].

At the same time, it is important to study the process of formation of the initial gas-dust cloud, the evolution of which leads to the formation of a protoplanetary, and then a planetary system.

The justification of the "widened" model is carried out by numerical simulation.

References:

- [1] T. Eneev, N. Kozlov The Dynamics of Planet Formation. Theory and Computer Simulation // Saarbrucken, Deutschland, Lap Lambert Academic Publishing, 2016, 140 p. ISBN: 978-3-659-85958-8.

ESCAPE OF ROCK-FORMING VOLATILE ELEMENTS AND NOBLE GASES FROM PLANETARY EMBRYOS

M. Benedikt^{1,2}, M. Scherf², H. Lammer², E. Marcq³, P. Odert¹, M. Leitzinger¹, N.V. Erkaev^{4,5}

¹ *Institute of Physics, IGAM, University of Graz, Universitätsplatz 5, 8010 Graz, Austria (markusbenedikt@gmx.at);*

² *Space Research Institute, Austrian Academy of Sciences, Schmiedlstr. 6, 8042 Graz, Austria;*

³ *LATMOS, Université de Versailles Saint-Quentin-en-Yvelines, Guyancourt, France;*

⁴ *Institute of Computational Modelling of the Siberian Branch of the Russian Academy of Sciences, 660036 Krasnoyarsk, and Siberian Federal University, 660041 Krasnoyarsk, Russian Federation;*

⁵ *Siberian Federal University, 660041 Krasnoyarsk, Russian Federation*

Keywords:

Planetary embryos, protoplanets, hydrodynamic escape, magma oceans, steam atmospheres, rock-forming elements

In the early evolution of planetary systems, protoplanets originate from the coagulation of dust and ice and initially reside embedded in the gas of the circumstellar disks. From isotope studies, it is expected that the Earth (and terrestrial planets) formed from pre-fractionated differentiated planetary embryos and a fraction of carbonaceous chondrites. Additionally, the importance of ureilite and enstatite chondrites for the evolution of Earth can also be argued by isotope studies. Large planetesimals and planetary embryos are differentiated bodies with sizes of several hundred to a few thousand kilometers. Planetary embryos form protoplanets via mutual collisions, which can lead to the development of magma oceans. During their solidification, significant amounts of the mantles' volatile contents may be outgassed. We show that the resulting steam atmospheres can be lost efficiently via hydrodynamic escape that drag heavier elements like noble gases, and outgassed rock-forming elements K, Na, Si, Mg, Rb etc. into space so that they are also lost. Planetary embryos that are later involved in terrestrial planet formation can be drier than previously expected. We model the outgassing and subsequent hydrodynamic escape of steam atmospheres from such embryos, including the efficient outflow of H that drags along heavier species like O, CO₂, CO, K, Na, Si, Mg, Rb etc., and noble gases (Ar, Ne) and their isotopes. The full range of possible EUV evolution tracks of a young solar-mass star is taken into account. We investigate the atmospheric/elemental escape from planetary embryos with masses of 0.5 Mars, 1 Mars, 1.5 Mars and 1 Moon at different orbital distances and the fractionation of these planetary embryos. Finally, we discuss the implications of our findings in relation to elemental composition of the bulk silicate Earth composition.

NATURAL OCTAHEDRONS OF VARIOUS SIZES INCLUDING HIDDEN ONES IN EARTH AND SATURN

G.G. Kochemasov

IGEM of the RAS, Staromonetny 35,119017Moscow, RF,kochem.36@mail.ru

Keywords:

Cosmic bodies, asteroids, Amalthea, Yanus, Steins, Ryugu, Earth, Saturn

Introduction:

The first hint on “diamond” shape in cosmos was presented by images of Amalthea (Fig. 9) – a small Jupiter satellite - acquired by Galileo mission. This hint was not adequately appreciated and did not evoke any discussion. Later on some features of polyhedron shapes were observed in some other asteroids (Mathilde, Ida, Eros, Dactyl, Steins) [1] but were noticed and commented only by a few observers [1, 2]. Now, wealth of small icy bodies are imaged by Cassini cameras and their sometimes almost artificial appearance (like the Plato’s polyhedrons and “flying saucers”) is commented [3–6]. Such a massive evidence of polyhedron shapes in cosmos claims for an explanation different from seldom impacts usually presumed.

The wave planetology [7–12 & others] main assertion is: “Orbits make structures”. As all celestial bodies move in non-round (elliptical, parabolic) orbits with periodically changing accelerations they all are subjected to an action of inertia-gravity forces. These forces arouse in them warping waves that in rotating bodies (but they all rotate!) acquire a stationary character and 4 directions of propagation (ortho- and diagonal). Interferences of these waves produce three kinds of tectonic blocks: uplifting (+), subsiding (-) and neutral (0). Their size depends on warping wavelengths. The longest fundamental wave 1 produces ubiquitous tectonic dichotomy – an opposition of two segments: uplifted and subsided, expanded and contracted ($2\pi R$ -structure). The first overtone wave 2 superposes on this segmentation smaller features - sectors (πR -structure, Figs. 4-11). Next overtones give smaller features.

An essence of tectonic dichotomy is in tendency of 4 interfering waves 1 to make from a body a tetrahedron – the simplest Plato’ figure [3, 4]. A dichotomous nature of this figure is revealed in opposition of a vertex and a face (cutting any of its 4 axes one always gets from one side a vertex, from another a face). In one direction three faces narrow towards a vertex (contraction), in opposite direction they expand towards a fourth face (expansion). Most often in small bodies (not only in satellites but also in asteroids and comets) one observes an oblong convexo-concave shape [12 & others] but sometimes at certain points of view a flatten concave side and a sharpened convex side are presented by such a way that a tetrahedron develops. Interfering waves 2 produce an octahedron. At the first time it was observed in a shape of Amalthea (see Kolva’s drawing of this satellite after Galileo mission), and name “diamond” was pronounced but no explanation followed. Now some octahedron faces one can observe at a number of small bodies, just to mention Phobos, Phoeba, Yanus Steins, Ryugu (Fig. 6–11). Interfering waves 4 produce a cube. Shorter wavelengths — more vertices in a polyhedron: tetrahedron 4, octahedron 6, cube 8 and so on. Various polyhedrons are present in a body simultaneously because the wave warping occurs in various wavelengths at the same time but particular viewpoints present better view of one of them (for examples, Yanus, Amalthea, Hyperion, Helene, Steins, Ryugu).

So, produced by warping waves polyhedron shapes, often detected in small bodies due to their weak gravity, present a real fundamental property of these cosmic bodies. In larger bodies this forms are smoothed by gravity making bodies globular, but still some vertices and edges can be distinguished with help of analyses of geology, geomorphology and geophysics. For an example, “famous” hexagon feature in the northern hemisphere of Saturn presents a face of structural tetrahedron, whereas the southern hemisphere “hurricane” is its opposite vertex. Thus looks the structural dichotomy of this giant

gas planet. The hexagon should be considered as combination of a tetrahedron (tectonic dichotomy) and an octahedron (the first overtone feature). The tetrahedron has three directions of faces, the octahedron-two directions of faces. $3 \times 2 = 6$. Thus appear the hexagon outlines (Fig. 1–3). This structure is volumetric as it goes deep at least for 100 km and up into the stratosphere for nearly 300 km [15].

A hidden octahedron is in the Earth (antipodal vertices: 1. New Guinea, 2. Equatorial Atlantic, 3. Easter Isl. 4. Pamirs-Hindukush, 5. Bering Strait, 6. Bouvet Island) (Fig. 4, 5). Its faces are continents and oceans on the Earth's surface and corresponding them inversely highs and depressions in the core mantle boundary (Fig.5 [13]).

Considered above natural octahedron shapes and structures give a regular line from small bodies to giant sizes-characteristic sizes: a portion of km – km – tens of km – hundreds of km – thousands of km – tens of thousands of km. Only a wave nature of such structurization must be considered.

Asteroids of Figs. 6–8 demonstrate geometric forms nearing octahedrons and fine intercrossing lineations reflecting stresses due to the wave formation of the bodies shape and tectonics.

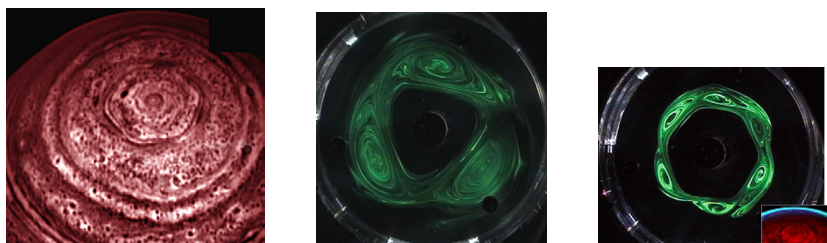


Fig. 1. Saturn, PIA18280, north pole hexagon; **Fig. 2.** A laboratory model producing a triangle image of Fig. 2, but making close to square outlines [14]; **Fig. 3.** The same as Fig. 2, but making close to square outlines [14];

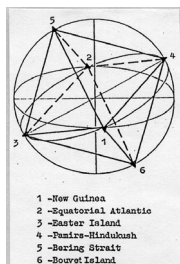


Fig. 4. Earth's octahedron frame;

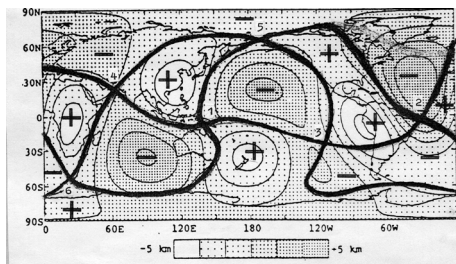


Fig. 5. Octahedron sectors (thick lines) and their inverse reflection in the core-mantle boundary [13];



Fig. 6. Asteroid Bennu, 0.56 km;



Fig. 7. Asteroid Ryugu, 0.92 km;

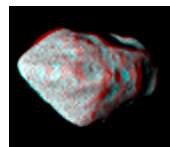


Fig. 8. Asteroid (2867)Steins, 4.6 km;



Fig. 9. Satellite Amalthea, PIA01074, 270×164×150 km;



Fig. 10. Satellite Yanus, PIA06613, 220×190×160 km;



Fig. 11. Satellite Phoebe, PIA06066, 230×220×210 km.

References:

- [1] ESA News. Steins: a diamond in the sky, 6 September, 2008 (<http://www.esa.int/rosetta>);
- [2] Kochemasov G.G. (1999) "Diamond" and "dumb-bells"-like shapes of celestial bodies induced by inertia-gravity waves // 30th Vernadsky-Brown microsymposium on comparative planetology, Abstracts, Moscow, Vernadsky Inst., 49-50;
- [3] Kochemasov G.G. (2006) The wave planetology illustrated – I: dichotomy, sectoring // 44th Vernadsky-Brown microsymposium "Topics in Comparative Planetology", Oct. 9-11, 2006, Moscow, Vernadsky Inst., Abstr. m44_39, CD-ROM;
- [4] Kochemasov G.G. (2008) Plato' polyhedra as shapes of small icy satellites // Geophys. Res. Abstracts, Vol. 10, EGU2008-A-01271, CD-ROM; [5] Porco C.C., Weiss J.W., Thomas P.C. et al (2006) LPSXXXVII, Abstract 2289.pdf;
- [6] NASA News releases-2007-142 Images of Saturn's small moons tell the story of their origin, December 6, 2007;
- [7] Kochemasov G.G. (1992) Concerted wave supergranulation of the solar system bodies // 16th Russian-American microsymposium on planetology, Abstracts, Moscow, Vernadsky Inst. (GEOKHI), 36-37;
- [8] Kochemasov G.G. (1994) 20th Russian-American microsymposium on planetology. Abstr., Moscow, Vernadsky Inst., 46-47;
- [9] Kochemasov G. G. (1998) Proceedings of international symposium on new concepts in global tectonics ('98 TSUKUBA), Tsukuba, Japan, Nov. 1998, 144-147;
- [10] Kochemasov G.G. (1999) Theorems of wave planetary tectonics // Geophys. Res. Abstr., , V.1, №3, p.700; [11] Kochemasov G.G. (2004) Mars and Earth: two dichotomies – one cause // In Workshop on "Hemispheres apart: the origin and modification of the martian crustal dichotomy", LPI Contribution # 1203, Lunar and Planetary Institute, Houston, p. 37;
- [12] Kochemasov G.G. (1999) On convexo-concave shape of small celestial bodies // Asteroids, Comets, Meteors. Cornell Univ., July 26-30, 1999, Abstr. # 24.22;
- [13] Morelli A. and Dzierwonski A.M. 1987. Topography of the core-mantle boundary and lateral homogeneity of the liquid core. // Nature, 1987, v. 325, # 6106, p. 678-683.
- [14] Barbosa A., Read P., Wordworth R., Sattera T., Yamazaki Y. Hiro. (2010) A laboratory model of Saturn's North Polar Hexagon // Icarus, v. 206, #2, p. 755-763;
- [15] Fletcher L.N., Orton G.S., Sinclair J.A. et al. (2018) A hexagon in Saturn's northern stratosphere surrounding the emerging summertime polar vortex // Nature, Nature communications, 03 Sept.2018, article #: 3564 (2018).

LIGHT SCATTERING BY DISCRETE RANDOM MEDIA: PITFALLS IN THE COMPARISON OF MODELS AND EXPERIMENTS

E.V. Petrova¹ and V.P. Tishkovets^{2,3}

¹ *Space Research Institute, Moscow, Russia, epetrova@iki.rssi.ru*

² *Institute of Radioastronomy, Kharkiv, Ukraine, tishkovets@rian.kharkov.ua*

³ *V.N. Karazin Kharkiv National University, Kharkiv, Ukraine*

Keywords:

atmosphereless celestial bodies, polarimetry, radiative transfer, coherent backscattering, shadow hiding, near-field effects

Introduction:

To retrieve the properties of particles composing the surfaces of atmosphereless celestial bodies from remote sensing data is not a trivial task, since a correct light-scattering model for densely packed discrete media is still lacking, which, in turn, is connected with a complicated problem of considering the interaction of scatterers in the near field [1].

At the same time, the model, which considers the scattering medium as composed of clusters located in the far zones of each other, shows a good agreement with laboratory measurements of polarization of non-absorbing loose samples and allows one to obtain some characteristics of the surface of high-albedo celestial bodies from polarimetric measurements [2-4]. For this, the Stokes parameters of the reflected light are calculated as a sum of the diffuse and coherent components obtained from the numerical solution of the radiative-transfer and weak-localization equations, respectively [5, 6]. The consideration of particles in the loose surface material (the regolith) as clusters allows the near-field interaction of scatterers to be partially accounted for.

Model verification:

A further verification of the model by different samples with thoroughly controlled properties faces problems, since such measurements are very rare. Moreover, due to computational reasons, we assume the constituents of clusters composing the medium to be spherical. Consequently, to test the model, we may use only the samples composed of rather small particles (with the size parameter $x = 2\pi r/\lambda < 2$), for which the resonance phenomena are not important, or the samples composed of spheres.

For the above reasons, we paid attention to the measurements of intensity and degree of linear polarization performed with three samples of powdery surfaces consisting of non-absorbing spherical particles 0.5, 1.0, and 1.5 mm across (with a small variance in size) in two spectral bands at 0.44 and 0.63 μm [7]. The comparison of our models with the phase curves measured in [7] has led us to the results we intend to discuss here.

The modeling phase profiles of intensity and polarization were calculated for the media composed of individual monodisperse and polydisperse spherical particles, clusters of identical spherical constituents (up to 200), spherical particles with stuck smaller particles of different number and size, and complex clusters of these spheres with stuck crumbs.

Since our previous analysis showed that the limitation of the present model influences much more the intensity profiles than the polarization ones [4], we will focus here only on comparison of the phase profiles of polarization. For the samples of larger particles ($D = 1$ and 1.5 mm or $x = 7-11$), the measured profiles exhibit resonance features, which are well reproduced in the modeling for the medium composed of individual polydisperse spheres. However, the polarization profiles measured in the sample of smaller particles ($x = 3.57$ and 2.49 for the blue and red spectral range, respectively) show no resonance features at all (though they might also be expected from the theory), and their appearance is close to that of natural high-albedo surfaces containing irregular particles, i.e., at small phase angles, there is an asymmetric negative branch of polarization with a minimum shifted to opposition.

At the same time, the phase profiles calculated for the medium composed of spherical particles with corresponding size parameters show, on the contrary, a noticeable branch of positive polarization in this phase domain. The latter is a result of the mostly negative polarization of light scattered by individual spheres of these sizes, especially at phase angles $<60^\circ$ (e.g., [8] and references therein). The modeling shows that this positive polarization feature can be weakened only by the interaction in large ensembles of such spheres, but the yielded phase curves of polarization still do not resemble the observed one.

We see a cause of the above disagreement in the fact that, according to the note made by the authors of [7], their smallest particles may deviate from spheres in shape. We attempted to model these deviations by considering the scattering by spheres of corresponding sizes with small stuck particles ($x \leq 1.0$) and by clusters of such complex particles. The obtained phase curves of polarization resemble the experimental ones, and their parameters strongly depend on the number and sizes of small stuck particles.

Concluding remarks:

The present analysis shows a high importance of a thorough control of all parameters of the scattering samples in laboratory experiments and an accurate modeling of the properties of scattering particles when testing the models.

The present modeling confirms that exactly the particles with sizes of an order of the wavelength and smaller or the inhomogeneities or irregularities of these sizes in larger particles are responsible for producing the negative branch of polarization of light scattered by many powdery surfaces in nature (regoliths).

References:

- [1] Tishkovets V.P., Petrova E.V., Mishchenko M.I. Scattering of electromagnetic waves by ensembles of particles and discrete random media // *J. Quant. Spectrosc. Rad. Trans.* 2011. V. 112. P. 2095–2127.
- [2] Tishkovets V.P., Petrova E.V. On applicability of the far-field approximation to the analysis of light scattering by particulate media // *J. Quant. Spectrosc. Rad. Trans.* 2016. V. 182. P. 24–34.
- [3] Tishkovets V.P., Petrova E.V. Reflectance model for densely packed media: estimates of the surface properties of the high-albedo satellites of Saturn // *Solar Syst. Res.* 2017. V. 51. P. 277–293
- [4] Petrova E.V., Tishkovets V.P., Nelson R.M., and Boryta M.D. Prospects for estimating the properties of a loose surface from the phase profiles of polarization and intensity of the scattered light // *Sol. Syst. Res.* 2019. Vol. 53. P. 172–180.
- [5] Mishchenko M.I., Dlugach J.M., Chowdhary J., Zakharova N.T. Polarized bidirectional reflectance of optically thick sparse particulate layers: an efficient numerically exact radiative-transfer solution // *J. Quant. Spectrosc. Rad. Trans.* 2015. V. 156. P. 97–108.
- [6] Tishkovets V.P., Mishchenko M.I. Approximate calculation of coherent backscattering for semi-infinite discrete random media // *J. Quant. Spectrosc. Rad. Trans.* 2009. V. 110. P. 139–145.
- [7] Bondarenko S., Ovcharenko A., Shkuratov Yu., Videen G., Eversole J., and Hart M. Light backscatter by surfaces composed of small spherical particles // *Applied Optics.* 2006. V. 45. P. 3871–3877.
- [8] Petrova E.V. and Tishkovets V.P. Light scattering by morphologically complex objects and opposition effects (a review) // *Sol. Syst. Res.* 2011. Vol. 45. P. 304–322.

INVESTIGATION OF THE ATMOSPHERELESS BODIES DUST DYNAMICS: EXPERIMENTAL SET-UP

I.A. Kuznetsov¹, A.V. Zakharov¹, A.N. Lyash¹, I.A. Shashkova¹,
G.G. Dolnikov¹, A.Yu. Poroikov²

¹ Space Research Institute of the RAS, Moscow, Russia, email: kia@iki.rssi.ru;

² National Research University "Moscow Power Engineering Institute",
Moscow, Russia

Keywords:

Dusty plasma, dust, dust dynamics, atmosphereless body, Moon, Experimental set-up

Introduction:

One of the complicating factors of the future robotic and human lunar landing missions is the influence of the dust. Meteorites bombardment has accompanied by shock-explosive phenomena, disintegration and mix of the lunar soil in depth and on area simultaneously. Therefore, the lunar soil has undergone melting, physical and chemical transformations.

Studying the properties of lunar dust is important both for scientific purposes to investigation the lunar exosphere component and for the technical safety of lunar robotic and manned missions.

The absence of an atmosphere on the Moon's surface is leading to greater compaction and sintering. Properties of regolith and dust particles (density, temperature, composition, etc.) as well as near-surface lunar exosphere depend on solar activity, lunar local time and position of the Moon relative to the Earth's magneto tail. Upper layers of regolith are an insulator, which is charging as a result of solar UV radiation and the constant bombardment of charged particles, creates a charge distribution on the surface of the moon: positive on the illuminated side and negative on the night side. Charge distribution depends on the local lunar time, latitude and the electrical properties of the regolith (the presence of water in the regolith can influence the local distribution of charge).

On the day side of Moon near surface layer there exists possibility formation dusty plasma system. Altitude of levitation is depending from size of dust particle and Moon latitude. The distribution dust particle by size and altitude has estimated with considering photoelectrons, electrons and ions of solar wind, solar emission.

Moreover, most of these processes take place on most body in the space without the atmosphere.

Experimental investigation of the dust dynamics near the atmosphereless bodies are quite challenging. Experimental set-up should include the sources of electrons, UV, ions (solar interaction), special materials. It also should be accurate registration system.

This work explains the steps for development the atmosphereless bodies conditions simulation in the experimental set-up, used registration system and results.

Acknowledgements:

This work was supported by the Russian Scientific Foundation (the grant № 17-12-01458).

WAVE EFFECTS IN DUSTY PLASMAS IN MARTIAN ATMOSPHERE

Y.N. Izvekova^{1,2}, S.I. Popel^{1,2}

¹ *Space Research Institute, Russian Academy of Sciences, ul. Profsoyuznaya 84/32, Moscow, 117997 Russia;*

² *Moscow Institute of Physics and Technology, 9 Institutskiy Pereulok, Dolgoprudnii, 141700 Russia*

Keywords:

Dust particles, plasma, Martian ionosphere, solar wind, high-frequency waves.

Introduction:

According to the missions of Viking and Pathfinder in the atmosphere of Mars particles with sizes in the range of 0.1–10.0 μm are constantly suspended. Also dust vortices raises particles up to 100 μm in size. Chemical composition of dust particles is dominated by SiO_2 (43.4 - 48.6%), Fe_2O_3 (17.5-18.2%), Al_2O_3 (7.8-8.3%) and MgO (6.0-7.5%). The mineralogical composition contains products of weathering of volcanic rocks origin, iron-bearing clay minerals, hematites (nanophase), etc.

The charge of dust particles depends on the size of dust particles, densities and temperatures of charged particles (ions, electrons and dust particles) and neutrals and so on. During the daytime the solar radiation spectrum and the work function of the substance of particles play an important role.

In the lower atmosphere effective charging occurs in dust vortices. Dust particles intensively collide with each other so the main mechanism for charging is triboeffect. The magnitude of the charge acquired can significantly exceed the charges acquired by dust particles as a result of the currents of electrons and ions.

Since Mars does not have a global magnetic field, the penetration of the solar wind into the ionosphere takes place. The presence of local magnetic fields leads to significant inhomogeneities in the Martian ionosphere. On the night side of the ionosphere there are areas of a sharp increase in the electron concentrations in areas where the magnetic field lines are perpendicular to the surface of the planet. In areas where the magnetic field is parallel to the surface the electrons of the solar wind do not penetrate the atmosphere and there are areas without ionization. Interaction of the plasma of the solar wind with a plasma containing dust particles can lead to the generation of high-frequency waves.

Waves associated with the presence of dust in a plasma system are considered. In the presence of plasma systems moving relative to each other plasma instabilities may arise leading to the generation of new types of waves.

Acknowledgements:

The work is supported by the Russian Science Foundation (project No 18-72-00119).

DUST IMPACT MASS-SPECTROMETER «METEOR-LD»

A.I. Demyanov¹, V.V. Vysochkin²

¹ *Institute for Geochemistry and Analytical Chemistry (GEOKHI) RAS 119991 Moscow, Kosygina 19, Russia, demyanovalexey@mail.ru;*

² *Institute for Geochemistry and Analytical Chemistry (GEOKHI) RAS 119991 Moscow, Kosygina 19, Russia, vvisochkin@mail.ru*

Keywords:

Cosmic dust, meteor, the Moon.

Assignment and application area

The Dust Impact Mass-Spectrometer METEOR-LD is designed to determine the chemical composition encountered of meteor particles, as well as to determine the spatial density of meteor particles along the Earth-Moon flight path and near the moon.

The purposes of the METEOR-LD device to determine:

- 1) Speed;
- 2) Mass;
- 3) Chemical composition;
- 4) Trajectories of cosmic dust (orbital characteristics).

Device design

The GEOKHI RAS in collaboration with the MEPhI has developed time-of-flight The Dust Impact Mass-Spectrometer with a target area ~ 300 (Fig. 1). The Dust Impact Mass-Spectrometer is developed on the basis of the Space Dust Detector METEOR-L (GEOKHI RAS) for the lunar orbital spacecraft Luna-Resurs-1 (Luna-26).



Fig. 1. General view of the Dust Impact Mass-Spectrometer METEOR-LD



Fig. 2. Photo of a model of the device (target-barrier removed)

A working model of the device was made and tested on the Particle Accelerator were carried out with a positive result (Fig. 2). METEOR-LD made as single block. On the top of the device there is a target-barrier that particles hit

and time-of-flight mass-spectrometer that allows to determine the chemical composition of the stuck particles. At the bottom of the device there is an electronics unit that ensures the operation of the device.

The operational principle of the apparatus

A single-mesh mass-reflectron [1] with a plane of symmetry perpendicular to the drawing plane through the axis of symmetry of the detector is selected as an ion-optical scheme of the analyzer. High-speed particles P collide with the target T in the form of "blinds", and the resulting ions are "pushed" by the field of the electron lens EL and "stretched" by the potential difference between the target and the deflecting plates DP. To ensure the collection of ions formed at different points of the target a small potential difference, depending on they coordinate, is additionally applied between adjacent plates. The working area of the target is $\sim 300 \text{ cm}^2$.

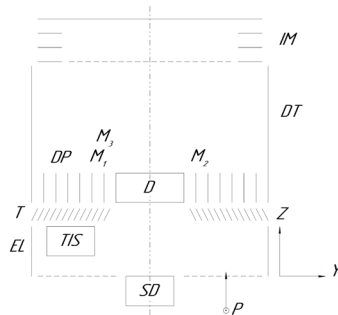


Fig. 3. Ion-optical scheme of the analyzer. T-target, DP deflecting plates, DT-no-field drift space, IM-single-grid ion mirror, D-detector, SD - starting detector, TIS-test ion source, P-analyzed microparticle, EL-electron lens, , , -ion packages with different values $M=m/e$.

The electrons formed at the moment of impact of the microparticle on the target are focused by an electronic lens and accelerated to the starting SD detector, which is necessary for the formation of the starting pulse for the launch of a multi-channel amplitude-time analyzer. The delay and time spread of receipt on the detector does not exceed 1-2 ns. A secondary electron multiplier SEM-7 was used as a starting detector.

The ion package formed at impact is divided by the time of flight in accordance with the mass-to-charge ratio of the ions (m/e), and after reflection in the ion mirror IM ion packages with different m/e (in Fig. 3) are collected on the detector D. A double herringbone assembly of rectangular microchannel plates with an effective detection area of 48 was used as a detector [2].

The technical characteristics are given in the table 1.

Table 1.

Dimensions of the device, mm	$\varnothing 252 \times 380$
Instrument mass, kg	4.5
Supply voltage, V	27
Power consumption, W	Not more than 12
The speed of the detected particles, km/s	3-35
The mass of the detected particles, g	

References:

- [1] Mamyryn B.A., Karataev V.P., Shmikk D.V., Zagulin V.A. The mass-reflectron, a new nonmagnetic time-of-flight mass spectrometer with high resolution // JETP. 1973. V. 64. No. 1. P. 82.
- [2] Sysoev A.A., Surkov Yu.A., Bandura D.R. et. al. A transit-time analyzer for determining the elemental composition of space dust particles// Instr. Exp. Techn. 1993. No. 4. P. 126 [in Russian].

AN EXPERIMENT AND DATA PROCESSING TECHNIQUE AIMED AT DETERMINING THE RADIAL SPEED OF SOLAR WIND INHOMOGENEITIES OF VARIOUS SPATIAL SCALES

S.F. Kolomiets, A.L. Gavrik, L.A. Lukanina, T.F. Kopnina

Fryazino branch of Kotel'nikov Institute of Radio-engineering and Electronics of Russian Academy of Sciences. acad. Vvedensky sq.1, Fryazino, Russian Federation;

Keywords:

occultation of the solar wind, coherent radio-source and spaced antennas, velocity measurement, dynamic structure of solar wind flows, filtering in a frequency domain.

Introduction:

The usage of spaced antennas suggests a more or less quantitative approach to the estimation of the speed of solar wind medium. However in the past, the group delay time (GDT) and the known distance between the beams were mainly used to determine the speed [1]. Fluctuations of the flow velocity in time domain, determined within such an approach, allow a qualitative assessment of the turbulent flow regime [1, 2]. The extensive experimental material processed with techniques based on the measurement of GDT indicates that a uniform and isotropic regime of solar wind turbulence is confirmed at distances of more than 15–20 solar radii [3] only. However, the capabilities of data processing and interpretation techniques developed based on the GDT are not enough to study of the reasons for deviations of the turbulent regime (from Kolmogorov's regime expected) at a close distance to the Sun, as they take the flow as a whole averaging all estimates over it. Therefore improvement of the technique itself is crucially required in order to make a finer analysis of the solar wind flows within the region in question.

A Novel Data Processing and Interpretation Technique:

The geometry of the occultation experiments with the coherent radio source mounted on a spacecraft orbiting the Sun determines the functional relationship between the frequency of fluctuations and the spatial scale of the inhomogeneities. Thus, the idea of a simplest analysis of a flow dynamic structure could consist in calculating the GDT in different frequency intervals after filtering of fluctuations in a frequency domain. A description of consistent approach to the interpretation of such estimates in the literature was not found. So in order to formulate and test the original way of interpreting such data, a series of numerical experiments and intensive theoretical studies were carried out. The former made it possible to establish the empirical rules of estimates formation, while the latter made it possible to explain it theoretically. Theoretical justification of the technique suggested was proposed using the dependences published in [4], and further developed both in works on measuring the velocity of ionospheric and tropospheric scattering inhomogeneities [5, 6]. Corresponding dependencies have never been considered in relation to signals after filtering in frequency domain.

An Experimental Test of The Technique Suggested

Application of the proposed methodology for estimating the velocity of a medium to real experimental data obtained near the Sun allows one to detect quite reliably a two-speed flow regime (when and if it exists) even while it is not detected by conventional methods developed based on GDT [7]. Accordingly, in a single-speed representation, such flows cannot be a source of homogeneous isotropic turbulence and must be excluded from consideration in turbulence of the solar wind studies.

Conclusion

A novel data processing and interpretation technique were suggested, theoretically justified and experimentally tested both on numerical models and

real experimental data. An analysis of scattering properties of the solar wind flow taken into the experimental test of the technique as well as the analysis of the fine structure of the flow in different parts of the frequency spectrum (coupled with the data of optical instruments), suggest that the conclusion about the existence of the inhomogeneous and anisotropic turbulence near the Sun can be formed when the streamer is crossed by radio sounding rays. Using the techniques suggested the dynamic processes in the latter can be studied separately from the "background" solar wind.

References:

- [1] Efimov A.I., et al. // Solar Physics, 2015. V. 290. P. 2397
- [2] Chashei I.V., et al. // Astron. & Astrophys. Transactions, 2007. V. 26. P. 611
- [3] Yakovlev O. I. and Pisanko Y. V. // Adv. Space Res., 2017. V. 61, P. 552
- [4] Briggs, B. H. et al. // Proc. of the Physical Soc. Section B, 1950. V. 63. P. 106.
- [5] Costa E. et al. // Radio Sci., 1988. V. 23, P. 141.
- [6] Doviak R. J. et al. // Radio Sci., V. 31, P. 157.
- [7] Chashei I.V., et al. // Adv. Space Res., 2005. V. 35. P. 2195

METHODS OF DETECTION OF FAILURES IN PHASE DATA OF GNSS AND THEIR INFLUENCE ON VALUE OF MEASUREMENTS OF THE TOTAL ELECTRON CONTENT.

G.G. Minasyan¹, I. A. Nesterov², Ya.A. Ilyushin³

¹ 119991 Moscow, GSP-1, Leninskie Gory, Lomonosov Moscow State University, bldg. 1, str.2 Faculty of Physics, minasyangg.msu@yandex.ru.

² 119991 Moscow, GSP-1, Leninskie Gory, Lomonosov Moscow State University, bldg. 1, str.2 Faculty of Physics, nia2002@yandex.ru.

³ 119991 Moscow, GSP-1, Leninskie Gory, Lomonosov Moscow State University, bldg. 1, str.2 Faculty of Physics, ilyushin@physics.msu.ru.

Keywords:

total electron content, TECU, GNSS, radio wave, propagation, sounding of the ionosphere.

Based on the analysis of the phase data of the global navigation satellite system, distributions of time derivatives of the $\$ L_1 \$$ phase frequency and the total electronic content are obtained. The change in the distributions of observed statistics of time derivatives of the total electron content was analyzed, because there are phase failures of signals of navigation satellites. According to the analysis of the statistics of the phase of signals, an assumption about the physical and technical reasons for phase failures was made. The correlation between time derivatives of the phase signals and the total electron content has been obtained, despite the apparent dependence of the latter on the phase of the signal. This ratio showed that neither direct nor inverse dependence of the change in the distribution of time derivatives in both of quantities was found.

Introduction:

The distance between the GPS satellite and the receiver can be estimated by calculating the pseudorange. To determine the pseudorange or the carrier phase of the radio wave on the GPS satellite – receiver path, the propagation time of the encoded signal should be measured [1]. VHF can produce three pseudo-range code measurements: C/A-code at frequency f_1 (denoted by C_1), P-code at frequency f_1 (denoted by P_1) and P-code at frequency f_2 (denoted by P_2) [2]. The key to the accuracy of the system is the fact that all signal components are precisely controlled by atomic clocks. These highly accurate frequency standards of GPS satellites produce the fundamental frequency of 10.23 MHz. Coherently derived from this frequency are (presently) two signals in the L-band, the f_1 and the f_2 carrier waves generated by multiplying the fundamental frequency by 154 and 120, respectively, yielding $f_1=1575.42$ MHz and $f_2=1227.60$ MHz [3]. Phase measurements of pseudo-range are calculated with formula: $D'f = \lambda\Delta\phi + \lambda N$, where $\lambda=c/f$; $\Delta\phi$ — measured by the receiver phase difference between the radio wave carrier received from the satellite and the signal of the same frequency generated in the receiver itself. Measured phase pseudo-ranges in radio wavelengths $D'f/\lambda$ at frequencies f_1 and f_2 are denoted as L_1 and L_2 respectively. Full pseudo-ranges along the phase trajectories for the frequencies f_1 and f_1 can be written as (1):

$$L_1\lambda_1 = D - \frac{c_4}{f_1^2}l + \Delta L_0 + \sigma_{L_1}, \quad L_2\lambda_2 = D - \frac{c_4}{f_2^2}l + \Delta L_0 + \sigma_{L_2}, \quad (1)$$

D — is the true distance between the receiver and the satellite, ΔL_0 — is the effective path lengthening due to the influence of the troposphere, clock mismatch, phase ambiguity of measurements, etc., $\sigma_{L_1,2}$ - random measurement errors [4]. The value of the total electronic content (TEC) along the beam of the GPS satellite receiver is determined by phase measurements at two frequencies with the formula (2) [5].

$$l = \frac{1}{40.308} \frac{f_1^2 f_2^2}{f_1^2 - f_2^2} [(L_1 \lambda_1 - L_2 \lambda_2) + \text{const}_{1,2} + \sigma_L], \quad (2)$$

where L_1, L_2 are the pseudo-ranges measured by the phase method in radio wavelengths; $\text{const}_{1,2}$ - ambiguity of phase measurements; σ_{L_i} - phase measurement error. The generally accepted unit of measurement for TEC is the TECU (Total Electron Content Unit), a unit of measurement of the total electronic content, equal to 10^{16} .

Objective:

The data from GPS satellites can contain gaps, noise, and various faults that are of a technical nature. In order to use them, pre-processing is necessary. First, because the data is used in TEC calculations. Secondly, the study of failures themselves, their connection with various factors is a separate topic for research considered in this paper.

Experimental Technique:

At the phase data obtained after preprocessing of files in the RINEX [6] format there are different noises, gaps and failures for a number of reasons: technical fault of satellites or stations, external impact on forming of a signal. We know that a signal are fixed by the station depending on different parameters of settings, with different temporary frequencies: 15, 30, 60 and 120 seconds. Thus, all data were grouped in continuous fragments of records of a phase for each satellite with a frequency of reception of $15(\Delta_{15})$ and $30(\Delta_{30})$ seconds.

Statistic Analysis:

Using dual frequency data the first and the second time derivatives were calculated for values and the TEC on two time intervals Δ_{15} and (Δ_{30}) . The statistics of the data from 01.01.2015 (day 1) to 31.12.2015 (day 365) were constructed for all measurements at more than 2000 stations and 32 satellites in one day. For a more detailed study of the behavior of the distribution of the L_i and TEC derivatives, histograms were constructed on several analytically significant ranges obtained in the course of calculations.

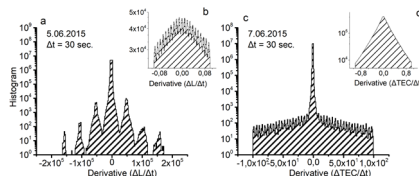


Fig. 1. The distribution of the values of the time derivative of the phase signal (left) and TEC (right) on different ranges.

The values of which correspond to the geometry of the satellite's motion relative to the station in the central part are noticeable (Fig. 1b). Since it is known that is the phase path of a radio signal, the satellite speed is a real value, which should vary in a narrow range of values, of the order of 4×10^3 . A parabola can approximate the central part. Increasing range construction by several orders, we note the appearance of a multimode structure (Fig.1a). Comparing values of derivatives forming this structure with formula (1), we understand that the derivative with respect to the phase path of the radio signal should not increase or decrease dramatically in a relatively short time $\Delta t = 30$, since the satellite's motion relative to the station is uniform, and there can be no abrupt change in the phase path. Consider these values from a physical point of view: suppose that a sharp change caused a rapid increase or decrease in TEC along a satellite-station beam, which should affect the phase derivative without sharp jumps, evenly. There are histograms of the distribution of the TEC derivative for 07.06.2015 ($K_p = 0.3$) at various intervals (right side of the Fig.1). There are values corresponding to the physical nature of emergence in the central part(hump) (Fig. 1d). The hump is approximated by gaussoidy and power functions with various coefficients. Increasing an interval to one order there are distribution tails which are approximated by power functions. At increase in an interval of distribution to two orders, we observe the following picture (Fig. 1c). Increasing an interval of distribution, promoted emergence of multi-

mode structure of the distribution of tails similar to structure of the distribution for derivative $\frac{\Delta L}{\Delta t}$. Thus, it is possible to make a conclusion that TEC values are formed by various mechanisms of both the physical and technical nature.

Dale of Faulty Data:

Dale of faulty data failures and ruptures of data can happen not only because of technical malfunction of a system satellite-receiver, but also because of various external factors. For a research of this assumption, we set restrictions derivant on L_1 and TEC, which were set above. Quantity of values, which didn't get into the specified interval on each station was calculated. The relationship of faulty values to total is expressed in percentage ratio (Fig.2).

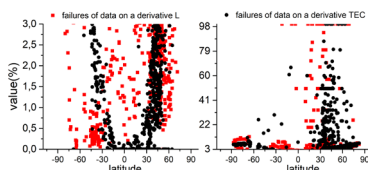


Fig.2. Statistics of a share of faulty data on stations at $0\% < P_{fail} < 3\%$ (left side) $3\% < P_{fail} < 100\%$ (right side) at 10.06.2015.

Conclusion:

The conclusions based on this part of the work are as follows:

- The distribution of L_1 and L_2 has a complex multimode character.
- The distribution of the TEC in general is smooth, but depending on the histogram interval, the resulting asymptotic distribution with large deviations from the mean is approximated by various power functions.
- The reasons for the appearance of large values in the phase data themselves do not lead to failure of the values of $\Delta TEC/\Delta t$. Thus, failures are caused by a set of different mechanisms.

References:

- [1] N.M.Gavrilov, Measurement of the characteristics of the atmosphere by the method of ground radio navigation satellite systems, St. Petersburg(Russia): University Research and Education Center "Modeling and Monitoring of Geospheres," 2007, pp.30-32 (in Russian).
- [2] Bernhard Hofmann-Wellenhof, Herbert Lichtenegger, Elmar Wasle. GNSS – Global Navigation Satellite Systems GPS, GLONASS, Galileo, and more, Austria: Institut für Navigation und Satellitengeodäsie Technische Universität Graz, 2008, p332.
- [3] Bernhard Hofmann-Wellenhof, Helmut Moritz. Physical Geodesy, Austria: Institut für Navigation und Satellitengeodäsie Technische Universität Graz, 2005, p.179.
- [4] I.D. Kozin, Satellite radio navigation systems, Almaty(Kazakhstan): KazATK, 2006, p.75 (in Russian).
- [5] Bernhard Hofmann-Wellenhof, Helmut Moritz. Physical Geodesy, Austria: Institut für Navigation und Satellitengeodäsie Technische Universität Graz, 2005, p.179.
- [5] I.K.Yasyukevich, The response of the ionosphere to solar and geophysical disturbing factors according to GPS, monograph. Irkutsk(Russia): ISU Publishing House, 2013, p.259 (in Russian).
- [6] Satellite data obtained from reception stations — 2018. [Online]. Available: <ftp://garner.ucsd.edu/pub/rinex>

OBSERVED RESPONSE OF EARTH'S LITHOSPHERE TO SOLAR WIND AND RADIATION BELT VARIATIONS

G.Ya. Khachikyan

Institute of Ionosphere, 050020, Almaty, Kazakhstan

Keywords:

Radiation belt, geomagnetic storm, electron bursts, earthquakes.

Introduction:

It is known for many years [1,2, and references in herein] that strong earthquakes may be preceded by electron bursts from the Earth's radiation belt along geomagnetic field lines penetrated in the future epicenters. It is reported, usually, that a time lag between electron bursts and earthquake occurrence consists of some hours or days. Present report shows that a time lag may reach up to 2 months between relativistic electrons precipitation from outer zone of radiation belt into the slot or inner zone due to strong geomagnetic storm with creating a new electron belt, and occurrence of strong earthquake near the footprint of geomagnetic field lines belonging to a new electron belt.

Results:

More than 25 years ago, the satellite "CRESS" and station "MIR" detected a new ring of relativistic electrons in the radiation belt after a strong geomagnetic storm on March 24, 1991 [3]. In that case, a belt of relativistic electrons has been formed around of geomagnetic line $L \sim 2.6$, and existed about of two years [3]. An analysis of seismic data for 1991 year, using the USGS global seismological catalog, shows that about of 2 months later, on May 30, 1991 a strong ($M=7.0$) earthquake occurred near the footprint of $L=2.69$ belonging to a new electron belt (coordinates of earthquake epicenter 54.57°N , 161.61°E). Another case, it was revealed in [4] that after geomagnetic storm on September 3, 2012, the Van Allen Probe satellites registered a new ring of relativistic electrons around of geomagnetic lines $L=3.0-3.5$. Data of global seismological catalog again show that almost 2 months later, on October 28, 2012 a strong ($M=7.8$) earthquake occurred near the footprint of $L=3.32$ belonging to a new electron belt (coordinates of epicenter 52.79°N , 132.1°W). In Figure 1, monthly amount of earthquakes with magnitude $M \geq 4.5$ which occurred in 1991 year near the footprint of $L = 2.5 - 2.7$ (left) and in 2012 year near the footprint of $L = 3.0 - 3.5$ (right) are presented. The results in Figure 1 prove that ~ 2 months after the both geomagnetic storms on March 24, 1991 and September 3, 2012, seismic activity was noticeably increased in regions penetrated by geomagnetic lines of new belts of relativistic electrons.

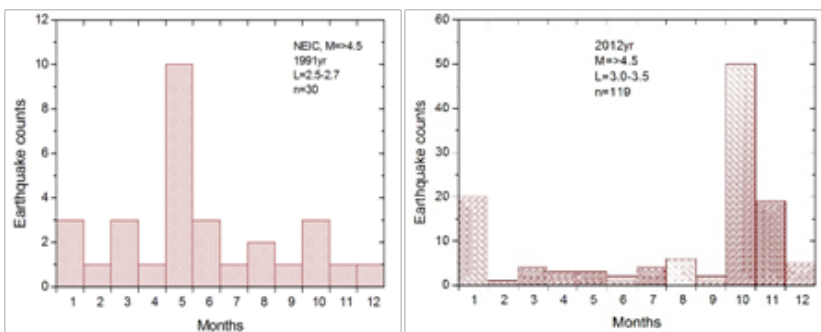


Fig. 1. Monthly amount of earthquakes with $M \geq 4.5$ occurred near the footprint of $L=2.5-2.7$ in 1991 year (left) and near the footprint of $L=3.0-3.5$ in 2012 year (right).

After strong geomagnetic storm on June 23, 2015, a new ring of relativistic electrons ($E=1.6$ MeV) appeared around geomagnetic lines $L=1.5-1.8$ and was persisted during ~ 11 months [5]. Figure 2, adapted from [5, their Fig. 6] demon-

strates this phenomenon, as was measured by the Magnetic Electron and Ion Spectrometer (MagEIS) instrument on the satellites Van Allen Probes. An analysis of earthquakes with magnitude $M \geq 4.5$ occurred in 2015-2016 years near the footprints of $L=1.5-1.8$ showed (Figure 3) that seismic activity in the footprint of these magnetic lines was sharply increased in September 2015, that again is about of 2 months after geomagnetic storm on 23 June, 2015 and relativistic electron bursts from the outer zone of radiation belt into the inner zone.

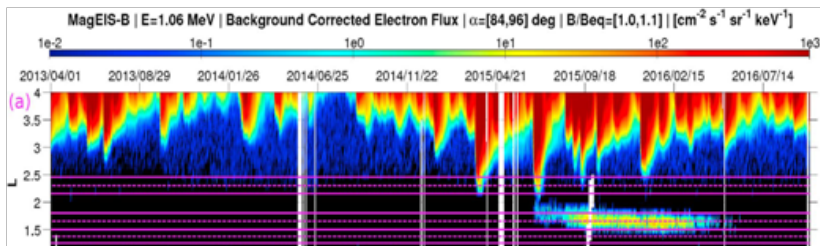


Fig. 2. MagEIS-B daily-averaged electron fluxes ($E=1.06$ MeV) from April 2013 to September 2016 plotted in L -versus-time format; a new ring of relativistic electrons appeared in inner radiation belt at $L=1.5-1.8$ after geomagnetic storm on June 23, 2015 [adapted from 5, their Figure 6].

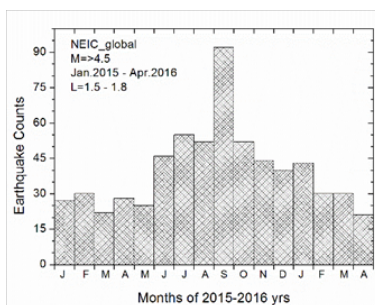


Fig. 3. Monthly amount of earthquakes with $M \geq 4.5$ occurred near the footprint of $L = 1.5 - 1.8$ from January 2015 to April 2016.

Conclusion:

The new results on increasing of seismic activity in the footprints of geomagnetic field lines belonging to the new belts of relativistic electrons created in the slot or inner zone of the radiation belt due to strong geomagnetic storms, may be useful for understanding physical mechanism of solar-terrestrial (including solar-lithosphere) relationships.

References:

- [1] Aleksandrin S. Yu., Galper A. M., Grishantzeva L. A., Koldashov S. V., Maslennikov L. V., Murashov A. M., Picozza P., Sgrigna V., and Voronov S. A. High-energy charged-particle bursts in the near-Earth space as earthquake precursors // *Ann. of Geophys. 2003*. V. 21. P. 597-602.
- [2] Anagnostopoulos, G. C., Vassiliadis, and Pulinet, S. Characteristics of flux-time profiles, temporal evolution, and spatial distribution of radiation-belt electron precipitation bursts in the upper ionosphere before great and giant earthquakes // *Ann. of Geophysics*. 2012. V. 55. doi:10.4401/ag-5365.
- [3] Galper M.A. Earth radiation belt // *Soros Educational Journal*. 1999. No. 6. www.eduhmao.ru/var/db/files/3456.9906_075.pdf
- [4] Thorne R.M., Li W., Ni B., Ma Q., Bortnik J., Baker D.N., Spence H.E., Reeves G.D., Henderson M.G., Kletzing C.A., Kurth W.S., Hospodarsky G.B., Turner D., and Angelopoulos V. Evolution and slow decay of an unusual narrow ring of relativistic electrons near $L \sim 3.2$ following the September 2012 magnetic storm // *Geophysical Research Letters*. 2013. V. 40. P. 3507-3511. doi:10.1002/grl.50627.
- [5] Claudepierre S. G., Reeves G. D., O'Brien T. P., Fennell J. F., Clemmons J. H., Looper M. D., Mazur J. E., Roeder J. L., Turner D. L. The hidden dynamics of relativistic electrons (0.7-1.5 MeV) in the inner zone and slot region // *Journal Geophys. Res. Space Physics*. 2017. V. 122. doi:10.1002/2016JA023719.

FEATURES OF THE SUN'S INFLUENCE ON THE EARTH LITHOSPHERE IN PERIODS OF MINIMAL ACTIVITY

N.P. Bulatova

Schmidt Institute of Physics of the Earth of Russian Academy of Sciences, Moscow, n.p.bulatova@mail.ru

Keywords:

sun, earthquakes, solar activity minima; 21-23 cycles.

Introduction:

The author made an attempt to statistically separate the time series of seismic events ($N > 500$) from 1973 to 2005 into sets related to the influence of individual groups of factors having different physical nature. The seismicity of the Earth is simultaneously influenced by both external cosmic influences: (tidal gravity, solar activity) and internal geological circumstances (the state of earthquake zones). Some scientists believe that the higher the solar activity (SA), the greater a probability of occurrence of seismic events, tsunamis, volcanic eruptions, etc. on Earth [3]. In this connection the surprising result was obtained by the author in 2004 [1]. So, the method of visualization of the statistical processing outcomes revealed the anticorrelation of the maxima of strong earthquakes with the minima of solar activity (SA) – W_{\min} (where W is Wolfe numbers) for 21-23 cycles. Preliminary result of this phenomenon study was presented in author's work [1,2,4,5].

Multifactor analysis of the phenomenon:

Changes in the planet Earth occurs as a result of the external energy sources impact on it in the near-earth space. As a result, areas of the lithosphere can be activated in the earth's shells and to be in a state of unstable equilibrium that can lead to an increase of seismic activity and an occurrence of earthquakes [2]. Traditionally, the Sun and the Moon were considered as sources of energy for such activation. Of course, it is also necessary to take into account the state of geological environment. It is known that strong earthquakes ($M \geq 7$) often occur as a result of tectonic or volcanoes movements of the earth's crust. For example, in subduction zones lithospheric plates can collide and crawl on each other. as a result of the movement of lithosphere blocks. Such movements require large amounts of energy.

Perhaps that is why strong earthquakes often occur in the phases of SA minima, when this energy is accumulated during a long time, so that when the required level of energy supply is reached, it appears in a seismic event.

During periods of SA maximum, it can be spent on less energy-intensive events with $M < 6$.

Of course, to the explanation of this phenomenon requires efforts of specialists of different Sciences: geologists, physicists, astrophysicists, etc. since the solution to this problem lies in the interdisciplinary field. Here we present the obtained result (Fig. 1), while without explanation of reasons for this phenomenon.

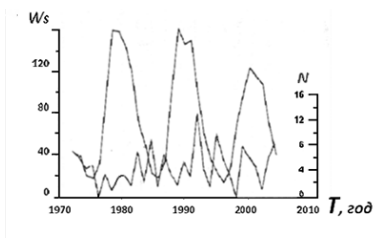


Fig. 1. The distribution of amounts of strong earthquakes $M \geq 7.0$ (N) for time T , where $T = 1973 - 2005$ y., demonstrating the attraction of N_{\max} to the periods of SA minima in 21-23 cycles (where W is Wolfe numbers), obtained by the visualization method.

This result was obtained by step-by-step allocation of time series trends in the range 1973-2005, [5].

These series obtained from databases (NE ISE [6]) were presented as sums of groups of time series of earthquakes (each with its own trend) associated with different generating sources: internal – geological circumstances , and external –astrophysical influences.

The last group of earthquakes N was compared with the solar activity having index W (Fig. 1).

Conclusion:

For the energy class of earthquakes $M \geq 7$, the anticorrelation of N_{\max} (seismic) and W_{\min} solar activity during 1973-2005 was obtained. The maxima time series of earthquakes N_{\max} have a attraction to the phases of minima – W_{\min} of solar activity.

References:

- [1] Bulatova N.P.: Spatial–temporal analysis of the Earth’s seismicity (in Russian). Ph.D. Moscow. IPhE (2004), 120 p.
- [2] Bulatova N. P. On the relationship of strong earthquakes ($M \geq 7$) with relative position of the Sun and the Moon (on the earthquake of December 26, 2004) // Geophysics of the XXI century: 2006. Proceedings of the Eighth geophysical readings named after V. V. Fedynsky. 2007. P. 279-285.
- [3] Sytinsky A.D.. On earthquakes and solar activity bond. *Physic of the Earth*. № 3. 110–112.(1991). Sytinsky A.D. On influence solar activity to seismicity of the Earth/ DAN SSSR. 208. №5 P.1078–1081 (1973).
- [4] Bulatova N.P. The latitudinal distribution of terrestrial seismicity in relation to the locations of the Sun and Moon. *Vulcanology and Seismology*, 2, P.57–78 (2005).
- [5] Bulatova N.P. The global multi factor model of seismic activity: priorities // Interdisciplinary Symposium on Complex Systems (ISCS 2013). Springer. Berlin. 2013. P.237-244.
- [6] Global Hypocenters Data Base, National Earthquake Information Center, U.S. Geological Survey, Denver, 1973–to present.

COMPLEX OF LOW-WEIGHT MINIATURE INSTRUMENTS FOR SPACE WEATHER MONITORING

A.Yu. Shestakov¹, S.D. Shuvalov¹, I.V. Zimovets¹, D.A. Moiseenko¹, O.L. Vaisberg¹, R.N. Zhuravlev¹, A.A. Nozik^{2,3}, E.M. Stadnichuk³, M.E. Zelenyi³

¹ *Space Research Institute of the Russian Academy of Sciences (IKI), 84/32 Profsoyuznaya Str, Moscow, Russia, 117997, sartiom1@yandex.ru;*

² *Institute for Nuclear Research of the Russian Academy of Sciences, 27 Fizicheskaya Str, Troits, Moscow, Russia, 108840*

³ *Moscow Institute of Physics and Technology (State University), 9 Institutskiy per., Dolgoprudny, Moscow Region, Russia, 141701*

Keywords:

Solar wind, space plasma, solar cosmic rays, space weather, ion spectrometer, electron analyzer, energetic particle telescope.

Introduction:

Our project is aimed at creating a prototype of a complex (set) of small-size light-weight scientific and measuring equipment for the diagnostics of corpuscular radiation of the Sun and the space environment necessary for monitoring and predicting the effects of space weather. This equipment complex will include a basic set of instruments for the diagnostics of solar corpuscular radiation: (1) a solar wind ion analyser (0.5–10 keV); (2) a solar wind electron analyser (30 eV–10 keV); (3) a telescope of solar energetic particles (electrons with energies of ~1–10 MeV, ions ~10–100 MeV/nucleon). We pay special attention to optimization of the instruments in terms of mass-dimensional characteristics, sensitivity, reliability, universality, the possibility of rapid modification. We believe that this set of equipment can later become a basic set for larger complexes of monitoring solar corpuscular and electromagnetic radiation, being developed in Russia. In recent decades, Russia has lost leading positions in this area, since, in practice, it almost did not launch spacecraft beyond the Earth's magnetosphere. The development of the proposed set of equipment should partially fill this gap of space instrumentation making, lay the foundation for the release of scientific and technical products, which in future could compete with analogues in the domestic and international markets. With a small modification, the equipment can also be used on spacecraft with orbits inside the magnetosphere (for diagnostics of plasma and energetic particles), with interplanetary orbits, at extraterrestrial bases (on the Moon, Mars, etc.).

We are presenting results of the second year of our project:

1. During the second year we have manufactured and successfully verified operational status of the PICA ion analyzer prototype. During preliminary tests we checked the detector performance and estimated electrostatic analyzer $\Delta E/E$ energy resolution, which was 10% that corresponds to model parameters.
2. The prototype of the ECOS electronic analyzer has been manufactured and passed the preliminary operability tests. During these tests we checked the operation of the position-sensitive detector and determined its spatial resolution. Spatial resolution of detector was estimated as 11 lines, which will allow to achieve the required analytical characteristics of the instrument.
3. The prototype of the proton part of the telescope of solar energetic particles (PPP-TSEP) has been manufactured. We tested several options for the geometry of the groove for attaching the optical fiber to the scintillator plates. The scintillator plates have been manufactured and tested. The measurements of the uniformity of light collection and light output were carried out. The temperature dependence of the registration efficiency of the silicon photomultipliers (SiPM) was studied. We built the calibration curves to adjust the offset voltage. A number of software tools based on CERN ROOT and Pandas for reading and processing mea-

surement results has been developed. The PPP-TSEP was tested on cosmic muons and at a source of beta radiation. All tests were carried out in a thermostatted box, isolated from external lighting. In measurements on cosmic muons, a uniform distribution of the number of events and the energy release per event in different layers of the detector was obtained. This result is consistent with expectations, since high-energy cosmic muons are minimally ionizing particles and pass the detector through without significant energy loss. When measuring energetic electrons (laboratory source Sr-90, maximum energy 2.8 MeV), characteristic amplitude spectra were obtained in the input layers. Preliminary tests show the good performance of the prototype.

THE OBSERVATION OF THE SOLAR FLARE ON THE NEUTRINO TELESCOPE

Khavroshkin O.B, Tsyplakov V.V.

Institute of Physics of the Earth, RAS

For the first time, using a neutrino telescope and ANRI effect in the study of solar activity, a low class solar flare was recorded. Given the high theoretical and applied interest in nature and the manifestation of solar flares, we note that the neutrino telescope expands the capabilities of the researcher: the existence of the neutrino component of the solar flare is shown.

Keywords:

solar flares, solar neutrino flux, ANRI effect.

Introduction

The present study was intended as a current, almost regular plan with a fairly ordinary result in advance. What was originally taken as an unknown external influence remained without careful study and only an exact coincidence with the solar flare moment, even if weak (class C), changed the structure of the study. As is well known, the study of solar flares is a subject of rapt attention and deserves both theoretical and experimental efforts. Already an early study of sunspots and recognition of the role of magnetic hydrodynamics led to conclusions about the special formation of flares (in the vicinity of the sunspot group, but outside the sunspot) [1]. According to Internet surveys, a solar flare as an explosive process of isolating different types of wave energy and solar matter emission has been studied in great detail, and since powerful flares are dangerous for society (energy release $\sim 6 \times 10^{25}$ Joules), much attention is paid to their prediction. Advances in the forecast of powerful outbreaks are quite modest and not deep in time — about 3 days. The power is determined in W / m^2 , the flash duration is \sim several minutes, the composition is mg-waves and plasma, the optical X-ray radiation reaches the Earth in 8.5 minutes, after several tens of minutes - powerful streams of charged particles and plasma clouds — after 2.3 days. The works in which solar neutrinos would be mentioned in the flare were not found, but there are studies that lead to serious conclusions [2].

Experiment

On April 4, the solar neutrino flux was observed at the intersection of the axis of the neutrino telescope equipped with a temperature detector of the neutrino flux. There was expected as usual to obtain interference patterns.

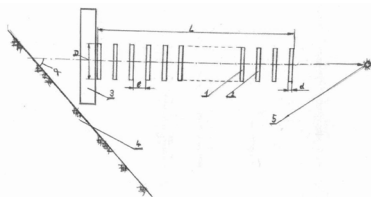


Fig.1. Neutrino telescope. The simplest series of regular disks from radioisotopes, where: L is the total length of the series; D —diameter of the disk; d is the disk thickness; l is the distance between the disks; — the axial line; 1.2 — Disks of the ΣN series, where N is the number of disks, α is the angle of installation of the telescope axis with respect to the basement plane, 3 —temperature detector, 4 is the basement plane, — 5 neutrino source (Sun).

The temperature detector is installed at the rear of a row of disks, while the outermost disk is on the opposite side facing the solar disk, which intersects along the normal and diameter with an axial line due to the rotation of the Earth. The purpose of the recording was to obtain a form of heat flux perturbation on the telescope detector during the passage of the solar neutrino flux during the intersection of the solar disk. Signal recordings with a 4-minute averaging of its level are statistically almost regular in nature and

refer to the initial stage of the study (for example, the construction of diffraction patterns). However, on April 4, the observation process was accompanied by unforeseen features (see Fig. 2). In addition to the usual temperature increase caused by the passage through the maximum of the solar neutrino flux ($N = 6 \times 10^{10}$ particles/sec. cm^2), there was another narrow peak with an amplitude that does not require confirmation of the reliability by statistical estimates. To search for the causes of its origin, publicly available data on solar flare activity were analyzed (Fig. 3).

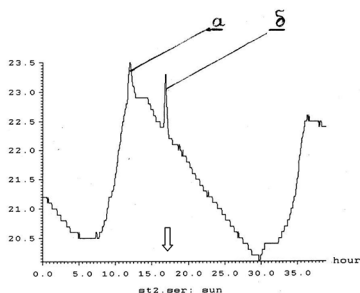


Fig. 2. The usual temperature record is the peak associated with the passage of the solar maximum or the main peak (a), and the peak associated with the flash on the Sun (b), the arrow indicates the flash point - T = 15h 52m UT.

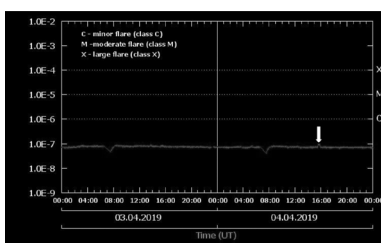


Fig. 3. Data of the flare activity of the Sun for 04/04/2019. At 15h 52min there is an outbreak of activity on the Sun in the form of an insignificant but significant peak (marked by an arrow), - T = 15h 52m UT.

Peak (b) fig.2 in time exactly corresponds to the peak of the solar flare (Fig. 3). Fig. 4 shows the spectral - time analysis (chart) of Fig. 2 data, according to which the observation period is clearly visible, having a gap at the moment of appearance of the pic.2, 3 peaks, since their amplitude did not correspond to the overall periodicity.

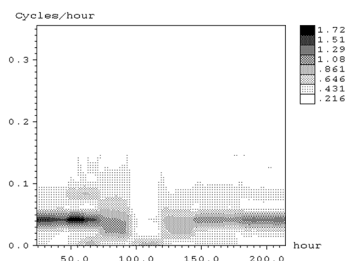


Fig.4. Spectral - time analysis (STA) data Fig.2.

Were compared records of observations of the activity of the Sun for 4.04. and 5.04. 2019 by calculating the mutual correlation function between observations of the Sun for 4.04 and 5.04. 2019 y. approximately at the same time intervals (Fig.5).

As follows from Fig. 5, the maximum correlation corresponds to the zenith orientation of the neutrino telescope to the solar disk. According to both of the above analysis and observational data, a flare at the Sun is accompa-

nied by a powerful jet of neutrino ejection. Let us estimate the ejection power (peak b) by comparing it with the main signal (peak-a), that is, by the amplitudes of the peaks a) and b). According to Fig. 2, peak a) is 23.5 C0 and peak b) is 23. 3C0 that is, their flows are comparable. If we assume that the peak b) appeared due to the growth from the peak curve a), then the power of its flux will be $\sim 1C0$ or ~ 109 neutrinos/cm²sec. Since a registered flash cannot be classified as a powerful one, this means that sufficiently powerful flashes according to the Catalog are accompanied by significantly larger neutrino emissions. Thus, observation of the solar disk with the help of the neutrino telescope [3] made it possible to detect a new type of solar flare, which, according to the adopted name system, should be called neutrino. According to [2], when the Sun is activated, extensive flare fields are observed, i.e., neutrino output from large areas of surface or near-surface structures and/or (volumes) of the central zone is emitted in the form of isolated powerful streams of limited diameter and not sufficiently strictly directed along the normal (radius of the Sun). Therefore, the existing estimates of the real flux without these features need to be revised, as well as the severity of the problem of the lack of neutrinos (never doubting the effect of neutrino oscillations). The existence of neutrino flares indicates their deep connection with the central zone or core of the Sun, which is in good agreement with the existence of the previously known [2] 11-year cycles, which speaks in favor of the influence of flares on volcanic and seismic activity. Similar effects, such as the role of solar neutrinos, in the activation of a volcano were also investigated previously [4]. As is known [2], proton flares are most suitable for forecasting flare activity. Neutrino flares are also likely to have good chances. Moreover, their registration in standby recording mode is easy and affordable. At the same time, if the intensity of the neutrino flux is moderate enough, then its impact on the seismically active region will lead to a decrease in the level of seismicity. Occur, as expressed by the famous physicist V. Tsarev, earthquake prevention. And the last - super flashes - the events are not frequent, but their manifestation involves many well-known dangers for modern civilization. The most powerful neutrino flux from such a flash will in itself be the source of many troubles: the explosive eruption of volcanoes in a near-critical state; growth of general and regional seismicity; unpredictable damage and accidents on nuclear systems and reactors, primarily nuclear power plants; the likely failure according to theoretical estimates of the failure of a nuclear weapon. So physicists from the Japanese KEK laboratory at the University of Hawaii showed that with a certain technical progress in the future, a neutrino beam can be used to detect and destroy enemy nuclear weapons. Unfortunately, an even more powerful beam is likely with a super flash, and its effectiveness guarantees the existence of the Henry effect [5, 6]. Earlier, in the study of lunar seismicity of flare origin, anomalies of seismograms were observed, which were interpreted as a manifestation of the neutrino fluxes of the Sun [7].

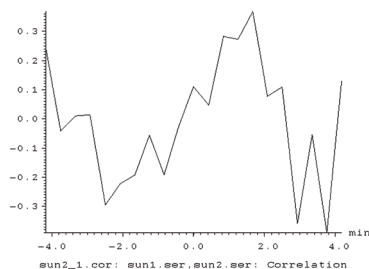


Fig.5. Mutual correlation function of records of neutrino fluxes of the Sun for 4.04 and 5.04. 2019 y.

Conclusion

1. Solar flares are accompanied by a powerful neutrino flux.
2. Solar flares are simple and affordable to register with a neutrino telescope.
3. The danger of super flashes greatly increases due to the simultaneously emerging powerful neutrino flux.

4. The neutrino component of solar flares can play a prominent role in Earth geophysics.

References

- [1] R. Bray, R. Loughhead. SUNSPOTS. Volume seven. The Astrophysics Series. Chapman and Hall LTD. London. 1964.
- [2] Solar flares. Siberian Branch of the Academy of Sciences of the USSR, Siberian Institute of Terrestrial Magnetism, Ionosphere and Radio Wave Propagation. Ed. "Science", M. 1982, 247p.
- [3] Khavroshkin, O.B., Tsyplakov V.V. Neutrino telescope and the effect of anomalous neutrino radiations - isotope (anri) absorption. engineering physics No. 2. 2019, P. 3–13.
- [4] O.B. Khavroshkin, S. A. Fedotov, V. V. Tsyplakov, A. N. Boyko. VOLCANOLOGY AND NEW GEOPHYSICS: REALITY AND PROSPECTS ON THE EXAMPLE OF YELLOWSTONE VOLCANO. VOLCANOLOGY AND SEISMOLOGY, 2019, No. 1, p. 25–35.
- [5] Khavroshkin O.B., Tsyplakov V.V. Anomalous neutrino radioisotopic (anri) absorption and nuclear reactor. engineering physics No. 10. 2016, pp.3-8.
- [6] O. B. Khavroshkin, V.V. Tsyplakov. Five Years after Discovery Abnormal Neutrino Radioactive -Isotope (ANRI) Absorption. Open Access Library Journal 2018, Volume 5, **** pp.1-17.
- [7] Satoshi Tanaka, Khavroshkin O.B., Tsyplakov V.V. Solar flares: seismic fields of the Moon and Earth. ENGINEERING PH

NEUTRINO TELESCOPE: PROBLEMS AND SOLUTION 3

O.B. Khavroshkin, V.V. Tsyplakov,

khavole @ ifz.ru

A brief review is given of the existing methods and devices currently used for recording astrophysical mostly solar neutrinos. These structures, as a rule, have significant, often cyclopean dimensions, insignificant sensitivity and difficulties in determining the direction to the neutrino source. New types of neutrino telescope are described, which are based on the physical effect of anomalous neutrino radioisotope (ANRI) absorption. One type has a high sensitivity, small dimensions, low cost, but also how all existing ones determine the direction of neutrino arrival through the interaction tracks. The other type of telescope, while maintaining these advantages, points to a neutrino source similarly to an optical one - by the direction of the axis of the design structure not on the neutrino interaction tracks, but on their source. The results of a successful test of the current layout are given. Keywords: astrophysical neutrinos, anomalous neutrino radioisotope (ANRI) absorption, neutrino telescopes based on the ANRI effect.

Neutrino telescope: understanding, operating principle, modeling. If we start with general concepts, we mention all known types that are classified by the nature of matter and the processes existing in it that need to be studied. Historically, the telescope first appeared as a device for working with optical signals as an element of electromagnetic fields belonging to the most common objects for studying a wide range of frequencies (from gamma and X-ray bands to radio signals). The telescope provides the collection and primary analysis of electromagnetic signals from astronomical and astrophysical distant objects and processes determine the direction to the source, estimate the power of the primary radiation. Detectors of cosmic dust particles, neutrinos and gravitational waves are also considered to be telescopes. Structurally, all the above instruments vary considerably therefore we consider only the neutrino telescope.

The neutrino telescope, like the dust, X-ray and gamma telescopes, works with a useful signal - a conglomeration of particles, but it records particles (neutrinos) regardless of the direction of their approach, that is, the radiation pattern is absent. The directionality is determined by the physical mechanism of neutrino registration, its interaction with the atomic nucleus of the working fluid (for example, specially purified water) and the subsequent interaction of nuclear particles with the environment (track). Since the capture cross section of the neutrino interaction is $\sim 10^{-43}$, only significant masses of water ($\sim 10^3$ tons and more) and a dense flux of solar neutrinos ($\sim 10^{12}$ particles per second / cm^2) allow observing rare interaction events in the form of optical flares — tracks from The resulting set of nuclear particles. The parameters of the tracks are judged on the power and direction of approach of the particles. The usual number of events is 3-10 neutrinos per day. Thus, the neutrino telescope practically does not correspond to the traditional concept the directivity is determined by the interaction of neutrinos in the working environment.

A tank telescope at a depth of 1490 m in the mine contained 610 tons of perchlorethylene was the first active neutrino telescope on which the first American scientist, Ray Davis, obtained the results, and in 1974 he announced reliable neutrino recording from the Sun. To continue the research, they decided to build new neutrino telescopes and work on possible solar nuclear cycles. In Russia, neutrino research laid the foundation for physics under the leadership of Academician G. T. Zatsepin and corresponding member A. Ye. Chudakov. The Neutrino Telescope of the Institute for Nuclear Research of the Russian Academy of Sciences is located in the North Caucasus, in the Baksan Gorge, at a depth of 350 m. an entire five-story house is set up under the protection of rocks.

The “cells” of a unique telescope house are made up of 3200 independent detectors of size 70X70X30 cm each, filled with a very sensitive liquid scintillation treks. The Baksan neutrino telescope can register neutrinos of both relatively low energies - (10-20 MEV) with the formation of a neutron star, and high, also astrophysical - (100 MEV). In the Baksan telescope, an electronic system that combines sensors that monitor light flashes in individual “cells” filled with a scintillation treks allows you to accurately determine the direction to the neutrino source in the sky. An interesting project DUMAND, provided for installation at a depth of 5 kilometers in the ocean lattice of 1 km³. Photomultipliers (PMTs) in transparent waterproof spheres should be strengthened at the lattice points. PMTs should register flashes of light arising in water during the superluminal passage of charged particles, the so-called Cherenkov’s effect.

Domestic physicists — G.A. Askorian and B.A. Dolgoshein and American T. Bowen proposed a sound method for recording neutrino traces in the ocean. With the passage of a fast particle from the interaction of neutrinos in the water along the route, the temperature and pressure increase, and a shock sound wave arises. The sound emitted when neutrinos interact with water is available for recording at a distance of about a kilometer, unlike light (~ 20 m.). It was supposed to create a grid of hydrophones: an area of 10x10 km and a height of 1 km. According to calculations, out of every 1010th degree of passing neutrinos, only one particle is absorbed. When cosmic rays collide with the nuclei of atoms of a substance (air, water, soil), short-lived particles are created - pi-mesons, which immediately break up into a pair of particles - muon (~ 200 electron masses) and neutrino.

By the energy and direction of motion of the muons, the corresponding characteristics of the neutrinos are judged. This is done in specially developed devices, called “neutrino telescopes”, and the experiments are carried out in conditions of minimal interference, for example, in deep caves or reservoirs (Lake Baikal), where in 1993. An initial telescope of 36 detectors at a depth of 1100 m, passed annual tests. In the Mediterranean, an underwater neutrino telescope of 320 vertical structures and detection units was planned. Each such unit is a complex technical system. In terms of the number of Cherenkov radiation detectors (about 400 thousand), the new neutrino telescope is one of the leaders. It is assumed that the angular resolution for neutrinos with energies above 10 TeV will be 0.1 degrees, which is 10 times greater than the angular resolution of Ice Cube in Antarctic Continent the neutrino energy range is from hundreds of GeV and is several orders of magnitude higher than the neutrinos of all flavors. Such data have significant plans.

However, this does not eliminate the need to create an efficient neutrino telescope.

To determine the direction of arrival of neutrino radiation from a specific celestial body, it is necessary to measure the angular distribution of the fission products caused by neutrinos. But in the case of neutrinos with energy of several MeV or less, this angular distribution with respect to the direction of the incident beam is very insensitive. This difficulty has not yet been resolved. The problem is greatly simplified for high-energy neutrinos, ~ 10⁹ eV, since particles produced by the interaction of neutrinos with nuclei, retain the direction of the incident neutrinos. The last “surprise” among the giant neutrino detectors is the Japanese Super Kamiokande. Located at a depth of 1000m, with a height of ~ 100m, the internal walls are equipped with 11000 PMTs, in fact a stainless steel tank filled with 50.000ton specially purified water. In the future - “Hyper - Kamiokande” exceeding its predecessor by 20 times. Further, let the reader appreciate the modern gigantism and the possibility of applying the effect of ANRI absorption **Neutrino telescope based on the ANRI absorption effect.**

A few years ago, the authors experimentally finally became convinced the reality of the existence of the effect of anomalous neutrino radioisotope (ANRI) absorption [1, 2]. Taking into account the applied and fundamental significance of the effect, as well as the need for thorough repetition and verification of the results of primary research, the authors methodically and technically

repeated the first successful work, but the registration processes for the ANRI effect were additionally duplicated using a parallel recording channel working on a different principle (the occurrence of a thermal field during decay processes). Both methods: radiometric and thermal, their results coincided with the data of the primary work, as well as among themselves. Thus, the existence of the ANRI effect is absolutely reliably proved [1]. This study actually draws a line under the primary study of the effect of absorption, and is the output of the applied technology of study on a broad front of new exploration, taking into account or based on previous results [2–25]. Indeed, in the initial study, which allowed not only to register the flux of solar neutrinos, but also to record the spectrum of the proper oscillations of the Sun which by the modulated flux of radio emission [1, 2].

Moreover, the actual neutrino detector based on the ANRI effect (see Fig. 2 [1]) by weight of the working radioactive substance did not exceed $\sim 10\text{g}$, which is less than the amount of the substance — specially purified Kamiokande water 10^{10} times; comparison of registration systems leads to an equally shocking surprise. Therefore, a comparison with the registration system “ICECUBE” in Antarctica is unnecessary. Such striking differences are explained by an increase in the neutrino capture section by a radioactive substance by a factor of 10^{30} [21]. But the neutrino detector used on the basis of the ANRI effect, as well as all previous ones, is not able to point towards the neutrino source by turning any of its construction side, that is, it is necessary to focus on the source along the neutrino interaction paths with the working substance nuclei. Without the ANRI effect, for example, the Kamiokande system works. Therefore, to create a genuine neutrino telescope capable of indicating the coordinates of the source, the neutrino power, the duration of the impact, it is necessary to combine the ANRI effect and the tracing principle, which is constructively quite realistic (Fig. 1).

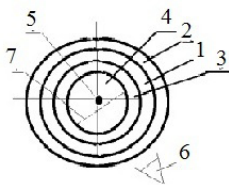


Fig. 1a. Autonomous transparent element of the neutrino telescope: 1— liquid transparent spherical layer from a radioisotope (for example, tritium heavy water); 2 — protective external anti-radiation shell of lead-enriched glass; 3—impermeable inner transparent shell; 4— liquid transparent scintillator solution; 5 — transparent point piezo receiver from polarized quartz; 6 — system for recording tracks of interaction of muon and neutrino fluxes with radioisotope 1; 7 — scintillation track.

Figure 1a shows an autonomous separate element of the neutrino telescope, including: a radioisotope element, external and internal bio-protection, phosphor, acoustic sensor and track recording system. It is desirable that all the above listed details be transparent. For increased sensitivity, a separate system is made up of separate units (1a) (Fig.1b). For a transparent bioprotection apply heavy grade glass (25% lead). The radioisotope can be transparent and in liquid form (for example, heavy tritium water). Even the spherical piezoelectric transducer is also optically transparent (acoustic quartz). The selection of such transparent properties of the working elements of the telescope makes it in many ways a device capable of studying the cosmic neutrino much better than previous systems and fabulously cheap. In addition, the telescope is available to work on most transport systems dimensions and weight is quite acceptable. More specifically, you can figure out the class of research problems. Probably, this type of neutrino telescope can be classified according to the ANRI effect, which completely determines the structure of the whole structure. That is, it can be designated as a neutrino telescope with an updated, but old scheme, according to which the direction to the source is determined by the response (for example, optical) of the working substance,

and the response does not depend on the orientation of the neutrino source of any characteristic part of the structure. We will abbreviate ANRI neutrino telescope (ANRINT). For efficiency, ANRINT may consist of a set of autonomous elements of the type fig. 1a., which will significantly increase the signal-to-noise ratio (Fig. 1b). By selecting the characteristics and parameters of the autonomous module (Fig. 1a), the operation of the entire neutrino telescope can be optimized.

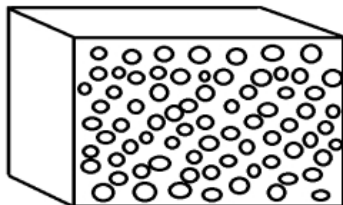


Fig. 1b. There is neutrino telescope from a set of individual modules of spherical type (Fig. 1a).

However, there is a need to create a neutrino telescope (NT) literally similar to optical or radio in terms of guidance, when the maximum signal from the neutrino stream corresponds to the direction of the NT axis to the neutrino source, especially considering many other works [25–38]. Such an NT will consist of two blocks: a block providing one of the main telescopic functions — the search and amplification of the useful signal and the block of registration of the primary amplified signal. Both units are operable only on the basis of the ANRI effect. Since the device of the registration unit is sufficiently developed, then the problems of the telescopic unit will be mainly investigated.

There is ANRINT with an axial focus on the source (ANRINTFS) or simply NTFs. Unfortunately, the concept of a lens for a neutrino flux is not feasible; therefore it is necessary to use another method to increase the flux intensity. Consider a series of regular identical disks from a radioisotope, installed along the axis at equal distances (Fig. 2).

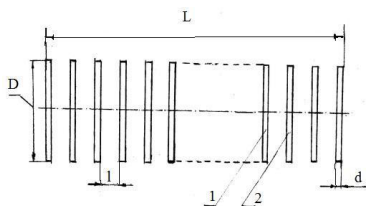


Fig. 2. Simplest series of regular disks from radioisotopes, where: L is the total length of the series; d is the disk thickness; l is the distance between the disks; - * - * - centerline; 1, 2 are the disks of the series $\sum N$, where N is the number of disks.

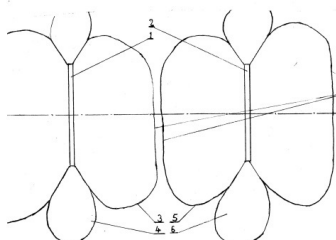


Fig. 3. Diagrams of radiation of the neutrino flux by regular round disks of radioactive materials: 1,2- radioactive disks; 3,5- diagrams of neutrino flux emission by the inner surfaces of disks 1,2; 4,6- diagrams of neutrino flux emission from the edges of disks 1,2; 7, 8 - external end surfaces of radiation diagrams of disks 1,2, forming the central, linear zone of the total radiation pattern of the total neutrino flux of a number of disks (Fig. 2) with a total length L .

Of interest is the total shape of the neutrino emission diagram by a series of disks (Fig. 2) depending on the distance between the disks, when basically each disk radiates the same form as the other neutrino flux (antineutrino), see the general picture — Fig. 3.

It is obvious that, in accordance with the properties of neutrinos (antineutrinos), the interaction processes of fluxes from individual disks affect both the emission of muons by each disk, and hence the neutrino, and the formation of the level of neutrinos of the surfaces of a series of disks, especially the extreme ones. That is, it is possible that the very stimulating interaction of a series of disks, which has some analogy with an optical quantum generator. In the case of the existence of such a feature, the selection of parameters of a number and characteristics of a radioactive substance will probably allow obtaining from the disk a constantly operating linear neutrino source (LNS), which does not require special equipment and observation, depending on the half-life of a radioisotope with an exceptionally long working time (radiation). Such a scheme in the future is very promising, since it can work on disks with highly active nuclear waste. However, first of all, we will consider the operation of a number of disks, shown in Figure 4, in the ANRITFS mode.

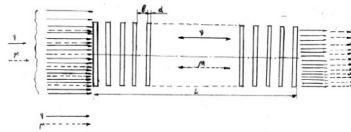


Fig. 4. Linear neutrino source in the neutrino telescope mode: γ , μ - denotes neutrino and muon fluxes; l is the distance between the inner planes of adjacent disks; d is the disk thickness; the arrows indicate the neutrino (solid) and muon fluxes (dotted lines); L is the length of a row of disks.

Since the fluxes γ , μ from natural sources multiply exceed the internal ones arising from the interaction of the disks, a more intensive interaction of the radioactive substance of the disks with external streams will occur, which will be enhanced by the interaction with the disks. These interaction processes are primarily determined by the angle of orientation of the axis of the linear neutrino source to the natural source. Such is the simplest amplification mechanism in the ANRITFS telescope of the neutrino signal (stream) from an external source. Let us consider the possibilities of increasing the efficiency of this gain, which are also connected with the zones of radioactive disks (Fig. 5).

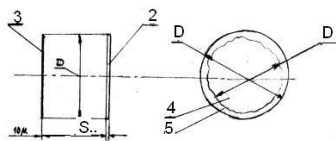


Fig. 5. An example of the disk structure by their emission zones γ , μ streams: 2 — a disk as an element of the neutrino source (LIN); 3 — the outer surface of the adjacent disk; 4 — the central zone of the disk, the radiation of which is mainly axial direction; 5 — edge zone of the disk, with a scattered radiation flux; D is the outer diameter of the disk; D_x is the diameter of the disk's radiation zone with predominantly axial radiation. Figures in fig. refer to the experimental sample.

According to fig.5 and in accordance with the laws of radiation of the edge zone of a flat surface, the peripheral zones of the disks do not play a noticeable role in the formation and enhancement of the radiation flux γ , μ from an external source. Therefore, to improve the ANRITFS telescope, it is necessary to exclude the role of the peripheral zone (Fig. 6).

As follows from the scheme in Fig. 6, the particle flux from the external disk, significant in area, takes an axial direction in the disk system and is enhanced by interaction with the disks. In this case, the linearization scheme of the flow direction and reduction of losses due to its dispersion by the peripheral zone of the disks can be improved with further increase in the activity of the radioisotope material of the disks (Fig. 7). For a rough estimate, the degree

of amplification is estimated by the ratio of the areas of the plates external to the last.

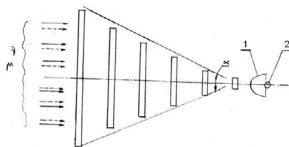


Fig. 6. Diagram of the ANRITFS telescope with more efficient use of disks: γ , μ - flow from external sources; α is the linear decrease angle of the diameters of the subsequent disks in order from external to last; 1-radioactive parabolic shell to receive an axial flow of particles from the last disk; 2- shell focus with radiometer or thermometer.

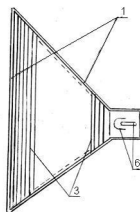


Fig. 7. Compact sensitive ANRINTS: 1 — durable sealed enclosure - radioactive screen; 3 — metal disks from a highly active isotope (for example, U-235); 6 — registration block. The most advanced version of ANRITS is durable, hermetic and compact; most suitable for use in mobile systems. The above qualitative representations of different types of telescopes allowed us to proceed to practical research.

Testing of the current layout of the simplest scheme ANRITFS

The simplest mock-up of the ANRITFS telescope or simply NT with the structure in accordance with Fig. 2 was tested, where: L -150mm; d-6mm; D -45mm; l-15 mm; ΣN – 10. The radioactive cesium isotope was used in the registrar unit; the useful signal was recorded using a thermal sensor. The main task of the test was to determine the reaction of the NT model with its axial orientation towards the Sun or calibration with the solar flux of neutrinos. The maximum of the radiation pattern coincides with the geometric axis of the series. The first tests led to encouraging results (Fig. 8).

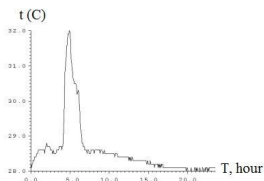


Fig. 8. Level of the signal from the telescope layout when passing its radiation pattern over the solar disk. The model itself consisted of 2 parts: the telescopic unit (TU) itself (diagram in Fig. 2) and the recorder (BR) of the neutrino flux at the outlet of the telescopic unit. The telescopic unit consisted of a set of 10 plastic discs filled with radioactive thorium ore, and located along with an interval of 15 mm. on a wooden rod directed toward the Sun. The recorder was designed as a neutrino temperature sensor based on Baikal uranium ore. It located behind the TU - a set of discs with thorium ore.

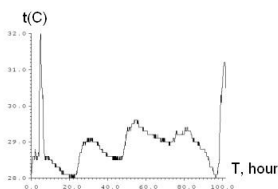


Fig. 9. Observations on the neutrino telescope for 4 days.

Fig. 9. shows the result of both the telescope aperture passing through the solar disk (at the beginning of Fig.8) and the effect of thorium tablets located across at the end of the observation (after 100 hours the telescope was rotated 90 degrees, that is, the disks were directed by ribs in the direction from The sun). From consideration of Figure 9, it follows that the temperature change of 3 degrees Celsius (from 29 to 32) occurred in about three hours, which corresponded to the time of NT aperture passing through the solar disk, taking into account the nature of ore heating. In Fig.9, thorium tablets were located across the sensor at the end of the figure 3 days after the first experiment. Figure 9 also clearly shows the usual daily fluctuations (day-night) of the temperature in the laboratory.

Further observations on NTs were carried out using a temperature unit — a recorder on the Cz 137 isotope and the former telescopic unit (Fig. 10). Variations in the sensor temperature from 27 ° C to 30 ° C degrees Celsius with background variations in the laboratory of 0.1 ° C were detected.

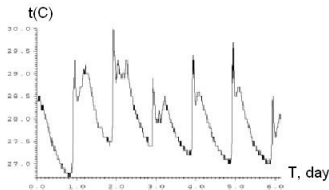


Fig. 10. Fragment of the recording of the neutrino telescope during the week.

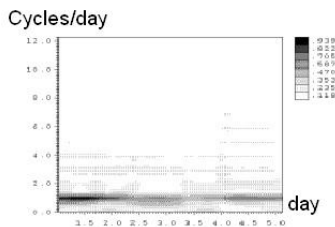


Fig. 11. Results of the spectral-temporal analysis of the recording Fig.10. In fig.11 the diurnal component and its higher harmonics are highlighted. Next, the second and sixth diurnal peaks in Figure 10 were identified and a correlation was made between them (Figure 12).

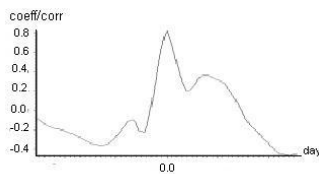


Fig. 12. Correlation coefficient between the 2nd and 6th peaks is about 0.8.

Then, a sliding correlation is determined between the whole implementation of Fig.10 and the selected daily peaks in a 10% window (Fig.13, 14).

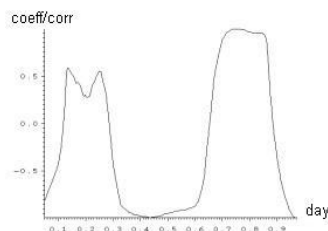


Fig. 13. These is correlation coefficient between the 2-nd peak and the whole implementation.

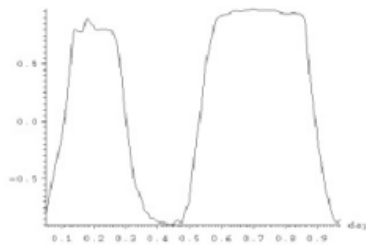


Fig. 14. There is correlation coefficient K between the 6th peak and the whole implementation; along the axis of the K value. The abscissa is the current time (days). The strong similarity of Fig.13, 14 confirms the physical reality of the work of NT.

Conclusion

1. Opened in 2013 the effect of anomalous neutrino radioisotope absorption (ANRI effect) allowed the simplest, inexpensive, and small-sized installations to ensure the continuous recording of solar oscillations in a modulated solar neutrino flux.
2. A simple method has been developed for creating a sensitive neutrino telescope (NT) based on ANRI - an effect that can not only continuously record the solar neutrino flux, but also along tracks - the direction of the neutrino approach from the source. Compared with the existing neutrino detection facilities, such an NT is many orders of magnitude more sensitive, simpler, easier, cheaper, and more accessible.
3. On the basis of the ANRI - effect, a working model of NT has been created and tested according to the principles of operation similar to the optical one. That is, it determines the direction to the source and amplifies the selected received neutrino signal. Structurally simple and can serve as a model for further development.

References

- [1] Khavroshkin O.B., Tsyplakov V.V. Anomalous Neutrino Radio - Isotopic (ANRI) Absorption Effect: 5 Years Later // Engineering Physics.
- [2] Khavroshkin O.B., Tsyplakov V.V. Sample ore radioactivity: monitoring // Engineering Physics. 2013. № 8. P.P. 53 ... 62.
- [3] Khavroshkin O., Tsyplakov V. Sun, Earth, radioactive ore: common periodicity. The Natural Science (NS). 2013. Vol. 5. № 9. Pp. 1001...1005.
- [4] Khavroshkin O., Tsyplakov V. Radioactivity of nuclei in a centrifugal force field. The Natural Science (NS). 2011. Vol. 3. № 8. Pp. 733...737.
- [5] Khavroshkin O.B., Tsyplakov V.V. Natural radioactivity as an open system // Engineering Physics. 2013. № 12.
- [6] Starodubov A.V., Khavroshkin O.B., Tsyplakov, V.V. From periodicities of radioactivity to cosmic and metaphysical oscillations // Metaphysics. 2014. No. 1. P. 137 149.
- [7] Khavroshkin O.B., Tsyplakov V.V. Hydrogen Maser: Solar Periodicities // Engineering Physics. 2014. № 3. P. 25 ... 31
- [8] Khavroshkin O.B., Tsyplakov V.V. Atomic-molecular metastable media and solar neutrinos // Engineering Physics. 2014. № 6. P. 40 ... 47
- [9] Rukhadze, A.A., Khavroshkin O.B., Tsyplakov, V.V. Periodicity of natural radioactivity // Engineering Physics. 2015. № 6. P. 26 ... 36
- [10] Khavroshkin O.B., Tsyplakov, V.V., Modulated Neutrino Flows: Astrophysical and Geophysical Periodicities, Engineering Physics. 2015. № 10. P. 27 ... 47
- [11] O. Khavroshkin, V. Tsyplakov. The Radioactivity of Nuclei & Solar Oscillations: New Experiments. NS. Vol. 8, No.1, January 2016 PP. 20-32 DOI: 10.4236/ns.2016.81003
- [12] Tarasov N.T., Tarasova N.V., Khavroshkin O.B., Tsyplakov V.V. SN1987A SUPERNOUS FLASH: SEISMIC RESPONSE. Engineering Physics. 2016. No. 6. P. 82-93.
- [13] Karagioz O.V., Izmailov V.P., Khavroshkin O.B., Tsyplakov V.V. CAVENTISH TORQUE SCALES AND CERNA HADRONNE COLLIDER: DIFFERENT DESTINIES AND RESULTS. Engineering Physics. 2016. No. 4. P. 3-8.
- [14] Khavroshkin O.B., Tsyplakov V.V. ANOMALOUS NEUTRINAL RADIOISOTOPIC (ANRI) ABSORPTION AND NUCLEAR REACTOR. Engineering Physics. 2016. № 10. P. 3-8.

- [15] Khavroshkin O.B., Tsyplakov, V.V. SOLAR NEUTRINO, MONOPOL, DION, AXION: SEARCH EXPERIMENTS. Applied physics and mathematics. 2017. No. 2. P. 3-10.
- [16] Khavroshkin O.B., Tsyplakov V.V. GRAVITATIONAL-WAVE EXPERIMENT: GEOPHYSICAL AND ASTROPHYSICAL COMPONENTS. Engineering Physics. 2016. No.8. P.56-63.
- [17] Nikolaev A.V, Khavroshkin O.B., Tsyplakov, V.V. STRUCTURE OF ASTROPHYSICAL COMPONENTS OF SEISMIC EMISSIONS AND NOISES Engineering Physics. 2016. No. 9. P. 69-73.
- [18] Khavroshkin O.B., Tsyplakov V.V. Devices for advanced physics research. Invention Journal of Research Technology in Engineering & Management (IJRTEM) Volume 2 Issue 4 || April 2018 || PP 59-63
- [19] Khavroshkin O.B., Tsyplakov, V.V. Neutrino: experiments, new results. Palmarium Academic Publishing. 2017, 265p.
- [20] Khavroshkin O.B., Tsyplakov V.V. Anomalous Neutrino Radioisotope (ANRI) Absorption and Background Antineutrinos of a Water-water Nuclear Reactor. SciFed Journal of Nuclear science SF J Nucl Sci, 2017, 1:1
- [21] Khavroshkin O. B., Tsyplakov V.V. Cavendish Torsion Balance and Hadron Collider at the Cern: Different Fates and Results. SciFed Journal of Nuclear Science SF J Nucl Sci, 2017.
- [22] Khavroshkin O.B., Tsyplakov V.V. Yellowstone`s Volcano and Sun: Fragments Selected Works. Journal of Geology and Geoscience. Volume 1(1): 2017, pp 1-5
- [23] A. Rukhadze A., Khavroshkin O.B., Tsyplakov, V.V. Graviton and neutrino: modulated flows or envelope waves. Engineering Physics. 2017. No. 10. P.71-85.
- [24] Khavroshkin O.B., Tsyplakov, V.V. Temperature fields of radioactive substances: temporary variations and applications. Engineering physics. 2017. No. 7. P.17-32.
- [25] Khavroshkin O.B., Tsyplakov V.V. Devices for advanced physics research. Invention Journal of Research Technology in Engineering & Management (IJRTEM) Volume 2 Issue 4 || April 2018 || PP 59-63
- [26] Y. A. Baurov, Y. G. Sobolev, Y. V. Ryabov. New Force, Global Anisotropy and the Changes in β -Decay Rate of Radioactive Elements. American Journal of Astronomy and Astrophysics 2014; 2(2): 8-19 Published online October 30.
- [27] Yu. A. Baurov. "On the Structure of Physical Vacuum and a New Interaction in Nature (Theory, Experiment and Applications)", Nova Science, New York, 2000.
- [28] Parkhomov A.G. Periodic and sporadic changes in the rate of beta decay found during long-term observations. Metaphysics. Science Magazine. M. 2014, № 1 (11), p. 124-136.
- [29] Jenkins J.H. et al. arXiv: 1207.5783v1 [nucl - ex] 24 Jul 2012
- [30] Lobashov V.M., Measurement of the Neutrino Mass in Beta Decay of Tritium, Vestnik RAN.- 2003-73 (1). - P. 14-27.
- [31] Baurov Yu.A., Sobolev, Yu.G., Kushniruk, V.F., et al. Experimental Studies of Changes in Velocity in the Rate of Beta-Decay of Radioactive Elements // Physical Thought of Russia.- 2000.- No. 1.- S. 1-7.
- [32] Baurov Y. A., Konradov A. A., Kushniruk V. F., etc. Experimental Investigation of Changes in Beta- Decay Rate of ^{60}Co and ^{137}Cs // Modern Physics Letters A.- Vol.16.- № 32.- P. 2081- 2101.
- [33] Falkenberg E. D. Radioactive decay caused by neutrinos?//Aperion, 8.-2001.- №2.-P.2081-2101
- [34] E. Fischbach, J. B. Buncher, J. T. Gruenwald et al. Time dependent Nuclear Decay Parameters: New Evidence for New Forces? Space Science reviews (2009) 145: 285-335 DOI 10, 1007/s 112 14-009-9518-5.
- [35] Iben I., Jr., Mahaffy J. Astrophys. J. (Lett.), 1976, v.209, p.L39.
- [36] Khavroshkin O.B., Tsyplakov V.V. Hydrogen maser: solar frequency. Engineering Physics. №3, 2014, M. p. 25-31.
- [37] Khavroshkin O.B., Tsyplakov, V.V. Atomic-molecular metastable media and solar neutrinos. Engineering Physics. №6, 2014, M. C. 40-47.
- [38] Dodonov V.V., Klimov A.B., Man'ko V.L. Low energy wave packet tunneling from a parabolic potential well through a high potential barrier. PHYSICS LETTERS A no. 1996. P. 41...48.

A NEW INVERSION OF THE PRANDTL-MEYER RELATION

R.T. Ferreyra¹, J.G. Gongora Rincon²,

¹ *Departamento de Matemática, Facultad de Ciencias Exactas Físicas y Naturales, Universidad Nacional de Córdoba, Argentina;*

² *Departamento de Aeronáutica, Facultad de Ciencias Exactas Físicas y Naturales, Universidad Nacional de Córdoba, Argentina;*

Keywords:

Expansion Waves, Flow Discontinuities, Convex Corner, Supersonic Flow.

Introduction:

The supersonic flow through convex corners generates flow discontinuities. A new inversion of the Prandtl-Meyer relation for expansion waves in supersonic flow is obtained. The contribution in the fields of Craters formation, Theoretical Fluid Dynamics and Computational Fluid Dynamics [1] is to be able to access to the Mach number of the fluid by the measured flow deflection obtained from high resolution images. A numerical treatment of this inversion can be found in the literature [2].

References:

- [1] Anderson J.D., Modern compressible flow with historical perspective. McGraw-Hill 2003. 760p.
- [2] Hall I.M., Inversion of the Prandtl-Meyer relation // Aeronautical Journal, 1975. P. 417-418.

EVIDENCE FOR INDIGENOUS MICROFOSSILS IN CARBONACEOUS CONDRITES

R.B. Hoover¹, A. Yu. Rozanov²

¹ U. S. Space and Rocket Center, One Tranquility Base, Huntsville, Alabama 35805, USA, RichardBHoover@ICloud.Com;

² Astrobiology Sector, Laboratory of Radiation Biology, Joint Institute for Nuclear Research, Dubna, Russia, 141980, Aroza@Paleo.ru

Keywords:

Carbonaceous Chondrites, Orgueil, Murchison, Microfossils, Biomolecules, Microalgae, Cyanobacteria, Diatoms, EDS, Nitrogen

Introduction:

Carbonaceous chondrites are a major clan of chondritic meteorites. The CI and CM groups are considered the most primitive of all carbonaceous meteorites. Their element compositions most closely resemble that of the Sun and the proto-solar nebula and contain high percentages (3% - 20%) of indigenous extraterrestrial water, and several weight % Carbon. The CI1 carbonaceous chondrites are of CI (Ivuna Type) chemical group and petrologic Type 1. Chondrules are present in all carbonaceous chondrites except Orgueil, Alais and the other CI1 meteorites where it is accepted that their chondrules were destroyed by extensive low temperature (<50 °C) aqueous alteration on the parent body. The CI1 meteorites exhibit and by their high degree (~20%) of indigenous water of hydration. The dominant mineral (62.6 %) of the Orgueil meteorite is Chlorite [(Fe, Mg, Al)₆(Si, Al)₄O₁₀(OH)₈] of the clay phyllosilicates mineral group (similar to terrestrial smectite or montmorillonite clay). Carbonaceous chondrite also contain carbonates, and iron oxides such as magnetite Fe₃O₄, limonite Fe₂O₃ · nH₂O and fragments and crystals of olivine, pyroxene, elemental iron, presolar diamonds, graphite and insoluble organic matter similar to kerogen [1-3]. The silicate minerals are more properly designated as serpentine rather than peridotite. The phyllosilicates and light element geochemistry provide indications of the surface conditions and processes on the parent body [4]. Clayton [5] found that the carbon isotopes of the Orgueil carbonates ($\delta^{13}\text{C} \sim +60 \text{‰}$) are very different from terrestrial carbonates of precambrian limestones and dolomites ($\delta^{13}\text{C} = +0.4 \text{‰}$) [6] or biological carbonates ($\delta^{13}\text{C} = 0 \text{‰}$ to -70‰) [7]. These findings provide direct evidence that the Orgueil carbon is indigenous to the stones and extraterrestrial in nature.

It is now well established that the carbonaceous chondrites contain a vast array of complex organic molecules. Sephton [8] reviewed carbonaceous chondrite organics including: amino acids, aliphatic and aromatic hydrocarbons; carboxylic, sulfonic and phosphonic acids; sugars, alcohols, ketones, aldehydes, amines, amides, nitrogen and sulfur heterocycles and abundant high molecular weight insoluble organic matter (IOM) similar to kerogen. Schmitt-Koplin et al. [9] analyzed the organics of the Murchison CM2 meteorite using Fourier transform ion cyclotron resonance/mass spectrometry (FTICR/MS) and found it to contain tens of thousands of indigenous and extraterrestrial molecular compositions, many of which are similar to known biomolecules found in living organisms. Indigenous and extraterrestrial protein amino acids (some with an excess of the L-enantiomer) as well as others with no known biological function have been detected in the Murchison CM2 [10, 11] and the Orgueil and Ivuna CI1 carbonaceous chondrites [12, 13]. It is important to note that only 8 of the 20 proteinaceous amino acids found in all known life forms have been detected in carbonaceous meteorites. Three (Adenine, Guanine and Uracil) of the five nucleobases essential for life have also been found [14] but the unstable nucleobases (thymine and cytosine) are absent in the carbonaceous meteorites. It would be impossible to contaminate a meteorite with modern microorganisms without also introducing all 5 nucleobases and all 20 amino acids that are abundant in the DNA, RNA, proteins and enzymes of all life forms known on Earth. Consequently the missing amino acids, nucleobases, RNA, DNA and a host of other life-critical provides clear and convincing evidence

that these carbonaceous meteorites have not been recently contaminated by living microorganisms [15]. Aerts et al. [16] conducted a DNA and RNA analysis of Orgueil using 16S and 18S rRNA PCR amplification methods sensitive enough to detect a single bacterial cell. The negative results of these test provides solid evidence that the Orgueil CI1 carbonaceous chondrite has not been contaminated by modern bacteria or other living microorganisms.

Materials and Methods: Samples of the Orgueil CI1 carbonaceous chondrite were provided by Musée Nationale d'Histoire de Paris; Musée d'Histoire Naturelle Victor Brun, Montauban and Planetary Studies Foundation, Galena, Illinois, USA. Samples of the Murchison CM2 carbonaceous chondrite were provided by Museums Victoria, Melbourne, Australia. Flame sterilized tools were used to fracture the meteorite fragments and mount them on new SEM stubs with the freshly fractured interior meteorite surfaces exposed. High resolution Secondary and Backscattered Electron images; Spot Element composition; and 2D X-ray Element Maps were obtained using Scanning Electron Microscopes with Energy Dispersive X-Ray Spectroscopy (EDS). at the NASA/Marshall Space Flight Center (USA); Paleontological Institute (RAS) and Joint Institute of Nuclear Research, Dubna (Russia).

Results:

The Orgueil CI1 and Murchison CM2 carbonaceous meteorites have been found to contain a great diversity of the permineralized or carbonized remains of recognizable fossils of aquatic cyanobacteria, prasinophytes and other microalgae and protists. The most abundant recognizable forms exhibit morphological features and sizes of filamentous cyanobacteria. These include both extant and extinct microorganisms. Diatoms have been detected in Orgueil, but they are extremely rare [17]. EDS spot data reveal the nitrogen content of these fossils is almost always below the EDS detection limit ($N < 0.5\%$). Since nitrogen is present in the amino acids, proteins, DNA and RNA molecules of all living cells (typically 2% to 20% atomic; the absence of nitrogen indicates the organisms died long before the meteorites entered Earth's atmosphere. The O/C and C/N ratios are similar to proterozoic biogenic kerogen ($O/C < 0.2$; $C/N \sim 100$ to 160 and the Orgueil microfossils are often infilled with magnesium sulfate.

Conclusion:

The Orgueil CI1 and Murchison CM2 carbonaceous chondrites contains a wide diversity of exceptionally well-preserved microfossils. Many are the, recognizable remains of large filamentous trichomic cyanobacteria with the specialized cells for nitrogen fixation (heterocysts) and evidence of distinctive reproductive modes (akinetes, hormogonia, and baeocytes). EDS data reveal C/N, C/S and O/C ratios consistent with ancient biological remains rather than modern microbial contaminants. Therefore these clearly biological forms are interpreted as indigenous remains of aquatic microorganisms that inhabited aqueous environments in the meteorite parent body and died long before the meteorites entered the atmosphere of Earth. .

References:

- [1] Endress, M., Bischoff, A. Mineralogy, degree of brecciation, and aqueous alteration of the CI chondrites Orgueil, Ivuna and Alais // *Meteoritics*. 1993. V. 28. P. 345-346.
- [2] Endress, M., Spettel, B. and Bischoff, A. Chemistry, Petrology, and Mineralogy of the Tonk CI1 chondrite: Preliminary results // *Meteoritics*. 1994. V 29. P. 462-463...
- [3] Endress, M., Bischoff, A. (1996). Carbonates in CI chondrites: Clues to parent body evolution // *Geochimica. et Cosmochimica Acta.*, 1996. V. 60. P. 489-507.
- [4] Bunch, T. E., Chang, S. Carbonaceous chondrites-II. Carbonaceous chondrite phyllosilicates and light element geochemistry as indicators of parent body processes and surface conditions // *Geochim. Cosmochim. Acta* 1980. V. 44. P. 1543-1577.
- [5] Clayton, R. N. Carbon isotope abundances in meteoritic carbonates // *Science*. 1963, V. 140. No. 3563. P. 192-193.
- [6] Schidlowski, M., Eichman, R., Junge, C. E. Precambrian sedimentary carbonates: carbon and oxygen isotope geochemistry and implications for the terrestrial oxygen budget. // *Precambrian Research*. 1975. V. 2. No. 1. P. 1-69.

- [7] McConnaughey, T. A. et al. Carbon isotopes in biological carbonates: Respiration and photosynthesis // *Geochim. et Cosmochim. Acta*. 1997. V. 61. No. 3. P. 611–622.
- [8] Sephton, M. A. (2005). Organic Matter in Carbonaceous Meteorites: Past Present & Future Research // *Philosophical Transactions of the Royal Society*, A. 2005. V. 363. P. 2229-2742.
- [9] Schmitt-Kopplin, P. et al. High molecular diversity of extraterrestrial organic matter in Murchison meteorite revealed 40 years after its fall // *Proceedings of the National Academy of Sciences*. 2010. V. 107. P. 2763-2768..
- [10] Engel, M. E., Nagy, B. Distribution and enantiomeric composition of amino acids in the Murchison meteorite // *Nature*. 1982. V. 296. P. 837-840.
- [11] Engel, M. E., Macko, S. A. The stereochemistry of amino acids in the Murchison meteorite // *Precambrian Research*. 2001. V. 106. P. 35-45.
- [12] Lawless, J. G., Kvenvolden, K. A., et al. Evidence for Amino-acids of Extraterrestrial Origin in the Orgueil Meteorite // *Nature*. 1972. V. 236. P. 66-67.
- [13] Ehrenfreund, P., Glavin, D. P., Botta, O. et al.. Extraterrestrial amino acids in Orgueil and Ivuna: Tracing the parent body of CI type carbonaceous chondrites // *Proceedings of the National Academy of Sciences*. 2001 V. 98. P. 2138-2141.
- [14] Callahan, M. P., et al. Carbonaceous Meteorites Contain a Wide Range of Extraterrestrial Nucleobases // *Proceedings of the National Academy of Sciences*. 2011. V. 108. P. 13995-13998.
- [15] Hoover, R.B. Comets, Carbonaceous Meteorites and the Origin of the Biosphere // In: Dobretsov N., Kolchanov N., Rozanov A., Zavarzin G. (eds) *Biosphere Origin and Evolution*. 2008. Springer, Boston, MA P. 55-65.
- [16] Aerts J. W. et al. A contamination assessment of the CI carbonaceous meteorite Orgueil using a DNA-directed approach.// *Meteoritics & Planetary Science*. 2016. V. 51. No. 5. P. 920-931.
- [17] Hoover, R.B., Rozanov, A. Yu., Krasavin, E. A., Ryumin, A. K., Kapralov, M. I. Diatoms in the Orgueil Meteorite // *Paleontological Journal*. 2018. V. 52. No. 13. P. 1647-1650.

THE INFLUENCE OF CYCLES OF SPACE WEATHER ON GEOCHRONOLOGY OF BIOLOGICAL AND CLIMATIC CHANGES

A.L. Kharitonov

Pushkov Institute of Terrestrial Magnetism, Ionosphere and Radio Wave Propagation of the Russian Academy of Sciences, 108840, Moscow, Troitsk, Kaluzhskoe High Way, 4, IZMIRAN, E-mail: ahariton@izmiran.ru

Keywords:

Structure and evolution of galaxies, paleo magnetic and paleo biological processes

Introduction:

Biological scientific problems which are related to the features of structure of our Galaxy and effluent from it general conformities to law of structure and evolution of natural physical processes of Galaxy Climate in the Solar Planetary system (SPS) and, in particular case, in the Earth are considered in this report. Many advanced studies are devoted sufficiently the questions of structure and evolution of galaxies [1-4]. But above all things interests us – whether there are what that general physical galactic conformities to law, showing up in the paleo magnetic field of the Earth, its paleo climatic, paleo biological processes?

There are different hypotheses about the origin of the magnetic field of spiral arms of our Galaxy [5]. As the noticeable magnetic field of galactic wind found out not in all our Galaxy, but only in its spiral arms, then can be assumed, that the density of the flow of the magnetic field of the galactic wind is non-uniform in Galaxy. The edge of spiral arms of galaxies, in accordance with the theory of Galactic spiral wave closeness [6], are the waves of closeness, and the process of their distribution is the hard rotation of waves. This theory assumes the presence of galactic shock waves (GSW) which are the area of the compressed interstellar gas, along the internal edge of galactic spiral wave. The galactic shock wave results in the compression to the interstellar gas, dust and there is the increase of concentration of such gas, dust in the area of wave front. It is assumed on the basis of this theory of galactic spiral waves of closeness, that orbit of our Solar Planetary system periodically intersects with the galactic shock waves of closeness of the spiral arms. Crossings of the orbit of the Solar Planetary system with the spiral arms can have three basic temporal periods: 1) at the late stage of evolution of our Galaxy (about 1 - 2 billions years ago) there is the temporal period ($T_1 = 185 \pm 35$ million years) which was needed, that the Solar Planetary system passed distance equal Galactic Year; 2) middle temporal period ($T_2 = 25 \pm 10$ million years) during which the Solar Planetary system passes between of the spiral arms; 3) temporal period ($T_3 = 3 \pm 1$ million years) during which the Solar Planetary system passes the zone of the edge of the Galactic arm where the front of the Galactic shock wave (GSW) is located. Thus, coming from maximum entropy spectral method (MESM) data about evolution of the different physical processes, for the Solar Planetary system can be selected three basic periodically repetitive temporal epochs: with the period (T_1) in 185 million years, to the slow evolution of all physical processes in the Solar Planetary system; other temporal epochs with the period (T_2) about 25 million years, with in relation to by the rapid evolution of all physical processes and finally third type of temporal epochs with the period (T_3) about three million years, related to relatively by the very rapid evolutionary changes of many physical parameters of the Solar Planetary system and Earth in particular.

If to analyse different geophysical (including paleo-magnetic scale) data literature sources [7-12] about more early period of evolution of Earth from Precambrian to the Permian period, presented in this paper too, it is possible to say that crossing of galactic arm spiral wave of closeness by the Solar Planetary system relatively is poorly reflected in geophysical information, except for stratum discontinuus, often related to the small changes of the

level of waters of the World Ocean. To crossings by Earth, in composition the Solar Planetary system, Sagittarius galactic spiral arm of closeness, in the temporal period of Precambrian ((№1)-2440, (№2)-1700, (№3)-960 millions years ago), it was related to the different tectonic-dynamical events of Precambrian phases of the tectonic deformation and cardinal changing of Lithosphere [10-11], including catastrophic change. For example, Permian-Triassic climatic and biological catastrophes of deaths of plankton and subsequent chain let of biological kinds, feedings to them, and grown of new kinds of different plants in the geological time period 280-225 m.y.a. In more early periods of crossing with the galactic spiral arm of closeness there was intensive bombardment meteorites of Earth and transition from the mantle Plume tectonics to Plate tectonics. In the period of passing the Solar Planetary system from the Sagittarius galactic spiral arm of closeness to the Persej galactic spiral arm, in the Earth, presumably, the phase of processes of tension prevailed (disintegration of continents and divergence them from each other).

And, vice versa, in the period of motion of the Solar Planetary system from the Persej galactic spiral arm to the Sagittarius galactic spiral arm (4655 m.y.a.) were compression forces in the Earth. In the period of crossing (3800, 2300, 805, 65 million years ago) of galactic spiral arm of closeness of Orion there were the large-scale freezings, changes of chemical composition of atmosphere (saltatory growth of oxygen and carbon dioxide) and gallop in the change of the organic world [12]. It is also possible to suppose certain influence of the magnetic field of galactic spiral arms of closeness on the inversion of the geomagnetic field. In the last time period (from 2 million years ago) passing of the Solar Planetary system within the limits of Sagittarius galactic spiral arm, the frequency of reversions of the geomagnetic field was bigger, as compared to the Carboniferous period, wherever inversions were not practically.

From reports, the temporal moment, when the Solar Planetary system in the last time crossed border of one of galactic arm concerns at the right time about 1.7 million years ago, in the Matuyama reversed epoch after the Gilsa polarity event on the geomagnetic time scale of inversions [13]. Now the solar-planetary system together with the Earth has entered 1.7 million years ago new Galactic Year with which it is possible to allocate on geological time scale and geomagnetic time scale [13]. Taking into account, it is possible to assume that in the future, during the time period, not less than 18-23 million years (if to consider that it will be the narrowest galactic arm) in the Earth expects the time period of enough quiet-stable galactic magnetic field at movement the Earth along the galactic orbit to the next meeting with the raised magnetic field and shock waves of other galactic arm. As the result it is possible to tell that during the temporal periods of the last Galactic Year, in the course of passage by the orbit of the Earth, as the part of the Solar Planetary system, certain coordinates of the galactic orbit were observed both the periods of blossoming of the biological kinds of the Earth, and the catastrophic natural phenomena, for various biological kinds of the fauna and the flora (Permian-Triassic biological accident 225 million years ago). We will try to show the role of special time points of the galactic orbit in evolution of biological kinds on the Earth.

It is considered that about 4670 million years ago has started to occur the gravitational attraction of particles cloud of the cold interstellar dust in one agglomeration which it is possible to name "cold" phase of development proto-planet Earth, proceeding during approximately three galactic cycles (1-3 galactic years). It is considered that, beginning approximately with the temporary period of 4000 million years, process of primary fusion of this huge mass of bound together particles under the influence of forces of gravitational compression began. That is approximately within one galactic year as the result of fusion there were processes of intensive differentiation and decontamination of primary substance of the proto-planet Earth. As the result, at a boundary about 3750 million years on the surface of the "hot" proto-planet there was the first water. As the result of impact of the magnetic field of the Sun and the solar wind on proto-planets electro-carrying out to heterogeneity Earth during this period could arise primary genera-

tion of own magnetic field. As considers the majority of biochemists, from the moment of emergence on water Earth, within the 5th galactic year, in the Kat-Archean stage, formation of stereo-isomers began, there were proteins and poly-nucleotides. That is live could arise from the lifeless. It is fixed that for the first time biological life on Earth appeared 3750 million years ago in the form of anaerobe archean bacterias and the eu bakterias existing at almost total absence of oxygen in the atmosphere. At the Pro-kariot stage of development of the biosphere on Earth it is possible to allocate two stage. The first stage, begun at the boundary 3750 million years ago and proceeding till 3500 million years ago when the archean bacterias similar to modern of methane-oxidizen bacteria, selen bacteria and to other bacteria of hydrothermal waters prevailed. Therefore we assume that evolution of biological kinds on Earth was defined by the prevailing chemical composition of actively allocated hydrothermal waters and volcanic gases. In the second stage the life developments on Earth, proceeding from 3500 to 3300 million years appeared eu bakteria that is in our opinion connected with significant increase in concentration of salts of carbonates in hydrothermal waters. Then 3300 million. years ago, in the Archean stage, they were replaced by photosynthesis of bacteria cyanogen.

References:

- [1] Hubble E.P. A general study of diffuse galactic nebulae // *The Astrophysical Journal*. 1922. V. 56. No. 3. P. 21-49.
- [2] Carey S.W. *Theories of the Earth and Universe // A History and Dogma in the Earth Sciences*. Stanford. California. 1988. P.1-12.
- [3] Narlicar J. *Complex Universe // Moscow*. Mir. 1985. P. 192-197.
- [4] Aynasto Y.V. *The evolution of galaxies // The problems of experimental and theoretical astronomy. Ser. The Measurements and Investigations of Universe*. Moscow-Leningrad. USSR. 1977. No. 6. P. 26-41.
- [5] Halton S.A. *The evolution of galaxies // About physical thingth*. Moscow. Nauka, 1967. No. 6, P. 92-110.
- [6] Maronchik L.S., Suchkov A.A. *Galaxy*. Moscow. Nauka, 1984. 392 p.
- [7] Milanovsky E.E. *About the correlation of frequency phase of geomagnetic field reversions, low World Ocean and phase of Earth's crust deformations in mesozoic and cenozoic // Geotectonica*. 1996. No. 1. P. 3-11.
- [8] Barenbaum A.A. *Circles of geological processes from new data about Galactic construction // Geodynamic basis of the predicting of oil and gas in the interior of the Earth. Proceeding of First USSR Conference*. Ch. 1. Moscow. MING. 1988. P. 262-264.
- [9] Sergeev V.N., Holl A.H., Zavarzin G.A. *The three milliards years ago: from procariot to ecariot*, *Nature*. 1996. No. 6. P. 54-67.
- [10] Glebovsky V.A., Shemiakin V.M. *Extraction and correlation of Precambrian // Regional geology and metal genesis*, 1996. No.5. P. 25-76.
- [11] Ozima M. *The history of the Earth*. Moscow. Znanie, 1983. 205 p.
- [12] Ushakov S.A., Yasmanov N.A. *The Continental drift and Earth's climate*. Moscow. Misl, 1984. 206 p.
- [13] Condie K.C. *Plate Tectonic and Crustal Evolution // Pergamon Press*. New York, 1975. 288 p.

3D MODELING OF TRANSIT OBSERVATIONS OF THE HOT EXOPLANETS

M.S. Rumenskikh, A.G. Berezutsky, I.B. Miroshnichenko, I.F. Shaikhislamov
Institute of Laser Physics SB RAS, Novosibirsk, Russia

The investigation of the atmospheres of close-orbit exoplanets and their interaction with incoming stellar wind becomes more important due to the planned launches of new space telescopes. In this paper, we study Gliese-436b, which belongs to the class of the planets named Warm Neptunes. Such planets have a mass and radius comparable to those of Neptune, but are located at a distances of <0.05 AU from parent star. The atmosphere of the planet is ionized due to proximity to the parent star and the interaction of planetary and stellar winds can be considered as the interaction of plasma flows.

The atmosphere of Gliese-436b consists mostly of hydrogen, and the Ly- α spectral line is actively absorbed in this medium. Thus, first transit measurements were carried out primarily for this line [1, 2]. The data show that absorption takes place at high speeds of ~ 100 km/s, which can be explained by the presence of atoms rapidly moving away from the star. From the transit curve and the absorption profile of the line, it is possible to predict the velocity of the outflow of the planetary atmosphere and how it interacts with the stellar plasma wind.

A 3D gas-dynamic model which takes into account the processes of recombination and plasma-photochemistry of plasma components was used in this work [3]. We have studied the processes occurring in the atmosphere of Gliese-436b, varying the parameters of its parent star. Comparing the modeled transits with the experimental ones presented in [1, 2], it is possible to predict the values of stellar wind parameters such as temperature, density and intensity of ultraviolet radiation.

The work was supported by the RNF project №18-12-00080.

- [1] Ehrenreich D., Bourrier V. // *Nature*, 2015, V. 522, P. 459-461
- [2] Lavie B., Ehrenreich D., Bourrier V. // *A&A*, 2017, V. 605
- [3] Shaikhislamov I. F. et al. // *MNRAS*, 2018, 481(4), 5315-5323.

WHY EARTH-LIKE N₂ ATMOSPHERES ARE MOST LIKELY NOT COMMON ON TERRESTRIAL PLANETS

L. Sproß^{1,2}, H. Lammer², M. Scherf²

¹ *Institute of Physics, University of Graz, Austria, laurenz.spross@edu.uni-graz.at*

² *Space Research Institute, Austrian Academy of Sciences, Graz, Austria*

Keywords:

Nitrogen, nitrogen cycle, atmospheric evolution, secondary atmospheres, outgassing, nitrogen fixation, atmospheric escape, plate tectonics

Introduction:

The present Earth's atmosphere is N₂-dominated. This feature provides diverse conditions for life in physical and chemical senses and shapes the habitat we live in. It is undisputed that nitrogen dominated the Earth's atmosphere throughout the Proterozoic, but it is not clear how it behaved in the time before and during the Great Oxidation Event transition (GOE). Understanding the early form of the geobiological cycle can not only give indications on the composition of the early Earth's atmosphere, it also helps us to comprehend the requirements for the evolution of N₂-dominated atmospheres on other rocky planets.

Scientific background:

The origin of a secondary atmosphere.

On Earth, the first time in which atmospheric nitrogen was possibly present in greater extend was the period of magma oceans in the early Hadean. Besides H₂, CO₂, and H₂O, also nitrogen might have been outgassed during the magma crystallization phase, but if outgassing or direct dissolution into the magmatic surface were dominating is still an open question [1–4]. The question which kind of molecules are outgassed in the Hadean is strongly linked to the redox state of the mantle, determining the initial conditions of the secondary atmosphere [5, 6]. A comparison between Venus and Earth, both having a comparable amount of atmospheric N₂ at present day, could motivate the assumption of early outgassed (and no more ingassed) nitrogen. On the other hand, CO₂ seems to have weathered into the surface, a process that is connected to the renewing of surface crust, to the oxidation of the planet and in consequence to an active tectonic regime. Furthermore, be it in the magma ocean phase or in the further course of Earth history, nitrogen outgassing is triggered by oxidation of ammonium in upper mantle minerals [7]. In the humid atmosphere after the crystallization phase, abiotic N₂ fixation (= depletion) processes such as impactor fixation and lightning are likely to have lowered the atmospheric N₂ partial pressure.

The interplay of CO₂ and N₂.

Under the young Sun's EUV irradiation, which was one to two orders higher than that of today [8], unprotected atmospheric N₂ suffers massive escape. The infrared-active CO₂ is capable of counteracting thermal escape through cooling the upper atmosphere and reducing the extend of the thermosphere [9]. A lack of a footprint of such an atmospheric escape in ¹⁴N/¹⁵N isotope ratios shows that sufficient CO₂ must have been present in the early Archean to protect atmospheric N₂. If only a low CO₂ partial pressure was present back then, a present-level N₂ partial pressure in the Archean is impossible. These considerations are also valid for exoplanets, especially for K- and M-type stars, since they are very active in EUV also in the long-term. At exoplanets orbiting such a star, CO₂ levels must be relatively high to allow an N₂-dominated atmosphere over long periods of time. On the other side CO₂ heats a planet's surface and therefore can hinder the condensation of water and the formation of oceans. This shows the complex interplay between CO₂ and N₂ as atmospheric constituents.

The geobiological nitrogen cycle in the Archean.

The nitrogen cycle is a complex interplay between the Earth's mantle, crust, and atmosphere, including its hydro- and biosphere. On Earth, its turnover is clearly dominated by biological processes [4, 10]. The biosphere is a crucial factor for maintaining the present Earth's atmospheric N_2 , since it recycles fixed nitrogen back into the atmosphere through denitrification and anaerobic ammonium oxidation. But for a young planet (with a biosphere), when the atmosphere was still reducing, such a strong return flux was not possible, while abiotic processes such as lightning and biological nitrogen fixation were active. Models of the thermal mantle evolution show that volcanic outgassing could not have balanced these sinks [11, 12]. This raises the question if early Earth's atmospheric N_2 partial pressure was as stable as it was during the Proterozoic. All in all, the early evolution of nitrogen still lies in the dark although it is an apparent feature of planet Earth. In combination with these strong outgassing fluxes, a low initial atmospheric nitrogen content as discussed in the previous paragraphs would indicate rather low atmospheric N_2 amounts on early Earth. To get a deep understanding of the processes and reservoir sizes in the first 2 Gyr of the Earth's life can also lead to information about the atmospheric development of terrestrial exoplanets.

O_2 and N_2 as indicators for life.

An N_2 - O_2 -dominated atmosphere as it has been present on Earth since the GOE is chemically not stable, which is once again only possible to maintain with the influence of life. This leads to the hypothesis of N_2 and O_2 as geo-bio-signature, since one needs active tectonics for reducing CO_2 and life for maintaining N_2 and O_2 over longer periods of time [4, 13].

Conclusion:

Our goal is to answer the open questions in the context of the Archean geobiological nitrogen cycle and the evolution of atmospheric N_2 through deep time. We develop a model for nitrogen outgassing and recycling and fixation, combined with estimates for atmospheric escape. The results we show constrain the Earth's early atmosphere evolution and show limits for the development of Earth-like habitats in other stellar systems.

References:

- [1] Wordsworth, R. D. Atmospheric nitrogen evolution on Earth and Venus // *Earth and Planetary Science Letters*. 2016, Vol. 447, P. 103–111.
- [2] Libourel, G., Marty, B., Humbert, F. Nitrogen solubility in basaltic melt. Part I. Effect of oxygen fugacity // *Geochimica et Cosmochimica Acta*. 2003, Vol. 67, No. 21, P. 4123–4135.
- [3] Kadik, A.A., Kurovskaya, N.A., Ignat'ev, Y.A., Kononkova, N.N., Koltashev, V.V., Plotnichenko, V.G. Influence of oxygen fugacity on the solubility of nitrogen, carbon, and hydrogen in FeO - Na_2O - SiO_2 - Al_2O_3 melts in equilibrium with metallic iron at 1.5 GPa and 1400°C // *Geochemistry International*. 2011. Vol. 49, No. 5, P. 429–438.
- [4] Lammer, H., Sproß, L., Grenfell, J.L., Scherf, M., Fossati, L., Lendl, M., et al. The Role of N_2 as a Geo-Biosignature for the Detection and Characterization of Earth-like Habitats // *Astrobiology*, in print. 2019. arXiv:1904.11716
- [5] Hirschmann, M.M. Magma ocean influence on early atmosphere mass and composition // *Earth and Planetary Science Letters*. 2012. Vol. 341–344, P. 48–57.
- [6] Gaillard, F., Scailliet, B., Pichavant, M., Iacono-Marziano, G. The redox geodynamics linking basalts and their mantle sources through space and time // *Chemical Geology*. 2015. Vol. 418, P. 217–233.
- [7] Mikhail, S., Sverjensky, D.A. Nitrogen speciation in upper mantle fluids and the origin of Earth's nitrogen-rich atmosphere // *Nature Geoscience*. 2014. Vol. 7, No. 11, P. 816–819.
- [8] Tian, F., Kasting, J.F., Liu, H.L., Roble, R.G. Hydrodynamic planetary thermosphere model: 1. Response of the Earth's thermosphere to extreme solar EUV conditions and the significance of adiabatic cooling // *Journal of Geophysical Research E: Planets*. 2008. Vol. 113, No. 5.
- [9] Lichtenegger, H.I.M., Lammer, H., Grießmeier, J.-M., Kulikov, Y.N., von Paris, P., Hausleitner, W., et al. Aeronomical evidence for higher CO_2 levels during Earth's Hadean epoch // *Icarus*. 2010. Vol. 210, No. 1, P. 1–7.
- [10] Galloway, J.N. *The Global Nitrogen Cycle*, in *Treatise on Geochemistry*, 2003. Vol. 8, Elsevier. P. 557–583.

- [11] Padhi, C.M., Korenaga, J., Ozima, M. Thermal evolution of Earth with xenon degassing: A self-consistent approach, *Earth and Planetary Science Letters*, 2012. Vol. 341–344, P. 1–9.
- [12] Korenaga, J. Thermal evolution with a hydrating mantle and the initiation of plate tectonics in the early Earth // *Journal of Geophysical Research*. 2011. Vol. 116, No. B12, 403.
- [13] Stüeken, E.E., Kipp, M.A., Koehler, M.C., Schwieterman, E.W., Johnson, B.W., Buick, R. Modeling pN_2 through Geological Time: Implications for Planetary Climates and Atmospheric Biosignatures // *Astrobiology*. 2016, Vol. 16, No. 12, P. 949–963.

HOW FUNGAL COMMUNITIES OF DESERT SOILS RESPOND TO IRRADIATION BY HIGH-ENERGY ELECTRONS (HEE)?

M.O. Kryuchkova ¹, E.A. Vorobyova ¹, A.E. Ivanov ^{1,2}, V.S. Cheptsov ^{1,3}, A.K. Pavlov ⁴

¹ Department of Soil Biology, Lomonosov Moscow State University, Moscow 119991, Russia (margo_kruchkova@mail.ru);

² A.N. Severtsov Institute of Ecology and Evolution, Russian Academy of Sciences, Moscow, 119071, Russia;

³ Space Research Institute, Russian Academy of Sciences, Moscow, 117997, Russia;

⁴ Ioffe Physical-Technical Institute, Russian Academy of Sciences, St. Petersburg, 194021, Russia

Keywords:

Micromycetes; resistance; extreme habitats; astrobiology; Mars.

Introduction:

Often, microbial communities of terrestrial habitats with extreme environmental conditions become model objects of astrobiology. Irradiation with high-energy electrons (HEE) is one of the factors limiting the preservation of the viability by microorganisms in the regolith of Mars. Thus, the purpose of this research was to study the effect of irradiation with HEE under low temperature and low pressure conditions on the micromycetes communities of arid soil.

Materials and Methods:

Soil samples of the upper horizon of gray soil (Negev desert, Israel) were the object of the study. The samples were irradiated in a special climatic chamber, which allows to maintain a pressure of $8-9 \times 10^{-3}$ Torr and a temperature of -130°C throughout the experiment. The samples were irradiated with the following doses: 0.05, 1, 2, 3, 4, and 5 MGy. One sample was exposed only to low temperature and low pressure, without irradiation, the other one was irradiated at room temperature and a pressure of 1 atm. with a dose of 0.05 MGy (RT, 1 atm.). To determine the colony forming units (CFU) number and the structure of the fungal communities, the method of soil dilutions and plating on solid nutrient media was used: the fungal Czapek agar and alkaline agar were used. Culturing was performed at 5, 25 and 37°C . Fungal biomass was determined by direct luminescence microscopy using a calcofluor white dye.

Results and Conclusions:

The number of fungal propagules in the control samples was $1-5 \times 10^4$ CFU/g of soil. The impact of low temperature and pressure did not have a significant impact on the number of CFUs. Irradiation with doses of 0.05 MGy and 1 MGy led to an increase in CFU by a factor of 5 – up to $11-20 \times 10^4$ CFU/g, whereas after irradiation with doses of 3, 4, and 5 MGy, a significant decrease in CFU down to 1×10^4 CFU/g was observed. The lowest CFU number was recorded after irradiation with 0.05 MGy (RT, 1 atm.) - 3×10^3 CFU/g of soil.

The greatest species diversity was observed in control samples - 25-35 species. The number of species in the most of irradiated samples was 13–15. Relatively high species diversity (20 species) among the irradiated samples was revealed after irradiation with a dose of 2 MGy. The lowest species diversity was recorded after irradiation with 0.05 MGy (RT, 1 atm.) - 5 species.

After irradiation with HEE, changes were also observed in the structure of the fungal communities: biodiversity was significantly lower in the irradiated samples compared to the control ones. After irradiation with doses of 1 and 2 MGy, the number of yeasts significantly increased. After exposure to doses of 3, 4, 5 MGy, and 0.05 MGy (RT, 1 atm), species were isolated only when cultivated at 25°C . In samples irradiated with high doses of HEE, species of the genera *Aspergillus* and *Penicillium* dominated, and in the sample that received the dose of 0.05 MGy (RT, 1 atm) the species of the genus *Trichoderma* dominated.

The biomass of fungal spores tended to decrease with increasing radiation dose.

As a result, it was shown that the fungal communities of desert soils retain viability after irradiation with high doses of HEE under low temperature and low pressure conditions. Doses of 0.05, 1, and 2 MGy had a stimulating effect on the fungal communities of desert soils, which resulted in an increasing in the number of fungal propagules. Higher doses (3, 4, and 5 MGy) had a suppressive effect: a significant decreasing in CFU numbers, spore biomass, and the absence of spore germination from the soil was observed when cultivated at 5 and 37° C. The greatest sterilizing effect was found after irradiation with a dose of 0.05 MGy (RT, 1 atm) - the lowest CFU count and the lowest biodiversity were revealed.

CZECH PARTICIPATION ON THE ARIEL TELESCOPE MISSION - REMOTE SENSING OF ASTEROID AND COMETARY IMPACT EVENTS

Růžena Ferusová Živorová,¹Martin Ferus

J. Heyrovsky Institute of Physical Chemistry, Czech Academy of Sciences, Dolejškova 3, CZ18223 Prague 8. Czech Republic, martin.ferus@jh-inst.cas.cz

Keywords:

exoplanets, Ariel, origin of life, impacts

Introduction:

ARIEL[1] (acronym “atmospheric Remote-sensing Infrared Exoplanet Large-survey,”) is the European Space Agency’s fourth medium-class mission. The goal of the Cassegrain three-axis telescope equipped with high tech spectrometer is to record the spectra of over 1000 known exoplanets from Jupiter and Neptune to super-Earth size in the 1.95-7.8 μm range. The telescope will examine their atmospheres, elemental and molecular composition and spectral analysis will focus on finding of interesting molecules and condensates. The Ariane 6-2 rocket will place the satellite in 2028 at the L2 Lagrange center, where it will provide the observations until 2032. Ariel will perhaps answer a wide range of fundamental questions of contemporary science concerning astrochemistry and physics of exoplanets, including the evolution of chemical environment on young worlds during period preceding origin of the first living structures. It will also evaluate the relevance between the distance of particular planet from the parent star of a given size and planetary type and its chemistry and composition, exoplanet climate, composition of their clouds, the atmospheric temperature and chemical profiles, their dynamics and their variability in time. The Czech Republic joined the Ariel project last year. In addition to manufacturing of mirrors for the optical system, the aim of Czech scientists is to create a catalogue of spectra of ARIEL target molecules, radicals and ions detected in exoplanet atmospheres, evaluation of critical parameters of the optical system with respect to the spectra of these molecules and finding of selected processes markers in planetary atmospheres with an emphasis on phenomena associated with high energy density events[2], [3].

References:

- [1] Tinetti G. et al.A chemical survey of exoplanets with ARIEL, 2018. V. 46 No. 1. P. 35–209.
- [2] Ferus M. et al.Formation of nucleobases in a Miller–Urey reducing atmosphere // PNAS. 2017. V. 114 No. 17. P. 4306-4311.
- [3] Ferus M. et al.High-energy chemistry of formamide: A unified mechanism of nucleobase formation// PNAS. 2015. V. 112 No. 3. P. 657-662.

BACTERIA SURVIVAL IN EUROPA'S SURFACE ICE AFTER PULSE EJECTION OF SUBSURFACE OCEAN WATER

V. Cheptsov^{1,2}, A. Pavlov³, D. Tsurkov³, A. Belov¹, E. Vorobyova¹, D. Frolov^{3,4}, G. Vasiliev³, V. Lomasov⁴

¹ Department of Soil Biology, Lomonosov Moscow State University, Moscow 119991, Russia (cheptcov.vladimir@gmail.com);

² Space Research Institute, Russian Academy of Sciences, Moscow 117997, Russia;

³ Ioffe Physical-Technical Institute, Russian Academy of Sciences, St. Petersburg 194021, Russia;

⁴ Peter the Great St. Petersburg State Polytechnic University, St. Petersburg 194021, Russia;

Keywords:

astrobiology; Europa; ionizing radiation; microorganisms; radioresistance; accelerated electrons.

Introduction:

Jupiter's satellite, Europa, is believed to have a subsurface ocean that might be a potential environment for the existence of extraterrestrial life. Observational data from the Hubble Space Telescope (HST) provide possible evidence for water plumes being ejected from the ocean to space and permanently renewing the icy surface of Europa. In this case, hypothetical microorganisms could be ejected from the ocean and frozen in the surface ice layer during the water eruption event. These potential life forms might remain in a dormant state for an undetermined extended period of time at a very low temperature in the surface ice layer. The viability of microorganisms after millions of years of cryoconservation should be limited by impact of ionizing radiation. The determination of the survival time and depth limits was the main aim of this study. We calculated irradiation rates depending on ice thickness, and performed irradiation (with accelerated electrons) of *Deinococcus radiodurans*, *Arthrobacter polychromogenes*, and *Methylobacterium* sp. bacteria embedded into a model of Europa's ice under simulated temperature and pressure conditions of Europa.

Materials and Methods:

A special vacuum chamber was developed for modelling the extreme irradiation of icy samples with bacteria under low temperature and low atmospheric pressure (−130 °C, 0.01 mbar) [1].

Strains *Deinococcus radiodurans* VKM B-1422T, *Arthrobacter polychromogenes* SN_T61, and *Methylobacterium* sp. KBP.AS.506 [2] were the objects of study. A solution of salts modeling the composition of Europa's ice was used for suspension of bacterial cells. There are no direct measurements of Europa's ice composition, but several studies assume Mg²⁺, Na⁺, and SO₄²⁻ to be the dominant ions within it. We follow the composition described by the authors of [3] to prepare the model ice samples (artificial Europa ice with bacteria). A solution of magnesium sulfate, sodium sulfate, and sulfuric acid at a ratio of 50:40:10 of molar percent with 35 g/L total concentration was used.

Ice samples irradiation was produced by the electron accelerator with electron energy in the range of 0.4–1.0 MeV. Four runs of irradiation were executed with doses of 5, 10, 50, and 100 kGy. Irradiation rates were 0.28 kGy/s for 5 and 10 kGy runs and 2.8 kGy/s for 50 and 100 kGy runs. The determination of the number of culturable bacteria in the samples was performed by plating on glucose–peptone–yeast agar (GPY) [2].

A GEANT4 toolkit was used first to calculate the energy absorbed in a unit water ice layer per incident particle with a certain total energy. The depth of the unit layer was considered to be 0.1 mm and its incident surface as 1 cm² with the total depth of the ice column being from 0.05 to 5000 mm. These absorbed energy/depth E_{abs} (E, d) profiles were calculated for electrons, pro-

tons, oxygen, and sulfur ions as incident particles. To imply these calculations to Europa's radiation environment, we used differential particle spectra $J(E)$ [counts per $\text{cm}^2 \text{ s sr MeV}$] from Table 1 in the work of [10]. To obtain total accumulated dose at each depth d , one has to numerically integrate $J(E) \times E_{\text{abs}}(E, d) dE$ for every sort of incident particle, which results in a dose rate profile. Thus, we obtain a one-year dose profile. A simple model of Europa resurfacing was introduced for the following calculations: A layer of "fresh ice" with varying thickness is added atop the ice profile and the calculation is then continued for further 1 million years. Ip et al. [4] proposed the static resurfacing rate of 12 m per 100 Myr, which was also taken into consideration. These computations were done with MATLAB software.

Results and Discussion:

After irradiation with doses of 5, 10, and 50 kGy, the number of cultivated cells of *Deinococcus radiodurans* VKM B-1422T decreased on 2, 3, and 6 orders of magnitude, respectively (Figure 1). *Arthrobacter polychromogenes* SN_T61 shown comparable survival rates - the number of viable cells decreased on 2, 5 and 6 orders of magnitude at 5, 10, and 50 kGy, respectively. *Methylobacterium* sp. KBP.AS.506 shown lower radioresistance and survived irradiation with 5 and 10 kGy doses only. Cultivated cells of all bacteria studied were not found in samples that were irradiated with the 100 kGy doses.

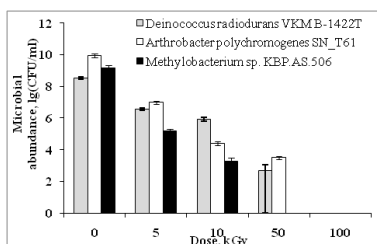


Fig. 1. Impact of high energy electrons irradiation on the number of *Deinococcus radiodurans* VKM B-1422T, *Arthrobacter polychromogenes* SN_T61, and *Methylobacterium* sp. KBP.AS.506 viable cells. Error bars are in accordance with the confidence interval for $p < 0.05$.

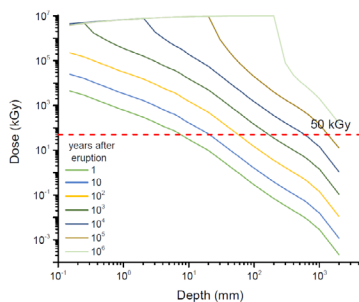


Fig. 2. Total dose accumulation rate in dependence on exposure time and "fresh ice" depth. Red dashed line demonstrates the upper limit of the bacteria survival in our experiment.

The total of all dose accumulation rates of considered incident particles is presented in Figure 2. The resulting dose rates for different particles are presented in [1]. High-energy protons and heavy ions profiles dramatically decrease with depth, thus their impact on the microorganisms' survival in the ice layer is significant only for depths less than 1 cm, even taking into account their higher biological efficiency compared with electrons. Despite the high total dose accumulation rate, the lethal dose does not accumulate in the ice layer at depths of 0.1–1 m until 1000–10,000 years after eruption. For lengths of time greater than 10,000 years, the dose is lethal in the region of interest. For exposure times from 1000 years onwards, we see a nearly constant (in comparison with the one-year profile) part emerging in the dose

profile. This is the effect of considering a static resurfacing rate from the work of [4] in our model. This effect might not be real case, but it has no significant impact on the main goals and conclusions of this work. At 0.01–0.1 m depths, the lethal dose is accumulated in 100 years, and for depths lower than 0.01 m, no viable cells would be present after only one year of radiation exposure.

Conclusion:

Our study demonstrates the ability of terrestrial microorganisms to survive high intensity radiation in conditions modelling shallow subsurface environments of Europa for a long time. Considering radiation dose accumulation as the limiting factor for microbial life survivability, we hypothesize that there is a chance to discover viable cells at an ice depth of 10–100 cm if the massive water release from the ocean of Europa occurred on a landing site 1000–10,000 years before.

References:

- [1] Pavlov A., Cheptsov V., Tsurkov D., Lomasov V., Frolov D., Vasiliev G. Survival of radioresistant bacteria on Europa's surface after pulse ejection of subsurface ocean water // *Geosciences*. 2019. V. 9. № 1. P. 9.
- [2] Cheptsov V., Vorobyova E., Belov A., Pavlov A., Tsurkov D., Lomasov V., Bulat S. Survivability of soil and permafrost microbial communities after irradiation with accelerated electrons under simulated Martian and open space conditions // *Geosciences*. 2018. V. 8. № 8. P. 298.
- [3] Orlando T.M., McCord T.B., Grievies G.A. The chemical nature of Europa surface material and the relation to a subsurface ocean // *Icarus*. 2005. V. 177. P. 528–533.
- [4] Ip W.H., Williams D.J., McEntire R.W., Mauk B.H. Ion sputtering and surface erosion at Europa // *Geophysical Research Letters*. 1998. V. 25. P. 829–832.

EDAPHIC BACTERIAL COMMUNITIES OF THE ARID MOJAVE DESERT: ASTROBIOLOGICAL IMPLICATION

A.A. Belov¹, V.S. Cheptsov^{1,2}, E.A. Vorobyova¹, N.A. Manucharova¹,
Z.S. Ezhelev¹

¹ Lomonosov Moscow State University, Soil science faculty, 119991, Russian Federation, Moscow, 1 Leninskie Gory Street, and.ant.be@gmail.com ;

² Space Research Institute, 117997, Russian Federation, Moscow, 84/32 Profsoyuznaya Street

Keywords:

Physiology of bacteria; extremotolerance; antibiotic resistance; soil; culturable bacterial communities; Mars analogue site

Introduction:

The arid Mojave Desert is one of the most significant terrestrial analogue objects for astrobiological research due to its genesis, mineralogy, and climate. However, the knowledge of culturable bacterial communities found in this extreme ecotope's soil is yet insufficient. The Mojave Desert is located in the southwest of the United States and covers an area of approximately 150 000 km², temperatures range from -10 to 50°C. Ten thousand years ago this territory was characterized by a humid climate and well-formed soil coverage, but the aridization of weather conditions and desertification of the region have led this area to its present state [1].

The total number of prokaryotic cells in the soil sample was detected $(5.8 \pm 1.7) \times 10^8$ cells per gram of soil. Cultured bacteria on PYG medium were detected at level $(8.0 \pm 0.5) \times 10^6$ colony-forming units (CFU) per gram and $(5.5 \pm 0.2) \times 10^6$ CFU/g at 25°C and 10°C, respectively. No CFU were detected after incubation at 50°C. Pigmented forms of microorganisms dominated in all the cultured communities isolated from the sample. Maximum diversity of colony morphotypes was observed at the mesophilic incubation temperature. Representatives of bacterial genera *Agrococcus*, *Arthrobacter*, *Bacillus*, *Brachybacterium*, *Brevibacterium*, *Cellulomonas*, *Georgenia*, *Janthinobacterium*, *Kocuria*, *Labedella*, *Leucobacter*, *Massilia*, *Microbacterium*, *Micrococcus*, *Mycetocola*, *Paracoccus*, *Planomicrobium*, *Pseudarthrobacter*, *Rufibacter*, *Salinibacterium*, and *Streptomyces*.

The analysis of the resistance to different stress-factors were performed for all of isolates. Temperature resistance spectra reveals the thermotolerant properties of communities cultured at 25°C. The wide pH ranges in which the metabolic activity is maintained were observed. It could be explained by contrast temperature conditions and precipitation regimes leading to a change in the solubility of the substances in the soil solution [2].

The studied region is characterized by a low content of water-soluble salts, however the moderate general resistance of isolated communities to the presence of sodium chloride or potassium chloride were observed. High resistance to magnesium perchlorate found is particularly important in the astrobiology-oriented review of the obtained results. Maintenance of metabolic activity in vitro in the presence of perchlorates, at concentrations significantly exceeding those found in the regolith of Mars [3], testifies their non-limiting role in the regolith.

Stress effects, such as low water availability, nutrients deficiencies, high levels of solar radiation, and wide temperature fluctuations in the surface soil of the Mojave Desert lead to the formation of physiological survival strategies for prokaryotes existing under these conditions [4, 5]. Our study revealed a high diversity (both taxonomic and morphophysiological) of culturable bacteria in the investigated soil. Species typical for various soils, including arid soils, and species that have not been previously isolated from hot arid soils were found in isolated bacterial communities. This suggests that the mechanisms of adaptation to cryo-arid and xero-arid conditions include similar

physiological processes and adaptations. The obtained spectra of metabolic activity in the gradients of physicochemical factors indicate predominantly mesophilic and neutrophilic optima of all the studied strains, mostly capable of maintaining metabolic activity in a wide range of conditions, up to extreme ones for individual strains. Extreme resistance levels were identified in bacteria of *Arthrobacter*, *Microbacterium*, *Bacillus*, *Planomicrobium*, *Kocuria*, *Leuobacter*, and *Pontibacter* genera.

The obtained results, considered together with the data of previous works [6–8], testify in favor of viability, functionality, and taxonomical diversity of soil bacterial communities in the central part of the Mojave Desert studied, which is considered as a terrestrial analogue of Martian regolith. The isolated strains require further characterization and description for potential biotechnological applications. Due to the low similarity of the nucleotide sequences of some individual strains to those found in the database, these isolates could be the representatives of undescribed species of culturable bacteria. The most resistant strains that have been found could be used as model objects in further astrobiological studies.

The Mojave Desert has undergone processes similar to those that took place on Mars and formed its current state. The properties of culturable bacterial communities revealed in this study indicate that they have adapted to survive in aggressive changing environmental conditions. Consequently, such communities could be considered as a model for further research of the Martian regolith habitability and the ability of terrestrial bacteria to adapt to extra-terrestrial conditions.

Acknowledgments:

This research was funded by Russian Foundation for Basic Research according to the research project № 18-34-00331, and partially by PRAS № 17 (Evolution of organic world. Role and influence of planetary processes), subprogram № 1.

References:

- [1] Abbey W., Salas E., Bhartia R., Beegle L.W. The Mojave vadose zone: A subsurface biosphere analogue for Mars. // *Astrobiology*. 2013. V. 13. P. 637–646
- [2] Makhalyane T.P., Valverde A., Gunnigle E., Frossard A., Ramond J.B., Cowan D.A. Microbial ecology of hot desert edaphic systems. // *FEMS Microbiology Review*. 2015. V. 39. P. 203–221
- [3] Clark B. C., van Hart D.C. The salts of Mars. // *Icarus*. 1981. V. 45. P. 370–378
- [4] Cockell C.S., Schwendner P., Perras A., Rettberg P., Beblo-Vranesevic K., Bohmeier M., Rabbow E., Moissl-Eichinger C. Wink L., Marteinson V., et al. Anaerobic microorganisms in astrobiological analogue environments: From field site to culture collection. // *International Journal of Astrobiology*. 2017. P. 1–15
- [5] Cloutis E.A., Craig M.A., Kruzelecky R.V., Jamroz W.R., Scott A., Hawthorne F.C., Mertzman S.A. Spectral reflectance properties of minerals exposed to simulated Mars surface conditions // *Icarus*. 2008. V. 195. P. 140–168
- [6] Preston L.J., Dartnell L.R. Planetary habitability: Lessons learned from terrestrial analogues. // *International Journal of Astrobiology*. 2014. V. 13. P. 81–98
- [7] Loughney K.M., Badgley C. Facies, Environments, and Fossil Preservation in the Barstow Formation, Mojave Desert, California. // *Palaios*. 2017. V. 32. P. 396–412
- [8] Rainey F.A., Ray K., Ferreira M., Gatz B.Z., Nobre M.F., Bagaley D., Small A.M. Extensive diversity of ionizing-radiation-resistant bacteria recovered from Sonoran Desert soil and description of nine new species of the genus *Deinococcus* obtained from a single soil sample. *Applied and Environmental Microbiology*. 2005. V. 71. P. 5225–5235.

PARAFAC ALGORITHM FOR RESOLVING FLUORESCENCESIGNATURESOF LIFE-SPECIFIC COMPOUNDS

F.A.I. Azar, I. Digel

FH AachenUniversity ofApplied Sciences, Heinrich-Mußmann-Straße 1, 52428 Jülich, digel@fh-aachen.de

Keywords:

fluorescence spectroscopy, autonomous navigation, emission-excitation matrix, PARAFAC

Introduction:

The project “Technologies for Rapid Ice Penetration and Subglacial Lake Exploration” (TRIPLE) has the goal of developing a deployable autonomous robotic system for the contamination-free scientific investigation of sub-glacial lakes. In order to perform the exploration mission, the AUV must be able to perform its own localization and navigate in an unknown environment. Specifically, in order to find a suitable area to sample for further testing, it must be able to distinguish and classify a target substance from mixture and determine its concentration gradient, along which it will travel.

The first payload prototype consisting of miniaturized (65mm x 65mm x 120mm) fluorescence spectrometer is already available. The device allows excitation of the sampleflowing through the cuvette by four LEDs. A photometric sensor (CMOS) then detects the emitted light of the sample and represents the intensity of the emitted wavelengths.

Although individual excitation-emission matrices (EEMs) obtained by fluorescence spectroscopy are mostly unique to the dissolved organic material at a given concentration, correct signal interpretation for the mixtures represents a challenge. A multi-way signal decomposition method known as PARAFAC (Tensor Rank Decomposition) can be used to extrapolate signals generated by individual components. Using unsupervised / supervised neural networks, we were able to recognize and to measure dissolvedorganic compounds such as NADH, FAD and ATP from their mixture(Figure).However, this technique still needs to be applied to the data obtained from miniaturized fluorescence spectrometer.

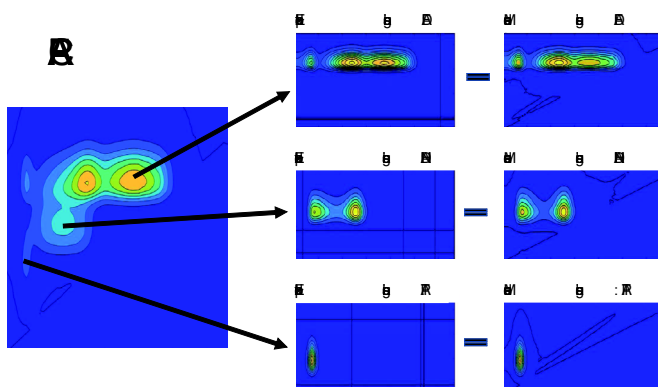


Fig. 1.